



IMAGING HERITAGE AND OTHER METAL SURFACES WITH X-RAY EXCITED OPTICAL MICROSCOPY

Word count: 96,902

Pieter-Jan M.G. Sabbe

Student number: 002005497430

Supervisors: Prof. Dr. Mieke Adriaens, Em. Prof. Dr. Mark Dowsett

A dissertation submitted to Ghent University in partial fulfilment of the requirements for the degree of
Doctor of Science: Chemistry

Academic year: 2017 - 2018

Artwork displayed on chapter pages:

Chapter 1

The Statue of Liberty at the entrance of the New York Harbour is listed on UNESCO's world heritage list and is most likely world's most famous piece of corroded metallic cultural heritage. Lady liberty is composed of thin copper sheets (over a steel framework) which received a *Verdigris* patina from mother nature . Verdigris contains, near the sea, a large amount of basic copper chlorides. Referred in this work as atacamite and paratacamite, these basic copper chlorides are abundantly discussed. The tablet of Lady Liberty is left unmodified to draw the attention on the colour of the verdigris.

Image downloaded from unsplash.com and is free of copyrights.

Chapter 2

The experimental hall and storage ring of the ESRF.

©P.Ginter /ESRF

Chapter 3

Detail of Andor CCD camera of XEOM 1.

©PJ.Sabbe

Chapter 4

Microscopic image of copper coupon in combination with a microscopic grid used in TEM. Providing either the coupon or the mesh with a patina allowed us to create well-defined microscopic regions of different copper corrosion products. The sample was used for evaluating the imaging features of XEOM1.

©PJ.Sabbe

Chapter 5

Detail of the sample stage of XEOM 1 with the evaluation sample in the imaging position.

©PJ.Sabbe

Chapter 6

Painting of 'The Mary Rose' by marine artist © Geoff Hunt, PPRSMA.

Reproduced with permission from the Mary Rose trust.

Chapter 7:

A Novel UV-C illumination module designed by the author of this work. The illumination module allows to perform some XEOM 1 experiments in the absence of synchrotron radiation.

©P.J.Sabbe

Chapter 8

The 'Pont d'Oxford' is just located next to the ESRF in Grenoble and bridges the Isère in order to connect the 'Polygone scientifique' with the French highway A48. Crossing this bridge, after an intense week of experiments, was typically a moment for me to reflect back on the experiments done and to answer the question "What's next?".

Image downloaded from: <http://mapio.net/pic/p-21854270/>

Chapter S

Example of a frameless copper-gold intrauterine device.

©D.Wildemeersch

NEDERLANDSTALIGE SAMENVATTING

LIST OF ABBREVIATIONS

CHAPTER 1: INTRODUCTION	1
1.1 CULTURAL HERITAGE, TANGIBLE AND INTANGIBLE REFERENCES TO THE PAST	2
1.1.1 CONSERVATION AND PRESERVATION OF METALLIC OBJECTS	2
1.2 SYNCHROTRON RADIATION TECHNIQUES IN A CULTURAL HERITAGE CONTEXT	4
1.3 X-RAY-EXCITED OPTICAL LUMINESCENCE (XEOL) AS A DETECTION SCHEME FOR X-RAY ABSORPTION SPECTROSCOPY (XAS)	6
1.3.1 XEOL	7
1.3.2 EXTENDED XEOL APPLICATIONS: TR-XEOL & 2D XEOL-XANES	8
1.3.3 XEOL-XAS	9
1.3.4 ODXAS 1	9
1.4 IMAGING CORROSION WITH XEOL-XAS	12
1.4.1 SCANNING PROBE AND FULL-FIELD XAS MICROSCOPY	12
1.4.2 XEOL-XAS IMAGING	14
1.4.3 TRANSMISSION AND FLUORESCENCE XAS MICROSCOPY	16
1.5 SYNCHROTRON RADIATION INDUCED SAMPLE DAMAGE	17
1.5.1 RADIATION INDUCED EFFECTS ON CULTURAL HERITAGE ARTIFACTS: SOME EXAMPLES	18
1.5.2 OBSERVATION OF X-RAY-INDUCED MODIFICATION OF CORRODED COPPER SURFACES.	19
1.6 IMAGING HERITAGE AND OTHER METAL SURFACES WITH X-RAY-EXCITED OPTICAL MICROSCOPY (XEOM)	21
1.6.1 SCOPE OF THE THESIS	22
1.7 BIBLIOGRAPHY	24
CHAPTER 2 : BACKGROUND & THEORY	31
2.1 SYNCHROTRON RADIATION	32
2.1.1 X-RAYS	32
2.1.1.1 Discovery	32
2.1.1.2 Properties of X-rays	33
2.1.2 SYNCHROTRON RADIATION: A STORY PASSED DOWN FROM GENERATION TO GENERATION	34
2.1.3 RADIATION FROM RELATIVISTIC ELECTRONS	35
2.1.4 DESIGN OF A THIRD GENERATION SYNCHROTRON	37
2.1.5 BEAM LINE LAYOUT	42
2.2 X-RAY ABSORPTION SPECTROSCOPY	44
2.2.1 PRINCIPLES OF X-RAY ABSORPTION	44
2.2.2 X-RAY ABSORPTION NEAR EDGE STRUCTURE (XANES)	49
2.2.3 EXTENDED X-RAY ABSORPTION FINE STRUCTURE (EXAFS)	51
2.2.3.1 Principles of EXAFS	51

2.2.3.2 The EXAFS equation	53
2.2.4 DATA PROCESSING	54
2.2.5 EXPERIMENTAL FEATURES	56
2.2.5.1 Transmission mode	56
2.2.5.2 Fluorescence yield mode	57
2.2.5.3 Electron yield mode	57
2.2.5.4 Optical yield mode	57
2.3 X-RAY-EXCITED OPTICAL LUMINESCENCE (XEOL)	58
2.3.1 THE PHYSICAL BASE OF THE XEOL PHENOMENON	58
2.3.2 XEOL-XAS	60
2.4 OTHER TECHNIQUES USED DURING THIS STUDY.	62
2.4.1 X-RAY DIFFRACTION (XRD)	62
2.4.1.1 Crystalline Structures	62
2.4.1.2 Principle of X-ray diffraction	63
2.4.1.3 Instrumentation	64
2.4.1.4 Data analysis	65
2.4.2 X-RAY PHOTOELECTRON SPECTROSCOPY (XPS)	66
2.4.2.1 Principle of X-ray Photoelectron Spectroscopy	66
2.4.2.2 Instrumentation	67
2.4.2.3 Data analysis	67
2.5 BIBLIOGRAPHY	68
CHAPTER 3: XEOM 1	73
<hr/>	
3.1 HARDWARE	74
3.1.1 OPTICAL COLUMN	75
3.1.1.1 sample stage section	76
3.1.1.2 Central optics section	76
3.1.1.3 CCD detector section.	79
3.1.2. LENS SYSTEM	80
3.1.2.1 Towards an achromatic lens system.	83
3.1.3 FILTER SYSTEM	84
3.1.3.1 Filters	84
3.1.4 DETECTORS	94
3.1.4.1 Optical light detector	94
3.1.4.2 X-ray detectors	98
3.1.5 ELECTRONICS INTERFACE FOR REMOTE CONTROL AND DATA ACQUISITION	99
3.2 SOFTWARE	102
3.2.1 CONTROL SOFTWARE	102
3.2.2 DATA PROCESSING SOFTWARE: <i>ESAPROJECT</i>	103
3.3 XEOM 1 INSTALLED AT THE ESRF	104
3.3.1 THE EUROPEAN SYNCHROTRON RADIATION FACILITY	104

3.3.2 BM28 XMAS, THE UK COLLABORATING RESEARCH GROUP (CRG)	105
3.3.2.1 XEOM 1 on XMaS	105
3.3.3 BM26A DUBBLE, THE DUTCH BELGIAN BEAMLINE	108
3.3.3.1 XEOM 1 on DUBBLE	109
3.3.4 Overview of beamtime allocations	110

CHAPTER 4: SYNTHESIS AND CHARACTERIZATION OF ARTIFICIALLY CORRODED COPPER SAMPLES

115

4.1 COPPER	116
4.1.1 COPPER COUPONS	117
4.1.2 COPPER GRIDS: A MESH FOR TRANSMISSION ELECTRON MICROSCOPY EXPERIMENTS	117
4.1.3 XEOL-XAS OF COPPER	118
4.2 CUPRITE	120
4.2.1 GREY CUPRITE PROTOCOL	121
4.2.2 XRD ANALYSIS OF GREY CUPRITE	121
4.2.2.1 Experimental details	121
4.2.2.2 Results and discussion	121
4.2.3 XPS ANALYSIS OF GREY CUPRITE	123
4.2.3.1 Experimental details	123
4.2.3.2 Results and discussion	123
4.2.4 XAS ANALYSIS OF GREY CUPRITE	126
4.2.4.1 Experimental details	126
4.2.4.2 Results and discussion	126
4.2.5 XEOL-XAS ANALYSIS OF GREY CUPRITE	128
4.2.5.1 Experimental details	128
4.2.5.2 Results and discussion	128
4.2.6 CONCLUSION	130
4.3 TENORITE	131
4.3.1 PROTOCOL	131
4.3.2 XEOL-XAS OF TENORITE	131
4.4 NANTOKITE	133
4.4.1 PROTOCOL	134
4.4.2 XEOL-XAS OF NANTOKITE	135
4.5 PARATACAMITE AND ATACAMITE	137
4.5.1 PROTOCOL	137
4.5.2 XEOL-XAS OF COPPER HYDROXYCHLORIDES	139
4.6 CONCLUSIONS	141

CHAPTER 5: EVALUATION OF XEOM 1 FOR CHEMICAL IMAGING OF METAL SURFACES **145**

5.1 OPERATION OF A XEOM 1 EXPERIMENT	146
5.2 IMAGING A HOMOGENEOUS CUPROUS CHLORIDE LAYER ON BRONZE SAMPLE	151
5.3 CHEMICAL MAPPING	152
5.3.1 EDGE HEIGHT MAPPING OF A TOPOLOGICAL INSULATOR	153
5.3.2 IMAGE STACK OF A CUPRITE GRID ON A COPPER SURFACE	156
5.3.3 IMAGE STACK OF A NANTOKITE GRID ON A CUPRITE SURFACE	162
5.4 CONCLUSIONS	165

CHAPTER 6: A MULTIMETHOD EXAMINATION OF ARCHAEOLOGICAL SAMPLES RETRIEVED FROM KING HENRY VIII'S FLAGSHIP: THE MARY ROSE **169**

6.1 THE MARY ROSE : 'THE NOBLEST SHIP OF SAIL'	170
6.2 TREASURES HARBOURED BY THE SHIP : TWO CHAIN MAIL LINKS	173
6.3 SIMULTANEOUS MULTIMETHOD ANALYSIS OF TWO CHAIN MAIL LINKS	175
6.3.1 EXPERIMENTAL SETUP	175
6.3.2 X-RAY FLUORESCENCE SPECTROSCOPY	176
6.3.3 X-RAY ABSORPTION SPECTROSCOPY : XAS & XEOL-XAS	178
6.3.4 CHEMICAL MAPPING OF THE CHAIN MAIL LINKS : XEOM ANALYSIS	180
6.3.4.1 Waveband survey of the corroded link MR81A2249	180
6.3.4.2 XEOM analysis of the corroded link MR81A2249	182
6.3.4.3 XEOM analysis of the conserved link MR81A1436	185
6.4 SR-XRD STUDY OF THE CHAIN MAIL LINKS	186
6.4.1 EXPERIMENTAL APPROACH	187
6.4.2 XRD ANALYSIS OF THE CORRODED CHAIN MAIL LINK MR81A2249	189
6.4.3 XRD ANALYSIS OF THE CONSERVED CHAIN MAIL LINK MR81A1436	191
6.5 CONCLUSIONS	194

CHAPTER 7: DESIGN OF AN UV-C ILLUMINATION MODULE FOR LABORATORY APPLICATIONS AND TESTING OF XEOM 1 **197**

7.1 INTRODUCTION	198
7.2 A NOVEL UV-C ILLUMINATION MODULE	200
7.2.1 DESIGN BRIEF AND CONSIDERATIONS	200
7.2.2 COMPONENTS	201
7.2.2.1 UV-C LED	201
7.2.2.2 LENS	202
7.2.2.3 Current source and Electronics	202
7.2.2.4 Heat sink and fan	203
7.2.3 DESIGN PROCESS	203
7.2.3.1 Experiments prior to design	203

7.2.3.2 Design	208
7.2.3.3 Final product	210
7.3 FIRST EXPERIMENTAL RESULTS	213
7.3.1 MEASUREMENTS TO ESTABLISH THE INFLUENCE OF THE OPTICS' ASPHERICAL CORRECTION ON THE RESOLUTION OF XEOM 1	213
7.3.1.1 Experimental aspects	214
7.3.1.2 Results and discussion	214
7.3.2 FINDING OPTIMAL FOCAL POSITION FOR EACH PASS BAND FILTER	217
7.3.3 ESTABLISHMENT OF 'ASTIGMATISM' IN THE XEOM 1 OPTICAL COLUMN	219
7.4 CONCLUSION	222
<u>CHAPTER 8: CONCLUSIONS</u>	<u>225</u>
8.1 PROJECT SUMMARY	226
8.2 FUTURE WORK	230
8.3 FINAL THOUGHTS	233
8.4 BIBLIOGRAPHY	234
<u>SUPPLEMENTARY CHAPTER: STUDY OF FRAMELESS COPPER AND COPPER-GOLD BEARING INTRAUTERINE DEVICES</u>	<u>235</u>
S.1 GENERAL INTRODUCTION	236
S.2 EVALUATION OF SITE-SPECIFIC IN UTERO CORROSION BEHAVIOUR OF COPPER SLEEVES FROM FRAMELESS INTRAUTERINE DEVICES .	237
S.2.1 INTRODUCTION	237
S.2.2 MATERIAL AND METHODS	239
S.2.2.1 Analysed samples	239
S.2.2.2 X-ray diffraction experiments	241
S.2.2.3 Scanning electron microscopy	242
S.2.2.4 Differential copper loss measurements	243
S.2.3 RESULTS AND DISCUSSION	243
S.2.3.1 X-ray diffraction patterns	243
S.2.3.2 SEM-analysis	246
S.2.3.3 Discussion	250
S.2.4 CONCLUSION	253
S.3 SITE-SPECIFIC IN VITRO COPPER RELEASE STUDY OF FRAMELESS INTRAUTERINE DEVICES IN A SIMULATED UTERINE SOLUTION.	254
S.3.1 INTRODUCTION	254
S.3.2 MATERIAL AND METHODS	254
S.3.2.1 Materials	254
S.3.2.2 Preparation of simulated uterine solution and stock solution.	256
S.3.2.3 Instrumentation	257

S.3.2.4 Standard curve for cupric ions	257
S.3.2.5 Sample analysis and sampling	258
S.3.3 RESULTS AND DISCUSSION	258
S.3.4 CONCLUSION	259
S.4 EVALUATION OF CORROSION BEHAVIOR OF COPPER-GOLD BEARING INTRAUTERINE DEVICES	260
S.4.1 INTRODUCTION	260
S.4.2 SR-XRD STUDY OF CU-AU CORROSION IN SIMULATED UTERINE SOLUTIONS USING A PORTABLE SPECTROELECTROCHEMICAL CELL	261
S.4.2.1 Material and methods	261
S.4.2.2 Results and discussion	265
S.4.2.3 Conclusions	266
S.4.3 IN VITRO COPPER RELEASE STUDY OF CU-AU FRAMELESS INTRAUTERINE DEVICES IN SIMULATED UTERINE SOLUTIONS	268
S.4.3.1 Material and methods	268
S.4.3.2 Results and discussion	269
S.4.3.3 Conclusions	270
APPENDIX	276
LIST OF PUBLICATIONS	298
CONFERENCE ATTENDANCE	299



Acknowledgements



'If I have seen further, it is by standing upon the shoulders of giants'

-Isaac Newton-

Contributions to science, regardless of their size or impact, are rarely the result of the work of an individual. Every scientist, like Newton, needs some pairs of strong shoulders to stand and rely on for scientific input, brilliant ideas, soothing comfort and necessary distractions.

Many wonderful people have joined me in my Ph.D. journey and provided me their shoulders to lean on. My scientific expedition at S12 lasted 7 years, a fact which does not facilitate my wish of making a complete list of people who I want to thank and acknowledge. However, allow me to try...

Eerst en vooral wil ik mijn promotor bedanken voor de kans die ze mij in 2010 gegeven heeft om de ESA groep te vervoegen. Mieke -voor één keer laat ik 'Professor' achterwege- oprecht bedankt voor alle kansen die je mij gegeven hebt om wetenschap uit te oefenen op een hoger niveau en dit te kunnen delen met de rest van de wereld. Het is echt niet vanzelfsprekend om een student op pad te sturen voor 7 conferenties in binnen- en buitenland, 4 studiebezoeken aan Warwick University, 1 Summer school in Chicago en maar liefst 15 meetsessies in de synchrotron. Toch heb ik hiervoor de kans gekregen. Bedankt voor alle vertrouwen.

A few sentences is probably insufficient in order to express my gratitude towards my co-supervisor, Professor Mark Dowsett. Mark, I count myself as very lucky to have had your guidance over the past 7 years. Thank you for sharing your passion of science with me and inspiring me to discover all the aspects that my research entailed. Without you, I'm sure I would have never subscribed for a lathe and milling course. If only I could convince Ana to make my garage look like yours ... Moreover, I appreciate all your tireless efforts (even during your retirement) to correct my papers, presentations and this thesis. I will never forget all the enriching discussions we had during the many beamtimes we shared. Thank you for providing me numerous answers to as many questions I had regarding physics, chemistry, engineering, optics, electronics, software, programming, computer science, synchrotrons, astronomy, English language, etc. Thank you for being a true mentor!

Oh, and before I forget, allow me to share the reason why I will never misuse 'as such' in the future as explained by one of your typical outbreaks of topical poetry:

*Oh no! He's gone and used "as such"
But I'll forgive, his first language is Dutch
As suches lurk in woods and grass
Leap out and bite you on the ass
Make you like a politician sound
And drive your rhetoric to the ground
They can be used but with great care
Else they breed and sneak in everywhere
(Much safer to insult a bear)
If you want to avoid some English hell
Here's a way to use them well
"I'm a virgin of this parish,
As such entitled to a Christian marriage"
But safer far to avoid the clutch
Of the dreaded sense free vicious as such.*

-Mark Dowsett-

Thanks to the members of the examination commission: Prof. Laszlo Vincze, Prof. Philippe Smet, Dr. Maria Alfredsson and Dr. Dirk Wildemeersch for the time spent in reviewing this thesis and their valuable comments in order to improve it. Special thanks to Prof. Karel Strijckmans for accepting to be chair of the examination commission, even after his retirement, and guiding the entire examination procedure in the right direction.

I would like to thank Ghent University for their financial support during my Ph.D. Moreover, the Fonds Wetenschappelijk Onderzoek (FWO), the Paul Instrument Fund, and the Engineering and Physical Sciences Research Council (EPSRC) are acknowledged for funding of the XEOM 1 equipment. The XMaS and DUBBLE beamlines are acknowledged for granting the numerous beam times necessary for conducting this research. A special thanks to the beam line staff of XMaS (Paul Thompson, Laurence Bouchenoire, Didier Wermeille and Simon Brown) and DUBBLE (Wim Bras, Dipanjan Banerjee, Miguel Silveira, Sergey Nikitenko and Stephen Bauters) for their support during the experiments.

Chapter 6 of this thesis would not have existed without the kindness of the Mary Rose trust and its head of collections, Prof. Mark Jones, for lending us the brass chain mail links. I am greatly indebted to them for providing the valuable archaeological artefacts and allowing us to investigate them.

Graag zou ik ook van dit moment gebruik maken om Jorge Alves Anjos en Davy de Pauw in de *spotlight* te plaatsen. Zonder hun hulp zou de XEOM 1 microscoop niet zó vlot en volautomatisch functioneren zoals ze dat nu kan. Daarnaast wil ik Jorge extra bedanken voor zijn hulp en gezelschap tijdens de laatste twee beamtimes; maar vooral voor de vele toffe momenten, babbels en lunchpauzes die we samen beleefd hebben. Muito obrigado !

A warm thank you is in place for all my fellow ESA & ASP group members. Elbeshary, Rosie, Annelies, Victoria, Farzin, Sara, Matt and Alice; thank you for all the enjoyable moments and the support you all have given me in your own particular way. It has been a pleasure to work with you all.

Michel, een apart blokje tekst voor jou! Heel graag zou ik je willen bedanken om een fantastische constante factor te zijn gedurende mijn doctoraatsperiode. Niemand anders kon soms beter de groeipijnen van een doctoraat begrijpen en inschatten dan jij. Bedankt voor je vele geduld, hulp en advies. Daarnaast onthou ik zeker en vast de vele memorabele momenten in ons bureau en ben ik dankbaar voor jouw 'The Big Bang Theory' collectie die je meebracht naar het ESRF. Desondanks het feit dat je voor Anderlecht supportert 😊, was je een perfecte collega waar ik altijd kon op rekenen! Hopelijk tot snel eens in Atlanta!

Walking to your room after an intensive night at the beamline while counting (apart from the hours of sleep left) the ESRF bunnies was for sure one of my favourite of many memorable moments in Grenoble. Matt, Rosie, Michel, Rita, Victoria and Jorge; many thanks for sharing that walk with me !

Naast doctoraatsstudent mocht je me samen met Jolien, Lien en Michel voor AAP houden. AAPjes, bedankt voor jullie team spirit ! Ik heb enorm veel voldoening kunnen en mogen halen uit mijn educatieve taak binnen het departement Analytische Chemie ofte WE08. Bedankt aan alle collega's die samen met mij getracht hebben de studenten te overtuigen van de geneugten van radiochemie. Annelies, Annelien, Tom, Eva en Pieter: dikke merci! Pieter, #thankyou voor de toffe attentie tijdens mijn laatste practicum en voor de vele hulp en interessante X-ray discussies op S12. #youtokeeponshiningbrightlikeanx-ray.

Graag ook een woordje van dank aan het administratief en technische personeel van de vakgroep. Zonder hen zou het werk als doctorandus en assistent bijna onmogelijk zijn. Chantal, Tine, Philip, Kris en Harry: bedankt voor alle hulp! Sylvia, *stief wel bedankt* voor de organisatie van alle teambuildings, kerstfeestjes en barbecues maar nog véél meer voor je luisterend oor, je hoog rots-in-de-branding gehalte en de vele grandioze momenten op het derde verdiep!

A final word of thanks to the many other wonderful people and colleagues I have met along the road at S12.

Deze scriptie vormt het ultieme sluitstuk van een twaalf jaar durend avontuur op de Sterre. De hulp, steun en plezier dat ik gekregen heb van mijn sterke achterban waren essentieel om deze periode tot een goed einde te brengen. Hierbij hoort een belangrijk vermelding en een welgemeende *dankjewel* , *thank you* en *gracias* ...

... voor het TOPteam van de Two. Bedankt voor de machtige ploegsfeer en speciaal bedankt aan Jochem aan wie ik mijn vele thesis stress kwijt kon tijdens het carpoolen van en naar de training en de match...

... voor mijn machtige chemie maten die al graag eens een tussenshotje drinken op een strand in Lagos ...

... voor Stijnie om gedurende een tweetal jaar een eersteklas roommate te zijn, 'Alsjeblieft!'...

... voor Joerik, Kristof, Stephanie en Inge. Bedankt voor de vele leuke momenten en reizen die we gehad hebben en nog zullen maken ...

... voor het #vakmanschap van www.decloedtkristof.be (beetje reclame maken mag) om de cover en de titelbladen van mijn thesis zo prachtig mooi te maken, ...

... voor de vele steun en berichtjes van mijn fantastische meter Tante Bet; voor de vele raad en levenswijsheden van Nonkel Willy en de vele interesse in mijn werk van Nonkel Étienne ...

... voor de knipoog die Tante Nicole zeker, van waar dan ook, naar mij stuurt. De bloem op het titelblad van dit hoofdstuk is dan ook mijn knipoog terug ...

... voor Bobon, doch klein van gestalte, mijn enige echte reus in dit gezelschap ...

... voor de onvoorwaardelijke steun van Zus & Koenraad. Bedankt voor de vele onvergetelijke momenten in het verleden, heden en de toekomst ...

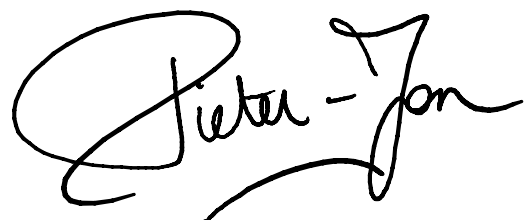
... voor mijn nichtjes Élena en Ella-Leonora y mis sobrinas Miranda y Valeria. Jullie onuitputtelijk enthousiasme doet alles relativeren. Gracias para siempre poner una sonrisa en mi cara ...

... para mi querido familia española. Mercedes, Alfonso, Helena y Ruben : Gracias por su cálida bienvenida a la familia y por hacerme sentir como en casa desde el primer día. Miles de gracias para compartir tu hija, hermana y cuñada conmigo aunque esto no puede ser fácil ...

... mijn schitterende ouders. Weinig woorden kunnen beschrijven hoe dankbaar en *preus* ik ben om jullie 'mama en papa' te mogen noemen. Bedankt voor alle kansen die jullie me gegeven hebben om hier te raken. Bedankt voor de onvoorwaardelijke steun en liefde en om altijd in mij te geloven ...

... para mi amor, Ana. Empecé este viaje solo pero muy rápidamente viniste a acompañarme (y adelantarme ... ;)) y para poner mi mundo al revés. Gracias por su profundo impacto en cada aspecto de mi vida, y por haberlo mejorado de todas las maneras imaginables. Habiendo terminado nuestro viaje en la universidad, estamos justo al comienzo de nuestra aventura de vida. ¡Hasta la luna y volver!

The end is not near, it's finally here!

A handwritten signature in black ink that reads "Pieter-Jan". The signature is written in a cursive, flowing style with a long horizontal stroke at the end.

Florida de Liebana, 30th of December 2017.

Nederlandstalige samenvatting

Erfgoedtoerisme vormt een belangrijke bron van inkomsten voor de Europese Unie [1]. Binnen de cultureel erfgoedverzameling vormen metallische objecten een belangrijk onderdeel. Het voortbestaan van deze metallische objecten is echter niet gegarandeerd omdat ze corroderen en degraderen onder invloed van tijd en andere externe factoren. Het is de taak van de conservator om deze corrosie en achteruitgang te bestrijden en maatregelen te treffen om hun overleving te verzekeren. Een behandeling kan pas opgestart worden nadat een diepgaande kennis verworven werd omtrent de chemische en fysische eigenschappen van de aangetroffen corrosielagen, en dit zowel op macro- als microscopisch niveau. Wanneer corrosie op een microscopisch niveau wordt benaderd zijn meer geavanceerde tools en analysemethodes noodzakelijk. Hiertoe behoren o.a. chemische beeldvormingstechnieken. Chemische beeldvormingstechnieken stellen onderzoekers in staat om zowel de samenstelling, structuur als andere chemische eigenschappen van complexe, heterogene materialen (zoals corrosielagen) op micrometerschaal in kaart te brengen. Veel van deze beeldvormingstechnieken zijn gebaseerd op het aftasten van het oppervlak volgens een raster met een X-stralenbundel van micrometerdimensies. Hoewel de beste laterale resolutie via deze weg verworven wordt, heeft recent onderzoek aangetoond dat de vermogensdichtheid van de hiervoor gebruikte X-stralenbundels voldoende groot zijn om de chemische eigenschappen van de corrosiedeklaag van het object aan te tasten [2]. Het continu ontwikkelen van nieuwe en innovatieve analytische methodes om corrosielagen vanuit verschillende perspectieven te onderzoeken, waarbij de integriteit van het historisch kunstvoorwerp bewaard blijft, is bijgevolg van groot belang voor de conservatiegemeenschap.

In een poging hiertoe bij te dragen werd in dit onderzoek de nadruk gelegd op de evaluatie en de verdere ontwikkeling van een nieuwe spectromicroscopische methode en bijhorend toestel voor de niet-destructieve en oppervlaktespecifieke chemische beeldvorming van corrosiedeklagen op cultuurhistorische en andere metalen in een gecontroleerde omgeving. XEOM 1, acroniem voor 'X-ray excited optical Microscopy 1', is een microscoop die XEOL licht capteert die opgewekt werd door synchrotron straling. XEOL, afkorting van 'X-ray excited Optical Luminescence', verwijst naar de elektromagnetische emissie uit het UV-VIS-IR gebied dat opgewekt wordt als gevolg van de interactie tussen het onderzochte monster en een X-straalbundel. XEOL is naast transmissie, fluorescentie en elektronenopbrengst een vierde detectiemethode om X-straalabsorptie spectra (XAS) te verwerven. Wanneer XEOL als detectiemethode voor X-straalabsorptiespectroscopie gebruikt wordt is de verworven informatie representatief voor de bovenste 200 nm van het monster. Een

kenmerk wat noodzakelijk is tijdens het bestuderen van oppervlaktefenomenen zoals corrosie.

Na **twee inleidende hoofdstukken** worden de hard- en softwarespecificaties, de installatie en de evaluatie van enkele componenten van XEOM 1 besproken in **hoofdstuk 3**. In **Hoofdstuk 4** wordt het productie- en karakterisatieproces van een set koperen testmonsters voorzien van een kunstmatig aangebrachte corrosiedeklaag besproken. Hoewel het toepassingsveld mogelijks veel breder is, werd in deze studie vooral de nadruk gelegd op het onderzoeken van gecorrodeerde koperen objecten van aanzienlijke cultuurhistorische waarde. Aangezien er veel van deze objecten onvervangbaar zijn en er vaak weinig voorkennis heerst over de aanwezige corrosiedeklagen zijn echte erfgoedobjecten geen ideale testmonsters voor de evaluatie van een nieuwe spectromicroscopische techniek. Een typische testmonster die gebruikt werd tijdens deze studie voor de evaluatie van XEOM 1 bestaat uit een koperen microrooster en coupon waarbij één van beide componenten voorzien is van een corrosiedeklaag. Eens beide componenten gecombineerd worden ontstaan scherp afgebakende microzones met verschillende koperchemie. Deze microzones zijn optimaal voor het bepalen van de laterale resolutie en de beeldvormingseigenschappen van de microscoop. Dit hoofdstuk analyseert uitvoerig de reactieproducten van de gebruikte recepten voor het produceren van nantokiet (CuCl), paratacamiet/atacamiet ($\text{Cu}_2(\text{OH})\text{Cl}_3$), tenoriet (CuO) en vooral cupriet (Cu_2O). Gevestigde technieken zoals XRD, XAS, XEOL-XAS en XPS, of een combinatie hiervan werden hiervoor gebruikt. Waar nodig werd het recept aangepast om de deklaag ook te kunnen produceren op meer fragiele substraten zoals het koperen microrooster.

In **hoofdstuk 5** worden de XEOM-meetresultaten van de verschillende testmonsters uitvoerig besproken, alsook de beschrijving van een procedure die gevolgd wordt tijdens het uitvoeren van een XEOM experiment. Tijdens een XEOM-experiment wordt XEOL emissie gecapteerd in tweedimensionaal beeld met behulp van een CCD-camera. Dergelijk beeld wordt genomen op verschillende energiepunten rond de absorptierand van koper (8979 eV) waardoor een energieafhankelijke beeldreeks gemaakt wordt. Vervolgens kan met esaProject, aangepast XEOM software, XEOL-XAS spectra geëxtraheerd worden uit deze XEOM-beeldreeks. Op deze manier kan chemische en structurele informatie gewonnen worden uit ofwel: één enkel pixel van het XEOM beeld, een door de gebruiker gekozen pixelregio ('region of interest', ROI) of het volledige XEOM beeld. Vervolgens kan de software alle spectra automatisch analyseren en, per spectra, bepaalde specifieke kenmerken isoleren. Een chemische kaart ontstaat dan wanneer deze specifieke kenmerken vertaald worden in een kleurcode en via deze kleur herafgebeeld worden op hun oorspronkelijke positie. Een typisch voorbeeld hiervan is de positie van de absorptierand van het onderzochte element wat een maat is voor zijn

oxidatietoestand. Op de eerste XEOM-beelden kunnen de verschillende corrosieproducten duidelijk waargenomen worden en dit vooral wanneer adequate optische filters gebruikt werden tijdens de acquisitie. Een chemische kaart die de verschillende oxidatietoestanden in beeld brengt van het testmonster kon evenwel geproduceerd worden. De laterale resolutie die momenteel behaald wordt is echter nog niet optimaal. Enerzijds kan dit toegeschreven worden aan het de sterk verschillende efficiëntie in XEOL productie van de verschillende koper corrosieproducten. Anderzijds hebben verschillende testen aangetoond dat, in het geval van XEOM metingen, er algemeen matig contrast verworven wordt wat een nadelige invloed heeft op de laterale resolutie van het toestel. Er werd geconcludeerd dat de optische kolom aangepast moet worden om dit nadelig effect weg te werken.

Nadat de initiële testfase afgerond werd, werd de uitdaging aangegaan om de corrosiedeklaag van enkele echte artefacten in kaart te brengen met XEOM 1. **Hoofdstuk 6** beschrijft de resultaten van een synchrotron-meetsessie waarbij simultaan XEOM, XANES en XEOL-XANES data verzameld werd in combinatie met een XRF-analyse van een geconserveerde en niet-geconserveerde maliënkolderringen die gevonden werden in het scheepswrak van de 'Mary Rose', het vlaggenschip van koning Henry VIII van Engeland. Deze informatie werd aangevuld met SR-XRD data, opgemeten via een relatieve nieuwe aanpak. Uit de resultaten blijkt dat beide ringen van messing gemaakt zijn en hoofdzakelijk in een anaerobe omgeving corrodeerden. Daarnaast blijkt het aannemelijk dat de corrosiedeklaag van de niet-geconserveerde ring sterk veranderde onder invloed van de omgevingsverandering na het ophalen van de zeebodem. Finaal kon het effect van de conservatiebehandeling duidelijk waargenomen worden in de verkregen data, waarbij het niet-destructief karakter van de XEOM techniek bevestigd werd.

Het gebrek aan synchrotron meettijd bleek al vanaf het begin één van de grootste beperkingen in dit onderzoeksproject. Om hieraan tegemoet te komen werd een alternatieve primaire excitatiebron ontworpen en ontwikkeld waarbij een UV-C LED in combinatie met een lens werd ingebouwd in nieuwe UV-C illuminatie module. De UV-C LED kan in combinatie met de lens een oppervlakte van $1 \times 1 \text{ mm}^2$ belichten met 255.6 nm UV-licht en een piekvermogen van 3 mW . Deze nieuwe module werd al gebruikt om de asferische correctie van de optische kolom te evalueren en om de optimale positie te vinden van focuslens (L3) in combinatie met verschillende optische filters. Daarnaast werd de module gebruikt om astigmatisme vast te stellen in XEOM 1's optische kolom. De resultaten van deze tests, alsook het ontwerps- en ontwikkelingsproces van de module werden uitvoerig beschreven in **hoofdstuk 7**.

Hoofdstuk 8 geeft een algemene conclusie van het gevoerde onderzoek.

Naast het onderzoek omtrent de chemische beeldvorming van corrosiedeklagen met XEOM 1, werd een aanzienlijke hoeveelheid onderzoek verricht naar de intra-uteriene corrosie van koperhoudende spiraaltjes, een populair anticonceptiemiddel. Aangezien deze studie moeilijk verenigbaar was onder de noemer van XEOM-onderzoek werd een **supplementair hoofdstuk** geweid aan de beschrijving van dit onderzoek. Koperhoudende spiraaltjes ('intrauterine devices', IUDs) bestaan vaak uit een plastic frame voorzien van een koperbron (huls of draad). Onder invloed van de intra-uteriene omgeving corrodeert de koperbron waarbij vrije koperionen ontstaan die de baarmoeder onontvankelijk maken voor conceptie. Hoewel de kennis bestaat dat het baarmoedervolume sterk kan verschillen tussen vrouwen onderling zijn koperhoudende spiraaltjes veelal enkel verkrijgbaar in één standaardgrootte. Incompatibiliteit tussen de baarmoeder en het spiraaltje kan leiden tot een resem aan onaangename randeffecten zoals: expulsie, pijn in de onderbuik, hevige uteriene bloedingen, etc. In deze studie werd het corrosiegedrag bestudeerd van frameleze koperhoudende spiraaltjes. Deze innovatieve spiraaltjes bestaan uit een reeks holle koperhulzen aaneengeregen via een flexibele hechtingsdraad. Via het gebruik van holle koperhulzen wordt in dit alternatieve design getracht de koperoppervlakte/IUD-volumeratio te vergroten en zo een oplossing te bieden aan de nadelige effecten van de spiraaltjes met frame. Via de analyse van *in utero* gecorrodeerde frameleze koperspiraaltjes met X-straal diffractie (XRD) en elektronenmicroscopie (SEM) werd aangetoond dat de nominale koperoppervlakte benaderd wordt door de koperoppervlakte die relevant is voor anticonceptie. Dit wordt in een latere paragraaf kwantitatief bevestigd met een *in vitro* experiment waarbij de koperafgifte van zowel de binnen- als de buitenkant van de koperhuls afzonderlijk bepaald worden met vlam atomaire-absorptiespectrometrie. De analyse van *in utero* gecorrodeerde koperhulzen leverde ook enkele belangrijke inzichten in de corrosieschaal van de *in utero* gecorrodeerde hulzen. Daar waar de literatuur de aanwezigheid van verschillende kopercorrosieproducten op *in utero* gecorrodeerde koperhoudende spiraaltjes beschrijft, werd via X-straal diffractie enkel de aanwezigheid van cupriet op de koperhulzen vastgesteld. Hoewel cupriet een belangrijk intermediair is in het corrosieproces werd via een apart experiment vastgesteld dat een deel van het aanwezige cupriet afkomstig is van gehydrolyseerd nantokiet. Dit vertekend beeld is het gevolg van een reinigingsproces met water van de spiraaltjes na verwijdering uit de uterus. In een laatste paragraaf werd de invloed van galvanische corrosie op de koperafgifte van het IUD bestudeerd. In een galvanische cel waarbij koper in contact wordt gebracht met het nobeler goud, fungeert koper als sacrificiële anode waardoor het sneller corrodeert en solvateert. Via de creatie van Cu-Au spiraaltjes wordt getracht de miniaturisatie van het spiraaltje verder te optimaliseren. Daarnaast bestaat het geloof dat een verhoogde intra-uteriene koperconcentratie mogelijks (gedeeltelijke) bescherming biedt tegen seksueel overdraagbare aandoeningen (SOA). Hoewel via SR-XRD aangetoond werd dat het

corrosieprofiel van koper onder invloed van goud verschuift naar meer oplosbare koperproducten, werd geen extra koperafgifte vastgesteld bij de Cu-Au frameleze spiraaltjes. Een nieuw ontwerp van deze Cu-Au spiraaltjes met een groter Cu-Au contactoppervlak dringt zich op om de afgifte-efficiëntie te verhogen. Het sputtercoaten van de Cu-cilinders met Au is hierbij een interessante piste om te volgen.

BIBLIOGRAFIE

[1] F. Cipolla-Ficarra, C. de Castro Lozano, E. Nicol, A. Kratky, M. Cipolla-Ficarra, *Human-Computer Interaction, Tourism and Cultural Heritage*, Springer Science & Business Media, 2011.

[2] A. Adriaens, P. Quinn, S. Nikitenko, M.G. Dowsett, Real Time Observation of X-ray-Induced Surface Modification Using Simultaneous XANES and XEOL-XANES., *Anal. Chem.* 85 (2013) 9556–9563.

List of abbreviations

a.u.	arbitrary units
APD	avalanche photodiode
ASP	analytical science projects
BE	binding energy
BM	bending magnet
BSA	bovine serum albumin
BSE	backscattered electrons
CCD	charge-coupled device
CW-XEOL	continous wave XEOL
DAQ	data acquistition system
eCell	electrochemical cell
EIU	electronics interface unit
EM	electromagnetic
ESA	electrochemistry & surface analysis
ESRF	European Synchrotron Radiation Facility
eV	electron volt
EXAFS	extended X-ray absorption fine structure
FAAS	flame atomic absorption spectroscopy
FLI	Finger Lakes Instruments
FLY	fluorescence yield
FWHM	full width at half maximum
ID	insertion device
IR	infrared
LCF	linear combination fitting
LED	light emitting diodes
LINAC	linear accelerator
ODXAS	optically detected/derived XAS
peCell	portable e-cell
PLY	photoluminescence yield
PMT	photomultiplier tube
QE	quantum efficiency
RF	radiofrequency
RMS	root mean square
ROI	region of interest
S/N	signal to noise ratio
SDD	silicon drift detector

SR	synchrotron radiation
SRS	Synchrotron Radiation Source (Daresbury)
SUS	simulated uterine solution
TEY	total electron yield
TR-XEOL	time resolved
UHV	ultra-high vacuum
UV	ultraviolet
UVFS	UV-graded fused silica
VIS	visible
XAFS	X-ray absorption fine structure
XANES	X-ray absorption near-edge structure
XAS	X-ray absorption spectroscopy
XEOL	X-ray-excited optical luminescence
XEOL-XAS	X-ray-excited optical luminescence X-ray absorption spectroscopy
XEOM	X-ray-excited optical microscopy
XPS	X-ray photoelectron spectroscopy
XRD	X-ray diffraction
XRF	X-ray fluorescence

A low-angle, close-up photograph of the Statue of Liberty, bathed in a warm, golden-yellow light. The statue's right arm is raised, holding the torch aloft. Her left arm is partially visible, holding several blue shopping bags. The background is a solid, bright yellow, creating a high-contrast, stylized effect.

Introduction

CHAPTER 1

1.1 CULTURAL HERITAGE, TANGIBLE AND INTANGIBLE REFERENCES TO THE PAST

"Societies retain evidence of their history to provide context, stability and inspiration to their cultures, which contributes to their development, growth and learning" – the justification given by Dillmann et al. [1] in order to explain the importance of what is left behind by our ancestors. The evidence alluded to by these authors, is based on tangible (architecture, art, archaeology, etc.) and intangible (social, political, religious and other practices) elements which comprise the cultural heritage of a nation. Intangible heritage in the form of professional craft knowledge is materialized in historic objects which, in turn, can offer tangible historical milestones that provide direct links to past events and people [2]. Additionally, tangible and intangible heritage have become a source of income for many countries, including European countries [3, 4]. For both these social and economic reasons, the endurance of the heritage components of our society is of great importance. Nevertheless, the decline of the physical aspect of our cultural heritage is unavoidable. *"Assets can degenerate through natural processes of decay, environmental influence or by direct effects of increased public access and tourism"* (as described by Adriaens and Dowsett in [5]). However, for most historic places and structures the main source of income is from tourists. In order to further attract tourists, and accordingly generate revenue these heritage sites have to be protected and preserved from damage and destruction, closing in this manner the paradoxical vicious circle¹.

Metals serve as a major ingredient to many tangible heritage objects and structures, but tend to degrade through corrosion. Even though in some cases layers of corrosion are intentionally produced to achieve particular aesthetic effects, in most cases corrosion is a result of the degradation of the metallic structure at its surface through chemical reactions with the environment. The surfaces of nearly all ancient metal objects which are buried in soil, immersed in fresh or salt water or exposed to air, rain and sun are prone to undergo these transformations. The partial or complete corrosion of the metallic core can lead to the impairment of the archaeological piece with resulting reduction in aesthetic value or loss of function [6, 7].

1.1.1 CONSERVATION AND PRESERVATION OF METALLIC OBJECTS

¹ In order to solve this problem, the PICTURE (Pro-active management of the Impact of Cultural Tourism upon Urban Resources and Economies) project financed by the European Commission aims to establish a sustainable management of cultural tourism [150].

It is generally accepted that actions are required to halt or mitigate the decline of unique objects of our cultural heritage [8]. It is the conservator's task to try to overcome this inherent instability of metallic heritage objects and prolong their survival. This responsibility is not easy and very delicate as their decisions must be guided by a set of ethical standards [9, 10]. These guidelines for ethical interventions depart from the position that *"the conservation process is governed by absolute respect for the aesthetic, historic and physical integrity of the work and requires a high sense of moral responsibility"*, as stated by Matero [11].

The extended endurance of heritage objects can be obtained through a variety of treatments which can be grouped into preventive and interventive conservation actions. Understandably, preventing corrosion is prioritized by a conservator. Preventive conservation is mostly associated with non-invasive methods which aim to impede corrosion via control of environmental factors that potentially promote corrosion: temperature, light, humidity and air pollution [12, 13].

A large number of objects, however, require physical or chemical interventions in order to treat and stop corrosion. A first and generally used practice to restore and conserve the corroded item is a cleaning procedure during which dirt is removed and the corrosion crust is (partially) dissolved [14]. Approaches include: mechanical cleaning [15], the use of chemical agents or the application of a laser [16, 17]. A typical example of the use of chemical agents is the treatment of corroded archaeological copper / bronze artifacts recovered from wet saline environments. Here, the aggressive chloride contamination is removed by soaking the object in sodium sesquicarbonate solutions in order to discard the water-insoluble cuprous chloride components [18, 19].

In the field of art, indications of corrosion on metallic artefacts are often accepted, and sometimes even desired. Some prefer the rich colour palette exhibited by the patina; others appreciate the reference to *"time past and time passing"* [18]. Nevertheless, under certain conditions, these objects remain at risk and action is still necessary. Cleaning remedies which remove or dissolve the entire corrosion layers are not suitable for this type of artefact. A better solution is the use of a stabilization treatment which maintains the details of the corrosion crust but tackles the active corrosion. Stabilization methods involve plasma cleaning [20] and electrochemical treatments for mechanical stripping or reduction of the corrosion crust [21–23].

Finally, in the case where preventive conservation is not sufficient to halt the attack of the surroundings, the artefact itself must be protected by adding material to seal it away from its environment. Within this *preservation* approach, the application of inhibitors or barrier coatings is popular. Addition of material to valuable objects,

often unique in nature, is not trivial as these coatings must ideally meet a series of stringent conditions, including:

- removability or re-treatability of the coating
- aesthetics of the object must be preserved
- application of the coating must not be complex
- inexpensiveness of the coating
- non-toxicity

Corrosion inhibitors react chemically with the artefact substrate to produce a stable surface whereas barrier protection coatings do not form any chemical bonds. The chemisorption of benzotriazole on copper to form a copper-benzotriazole barrier between e.g. cuprous chloride and moisture of the atmosphere is a well-known application of an inhibitor [24]. Although the distinction between inhibitors and protective coatings is mainly dependent on the reactivity of the artefact substrate; paraffin wax [25], microcrystalline waxes [26] and varnishes [27–29] are often divided in the barrier protection subgroup.

Identifying the condition of the metallic artefact is the initial step in establishing a methodology for its stabilization and conservation or preservation. Advanced analytical methods and techniques are essential in this endeavour, as they provide the required resources to understand the chemistry and structure of corroded metallic objects under investigation [30]. Additionally, they aid in understanding and elucidation of the corrosion routes responsible for an object's deterioration, which - in turn - contributes to the development of corrosion prevention strategies. A large-scale facility such as a synchrotron provides a wealth of analytical possibilities which are unavailable in smaller scale laboratories. Therefore synchrotron radiation (SR) methods have become very popular for researchers in the field of cultural heritage. A brief overview is presented in the following paragraph.

1.2 SYNCHROTRON RADIATION TECHNIQUES IN A CULTURAL HERITAGE CONTEXT

The use of synchrotron radiation in heritage science was first mentioned in 1986 by Harbottle et al. who anticipated that SR-based techniques would “*quickly take a prominent place in archeometric research*” [31, 32]. Ever since 1986, synchrotron radiation has become an increasingly important tool for research in the fields of art, archeometry and the conservation of objects with cultural heritage significance. Synchrotrons provide intense beams of electromagnetic radiation of tunable energy/wavelength, mainly used in the X-ray regime, with low angular divergence (strong natural collimation), selectable polarization and well-defined pulsed time

structure and beam patterns. These unique properties allow measurements to be performed on millimetre to nanometre sized samples and on a short timescale. Experimental techniques that benefit from SR used in conservation and archeometric studies are broad and all serve a similar purpose: identify constituent materials of samples, characterize product alteration and its pathways or assess certain conservation/stabilization measures. A brief overview is given below:

X-ray fluorescence spectroscopy (XRF) relies on the detection of characteristic X-ray radiation (fluorescence) emitted by the excited chemical elements after absorption of primary X-rays (see chapter 2 for more detail). Analysing XRF spectra can yield qualitative (elemental) and (semi-)quantitative information. Laboratory XRF equipment nowadays is sufficiently powerful to perform standard elemental analysis. The power of synchrotron XRF (SR-XRF) lies in its sub-ppm level detectability, reduced measurement times (with similar statistics) which are extra beneficial during the acquisition of 2D [33, 34] or 3D maps [35, 36], the use of microscopic [37] and nanoscopic [38] beam size to obtain high spatial resolution and the possibility to interleave XRF in multimodal measurements with X-ray absorption spectroscopy (XAS) and X-ray diffraction (XRD) (see below). The use of (SR)-XRF is one of the most often applied methods used in heritage science for the analysis of metallic objects [39], paint layers [34, 40], ancient glass [41], ceramics [42] and inks [43, 44].

X-ray diffraction (XRD) occurs when X-rays are coherently scattered from a periodic structure of atoms with interatomic distances of similar scale to the X-ray wavelength (see 2.4.1 for a more detailed description) [45]. Its main use in art and archaeology lies in the identification and quantification of crystalline compounds in a mixture. The investigation of amorphous systems (e.g. glasses) is limited by the lack of ordered structure, however important information can be obtained on average interatomic and intermolecular distances [46]. When XRD is performed on a synchrotron infrastructure (SR-XRD), it can provide information on a short timescale (seconds), which permits time-lapse measurements. This can be particularly useful for real time observation of e.g. corrosion growth on metallic substrates in controlled environments. Information provided by these experiments helps in the elucidation of the corrosion mechanisms involved. Our research groups, Electrochemistry and Surface Analysis (ESA) at Ghent University and Analytical Science Projects (ASP) at Warwick University, have used time-lapse XRD in combination with an electrochemical/environmental cell (eCell) [47] on many occasions for corrosion research on copper [48], bronze [49], lead [50] and silver [51].

X-ray absorption spectroscopy (XAS) is based on the change in absorption of X-rays as a function of X-ray energy when tuned across the *absorption edge* of a given atomic constituent of interest in the material. Spectroscopy in the vicinity of the absorption edge is referred to as X-ray absorption near-edge structure (XANES) and

post-edge region spectroscopy is better known as extended X-ray absorption fine structure (EXAFS) [52]. Unlike XRF and XRD, laboratory XAS instruments are not readily available, even though they exist [53, 54]. The application of XAS is mainly restricted to synchrotron facilities primarily due to the highly monochromatic, tunable energy X-rays provided at high flux. XAS offers a combination of features, particularly well-suited for the analysis of heritage objects. The technique complements XRD as it probes the short-range order of a material [55]. Accordingly it is suitable for a wide variety of materials, both crystalline and amorphous. Since XANES provides straightforward access to the oxidation state of the sample under investigation, it can serve as a tool to monitor in-situ chemical modifications. The use of XAS for in the investigation of metals [56–59], paint pigments [40, 60, 61], antique glasses [62], glazes [63, 64], ceramics [65], wood [66] and inks [67] has been reported.

Besides XRF, XRD and XAS, many other synchrotron supported techniques are being used in heritage science. Beyond the scope of this thesis, the use of synchrotron-based Fourier transform infrared micro-spectroscopy (SR-FTIR) [68], small-angle X-ray scattering (SAXS) [69] and X-ray Tomography [70] are reported elsewhere in more detail.

1.3 X-RAY-EXCITED OPTICAL LUMINESCENCE (XEOL) AS A DETECTION SCHEME FOR X-RAY ABSORPTION SPECTROSCOPY (XAS)

It must be emphasized that, in order to study the complexity that heritage samples exhibit, the use of more than one analytical technique is necessary. For metallic samples, it is noteworthy that deterioration is not primarily associated with alterations throughout the bulk of the material as corrosion crusts are initially limited to the outermost superficial layer.

Analysing surface specific events is more challenging in the sense that signals originating from the bulk may significantly swamp the chemical signal which is surface-born. For this reason X-ray-excited optical luminescence (XEOL) was explored by our groups as an alternative pathway to obtain XAS spectra for monitoring corrosion. XEOL is appealing in its potential to improve on the lack of surface specificity of complementary X-ray based techniques using X-ray beam energies over a few *keV* [71].

1.3.1 XEOL

X-ray-excited optical luminescence refers to the emission of optical photons from the near UV to the near IR upon absorption of X-rays. A description of the complex physical processes that precede the emission of XEOL is given in chapter 2 (see 2.3) [72]. Optical (UV/Vis) light can either be created with more conventional excitation sources (e.g. a discharge lamp, LASER, UV LED see chapter 7) or with a synchrotron radiation source. The high-energy resolution provided by a synchrotron allows the addressing of different chemical sites by selective excitation of specific edges and consequently decay channels in the sample. Of equal importance is its high brilliance which allows performing the measurements on a reasonable timescale. Finally, the energy tunability allows one to perform XEOL-XAS measurements and the pulsing time character of a synchrotron makes it possible to perform time resolved measurements (TR-XEOL) [73–75].

Research on XEOL has had a long history since its discovery simultaneously with the X-ray [72, 76], even though Röntgen was not aware of this at the moment when he observed the glowing barium platinocyanide. Ever since, many materials have been utilized to convert X-rays into visible or ultraviolet light in order to visualize the X-rays efficiently as such or on photographic films. CaWO_4 , for example, was distinguished from more than 8000 other chemicals by Edison as being extremely luminescent [77]. In addition to this exploration for X-ray scintillators, many attempts have been made in order to utilize XEOL for chemical and physical analysis.

A first important application of XEOL spectroscopy was the analysis of rare earth elemental impurities [72]. During a XEOL spectroscopy experiment, the photoluminescent response upon X-ray interaction is detected per unit of optical wavelength. This basic form of XEOL spectroscopy is also sometimes described as continuous wave XEOL (CW-XEOL) [73]. Detection limits in the range of 1 *ppm* – 1 *ppb* were obtained for the analysis of most rare-earth elements (Tb, Dy, Eu, Gd) in high purity inorganic hosts [78, 79]. Other early applications of XEOL spectroscopy involve the identification of *polynuclear aromatic hydrocarbons (PAH)* in environmental samples [80].

XEOL has been proven to be a valuable tool in studying the physicochemical properties of new nanostructured materials. Nanostructures possess a unique optical-structural property correlation in which they often exhibit significant band-edge emission, which is not the case for their counterpart bulk materials [81]. These innovative materials were recognized as very promising for optoelectronic devices such as light emitting diodes (LEDs), flat panel displays, photovoltaic devices, etc. in the early 2000s and are now a commercial reality [82]. XEOL exhibits essential features for studying these and future nanomaterials: element specificity, good

quantum efficiency, easy approach to time resolution, sensitivity to both crystalline and amorphous systems with or without incorporated defects or dopants [83, 84]. Within the field of nanoscaled systems with interesting luminescent features for optoelectronic applications studied with XEOL spectroscopy, the literature refers to ZnO [83–85], ZnS [82, 86], TbCl₃ [84], TiO₂ [87], porous Si [74, 88–90] and carbon based nanostructures [91]. A review of the trends on this nanomaterials topic was given by Tsun-Kong Sham in [81].

For completeness, it should also be mentioned that XEOL has also been used extensively in the study of Ru-doped organic light-emitting diodes (OLED) [92], molecular beacons (optical tags in biological studies) [93], nanosized photocatalysts for water splitting [94] and gold (I) complexes with organic ligands [75].

1.3.2 EXTENDED XEOL APPLICATIONS: TR-XEOL & 2D XEOL-XANES

In order to support the research of the emerging materials discussed above, techniques derived from XEOL spectroscopy have been developed. Within this context attention will be drawn to: time resolved XEOL (TR-XEOL) and two-dimensional XEOL-XANES (2D XEOL-XANES).

Time resolved XEOL benefits from the pulsed time-structure featured by third generation synchrotrons operating in top-up mode (see chapter 2.2.3) [81]. TR-XEOL monitors the time dependent decay, typically in the sub-nanosecond time frame, of the XEOL emission intensity following the absorption of a synchrotron X-ray pulse [74]. The decay curve provides information regarding the lifetime of an excited state. Additionally, during short and long time window measurements, extra information can reveal the relative contributions of long and short lived states. Typically, long lived states represent spectral features originating from defect states [95].

Two-dimensional XANES-XEOL spectroscopy is a novel mapping extension to XEOL developed to further the knowledge on the correlation between the structural and optical properties of nanomaterials. The technique, both operational in energy and time domain, permits the user to track the efficiency of X-ray-excited luminescence channels across the absorption edge of nanostructures of different size and morphology. In the energy domain, this is done by acquiring a full range (Continuous Wave, CW) of XEOL per excitation energy and displaying the results in a colour coded intensity map [94]. In the time domain this is done in a similar fashion where the measured lifetime is correlated with resolved XEOL wavelength. Results for ZnO nanowires [85], hierarchical TiO₂ [87] nanostructures and GaN-ZnO photocatalysts [94] have been reported.

1.3.3 XEOL-XAS

As described above, XEOL can serve as an independent spectroscopic tool. Nonetheless, since the excitation of a core electron is essential for XEOL to occur, a combination of XEOL detection and the energy tunability of synchrotron radiation might provide interesting information. Indeed, provided the stochastic background fluorescence and phosphorescence is sufficiently weak, XEOL is suitable as a vehicle for XAS signatures providing information on the chemical state and short-range atomic order with additional surface specificity [96]. This spectroscopic tool has been referenced elsewhere many times as optically detected (or derived) X-ray absorption spectroscopy (OD-XAS), in this work however it was chosen to retain a more general term: XEOL-XAS.

In 1978, Bianconi et al. reported the first observation of the close relationship between the fine structures of absorption spectra in XEOL yield and fluorescence yield mode, both recorded from a 2 mm thick CaF_2 single crystal across the Ca *K*-edge [97]. The concept of using XEOL as an information carrier for XAS was further explored by Goulon et al. In 1983, they demonstrated the possibility to measure selectively a ZnO spectrum in a ZnO – Zn *meso*-tetraphenylporphyrin (Zn TTP) mixture by addressing the XEOL detection mode [98]. By doing this, they claimed that XEOL-XAS could add site selectivity to XANES and EXAFS measurements. This enthusiasm was later tempered by Soderholm et al. who stated that site specificity was absent in many cases, possibly due to energy transfer mechanism between a donors and emitters [99]. Furthermore, Soderholm et al. argued that under certain circumstances, the XEOL signal did not carry any accessible EXAFS or XANES [91]. Much later Sham and Rosenberg alleged that site selectivity should be evaluated for each situation at the desired absorption edge, but measuring at lower X-ray energy and the use of nanostructures benefits in achieving this [74].

1.3.4 ODXAS 1

It can be concluded from the literature study above that most interests and developments of XEOL-based techniques have been in the soft X-ray regimes. Near the end of the previous decade, our research groups ESA & ASP (under the leadership of the supervisor and co-supervisor of this work) explored the use of XEOL to obtain XAS spectra for monitoring corrosion in the hard X-ray regime. It was demonstrated that spectral features observed in broadband XEOL-XANES and XEOL-EXAFS spectra for pure copper and derivative corrosion products are closely related to those taken with fluorescent XAS [5, 71]. The concerns expressed earlier by Soderholm et al. [99] were addressed to this extent and proven not to be too problematic in the case of copper and a set of copper corrosion products with cultural heritage relevance. Additionally, it was found that XEOL-XAS spectra

recorded from thin corrosion layers on metal are much more characteristic of the corrosion layer than their fluorescence counterpart, which points out the enhanced surface specificity in comparison with conventional XAS [71]. Another significant feature of the technique appears to be that the data can possibly be collected in controlled gaseous or liquid environments. Initial tests hinted that data did not suffer from self-absorption effects when radiation is forced to escape through fluid, whereas in counterpart XAS measurements the data are dominated by the fluid chemistry. For this reasons, the technique was regarded to be an attractive prospect in the corrosion study of metallic heritage artefacts. This work reached the cover of *Analytical Chemistry* on 15 November 2008 (Figure 1.1) [5, 71].

The results establishing the proof-of-principle of XEOL as a corrosion monitoring tool were acquired with ODXAS 1 [100]. ODXAS 1 is a portable XEOL detection system and a precursor instrument to XEOM 1 which is evaluated herein. ODXAS 1 is designed to transport a maximal amount of XEOL-emitted photons via a basic two-lens optical system to the detector [100, 101]. The optical system incorporates an objective lens to capture the XEOL flux from the sample; a condenser lens to guide the light to the detector and a broadband photomultiplier tube [100]. ODXAS 1 is designed to interface easily with an electrochemical/environmental cell developed earlier by the group – the eCell [102]. The body of the eCell, manufactured out of PCTFE, is highly chemically resistant and allows for introduction of corrosive environments for in-situ data collection. The eCell is designed in such a way that the sample is the working electrode of a 3-electrode system (in addition to a Pt counter electrode and a reference electrode). Consequently, electrochemical data can be gathered simultaneously to X-ray measurements (XRD and in principle XAS and XEOL-XAS) to provide supplementary information on the nature of the corrosion mechanism. All experiments of such type may be collected under the heading of spectroelectrochemistry. Since the eCell is translucent, an extra requirement is that the experiment must be conducted in the dark, to avoid unwanted stray light. Figure 1.2 shows a section through the solid model of ODXAS 1 and the deployment of the instrument in conjunction with the eCell at the BM28 XMaS beamline at the ESRF.

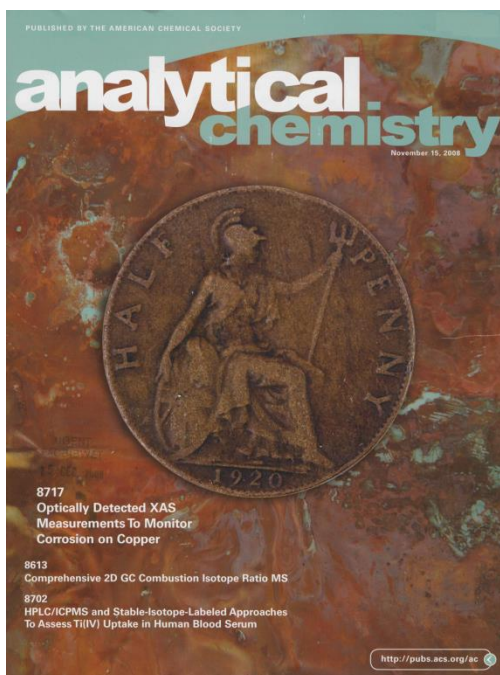
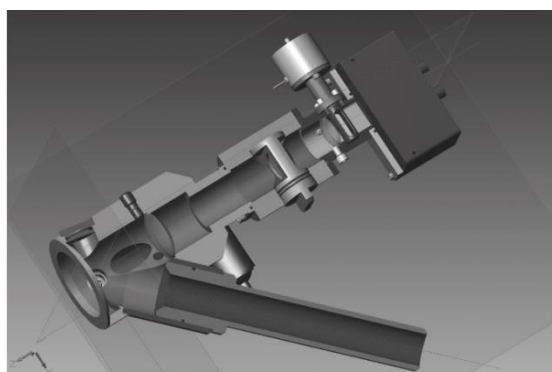
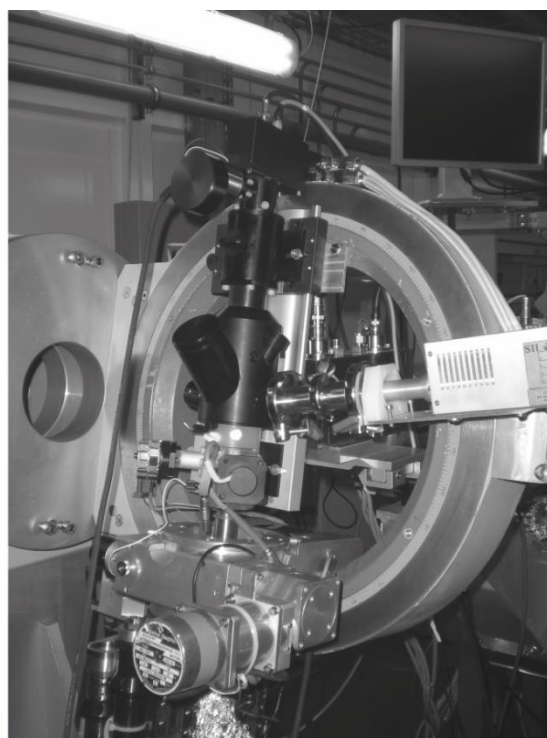


Figure 1.1

Cover of Analytical Chemistry of 15 November 2008



[A]



[B]

Figure 1.2

[A] Cross-section view of ODXAS 1, precursor to XEOM 1. 3D solid model was made by Mark Dowsett.

[B] ODXAS 1 installed in conjunction with the eCell in the experimental hutch of BM28 (XMaS) at the ESRF. ODXAS 1 was designed and machined by Mark Dowsett.

The primary limitation of ODXAS 1 is that measurements are volume-integrated over the X-ray exposed part of the sample; hence no lateral resolution is provided by the system [100]. The results represent average information from the analysed sample volume and the assumption has to be made that this average information is representative for the entire sample. However, the targeted heritage materials can possess a very complex heterogeneous nature. Firstly, the pristine artefact can exhibit heterogeneous features as it is commonly crafted out of a multimaterial mixture of simple compounds. Furthermore, since corrosion processes do not generally evolve homogeneously over a metal surface, the corrosion crust can add extra heterogenic complexity to the sample. In order to break down this complexity, a microscopy approach for XEOL-XAS was explored. XEOM 1 is the result thereof.

1.4 IMAGING CORROSION WITH XEOL-XAS

With few exceptions, materials are heterogeneous in nature, therefore analytical techniques which feature spatial resolution are desirable. Corroded heritage and other metals or alloys fall within this category and analyses performed on these materials would greatly benefit from lateral resolution. To build on the promising results that were acquired with ODXAS 1 and to remedy its lack of lateral resolution, XEOM 1 was designed. XEOM 1 is a full-field XEOL-XAS microscope for chemical mapping of corroded and other metal surfaces on a reasonable timescale [96, 101, 103]. Even though a number of research fields would benefit from chemical mappings provided by XEOM 1, heritage metal analysis with in particular corrosion research was initially targeted during this research.

Full-field imaging is only one of the possible approaches which can be followed to image the surface a sample. The difference between full-field imaging and scanning probe imaging is explained in section 1.4.1. The use of XEOL as an information source for chemical imaging is not novel and has been explored in the past. In section 1.4.2, an overview of the existing literature regarding XEOL imaging is provided. Finally, an overview is given in section 1.4.3 on X-ray absorption spectroscopy imaging in other detection modes: transmission mode and fluorescence mode.

1.4.1 SCANNING PROBE AND FULL-FIELD XAS MICROSCOPY

Chemical and structural imaging with spatial resolution can be achieved by basically 3 different approaches which differ by their illumination properties. One can distinguish between scanning probe, full-field and projection microscopy [104, 105].

Projection microscopy, a lensless imaging technique, is outside the scope of this work and is accordingly not discussed.

In a scanning probe microscopy system, a strongly demagnified X-ray beam is focused into a small spot on a specimen which is raster scanned in two dimensions perpendicular to the optical axis [106]. Before moving onto an adjacent point, the X-ray probe dwells for a limited time on each point to record emission signal (XEOL, fluorescent X-rays, electron yield, etc.). This way, the total image is formed pixel by pixel (or voxel by voxel when the sample is scanned in three dimensions). When the X-ray energy is scanned across a particular absorption edge during the dwell time of the X-ray beam, an XAS spectrum can be recorded per pixel. This way a spatially resolved XAS map can be recorded. The spatial resolution is defined by the dimensions of the X-ray probe or by the dimensions of its interaction volume. The spatial resolution at a synchrotron source has reached 10 *nm* for soft X-rays [107] and below 30 *nm* in the hard X-ray regime where 1 nm resolutions are expected in future synchrotrons [108, 109]. Whether such narrow probes lend themselves to perform XEOL-XAS spectromicroscopy is nevertheless uncertain. The drawback of this scanning technique is that a prohibitive amount of collection time is required to cover only a few micrometres, let alone a complete field of view. An advantage of this method is that different information channels can be collected from the same point on the sample using parallel detection [96, 110]. A schematic illustration of scanning probe imaging approach is given in Figure 1.3 A.

The alternative to a scanning probe approach is the use of a full-field imaging system. In a full-field microscope focusing optics are used to illuminate a relatively large area on the sample and other optics provide a magnified projection of the emission onto a pixelated detector, e.g. a charge coupled device (CCD) [104]. The ultimate lateral resolution in this imaging scheme is determined by lens aberrations or by pixel-array detector limitations such as pixel size and cross talk between pixels in the detector [96]. Advantageous to this method is that XAS profiles can be obtained in more moderate measuring times (with sufficient statistics) since each part of the image can be simultaneously acquired [111, 112]. Additionally, considering that relocation of the X-ray beam (e.g. due to monochromator scanning) does not affect the produced image, no realignment procedures are necessary. Nevertheless, the scanning micro- or nanoprobe method will achieve the highest lateral resolution. A schematic illustration of full-field imaging approach is given in Figure 1.3 B.

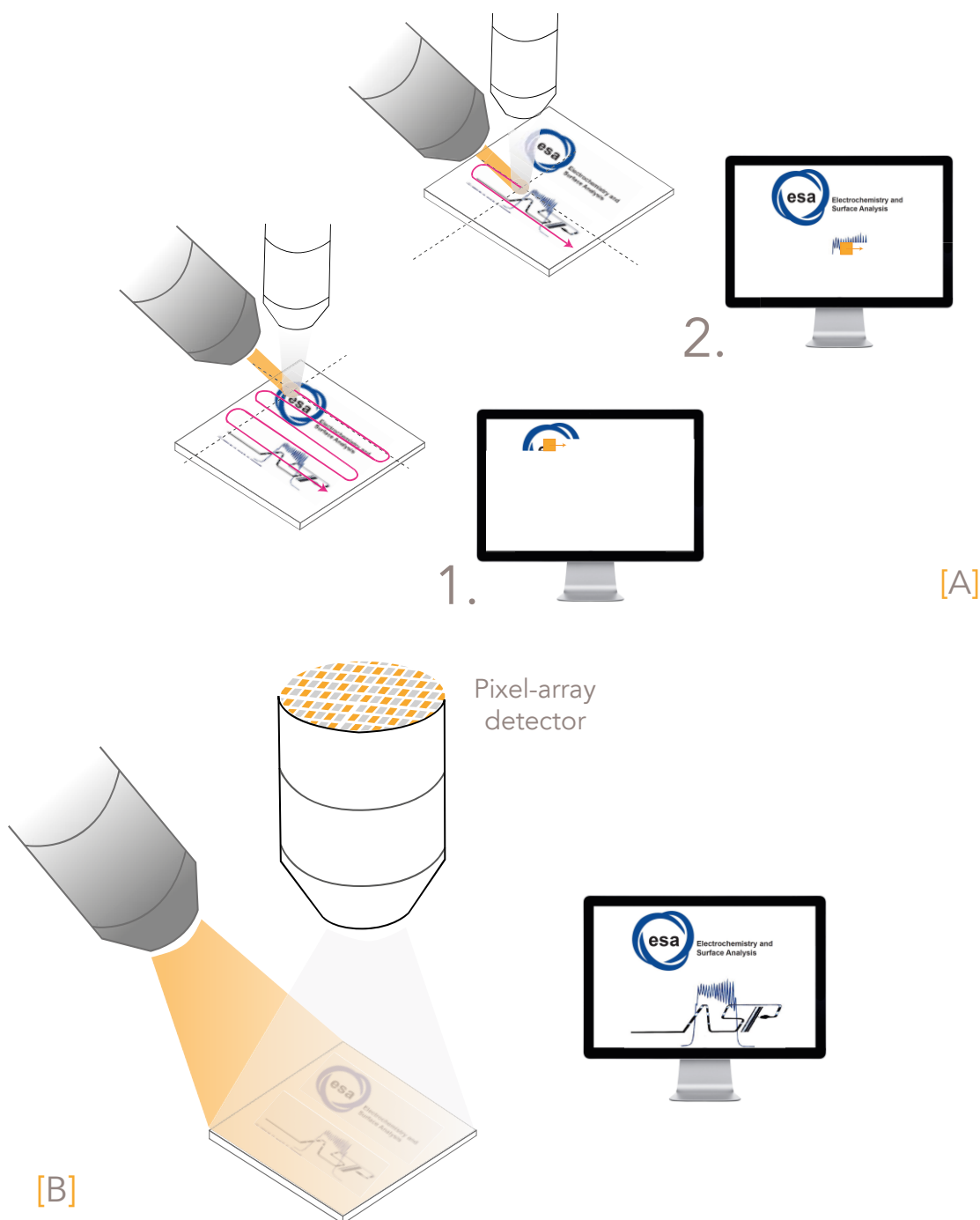


Figure 1.3

[A] Schematic illustration of imaging via a scanning microprobe approach

[B] Schematic illustration of a full-field imaging approach

1.4.2 XEOL-XAS IMAGING

XEOL spatial mapping has been explored in the past to investigate the texture of materials with lateral resolution (lateral resolutions differ between different approaches followed) [72, 113–115]. Previously used XEOL-mapping systems were

designed to investigate the materials discussed in section 1.4.1 (semiconductors, nanostructured materials) and are different from the corroded archaeological examples given in this work. In conjunction with the previous section, XEOL-XAS imaging methods can be subdivided into scanning probe and full-field imaging techniques.

Martínez-Criado et al. described a system for beamline ID22 at the European Synchrotron Radiation Facility (ESRF) for scanning luminescence spectroscopy with a hard X-ray microbeam to image optical heterogeneities in, e.g., GaN [115]. Another scanning XEOL microscopy system was installed by Vyvenko et al. in beamline 7T-WLS/1 (mySpot) of the BESSY synchrotron in Berlin. The system, named μ -SXEO, registered successfully the spatial distribution of band-band luminescence in multi-crystalline silicon [116]. The lateral resolution obtained by this system is in the micrometre range, although Martínez-Criado et al. published more recently chemical maps with < 100 nanometre resolution [117, 118]. Other groups achieved extreme lateral resolution (nm scale) by linking of established scanning microscopy techniques with the use of synchrotron radiation. Within this respect, for instance, Ishii et al. [119] achieved nanometre-order lateral resolution by coupling a scanning capacitance microscopy module to the synchrotron beamline. They detected the absorption fine structure by measuring the changes in sample capacitance that resulted from X-ray bombardment [119, 120]. Lacheri et al. designed a similar XAS scanning near-field optical microscope (XAS-SNOM) with a tapered optical fibre probe to detect the XEOL of an irradiated sample. This approach allows element-specific profilometry (cross-section profile) to be performed next to chemical imaging [121–123].

Full-field XEOL-XAS imaging systems are few in number. Prior to XEOM 1, the only previous instrumentation constructed for XEOL-XAS imaging in a synchrotron environment was CLASSIX (Chemistry, Luminescence And Structure of Surfaces by micro-Imaging X-ray absorption) developed by Nigel Poulton, Bruce Hamilton and others [113, 124]. CLASSIX1 was developed in the mid 2000's as a successor to the MoLES system (mobile luminescence end station), which was used for acquisition of wavelength-resolved XEOL-XAS spectra in the study of luminescence processes [114, 125]. CLASSIX1 was designed as a portable end-station to operate mainly on standard beamlines at the Synchrotron Radiation Source or SRS (Daresbury, United Kingdom). The system consisted of an ultra-high vacuum (UHV) compatible sample chamber containing a cryostat for creating low temperature environments [113]. The imaging section consisted out of focusing and imaging optics, a spectral dispersion system and a CCD detector. The spectral dispersion system consisted out of a filter wheel holding 105 optical filters to select specific bands in the emission. CLASSIX1 has been used, for example, to investigate the chemistry and structure of nanoporous alumina [113] and for XEOL-XANES structural mapping of boron nitride

(BN), a wide band gap semiconductor [126]. Unfortunately CLASSIX was not adopted elsewhere when the SRS closed in August 2008 and is hence no longer being operated.

Alongside of CLASSIX, Rosenberg et al. recently explored the use of a commercially available optical microscope mounted on a beamline end station for full-field elemental and magnetic sensitive XEOL imaging of solar cell materials [127].

1.4.3 TRANSMISSION AND FLUORESCENCE XAS MICROSCOPY

Full-field transmission X-ray microscopy (TXM) with XANES spectroscopy has been used in the past to follow two-dimensional (and three-dimensional) morphological and chemical changes in relatively large volumes at high resolution [111, 128–130]. The studied sample is excited with a large footprint X-ray beam and the signal transmitted through the sample is monitored using a CCD-based detection system. When a series of distinct images is recorded upon scanning the photon energy across the X-ray absorption edge of the element of interest, laterally resolved XANES spectra can be extracted by processing the intensity change of each pixel as a function of energy. Features conveying chemical or structural information, e.g. edge position as mirror for the oxidation state, can subsequently be expressed for each pixel in a two-dimensional colour map. TXM-XANES instrumentation has been installed in, for example, the BL 6-2 C beamline at the Stanford synchrotron radiation lightsource (SSRL, Stanford, California, USA) [111] and modern optics made it possible to push the lateral resolution for TXM systems down to about 30 nm in the hard X-ray region [129, 131] and sub-15 nm in the soft X-ray region [38]. Transmission full-field XANES chemical mapping has been applied in the field of cultural heritage by Meirer et al. to study the firing conditions of Roman ceramics [111].

The drawback of transmission mode XANES is that the data quality is very much dependent on the sample characteristics [112]. When the sample is not optimal in terms of thickness, this might result in either too strong absorption of the primary X-ray beam in case of a thick sample or too weak X-ray interaction with the (thin) sample upon transmission. The use of recording XANES profiles in fluorescence mode might provide a solution for sample thickness and/or low analyte concentration related problems. Tack et al. [112] proposed the use of an energy dispersive pnCCD detector, the SLcam, for full-field fluorescence mode XANES imaging. The use of this detection system allowed them to obtain spatially resolved coordination state and chemical speciation information on large sample area (> 4 mm²) with microscopic resolution of dilute and non-transparent samples. Application of a full-field approach resulted in the collection of about 70 000 XANES spectra in a

time frame of less than 15 hours. This is an achievement which would not have been possible upon using a raster scanning procedure. XANES imaging carried out by the more conventional raster scanning technique requires much longer scanning times to obtain good statistics for a similar imaged area and energy resolution window with respect to full-field imaging [104, 111, 112]. Nonetheless, raster scanning XANES imaging has been used to image confined areas or volumes: e.g. to observe Fe-rich mineral inclusions from diamonds found deep in the Earth's crust [132, 133]. The advent of large-area array detectors with considerable improvements in solid angle and signal throughput, such as Maia [134], provide new perspectives for mapping larger areas with very high resolution in raster scanning mode. These state-of-the-art detection systems allow for dwell times per pixel in the millisecond range. Accordingly, this results in collecting chemical maps with acquisition times and acquired X-ray doses that are up to 2-3 orders of magnitude lower than those obtained with conventional solid state detectors [134, 135]. Recently Monico et al. [135] published full spectral (FS) XANES maps registered with a Maia detector from chrome yellow pigments from a number of paintings by Vincent van Gogh. A full XANES stack of 125 steps recording an area 420 μm x 150 μm with a lateral resolution of about 1 μm could be obtained in 8 hours at the P06 beamline of the PETRA III synchrotron (Hamburg, Germany).

1.5 SYNCHROTRON RADIATION INDUCED SAMPLE DAMAGE

As is apparent from the preceding section, a choice must be made during the design process of a chemical mapping tool whether a scanning microprobe approach will be followed or a full-field imaging system will be pursued. In general, microprobe systems provide higher lateral resolution over full-field imaging systems but require much longer measurement times, especially in the case of recording X-ray absorption spectra where an extra energy dimension has to be scanned [40, 112, 136].

On another note, but nevertheless of extreme importance, is it imperative that knowledge is gathered to which extent the probing X-rays themselves can damage or induce modifications in the sample. With the exception of biocrystallography, X-ray experimentation has been considered for a long time as being completely non-destructive [137, 138]. However, since the use of intense radiation sources has increased for the analysis of a wide range of cultural heritage samples, the associated risk of radiation damage has become a subject of discussion in conservation communities [139]. In this context, lately, efforts are undertaken to raise awareness with researchers of possible radiation-induced side effects during analysis of heritage

artefacts. These efforts include, for example, the publication of review articles on the potential consequences of ion beam analysis (IBA) methods [140] or intense radiation sources in general [139].

For a long time, experiments were categorized as 'destructive' or 'non-destructive' based on whether the analysis had altered the visual appearance of the analysed object. However, despite the fact that it can serve as a first level of inspection, visible damage is not the only radiation-induced side effect. Investigation with intense beams of energetic photons entails a number of important processes that may induce changes in materials [139]. Direct effects can be of primary or secondary order in which, respectively, the incident photon reacts immediately with the target atom/molecule or secondary products of primary X-ray interaction (fluorescent photons, Auger electrons) react with their surroundings. In some cases, these interactions can create a chemically reactive environment which triggers a variety of different processes: atom abstraction, oxidation, dissociation, polymerization, etc. [137, 139]. The latter effects are subcategorized under indirect radiation effects. In addition to the radiation induced chemical effects, thermal effects should not be underestimated. Upon irradiation of the object, a large part of the photon energy will be dissipated via the activation of vibrational or lattice modes. Depending on the thermal conductivity of the sample, this can lead to substantial heating which may lead to: mechanical expansion, melting or an acceleration of the chemical reactions described above [139].

1.5.1 RADIATION INDUCED EFFECTS ON CULTURAL HERITAGE ARTIFACTS: SOME EXAMPLES

The alteration effects as a result of X-ray exposure on different types of cultural heritage materials have been documented in the past and reviewed by Bertrand et al. [139]. Most sensitive are organic (bio)materials (fabrics, paper, parchment, wood, dyes, varnishes) because organic bonds are easily broken due to primary or secondary radiation interactions. Some examples:

- During X-ray investigation of wood samples from the seventeenth-century warship 'Vasa', Sandström et al. [141] observed a sulphur and sulphate signal alteration as a result of prolonged X-ray exposure during XPS measurements.
- Mantler et al. [142] reported the permanent yellowing, brittleness and mechanical decomposition of paper samples upon using a 3 kW radiation source for several minutes and more.
- Potential physical damage during synchrotron microtomography studies on modern and fossil teeth and bones were documented by Richards et al. [143]. Even at the lowest energy and shortest duration of exposure, the hydroxyapatite crystals in the teeth were affected and resulted in colour changes.

Even though inorganic materials are less prone to radiation damage, radiation induced effects have been reported in this class of cultural heritage materials:

- Wilke et al. demonstrated that exposure to X-rays during XANES acquisition affected the oxidation state of iron in most iron gall inks [144].
- A similar beam induced reduction of Fe(III) to Fe(II) was observed by Gervais et al. in Prussian blue paint pigment during XAS analysis [145].
- Monnier et al. identified the presence of S(IV) artifacts, attributed to radiation exposure, in X-ray absorption spectra recorded at the S *K*-edge from corrosion layer samples of the iron chain recovered from the cathedral of Amiens [57]. Another example of significantly biased information of X-ray analysis on corrosion crusts on copper surfaces is described into more detail in the next section 1.5.2

Alternatively, irradiation might also induce non-permanent changes in the investigated material. An example of this phenomenon occurs when the nonradiative energy delivered after the X-ray induced electron-hole pair formation leads to a distortion within the crystal structure. This distortion is typically associated with the formation of electrons trapped within an anionic vacancy, which are referred to as colour centres or F-centres as they produce colouration in perfect colourless crystals. Once the irradiation source is removed, the colour centres will fade over time to the initial state [146].

1.5.2 OBSERVATION OF X-RAY-INDUCED MODIFICATION OF CORRODED COPPER SURFACES.

Observing beam-induced changes in a material is an experiment in itself. One such, carried out by the supervisors of this thesis and published in *Analytical Chemistry* [100] is described here. In the paper, the influence of the beam size (consequently also beam power density) on XEOL-XAS measurements made in air on artificially corroded copper and bronze samples is discussed. Metals are among the most radiation-resistant materials. Their high thermal and electrical conductivity reduces the impact of heating and charging effects arising from beams. However, prolonged exposure to radiation can accelerate oxidation and corrosion, especially in the presence of water and oxygen [139]. Corrosion crusts are far more sensitive to radiation effects than pure metals or alloys.

As an example to illustrate the modifying potential of micro sized X-ray beam, repetitive XEOL-XAS and XAS measurements were performed with micro (4.5 x 5.2 μm) and macro (1 x 6 mm) footprint X-ray beams on a copper coupon artificially corroded with nantokite (CuCl). The results are discussed in more detail in the original paper but are reproduced with permission of Dr. Darla Henderson (Assistant

Director of Open Access Program of the American Chemical Society (ACS) and Analytical Chemistry journal) in Figure 1.4.

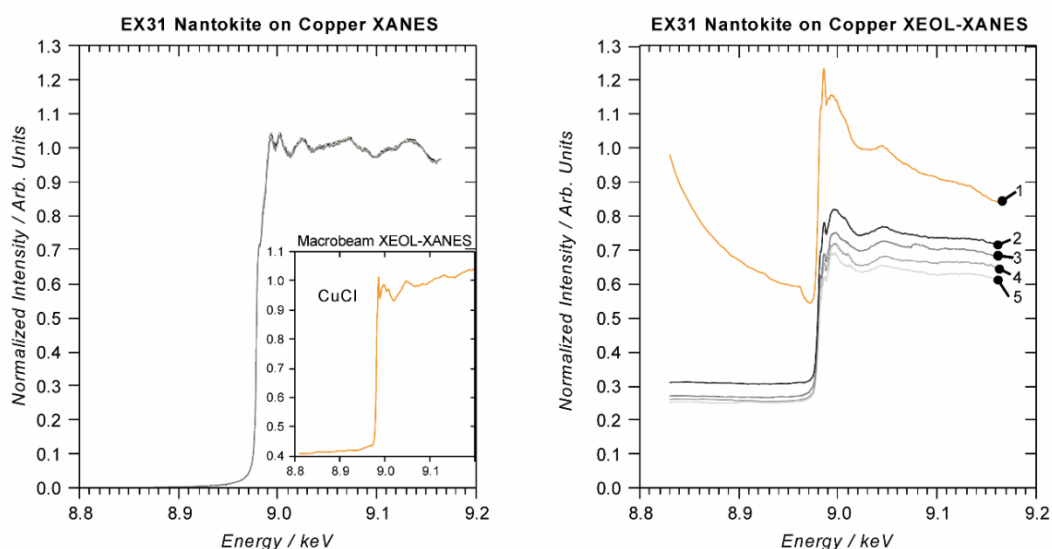


Figure 1.4

Microbeam scans of XANES (left) and XEOL-XANES (right) from nantokite (CuCl)-coated copper with macrobeam XEOL-XANES of nantokite as an inset. Spectra 1-5 are a sequence of 5 consecutive XANES across the Cu K-edge. The 5 spectra in the fluorescence set (left) are superimposed within noise level and are entirely characteristic of copper. The macrobeam XEOL-XANES is characteristic of nantokite. The first of 5 microbeam XEOL-XANES spectra is showing a rapidly decaying background suggesting the loss of a phosphorescent emitter and the decomposition to paratacamite under the beam.

Reproduction of Figure 6 published in Analytical chemistry [99]

(<http://pubs.acs.org/doi/pdf/10.1021/ac401646q>) Apart from the colour of the graphs, no modifications were made to the graph nor the caption.

Nantokite is a corrosion product typically found on heritage artifacts recovered from marine environments. Figure 1.4 displays on the left side 5 consecutive fluorescence XAS scans recorded with a microbeam provided by the I18 beamline of the Diamond Light Source (Didcot, UK). The microprobe beam featured a flux of $1 \times 10^{12} \text{ s}^{-1}$, which corresponds at 9000 eV (or $1.441959 \times 10^{-15} \text{ J}$) to a 61.3 W mm^{-2} input power density in a $4.5 \times 5.2 \text{ }\mu\text{m}$ beam spot size. The data are completely characteristic of the underlying bulk copper and no features characteristic of the thin surface nantokite layer are visible. All consecutive scans overlap within the noise level, indicating that there are no measurable changes in the sample bulk as a consequence of irradiation. A trained eye can recognize that XEOL-XAS signal recorded in parallel during the same experiment (Figure 1.4, right hand side) shows the presence of a mixture of nantokite and paratacamite. This feature highlights the surface sensitivity of the XEOL detection scheme for X-ray absorption spectroscopy. In contrast to the XAS

data, the successive XEOL-XAS spectra cannot be superimposed indicating a changing surface chemistry as a result of X-ray interaction. It appears that the nanotokite coating is being gradually hydrolysed to paratacamite in the beam. Similar measurements recorded with a $20 \mu\text{W mm}^{-2}$ macroprobe beam ($1 \times 10^{11} \text{s}^{-1}$ photons at 9000 eV in $1 \times 6 \text{ mm}$) remained stable over time showing that no surface modification was induced by the X-ray beam (Figure 1.4, left side, inset).

As can be concluded from the measurements published in [100], X-irradiation can change or damage the surface considerably more than the underlying material. This might be a consequence of the X-ray induced interaction with the air in the top few atomic layers or the surface reaction with the created O_3^- radicals (resultant of X-ray/air reaction). The loss of information due to radiation damage or the retrieval of misleading or biased information, even without visible damage, constitutes a major analytical risk. Therefore, exposure to higher power density X-ray beams must be avoided as much as possible. One of the possible mitigation strategies to be followed is the use of broader, low input power density X-ray beams.

The above results by Dowsett and Adriaens were used to justify the choice of a full-field rather than a scanned probe design for XEOM 1.

1.6 IMAGING HERITAGE AND OTHER METAL SURFACES WITH X-RAY-EXCITED OPTICAL MICROSCOPY (XEOM)

The information obtained from studying ancient materials and the development of their conservation approaches is strongly dependent on the development of new techniques for physical and chemical analysis [147]. In this contribution, we propose a novel modular system for the non-destructive chemical imaging of corroded and other heritage metal surfaces. Major problems with existing techniques include: a lack of lateral resolution, surface specificity, a requirement for a high vacuum, sample damaging beam conditions and/or the time consumed in producing chemical maps of large surfaces. The application of XEOM 1, a new full-field spectromicroscopy system employing XEOL as a detection scheme for XAS, can be useful in the endeavour to circumvent these deficiencies. XEOM 1 builds on the promising results that were acquired previously with ODXAS 1 and is a logical next step in this project.

XEOM 1 is designed as a portable synchrotron end-station which can potentially be installed with minimal effort in a large number of beamlines in synchrotrons all over the world. From this point of view, our system is different from other XEOL set-ups as they are dedicated to a particular beamline: e.g. I18 at DLS (Didcot, UK) [73, 148] or ID22 at the ESRF (Grenoble, France) [149]. XEOM 1 has been installed and synchronized successfully with BM26A (DUBBLE) and BM28 (XMaS) bending magnet

beamlines at the ESRF. Both beamlines delivered a beam with a large beam footprint to minimize X-ray induced side effects to the studied samples. This can be particularly important in the field of cultural heritage research, as any alteration to the artefact is seen as a negative evolution along the path that ultimately leads to artefact destruction and disappearance. An additional benefit to the application of XEOM 1 in heritage science is that the instrument can accommodate objects of various shapes and is able to operate in air or a controlled environment.

Laterally resolved XEOL-XAS provided by XEOM maps collected simultaneously with XAS and processed in tandem may create a powerful alternative analytical technique for the investigation of corrosion in heritage materials.

1.6.1 SCOPE OF THE THESIS

This document contains an account of the extensive evaluation process, the continued development and the application of XEOM 1 during multiple beam time allocations. It has to be emphasized that XEOM 1, and therefore also this work, is the result of the close collaboration between the ESA (under the leadership of Prof. Annemie Adriaens) and ASP research groups and EVA surface analysis (the latter both managed by Prof. Mark Dowsett). This document is subdivided into 8 different chapters, each addressing a different aspect of this research:

- **Chapter 1** introduces the reader to the main concerns of the conservation and preservation of our cultural heritage. An explanation is given why analytical tools, with synchrotron based techniques in particular, are crucial in the process of protecting our cultural heritage. XEOM 1 is introduced as a valuable asset in this struggle and its conceptual design is discussed in detail. The chapter features a literature study on the use of XEOL and XEOL-XAS in other fields, XAS and XEOL-XAS imaging and the current awareness of the potential damaging character of high intense X-rays.
- **Chapter 2** provides background and an in-depth explanation of the methodology used in this work. Much attention is paid to: the nature of X-rays, the structure and operating principle of the synchrotron, X-ray absorption spectroscopy and the origin of X-ray-excited optical luminescence.
- **Chapter 3** discusses the hard- and software features of XEOM 1 instrument and its components. Additionally, an overview is given of the allocated beam times at BM26 A and BM28 of the ESRF.
- **Chapter 4** describes the amount of work done in producing and characterizing artificially corroded analogues of naturally occurring corrosion products with cultural heritage relevance. Moreover, in order to evaluate XEOM 1, well characterized patterned assessment samples are necessary. The approach followed to overcome this problem is discussed in this chapter.

- **Chapter 5** presents the evaluation and assessment of XEOM 1 as a spectromicroscopy tool for investigating metal surfaces. The results from the measurements recorded of the evaluation samples, exhibiting a spatially varying patination establishing the ground work for imaging copper and relevant copper corrosion products, are presented and discussed.
- **Chapter 6** presents and comments on the first application of XEOM 1 on a genuine cultural heritage artefact: chemical maps recorded from a brass chain mail link recovered from the Mary Rose, the wreck of Henry VIII's flagship.
- One of the main limitations in the evaluation process of XEOM 1 is the unavoidably restricted access to a synchrotron. **Chapter 7** presents the design and application of an accessory UV-C illumination source to XEOM 1. In this chapter, we examine whether this can be a useful alternative for experiments outside the synchrotron such as performing optical tests.
- **Chapter 8** provides a summary of the project and conclusions are drawn as a final evaluation of this thesis. Additionally, some final thoughts are given for future work.
- Outside the scope of metal surface imaging with XEOM, but within the field of copper corrosion, a case study on in utero corrosion of frameless copper intrauterine devices has been added to this thesis. This **Supplementary chapter** is the result of a considerable amount of work performed on this project over the past years in collaboration with Dr. Dirk Wildemeersch. Since this body of work was difficult to unify with the rest of this thesis, this additional chapter is built up as a separate research product with a distinct introduction, methodology, results & discussions and conclusion section.

1.7 BIBLIOGRAPHY

- [1] P. Dillmann, D. Watkinson, E. Angelini, A. Adriaens, *Corrosion and Conservation of Cultural Heritage Metallic Artefacts*, Elsevier, 2013.
- [2] K.M. Darain, M.Z. Jumaat, M. Nazimuddin, A. Ahsan, R. Rashid, M.M.A. Aziz, M. Obaydullah, A.B.M.S. Islam, A review of the corrosion behaviour of metallic heritage structures and artifacts, *J. Teknol.* 77 (2015) 206–218.
- [3] D.J. Timothy, *Cultural Heritage and Tourism*, Channel View Publications, 2011.
- [4] F. Cipolla-Ficarra, C. de Castro Lozano, E. Nicol, A. Kratky, M. Cipolla-Ficarra, *Human-Computer Interaction, Tourism and Cultural Heritage*, Springer Science & Business Media, 2011.
- [5] A. Adriaens, M. Dowsett, The coordinated use of synchrotron spectroelectrochemistry for corrosion studies on heritage metals., *Acc. Chem. Res.* 43 (2010) 927–35.
- [6] F. Mathis, J. Salomon, S. Pagès - Camagna, M. Dubus, D. Robcis, M. Aucouturier, S. Descamps, E. Delange, in: *European Federation of Corrosion (EFC) Series*, Woodhead Publishing, 2007, pp. 219–238.
- [7] E. Angelini, F. Rosalbino, S. Grassini, G.M. Ingo, T. De Caro, in: *European Federation of Corrosion (EFC) Series*, Woodhead Publishing, 2007, pp. 203–218.
- [8] A. Adriaens, G. Demortier, COST Actions G1 and G8: EU programs on the use of radiation in art and archaeometry, *Nucl. Instruments Methods Phys. Res. Sect. B Beam Interact. with Mater. Atoms* 226 (2004) 3–9.
- [9] A.I. for Conservation, *AIC code of ethics and guidelines for practice, Technical report*, 1994.
- [10] E. confederation of conservators-restorer's Organizations, *Practical guidelines, technical report*, 2002.
- [11] F. Matero, Ethics and policy in conservation, *Getty Conserv. Inst. Newsl.* 15 (2000) 5–8.
- [12] K. Gysels, F. Delalieux, F. Deutsch, R. Van Grieken, D. Camuffo, A. Bernardi, G. Sturaro, H.J. Busse, M. Wieser, Indoor environment and conservation in the Royal Museum of Fine Arts, Antwerp, Belgium, *J. Cult. Herit.* 5 (2004) 221–230.
- [13] D. Watkinson, in: P.D.W.A.B.T.-C. and C. of C.H.M.A. Adriaens (Ed.), *European Federation of Corrosion (EFC) Series*, Woodhead Publishing, 2013, pp. 9–36.
- [14] C. Ewen, *Artifacts*, Altamira Press, 2003.
- [15] P. Cridlebaugh, Formulating ethics and standards in archeology, *Chicora Found.* (1990).
- [16] M. Matteini, C. Lalli, I. Tosini, A. Giusti, S. Siano, Laser and chemical cleaning tests for the conservation of the Porta del Paradiso by Lorenzo Ghiberti, *J. Cult. Herit.* 4, Supplem (2003) 147–151.
- [17] C. Degrigny, E. Tanguy, R. Le Gall, V. Zafirooulos, G. Marakis, Laser cleaning of tarnished silver and copper threads in museum textiles, *J. Cult. Herit.* 4, Supplem (2003) 152–156.
- [18] D.A. Scott, *Copper and Bronze in Art: corrosion, colorants, conservation*, The Getty conservation institute : Los Angeles, 2002.
- [19] I.D. Macleod, Conservation of corroded copper alloys: a comparison of new and traditional methods for removing chloride ions, *Stud. Conserv.* 32 (1987) 25–40.
- [20] E.G. Ioanid, A. Ioanid, D.E. Rusu, F. Doroftei, Surface investigation of some medieval silver coins cleaned in high-frequency cold plasma, *J. Cult. Herit.* 12 (2011) 220–226.
- [21] L. Bertolini, M. Carsana, E. Redaelli, Conservation of historical reinforced concrete structures damaged by carbonation induced corrosion by means of electrochemical realkalisation, *J. Cult. Herit.* 9 (2008) 376–385.
- [22] L.M. Ottosen, C. Dias-Ferreira, A.B. Ribeiro, Electrochemical desalination of historic Portuguese tiles – Removal of chlorides, nitrates and sulfates, *J. Cult. Herit.* 16 (2015) 712–718.
- [23] T. Palomar, B. Ramírez Barat, E. García, E. Cano, A comparative study of cleaning methods for tarnished silver, *J. Cult. Herit.*
- [24] R.B. Faltermeier, A CORROSION INHIBITOR TEST FOR COPPER-BASED ARTIFACTS, *Stud. Conserv.* 44 (1998) 121–128.
- [25] K. Schaefer, D.J. Mills, The application of organic coatings in conservation of archaeological objects excavated from the sea, *Prog. Org. Coatings* (2016).
- [26] S. Goidanich, L. Toniolo, S. Jafarzadeh, I.O. Wallinder, Effects of wax-based anti-graffiti on copper patina composition and dissolution during four years of outdoor urban exposure, *J. Cult. Herit.* 11 (2010) 288–296.
- [27] P. Kotlík, K. Doubravová, J. Horálek, L. Kubáč, J. Akerman, Acrylic copolymer coatings for protection against UV rays, *J. Cult. Herit.* 15 (2014) 44–48.
- [28] V. Pitthard, R. Stone, S. Stanek, M. Griesser, Claudia-Kryza-Gersch, H. Hanzer, Organic patinas on Renaissance and Baroque bronzes–Interpretation of compositions of the original patination by using a

- set of simulated varnished bronze coupons, *J. Cult. Herit.* 12 (2011) 44–53.
- [29] C.E. Rogge, The varnished truth: The recipes and reality of tintype coatings, *J. Cult. Herit.* 15 (2014) 57–63.
- [30] A. Adriaens, Non-destructive analysis and testing of museum objects: An overview of 5 years of research, *Spectrochim. Acta - Part B At. Spectrosc.* 60 (2005) 1503–1516.
- [31] G. Harbottle, B.M. Gordon, K.W. Jones, Use of synchrotron radiation in archaeometry, *Nucl. Instruments Methods Phys. Res. Sect. B Beam Interact. with Mater. Atoms* 14 (1986) 116–122.
- [32] M. Cotte, J. Susini, J. Dik, K. Janssens, *Spectroscopy for Art Conservation: Looking Back*, 43 (2010) 705–714.
- [33] K. Janssens, W. De Nolf, G. Van Der Snickt, L. Vincze, B. Vekemans, R. Terzano, F.E. Brenker, Recent trends in quantitative aspects of microscopic X-ray fluorescence analysis, *TrAC Trends Anal. Chem.* 29 (2010) 464–478.
- [34] J. Dik, K. Janssens, G. Van der Snickt, L. van der Loeff, K. Rickers, M. Cotte, Visualization of a lost painting by Vincent van Gogh using synchrotron radiation based X-ray fluorescence elemental mapping, *Anal. Chem.* 80 (2008) 6436–42.
- [35] I. Mantouvalou, T. Wolff, O. Hahn, I. Rabin, L. Lühl, M. Pagels, W. Malzer, B. Kanngiesser, 3D Micro-XRF for Cultural Heritage Objects: New Analysis Strategies for the Investigation of the Dead Sea Scrolls, *Anal. Chem.* 83 (2011) 6308–6315.
- [36] L. Vincze, B. Vekemans, F.E. Brenker, G. Falkenberg, K. Rickers, A. Somogyi, M. Kersten, F. Adams, Three-Dimensional Trace Element Analysis by Confocal X-ray Microfluorescence Imaging, 76 (2004) 6786–6791.
- [37] K. Janssens, G. Vittiglio, I. Deraedt, A. Aerts, B. Vekemans, L. Vincze, F. Wei, I. Deryck, O. Schalm, F. Adams, A. Rindby, A. Knöchel, A. Simionovici, A. Snigirev, Use of Microscopic XRF for Non-destructive Analysis in Art and Archaeometry, *X-Ray Spectrom.* 91 (2000) 73–91.
- [38] A. Sakdinawat, D. Attwood, Nanoscale X-ray imaging, *Nat. Photonics* 4 (2010) 840–848.
- [39] B. Constantinescu, R. Bugoi, V. Cojocaru, R. Simon, D. Grambole, F. Munnik, E. Oberländer-Târnoveanu, Elemental analysis through X-ray techniques applied in archeological gold authentication — the case of Transylvanian gold and of the Dacian bracelets, *Spectrochim. Acta Part B At. Spectrosc.* 64 (2009) 1198–1203.
- [40] K. Janssens, M. Alfeld, G. Van der Snickt, W. De Nolf, F. Vanmeert, M. Radepon, L. Monico, J. Dik, M. Cotte, G. Falkenberg, C. Miliari, B.G. Brunetti, The use of synchrotron radiation for the characterization of artists' pigments and paintings., *Annu. Rev. Anal. Chem.* 6 (2013) 399–425.
- [41] Ž. Šmit, K. Janssens, O. Schalm, M. Kos, Spread of façon-de-Venise glassmaking through central and western Europe, *Nucl. Instruments Methods Phys. Res. Sect. B* 213 (2004) 717–722.
- [42] A. Guilherme, G. Buzanich, M. Radtke, U. Reinholz, J. Coroado, J.M.F. Dos Santos, M.L. Carvalho, Synchrotron micro-XRF with Compound Refractive Lenses (CRLs) for tracing key elements on Portuguese glazed ceramics, *J. Anal. At. Spectrom.* (2012) -.
- [43] O. Hahn, Analyses of Iron Gall and Carbon Inks by Means of X-ray Fluorescence Analysis: A Non-Destructive Approach in the Field of Archaeometry and Conservation Science, *Restaurator* 31 (2010) 41–64.
- [44] H. Mommsen, T. Beier, H. Dittmann, D. Heimermann, A. Hein, A. Rosenberg, X-ray fluorescence analysis with synchrotron radiation on the inks and papers of incunabula, *Archeometry* 38 (1996) 347–357.
- [45] Y. Waseda, E. Matsubara, K. Shinoda, *X-Ray Diffraction Crystallography; Introduction, examples and solved problems*, 2011.
- [46] L. Bertrand, L. Robinet, M. Thoury, K. Janssens, S.X. Cohen, S. Schöder, Cultural heritage and archaeology materials studied by synchrotron spectroscopy and imaging, *Appl. Phys. A* 106 (2012) 377–396.
- [47] M. Dowsett, A. Adriaens, Cell for simultaneous synchrotron radiation X-ray and electrochemical corrosion measurements on cultural heritage metals and other materials., *Anal. Chem.* 78 (2006) 3360–5.
- [48] M. Dowsett, A. Adriaens, C. Martin, L. Bouchenoire, The use of synchrotron X-rays to observe copper corrosion in real time., *Anal. Chem.* 84 (2012) 4866–72.
- [49] R. Grayburn, M.G. Dowsett, M. Hand, P.-J. Sabbe, P. Thompson, A. Adriaens, Bronze Disease Revealed? A synchrotron X-ray diffraction study of nantokite hydrolysis, *Corros. Sci.* 91 (2014) 220–223.
- [50] R. Grayburn, M. Dowsett, M. De Keersmaecker, E. Westenbrink, J.A. Covington, J.B. Crawford, M. Hand, D. Walker, P.A. Thomas, D. Banerjee, A. Adriaens, Time-lapse synchrotron X-ray diffraction to monitor conservation coatings for heritage lead in atmospheres polluted with oak-emitted volatile organic compounds, *Corros. Sci.* 82 (2014) 280–289.
- [51] R. Wiesinger, R. Grayburn, M. Dowsett, P.-J. Sabbe, P. Thompson, A. Adriaens, M. Schreiner, In situ time-lapse synchrotron radiation X-ray diffraction

- of silver corrosion, *J. Anal. At. Spectrom.* 30 (2015) 694–701.
- [52] G. Bunker, Introduction to XAFS, (2010) 268.
- [53] K. Sakurai, X. Guo, Recent performance of laboratory-scale X-ray absorption fine structure instruments, *Spectrochim. Acta Part B At. Spectrosc.* 54 (1999) 99–107.
- [54] G.T. Seidler, D.R. Mortensen, a J. Remesnik, J.I. Pacold, N. a Ball, N. Barry, M. Styczinski, O.R. Hoidn, A laboratory-based hard x-ray monochromator for high-resolution x-ray emission spectroscopy and x-ray absorption near edge structure measurements., *Rev. Sci. Instrum.* 85 (2014) 113906.
- [55] J.E. Penner-Hahn, X-ray Absorption Spectroscopy, *Compr. Coord. Chem. II* (2003) 159–186.
- [56] J. Monnier, S. Réguer, D. Vantelon, P. Dillmann, D. Neff, I. Guillot, X-rays absorption study on Medieval corrosion layers for the understanding of very long-term indoor atmospheric iron corrosion, *Appl. Phys. A. Mater. Sci. Process.* 99 (2010) 399–406.
- [57] J. Monnier, D. Neff, S. Réguer, P. Dillmann, L. Bellot-Gurlet, E. Leroy, E. Foy, L. Legrand, I. Guillot, A corrosion study of the ferrous medieval reinforcement of the Amiens cathedral. Phase characterisation and localisation by various microprobes techniques, *Corros. Sci.* 52 (2010) 695–710.
- [58] I. De Ryck, A. Adriaens, E. Pantos, F. Adams, A comparison of microbeam techniques for the analysis of corroded ancient bronze objects, *Analyst* 128 (2003) 1104.
- [59] A. Adriaens, M. Dowsett, G. Jones, K. Leysens, S. Nikitenko, An in-situ X-ray absorption spectroelectrochemistry study of the response of artificial chloride corrosion layers on copper to remedial treatment, *J. Anal. At. Spectrom.* 24 (2009) 62–68.
- [60] L. Monico, G. Van Der Snickt, K. Janssens, W. De Nolf, C. Miliani, J. Verbeeck, H. Tian, H. Tan, J. Dik, M. Radepon, M. Cotte, Degradation Process of Lead Chromate in Paintings by Vincent van Gogh Studied by Means of Synchrotron X-ray Spectromicroscopy and Related Methods. 1. Artificially Aged Model Samples, *J. Anal. Chem.* 83 (2011) 1214–1223.
- [61] M. Cotte, J. Susini, V.A. Solé, Y. Taniguchi, J. Chillida, E. Checroun, P. Walter, Applications of synchrotron-based micro-imaging techniques to the chemical analysis of ancient paintings, *J. Anal. At. Spectrom.* 23 (2008) 820.
- [62] O. Schalm, K. Proost, K. De Vis, S. Cagno, K. Janssens, F. Mees, P. Jacobs, J. Caen, Manganese staining of archaeological glass: The characterization of mn-rich inclusions in leached layers and a hypothesis of its formation, *Archaeometry* 53 (2011) 103–122.
- [63] S. Padovani, D. Puzzovio, C. Sada, P. Mazzoldi, I. Borgia, a. Sgamellotti, B.G. Brunetti, L. Cartechini, F. D’Acapito, C. Maurizio, F. Shokoui, P. Oliyai, J. Rahighi, M. Laméhi-Rachti, E. Pantos, XAFS study of copper and silver nanoparticles in glazes of medieval middle-east lustreware (10th–13th century), *Appl. Phys. A* 83 (2006) 521–528.
- [64] S. Padovani, C. Sada, P. Mazzoldi, B. Brunetti, a. Giulivi, F. D’Acapito, G. Battaglin, Copper in glazes of renaissance luster pottery: Nanoparticles, ions, and local environment, *J. Appl. Phys.* 93 (2003) 10058–10063.
- [65] a. D. Smith, T. Pradell, J. Roqué, J. Molera, M. Vendrell-Saz, A.J. Dent, E. Pantos, Color variations in 13th century hispanic lustre – An EXAFS study, *J. Non. Cryst. Solids* 352 (2006) 5353–5361.
- [66] M. Sandström, F. Jalilehvand, E. Damian, Y. Fors, U. Gelius, M. Jones, M. Salomé, Sulfur accumulation in the timbers of King Henry VIII’s warship Mary Rose: a pathway in the sulfur cycle of conservation concern., *Proc. Natl. Acad. Sci. U. S. A.* 102 (2005) 14165–14170.
- [67] K. Proost, K. Janssens, B. Wagner, E. Bulska, M. Schreiner, Determination of localized Fe²⁺/Fe³⁺ ratios in inks of historic documents by means of μ -XANES, *Nucl. Instruments Methods Phys. Res. Sect. B Beam Interact. with Mater. Atoms* 213 (2004) 723–728.
- [68] M. Cotte, P. Dumas, Y. Taniguchi, E. Checroun, P. Walter, J. Susini, Recent applications and current trends in Cultural Heritage Science using synchrotron-based Fourier transform infrared micro-spectroscopy, *Comptes Rendus Phys.* 10 (2009) 590–600.
- [69] L. Bertrand, J. Doucet, P. Dumas, a Simionovici, G. Tsoucaris, P. Walter, Microbeam synchrotron imaging of hairs from ancient Egyptian mummies., *J. Synchrotron Radiat.* 10 (2003) 387–92.
- [70] P. Reischig, J. Blaas, C. Botha, A. Bravin, L. Porra, C. Nemoz, A. Wallert, J. Dik, A note on medieval microfabrication: the visualization of a prayer nut by synchrotron-based computer X-ray tomography., *J. Synchrotron Radiat.* 16 (2009) 310–3.
- [71] M.G. Dowsett, A. Adriaens, G.K.C. Jones, N. Poolton, S. Fiddy, Optically Detected X-ray Absorption Spectroscopy Measurements as a Means of Monitoring Corrosion Layers on Copper, *Anal. Chem.* 80 (2008) 8717–8724.
- [72] A. Rogalev, Goulon, in: T.K. Sham (Ed.), *Chemical Applications of Synchrotron Radiation Part*

II: X-ray Applications2, World Scientific, Singapore, 2002, pp. 707–760.

[73] R.P. Taylor, a. a. Finch, J.F.W. Mosselmans, P.D. Quinn, The development of a XEOL and TR XEOL detection system for the I18 microfocuss beamline Diamond light source, *J. Lumin.* 134 (2013) 49–58.

[74] T.-K. Sham, R. a Rosenberg, Time-resolved synchrotron radiation excited optical luminescence: light-emission properties of silicon-based nanostructures., *Chemphyschem* 8 (2007) 2557–67.

[75] P.S.G. Kim, Y. Hu, M.C. Brandys, T.J. Burchell, R.J. Puddephatt, T.K. Sham, X-ray-excited optical luminescence (XEOL) and X-ray absorption fine structure (XAFS) studies of gold(I) complexes with diphosphine and bipyridine ligands, *Inorg. Chem.* 46 (2007) 949–957.

[76] J. Maddox, The sensational discovery of X-rays, *Nature* 375 (1995) 183.

[77] T.A. Edison, Fluorescent electric lamp., (1907) US865367 A.

[78] F. Ions, V.A. Fassel, Analytical Applications of X-Ray Excited Optical Luminescence Direct Determination of Rare Earth Nuclear Poisons in Zirconia, *Anal. Biochem.* 46 (1974) 997 – 999.

[79] A.P. D'Silva, V.A. Fassel, X-ray excited optical fluorescence of trace rare earths in yttrium phosphate and yttrium vanadate hosts. Part per giga level determination of rare earth impurities in yttrium oxide, *Anal. Chem.* 45 (1973) 542–547.

[80] A.P. D'Silva, G.J. Oestreich, V.A. Fassel, X-ray Excited Optical Luminescence of Polynuclear Aromatic Hydrocarbons, *Anal. Chem.* 48 (1976) 915–917.

[81] T.K. Sham, Nanoparticles and nanowires: synchrotron spectroscopy studies, *Int. J. Nanotechnol.* 5 (2008) 1194.

[82] M. Murphy, X. Zhou, F. Heigl, T. Regier, T. Sham, An X-Ray Excited Optical Luminescence (XEOL) Analysis of Mn²⁺ Doped ZnS Nanostructures, *Nanostructures* 12–14.

[83] L. Armelao, F. Heigl, A. Ju, R.I.R. Blyth, T. Regier, X. Zhou, X-ray Excited Optical Luminescence Studies of ZnO and Eu-Doped ZnO Nanostructures, (2007) 10194–10200.

[84] F. Heigl, A. Jürgensen, X.-T. Zhou, S. Lam, M. Murphy, J.Y.P. Ko, T.K. Sham, R.A. Rosenberg, R. Gordon, D. Brewster, T. Regier, L. Armelao, Dynamic View on Nanostructures: A Technique for Time Resolved Optical Luminescence using Synchrotron Light Pulses at SRC, APS, and CLS, *AIP Conf. Proc.* (2007) 1202–1205.

[85] Z. Wang, X. Guo, T.-K. Sham, 2D XANES-XEOL

mapping: observation of enhanced band gap emission from ZnO nanowire arrays, *Nanoscale* 6 (2014) 6531.

[86] R. a. Rosenberg, G.K. Shenoy, F. Heigl, S.T. Lee, P.S.G. Kim, X.T. Zhou, T.K. Sham, Effects of in situ vacuum annealing on the surface and luminescent properties of ZnS nanowires, *Appl. Phys. Lett.* 86 (2005) 1–3.

[87] J. Li, L. Liu, T.-K. Sham, 2D XANES–XEOL Spectroscopy Studies of Morphology-Dependent Phase Transformation and Corresponding Luminescence from Hierarchical TiO₂ Nanostructures, *Chem. Mater.* 27 (2015) 3021–3029.

[88] N. Daldosso, F. Rocca, I.P. Trento, New EXAFS Measurements by XEOL and TEY on Porous Silicon, *J. Porous Mater.* 172 (2000) 169–172.

[89] N. Daldosso, G. Dalba, P. Fornasini, R. Grisenti, F. Rocca, Size and surface effects in porous silicon studied by X-ray absorption spectroscopy, *Phys. Status Solidi a-Applied Res.* 102 (2003) 98–102.

[90] N. Daldosso, M. Luppi, S. Ossicini, E. Degoli, R. Magri, G. Dalba, P. Fornasini, R. Grisenti, F. Rocca, L. Pavesi, S. Boninelli, F. Priolo, C. Spinella, F. lacona, Role of the interface region on the optoelectronic properties of silicon nanocrystals embedded in SiO₂, *Phys. Rev. B* 68 (2003) 085327.

[91] J. Zhou, X. Zhou, R. Li, X. Sun, Z. Ding, J. Cutler, T.-K. Sham, Electronic structure and luminescence center of blue luminescent carbon nanocrystals, *Chem. Phys. Lett.* 474 (2009) 320–324.

[92] Y. Hu, A. MacLennan, T.K. Sham, Electronic structure and optical luminescence studies of Ru based OLED compounds, *J. Lumin.* 166 (2015) 143–147.

[93] P.-S.G. Kim, N.O. Petersen, T.K. Sham, Y.F. Hu, Soft X-ray excited optical luminescence (XEOL) studies of fluorescein isothiocyanate (FITC) and FITC-labeled proteins, *Chem. Phys. Lett.* 392 (2004) 44–49.

[94] M.J. Ward, W. Han, T. Sham, 2D XAFS - XEOL Mapping of Ga_{1-x}Zn_xN_{1-x}O_x Nanostructured Solid Solutions, *J. Phys. Chem. C* 115 (2011) 20507–20514.

[95] T.-K. Sham, Photon-in/photon-out spectroscopic techniques for materials analysis: some recent developments., *Adv. Mater.* 26 (2014) 7896–901.

[96] M. Dowsett, M. Hand, P.-J. Sabbe, P. Thompson, A. Adriaens, XEOM 1 - A novel microscopy system for the chemical imaging of heritage metal surfaces, *Herit. Sci.* 3 (2015) 14.

[97] A. Bianconi, D. Jackson, K. Monahan, Intrinsic luminescence excitation spectrum and extended x-ray absorption fine structure above the K-edge in

- CaF₂, Phys. Rev. B 17 (1978) 2022–2024.
- [98] J. Goulon, P. Tola, M. Lemonnier, J. Dexpert-Ghys, On a site-selective exafs experiment using optical emission, Chem. Phys. 78 (1983) 347–356.
- [99] L. Soderholm, G.K. Liu, M.R. Antonio, X-ray excited optical luminescence (XEOL) detection of x-ray absorption fine structure (XAFS), J. Chem. Phys. 109 (1998) 6745 – 6752.
- [100] A. Adriaens, P. Quinn, S. Nikitenko, M.G. Dowsett, Real Time Observation of X-ray-Induced Surface Modification Using Simultaneous XANES and XEOL-XANES., Anal. Chem. 85 (2013) 9556–9563.
- [101] M. Hand, Development of an X-ray Excited Optical Luminescence Microscope (XEOM) Ph.D. Dissertation, University of Warwick, June 2014.
- [102] M. Dowsett, A. Adriaens, Cell for simultaneous synchrotron radiation X-ray and electrochemical corrosion measurements on cultural heritage metals and other materials., Anal. Chem. 78 (2006) 3360–5.
- [103] P.-J. Sabbe, M. Dowsett, M. Hand, R. Grayburn, P. Thompson, W. Bras, A. Adriaens, Evaluation of an X - ray-Excited Optical Microscope for Chemical Imaging of Metal and Other Surfaces, Anal. Chem. 86 (2014) 11789–11796.
- [104] F. Adams, C. Barbante, *X-Ray Imaging*, 2015.
- [105] J. Baruchel, P. Bleuet, A. Bravin, P. Coan, E. Lima, A. Madsen, W. Ludwig, P. Pernot, J. Susini, Advances in synchrotron hard X-ray based imaging, Comptes Rendus Phys. 9 (2008) 624–641.
- [106] I.M. Ternov, Synchrotron radiation: basics, methods and applications., Uspekhi Fiz. Nauk 165 (1995) 429.
- [107] W. Chao, B.D. Harteneck, J.A. Liddle, E.H. Anderson, D.T. Attwood, Soft X-ray microscopy at a spatial resolution better than 15 nm, Nature 435 (2005) 1210–1213.
- [108] L. Alianelli, D. Laundry, S. Alcock, J. Sutter, K. Sawhney, Development of Hard X-ray Focusing Optics at Diamond Light Source, Synchrotron Radiat. News 29 (2016) 3–9.
- [109] C.G. Schroer, G. Falkenberg, Hard X-ray nanofocusing at low-emittance synchrotron radiation sources, J. Synchrotron Radiat. 21 (2014) 996–1005.
- [110] T. Sham, R. Gordon, RIXS, XEOL and XEOL Imaging of Rare-earth Phosphors at the L_{3,2}-edges., AIP Conf. Proc. 1234 (2010) 133–136.
- [111] F. Meirer, Y. Liu, E. Pouyet, B. Fayard, M. Cotte, C. Sanchez, J.C. Andrews, A. Mehta, P. Sciau, Full-field XANES analysis of Roman ceramics to estimate firing conditions—A novel probe to study hierarchical heterogeneous materials, J. Anal. At. Spectrom. 28 (2013) 1870.
- [112] P. Tack, J. Garrevoet, S. Bauters, B. Vekemans, B. Laforce, E. Van Ranst, D. Banerjee, A. Longo, W. Bras, L. Vincze, Full-Field Fluorescence Mode Micro-XANES Imaging Using a Unique Energy Dispersive CCD Detector., Anal. Chem. (2014).
- [113] M.E. Nasir, B. Hamilton, D.W.E. Allsop, Optical measurements of nanoporous anodic alumina formed on Si using novel X-ray spectroscopy set up CLASSIX, Nucl. Instruments Methods Phys. Res. Sect. B Beam Interact. with Mater. Atoms 268 (2010) 251–253.
- [114] F. Quinn, N. Poolton, A. Malins, E. Pantos, C. Andersen, P. Denby, V. Dhanak, G. Miller, The Mobile Luminescence End-Station , MoLES: a new public facility at Daresbury Synchrotron research papers, (2003) 461–466.
- [115] G. Martínez-Criado, B. Alen, a. Homs, a. Somogyi, C. Miskys, J. Susini, J. Pereira-Lachataignerais, J. Martínez-Pastor, Scanning x-ray excited optical luminescence microscopy in GaN, Appl. Phys. Lett. 89 (2006) 221913.
- [116] O. Vyvenko, T. Arguirov, W. Seifert, I. Zizak, M. Trushin, M. Kittler, Scanning X-ray excited optical luminescence microscopy of multi-crystalline silicon, Phys. Status Solidi Appl. Mater. Sci. 207 (2010) 1940–1943.
- [117] G. Martínez-Criado, B. Alén, J. a. Sans, a. Homs, I. Kieffer, R. Tucoulou, P. Cloetens, J. Segura-Ruiz, J. Susini, J. Yoo, G. Yi, Spatially resolved X-ray excited optical luminescence, Nucl. Instruments Methods Phys. Res. Sect. B Beam Interact. with Mater. Atoms 284 (2012) 36–39.
- [118] G. Martínez-Criado, J.A. Sans, J. Segura-Ruiz, R. Tucoulou, A. V. Solé, A. Homs, J. Yoo, J.G.-C. Yi, B. Alén, X-ray excited optical luminescence imaging of InGaN nano-LEDs, Phys. Status Solidi 9 (2012) 628–630.
- [119] M. Ishii, T. Uchihashi, X-ray absorption measurement by scanning capacitance microscopy, Phys. B Condens. Matter 340-342 (2003) 1142–1146.
- [120] M. Ishii, Y. Tanaka, T. Ishikawa, S. Komuro, T. Morikawa, Y. Aoyagi, Site-selective x-ray absorption fine structure analysis of an optically active center in Er-doped semiconductor thin film using x-ray-excited optical luminescence, Appl. Phys. Lett. 78 (2001) 183.
- [121] S. Larcheri, F. Rocca, D. Pailharey, F. Jandard, R. Graziola, a Kuzmin, R. Kalendarev, J. Purans, A new tool for nanoscale X-ray absorption spectroscopy and element-specific SNOM microscopy., Micron 40 (2009) 61–5.
- [122] S. Larcheri, F. Rocca, F. Jandard, D. Pailharey,

- R. Graziola, A. Kuzmin, J. Purans, X-ray excited optical luminescence detection by scanning near-field optical microscope: A new tool for nanoscience, *Rev. Sci. Instrum.* 79 (2008).
- [123] D. Pailharey, Y. Mathey, F. Jandard, S. Larcheri, F. Rocca, a Kuzmin, R. Kalendarev, J. Purans, G. Dalba, R. Graziola, O. Dhez, Nanoscale x-ray absorption spectroscopy using XEOL-SNOM detection mode, *J. Phys. Conf. Ser.* 93 (2007) 012038.
- [124] N. Poolton, B. Towlson, B. Hamilton, D. Evans, New instrumentation for micro-imaging X-ray absorption spectroscopy using optical detection methods, *Nucl. Instruments Methods Phys. Res. Sect. B Beam Interact. with Mater. Atoms* 246 (2006) 445–451.
- [125] N.R.J. Poolton, L. Botterjensen, P. Denby, T. Nakamura, B. Hamilton, E. Pantos, High-sensitivity instrumentation for spectrally-resolved optically detected X-ray absorption spectroscopy, *Nucl. Instruments Methods Phys. Res. Sect. B Beam Interact. with Mater. Atoms* 225 (2004) 590–598.
- [126] N.R.J. Poolton, B.M. Towlson, D.A. Evans, B. Hamilton, Synchrotron–laser interactions in hexagonal boron nitride: an examination of charge trapping dynamics at the boron K -edge, *New J. Phys.* 8 (2006) 76–76.
- [127] R. a Rosenberg, S. Zohar, D. Keavney, R. Divan, D. Rosenmann, a Mascarenhas, M. a Steiner, Elemental and magnetic sensitive imaging using x-ray excited luminescence microscopy., *Rev. Sci. Instrum.* 83 (2012) 073701.
- [128] G.J. Nelson, W.M. Harris, J.R. Izzo, K.N. Grew, W.K.S. Chiu, Y.S. Chu, J. Yi, J.C. Andrews, Y. Liu, P. Pianetta, Three-dimensional mapping of nickel oxidation states using full field x-ray absorption near edge structure nanotomography, *Appl. Phys. Lett.* 98 (2011) 10–13.
- [129] Y. Liu, J.C. Andrews, J. Wang, F. Meirer, P. Zhu, Z. Wu, P. Pianetta, Phase retrieval using polychromatic illumination for transmission X-ray microscopy., *Opt. Express* 19 (2011) 540–545.
- [130] Y. Liu, F. Meirer, J. Wang, G. Requena, P. Williams, J. Nelson, A. Mehta, J.C. Andrews, P. Pianetta, 3D elemental sensitive imaging using transmission X-ray microscopy, *Anal. Bioanal. Chem.* 404 (2012) 1297–1301.
- [131] G. Schneider, P. Guttmann, S. Heim, S. Rehbein, F. Mueller, K. Nagashima, J.B. Heymann, W.G. Müller, J.G. McNally, Three-dimensional cellular ultrastructure resolved by X-ray microscopy., *Nat. Methods* 7 (2010) 985–987.
- [132] G. Silversmit, B. Vekemans, K. Appel, S. Schmitz, T. Schoonjans, F.E. Brenker, F. Kaminsky, L. Vincze, Three-Dimensional Fe Speciation of an Inclusion Cloud within an Ultradeep Diamond by Confocal mu-X-ray Absorption Near Edge Structure: Evidence for Late Stage Overprint, *Anal. Chem.* 83 (2011) 6294–6299.
- [133] G. Silversmit, B. Vekemans, S. Nikitenko, S. Schmitz, T. Schoonjans, F.E. Brenker, L. Vincze, Spatially resolved 3D micro-XANES by a confocal detection scheme, *Phys. Chem. Chem. Phys.* 12 (2010) 5503.
- [134] C.G. Ryan, R. Kirkham, R.M. Hough, G. Moorhead, D.P. Siddons, M.D. de Jonge, D.J. Paterson, G. De Geronimo, D.L. Howard, J.S. Cleverley, Elemental X-ray imaging using the Maia detector array: The benefits and challenges of large solid-angle, *Nucl. Instruments Methods Phys. Res. Sect. A Accel. Spectrometers, Detect. Assoc. Equip.* 619 (2010) 37–43.
- [135] L. Monico, K. Janssens, M. Alfeld, M. Cotte, F. Vanmeert, C.G. Ryan, G. Falkenberg, D.L. Howard, B.G. Brunetti, C. Miliani, Full spectral XANES imaging using the Maia detector array as a new tool for the study of the alteration process of chrome yellow pigments in paintings by Vincent van Gogh, *J. Anal. At. Spectrom.* 30 (2015) 613–626.
- [136] M. a. Marcus, X-ray photon-in/photon-out methods for chemical imaging, *TrAC - Trends Anal. Chem.* 29 (2010) 508–517.
- [137] M. Moini, C.M. Rollman, L. Bertrand, Assessing the impact of synchrotron X-ray irradiation on proteinaceous specimens at macro and molecular levels., *Anal. Chem.* 86 (2014) 9417–22.
- [138] P. O'Neill, D.L. Stevens, E. Garman, Physical and chemical considerations of damage induced in protein crystals by synchrotron radiation: a radiation chemical perspective, *J. Synch. Rad.* 9 (2002) 329–332.
- [139] L. Bertrand, S. Schöeder, D. Anglos, M.B.H. Breese, K. Janssens, M. Moini, A. Simon, Mitigation strategies for radiation damage in the analysis of ancient materials, *TrAC Trends Anal. Chem.* 66 (2015) 128–145.
- [140] A. Zucchiatti, F. Agullo-Lopez, Potential consequences of ion beam analysis on objects from our cultural heritage: An appraisal, *Nucl. Instruments Methods Phys. Res. Sect. B-Beam Interact. with Mater. Atoms* 278 (2012) 106–114.
- [141] M. Sandström, F. Jalilehvand, I. Persson, U. Gelius, P. Frank, I. Hall-Roth, Deterioration of the seventeenth-century warship Vasa by internal formation of sulphuric acid., *Nature* 415 (2002) 893–897.
- [142] M. Mantler, J. Klikovits, Analysis of art objects and other delicate samples: Is XRF really non-destructive ?, *Powder Diffr.* 19 (2004) 16–20.

[143] G.D. Richards, R.S. Jabbour, C.F. Horton, C.L. Ibarra, A.A. MacDowell, Color changes in modern and fossil teeth induced by synchrotron microtomography, *Am. J. Phys. Anthropol.* 149 (2012) 172–180.

[144] M. Wilke, O. Hahn, A.B. Woodland, K. Rickers, The oxidation state of iron determined by Fe K-edge XANES—application to iron gall ink in historical manuscripts, *J. Anal. At. Spectrom.* 24 (2009) 1364.

[145] C. Gervais, M.-A. Languille, S. Reguer, M. Gillet, E.P. Vicenzi, S. Chagnot, F. Baudelet, L. Bertrand, “Live” Prussian blue fading by time-resolved X-ray absorption spectroscopy, *Appl. Phys. A* 111 (2013) 15–22.

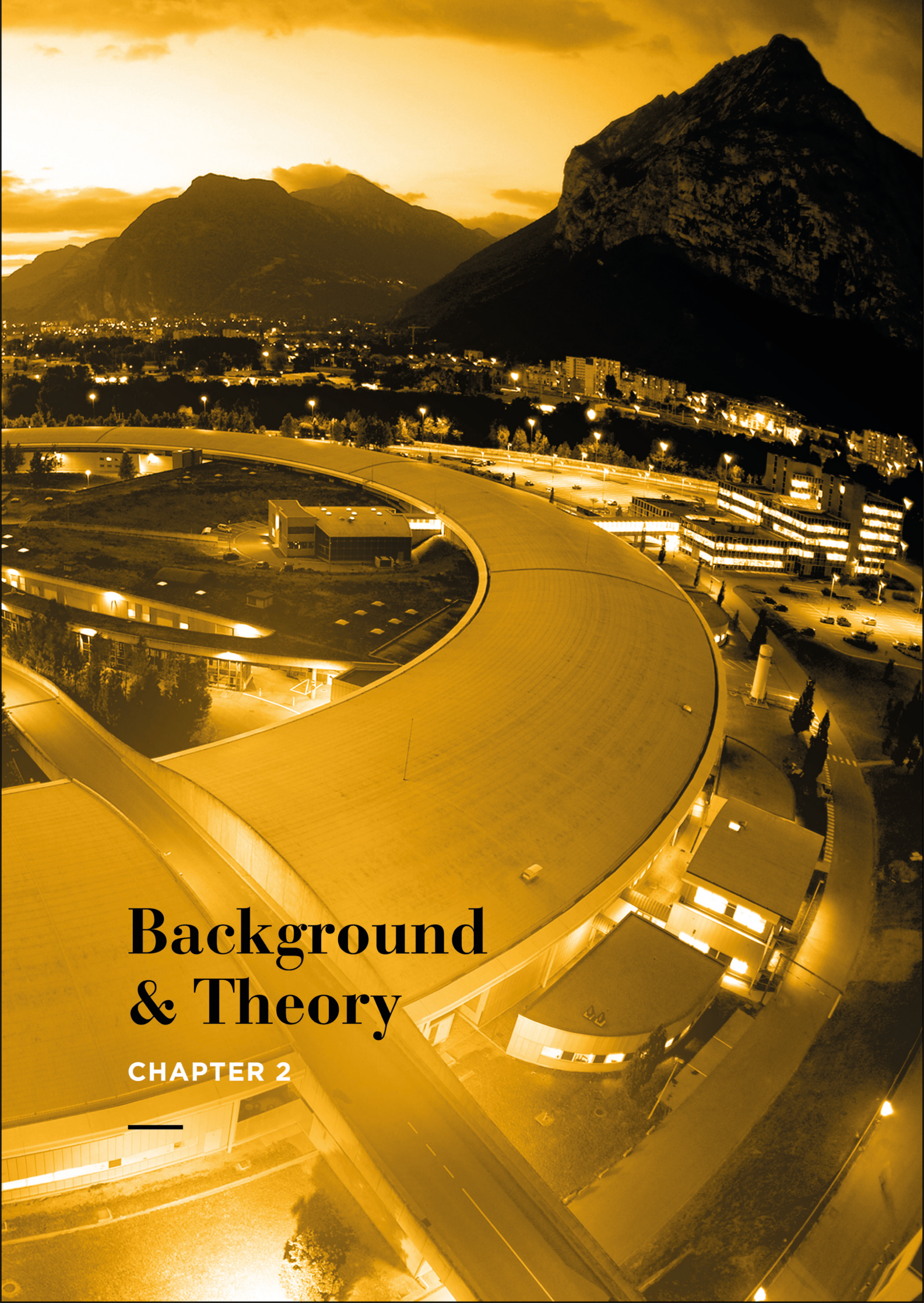
[146] D. Jaque, *An Introduction to the An Introduction to the Optical Spectroscopy*, 2005.

[147] L. Bertrand, D. Vantelon, E. Pantos, Novel interface for cultural heritage at SOLEIL, *Appl. physics. A, Mater. Sci. & Process.* 83 (2006) 225–228.

[148] J.F.W. Mosselmans, R.P. Taylor, P.D. Quinn, a Finch, G. Cibin, D. Gianolio, a V Sapelkin, A time resolved microfocus XEOL facility at the Diamond Light Source, *J. Phys. Conf. Ser.* 425 (2013) 182009.

[149] G. Martínez-Criado, B. Alén, J.A. Sans, A. Homs, I. Kieffer, R. Tucoulou, P. Cloetens, J. Segura-Ruiz, J. Susini, J. Yoo, G. Yi, Spatially resolved X-ray excited optical luminescence, *Nucl. Instruments Methods Phys. Res. Sect. B Beam Interact. with Mater. Atoms* 284 (2012) 36–39.

[150] A. Dupage, J. Teller, E. Dumont, Pro-Active Mangagement of the Impact of Cultural Tourism upon Urban Resources and Economics, [accessed 12/01/2016].

An aerial night photograph of a large, curved, illuminated building complex, possibly a university or government building. The building is illuminated from within, and its curved roofline is prominent. In the background, a city is visible with lights, and a large, dark mountain range dominates the upper portion of the image. The sky is a warm, golden yellow, suggesting sunset or sunrise. The overall scene is bathed in a warm, golden light.

Background & Theory

CHAPTER 2

Although this manuscript is an account of the research done in the last 5 years or so, the basic concepts which underpin the work, such as chemical imaging and the induction of optical light by X-rays, arose together with the first encounter of X-rays over a century ago. In chapter 2, the description of these basic concepts is given. The chapter opens with a description of synchrotron radiation and is followed by an explanation of the basic principles of X-ray absorption spectroscopy (XAS) and X-ray-excited optical luminescence (XEOL), two techniques which compose the physical foundation of XEOM. Finally, information regarding auxiliary techniques used in this work is covered in a section at the end of this chapter.

2.1 SYNCHROTRON RADIATION

2.1.1 X-RAYS

2.1.1.1 Discovery

X-rays were discovered in 1895 by Wilhelm Conrad Röntgen (Figure 2.1 A) at the University of Würzburg, Bavaria. He found that when running a high-voltage discharge tube (Crookes tube) enclosed in a thick black paper excluding all visible stray light, a green glow was emitted by a remotely positioned fluorescent screen containing crystals of barium platinocyanide ($\text{BaPt}(\text{CN})_4$) [1, 2]. Ironically, this observation of the optical activity from the fluorescent screen by Röntgen is also the first description of the observation of X-ray-excited optical luminescence (XEOL), a phenomenon which plays a pivotal role in this thesis. Investigating the cause of this green glow, Röntgen concluded that the discharge must have created a new form of invisible radiation with a strong penetrating character that could escape the confines of the glass discharge tube and its surrounding covering. To highlight the unknown nature of this new type of radiation, Röntgen referred to it as 'X' -rays [3]. The penetrating power of X-rays and their ability to stain photographic plates were recognized early on by Röntgen and led quickly to a first application exploiting these features. In radiography, the earliest sort of X-ray based chemical imaging: internal structures are visualized through the various X-ray absorption properties of different materials. For a given energy, materials with a higher electron density tend to absorb more X-rays than those with lower electron density [4]. This is clearly visible in one of the most famous images in photographic history, the radiographic image of the hand of Röntgen's wife Anna Berthe Ludwig (Figure 2.1 B). The image displays finger and hand bones as well as a ring which correspond to darker areas in the radiograph as a consequence of the higher X-ray absorbing nature of the calcium phosphates in the bones and presumably the gold in the ring. The boney structure

is surrounded by the penumbra of the flesh, composed mainly of low electron density elements (H, C, N, O and P) hence throwing a fainter shadow onto the photographic plate [4].

For his discovery Röntgen was awarded the first Nobel Prize in physics in 1901 [5]. It was the first of six to be awarded in the field of X-rays by 1927.



Figure 2.1

[A] Wilhelm Conrad Röntgen (27 March 1845 – 10 February 1923).
Source : <https://commons.wikimedia.org/wiki/File:Roentgen2.jpg>

[B] 'Hand mit Ringen' (Hand with Rings) , first X-ray photogram of the left hand of Anna Bertha Ludwig taken on December 22, 1895. The darker areas correspond to the finger and hand bones and to the ring around Anna Bertha Ludwig's ring finger.
source : <http://science.hq.nasa.gov/kids/imagers/ems/xrays.html>

2.1.1.2 Properties of X-rays

X-rays are a type of shortwave electromagnetic radiation not produced through nuclear decay which exhibits wavelengths typically between 0.01 and 10 nm. The wavelength range corresponds approximately to the energy range of 0.12 to 123 keV or to the frequency range of 3×10^{16} Hz – 3×10^{19} Hz [6]. Wavelength, energy and frequency scale are mutually convertible via Equation {2.1}:

$$E = h\nu = \frac{hc}{\lambda}, \quad \{2.1\}$$

where $h = 6.626 \times 10^{-34}$ J.s is Planck's constant, ν is the frequency of the radiation in Hz, $c = 2.9979 \times 10^8$ m.s⁻¹ is the speed of light in vacuum and λ is the wavelength of light in vacuum, given in metres [6, 7].

Within the X-ray region an arbitrary subdivision can be made between hard and soft X-rays: X-rays with a photon energy below 10 keV are considered as soft X-rays while radiation in the 10 – 100 keV are considered as hard X-rays.

2.1.2 SYNCHROTRON RADIATION: A STORY PASSED DOWN FROM GENERATION TO GENERATION

The most versatile source of X-rays used for a wide range of spectroscopic applications and other techniques is undoubtedly the synchrotron radiation source. The spectrum produced, depending on the beam line, extends from the far infrared to the hard X-ray regime, with intensities many of orders of magnitude greater than those produced by laboratory-based sources [8]. Ironically, the unique properties of synchrotron radiation were not recognized at the moment of their initial observation, the 24th of April 1947 at the General Electric Research Laboratory in Schenectady (New York) [9]. At first, synchrotron radiation was regarded as a redundant side effect and an unavoidable source of energy loss in particle accelerators for high energy physics research. Later on, after Tomboulion and Hartman [10, 11] reported the advantages of synchrotron radiation, this perception shifted and the utility of synchrotron radiation was recognized. Ever since, the design of synchrotron facilities has gone through several updates, each defining the start of a new synchrotron generation [12].

- **First generation :**

First generation synchrotron facilities are sometimes referred as parasitic facilities, as these synchrotrons were primarily built as particle accelerators for high-energy and nuclear physics experiments such as particle collision experiments [13]. SURF I (Synchrotron Ultraviolet Radiation Facility I, National Institute of Standards and Technology, Gaithersburg, Maryland) is considered as the first facility for regular users of synchrotron radiation.

- **Second generation:**

The advancement towards efficient electron storage rings for long-term operation initiated the second generation in synchrotron facilities [13]. The SRS (Synchrotron Radiation Source, Daresbury, UK, 2 GeV) facility is regarded as the first dedicated facility built for the production of synchrotron radiation mainly in the X-ray energy range (1981) [14].

- **Third generation:**

The progression towards third generation synchrotrons came along with the inclusion of insertion devices (wigglers and undulators, see below) in the storage ring [8, 13]. These devices were added to obtain optimum brilliance (amount of power per unit frequency, surface area and solid angle, see below). The first 3rd generation facility was completed in 1994 and was the European Synchrotron Radiation facility (ESRF, Grenoble, France, 6 GeV) [15], also the synchrotron where all the experiments described in this thesis have been conducted.

Now there are over 50 synchrotron light sources around the world carrying out a huge range of experiments with applications in a wide variety of research fields [16]. Beyond this, a next generation of synchrotrons is coming of age, in which an even greater brilliance and coherence is pursued. The current drive is towards the achievement of an additional 3 to 10 orders of magnitude in peak brilliance over modern 3rd generation synchrotrons, by the addition of so-called energy recovery linacs (ERLs) and free electron lasers (FELs) [17].

2.1.3 RADIATION FROM RELATIVISTIC ELECTRONS

Accelerating charged particles spontaneously emit electromagnetic radiation [18]. Synchrotron radiation is the result of transverse acceleration of charged particles producing motion in a curved path. In a synchrotron facility, relativistic charged particles are forced to follow a curved trajectory which results in the emission of radiation in a narrow pencil-like beam in the same direction of the electron motion (Figure 2.2) [13]. The radiation received by an experimental station, positioned tangentially to the synchrotron storage ring, will be subjected to an enormous relativistic Doppler shift in which its wave fronts are intensely compressed. Consequently the wavelength of the emission is shifted towards the X-ray regime [8, 13].

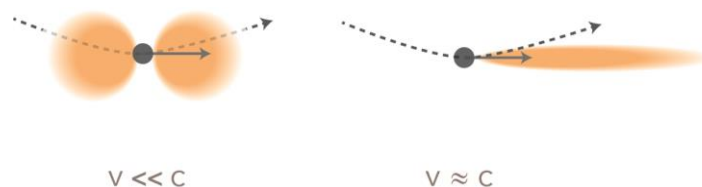


Figure 2.2

Electromagnetic radiation emitted by charged particles being accelerated to travel at velocities in the sub-relativistic regime ($v \ll c$) display an isotropic dipole radiation pattern. In contrast, particles travelling closely to the speed of light emit electromagnetic radiation in a very narrow cone in the direction of the travelling electrons.

The synchrotron-produced X-rays have unique properties that make them extremely advantageous over other X-ray sources [8]. These unique properties are:

- **High intensity and spectral brightness**

SR-beam intensities are many orders of magnitude higher than those produced by conventional X-ray sources. This can enable measurements to be conducted at great speed and with superior statistics. Intensity of synchrotron radiation can be quantified by the Flux F which is the number of photons per time and energy interval:

$$F = \frac{\text{photons}}{\text{s} \cdot (0.1\% \text{ bandwidth})}. \quad \{2.2\}$$

The quality of a photon source must be evaluated based upon the effectiveness for practical applications. Although the possibility of radiation damage must not be underestimated (see Chapter 1), high flux beams concentrated into a small beam footprint can serve many applications. Synchrotron intensity is characterized through spectral brightness B , a quantity sometimes referred to as '*Brilliance*', in which the photon flux emitted per second per bandwidth per unit solid angle and unit source area are taken into account [19]:

$$B = \frac{\text{photons}}{\text{s} \cdot \text{mm}^2 \cdot \text{mrad}^2 \cdot (0.1\% \text{ bandwidth})}. \quad \{2.3\}$$

Synchrotron sources possess high spectral brightness because of their high flux and low angular divergence

- **Broad spectral range**

The range of electromagnetic radiation which can be addressed by a synchrotron is very broad going from infrared up to hard X-rays. Narrow bands from this broad spectral range can be accessed with a monochromator (see below).

- **High degree of polarization**

The polarization of the X-rays coming from the storage ring depends on the point of observation. In the plane of the electron beam orbit, the radiation is mostly linearly polarized [20]. Within the range of few milliradians away from the orbital plane of the electron beam, elliptically polarized emission can be observed. Both types of polarization can be important for specific experiments, e.g. background reduction in X-ray emission type experiments.

- **Pulsed time structure**

Synchrotron light is not continuously emitted but has a pulsed time structure in which short bursts of X-rays (typically below 0.1 ns) are separated by narrow time windows in which radiation is absent (typically ns up to μ s). A pulsed beam structure is required when radiofrequency cavities (see below) are used for electrodynamic acceleration of the electrons in the storage ring in order to maintain the beam energy. An example, relevant to the analytical technique XEOL used in this thesis, which benefits from the time resolution in SR is: Time-resolved X-ray excited optical luminescence (TRXEOL) [21, 22]. TRXEOL is an analytical tool which exploits the pulsing character of a synchrotron source in order to determine the lifetime of an excited state that emits optical photons in light-emitting materials [22].

2.1.4 DESIGN OF A THIRD GENERATION SYNCHROTRON

Figure 2.3 displays a schematic representation of the most important components of a modern (3rd generation) synchrotron source [8]. The five main components which can be encountered in such a facility are discussed in more detail below.

Electron gun & linear accelerator

The charged particles most commonly used to produce radiation with synchrotrons are electrons. Free electrons are normally generated by thermionic emission from a hot filament of an electron gun and are directly injected into a linear accelerator (LINAC). The LINAC pre-accelerates the electrons to about 100 MeV before they are injected into a booster ring [23].

Booster ring

A booster ring receives electrons from the LINAC and further accelerates the electrons until they achieve the energy of the electrons in the main storage ring (GeV regime, e.g. ESRF = 6 GeV). When the electrons have obtained a relativistic speed, they are periodically injected into the main storage ring to maintain storage ring current as the electrons lose energy during their residence in the storage ring. Beam refill occurs typically when the ring current has dropped to 70% of its initial value. Users always have to bear in mind beam refills when planning a long experiment, as the experiment has to be suspended during injection of electrons into the storage ring. A new trend is to operate the synchrotron in 'top-up' mode, in which the ring current is quasi-continuous due to frequent (every 2 minutes) small injections from the booster ring into the storage ring [8, 13, 23].

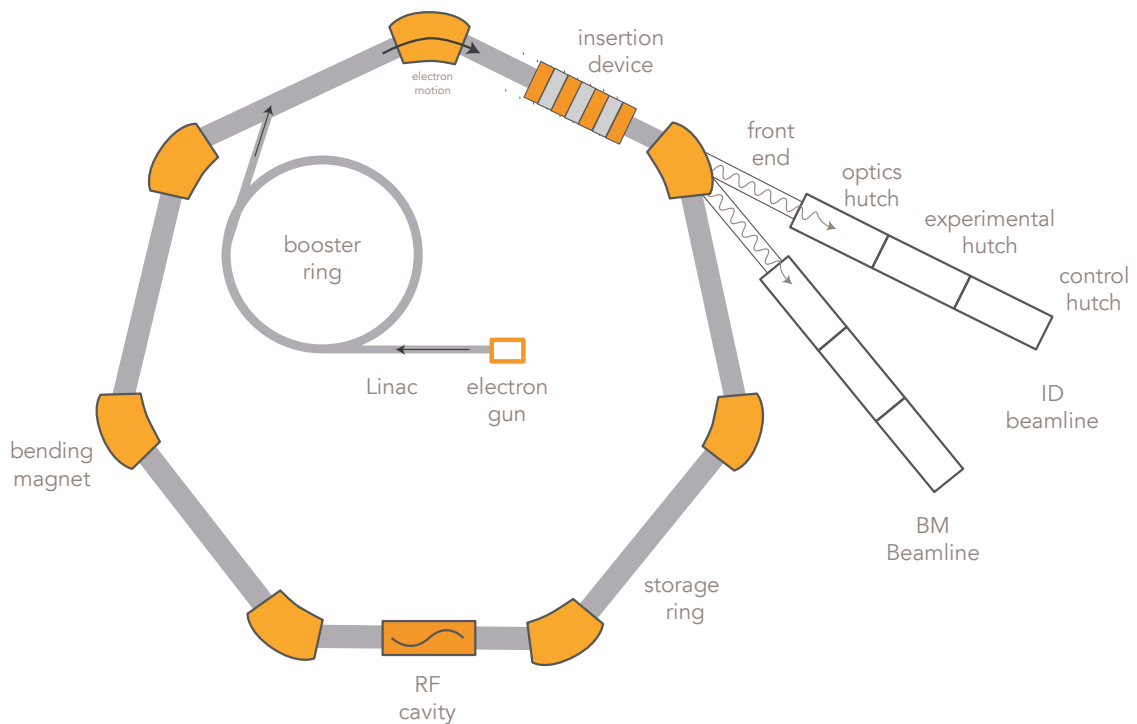


Figure 2.3

Schematic representation of the major components of a modern third generation synchrotron facility. One must bear in mind that the components depicted are not to scale and in reality the number of arced and straight sections is much greater.

Illustration after Figure 3.1 in P. Wilmott, 'An introduction to Synchrotron Radiation: techniques and applications', 2011, page 41.

storage ring

The storage ring incorporates a magnet lattice, in which an array of magnets is placed in a closed circular path to guide the relativistic electrons introduced by the booster ring. Typically, the circumference of the ring is hundreds of meters, e.g. the ESRF has a circumference of 843 m [15]. An ultra-high vacuum tube system connects the elements from the magnet lattice, hence maintaining the high energy of the relativistic electrons by preventing collision with gas molecules. Three types of magnets (Figure 2.4) can be encountered in the storage ring which help to keep the electrons in a closed orbit [8, 13, 23]:

- **dipole or bending magnet (BM):** The primary use of a BM is to deflect the path of the high energetic electrons and maintain its closed, circular character. As described below into more detail, a bending magnet is also a source of electromagnetic radiation.

- **Quadrupole magnet:** Quadrupole magnets act as beam shaping elements. Bending magnets introduce divergence in the electron beam. Quadrupole magnets are placed before and after a bending magnet to compensate for this effect, hence also maintaining a high particle density in the storage ring.
- **Sextupole magnet:** Sextupole magnets, named after their design with six opposing magnets, complement quadrupole magnets and correct for chromatic aberrations created during the focusing process of the quadrupole magnets.

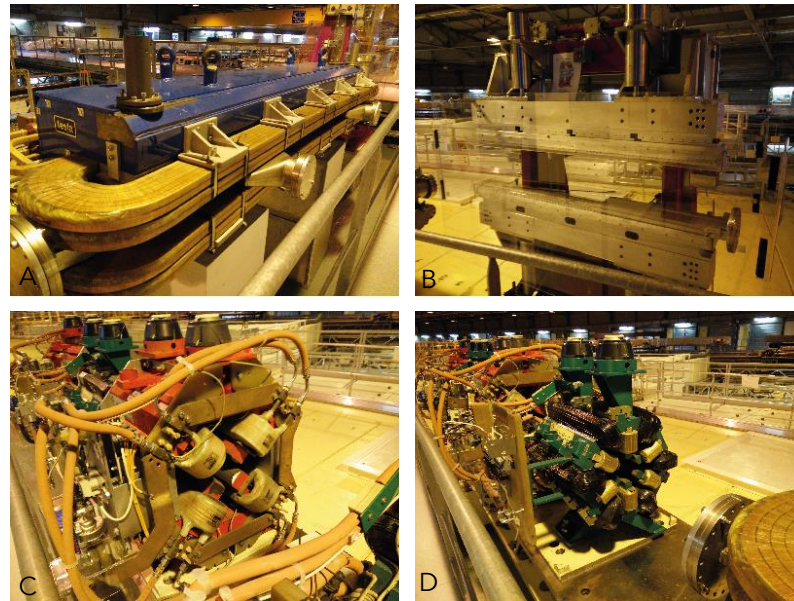


Figure 2.4

Pictures taken of bending magnet (A), undulator (B), quadrupole magnet (C) and hexapole magnet (D) on display in the experimental hall of the ESRF. (Thanks to Stephen Bauters ©)

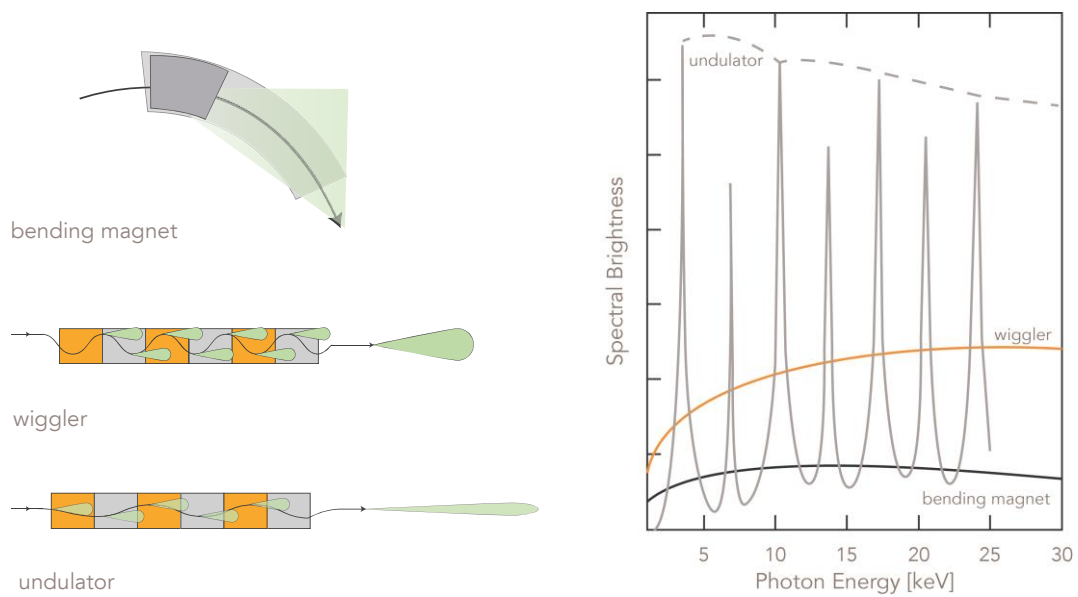
Indispensable parts of the storage ring are the magnetic structures which serve as the source of electromagnetic radiation. Bending magnets (BM) and Insertion devices (ID) fall into this category (Figure 2.5):

- **Bending magnets:** Synchrotron radiation is emitted when the relativistic electrons are accelerated by the Lorentz force arising upon passage through the magnetic field of the bending magnet. The bending-magnet radiation retains a flattened cone shape with a cone angle determined by the angular change of the electron path and the natural photon beam divergence [8, 13, 23]. Radiation by a bending magnet is emitted in a broad spectrum reaching, in principle, from microwaves up to the critical photon energy after which the intensity rapidly declines. A photon flux of $10^{12} - 10^{14} \text{ s}^{-1}$ with X-rays in the hard X-ray regime could be expected from a bending magnet which is approximately a factor of $10^4 - 10^5$ greater than a laboratory source. Nevertheless, as can be seen in Figure 2.5 B [24], bending magnets provide a limited

spectral brightness as compared to wigglers and undulators , which will be discussed in the next section.

- **Insertion devices:** Insertion devices (ID) are periodic magnetic structures installed in the straight sections of the storage ring and characterize 3rd generation synchrotrons. Electrons passing through the array of dipole magnets with alternating polarity start to oscillate perpendicularly to the direction of their motion and therefore emit synchrotron radiation during each individual wiggle [13]. Insertion devices are of two kinds: *wigglers* and *undulators* [25]. The devices are distinguished from one another by the strength of the amplitude of the induced oscillations by the magnetic structures. Wiggler radiation is the result of relativistic electrons ‘wiggling’ around their straight path in such a fashion that the excursions of the wiggling electron are significantly larger than the natural cone angle ($1/\gamma$) of the synchrotron radiation [8]. As a result, no overlap can occur between the radiation cone of each wiggle and the total radiation observed is the incoherent sum of the radiation emitted by each individual pole. Therefore the overall characteristics of the beam are similar to those of a bending magnet with the same magnetic field, but the intensity increased by a factor $2N$, with N representing the number of poles of the magnetic structure (Figure 2.5).

In contrast, undulator radiation is produced by a multipole magnet causing the electron to undulate through excursions smaller than the natural opening angle $1/\gamma$ [13]. Hence, radiation cones overlap and interfere coherently producing highly collimated and extremely bright radiation with a set of spectrally narrow peaks (a fundamental one and harmonics). The intensity of undulator radiation is increased by a factor equal to the square of the number of poles, N^2 , with respect to bending magnet radiation [8].



[A]

[B]

Figure 2.5

[A] Schematic illustration depicting the radiation characteristics of a Bending Magnet and the Insertion devices like a wiggler and an undulator.

[B] Brilliance of radiation emitted by different EM sources in a synchrotron: bending magnet, wiggler and undulators. Reproduced from [24].

Radio-frequency (RF) cavity

Radio-frequency cavities are necessary to maintain the orbital energy of the electrons in the storage ring and hence the stability of the orbiting electron bunches. The radiofrequency cavity system restores the kinetic energy, lost by the electrons due to emission of synchrotron radiation at the bending magnets and insertion devices. Electron energy is restored by providing the electrons a small boost during every passage through the radio-frequency cavity. [8, 13, 23].

Beam line

The experimental stations installed tangentially to the storage ring after a bending magnet or after an insertion device in a straight section are beam lines and are discussed into more detail in section 2.1.5.

2.1.5 BEAM LINE LAYOUT

The beam lines of a synchrotron are the experimental stations where scientists set up their experiments and collect data. Each beam line maintains components that depend on the experimental methods for which they are used. Figure 2.6 displays typical components found on a beam line.

Generally, a synchrotron beam line can be divided in two main parts : the optical section and the experimental station [8]. The optical section is connected with the storage ring through the beam line *front end*, a term generally used to describe the beam line components in the ring tunnel. The instruments installed in the front end are necessary for: positioning of the beam, to define angular acceptance, to block superfluous Bremsstrahlung radiation and filter out unwanted low-energy radiation. Just after the front end, a low absorbing window (typically made from beryllium or a polymer) is installed to interface the beam line and storage ring vacuums. Slits and apertures are also present in the optical section, they are used to define the angular and linear dimensions of the beam and to eliminate spurious beam scattered from the optics. X-ray mirrors are placed up- and downstream from the monochromator. They are used both primarily as a focusing and collimation device, whereas downstream mirrors also serve as high-energy cut-off filters to remove unwanted higher order harmonics delivered by the monochromator [8, 13].

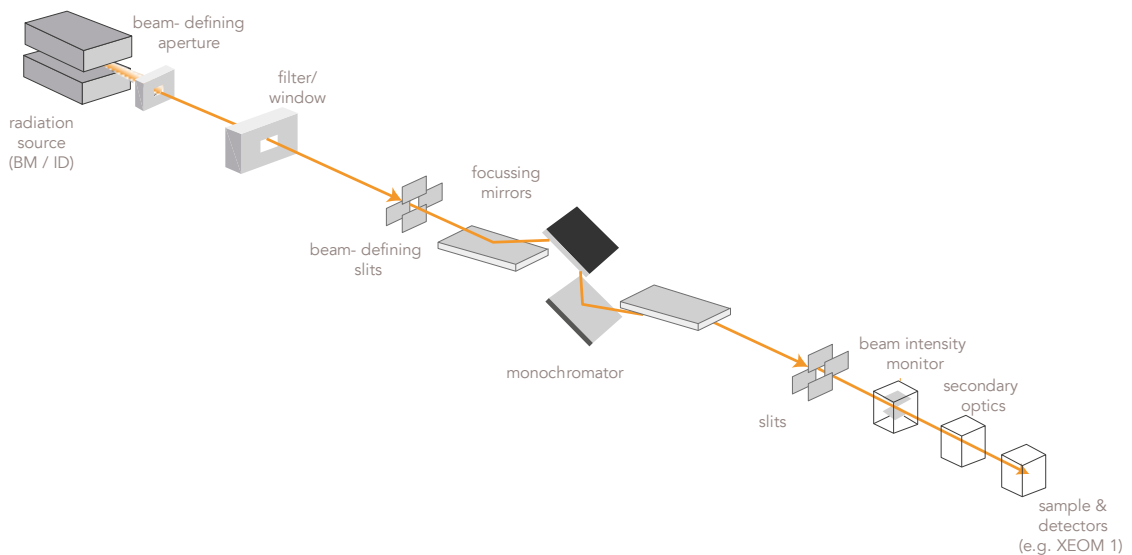


Figure 2.6

Schematic overview of the optics of a typical beamline.

The role of the monochromator is to deliver an X-ray beam with a well-defined photon energy with narrow bandwidth, as little as 0.1 eV, chosen by the user. In double crystal X-ray monochromators (Figure 2.7), diffraction from 2 perfect parallel

crystals (typically Si 111 or Ge or diamond) is used to monochromate the beam according to Bragg's law:

$$2 d \sin \theta = n\lambda, \quad \{2.4\}$$

where d is the spacing of the crystal lattice planes, λ is the wavelength and θ is the incident angle. In order to select a certain wavelength, θ is varied by rotating the pair of crystals [26]. X-ray absorption spectroscopy (or XEOL-XAS, see sections 2.2 & 2.3) requires that the photon energy is gradually changed and scanned across the absorption edge of a certain element. Beam line monochromators answer to this requirement with a high resolution and reproducibility. Other X-ray optical components such as: compound refractive lenses (CRLs), zone plates, capillaries, etc. are not discussed here as they are outside the scope of this thesis [8].

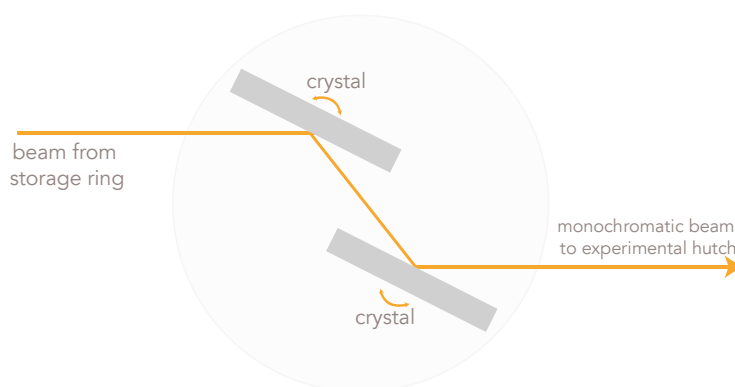


Figure 2.7

Basic geometry of the double-crystal monochromator

The equipment installed in the experimental hutch is, more than any other beam line components, defined by the type of experiment to be conducted. As most pieces of this equipment are not quickly interchangeable, each beam line is dedicated to a certain analytical method. Therefore the experimentalist must evaluate the beam line features carefully to determine whether the beam line is suitable for his/her experiment, before submitting a beam time proposal. A description of the instrumentation applied during experimentation in this work can be found in chapter 3.

The experimental station is secured with a hutch interlock system (HIS) to protect users from exposure to high radiation doses when the X-ray beam lines are operating [27]. For a safe operation of the instruments when the beam is 'on', users control the instruments from a control hutch, mostly located adjacent to the experimental hutch.

This implies that all instrumentation must have the potential to be remotely controlled, as is the XEOM hardware.

2.2 X-RAY ABSORPTION SPECTROSCOPY

X-ray absorption spectroscopy (XAS) was developed in the early 1970s by Sayers et al. [28] and is a unique tool for investigating the atomic environment around specific elements contained within a material. Apart from the qualitative information provided by the 'fingerprint' of the absorption spectrum, structural and chemical information on the local environment is embedded in the X-ray absorption fine structure (XAFS) [29].

The fine structure is generally divided into two regimes: X-ray absorption near edge structure (XANES) and extended X-ray absorption fine structure (EXAFS). Each regime reveals different information regarding the probed atom, i.e. its oxidation state and coordination geometry is embedded within the XANES, while the EXAFS exposes its local molecular structure [30, 31]. Since XAS is an atomic probe, few constraints are placed on the samples that could possibly be studied. XAS spectra can be collected on mixtures of gases, liquids and/or solids with minimal or no sample pretreatment [30]. Moreover, the theory and interpretation on which XAS relies, does not require any assumption of symmetry or periodicity. Hence XAS can yield short range order information for both crystalline and amorphous materials, which can be complementary to long range order info provided by X-ray diffraction (XRD) [8]. For all of the reasons mentioned above, XAS is an excellent tool for yielding information to aid in the archeometric analysis of corrosion on rare/precious metallic samples.

2.2.1 PRINCIPLES OF X-RAY ABSORPTION

The physical quantity that XAS practitioners are concerned with is the absorption coefficient $\mu(E)$. This coefficient reflects the probability of X-rays being absorbed by a sample. Beer's Law states that:

$$I = I_0 e^{-\mu t}, \quad \{2.5\}$$

where I is the transmitted X-ray intensity and I_0 is the X-ray intensity impinging on the sample [32]. The value I decreases exponentially with the sample thickness t and the absorption coefficient μ . The magnitude of the absorption coefficient is determined by two X-ray-matter interactions:

- **Photoelectric absorption:**

During the photoelectric absorption of X-ray photons, the incoming X-ray is fully absorbed by an atom and its energy is transferred to one of the bound electrons which leaves the absorbing atom as a photoelectron [33]. This effect only occurs on the condition that the energy of the incoming X-ray is greater than the binding energy of the electron. After emission, the kinetic energy of the photoelectron E_e , depends on the photon energy $h\nu$ and the binding energy E_0 of the initial electron level as expressed in equation {2.6} [34]:

$$E_e = h\nu - E_0. \quad \{2.6\}$$

The probability of this event is expressed by the photoelectric effect cross section τ (photoionization cross section) and is dependent on the atomic number Z and incident X-ray energy E , and can be approximately expressed as follows [34, 35]:

$$\tau(Z, E) \simeq C \frac{Z^4}{E^{3.5}}, \quad \{2.7\}$$

where C is a constant. The photoelectric cross section is a steeply decreasing function of energy. Every time the photon energy crosses a threshold corresponding to the binding energy of a deeper layer of electrons, a sudden steep increase in photoionization cross section can be observed. This discontinuity is characteristic for a given shell and is referred to as an *absorption edge* [31]. The photoelectric effect is the dominant mode of interactions of photons with an energy less than 100 keV.

- **Scatter interactions:**

The dominant scattering particle for X-rays in matter is the electron. Elastic scattering occurs when the electric field of an incident electromagnetic wave sinusoidally accelerates the scattering electron and consequently forces it to move at the same frequency as the incoming wave, thus reradiating light at exactly the same wavelength [23]. Elastic or coherent scattering of electromagnetic radiation on a free charged particle is called *Thomson scattering* [6]. When X-rays are being scattered of bound atomic electrons (in which the atom itself is neither ionized nor excited) and during which the energy of the scattered photon remains unchanged, *Rayleigh scattering* is in place [36]. Rayleigh scattering occurs predominantly at lower energies and for heavier elements (high Z materials) [8].

Arthur H. Compton noticed in 1923 that when monochromatic X-rays are scattered from graphite, some flux at energies a little below the primary energy was emitted [37]. The energy E_C of the inelastically scattered photon can be determined approximately using the Compton formula:

$$E_C = \frac{E_0}{1 + \frac{E_0}{m_e c^2} (1 - \cos\theta)}, \quad \{2.8\}$$

where E_0 is incident photon energy, m_e is the electron rest mass, c speed of light in vacuum and θ is the scattering angle. The effect of Compton scattering on the total cross section is small with respect to elastic scattering.

In a material including n elements each with a weight fraction w_i , the absorption coefficient of the irradiated sample is reduced to:

$$\mu(E) = \sum_{i=1}^n w_i \sigma(Z_i, E), \quad \{2.9\}$$

where $\sigma(Z, E)$ is the total interaction cross section (combining photoelectric absorption and scatter interactions) which is dependent on the atomic number Z and excitation energy E . At most X-ray energies, $\mu(E)$ decreases smoothly with increasing X-ray energy according to:

$$\mu \approx \frac{\rho Z^4}{A E^3}, \quad \{2.10\}$$

where ρ and A are respectively the sample density and the atomic mass [6].

The total interaction cross section of copper, and its components, as a function of incident X-ray energy was calculated with xraylib library for X-ray-matter interactions by Schoonjans et al. [38] and is plotted in Figure 2.8. The smooth decrease postulated by {2.10} can be observed. However, around 1000 and 10000 eV, two discontinuities can be observed. These are the absorption edges as referred to earlier [31].

For a given shell, the absorption energy increases with atomic number. Greater atomic numbers have more positively charged nuclei which correlate with a greater binding energy of an electron in a given atomic orbital. The nomenclature of absorption edges corresponds to the core electron state being excited, e.g.

scanning the K-edge is accompanied by the excitation of a 1s electron, while exciting a 2s, 2p_{1/2} or a 2p_{3/2} electron results respectively in addressing the L₁, L₂ and L₃ edges [29, 30].

Figure 2.9 gives an example of an X-ray absorption spectrum of paratacamite (mineralogical name of Cu₂(OH)₃Cl) collected at the Cu *K*-edge in fluorescence mode (see below) during beam time X (see Table 3.6). As the energy of the X-ray is swept across the absorption *K*-edge of copper (8979 eV), a sharp rise in absorption is observed. Typically, the absorption spectrum can be subdivided into four distinct energy regimes. The minor features in the *pre-edge region* are the result of electron transitions of core-electrons to empty bound states [8]. In the *rising-edge* region a sharp jump in absorption is observed as consequence of the high probability of photoelectric absorption. The ejected photoelectrons possess low kinetic energy in the *XANES* region (sometimes also indicated as NEXAFS, near-edge X-ray absorption fine structure) and experience strong multiple scattering by the surrounding atoms [32]. Single scattering is dominant in the *EXAFS* region, as the ejected photoelectrons leave with larger kinetic energies. The dividing energies between the different regimes are mainly arbitrary as transitions between these regions represent a gradual change in the dominant physical process taking place [29].

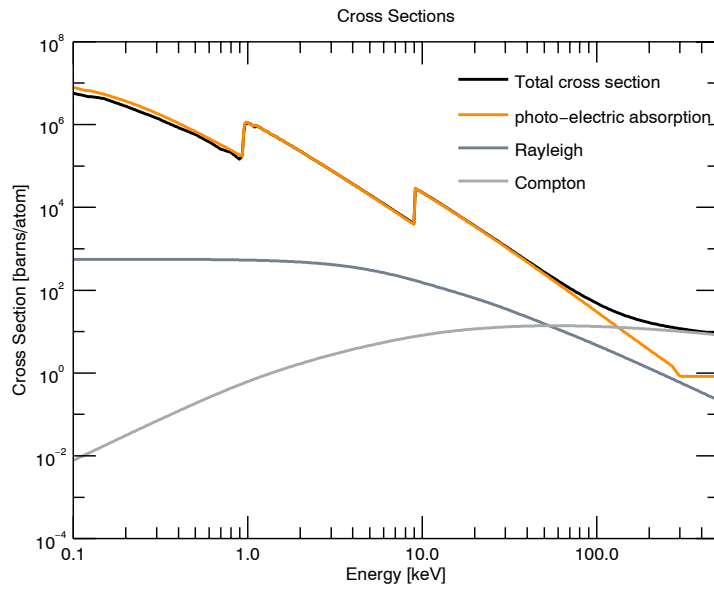


Figure 2.8

The Total cross section for X-ray interaction with Cu as function of photon Energy. Values were taken from [38] through the *xraylib* interface .

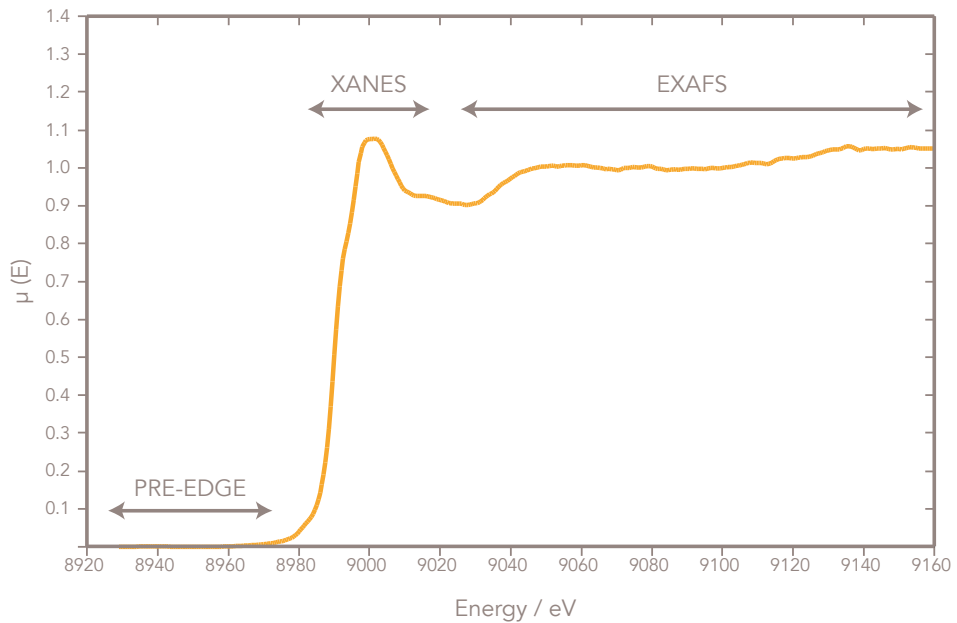


Figure 2.9

The different regions of a typical X-ray absorption spectrum of paratacamite ($\text{Cu}_2(\text{OH})\text{Cl}$) obtained in fluorescence mode. Spectral features found in the pre-edge, XANES and EXAFS region all result from molecular physical processes and are the source of a variety of information.

2.2.2 X-RAY ABSORPTION NEAR EDGE STRUCTURE (XANES)

In the vicinity of the absorption edge, the energy of the ejected photoelectrons is relatively low, so low that they might not be ejected into the continuum. The longer mean free path that accompanies this lower kinetic energy favours multiple scattering events, i.e. it is very likely that the departing photoelectron will scatter with more than one shell of neighbouring atoms [39]. In contrast to the EXAFS energy domain where single scattering contributions dominate and EXAFS theory provides a 'straightforward' equation for data fitting and structural refinement, multiple scattering events complicate XANES theory substantially. Notwithstanding recent progress in *ab-initio* XANES modeling [40, 41] and data refinement procedures [42], phenomenological interpretation of XANES features is well established and can provide fast qualitative and semi-quantitative information. Amongst these approaches, several were practiced during this research:

- **Fingerprinting**

The most straightforward approach to analysis is fingerprinting, which refers to identification of certain compounds without applying any calculations but by comparison to spectra of known substances – empirical standards [39]. Essential in fingerprinting analysis is the collection of a library of reference spectra of standardized materials: powders, foils, etc. Either entire spectra can be compared or just individual spectral features can be used as an argument in the determination of a compound. A classic example of a spectral feature which aids in rapid recognition of a certain material is the appearance of a *white line*. A white line is a sharp feature at the top of the edge showing much higher absorption than that seen in the adjacent EXAFS region. The term 'white line' originates from the days where X-ray spectra were collected on photographic films and the sudden intense absorption upon crossing the edge left the photographic negative unexposed, creating literally a white line [39, 43]. An example of a white line can be seen in the X-ray absorption spectrum of nantokite in Figure 4.7 D.

- **Edge Shift**

The absorption edge energy is defined as a particular energy point on the steep part of the absorption edge spectrum [30]. However, the method for designating the absorption edge energy is not standardized. It can be allocated to energy at half-height of the edge jump or as the maximum in the first derivative to energy [31]. Despite this ambiguity, edge energies have proven to be very efficient in defining the oxidation state of the absorber [44]. The edge energy for an element in a higher oxidation state is usually shifted several electron volts to a higher X-ray energy. Core

level electrons are more tightly bound in a charged atom with respect to a neutral atom, resulting in an increased energy required to eject the core electron from its bound state. Provided a proper energy calibration on a set of reference compounds has been carried out, determination of the edge position can be used to assign rapidly the oxidation state of the absorber [45]. Surface specific chemical mapping, the key intended application of XEOM 1, will benefit greatly from this phenomenon as described into more detail in chapter 5.

■ Linear combination Analysis (LCA)

Linear combination analysis or linear combination fitting (LCF) is a method for quantifying relative amounts of constituent chemical species in mixtures and multiphase compounds [39]. The underlying principle of this technique is the additive nature of the absorption from each constituent in the sample. If a sample contains, for example, a homogeneous mixture of 50 % Cu₂O (cuprite) and 50 % CuO (tenorite), the absorption coefficient of the multiphase sample will be the sum of the absorption coefficients of cuprite and tenorite, each weighted by 50%. During the analysis, the normalized experimental spectrum μ_{exp} of the unknown sample is fitted to a theoretical curve μ_{th} calculated as a linear combination of normalized reference spectra of the assumed constituent compounds weighted by fraction of the absorber α_j in the j^{th} environment [46].

$$\mu_{exp} = \sum_j \alpha_j \mu_{th} \quad \{2.11\}$$

Failing LCA procedures might suggest that a necessary constituent is not present in the library of standards used to fit the experimental data. This can be valuable information but reveals at the same time the bottleneck of this procedure as reference spectra for all compounds in the mixture are required [39].

2.2.3 EXTENDED X-RAY ABSORPTION FINE STRUCTURE (EXAFS)

2.2.3.1 Principles of EXAFS

Further away from the absorption edge, the XANES region is followed by the EXAFS part of the X-ray absorption spectrum. The EXAFS energy regime typically starts at 20 to 30 eV after the absorption edge and extends to 1000 eV post-edge or higher [30, 31].

In the post-edge division of the absorption spectrum, the absorbed X-ray excites a bound electron into the continuum. This newborn photoelectron, best described as a spherical wave propagating outwards from the absorber atom, possesses a certain kinetic energy given by equation {2.6}. From 20 eV on, the photoelectron is sufficiently energetic so that single scattering becomes dominant over multiple scattering, i.e. the more difficult interpretable phenomenon as observed in XANES.

The EXAFS signal is created when the outgoing spherical electron wave backscatters from the nearest neighbour shell of atoms, therefore creating a pattern of constructive and destructive interference [29, 30, 32]. The top part of Figure 2.10 displays a schematic representation of this event where a spherical photoelectron wave emitting from a central absorber (orange) is scattered off a shell of neighbouring atoms (grey). The resultant superposition of scattered waves (grey dotted line concentric circles) with the emerging photoelectron wave (orange full line concentric circles) modulates the amplitude of the photoelectron wave function through constructive and destructive interference, an effect which directly influences the sample's absorption probability and therefore also the absorption coefficient $\mu(E)$.

The bottom part of Figure 2.10 gives an XAS spectrum of metallic copper. The different spectral features, indicated by A, B and C, are the result of different effects of absorption at different energies. In the pre-edge region (Figure 2.10 A) the incoming X-ray is not sufficiently energetic to excite a core electron into the continuum, hence no interference can occur. Past the edge and in the EXAFS region, emerging photoelectron waves are being created. In the theoretical case where the absorbing atom has no backscattering neighbours a smooth, oscillation-free, monotonically decaying curve as described by {2.10} would be observed (Figure 2.10, spectrum, blue dotted line). This curve will prove its importance during data processing and will serve as a background function $\mu_0(E)$. When neighbouring atoms are present and the round-trip distance of the outgoing and scattered wave is a whole number of wavelengths, the outgoing and scattered photoelectron wave meet each other in phase at the absorber atom. This constructive interference results in an

increased electron wave amplitude and therefore also an enhanced absorption coefficient $\mu(E)$ with respect to the atomic absorption $\mu_0(E)$ (Figure 2.10 B).

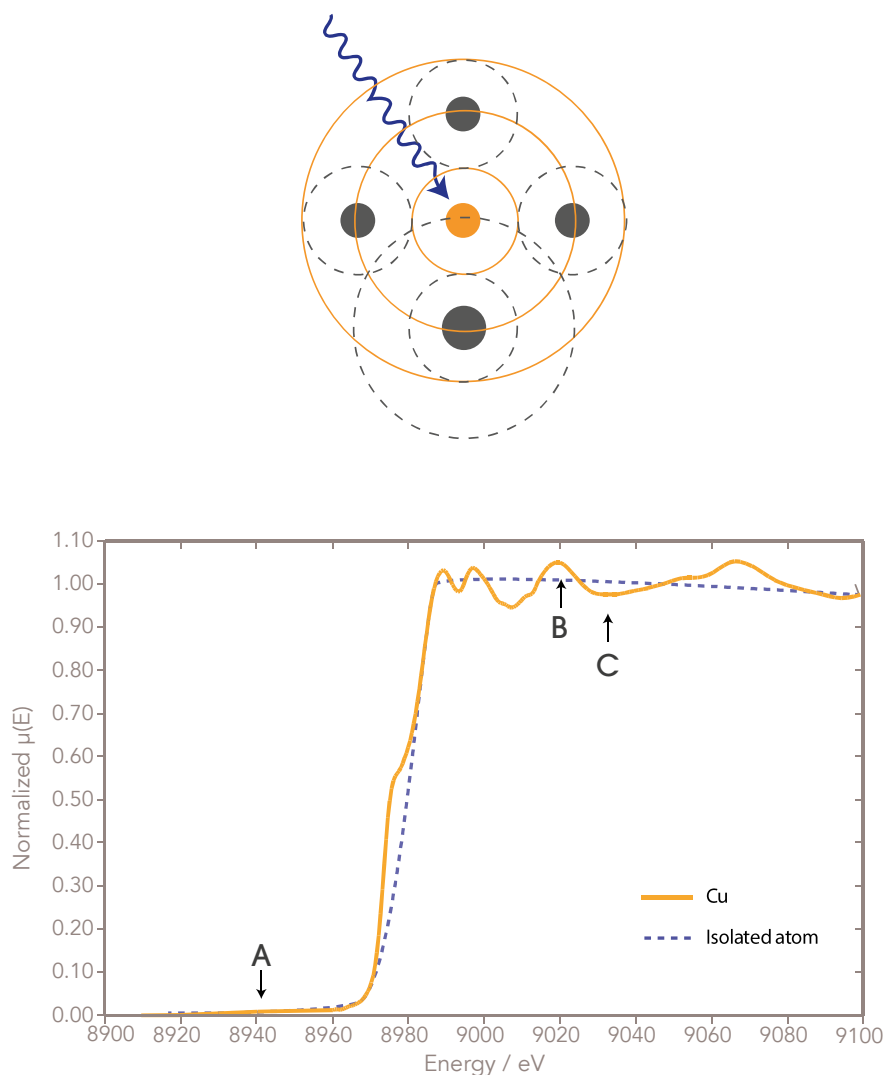


Figure 2.10

The top schematic represents the scattering of a spherical photoelectron wave emitted by a central absorbing atom (orange) and a shell of neighbouring atoms (grey). The solid orange circles represent the outgoing photoelectron wave while the dashed grey circles indicate the portion of the wave being backscattered of the neighbouring atoms. The bottom graph displays the X-ray absorption spectrum, measured in fluorescence yield mode, of pristine copper across the Cu *K*-edge (8979 eV). Top illustration is reproduced and adapted from [49].

Changing conditions for photoelectron energy and/or interatomic distances can alter the phase and hence the interference pattern [47]. A shorter photoelectron wavelength (higher energy) might result in more destructive interference. At this stage, the outgoing and scattered parts of the photoelectron wave are out of phase and destructive interference takes place. This results into a minimum of the EXAFS oscillations and consequently a diminished X-ray absorption probability with respect to $\mu_0(E)$ (Figure 2.10 C) [31].

2.2.3.2 The EXAFS equation

The fluctuations of $\mu(E)$ with respect to $\mu_0(E)$ due to interference of the outgoing and backscattered waves is called the EXAFS function χ (see below). These fluctuations embed information regarding: the type and amount of neighboring atoms around the absorber, inter atomic distances and deviation on this distance due to disorder (i.e. Debye-Waller factor) [28, 48, 49].

EXAFS is best understood in terms of its wave behaviour, hence the outgoing photoelectron wave is described by wavenumber k where:

$$k = \frac{2\pi}{\lambda} = \sqrt{\frac{2m_e(E - E_0)}{\hbar^2}}, \quad \{2.12\}$$

where λ is the de Broglie wavelength of the photoelectron, E_0 is the absorption edge energy and E the incoming X-ray energy, m_e the electron mass and \hbar is Planck's constant divided by 2π [29].

EXAFS is concerned with oscillations well above the absorption edge. As they tend to dampen out well above the edge, EXAFS is commonly defined as the fractional modulation $\chi(k)$:

$$\chi(k) = \frac{\mu(k) - \mu_0(k)}{\mu_0(k)}. \quad \{2.13\}$$

The apparent amplitude, shape and frequency of the EXAFS oscillations are reliant on the distance and the nature of the near-neighbour coordination shells. [32] All these features are described in the EXAFS equation published by Stern in 1978 [48] :

$$\chi(k) = S_0^2 \sum_j \frac{N_j}{kR_j^2} |f_j(k, r)| e^{-2k^2\sigma_j^2} e^{\frac{-2R_j}{\lambda_j(k)}} \sin(2kR_j + \delta_j(k, r)), \quad \{2.14\}$$

where:

- S_0^2 is an amplitude reduction factor to take the perturbed original state (shake-up / shake-off effects) of the absorber atom into account [50].
- N_j and R_j are respectively the number of equivalent and equidistant atoms in the j^{th} shell at distance R
- $f_j(k, r)$ is the backscattering amplitude
- $e^{-2k^2\sigma_j^2}$ is a Debye-Waller factor necessary for approximating the effects of thermal and static disorder on R_j

- $e^{-2R_j/\lambda_j(k)}$ is a correction factor for photoelectron loss by means of inelastic scattering, $\lambda_j(k)$ represents the electron mean free path
- $\delta_j(k, r)$ is determined by the phase shift introduced by the photoelectron travelling through the potential wells of the absorbing and backscattering atom.

The spectroscopist attempts to reveal the embedded information by fitting his experimentally obtained EXAFS data to a theoretical model based upon equation {2.14}. This fitting process is done on the Fourier transform of the obtained EXAFS data expressed as function of k .

Fourier transformation of the EXAFS function will decompose this sine wave superposition (as dictated by equation {2.14}) into its different constituent frequencies [51]. Accordingly, when the EXAFS signal is expressed as function of photoelectron wave number k (inverse distance), Fourier transformation will yield a plot in real space. Location of the different peaks in this R -space plot can then be associated with the distance at which different scattering shells are located around the absorber (R_j in equation {2.14}). Software programs such as FEFF [40, 52, 53] allow to simulate scatter path intensities which can subsequently be fitted to the different scatter paths observed in the R -space plot. Finally this process allows to quantify the radii of the neighboring shells R_i , the accompanying coordination number N_i , the amplitude reduction factor S_0^2 and phase shift factor σ [32].

2.2.4 DATA PROCESSING

Before structural information can be obtained from XAS spectra, the EXAFS signal needs to be extracted from the raw data by a process better known as 'data reduction'. The procedure of data reduction, as illustrated for copper in Figure 2.11 involves the following steps [29, 32, 39, 54] :

1. **Removal of pre-edge background:** due to the absorption by less bound electrons, the absorption spectrum generally is situated on top of a background. The background is removed by subtraction of a fitted polynomial function through the pre-edge region.
2. **Determination of E_0 :** the edge-position value E_0 is initially (most commonly) determined by finding the maximum of the first derivative of the spectrum.
3. **Normalization:** The spectrum is normalized to unit edge step to factor out sample thickness, concentration, settings in experimental set-up etc. Normalization is done by calculating the difference between extrapolated pre-

edge and post-edge fits at the determined edge-position E_0 and dividing the spectrum by this value.

4. **Interpolation of atomic background:** The atomic background μ_0 is approximated in the post-edge region by fitting a spline function. Great care should be taken that no fine structure is removed during this process.
5. **Isolation of $\chi(k)$** : this is done accordingly with equations {2.12} and {2.13}
6. **k -weight $\chi(k)$ and Fourier transform into R -space:** At high k -values, the EXAFS signal has the tendency to dampen out. To enhance these weak oscillations at higher k values $\chi(k)$ is multiplied by k^2 or k^3 . This function is subsequently Fourier transformed, ultimately revealing characteristic lengths associated with the interatomic distance R_j from equation {2.14}.

After these 6 preprocessing steps, the EXAFS data is ready to be fitted as discussed above. For XANES analysis however, data reduction is already completed once the spectrum is normalized in step 3.

Various software suites are currently available for XANES analysis and EXAFS fitting. Amongst them popular software sets are the Demeter package [53], Viper [55] and GNXAS [56]. In this research the Demeter package (i.e. the novel Horae suite) developed by Bruce Ravel was applied for data reduction of XAS data (not XEOL-XAS as explained in chapter 4). The Demeter package contains a set of graphical user interface programs, each aiding in a different step of the XAS data processing. ATHENA supports preprocessing of EXAFS data (data reduction) and allows for semi-quantitative analysis of XANES spectra. ARTEMIS fits the experimental reduced EXAFS data to theoretical standards using the FEFF engine (Matthew Newville) [52] in order to extract physical parameters as discussed above.

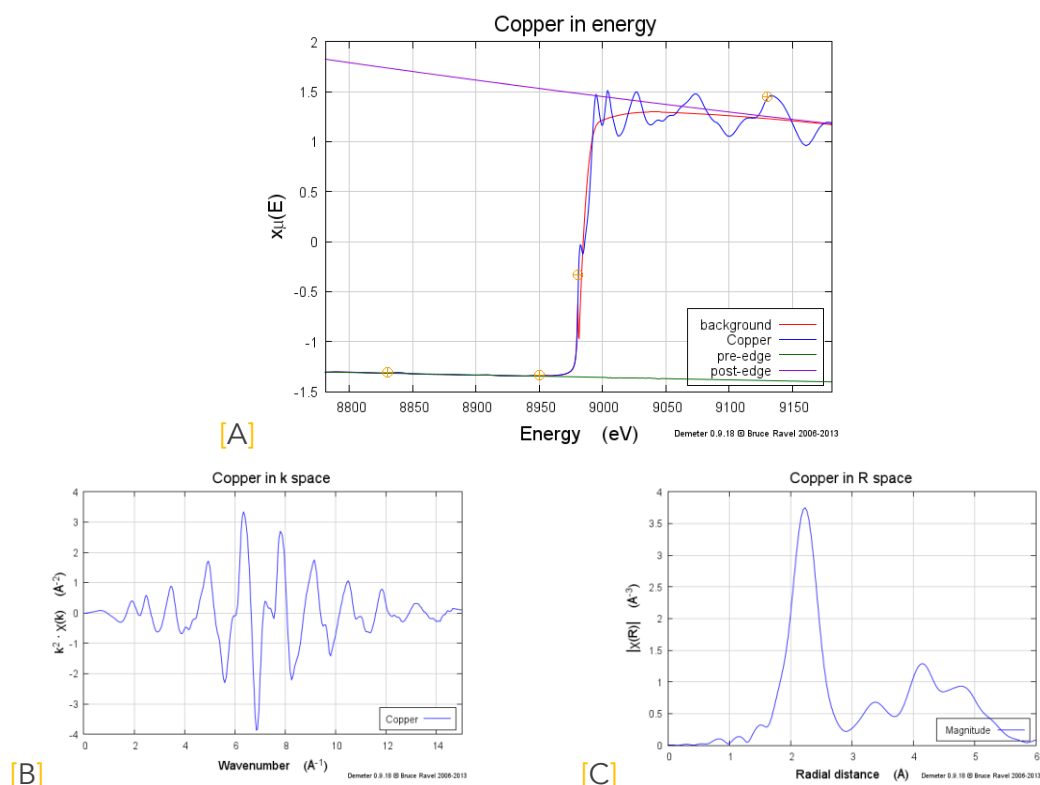


Figure 2.11

Different steps of the data reduction process of Cu-foil in ATHENA [52]

[A] Cu K-edge EXAFS of Cu (metal foil) with corresponding pre-edge and post-edge splines and atomic background μ_0 .

[B] Resulting k^2 weighted $\chi(k)$ spectrum.

[C] R-space plot resulting from the Fourier transform of $\chi(k)$.

Reference data downloaded from XAFS Spectra Library (beta)

(<http://cars.uchicago.edu/xaslib/spectrum/606>). Particular data set was recorded of a Cu foil at room temperature by Matthew Newville at 13ID at the APS (Chicago, Illinois, USA)

2.2.5 EXPERIMENTAL FEATURES

As mentioned earlier, executing an XAS experiment comes down to measuring the absorption coefficient at various energy points across the absorption edge of a certain element. In general, the absorption coefficient can be measured by directly comparing the intensities of the incoming and transmitted X-ray beam (transmission mode) or indirectly by measuring the intensity of a decay product of the absorption process with respect to the incoming X-ray intensity (fluorescence mode, electron yield mode and optical yield mode) [30].

2.2.5.1 Transmission mode

The simplest and most direct way of recording an XAS spectrum is in transmission mode. In transmission mode both incoming (I_0) and transmitted X-ray beam (I_t) are

measured by gas ionization chambers placed before and after the sample. Samples suitable for data acquisition in transmission mode must meet certain conditions: the samples must be concentrated, highly homogenous, exhibit constant thickness and must be free of pinholes [47].

2.2.5.2 Fluorescence yield mode

In fluorescence yield mode (FLY), the intensity of secondary characteristic X-ray lines produced upon X-ray absorption I_f is measured normalized to the primary X-ray intensity I_0 to determine the absorption coefficient. In fluorescence geometry, an energy dispersive detector (in this work an avalanche photodiode or a Vortex® silicon drift detector, see chapter 3) measures the fluorescent X-rays and is mounted (ideally) with the chip surface at 90° to the sample surface. The benefit of this orientation is twofold; both detection of secondary fluorescent X-rays is maximized over unwanted backscattered primary X-rays as well as the reduction of 'self-absorption' effects in thicker samples [6]. Data acquisition in fluorescence mode offers an alternative for samples which are unsuitable for transmission mode acquisition: e.g. highly dilute samples, non-homogeneous samples, too thick samples, etc. [30].

2.2.5.3 Electron yield mode

An alternative detection route for measuring the absorption coefficient involves the measurement of electrons emitted during the X-ray absorption event. The total electron yield (TEY) consists primarily of photoelectrons and Auger electrons. Commonly TEYXAS measurements are conducted in vacuum chambers, equipped with electrodes suitable for electron detection, to minimize electron loss due to absorption of air particles. Nonetheless, measurements carried out in ambient environments have been reported as well [57, 58]. Given the relatively short mean free path of the electrons, recording XAS spectra in TEY is highly surface sensitive and therefore sometimes referred to as surface extended X-ray absorption fine structure (SEXAFS) [59].

2.2.5.4 Optical yield mode

A final indirect mode to measure X-ray absorption spectra is the detection mode which plays a pivotal role in the work presented. X-ray-excited optical luminescence (XEOL) is electromagnetic emission in the optical range produced during a radiative process subsequent to X-ray absorption [60]. The XEOL phenomenon and its existence as XAS variant is described in more detail in the following section 2.3.

2.3 X-RAY-EXCITED OPTICAL LUMINESCENCE (XEOL)

Luminescence can be described as the emission of UV/VIS/IR radiation by a material as a result of its interaction with an incident energy [61]. This incident energy can be of different nature: visible or UV light generate *photoluminescence* (PL), electron beams can create *cathodoluminescence* (CL) and X-rays cause *X-ray-excited Optical Luminescence* (XEOL) [61, 62]. First successes of XEOL [63–65] to unravel the physics of certain luminescence phenomena combined with improving synchrotron light sources has led to the use of XEOL as a detection scheme for X-ray absorption [66].

Notwithstanding the lack of a detailed theory of XEOL, understanding the complex mechanisms involved in the production of XEOL can be important to interpret XEOL-XAS data. Hence an overview of the primary physical processes involved in the production of XEOL is given below in paragraph 2.3.1. Subsequently, the analytical use of XEOL-XAS is discussed in paragraph 2.3.2.

2.3.1 THE PHYSICAL BASE OF THE XEOL PHENOMENON

XEOL is an X-ray-photon in / optical-photon out process which measures the resultant photoluminescence yield (PLY) of the de-excitation process after excitation of a core-level electron of an atom in a chemical environment [67].

A general and detailed description of the XEOL-process has not yet been provided. This is mainly due to the nature of the process being material dependent (type, composition, crystallinity, defects, etc.) and hence difficult to generalize. Nevertheless, a description for the primary physical events taking place in the XEOL production in crystalline semiconductors is depicted in Figure 2.12. This complex phenomenon may be split into three subsequent, independent steps [60, 68]:

1. **X-ray absorption and subsequent formation of thermalized secondary excitations:** The X-ray absorption process excites a core electron of a chemically bound atom (e.g. an atom in a molecule, an atom in a semiconductor, a Cu-atom in a cuprite patina, etc.) into either a previously unoccupied electronic state (bound or quasi-bound) or into the vacuum continuum. Witness of this absorption process is a core hole and an excited absorber atom. Subsequent de-excitation of the system occurs through either a radiative pathway with the emission of a fluorescent X-ray or non-radiatively via Auger electron emission and the creation of outer holes [67]. As they travel through the absorbing medium, these emission products (including the initially created photoelectron) will interact with matter along their track through absorption and inelastic scattering resulting in the creation of shallower secondary electron holes and less energetic secondary electrons. In turn, the electron holes left behind in these shallower levels are filled by still shallower electrons accompanied

with emission of even less energetic electrons. Such cascade process finishes when the electrons and holes settle respectively in the bottom of the conduction band (LUMO for molecules) and the top of the valence band (HOMO for molecules). This process, better known as *thermalization*, continues producing electron-hole pairs until the energy is too low for further electronic excitation [22, 67, 69]. The electron-hole pair is an important type of secondary electronic excitation which will eventually give rise to the optical luminescence. In contrast to semi-conductors, the luminescent emission in metals (such as Cu, Ag, and Au) is derived from secondary electronic excitations resultant from transitions between the conduction band and electron holes located within the d-bands [70–72].

2. **Energy transfer and subsequent excitation of luminescent centres:** Following the multiplication of secondary electron-hole pairs and simultaneous thermalization, the electronic excitations undergo relaxation. The released energy which accompanies this process is transferred to luminescence centres. The mechanism through which this occurs is complex and is dependent on temperature, concentration of defects in crystals and dopant concentration [60]. Three basic energy transfer mechanism for XEOL were proposed in [60], for which *photoconductivity* is considered as a good candidate to describe the energy transfer within semiconductors. In photoconductivity; electrons and holes are trapped by and transfer their energy into a so-called *activator*. Activators are sometimes deliberately introduced in a host lattice as dopants to increase the luminescence quantum yield of a material (as in scinitillators). A more detailed explanation of this mechanism is outside the scope of this thesis and can be found in [60].
3. **Relaxation of luminescent centres with emission of optical photons:** As shown for a semiconductor in Figure 2.12, secondary electrons and holes fall at the bottom of the conduction band and the top of the valence band respectively. The electron and hole can recombine radiatively, emitting photons with an energy equal to the energy difference between the band gap energy and the binding energy of the electron-hole pair. This emission is referred to as near bandgap emission by Sham in [67]. In the instance of imperfect crystals, defect states (e.g. traps, vacancies, impurities) are present within the bandgap. Crystal defects can significantly alter the material's emission pattern as energy can be transferred to these defect states during step 2 (see above) of the XEOL process. Subsequent radiative recombination leads to light emission in longer wavelengths at the expense of the near bandgap emission. Alternatively, non-radiative relaxation of the electron-hole pair is also possible by means of phonon formation or radiation induced local annealing which is at the expense of the XEOL yield [69].

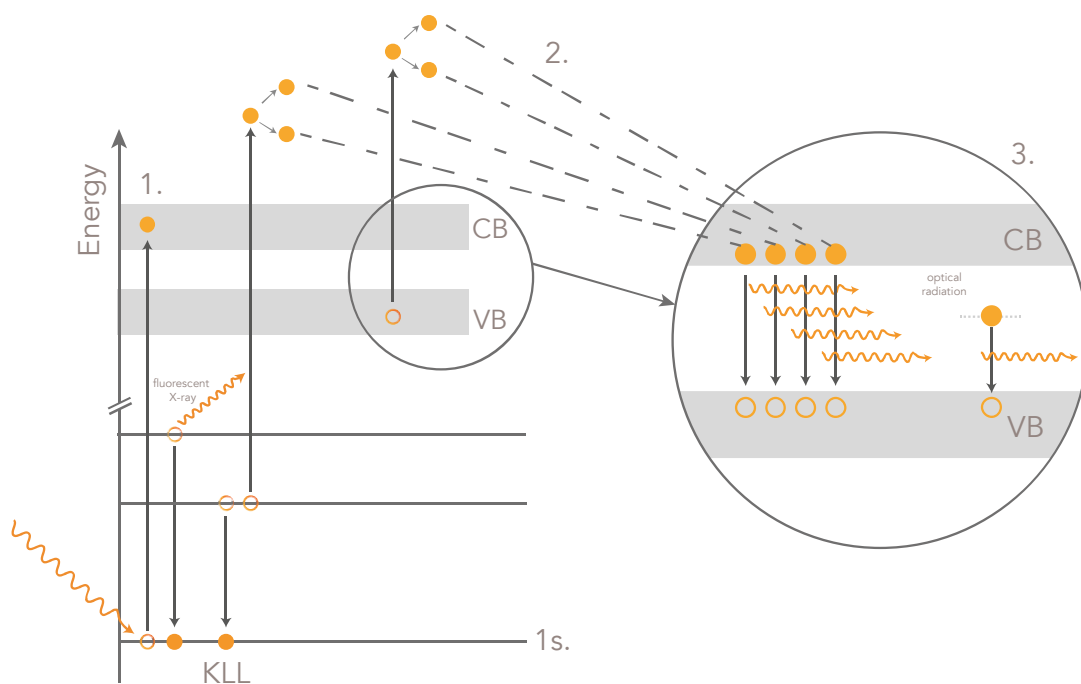


Figure 2.12

Energy diagram displaying absorption and luminescence processes responsible for XEOL. Solid circles represent electrons and open circles represent holes, while defect states are represented by dashed lines in the band gap. Image adapted from [59].

2.3.2 XEOL-XAS

Since the intensities of characteristic secondary fluorescence X-rays and secondary electrons are directly related to the creation of the core hole, their yield is generally proportional to the absorption coefficient. Accordingly, FLY and TEY are customary used to track XANES and EXAFS in X-ray absorption spectroscopy (see 2.2.5). Furthermore, XEOL can also be used as a carrier of X-ray absorption signatures [73]. This is because the optical light resulted from contributions from particular radiative transitions excited downstream from the core-level photoexcitation. Therefore the absorption coefficient is modulated in the same way when the excitation energy is tuned across the absorption edge of interest [74, 75]. Nevertheless, this contribution has to compete with optical emission arising from non-resonant excitation of states below the core level and therefore has to be sufficiently intense in order to be discernible [74]. The literature name for this spectroscopy is varies: optical XAFS [76], XEOL-XAS [75] or ODXAS (where both Optically Detected XAS [77, 78] or Optically Derived XAS [61] are used) are known as the collective spectroscopy and individually as XEOL-XANES and XEOL-EXAFS [74]. In this work the terminology of XEOL-XAS as the collective spectroscopy and XEOL-XANES and XEOL-EXAFS has been adopted.

XEOL-XAS can probe the electronic state, optical properties and local atomic order (XEOL-XAFS or ODXAS) of a specimen in an element and excitation specific fashion.

Since few limitations are imposed on the samples reports were registered for XEOL experiments in gases (no XEOL-XAS) [79], liquids [80] and solids in various forms: powder [77, 81], thin film [73, 82], bulk solids [83] and nanostructures [84–86].

Upon interpreting the behavior of XEOL-XAS spectra it is important to understand that the XEOL response of the targeted sample is not uniform across the scanned energy range (edge included) [73]. This means that the XEOL process, as described in the previous section 2.3.1, can alter significantly when the absorption edge of an element is crossed. Below the absorption edge, there is insufficient energy to excite core electrons and produce fluorescent X-rays or Auger electrons. Thus, optical luminescence is only function of electron-hole pair production following excitation of shallow valence electrons as well as background luminescence due to non-resonant excitation processes [73]. Across the absorption edge, the X-ray penetration depth decreases abruptly at the edge threshold. At this point, the XEOL intensity can be very sensitive to this rapid increase in absorption compared to the excitation below the edge. In some cases this might result in a decrease of electron-hole pair production as new optical channels are opened and the core hole has decayed [67]. Moreover, when emission products (Auger electrons, photoelectrons, fluorescent X-rays) created in the surface and near-surface regions can escape the surface without contributing to the thermalization process a reduction in the production of secondary electronic excitations can occur [84]. In some case this can lead to a phenomenon unique to XEOL-XAS spectra: *inverted edges*. The origin of inverted edges has been extensively studied by Emura et al. [54, 69] and appears to be dependent on the nature of the sample. It is for the reasons described above (high background, possible inverted edges, non-linearity of XEOL signal) that Soderholm et al. [87] published in 1998 a rather pessimistic paper on the use and survival of XEOL as a detection scheme for recording X-ray absorption spectra. He cautions that care is needed when attempting to extract structural parameters from XEOL-EXAFS data. Nevertheless, our groups have shown elsewhere [77] that it is possible for XEOL-XAS to detect thin surface corrosion layers on heritage metals. The extracted data, representing the top 200 nm of the sample, displayed no inverted edges and in most cases a strong similarity to FLY spectra were observed. Therefore, in the case of copper and its corrosion products, the distrust of Soderholm et al. should be mitigated and XEOL-XAS should at least be regarded as being suitable for fingerprinting purposes. Further investigation should reveal whether this is also true for other metals.

2.4 OTHER TECHNIQUES USED DURING THIS STUDY.

As described in the introduction (chapter 1), complex samples such as the corrosion crust of heritage metals, are rarely described and characterized by one single technique. Usually a set of techniques is used that provide complementary information. Moreover, in order to assess the lateral resolution of XEOM 1, a handcrafted sample was used. As a priori knowledge on the composition of this sample is desired some other analytical techniques were used. Below a brief description of these techniques is given.

2.4.1 X-RAY DIFFRACTION (XRD)

2.4.1.1 Crystalline Structures

Crystalline materials are characterized by the long-range periodic configuration of atoms. A distinction can be made between single crystals, in which the long-range order is maintained over the whole volume of the material, and polycrystalline materials in which small single-crystal regions separated by grain boundaries are observed [88].

The smallest subset of atoms which constitutes the repeating pattern in the crystal, is known as the unit cell of a crystal. The size and shape of the unit cell are designated by the lattice parameters which comprise both length units a , b , c and interaxial angles: α, β, γ [89, 90] (Figure 2.13 A). Only seven unit cell shapes are known that can be stacked to fill three-dimensional shapes, where each of seven define a unique crystal system. In descending order of symmetry there are: cubic, tetragonal hexagonal, rhombohedral, orthorhombic, monoclinic and triclinic crystal systems [91]. In turn, depending on the unit cell being primitive or centred, these 7 crystal systems give rise to 14 different crystal point lattices. In such a point lattices, also known as Bravais lattice, each point is occupied by one atom or a group of atoms [92].

During the analysis and description of crystals, it is important to consider its symmetry. Within this perspective, it is known that for each crystal system a set of compatible symmetry operations can be composed. In total of 32 different sets of symmetry operations (rotation, reflections, etc.) are defined as crystallographic point groups. Combining the 14 Bravais lattices with these 32 point groups yields a total of 230 space groups. This broad range of space groups represent all the possible ways a unit cell (motif) can be arranged in a periodic way in three-dimensional space [90]. Hence all known crystals can be defined by such a unique space group, information which is collected in the International Tables for Crystallography [93].

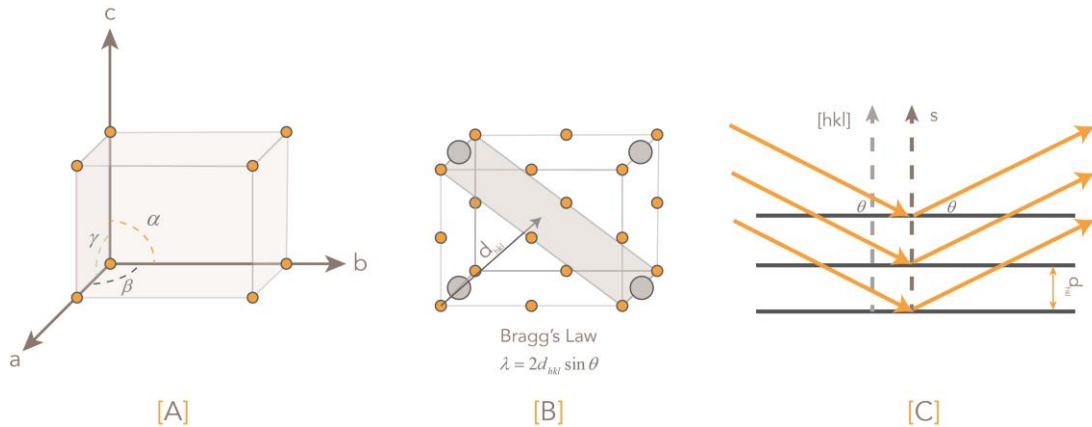


Figure 2.13

[A] A primitive unit cell described by the lattice parameters (a, b, c) and (α, β, γ)

[B] Example of the determination of Miller indices of a crystal plane (hkl)

[C] The position of diffraction peaks are determined by the distance between parallel planes of atoms according to Bragg's Law.

2.4.1.2 Principle of X-ray diffraction

If atoms are regularly arranged in space, as they are in crystalline materials, then an incident beam of X-rays will be scattered off in a number of well-defined directions. The direction at which scattered X-rays can be observed are directly related to the spacing between the planes of atoms in the crystalline material [94]. This phenomenon is well-known as X-ray diffraction and is commonly used to provide information on crystalline materials, even though it can provide some information on amorphous solids as well [95].

The diffraction peaks within a diffraction pattern are associated with planes of periodically ordered (groups of) atoms. Miller indices provide a way of uniquely describing a set of planes within a crystal lattice. The indices, denoted by the letters hkl , are defined by the reciprocal value of the axial intercept of a plane of atoms with the unit cell (Figure 2.13 B) [6]. The vector \mathbf{d}_{hkl} extends from the origin of the unit cell to the plane (hkl) and is normal to the (hkl) plane [13]. The vector \mathbf{d}_{hkl} is used in Bragg's law to determine where diffraction peaks will be observed.

Bragg's law provides a model to describe the required conditions for diffraction of X-rays by a crystal [26]. Bragg's law defines the angle where X-rays, scattered off parallel planes of atoms, interfere constructively. Under this condition, a diffraction peak will be observed within the diffraction pattern. Bragg's law is defined by the following formula:

$$n\lambda = 2d_{hkl} \sin \theta, \quad \{2.4\}$$

where λ is the wavelength of the incident X-rays, d_{hkl} is the interplanar spacing described by the vector detailed above and θ is the Bragg angle (as in Figure 2.13 C) at which one observes a diffraction peak and ultimately n is an integer number describing the order of the reflection. In most diffractometers, the X-ray wavelength λ is fixed. Consequently, for first order of diffraction ($n=1$), diffraction of the family of planes (hkl) will result in the observation of a peak in the diffraction pattern at the specific angle 2θ . An additional requirement is the obligation for the plane normal $[hkl]$ (as in Figure 2.13 C) to be parallel to the diffraction vector S , which is the vector bisecting the angle between the incident and diffracted beam [94].

2.4.1.3 Instrumentation

2.4.1.3.1 Laboratory Instrumentation

In powder diffraction laboratory instrumentation the X-ray tube, the sample and the scintillation detector (technically a photomultiplier tube with scintillating screen) are commonly placed in *Bragg-Brentano* geometry. In this Bragg-Brentano set-up, $\theta:2\theta$ instrumentation (e.g. Siemens D5000) and $\theta:\theta$ instrumentation (e.g. PANalytical X'Pert Pro) are available. The former consists of a fixed X-ray tube, a sample rotating at θ°/min and the detector rotating at $2\theta^\circ/\text{min}$. In contrast, for the latter case, the sample is fixed between a rotating X-ray tube (at θ°/min) and the detector (rotating at $-\theta^\circ/\text{min}$) [89].

In this work two different diffractometers have been used. For the characterization of a grey cuprite patina (Chapter 4) a Siemens D5000 diffractometer (Bruker, AXS S.A.S., France) of the Department of Materials Science and Engineering was used (with great thanks to Prof. Kim Verbeken, Ghent University). This instrument is equipped with a Ge focusing monochromator to produce Mo- K_α radiation ($\lambda=0.7108 \text{ \AA}$). Samples are mounted in ($\theta:2\theta$)-geometry and the sample is mounted on a rotating sample holder to minimize preferential orientation in the sample. In order to characterize the in utero corroded Cu-IUDS (supplementary chapter) a Panalytical X'Pert Pro Multipurpose Diffractometer (PANalytical, Almelo, The Netherlands) from the Department of Physics (thanks to dr. David Walker and Prof. Pam Thomas, University of Warwick) was used. This more advanced instrument is equipped with a

curved Ge focusing monochromator to produce Cu $-K_{\alpha 1}$ radiation ($\lambda=1.540598 \text{ \AA}$). The instrument is equipped with a PIXcel® solid-state detector (PANalytical, Almelo, The Netherlands), where the incident X-rays create electron-hole pairs in a p-i-n-diode array which offers parallel detection.

2.4.1.3.2 Synchrotron Two-Dimensional XRD

Synchrotron two-dimensional X-ray diffraction refers to X-ray diffraction applications where synchrotron generated diffracted X-rays are detected with a two-dimensional detector. Measurements recorded with such a setup benefit from the well-defined, monochromatic and highly parallel X-ray beams provided by the synchrotron [96]. Moreover, due to the highly intense nature of synchrotron radiation, diffractograms of an adequate resolution can be obtained in a much smaller space of time (s range) than laboratory instruments, allowing for time-lapse measurements. Two-dimensional diffraction patterns contain more information than a one-dimensional profile collected with laboratory diffractometers. It is for instance possible to get immediately an idea of the grain size in metallic alloys, the presence of single crystals or preferred orientation by looking at the ring structure in the unprocessed diffractograms [97].

SR-XRD in this work were collected using a Mar CCD 165 detector (Mar USA Inc., Evanston, IL, USA), consisting of 2048 x 2048 individual elements with a pixel size of 80 μm , at the BM28 end station (XMaS, ESRF, for more details on the end-station see Chapter 3). The samples were mounted in an electrochemical/environmental cell (eCell, [98]) or a portable eCell (peCell, [99]) for in-situ measurements or on a custom sample carousel (designed and devised by Prof. Mark Dowsett). The in-situ cells or the sample carousel were in turn mounted on an eleven-axis Huber diffractometer present in the BM28 beam line. For more information regarding the experimental parameters, the reader is referred to the respective experiments.

2.4.1.4 Data analysis

Diffraction patterns obtained with laboratory instrumentations or 2D diffractograms obtained at the synchrotron were processed with the XRD processing subunit of esaProject (© Mark Dowsett, EVA Surface Analysis). The software can extract diffraction patterns from a variety of data formats. The extraction process involves reprojection of the elliptical rings from the two-dimensional images to straight lines which are subsequently summed for each row and integrated to one-dimensional XRD patterns (Intensity vs. 2θ). This process can be done for single images or batch processed for larger data sets. esaProject can perform (among other features): normalization, background subtraction and peak smoothing operations on the 1D pattern.

To compare peaks on a common scale, the 2θ -space is converted to q -space according to Bragg's law and the following relation:

$$q = \frac{2\pi}{d} = \frac{4\pi \sin \theta}{\lambda}. \quad \{2.15\}$$

For qualitative analysis, all reflections were identified using reference diffraction patterns downloaded from the MinCryst database [100, 101].

2.4.2 X-RAY PHOTOELECTRON SPECTROSCOPY (XPS)

2.4.2.1 Principle of X-ray Photoelectron Spectroscopy

In X-ray photoelectron spectroscopy (XPS) electrons are emitted from a specimen as a result of the interaction between the sample surface and a flux of photons of characteristic energy (e.g. Mg- K_α , Al- K_α) [102]. These X-ray photons interact directly with core electrons of the sample atoms resulting in the emission of a photoelectron (Figure 2.14) with a kinetic energy (E_k) approximated by the difference between the incident photon energy ($h\nu$) and the binding energy (E_B):

$$E_B = h\nu - E_k - W, \quad \{2.16\}$$

W is the spectrometer work function, an instrumental figure determined during calibration of the spectrometer [103]. The spectrometer analyzes the energy of the emitted electrons and builds a spectrum by plotting the measured amount of electrons with respect to its binding energy or kinetic energy. Typically the x-axis displays the kinetic energy with increasing energy to right; hence binding energy increases from right to left. Emission of a photoelectron leaves the atom in an excited state. Relaxation can occur through emission of an Auger Electron, which will also be observed in the XPS spectrum. The inelastic mean free path of photoelectrons is defined by its probability to suffer an energy loss. Furthermore the probability that the electron analyzer receives the electron is defined by the attenuation length [104]. In both cases, kinetic energy and matrix limit the information depth to the first nanometers below the surface of the sample. Even though peaks originating from valence levels at low binding energies are present, the main information in XPS spectra come from core level peaks and Auger peaks. The chemical state of an atom can for instance be elucidated as this strongly affects the binding energies of core electrons [103, 104].

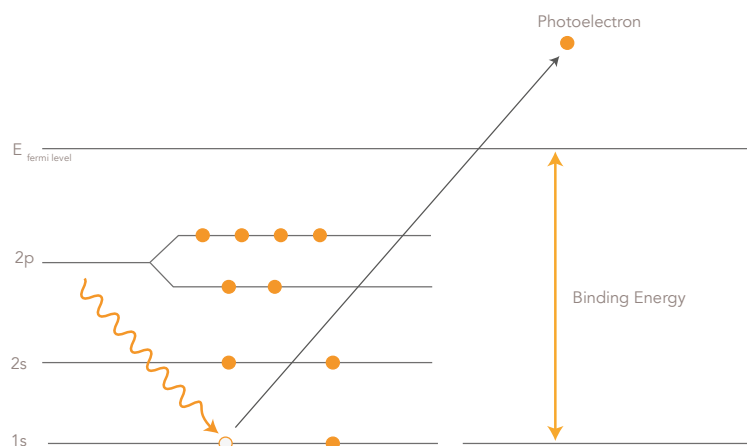


Figure 2.14
Schematic representation of the XPS process.

2.4.2.2 Instrumentation

The sample is housed in an ultrahigh vacuum (UHV)-based stainless steel chamber surrounded by an X-ray source with monochromator for excitation of the sample, a concentric hemispherical electron analyzer for energy separation of the emitted electrons followed by a detection system.

In this work, all measurements were carried out using an S-Probe monochromatized XPS spectrometer (Surface Science Instruments, VG Scienta, Pleasanton, CA, USA). The instrument is equipped with an Al-K_{α} X-ray source ($h\nu = 1486.6 \text{ eV}$) monochromatized by quartz crystal monochromators. The source is operated at 10 kV and a power of 200 W. A concentric hemispherical analyzer receives electrons from the sample at a take-off angle of 45° and is set so that the pass energy is 107.5 eV. Finally the energy resolved electrons are measured using a SSI position-sensitive detector of $40 \text{ mm} \times 40 \text{ mm}$ with a width of 13.70 eV. The pressure throughout the measurements was maintained at 2×10^{-9} mbar.

2.4.2.3 Data analysis

The core-level binding energy shifts observed in XPS spectra provide a local probe of the changes in the electronic structure of an atom in different environments in molecules and solids [105]. Moreover, the presence or absence of satellite peaks in the vicinity of XPS core lines can aid in data analysis. Practically, references to standard spectra of compounds are used for qualitative analysis of the XPS spectra and binding energy shifts provide information regarding the chemical state of a material. In this work, chemical compositions were analyzed using the CasaXPS software package (version 2.3.13, Casa Software Ltd.) was used in combination with the NIST X-ray Photoelectron Spectroscopy Database [106]. Adjacent to qualitative information, XPS spectra yield quantitative information as the number of electrons recorded for a given transition is proportional to the number of atoms at the surface.

Quantitative information was extracted out of XPS peak spectra by curve fitting procedures carried out in CasaXPS. The software uses a Shirley algorithm [107] for background subtraction and a Gauss-Lorentz cross-product for actual peak fitting. The use of relative sensitivity factors from the CasaXPS library aid in the determining the proportion between the peak intensity and the relative concentration of the emitting element.

2.5 BIBLIOGRAPHY

- [1] K. Garcia, *Wilhelm Roentgen and the Discovery of X-Rays*, Mitchell Lane Publishers, 2003.
- [2] A.K. Esterer, *Discoverer of X-ray: Wilhelm Conrad Röntgen*, J. Messner, 1968.
- [3] J. Maddox, The sensational discovery of X-rays, *Nature* 375 (1995) 183.
- [4] F. van Gelderen, *Understanding X-Rays: A Synopsis of Radiology*, Springer Berlin Heidelberg, 2003.
- [5] The Nobel Prize in Physics 1901". Nobelprize.org. Nobel Media AB 2014. Web. 29 Sep 2015. <http://www.nobelprize.org/nobel_prizes/physics/laureates/1901/index.html>.
- [6] R.E. Van Grieken, A.A. Markowicz, *Handbook of X-ray Spectrometry: Methods and Techniques*, Marcel Dekker Inc., 1993.
- [7] G.S. Smith, *An Introduction to Classical Electromagnetic Radiation*, Cambridge University Press, 1997.
- [8] P. Willmott, *An Introduction to Synchrotron Radiation: techniques and applications*, first edit., Wiley, Chichester, 2011.
- [9] F.R. Elder, R. V Langmuir, H.C. Pollock, Radiation from Electrons Accelerated in a Synchrotron, *Phys. Rev.* 74 (1948) 52–56.
- [10] D.H. Tombouliau, P.L. Hartman, Spectral and Angular Distribution of Ultraviolet Radiation from the 300-Mev Cornell Synchrotron, *Phys. Rev.* 102 (1956) 1423–1447.
- [11] P.L. Hartman, D.H. Tombouliau, Far Ultraviolet Radiation from the Cornell Synchrotron, *Phys. Rev.* 91 (1953) 1577–1578.
- [12] A. Thompson, D. Attwood, E. Gullikson, M. Howells, K.-J. Kim, J. Kirz, J. Kortright, H. Winick, I. Lindau, Y. Liu, P. Pianetta, A. Robinson, J. Scofield, J. Underwood, G. Williams, *X-ray Data Booklet*, 2009.
- [13] S. Mobilio, F. Boscherini, C. Meneghini, *Synchrotron Radiation: Basics, Methods and Applications*, Springer Berlin Heidelberg, 2014.
- [14] A.L. ROBINSON, Experiments Begin at Daresbury's SRS, *Science* (80-.). 213 (1981) 852–856.
- [15] R. Haensel, The European Synchrotron Radiation Facility, *Nucl. Instruments Methods Phys. Res. Sect. A Accel. Spectrometers, Detect. Assoc. Equip.* 266 (1988) 68–73.
- [16] [Http://www.lightsources.org/](http://www.lightsources.org/), Lighsources.org, Accessed 2015-01-05.
- [17] W.E. White, A. Robert, M. Dunne, The Linac Coherent Light Source, *J. Synchrotron Radiat.* 22 (2015) 472–476.
- [18] J. Larmor, On a dynamical theory of the electric and luminiferous medium, *Philos. Trans. R. Soc.* (1897) 205 – 300.
- [19] D.M. Mills, J.R. Helliwell, Å. Kvik, T. Ohta, I.A. Robinson, A. Authier, Report of the working group on synchrotron radiation nomenclature - Brightness, spectral brightness or brilliance?, *J. Synchrotron Radiat.* 12 (2005) 385.
- [20] J.E. Fernández, Polarization effects in X-ray / matter interactions, *J. Trace Microprobe Tech.* 14 (1996) 489–516.
- [21] F. Heigl, A. Jürgensen, X.-T. Zhou, S. Lam, M. Murphy, J.Y.P. Ko, T.K. Sham, R.A. Rosenberg, R. Gordon, D. Brewster, T. Regier, L. Armelao, Dynamic View on Nanostructures: A Technique for Time Resolved Optical Luminescence using Synchrotron Light Pulses at SRC, APS, and CLS, *AIP Conf. Proc.* (2007) 1202–1205.
- [22] T.-K. Sham, R.A. Rosenberg, Time-resolved synchrotron radiation excited optical luminescence: light-emission properties of silicon-based nanostructures., *Chemphyschem* 8 (2007) 2557–67.
- [23] I.M. Ternov, *Synchrotron radiation: basics, methods and applications.*, *Uspekhi Fiz. Nauk* 165 (1995) 429.
- [24] DESY online available: http://photon-science.desy.de/sites/site_photon-science/content/e62/e189219/e189248/e189389/e196698/e189414/

Spectra_eng.png, [Accessed november 2015].

[25] G. Brown, K. Halbach, J. Harris, H. Winick, Wiggler and undulator magnets—A review, *Nucl. Instr. Meth.* 208 (1983) 65–77.

[26] W.H. Bragg, W.L. Bragg, The reflection of X-rays by crystals (I), *Proc. R. Soc. London* 88 (1913) 428–438.

[27] T.F. Lin, J.P. Wang, S. Radiation, *The Safety Interlock System of Synchrotron Radiation Research Center*, (1996).

[28] D.E. Sayers, E.A. Stern, F.W. Lytle, New Technique for Investigating Noncrystalline Structures: Fourier Analysis of the Extended X-Ray Absorption Fine Structure, *Phys. Rev. Lett.* 27 (1971) 1204–1207.

[29] G. Bunker, *Introduction to XAFS*, (2010) 268.

[30] S. Kelly, D. Hesterberg, B. Ravel, Analysis of soils and minerals using X-ray absorption spectroscopy, *Methods Soil Anal. Part 5—Mineralogical Methods* (2008) 387–463.

[31] J.E. Penner-Hahn, X-ray Absorption Spectroscopy, *Compr. Coord. Chem. II* (2003) 159–186.

[32] M. Newville, *Fundamentals of XAFS*, *ReVision* (2004) 43.

[33] J. Als-Nielsen, D. McMorrow, in: *Elements of Modern X-ray Physics*, John Wiley & Sons, Inc., 2011, pp. 1–28.

[34] S. Tavernier, in: *Experimental Techniques in Nuclear and Particle Physics*, Springer, Heidelberg, 2010, pp. 23 – 53.

[35] T. Schoonjans, *Three Dimensional Quantitative X-ray Fluorescence at the micro- and nanoscopic level: methodological development and applications*. Ph.D Dissertation, Ghent Univ. (2012).

[36] J.E. Fernández, Rayleigh and Compton scattering contributions to x-ray fluorescence intensity, *X-Ray Spectrom.* 21 (1992) 57–68.

[37] A.H. Compton, A Quantum Theory of the Scattering of X-rays by Light Elements, *Phys. Rev.* 21 (1923) 483–502.

[38] T. Schoonjans, A. Brunetti, B. Golosio, M. Sanchez del Rio, V.A. Solé, C. Ferrero, L. Vincze, The xraylib library for X-ray-matter interactions. Recent developments, *Spectrochim. Acta Part B At. Spectrosc.* 66 (2011) 776–784.

[39] S. Calvin, *XAFS for everyone*, CRC press, Boca Raton, 2013.

[40] J.J. Rehr, J.J. Kas, F.D. Vila, M.P. Prange, K.

Jorissen, Parameter-free calculations of X-ray spectra with FEFF9, *Phys. Chem. Chem. Phys.* 12 (2010) 5503–5513.

[41] Y. Joly, X-ray absorption near-edge structure calculations beyond the muffin-tin approximation, *Phys. Rev. B* 63 (2001) 125120.

[42] W. Gawelda, V.-T. Pham, M. Benfatto, Y. Zaushitsyn, M. Kaiser, D. Grolimund, S.L. Johnson, R. Abela, A. Hauser, C. Bressler, M. Chergui, Structural Determination of a Short-Lived Excited Iron(II) Complex by Picosecond X-Ray Absorption Spectroscopy, *Phys. Rev. Lett.* 98 (2007) 57401.

[43] M. Brown, R.E. Peierls, E.A. Stern, White lines in X-ray absorption, *Phys. Rev. B* 15 (1977) 738–744.

[44] J.A. Kirby, D.B. Goodin, T. Wydrzynski, A.S. Robertson, M.P. Klein, State of manganese in the photosynthetic apparatus. 2. X-ray absorption edge studies on manganese in photosynthetic membrane, *J. Am. Chem. Soc.* 103 (1981) 5537–5542.

[45] a Vairavamurthy, Using X-ray absorption to probe sulfur oxidation states in complex molecules, *Spectrochim. Acta Part A Mol. Biomol. Spectrosc.* 54 (1998) 2009–2017.

[46] M. Benfatto, C. Meneghini, in: S. Mobilio, F. Boscherini, C. Meneghini (Eds.), *Synchrotron Radiation SE - 7*, Springer Berlin Heidelberg, 2015, pp. 213–240.

[47] C.S. Schnorr, M.C. Ridgway, *X-Ray Absorption Spectroscopy of Semiconductors*, Springer Berlin Heidelberg, 2014.

[48] E.A. STERN, Structure determination by X-ray absorption, *Contemp. Phys.* 19 (1978) 289–310.

[49] D.C. Koningsberger, R. Prins, *X-ray absorption : principles, applications, techniques of EXAFS, SEXAFS, and XANES*, New York : Wiley, 1988.

[50] P. Persson, S. Lunell, a Szöke, B. Ziaja, J. Hajdu, Shake-up and shake-off excitations with associated electron losses in X-ray studies of proteins., *Protein Sci.* 10 (2001) 2480–4.

[51] A. Gaur, B.D. Shrivastava, H.L. Nigam, X-Ray Absorption Fine Structure (XAFS) Spectroscopy – A Review, *Proc Indian Natn Sci Acad Spl. Issue, Part B* 79 (2013) 921–966.

[52] M. Newville, IFEFFIT : interactive XAFS analysis and FEFF fitting, *J. Synchrotron Radiat.* 8 (2001) 322–324.

[53] B. Ravel, M. Newville, ATHENA, ARTEMIS, HEPHAESTUS: data analysis for X-ray absorption spectroscopy using IFEFFIT., *J. Synchrotron Radiat.* 12 (2005) 537–41.

- [54] G. Silversmit, Chapter 2: EXAFS, extended X-ray absorption Fine structure, (2011).
- [55] K. V Klementev, Extraction of the fine structure from x-ray, 34 (2001) 209–217.
- [56] A. Filipponi, A. Di Cicco, X-ray-absorption spectroscopy and n-body distribution functions in condensed matter. II. Data analysis and applications, *Phys. Rev. B* 52 (1995) 15135 – 15149.
- [57] M. SALMERON, R. SCHLOGL, Ambient pressure photoelectron spectroscopy: A new tool for surface science and nanotechnology, *Surf. Sci. Rep.* 63 (2008) 169–199.
- [58] Y. Tamenori, Electron yield soft X-ray photoabsorption spectroscopy under normal ambient-pressure conditions, *J. Synchrotron Radiat.* 20 (2013) 419–425.
- [59] P.. Citrin, X-ray absorption spectroscopy applied to surface structure: SEXAFS and NEXAFS, *Surf. Sci.* 299-300 (1994) 199–218.
- [60] A. Rogalev, Goulon, in: T.K. Sham (Ed.), *Chemical Applications of Synchrotron Radiation Part II: X-ray Applications*, World Scientific, Singapore, 2002, pp. 707–760.
- [61] R.P. Taylor, A.A. Finch, J.F.W. Mosselmann, P.D. Quinn, The development of a XEOL and TR XEOL detection system for the I18 microfocuss beamline Diamond light source, *J. Lumin.* 134 (2013) 49–58.
- [62] L. Bertrand, L. Robinet, M. Thoury, K. Janssens, S.X. Cohen, S. Schöder, Cultural heritage and archaeology materials studied by synchrotron spectroscopy and imaging, *Appl. Phys. A* 106 (2012) 377–396.
- [63] F. Ions, V.A. Fassel, Analytical Applications of X-Ray Excited Optical Luminescence Direct Determination of Rare Earth Nuclear Poisons in Zirconia, *Anal. Biochem.* 46 (1974) 997 – 999.
- [64] A.P. D’Silva, V.A. Fassel, X-ray excited optical fluorescence of trace rare earths in yttrium phosphate and yttrium vanadate hosts. Part per giga level determination of rare earth impurities in yttrium oxide, *Anal. Chem.* 45 (1973) 542–547.
- [65] A.P. D’Silva, G.J. Oestreich, V.A. Fassel, X-ray Excited Optical Luminescence of Polynuclear Aromatic Hydrocarbons, *Anal. Chem.* 48 (1976) 915–917.
- [66] A. Bianconi, D. Jackson, K. Monahan, Intrinsic luminescence excitation spectrum and extended x-ray absorption fine structure above the K-edge in CaF₂, *Phys. Rev. B* 17 (1978) 2022–2024.
- [67] T.-K. Sham, Photon-in/photon-out spectroscopic techniques for materials analysis: some recent developments., *Adv. Mater.* 26 (2014) 7896–901.
- [68] D.J. Robbins, On Predicting the Maximum Efficiency of Phosphor Systems Excited by Ionizing Radiation, *J. Electrochem. Soc.* 127 (1980) 2694.
- [69] Z. Wang, X. Guo, T.-K. Sham, 2D XANES-XEOL mapping: observation of enhanced band gap emission from ZnO nanowire arrays, *Nanoscale* 6 (2014) 6531.
- [70] J. Roqué, N.R.J. Poolton, J. Molera, a. D. Smith, E. Pantos, M. Vendrell-Saz, X-ray absorption and luminescence properties of metallic copper nanoparticles embedded in a glass matrix, *Phys. Status Solidi* 243 (2006) 1337–1346.
- [71] A. Mooradian, Photoluminescence of metals, *Phys. Rev. Lett.* 22 (1969) 185–187.
- [72] G.T. Boyd, Z.H. Yu, Y.R. Shen, Photoinduced luminescence from the noble metals and its enhancement on roughened surfaces, *Phys. Rev. B* 33 (1986) 7923–7936.
- [73] A. Adriaens, P. Quinn, S. Nikitenko, M.G. Dowsett, Real Time Observation of X-ray-Induced Surface Modification Using Simultaneous XANES and XEOL-XANES., *Anal. Chem.* 85 (2013) 9556–9563.
- [74] M. Dowsett, M. Hand, P.-J. Sabbe, P. Thompson, A. Adriaens, XEOM 1 - A novel microscopy system for the chemical imaging of heritage metal surfaces, *Herit. Sci.* 3 (2015) 14.
- [75] P.-J. Sabbe, M. Dowsett, M. Hand, R. Grayburn, P. Thompson, W. Bras, A. Adriaens, Evaluation of an X - ray-Excited Optical Microscope for Chemical Imaging of Metal and Other Surfaces, *Anal. Chem.* 86 (2014) 11789–11796.
- [76] T. Murata, K. Harada, S. Emura, T. Moriga, M. Nomura, K.R. Bauchspiess, H. Maeda, Luminescence yield spectra through X-ray excitation - optical XAFS, *Nucl. Instruments Methods Phys. Res. Sect. A Accel. Spectrometers, Detect. Assoc. Equip.* 319 (1992) 290–294.
- [77] M.G. Dowsett, A. Adriaens, G.K.C. Jones, N. Poolton, S. Fiddy, Optically Detected X-ray Absorption Spectroscopy Measurements as a Means of Monitoring Corrosion Layers on Copper, *Anal. Chem.* 80 (2008) 8717–8724.
- [78] N. Poolton, B. Towilson, B. Hamilton, D. Evans, New instrumentation for micro-imaging X-ray absorption spectroscopy using optical detection methods, *Nucl. Instruments Methods Phys. Res. Sect. B Beam Interact. with Mater. Atoms* 246 (2006) 445–451.
- [79] R.A. Rosenberg, C.-R. Wen, K. Tan, J.-M. Chen, Production of excited neutral and ionic

photofragments following core-level excitation in molecules, *J. Chem. Phys.* 92 (1990) 5196.

[80] T.K. Sham, P. Kristof, R.A. Holroyd, Photoconductivity and luminescence measurements in liquids exposed to 4–6-keV x rays, *Rev. Sci. Instrum.* 63 (1992) 1198.

[81] S. Emura, T. Moriga, J. Takizawa, M. Nomura, K.R. Bauchspies, T. Murata, K. Harada, H. Maeda, Optical-luminescence yield spectra produced by x-ray excitation, 47 (1993) 6918–6930.

[82] P.-J. Sabbe, M.G. Dowsett, M. De Keersmaecker, M. Hand, P. Thompson, A. Adriaens, Synthesis and surface characterization of a patterned cuprite sample: Preparatory step in the evaluation scheme of an X-ray-excited optical microscopy system, *Appl. Surf. Sci.* 332 (2015) 657–664.

[83] N. Daldosso, F. Rocca, I.P. Trento, New EXAFS Measurements by XEOL and TEY on Porous Silicon, *J. Porous Mater.* 172 (2000) 169–172.

[84] M.J. Ward, W. Han, T. Sham, 2D XAFS - XEOL Mapping of Ga_{1-x}Zn_xN_{1-x}O_x Nanostructured Solid Solutions, *J. Phys. Chem. C* 115 (2011) 20507–20514.

[85] D. Pailharey, Y. Mathey, F. Jandard, S. Larcheri, F. Rocca, a Kuzmin, R. Kalendarev, J. Purans, G. Dalba, R. Graziola, O. Dhez, Nanoscale x-ray absorption spectroscopy using XEOL-SNOM detection mode, *J. Phys. Conf. Ser.* 93 (2007) 012038.

[86] M. Murphy, X. Zhou, F. Heigl, T. Regier, T. Sham, An X-Ray Excited Optical Luminescence (XEOL) Analysis of Mn²⁺ Doped ZnS Nanostructures, *Nanostructures* 12–14.

[87] L. Soderholm, G.K. Liu, M.R. Antonio, X-ray excited optical luminescence (XEOL) detection of x-ray absorption fine structure (XAFS), *J. Chem. Phys.* 109 (1998) 6745 – 6752.

[88] D. Sands, *Crystals and lattices*, Dover Publications, 1969.

[89] B.E. Warren, *X-Ray Diffraction*, Dover Publications, 2012.

[90] W.H. Zachariasen, *Theory of X-Ray Diffraction in Crystals*, Dover Publications, 2004.

[91] S. Hall, B. McMahon, *International tables for crystallography Volume G: definition and exchange of crystallographic data.*, Springer Netherlands, 2005.

[92] A. Bravais, Mémoire sur les systèmes formés par les points distribués régulièrement sur un plan

ou dans l'espace, *J. Ec. Polytech.* 19 (1850) 1–128.

[93] T. Hahn, *International Tables for Crystallography, Space-Group Symmetry*, Wiley, 2005.

[94] C. Suryanarayana, M.G. Norton, in: *X-Ray Diffraction A practical Approach*, Plenum Press, New York, 1998, pp. 223–236.

[95] A. Guinier, *X-ray diffraction in crystals, imperfect crystals and amorphous bodies*, Dover Publications, 1994.

[96] B. He, U. Preckwinkel, K. Smith, Fundamental of Two-dimensional X-ray Diffraction (XRD), *Adv. X-ray Anal.* 43 (2000) 273–280.

[97] B.B. He, in: *Two-Dimensional X-Ray Diffraction*, John Wiley & Sons, Inc., 2009, pp. 218–248.

[98] M. Dowsett, A. Adriaens, Cell for simultaneous synchrotron radiation X-ray and electrochemical corrosion measurements on cultural heritage metals and other materials., *Anal. Chem.* 78 (2006) 3360–5.

[99] R. Grayburn, Spectroelectrochemical techniques for the conservation of metallic artefacts, Ph. D. Dissertation, Ghent Univ.

[100] A. V Chichagov, D.A. Varlamov, R.A. Dilanyan, T.N. Dokina, N.A. Drozhzhina, O.L. Samokhvalova, T. V Ushakovskaya, MINCRYST: a crystallographic database for minerals, local and network (WWW) versions, *Crystallogr. Reports* 46 (2001) 876–879.

[101] MinCryst [online] Available: <http://database.iem.ac.ru/mincryst/index.php>, [accessed june 2014].

[102] P. van der Heide, *X-ray Photoelectron Spectroscopy: An introduction to Principles and Practices*, Wiley, 2011.

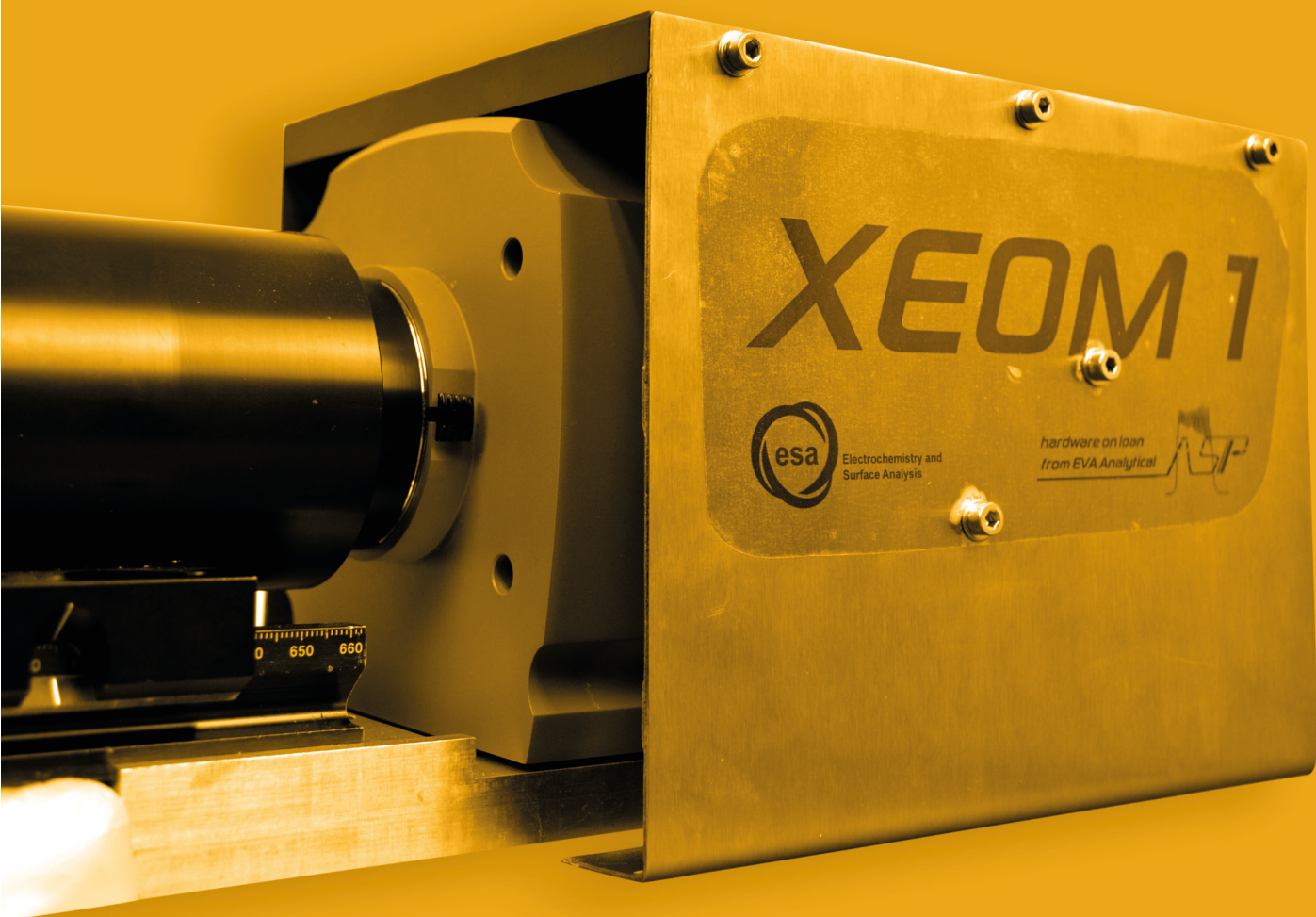
[103] S. Hofmann, *Auger- and X-ray Photoelectron spectroscopy in Materials Science*, Springer, 2013.

[104] J.F. Watts, *An introduction to Surface Analysis by Electron Spectroscopy*, Oxford University press, Oxford, 1990.

[105] Z. Zeng, X. Ma, W. Ding, W. Li, First-principles calculation of core-level binding energy shift in surface chemical processes, *Sci. China Chem.* 53 (2010) 402–410.

[106] A.V. Naumkin, A. Kraut-Vass, S.W. Gaarenstroom, C.J. Powell, NIST X-ray Photoelectron Spectroscopy Database, [accessed online june 2014]].

[107] D.A. Shirley, High-Resolution X-Ray Photoemission Spectrum of the Valence Bands of Gold, *Phys. Rev. B* 5 (1972) 4709–4714.



XEOM 1

CHAPTER 3



The portable XEOL spectromicroscopy system was given the name: XEOM 1, short for X-ray-excited optical microscope 1. In this chapter, the instrumental features of XEOM 1 will be discussed. The design of novel analytical instrumentation as XEOM 1 is not static, but the result of a dynamic evolution over the years. This chapter will therefore also shed light on the modifications and upgrades that XEOM 1 has undergone since the beginning of this doctoral study; September 2010.

It must be stated clearly beforehand that the mechanical design and manufacture of the optical column and its auxiliary components is the work of the co-supervisor of this thesis, Prof. Mark Dowsett. The lens system was designed and modelled by Matthew Hand and the lenses itself were made by Knight Optical (Harrietsham, UK). The new electronics interface unit was designed and devised by Prof. Mark Dowsett and my colleague Jorge Alves Anjos, the initial one was made by Adrian Lovejoy (electronics Workshop, Department of Physics, The University of Warwick). The filter wheel was designed by Prof. Mark Dowsett and made by Davy De Pauw (Workshop of the Faculty of Science, S4-bis, Ghent University). The software was written by both Prof. Mark Dowsett and Matthew Hand. The input of the author is the evaluation of all components, aiding toward new and improved setups and the coordination of updates when this was done between Ghent and the UK. This chapter is partially based on published descriptions of the system, which can be found in the articles issued by Analytical Chemistry and Heritage Science [1, 2] and the Ph.D. dissertation written by my former colleague Matthew Hand [3].

3.1 HARDWARE

The hardware of the XEOM 1 system was designed and built in a modular fashion in order to enhance the portability and transportability of the instrument. Apart from the optical column; XEOM 1 incorporates: a control and data acquisition system, an electronics interface unit, a set of detectors and a portable computer with control and data processing software. This approach allows XEOM 1 to be used as a stand-alone system in a laboratory environment where an alternative excitation source is being used, e.g. a UV-C LED (see chapter 7). When a beam time allocation is granted, the entire system can be dismantled and sent to the synchrotron packed into three hard-shell suitcases. In what follows a concise description of the XEOM 1 hardware is given and, where necessary, discussed.

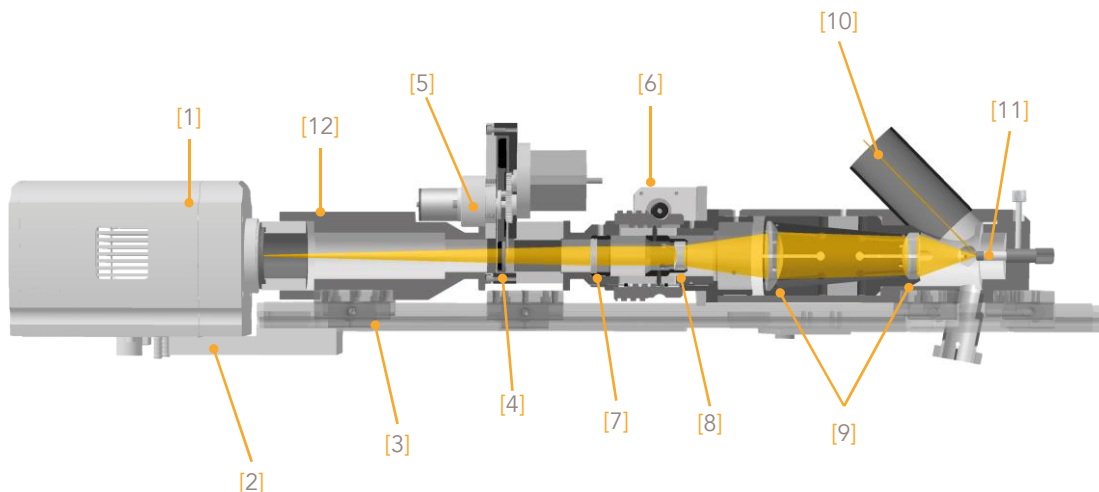


Figure 3.1

3D section view of the XEOM 1 microscopy system : [1] Andor Ikon-L camera with broadband CCD, [2] aluminum extension plate to optical rail to mount Andor Ikon-L, [3] Melles Griot optical rail, [4] filter, [5] filter wheel carrier for 10 filters, [6] remote focusing mechanism, [7] projector lens, [8] focusing /collimating lens, [9] aspherical doublet objective, [10] X-rays (entering through one of six possible ports), [11] sample housing (may be replaced with electrochemical/environmental cell), [12] camera tube.

After M.G. Dowsett (2014) solid model for XEOM1



Figure 3.2

Photograph of the optical column of XEOM 1 with its components. All the elements described in the caption of Figure 3.1 can also be seen in the photograph.

3.1.1 OPTICAL COLUMN

A 3D section view of optical column the XEOM 1 instrument is given in Figure 3.1 and a photograph of the system is given in Figure 3.2. The housing of the microscope and its major constituent elements have been primarily constructed of black acetal copolymer (see Figure 3.2). Experiments prior to designing ODXAS 1 confirmed the low intrinsic visible fluorescence under X-ray excitation of the material.

Apart from this, its light-tightness and the low reflectivity it exhibits make the acetal appropriate for XEOL experimentation. Additionally, its lightness (compared to metal components) and robust, impact proof character enhance the transportability of the system. All components of the optical column come together on a graduated optical rail, which is, in turn, installed on the beamline. The graduation allows precise (re-) alignment of the optics.

The body of the microscope comprises three main sections: a sample stage section, a central optics section and a final section for mounting the CCD camera. In what follows all sections are discussed in more detail.

3.1.1.1 sample stage section

The first section consists of a sample stage end cap (annotation 11 in Figure 3.1) which is surrounded by a number of angle ports at 10° , 45° and 60° with respect to the plane perpendicular to the optical axis. The sample stage is the base for a set of bespoke sample holders that allow coupons, grids and powders to be placed precisely in the focal plane of the microscope optics and centred in the field of view of the CCD camera (Figure 3.3). The angle ports serve as a mounting point for modular accessories such as: X-ray (avalanche photodiode or silicon drift detector) and optical luminescence (photomultiplier tube) detectors for supplementary experiments, a webcam for live sample inspection, a sample illumination system and a connector for inert gas supply to prevent beam-induced ozone damage to the samples (Figure 3.3 IV). The angle ports permit the X-ray beam to enter the microscope and target the sample. The choice of ports provided by the manifold ensures that the microscope can be mounted in different ways on different beamlines, thus emphasizing the portability of the instrument. When an angle port is not being used during an experiment, the entrance of the port is blocked with a plug in order to keep the system light tight at any time. The first section can be replaced by an electrochemical cell when spectroelectrochemical experiments are intended [4].

3.1.1.2 Central optics section

The central section of the column houses the lenses, optical filters in a single filter or a filter wheel carrier and a remotely controlled focusing mechanism. A complete overview of the lenses installed is given in 3.1.2.

3.1.1.2.1 Focus module

For safety reasons, it is necessary to control all equipment from a control hutch, adjacent to the experimental hutch. Remote focusing is done by driving a NEMA-17 frame stepper motor from a computer with the esaXsec software installed (see below). The stepper motor drives a worm which drives a worm gear machined into a rotating sleeve which surrounds the focus lens carrier. Driving the stepper motor



Figure 3.3

Sample holders tailored for 12.5 mm diameter coupons (I), TEM grid samples for microscope assessment (II) , powdered samples (III) . All sample holders screw on the mount point of the XEOM 1 end cap, which ensures that the sample is centred in the field of view of the detector. The final part (IV) is a plug that serves as a connector between gas tubing and a 10° angle port This piece enables the optical column to be filled with an inert gas (e.g. He) in order to prevent beam-induced ozone damage .

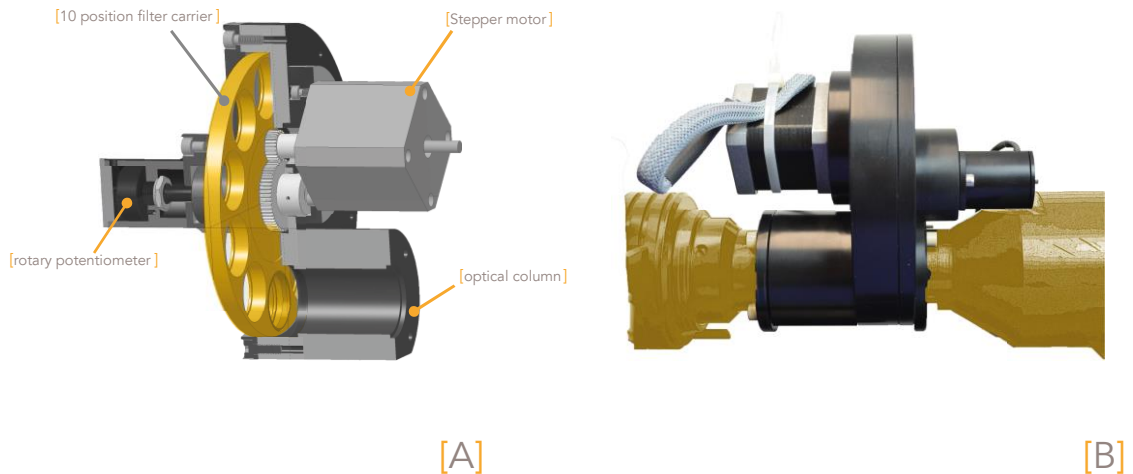


Figure 3.4

[A] 3D section view drawing of the filter wheel. The filter wheel has 10 positions for 25 mm diameter lenses. After M.G. Dowsett (2014) solid model for the filter wheel.

[B] Image of the filter wheel installed on XEOM 1.

clockwise or counter clockwise forces the rotating sleeve to rotate and allows one to move the focus lens towards the blue focal position or the red position. The worm drive mechanism also guides a linear potentiometer which provides feedback regarding the position of the focusing lens. Assessing the voltage across this potentiometer allows the user to determine exactly the position of this lens. For this reason, focus lens positions in later chapters are expressed in Volts. The precision of the focusing mechanism can be narrowed down to within approximately 2 nm of the targeted wavelength [3].

3.1.1.2.2 Filter carrier module

The final part of the central optics section is a module for wavelength selection of the emission passed through the lenses. This wavelength selection is done by a set of band pass filters. A complete overview and discussion of the filters used during this work is given in section 3.1.3. Essentially, the quality of the data is not dependent on the position of the filter section. However, some conditions must be met. First of all, the filters may not be hit by backscattered X-rays. These X-rays would create unwanted secondary fluorescence in the different layers of refractive materials from which the filters are composed. Then, the purchased filters are all (only) 25 mm in diameter, which means that the filters must be placed inside the condensed beam. This beam shape is only present downstream of the focusing lens. Finally, most of the filters used during this research are interference filters. Interference filters allow certain wavelengths to be transmitted based on the creation of an interference pattern, a process which is very angle sensitive. Therefore, the filters will only deliver its desired effect when the incoming light bundle is close to parallel. For all these reason, it was chosen to incorporate the filter section downstream of the projection lens L4.

The majority of the experiments carried out with XEOM 1 were done with a single filter carrier in place. Consequently, when a spectral survey has to be carried out, the filter in place had to be changed manually. The procedure of swapping the filters involved: turning off the X-ray beam, opening the experimental hutch, changing the filters, performing the search procedure, closing the hutch and ultimately switching on the X-rays again. This procedure required a considerable amount of time which is at the expense of valuable beamtime to collect data. Therefore it is desirable to avoid changing the filters manually and automate the process. Therefore, a system was designed capable of holding 10 filters simultaneously which can be remotely operated to change the filter. Figure 3.4 A shows a 3D section view of the filter wheel and its components and Figure 3.4 B displays the filter wheel installed on microscopy system. The body of the filter wheel was machined, like other components of XEOM 1, from black acetal copolymer. The module is bolted on one side with the focusing section and engages on the other side with a spigot machined on the camera tube. The filter wheel is 116 mm in diameter and can hold ten 25 mm diameter filters. The filter wheel is interfaced with a high torque stepper motor via two gears with a gear ratio of 58/24 (filter wheel gear / stepper motor gear). The NEMA 17 stepper motor steps, depending on its settings, 200 (full step) or 400 times (half step) in order to make a complete revolution. Taking the gear ratio into account, 482 or 964 steps are necessary for the filter wheel to make one revolution. Accordingly, this provides angular resolution of either 0.74 ° or 0.37 ° per step. Since the centres of the filters are 44 mm away from the filter wheel axis, this angular resolution corresponds with a lateral resolution of 0.56 mm or 0.28 mm. It was

chosen to set the stepper motor at half step, this way the filters could be aligned with the centre of the optical column to within 0.28 mm.

In order to keep track of the position of the filter wheel, the axis of the filter wheel engages with the shaft of a rotary servo-potentiometer. The pot is provided with 10 V from the electronics interface unit (EIU – see section 3.1.5). Rotation of the filter wheel forces the wiper inside the potentiometer to move correspondingly and adapt the internal resistance perceived by the voltage. Consequently, depending on the filter wheel position, a value between 0 – 10 V is registered by one of the analog inputs of the Agilent data acquisition system (DAQ) module. Software required to operate the filter wheel is incorporated in the esaXSec software. In order for the software to operate correctly, a calibration procedure is required. During a calibration procedure, each filter is associated with a rotary position read out by the potentiometer and the number of steps by the stepper motor required to move to the next filter is determined. When these values are entered in the software, the algorithm will determine how many steps are required from the stepper motor to bring the user selected filter in place. In future updates, each filter will also be associated with a value, determined by the linear potentiometer, for optimal position of the focusing for the selected wavelength. This way, the extensive operational procedure to find optimal focus prior to the actual X-ray imaging will be considerably shortened.

3.1.1.3 CCD detector section.

The final section of the optical column holds the camera tube and the CCD-camera or other detector. A complete overview of the specifications of the detectors applied during this research is given in section 3.1.4.

The camera is housed in a box lined with 0.5 mm self-adhesive lead sheet and the camera tube was provided with the same coating. This measure had to be taken since the loss of data was observed during initial experiments with an unprotected camera. The assumption was made that the loss of data was the result of backscattered X-rays entering the ventilation grills of the camera, building up charge at a critical area in the electronics and forcing the camera to flush after a certain period of time. Performing the experiments with the lead protected set-up avoided this problem, a result which supports the assumption made. For each CCD camera, a custom camera tube was made. The camera tube used in combination with the Andor camera is lined with lead and painted matt black inside to suppress scattered light. The FLI camera is mounted via a flange of the camera body which slides in the camera tube and is held in place by 4 screws. The Andor system is provided with an F-mount bayonet fitting, a commercial three-lug bayonet lens mount introduced by Nikon in 1959 [5]. Accordingly, an F-mount bayonet flange, recovered from a defective lens, is attached to the end of the camera tube prepared for the Andor

system. Since the F-mount fitting (which was apparent from a series of dark count measurements) appeared to be not completely light-tight, an extra stray light blocking cap was added to the connection.

3.1.2. LENS SYSTEM

One of the major benefits of imaging XEOL is that optical emission provided can be guided generally more easily than fluorescent X-rays. This allows the XEOM optical equipment to be in general, relatively simple. Nevertheless, a considerable amount of care must be taken when designing a full-field imaging system. In particular the optical aberrations of the lens system must be reduced to a minimum as this will influence disadvantageously the final image quality and consequently also the extracted data. A basic configuration was proposed which aimed to maximize XEOL collection capability with respect to both bandwidth and overall intensity, which would benefit image quality and ultimately lead to reduced measurement times. Subsequently, this design was further optimized computationally with the ray tracing software package OSLO (Optics Software for Layout and Optimization) [6].

The XEOM optical system consists of four lenses. At 50 mm from the sample face, the first of an objective doublet (L1) of plano-convex aspheres collects a relatively large solid angle of the X-ray induced light. After passing the second asphere (L2), the light is guided through a bi-concave lens (L3) which serves as a collimating and focusing element (driven by the stepper motor). Finally, L4 is a weak bi-convex lens used to project the image onto the sensor surface. An overview of the lenses of XEOM 1 is given in Table 3.1.

Lens	diameter	geometry	function
L1	40 mm	plano-convex	objective
L2	60 mm	plano-convex	objective
L3	25 mm	bi-concave	focussing/ collimating
L4	30 mm	bi-convex	projecting

Table 3.1

Overview of the UV-grade fused Si lenses used in XEOM 1. Lenses are enumerated downstream from the sample position.

All lenses are fabricated from UV-grade fused silica (UVFS) (Knight Optical, Harrietsham, UK). This material, a synthetic amorphous silicon dioxide of extremely high purity, is often used in astronomical imaging systems. It was chosen because of its transparent character in the targeted XEOL wavelength region (250 – 1000 nm) and its low intrinsic fluorescence. It is very probable that a significant flux of X-rays, mostly as backscatter from the sample or end-cap of the microscope, will strike the objective lenses. Any light that might be generated by this process would raise considerably the background noise level in the measurement or possibly be present as a measurement artefact in the data. Lenses are often covered with an anti-reflectivity coating to minimize losses of intensity caused by the reflection of light at the air-glass interface of each lens front. Since these coatings can be prone to the production of secondary emission as described above, it was chosen to purchase lenses without such a coating. Even without the coating, the fused silica should exhibit a flat transmission above 93% per lens in the required wavelength range of 250 – 1000 nm (and beyond), according to the lens manufacturer [7]. This was confirmed by an experiment conducted by the author. Transmission profiles in the range of 200 – 1100 nm were recorded with a UVmini-1240 UV-Vis spectrophotometer (Shimadzu Corporation, Kyoto, Japan). Before the lenses were measured, the instrument baseline was measured and subtracted of all the subsequent measurements. Figure 3.5 displays the results of this experiment. Clearly, the objective doublet elements (L1 & L2) and the projector lens (L4) show a flat transmission well above 90% in the wavelength range of 250 – 1100 nm. In the small area between 200 and 250 nm, a transmission of 80% and higher is measured. Whereas the plano-convex and the bi-convex lenses force the light rays to converge to a focal point, the bi-concave focusing lens (L3) has a diverging effect. The light coming from the halogen or deuterium lamp from the spectrophotometer is also subjected to the diverging effect of this lens. After passage through the lens, a considerable amount of the input flux will be refracted by this lens to an area outside the field-of-view of the detector. This will lead to a lower amount of counts perceived by the detector and accordingly to lower transmission (T%). The magnitude of this effect will be smaller or larger depending on the position of the lens in the beam. This is exactly what is observed in the spectra obtained for focusing lens L3, as depicted in Figure 3.5. The measurement was repeated three times, where the position of the lens with respect to the detector was changed during each experiment. During these measurements the transmission efficiency remained, more or less, flat in the 200-1100 nm wavelength range and average transmission varied between 35 – 50 T%. As mentioned above, it would be wrong to conclude that the focusing lens is defective. On the contrary, the lens diverges the light as it should. Unfortunately is the solid angle of the detector in the spectrophotometer not sufficiently large to collect all the refracted light.

The absolute position of each lens and the lens spacing is of critical importance for the desired behaviour of the microscope. To assure all lenses are spaced and positioned correctly according to the design, cartridges with a collet mechanism to hold the lens were made. Once all the lenses are in place an overall transmission of 70% is obtained and the overall magnification of the microscope is 12 [1].

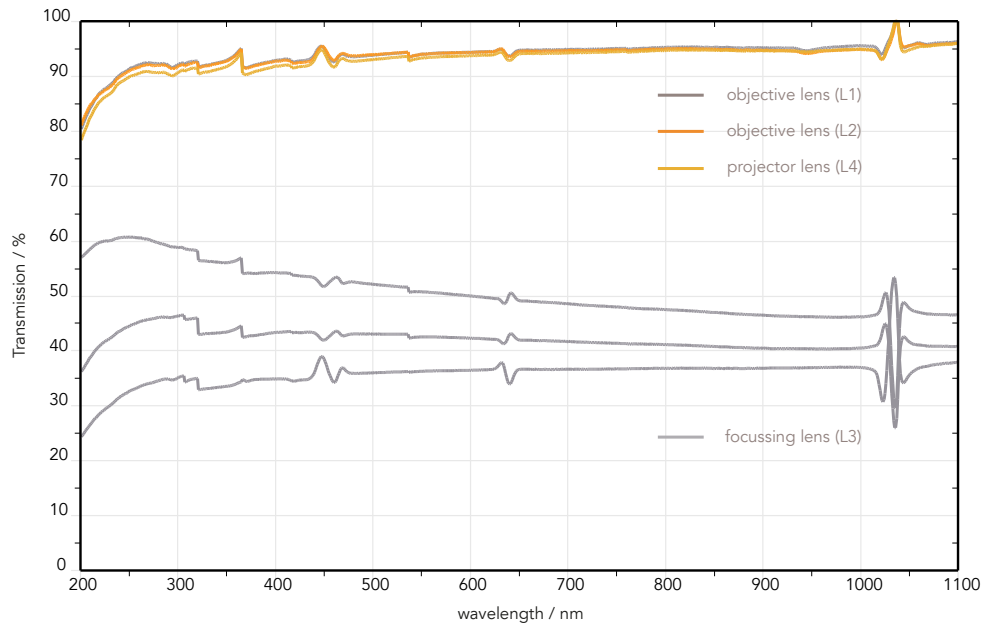


Figure 3.5

Transmission profiles of four UV-grade fused silica lenses built into XEOM 1 (L1 – L4). L1, L2 and L4 exhibit flat transmission profiles well above 90% in the targeted 250 – 1100 nm region. The bi-concave focussing lens has a dispersive effect on the passing radiation, which makes a proper measurement of this lens on its own very difficult.

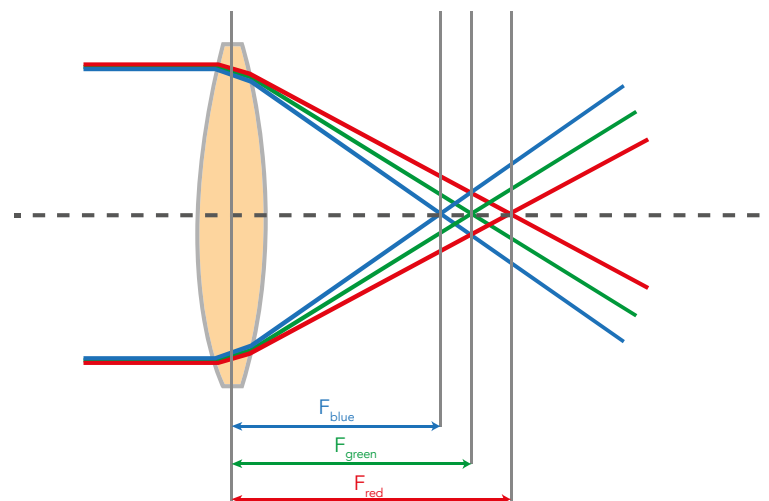


Figure 3.6

Chromatic aberration is the variation in focus as a result of the wavelength dependency of the refractive index.

3.1.2.1 Towards an achromatic lens system.

The fused silica lens system was designed to maximize light collection efficiency with respect to either bandwidth and overall intensity. However, the consequence of making all lenses of a single material is that the optical system inherently suffers from chromatic aberrations in which optical photons with a different wavelength will be focused into different spots along the optical axis (see Figure 3.6). In a system where the image distance is fixed, only one wavelength will be in focus with the image plane while other wavelengths will be blurred. XEOM 1 clearly exhibits chromatic aberration, which makes filtering of XEOL-emission crucial in order to acquire well-resolved images.

Achromatic lenses reduce the effect of chromatic aberration. Achromatic lens systems are typically arranged in doublets in which one lens of certain refractive index has a converging effect while another lens of different refractive index is diverging. Once combined, often both lenses are cemented together, the over-focusing effect of one lens is compensated by under-focusing of the other lens resulting in an identical focal spot for light of different colour. Clearly, the advantage of such a polychromatic optics would be :

- improved and sharper imaging of samples emitting XEOL in a broad waveband,
- application of all filters at exactly the same focal length,
- obtaining images for different colours with identical magnification,
- the avoidance of the time-consuming focusing process at the expense of valuable beamtime.

Moreover, while performing XEOL-XAS spectroscopy, we have learned that different optical channels might close or open at different energy points across the absorption edge. In an experiment where no filter is applied, in order to maximize light collection and reduce measuring time, this would mean that the position of the focus lens must be adjusted at every point across the absorption edge in the current system. Clearly, this is a process which is preferably omitted and could be avoided in an achromatic system. All these arguments prove that the acquisition of achromats should be a next step in improving XEOM 1.

Until recently, the broadband achromatic lens available were not useful for XEOM applications since transmission range of these lenses were restricted to the visible range. With the advent of doublet or lenses made from UV-grade fused silica and CaF_2 , this problem might be solved as they provide a consistent focal point for wavelengths ranging from 193 to 1000 nm [8]. Replacement of the current lenses by these achromats is not straightforward however. Firstly, funding must be found since each lens costs approximately 2000 EUR. Secondly, CaF_2 is known to be an efficient XEOL emitter since the first XEOL-XAS profile was recorded of CaF_2 by Bianconi et

al. in 1978 [9]. Accordingly, interaction of primary or secondary X-rays must be omitted at all time in order not to complicate the XEOL-data. Therefore, in the particular case of XEOM 1, achromatic correction might be supplied by a CaF_2 / fused silica doublet in which the fused silica faces the sample and shields the CaF_2 from any X-rays. Such a doublet combination in which the high dispersion component precedes the low dispersion component is known as the Steinheil configuration [10].

3.1.3 FILTER SYSTEM

Being able to select certain wavebands out of the polychromatic XEOL is of critical importance to perform both XEOM and XEOL-XAS experiments. In the first place determination and imaging of specific emission lines may reveal details on the optical properties and its correlation with the structural features of the investigated material. Furthermore filtering of the emission is important in order to obtain chemical maps with high contrast and spatial resolution because the system is not achromatic.

At the end of 2015, the carrier for the focusing lens was replaced with a newer model. During beamtime allocation X in July 2015 (see Table 3.6) it was observed that only a poor focus could be obtained in the blue – UV range, even with narrow band filters in place. The diverging lens L3 makes the converging ray bundle, leaving the objective doublet (L1-L2), to travel more parallel towards the projecting lens L4. As can be deduced from Figure 3.6, the objective pair is more strongly converging for wavelengths in the blue and UV band. Therefore the diverging L3 has to be translated towards the objective doublet for focussing shorter wavelengths (blue) onto the imaging plane and towards the CCD camera for focussing the longer wavelengths (red). The focusing mechanism is designed and devised in such a way that L3 cannot move outside the range of pre-set limits. These pre-set limits are, among others, dependent on the dimensions of the lens carrier. A misconception on the convention of certain parameters used during the design of the optical system led to the construction of the focus lens carrier which was slightly too short. As a result, the focusing lens in the focusing mechanism could not be shifted far enough away from the detector side in order to correctly focus for the blue and UV wavelengths. This complication could not have been discovered without the purchase of the new bandpass filters prior to the July 2015 beamtime. With the installation of the new longer lens cartridge, this problem was solved.

3.1.3.1 Filters

In what follows an overview is given of the different sets of filters that have been purchased and used over the years with the XEOM 1 system.

3.1.3.1.1 Dichroic Filters

The first set of filters which were used in combination with the XEOM 1 microscope was a set of additive and subtractive dichroic filters [11]. The purpose of a dichroic filter is to split a light beam into, at least, two separate bands which are either reflected or transmitted [12]. The dichroic filters that were used during this research were inherited from ODXAS 1 and were purchased at the time with Edmund Optics Ltd. (York, UK). The filters came in a set consisting of the three additive primary colours (red, green and blue) or of three subtractive colours (cyan, yellow and magenta). An overview of pass band characteristics of the dichroic filters according to the Edmund Optics specification sheets is given in Table 3.2.

	filter	centre wavelength (nm)	bandwidth (nm)	pass band (nm)
additive	Red (52-231)	657	150	600 - 750
	Green (52-534)	537	75	500 - 575
	Blue (52-531)	450	100	400 - 500
subtractive	Cyan (52-537)	500	200	400 - 600
	Magenta (52-540)	450 & 650	100 / 100	400 - 500 & 600 - 700
	Yellow (52-543)	600	200	500 - 700

Table 3.2

Overview of the characteristics of the additive and subtractive dichroic filters. The displayed numbers are copied from the specification sheets supplied by the manufacturer.

As mentioned earlier, the additive and subtractive dichroic filters were only used during the first beamtime allocations where XEOM 1 was installed. We suspected the presence of additional pass bands outside the 400 – 700 nm region documented on the specification sheets supplied by Edmund Optics. These doubts were the result of the observation of multiple foci during the attempt to find optimal focus of copper and cuprite XEOL signal with a dichroic filter in place. The focusing procedure consists of continuous acquisition of images (of short exposure time, e.g. 1 s) while scanning the lens across its range, which is imposed by the XEOM hardware. Finding an optimal focus is not yet controlled by an algorithm, but for the time being, it is dependent on the judgment of the user. The observation of multiple foci is possible when broadband emission is imaged with no filter in place or when a sample luminesces at various distinct wavelengths within the transmission window of the used filter. An alternative explanation can be the existence of multiple regions or

extremely broad regions where the dichroic filter transmits the light. This suspicion was strengthened by an experiment in which a cuprite lattice was imaged where initially only the green dichroic filter (pass band approximately 500- 600 nm) was put in place and subsequently both the green dichroic filter and a Schott KG1 colour glass envelop filter (pass band approximately 350 – 650 nm, see Table 3.4 and Figure 3.10 below). It could be concluded that when both filters were affecting the transmitted signal, the total signal intensity was cut down by a factor of 40. The results of this experiment are described in more detail on page 112 and 113 of [3].

In order to obtain a definitive answer, the dichroic filters were subjected to a similar experiment as described above for the UVFS lenses of XEOM 1. Transmission profiles of the filters were recorded across the Shimadzu UVmini 1240 instrumental range (200 – 1100 nm) and background subtracted over this range. The results display the transmission percentage in function of the monochromatic wavelength and are depicted in Figure 3.7 A (additive filters: red, green and blue) and Figure 3.7 B (subtractive filters: cyan, yellow and magenta). It could be concluded that for both sets, the information supplied by the manufacturer was misleading. It is clearly visible that all filters are transparent in the region of 800 nm and higher (far red to infrared) and XEOL emission in this region will not be rejected. Moreover, since the intensity of the cuprite XEOL signal was reduced by such a high factor, it must be concluded that the majority of the cuprite signal is being emitted in the infrared region (for more see chapter 4 & 5). The presence of these multiple pass-bands in the dichroic filters confirm the hypothesis made as a result of the presence of multiple focal points. In consequence it must be concluded that these dichroic filter sets are unsuitable for imaging purposes. Only in combination with envelope filters (see below) they would be suitable, but more straightforward is the acquisition of alternative sets.

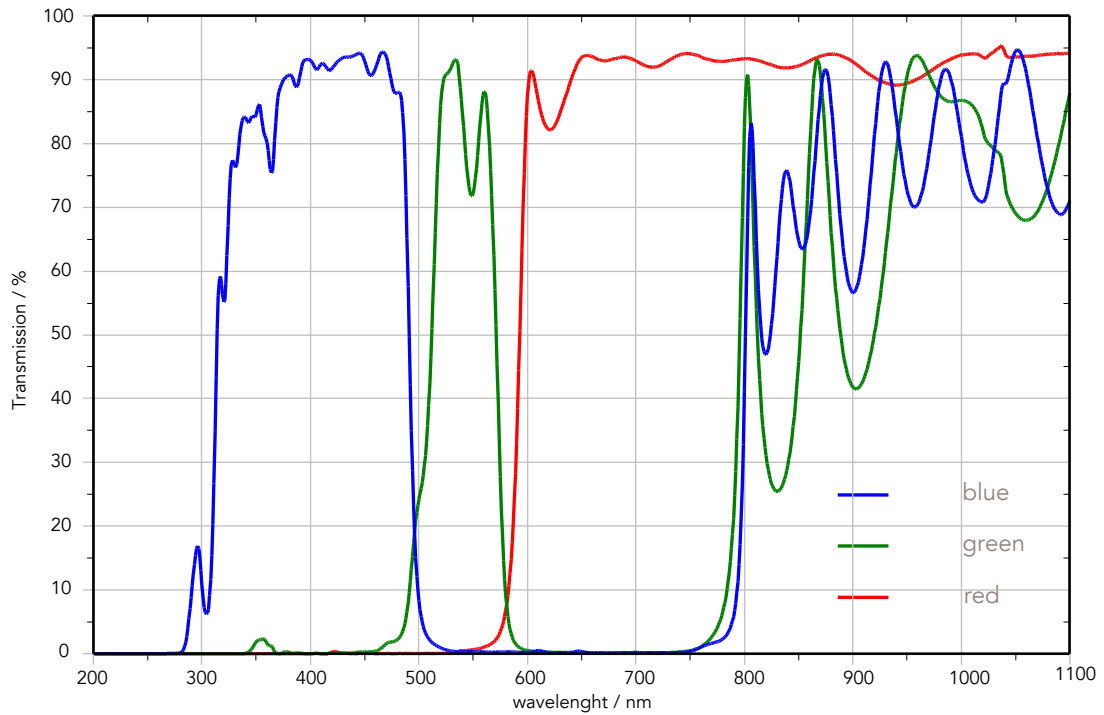


Figure 3.7 A

Transmission profile for red, green and blue additive dichroic filter set of Edmund Optics in the range of 200 – 1100 nm recorded with the Shimadzu UVmini 1240. The specification sheet of the manufacturer only displayed the data in the 400 – 700 nm range.

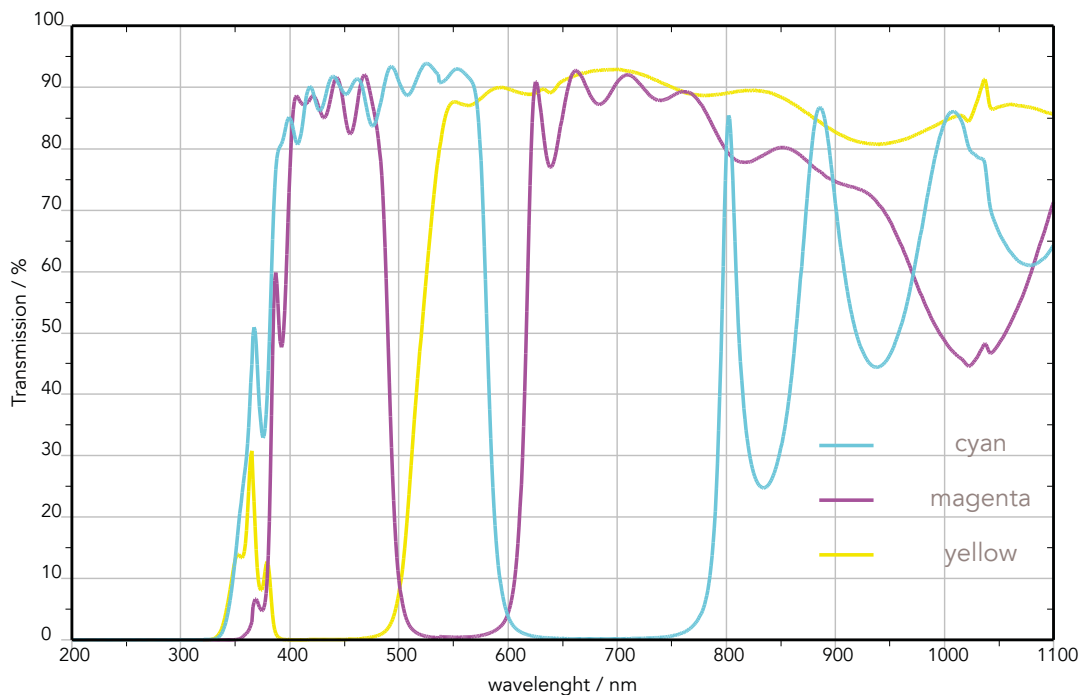


Figure 3.7 B

Transmission profile for cyan, magenta and yellow subtractive dichroic filter set of Edmund Optics in the range of 200 – 1100 nm recorded with the Shimadzu UVmini 1240. It is clear that these filters exhibit multiple pass-bands which render them not suitable for imaging purposes.

3.1.3.1.2 Fluorescence Line Filters

In order to expand the existing set of additive and subtractive dichroic interference filters; a new set of red, green, blue and UV TECHSPEC® fluorescence line filters was purchased with Edmund Optics [13]. An overview of the specifications of the fluorescence line filters is given in Table 3.3. The working principle of fluorescence line filters is similar to the one of dichroic filters, i.e. unwanted wavelengths are reflected opposed to colour glass filters which absorb them. Both the used dichroic filters and fluorescence line filters are interference filters.

An interference filter consists of several thin-layer coatings of different refractive index which are deposited on an optically flat transparent substrate. Figure 3.8 illustrates the simple system of a single thin-layer coating on a substrate. At the interface between two materials of different refractive index (either air, the substrate, a high refractive index thin-layer coating or a low refractive index thin-layer coating) an incoming light wave will be partly reflected and partly transmitted, as depicted in Figure 3.8. The interplay between transmitted and reflected light waves at the successive layers of different refractive index result in the creation of an interference pattern. In this pattern, reflected and transmitted waves will either be reinforced (constructive interference) or dampened out (destructive interference) when they are respectively in phase or out of phase for a half wavelength. Adjusting the nature of layered structure: refractive index of each layer, thickness of the layer, succession of the layers, etc. allows the manufacturer to shape the bandpass of these filters.

filter	centre wavelength (nm)	bandwidth (nm)	pass band (nm)
Red (84 - 103)	628	32	612 - 644
Green (67 - 031)	534.5	43	513 - 556
Blue (67 - 027)	472	30	457 - 487
UV (84 - 093)	377	50	352 - 402

Table 3.3

Overview of the characteristics of the red, green, blue and UV fluorescence line filters. The displayed numbers are copied from the specification sheets supplied by the manufacturer.

In order to avoid problems as with the previous set, these filters were also measured with the Shimadzu UVmini 1240 spectrophotometer. The results of this experiment are shown in Figure 3.9. The fluorescence line filters exhibit a narrow pass band in which they transmit light at 95 % or more. Of equal importance, is the confirmation that all light outside this pass band is effectively blocked. However, it must be noted

that the UV fluorescence filter becomes transparent for wavelengths higher than 1000 nm and the green fluorescence filter for wavelengths higher than 1100 nm. In essence, this cannot provide any substantial problems since the Quantum efficiency of the CCD sensor of both the FLI and Andor camera are very low at these long wavelengths.

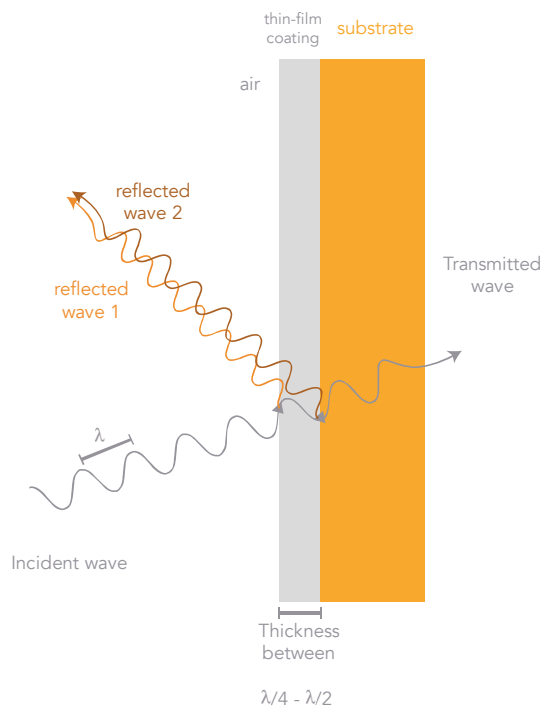


Figure 3.8

A light wave entering a thin-film layer is partially reflected and partially reflected backwards at both the air/thin-film layer interface and the thin-film layer / substrate interface. Adapting the thickness of the thin film to $\lambda/4$, in which λ is the chosen wavelength, will result in a phase difference of $\lambda/2$ between waves reflected away from the first and second interface. Consequently, a layer thickness of $\lambda/4$ entails destructive interference for reflected waves while a layer thickness of $\lambda/2$ entails constructive interference.

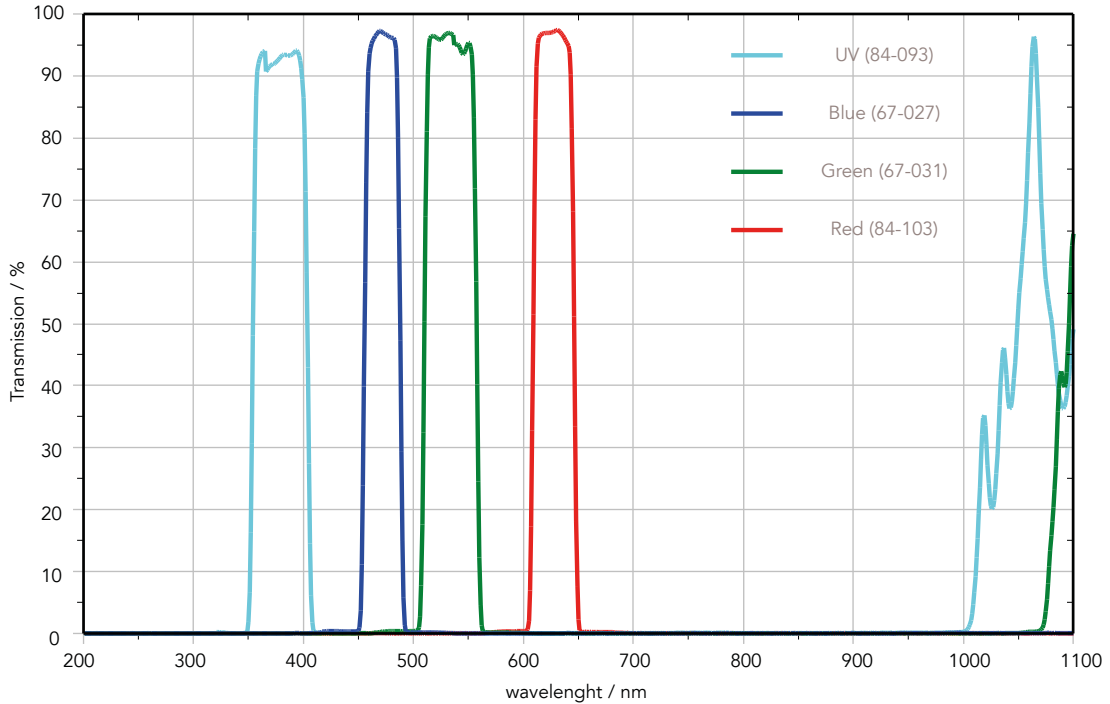


Figure 3.9

Transmission profile for blue, green, red and UV fluorescence line filter.

3.1.3.1.3 Envelope filters and wide pass-band filters

Table 3.4 gives an overview of a combination of wide pass-band filters and cut-of filters bought over the years. The short pass and the longpass filters are dichroic filters which were purchased together with the additive and subtractive dichroic filters at Edmund Optics [14, 15]. As can be seen in Figure 3.10, both shortpass and longpass transmit over 90 % in their specified pass window. However, unfortunately both filters are also transparent up to 95 % in regions outside their specifications. Both filters exhibit a crenelated pattern in these areas. As these additional pass bands transmit unwanted wavelengths onto the imaging sensor resulting in poorer contrast and lateral resolution, these filters are not suited for our intended imaging application. Aside from the interference filters, the features of 3 colour glass filters are shown in Table 3.4 and Figure 3.10. Colour glass filters 716 FHC 25 (made from Schott KG1 glass) [16] and 330 FCS 25 (made from Schott UG11 glass) [17] were purchased to demonstrate the presence of additional pass bands in the RGB and CMY dichroic filter sets. In combination with these filters, they can serve as an envelope to absorb unwanted light transmitted through the defective regions of these sets. Finally, the 780 FCS 25 colour glass filter [15] was purchased recently with Knight Optical, for experiments which require a longpass transmittance. Figure 3.10 confirms that the transparency is lower than 1 % in the region below its cut off at 780 nm.

filter	manufacturer	type	pass band (nm)
780 CS 25	Knight Optical	colour glass	780 - 2800
716 FHC 25 KG1	Knight Optical	colour glass	300 - 750
330 FCS 25 UG11	Knight Optical	colour glass	280 - 370
shortpass (47 - 286)	Edmund Optics	interference	250 - 450
longpass (47 - 620)	Edmund Optics	interference	775 - 2000

Table 3.4

Overview of the characteristics of short- and longpass interference filters and colour glass filter. The displayed numbers are copied from the specification sheets supplied by the manufacturer.

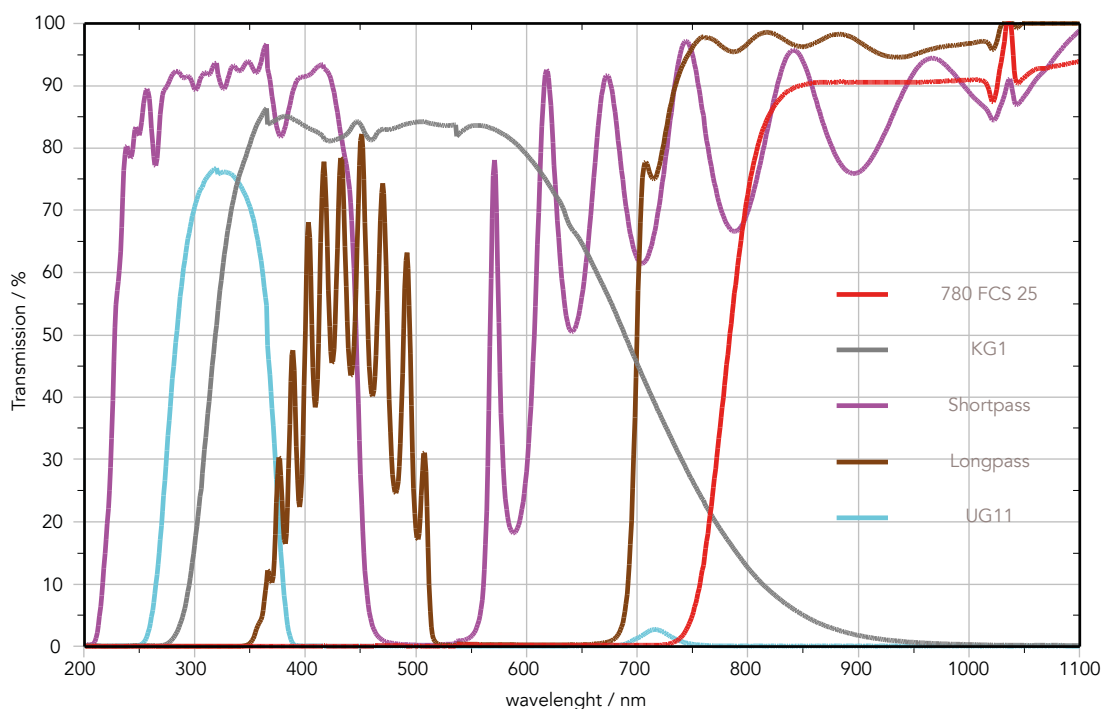


Figure 3.10

Transmission profiles for short- and longpass filters, colour glass KG1 & UG11 filters and 780 FCS 25 from Edmund optics.

3.1.3.1.4 Standard and extra broadband bandpass filters.

Of the filters discussed so far only the fluorescence line filters and, to a certain extent, the colour Schott glass filters (KG1 and UG11) are useful for imaging luminescence emission characteristics, as they do not possess additional pass bands. However, the bandwidth of the fluorescence line filters is narrow and the set in house

doesn't allow us to survey the complete XEOL spectrum. On account of this restriction, a set of 5 broadband bandpass interference filters (FIR) [18] and 7 extra broadband bandpass interference filters (FIW) [19] were purchased from Knight Optical. An overview of the features of these filters according to their specification sheets is given in Table 3.5. The broadband filters all have a full width at half maximum (FWHM) bandpass of 40 nm, whereas the bandpass for the extra broadband filters varies between 65 nm and 75 nm. The broadband set is suitable for mapping the luminescence emission characteristics of the micro-imaged sample, whereas the extra broadband are useful where extra sensitivity is required to collect spectra of weakly emitting samples. All filters were subjected to a transmission experiment with the UVmini 1240, which showed that all the specifications claimed by Knight Optical could be confirmed. The results of this experiment for the broadband bandpass filters is given in Figure 3.11 A and for the extra broadband bandpass filters in Figure 3.11 B. Inside the passband, the transmission is 70% or more for most of the filters except for the filters in the UV and blue area (400 FIR 25 and 450 FIR 25). Together with the UV filters (UG11 and fluorescence line) we already had, the complete set of filters covers the range of the CCD detector (250 nm – 1000 nm) without much overlap and with minimal gaps. Accordingly, repeating an experiment with a different filter in place allows us to observe the band in which the sample is emitting XEOL. Although it is planned to install a spectroscopic arm in the next generations of XEOM 1, already it is possible to perform a spectral survey with a resolution down to 40 nm without such a spectroscopic section installed.

filter	centre wavelength (nm)	bandwidth (nm)	pass band (nm)
400 FIR 25	400	40	385 - 425
450 FIR 25	450	40	430 - 470
600 FIR 25	600	40	585 - 625
650 FIR 25	650	40	635 - 675
700 FIR 25	700	40	680 - 720
500 FIW 25	500	70	465 - 535
550 FIW 25	550	70	515 - 585
600 FIW 25	600	65	570 - 630
650 FIW 25	650	75	615 - 690
700 FIW 25	700	70	665 - 735
750 FIW 25	750	65	720 - 785
800 FIW 25	800	65	770 - 835

Table 3.5

Overview of the characteristics of broad and extra broad bandpass filters from Knight Optical. The displayed numbers are copied from the specification sheets supplied by the manufacturer.

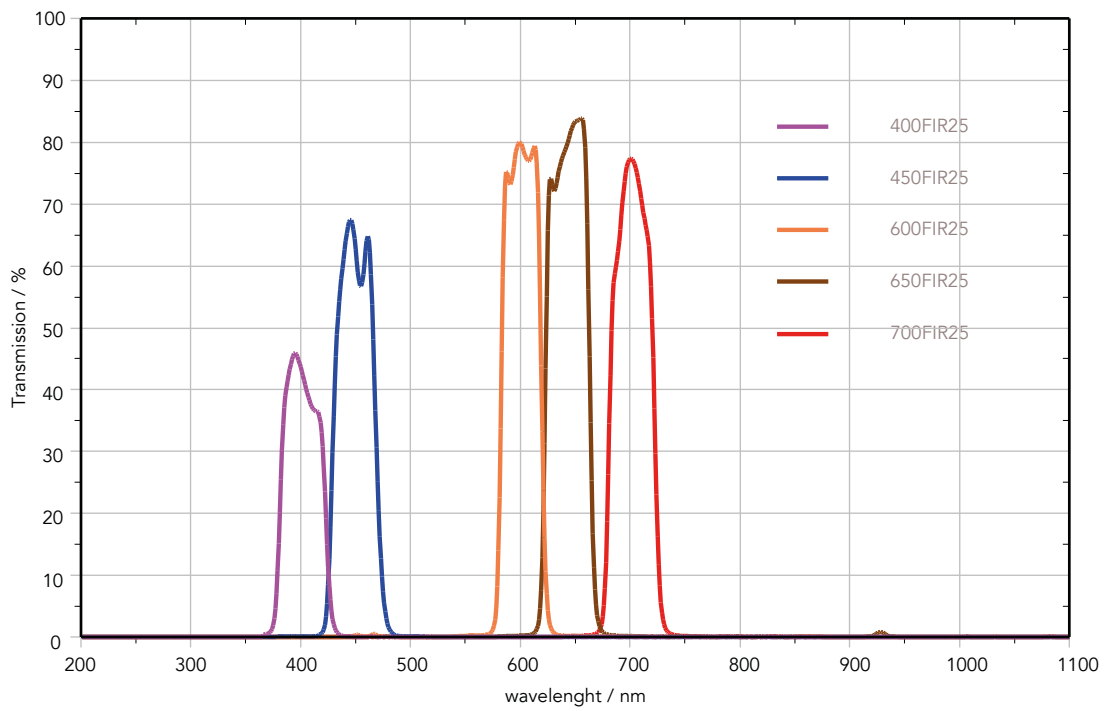


Figure 3.11 A

Overview of transmission profiles of broadband bandpass filters from Knight Optical.

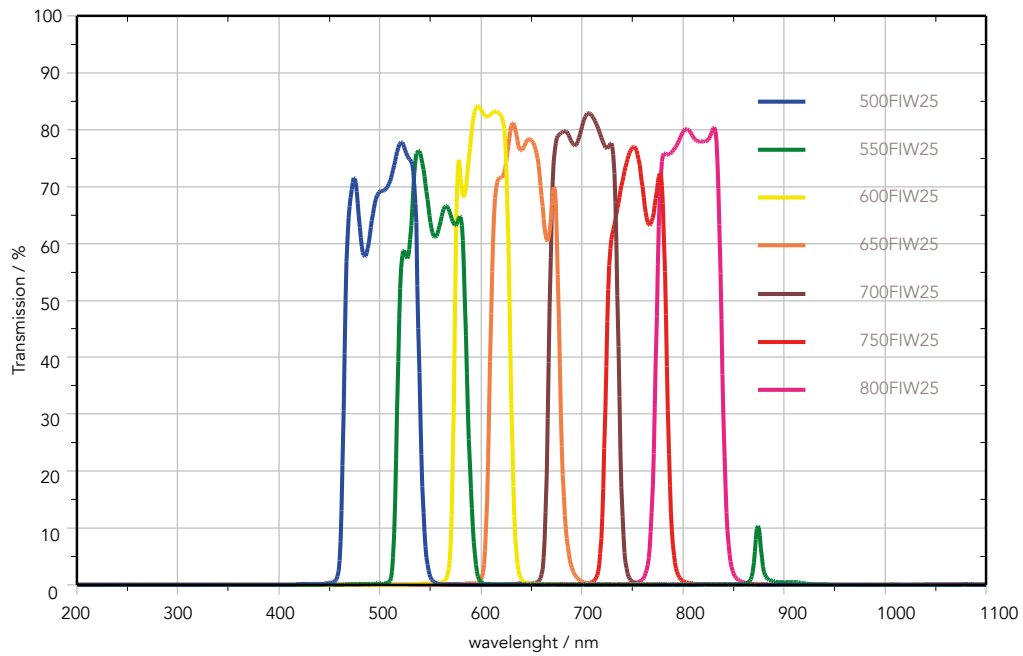


Figure 3.11 B

Overview of transmission profiles of extra broadband bandpass filters from Knight Optical.

3.1.4 DETECTORS

The interaction of a highly intense beam of X-rays with matter gives rise to a large number of physical processes taking place in and beyond the primary interaction volume. The result of such a process might be the emission of a fluorescent X-ray or optical photon, a photoelectron, an Auger electron, etc. Selecting an adequate detector to record the emission determines the corresponding spectroscopy which is obtained. Since these phenomena occur simultaneously, though with different efficiency, mounting an array of detectors around the sample allows the user to perform different spectroscopies concurrently. The design of XEOM 1 supports this multi-method approach and allows for simultaneous acquisition of XEOM, XEOL-XAS, XAS data and XRF to a certain extent.

3.1.4.1 Optical light detector

The resultant optical photons as a decay product of the X-ray absorption process form the basis of XEOL-XAS spectra and XEOM images. In order to obtain lateral resolution within two-dimensional images for XEOM, a visible light sensitive 2D pixel-array detector in the form of a charge-coupled device (CCD) was used. To acquire XEOL-XAS spectra representing the average optical yield of the interaction volume, a photomultiplier tube (PMT) was mounted.

3.1.4.1.1 FLI Microline ML1109 CCD camera

A CCD is a two-dimensional array of light sensitive elements (pixels) formed in an integrated circuit etched onto silicon substrate. Camera electronics process charges, generated by photons captured in a pixel, into a two-dimensional representation of the light pattern which fell on the device [20].

The Microline ML1109 spectroscopy CCD camera assembled by Finger Lakes Instruments (FLI LLC, Lima, New York, USA) equipped with a back-thinned Hamamatsu S10140-1109 CCD chip (Hamamatsu Photonics K.K., Shizuoka, Japan) was the first CCD camera purchased and installed on XEOM 1 [21, 22]. The Hamamatsu chip is rectangular in shape (24.58 x 6.072 mm) and houses a two-dimensional array of 2048 by 506 pixels, each 12 μm x 12 μm large. The efficiency with which photoelectrons are generated on the silicon substrate of the CCD chip is wavelength dependent and is described by the Quantum Efficiency (QE). The QE of the FLI camera is charted, together with the Andor camera QE and the photomultiplier tube QE, on Figure 3.12. QEs are improved by the application of anti-reflection coatings and the use of back-thinned chips. In back-thinned, or back-illuminated CCDs, the engineering of the chip is reversed and incident light can generate photoelectrons unimpeded [23]. The dynamic range of a CCD expresses its ability to record simultaneously very low light intensities alongside bright fluxes of optical photons. The dynamic range is typically defined as the ratio of the pixel full-

well capacity (maximum number of electrons in a single pixel) over the camera noise. With a full-well capacity of 75 000 e^- and a system noise of 10 e^- (per pixel at digitization speed of 500 kHz) , the dynamic range of the FLI camera is 7500. All CCDs benefit from working at lower temperatures, since thermal energy can be intense enough to generate charges in the CCD chip which are indiscernible from charges initiated by photons. This source of noise is known as dark current [24]. During operation, the FLI camera is typically cooled down to 65° below ambient temperatures by a thermoelectric Peltier cooling element. At this temperature (approx. : -40°C) the dark noise is on average lower than 0.4 e^- per pixel per second.

CCD sensor deficiency

The FLI camera was replaced, much earlier than intended, after only a few deployments. The major reason for this was the existence of a severe defect in the Hamamatsu CCD chip. Figure 3.13 is a test image recorded from a uniformly illuminated phosphorescent sheet and exhibits some artifacts which were visible in most of the data acquired. These consist of a series of luminous arcs running from top to bottom and a distribution of dark spots across the image. A set of experiments were carried out by Matt Hand in order to discover the origin of these features. A detailed description of these experiments can be found in [3]. The absence of the artifacts in dark frame images and their position and appearance being dependent on the angular distribution of the light source, pointed the conclusion towards geometry imperfections of the Hamamatsu chip. In fact, the surface of the CCD is wrinkled. Since the sensor is not provided with any anti-reflection coating, a fraction of the incoming light might be reflected of the sensor onto the distorted regions of the chip surface. In this particular case the distortion act as a concave mirror with a focal length approximately equal to twice the distance between the chip surface and the inner plane of the fused silica camera window. Therefore, the backscattered light is refocused by these concave distortions onto the CCD appearing as bright arcs on all images. The existence of dark spots across the field of view was attributed to dust particles on the surface of the sensor or the inside of the cover slip. Since the front of a CCD is typically sealed from its environment, the presence of dust particles does arise suspicion in the correct processing of the chip into the camera body or the suffering of the sensor compartment to an external stress source.

Since the presence of these artifacts inherently complicate the data recorded and no image corrections schemes can be applied to remedy for this, we were forced to purchase a new CCD camera. After an extensive selection process, the choice fell on an Andor Ikon-L.

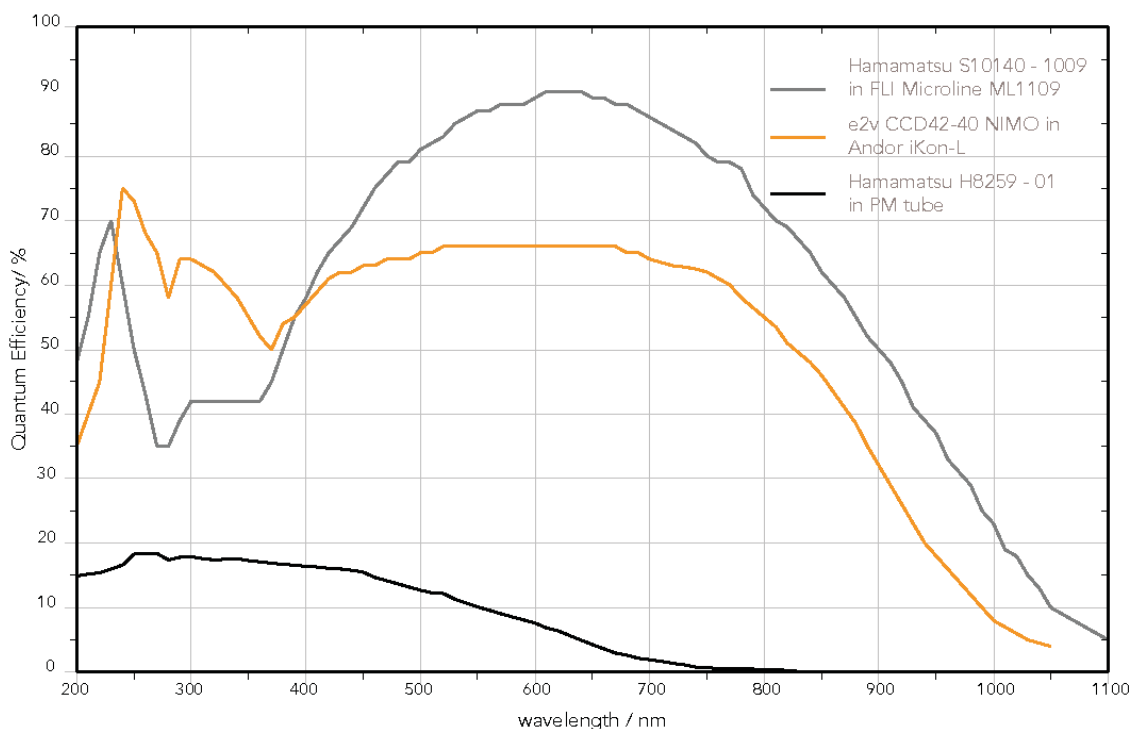


Figure 3.12

Quantum efficiency curves for the Hamamatsu and e2v CCD sensors installed in respectively the FLI and Andor camera and the Hamamatsu H8259-01 chip installed in the PMT. Data was reproduced from the data sheets supplied by the manufacturer. The QE of the Hamamatsu H8259-01 was recalculated from the peak efficiency curves provided by the manufacturers according to equation {3.1} – {3.2}.

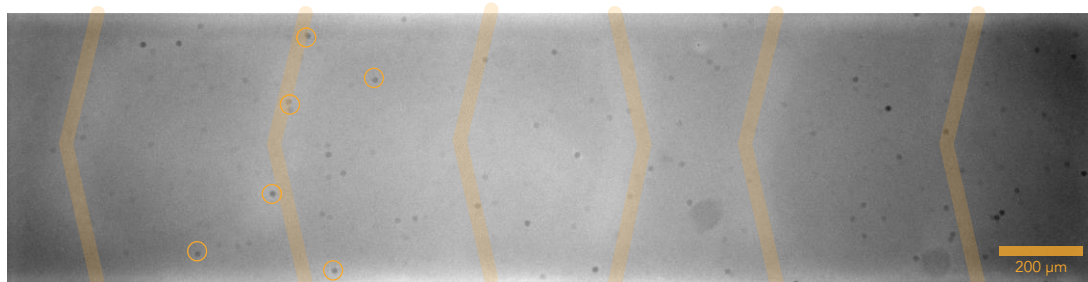


Figure 3.13

Image recorded with the FLI camera from uniformly illuminated phosphorescent screen in which the shortcomings of the CCD sensor are being exposed. The orange lines highlight the observed luminescent arcs in each image whereas the orange circles mark some of the dust particles observed.

3.1.4.1.2 Andor Ikon-L CCD camera

To replace the FLI camera, an Ikon-L 936 manufactured by Andor Technology (Andor Technology Ltd., Belfast, Northern Ireland) equipped with a back-illuminated e2v CCD42-40 NIMO CCD sensor with UV-enhanced coating (e2v technologies Ltd., Chelmsford, UK) was purchased [25, 26].

The specifications of the Andor camera are almost in all respects better than those for the FLI camera. A larger field of view is available due to the larger e2v chip. The sensor is square shaped (27.6 x 27.6 mm) and houses an array of 2048 x 2048 square pixels, each 13.5 x 13.5 μm large. The wavelength dependent quantum efficiency of the e2v CCD chip is displayed in Figure 3.12. The back-thinned sensor is provided with an UV-enhanced coating in order to obtain a flat quantum efficiency profile over the desired wavelength range. Unfortunately, the application of a UV-enhanced coating seems to be at the cost of a lower QE for the visible wavelengths with respect to standard broadband coatings. Each pixel can hold up to 100 000 e^- before saturation occurs and typical system noise is 31.5 e^- (RMS) at maximum digitization speed of 5 MHz, resulting in a (minimum) dynamic range of 3175.

Typically, during a XEOM experiment, an area of 4 by 4 pixels is recombined (binned) to one pixel. Although this is at cost of lateral resolution, the full-well capacity is increased by a factor 16. Combining this with a reduced system noise, as a result of the lower read out rate required for less pixels, the dynamic range can be considerably improved through binning, an operation which is equally possible in the FLI system. The cooling system of the Andor camera consists of a 5-stage thermoelectric cooling system enabling the large area sensor to be cooled down to approximately -70°C, resulting in a typical dark current of less than 0.4 e^- per pixel per second at this temperature. Additionally, this value can be reduced by using the supplementary water cooling system.

3.1.4.1.3 Hamamatsu H8259-01 photomultiplier tube

The Hamamatsu H8259-01 broadband photomultiplier tube (PMT) was used as an optical photon counting device in the customarily designed XEOL detector for ODXAS 1 [27]. Apart from the photon counting head, the detector was equipped with a biconvex fused silica lens and an external shutter mechanism. With the advancement of ODXAS 1 to XEOM 1, the PMT detector is recycled as a secondary detector on XEOM 1. With a suitable adapter, the PMT can be mounted on either of the angle ports surrounding the sample stage. The PMT allows to acquisition of a total XEOL spectrum, representative of the beam interaction volume, in experiments where no lateral resolution is required. The PMT is plugged into one of the SPEC-driven beamline counters during the experiments. *SPEC* is a unix-based software package purchased by XMaS for instrumental control and data acquisition [28]. This way, the XEOL response of a sample can be plotted rapidly when the sample is moved relatively with respect to the beam. Such an operation, a *dscan* according to the SPEC syntax, can aid enormously during the alignment procedure of the sample within the X-ray beam.

The QE of the PMT is also plotted in Figure 3.12. However, the specification for the wavelength dependent detection efficiency for the PMT was given in peak count

sensitivity, a quantity described in $s^{-1} \cdot pW^{-1}$. In order to determine the PMT's quantum efficiency, and to compare with the FLI and Andor camera, the following conversion has to be made: for 600 nm photons, the peak sensitivity of the PMT is 2.3×10^5 counts per second, per incoming pW of radiation.

$$E = \frac{h.c}{\lambda} = \frac{6.63 \cdot 10^{-34} \times 3 \cdot 10^8}{600 \cdot 10^{-9}} \frac{[J.s] \times [m.s^{-1}]}{m} = 0.033 \cdot 10^{-17} J, \quad \{3.1\}$$

in 1 pJ there are $3 \cdot 10^6$ photons of 600 nm according to:

$$\frac{1 \cdot 10^{-12} [J]}{0.033 \cdot 10^{-17} [J]} = 3 \cdot 10^6. \quad \{3.2\}$$

Consequently :

$$Q.E. = \frac{\text{peak sensitivity}}{\text{incident photon flux}} \times 100\% = \frac{2.3 \cdot 10^5 \text{ [cts.s}^{-1}\text{]}}{3 \cdot 10^6 \text{ [photons]}} \times 100\% = 7.59\%. \quad \{3.3\}$$

All values in Figure 3.12 were processed according to this method. Clearly the QE of the PMT is much lower than the CCD sensors used in the project, and the addressable wavelength band is much more restricted with respect to the CCD sensors. Nevertheless, the PMT during has been proven to be a valuable asset during experiments, partly because of its wide dynamic range.

3.1.4.2 X-ray detectors

Apart from UV-visible-IR sensitive detectors, X-ray detecting instruments have been mounted on XEOM to perform simultaneous XAS and XRF experiments. Both an avalanche photodiode and an energy dispersive silicon drift detector have been used for these purposes.

3.1.4.2.1 Avalanche Photodiode

On many occasions an avalanche photodiode (APD) detector supplied by the beamline (both by the DUBBLE and XMaS beamline) has been installed to record parallel fluorescence X-ray absorption spectra. APD detectors are light, compact and offer a wide dynamic range and good linearity. On XMaS, the cylindrical detector houses a silicon avalanche photodiode chip (Perkin Elmer Inc., Hopkinton, Massachusetts, USA) [29]. The active area of the chip is 5 mm x 5 mm and is protected from instant saturation by an 80 μ m thick Be window. The face of the detector is fitted with a KF-16 vacuum flange. An acetal adapter, complementary to the KF-16 flange, was made for easy mounting of the APD on one of vacant angle ports. At the conventional X-ray fluxes used during the XEOM experiments, X-ray

detectors are prone to saturation. In order to prevent this, attenuating materials must be placed in front of the detector to reduce the fluorescent X-ray flux. The APD was commonly mounted via a black ABS or acetal copolymer tube on the microscope. Due to its light nature, the weight of the APD could be completely supported by the connection with the angular port itself. Accordingly the distance at which enough X-rays were absorbed by air in order to prevent saturation was determined and used as the length for the black ABS tubing.

3.1.4.2.2 Vortex® Si drift detector

On XMaS, the Vortex® (Hitachi Ltd., Tokyo, Japan) Si drift detector (SDD) was installed alternative to the use of the APD detector for X-ray detection. A motivation to use this detector is its ability to detect X-rays with a better energy resolution than the APD. Apart from the fluorescence XAS, this allows us to perform elemental analysis by recording XRF spectra with the same detector (when the primary X-ray energy is set high to e.g. 15 keV). The Vortex® multi-cathode system houses a 50 mm² high purity silicon CMOS chip and provides an energy resolution of < 136 eV FWHM for the Mn K_{α} line [30]. The detector at XMaS is equipped with a 25 μ m thick Be window to prevent instantaneous saturation and condensation on the device surface. The window is mounted onto a KF-40 vacuum flange which aids in reducing the absorption of secondary X-rays by air. Because the Vortex® detector is considerably heavier than the APD detector, the approach used to mount the APD detector could not be followed. The flat chi-circle of the Huber diffractometer was used as an extra support to hold the Vortex® detector. This meant that the detector had to be mounted much closer to the sample, a position in which the saturation issue appears. To overcome this problem, a 400 μ m thick aluminium foil was placed on the camera face to further attenuate the fluorescent X-ray flux. Figure 3.16 shows the XEOM 1 setup with the Vortex® SDD installed on one of the 10° angle ports.

3.1.5 ELECTRONICS INTERFACE FOR REMOTE CONTROL AND DATA ACQUISITION

When working in a synchrotron facility, for safety reasons, all instrumentation must be remotely controllable from a user control cabin when an X-ray session takes place. XEOM 1 was designed to be as portable and autonomous as possible so it could be installed as an end-station on different beamlines and can be operated in a laboratory environment outside the synchrotron.

Figure 3.14 displays a schematic diagram of the data acquisition system (DAQ) and electronics interface unit (EIU) necessary for data acquisition and (remote) control of XEOM 1. All XEOM 1 related experiments are controlled from a laptop on which the control software 'eCell controller' and 'esaXSec' are installed. Recently a Dell

Precision M6800 Mobile workstation (Dell, Round Rock, Texas, USA) provided with a Intel Core i7-4810MQ Processor (Intel, Santa Clara, California, USA) and 32 GB DDR3L random access memory was purchased. The CCD cameras (both FLI and Andor system) are directly connected to the laptop via a USB interface. When in the synchrotron, the USB cables between the laptop in the control hutch and the instrumentation in the experimental hutch must pass through a safety chicane. Since the length of the USB cable required to reach the instrumentation sometimes exceeded 5 metres, we use USB repeater cables provided with amplifiers in order to preserve the signal.

Other hardware, which is not under direct control of the laptop, is driven by the software through the combination of a DAQ interface and a custom made electronics box. The DAQ interface consists of two Agilent U2353A multifunction cards mounted in an Agilent U2781A modular chassis (Keysight Technologies (Agilent), Santa Clara, California, USA) because of its robustness and possibility for further expansion [31, 32]. Each multifunctional card carries a set of analogue and digital inputs/output channels and analog or digital trigger capabilities. The DAQ is connected to the laptop via a USB 2.0 interface and each DAQ module card is connected to the EIU via two SCSI 68-way connectors. The software on the laptop computer drives the EIU, through the DAQ, which encloses an assembly of electronic components and integrated circuits required for the correct operation of XEOM 1. The EIU contains functionalities to:

- drive the stepper motors of the focusing section and the filter wheel,
- read out the position of the focus lens and filter wheel,
- control the shutter mechanisms of a the PMT and a LED illumination system,
- switch on/off of a LASER and a filament lamp,
- regulate the light intensity of a LED and filament lamp,
- send and receive trigger pulses to/from the beamline.

Apart from the electronics necessary for driving XEOM 1, the EIU contains a module to perform spectroelectrochemistry experiments with the eCell and the peCell [33, 34].

The original system was designed and built by Matt Hand, Mark Dowsett and Adrian Lovejoy and a detailed description of the operation of the electronics can be found in [3], since this is outside the scope of this thesis. Within the original system, the electronic components were arranged on two layers in a metal chassis. Since the development of the electronics appeared to be a dynamic process, modules and components were added and removed over the years, leaving the electronics box in a disorganized state at a certain point. In 2014 the system was rebuilt by Jorge Anjos. A modular approach was chosen in which all necessary electronic components

were combined on separate circuit boards. Since the two layer approach lead to unserviceability when working on the electronics, the system was rebuilt in a compacPRO (Schroff GmbH, Straubenhardt, Germany) case [35]. The case allows easy insertion and removal of the circuit boards in case when the electronics require adjustments. Additional unused slots provide the possibility of further expansion.

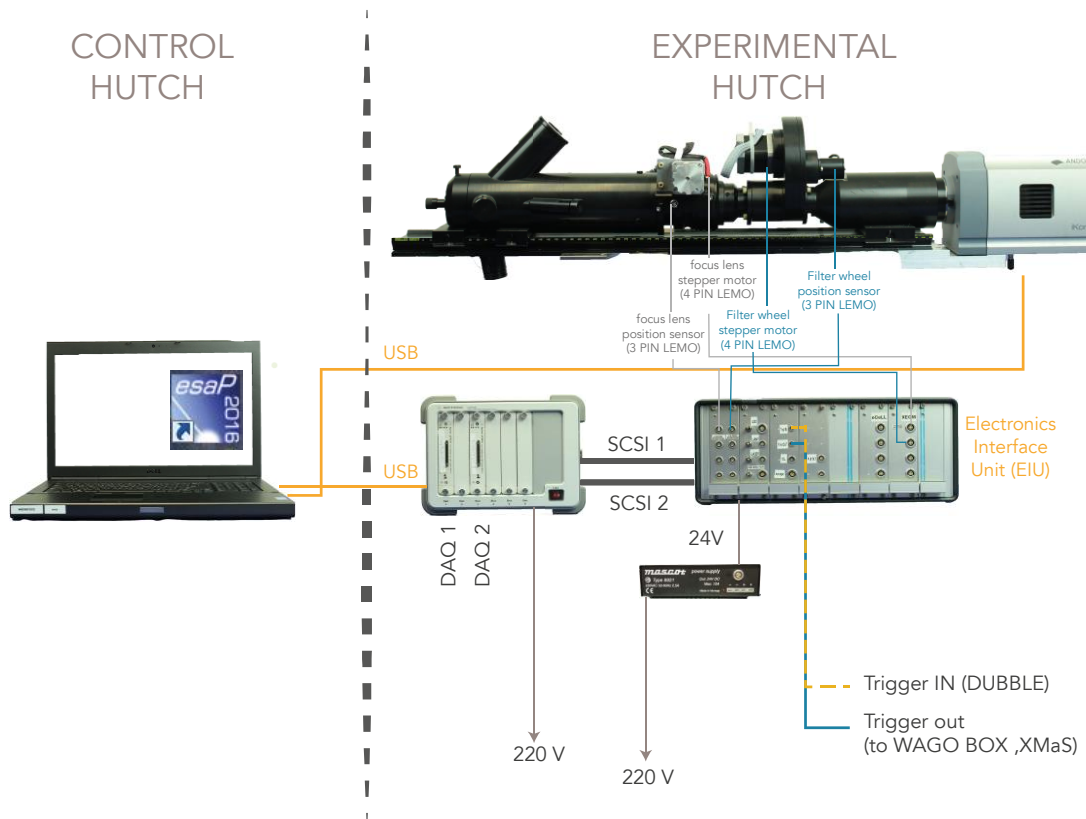


Figure 3.14

Diagram of a typical setup of the data acquisition system, electronics interface unit and the XEOM 1 optical column when installed on a beamline.

3.2 SOFTWARE

3.2.1 CONTROL SOFTWARE

In order to control all aspects of the XEOM 1 microscopy system and to automate data acquisition, a custom software program *eCell controller* was written. As the name suggests, *eCell controller* was originally made to coordinate experiments performed with the eCell. Since the eCell was mainly driven by the same EIU, Matt Hand and Mark Dowsett have used the software already present as a foundation to further develop the software required to drive XEOM 1. To prevent confusion, the program was later on renamed to *ASP* by Matt Hand. *ASP* is a program written in the high-level language Visual Basic .NET and is intended to run on a Microsoft® Windows operating system. Apart from the user interface (UI) and the user control for the different possible experiments, the source code combines a set of modules imported from different software development kits (SDK), each supplied with a piece of hardware implemented in XEOM 1. The FLI camera, the Andor camera and the Agilent DAQs are some examples of such a hardware components. The definitions and functions provided by these software libraries allow the programmer to address simultaneously different functionalities from different pieces of hardware and make them interoperable.

Most important for XEOM purposes is the image capture functionality, which permits the user to automatically acquire XEOM image stacks. The capture control window is a graphical user interface (GUI) which guides the user to prepare an experiment. *Capture control* allows the user to:

- select a certain camera (FLI or Andor),
- apply camera parameters such as: temperature, exposure time, binning parameters, cropping of sensor area;
- translate the focus lens while continuously capturing images (focus capture) to find optimal focus for a certain sample and filter,
- control auxiliary components like: LED or filament lamp illuminator, LASER, PMT shutter.

When all necessary settings are completed, a trigger capture can be initiated. During the trigger capture, image acquisition is synchronized with the stepping of the beamline monochromator (see 3.3.2.1 and 3.3.3.1 for more information). At this point, both our software and the beamline operation software run independently with the joint purpose to record a XEOM image at every point in the chosen energy interval across the absorption edge. Therefore, it is clear that time parameters on both system must be carefully selected. The result of any '*capture*' procedure is the output of an *.eccd*-file with or without an accompanying *.tiff* image. The *.eccd*-file

format is a bespoke file format (by Matt Hand & Mark Dowsett) with a human readable header and binary data block. After completion of the experiment, the .eccd-file image stack serves as input for *esaProject* (see below) where further data processing is handled. For a complete overview of the features and functionalities of *eCell controller/ ASP* see reference [3].

With the advent of new modules, such as the filter wheel, in the XEOM 1 project; new software had to be written in order to make it operational. Alongside of these upgrades, the initiative was taken to rewrite the software into a program where the *eCell/peCell* and XEOM 1 capabilities are more separated and function independently. *esaXSec* is the result of this innovation and is currently being further developed by Mark Dowsett.

3.2.2 DATA PROCESSING SOFTWARE: *esaProject*

After acquisition of raw XEOM data and preliminary processing by *ASP* and *esaXSec*, all post-processing operations on the data is done in *esaProject*. *esaProject* is a software suite for extraction, processing and presentation of XRD, XAS, XEOL-XAS and XEOM data sets. The program has been continuously developed by Mark Dowsett since 2006 [36]. The source code is written in Visual Basic .NET and an executable file can be installed on any computer running a 32-bit or 64-bit Microsoft® Windows operating system (from Windows XP onwards).

Individual images or complete sets of images (image stacks) can be imported into the XEOM portion of *esaProject*. Images can be previewed as false-colour intensity maps displaying the intensity value stored in each pixel. The colour display of each previewed image can subsequently be manipulated to highlight or hide particular features by adjusting brightness and threshold controls. A built-in 'image calculator' allows for a number of mathematical operations to be performed between images on a pixel-by-pixel basis or between an image and a constant value. Within this perspective, the process in which each image is divided by a parameter representing fluctuations in primary X-ray intensity is automated in a separate normalization feature of the program. Moreover, the code offers the capability to extract XEOL-XAS spectra through pixel-by-pixel integration of the intensity from different regions of interest (ROI) or from the entire image (total spectrum). Features of the resulting spectra can be further processed by *esaProject* into colour-coded chemical maps or the individual spectra may be forwarded to the spectrum processing portion of *esaProject* where they can be further analysed. Alternatively, extracted absorption spectra can be exported in formats suitable for other software packages designed for XAFS data analysis, e.g., the Horae suite (i.e. Athena, Artemis, Hephaestus) [37]. Lastly, *esaProject* is equipped with its own plotting capability in order to produce graphs suitable for publication. More information on the XEOM processing features

of esaProject can be found in chapter 5, however a complete overview is given elsewhere [3, 38].

3.3 XEOM 1 INSTALLED AT THE ESRF

3.3.1 THE EUROPEAN SYNCHROTRON RADIATION FACILITY

All measurements performed with XEOM 1 were, up till now, performed at the European Synchrotron Radiation Facility (ESRF). The experimental hall contains the 844 meter circumference storage ring and 40 tangentially adjacent beamlines. The storage ring circulates electrons at 6.04 GeV which are fed from a 300 m circumference 6 GeV booster ring in turn fed by a LINAC pre-injector. The source is optimised to deliver X-rays ranging from 1 – 100 keV and the maximum operating current of the storage ring at which the highest X-ray fluxes can be delivered is 200 mA [39].

Since 2009, the ESRF has been the subject of an upgrade program. During a first phase, which ended in 2015, a new experimental hall was constructed alongside 19 novel experimental end-stations. Next in line is the construction and commission of a new – first of a kind- ‘Extremely Brilliant Source’ (ESRF-EBS) storage ring over the period of 2015 – 2022. The EBS aims to improve the storage ring efficiency by enhancing brilliance and coherence by a factor 100 and reducing energy costs by 20%. Other components of this ambitious upgrade involve the improvement of the beamline and scientific instrumentation portfolio and to pursue the ‘data as a service’ strategy in order to take maximal benefit of the new high performance X-ray source [40].

XEOM 1 has been installed both on BM28 and BM26A in the past. The nature of the experiments that a user wants to perform determines the choice of beamlines. Within this respect, both beamlines provide characteristics which are desirable for performing a XEOM experiment. Both BM28 and BM26A, as the acronym predicts, utilize a bending magnet as X-ray source. The BM delivers an X-ray beam with a relatively large beam footprint with an acceptable flux uniformity and an energy range which allows to address the absorption edges of our interest (Cu, Pb, Zn, Sn, etc.). In the following sections a more detailed overview of the features of each beamline is given accompanied by a description of the mounting and interfacing of XEOM 1 with each beamline.

3.3.2 BM28 XMAS, THE UK COLLABORATING RESEARCH GROUP (CRG)

The XMaS beamline is situated on the soft sector of bending magnet (dipole) 28 of the ESRF and was originally designed for studying the X-ray diffraction of magnetic materials, hence the acronym: X-ray Magnetic Scattering, XMaS [41]. Nowadays, the instrumentation available allows to address a wide range of X-ray techniques making use of a polychromatic (white) or monochromatic X-ray beam in the range of 2.4 to 15 keV. Apart from diffraction experiments, users have been carrying out resonant elastic X-ray scattering, grazing incidence reflectivity, small angle scattering and various spectroscopy experiments. XMaS is the result of a collaborative project of Warwick and Liverpool Universities, funded by the UK Engineering and Physical Sciences Research Council (EPSRC)[42].

The optics, illustrated schematically in Figure 3.15, comprise a set of slits and mirrors to define a beam size at sample of max. 0.8 mm (vertical) by 0.5 mm (horizontal) at full width at half maximum (FWHM). The white beam slits are followed downstream by a double crystal monochromator, located at a distance of 24.3 m from the source. The monochromator comprises two plane silicon 111 crystals in a crystal cage and selects a monochromatic X-ray energy with a resolution of $\Delta E/E = 1.7 \times 10^{-4}$ in the range of 2.4 to 15 keV [43]. The majority of the incident SR power is absorbed by the first Si 111 crystal which is therefore equipped with a water cooling system. Higher harmonics to the selected X-ray energy transmitted by the monochromator can be rejected further downstream by harmonic rejection mirrors if they complicate data interpretation. The monochromator is followed by a toroidal mirror made of single crystal silicon with a rhodium coating for enhanced reflectivity. A pneumatically actuated bending mechanism can deform the cylindrical mirror creating a toroidal surface which focusses the beam with the desired dimensions onto the sample surface [41]. To reduce the flux delivered to the sample, one single or a combination of attenuating foils can be placed in the beam. Complete attenuation of the X-ray beam is obtained by a station shutter which must be closed before entering the experimental station. An additional fast shutter allows the exact exposure time of the sample to the SR to be controlled. The intensity of the X-ray beam flux can be monitored in a number of different ways. Aside from values registered from a scatter foil [41, 42] or a nickel grid [41, 42], the flux intensity can be recorded by an ion chamber.

3.3.2.1 XEOM 1 on XMaS

XEOM 1 is mounted in the experimental hutch on an 11-axis Huber four-circle diffractometer. The primary purpose of the Huber diffractometer is to precisely align the sample in the X-ray beam and automatically guide the motion of sample and detectors during sophisticated diffraction and scatter experiments. When the θ -angle

(angle between the X-ray beam and sample surface) of the diffractometer is set to 90° , the χ -circle of the diffractometer is oriented parallel to the X-ray beam and serves as an excellent mounting platform for the optical rail of XEOM 1. After the incident X-rays are aligned with a pin representing the centre of rotation of the goniometer, the XEOM is mounted so that the sample coincides with the centre of rotation. Subsequently the χ -circle is rotated 30° which allows the X-rays to enter the microscope through one of the 60° angle ports and hit the sample. Although XEOM 1 operates at ambient pressure, the soft primary X-rays need to be guided in vacuum as closely as possible to the sample in order to prevent X-ray absorption by air. Accordingly the vacuum tubes of the beamline reach until the entrance of the angle port. Figure 3.16 displays the XEOM 1 setup deployed at XMaS.

3.3.2.1.1 Dark experimental station

In contrast to experiments where (secondary) X-rays are being detected, ambient light is a source of unwanted background signal during XEOL measurements which has a considerable adverse effect on the sensitivity of the technique. In order to exclusively detect optical light induced by X-ray interaction XEOL-based measurements have to be performed in a completely dark experimental hutch. Therefore all lights and monitors were switched off and LED's from beamline hardware were covered with aluminium foil.

3.3.2.1.2 Interfacing with XMaS

As described up till now, XEOM 1 was designed to be operated independently from the beam line operating software. However, for automated data acquisition, synchronization between the XEOM 1 and the beamline operation is necessary. Performing a XEOM experiment, as described in more detail in Chapter 5, entails recording XEOL with the CCD camera on different energy points across the absorption edge of an element of choice. Thus the opening and closing of the CCD camera shutter has to be synchronized with stepping of the beamline monochromator.

The approach for synchronizing XEOM 1 with XMaS has been adopted from experiments carried in the eCell in which the movement of the working electrode was synchronized with the fast X-ray shutter [44]. In this approach, the beamline monochromator waits for a signal coming from XEOM 1 in order to step to a next energy point. This signal exists in the form of a transistor-transistor logic (TTL) pulse produced by the XEOM 1 electronics interface unit after data acquisition has finished. This pulse is fed into a WAGO Ethernet TCP/IP programmable fieldbus controller 750-842 (WAGO Kontakttechnik GmbH & Co. KG., Minden, Germany) which outputs an ethernet signal which forces the monochromator to step [3]. The ethernet signal replaces pulses coming from a time frame generator, which are

normally used during automated time dependent measurements. Enabling or disabling control by the WAGO box is done by executing or halting a SPEC-programmed macro (`wago_trig_on`, `wago_trig_off` or `wago_trig_wait`).

This approach is versatile in a way that it allows us to control XEOM 1 independently from the beamline, but benefits from the functions built into SPEC to perform different experiments (time scans, energy scans, position scans).

Initially this approach was not entirely successful. During several experiments, the monochromator missed certain trigger events sent by the WAGO box which resulted in missed data points. This problem was solved by either: clearing the beamline ethernet which was, on certain occasions, saturated by information coming from the synchrotron operation centre providing information of the status of the X-ray beam; increasing the WAGO pulse duration from 20 ms to 50 ms [3]; and rewriting of the WAGO macro (thanks to Didier Wermeille).

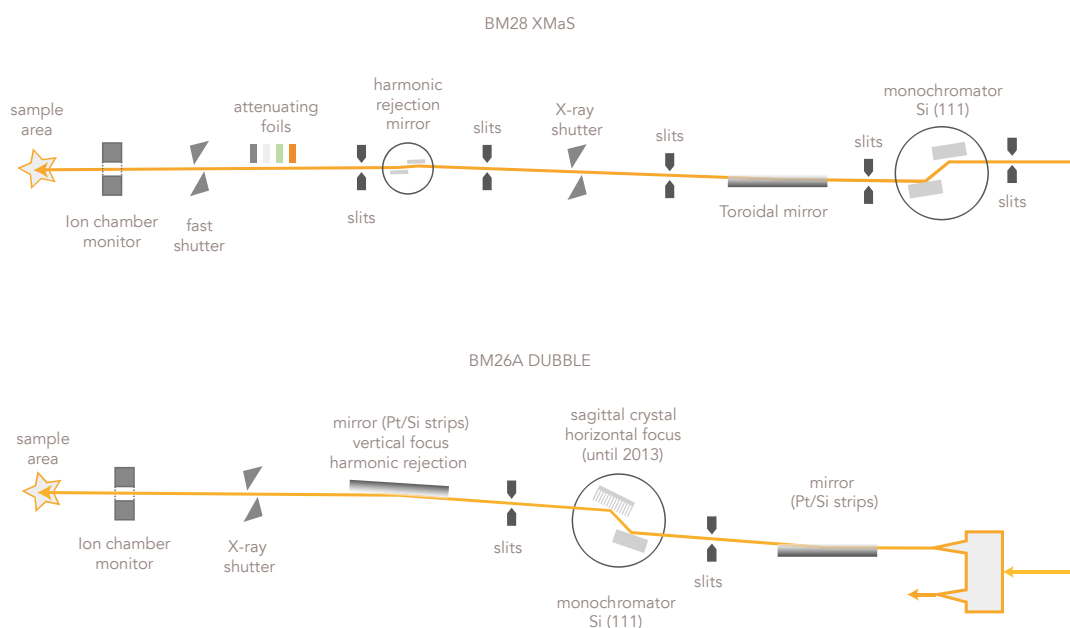


Figure 3.15

Diagram of the X-ray optics on BM28 (XMaS) and BM26A (DUBBLE) of the ESRF. All elements should be considered from a side-view perspective where the X-rays coming from the storage ring enter the optics from the right. All elements are not to scale.

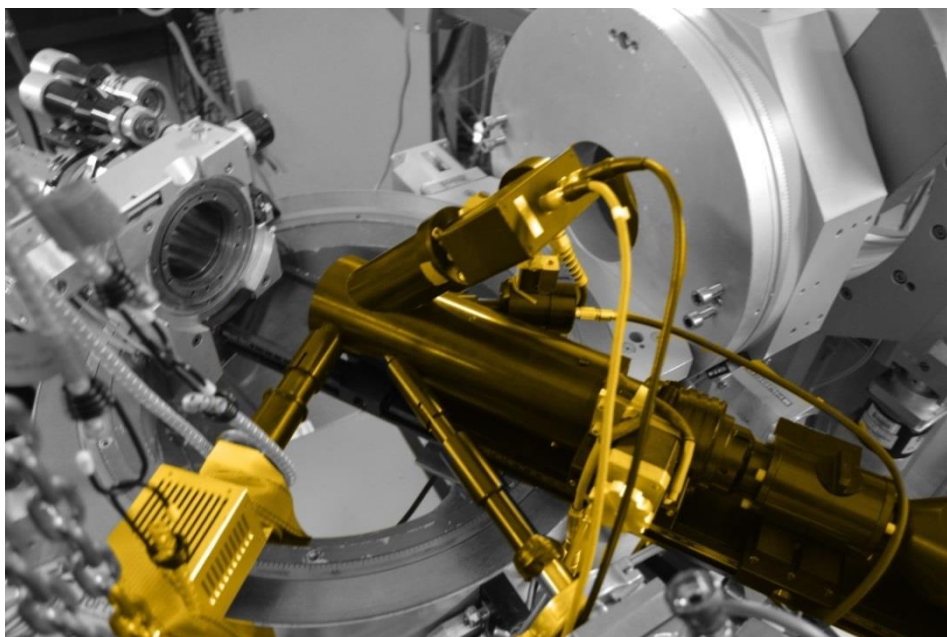


Figure 3.16

XEOM 1 installed on XMaS during beamtime X. In order to deduce the beamline parts from the XEOM 1, a yellow overlay was given to the XEOM 1 parts. The PMT and the Vortex® SDD are installed as secondary detectors on respectively the large 45° and 10° angle ports. X-rays enter through one 30° angle port, while the other 30° angle port is fitted with a LED illuminator.

3.3.3 BM26A DUBBLE, THE DUTCH BELGIAN BEAMLINE

The Dutch-Belgian Beamline (DUBBLE) operates as a CRG at the ESRF funded by the Dutch Science Foundation (NWO) and the Research Foundation - Flanders (FWO). The beamline is situated on dipole magnet sector 26 of the ESRF and is split into a soft and a hard energy branch, respectively BM26A and BM26B. The hard energy beamline was designed to support both small angle scattering (SAXS) and wide angle scattering (WAXS) while the softer energy branch A is mainly dedicated to X-ray Absorption Spectroscopy (XAS) [45]. XEOM 1 was only installed on BM26A, therefore the optics of only this part of the beamline are being described.

As can be seen on Figure 3.15 , a part of polychromatic X-ray beam coming from the storage ring enters the optics section of the soft line after having been separated by the radiation fraction intended for the hard line by a splitter vessel. The soft X-rays are collimated and focused on the first crystal of the double crystal monochromator by a cooled mirror accommodated with Pt and Si strips [46]. The double-crystal Si 111 monochromator can select monochromatic X-rays in the range of 5 – 40 keV with a resolution of $\Delta E/E = 1.74 \times 10^{-4}$. During the deployments of XEOM 1 at DUBBLE, the second Si 111 crystal of the monochromator could be bent into a cylindrical shape in which the crystal can also function as a horizontal focusing element apart from its wavelength selection capacities [47]. Advantage was taken of this sagittal

focusing capacity of the monochromator in order to maximize the beam flux, and accordingly XEOL yield, within the field of view of XEOM 1. Unfortunately, this feature was removed during the lifetime of the project. Due to the removal of the sagittal focussing in 2013 at DUBBLE, the beamline is no longer suitable for XEOM imaging experiments due to lack of sufficient beam flux.

Immediately downstream of the monochromator, a second Pt/Si mirror served as a vertical focusing element and a tool to suppress the higher harmonics of the primary X-ray energy. The combination of slits and mirrors can yield a typical beam size of 5 mm (horizontal) by 1 mm (vertical) at the sample. [46].

3.3.3.1 XEOM 1 on DUBBLE

XEOM 1 was installed for the first time in DUBBLE in December 2010. After several different attempts, the following solution was found to provide the most reliable and secure mounting of the XEOM 1 system. An overview of this approach can be seen in Figure 3.17 . Unlike the mounting approach followed on XMaS, the microscope was rotated by 90° with respect to its optical axis. The optical rail, holding all separate XEOM modules together, is affixed to an aluminium X95 profile via a joint of two rail carriers perpendicularly bolted together. This approach allows the microscope to be roughly aligned with the X-ray beam with two degrees of freedom. The X95 rail itself is mounted on a combination of X-Y and Z motorized sample stages for precise alignment of the sample in the X-ray footprint. On DUBBLE, the X-ray beam enters the microscope through the 45° angle port. Since the beamline vacuum only extends until just before the first ion chamber, which is mounted adjacent to the wall of the experimental hutch, the microscope could not be mounted in a geometry in which the 45° angle entrance port is placed just after the ion chamber. This implies that the large diameter 45° angle port could serve as an entrance port for unwanted stray light. This problem was solved by fitting a black ABS extension tube between the exit slit of the ion chamber and the entrance port of XEOM and operating in a completely dark hutch. Secondly, a considerable amount of air can steal X-ray flux before impact on the sample, resulting in lower XEOL yield and accordingly longer measurement times. On that account, this setup could be improved during future beam time allocations in which an evacuated tube could be placed between the microscope and the ion chamber.

3.3.3.1.1 Interfacing with DUBBLE

Interfacing XEOM 1 with the DUBBLE beamline to automate image stack acquisition was done by Matt Hand and Mark Dowsett with help of the DUBBLE beamline staff [3]. Contrary to the approach followed in XMaS, the EIU of XEOM 1 receives a triggering pulse from the beamline time frame generator which guides the monochromator and other hardware for time dependent measurements. This trigger

informs XEOM 1 to open the CCD camera shutter and to start acquisition of the data point. From that moment on, the XEOM soft- and hardware waits for another trigger to repeat this process. Since scanning the monochromator and acquiring XEOM images are respectively controlled by the beamline operating system and the XEOM 1 operating system, acquisition times on each control system must be decided carefully. Within this respect must the acquisition time of the beamline counting system always be approximately 5 – 10 seconds larger than the acquisition time of the XEOM system. Accordingly, the XEOM system is given the time to read out, download and store the data before another trigger is received.

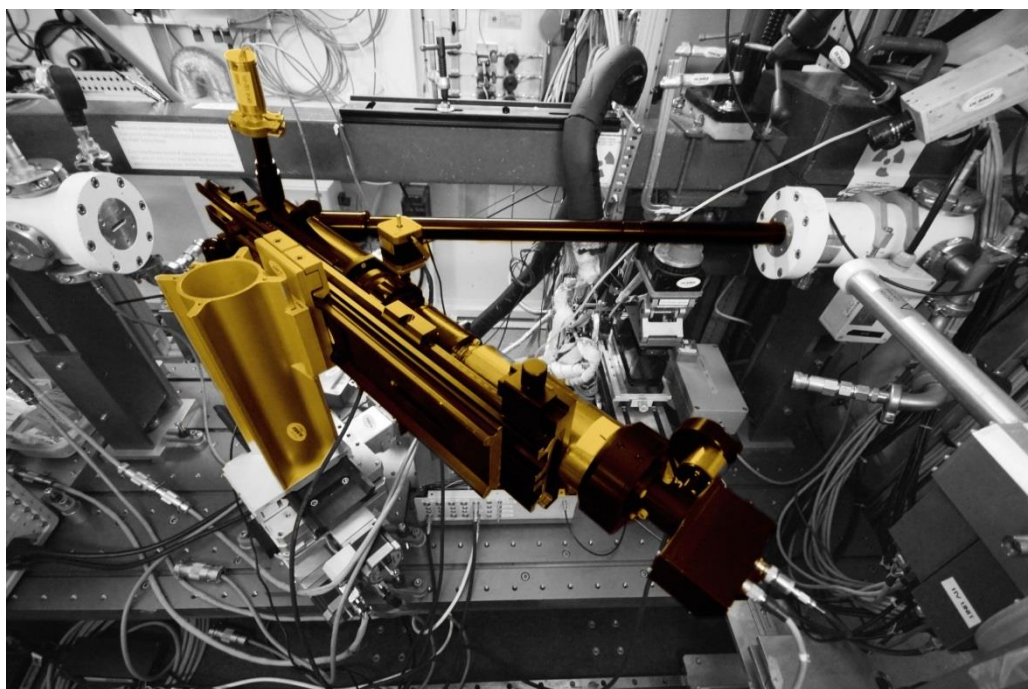


Figure 3.17

XEOM 1 installed on XMaS during beamtime VI. Image of the setup was taken with a fisheye lens. In order to deduce the beamline parts from the XEOM 1, a yellow overlay was given to the XEOM 1 parts. During this particular experiment, the PMT was mounted in the camera position and the APD was used as X-ray detector.

3.3.4 Overview of beamtime allocations

During the course of this research, we were given the opportunity to install XEOM 1 on XMaS and DUBBLE during a set of beamtime allocations. Table 3.6 gives a chronological overview of this beamtime allocations along with the correspondent beamline, date and beamtime subject. Each allocation is listed with a Roman number, to which will be referred to in the following chapters when a certain data set is being presented. It should be mentioned that on several beam time allocations, part of the time was made available for XEOM experiments and a part was dedicated to XRD measurements to support other research projects. Due to the limited quality

of the data obtained during beamtime XII as a result of insufficient flux, partly because of the removal of the sagittal focussing of the beamline, and experimental issues the data of this beamtime are not presented in the thesis. Nevertheless since the work done prior to and during beamtime XII fits into the larger framework of this thesis, its reference was included in the list.

Number	beamtime allocation code	beamline	date	title project
I	26-01 884	BM26A	16/12/10 - 20/12/10	Towards parallel μ XEOL imaging, XAS & XRD for studying the evolution of surface chemistry in real time
II	28-01 913	BM28	10/02/11 - 15/02/11	First applications of a new XEOL microscope for spectroelectrochemistry
III	28-01 928	BM28	11/05/11 - 14/05/11	Real time XEOL microscopy monitoring of chemical reactions in an electrochemical cell: exploring the limitations
IV	26-01 904	BM26A	15/06/11 - 20/06/11	Real time measurement of the growth of carboxylate coatings on lead
V	28-01 952	BM28	07/09/11 - 12/09/11	Establishment of a novel X-ray microscope: XEOM 1
VI	26-01 926	BM26A	30/11/11 - 05/12/11	High lateral resolution fast X-ray microscopy on a bending magnet using XEOM 1
VII	28-01 988	BM28	25/10/12 - 30/10/12	Chemical mapping of a topological insulator and other samples on the micron scale using XEOL
VIII	28-01 1002	BM28	03/07/13 - 09/07/13	Time lapse XRD, XAS & XEOL of heritage silver corrosion in a controlled environment
IX	28-01 1060	BM28	23/10/14 - 27/10/14	Time resolved copper corrosion for anticonception by a novel copper-gold intrauterine device
X	28-01 1114	BM28	08/07/15 - 13/07/15	X-ray-excited optical luminescence microscopy study of the state of conservation of objects from the Mary Rose
XI	28-01 1145	BM28	02/03/16 - 08/03/16	Parallel XRD, XAS and XEOL-XAS study of artifacts from Henry VIII's flagship, the Mary Rose
XII	26-01 1070	BM26A	02/06/16 - 05/06/16	A XEOL study of de-excitation channels and end states across K and L levels in metals


Table 3.6:

Overview of granted beamtime allocations during the course of this research.

3.4 BIBLIOGRAPY

- [1] M. Dowsett, M. Hand, P.-J. Sabbe, P. Thompson, A. Adriaens, XEOM 1 - A novel microscopy system for the chemical imaging of heritage metal surfaces, *Herit. Sci.* 3 (2015) 14.
- [2] P.-J. Sabbe, M. Dowsett, M. Hand, R. Grayburn, P. Thompson, W. Bras, A. Adriaens, Evaluation of an X-ray-Excited Optical Microscope for Chemical Imaging of Metal and Other Surfaces, *Anal. Chem.* 86 (2014) 11789–11796.
- [3] M. Hand, Development of an X-ray Excited Optical Luminescence Microscope (XEOM) Ph.D. Dissertation, University of Warwick, June 2014.
- [4] M. Dowsett, A. Adriaens, Cell for simultaneous synchrotron radiation X-ray and electrochemical corrosion measurements on cultural heritage metals and other materials., *Anal. Chem.* 78 (2006) 3360–5.
- [5] Nikon, Nikon F-mount.
- [6] L.R. Corporation, OSLO (Optics Software for Layout and Optimization).
- [7] Thorlabs, uncoated UV fused silica, (2016).
- [8] E. Optics, UV-to-NIR corrected triplet lenses, <http://www.edmundoptics.com/optics/optical-lenses/achromatic-lenses/uv-to-nir-corrected-triplet-lenses/2479/> accessed 2016–02–22.
- [9] A. Bianconi, D. Jackson, K. Monahan, Intrinsic luminescence excitation spectrum and extended x-ray absorption fine structure above the K-edge in CaF₂, *Phys. Rev. B* 17 (1978) 2022–2024.
- [10] W.J. Smith, *Modern Optical Engineering*, 2000.
- [11] E. Optics, Additive and Subtractive dichroic color filters, <http://www.edmundoptics.com/optics/optical-filters/color-dichroic-filters/additive-subtractive-dichroic-color-filters/1734/> accessed 2016–02–22.
- [12] H.A. MacLeod, *Thin-Film Optical Filters, Third Edition*, CRC Press, 2001.
- [13] E. Optics, Techspec Fluorescence Bandpass Filters, <http://www.edmundoptics.com/optics/optical-filters/bandpass-filters/fluorescence-bandpass-filters/3227/> accessed 2016–02–22.
- [14] E. Optics, Shortpass Filter, <http://www.edmundoptics.com/optics/optical-filters/shortpass-edge-filters/shortpass-filters/47286/> accessed 2016–02–22.
- [15] K. Optical, longpass colour glass filter, <http://www.knightoptical.com/stock/optical-components/uvvisnir-optics/filters/long-pass-filters/colour-glass-longpass-filters/colour-glass-filter-25mmdia780nm-long-pass/> accessed 2016–02–27.
- [16] K. Optical, KG1 toughened filter, <http://www.knightoptical.com/stock/optical-components/uvvisnir-optics/filters/short-pass-filters/kg1-heat-glass-filters/kg1-toughened-filter-25mmdia/> accessed 2016–02–27.
- [17] K. Optical, UG11 colour glass filter, <http://www.knightoptical.com/stock/optical-components/uvvisnir-optics/filters/band-pass-filters/colour-glass-bandpass-filters/colour-glass-filter-25mmdia330nm-band-pass/> accessed 2016–02–27.
- [18] K. Optical, Broadband Interference bandpass filters, <http://www.knightoptical.com/stock/optical-components/uvvisnir-optics/filters/band-pass-filters/interference-bandpass-filters-broadband-visnir-range-400nm---940nm/> accessed 2016–02–27.
- [19] K. Optical, Extra broadband interference bandpass filters, <http://www.knightoptical.com/stock/optical-components/uvvisnir-optics/filters/band-pass-filters/interference-bandpass-filters-extra-broadband-visnir-range-500nm---960nm/> accessed 2016–02–27.
- [20] J.R. Janesick, T. Elliott, S. Collins, M.M. Blouke, J. Freeman, Scientific charge coupled devices, *Opt. Eng.* 26 (1987) 692 – 714.
- [21] F.L. Instruments, FLI Microline ML1109.
- [22] Hamamtsu, Hamamatus S10140-1009.
- [23] J.W. Beletic, Scientific Detectors for Astronomy, *Astronomy* 300 (2004) 489–492.
- [24] S.B. Howell, *Handbook of Ccd Astronomy*, (2006) 208.
- [25] Andor Technologies, Andor Ikon-L 936.
- [26] E. Technologies, e2v CCD42-40 NIMO back illuminated chip.
- [27] Hamamatsu, Photon counting head H8259-01.
- [28] Certif Inc., SPEC, software for diffraction, <https://certif.com/content/spec/> (2017).
- [29] P. Elmer, Si avalanche photodiode chip.
- [30] H.H. technologies S. America, Vortex (r) X-ray detector.

- [31] K. Technologies, U2353A 16-channel 500kSa/s USB modular multifunction DAQ.
- [32] K. Technologies, U2781A USB modular products chassis.
- [33] M. Dowsett, A. Adriaens, Cell for simultaneous synchrotron radiation X-ray and electrochemical corrosion measurements on cultural heritage metals and other materials., *Anal. Chem.* 78 (2006) 3360–5.
- [34] R.A. Grayburn, M.G. Dowsett, P.-J. Sabbe, D. Wermeille, J.A. Anjos, V. Flexer, M. De Keersmaecker, D. Wildermeersch, A. Adriaens, SR-XRD in situ monitoring of copper-IUD corrosion in simulated uterine fluid using a portable spectroelectrochemical cell, *Bioelectrochemistry* 110 (2016) 41–45.
- [35] Schroff, Compac Pro Case.
- [36] A. Adriaens, M.G. Dowsett, K. Leyssens, B. Van Gasse, Insights into electrolytic stabilization with weak polarization as treatment for archaeological copper objects., *Anal. Bioanal. Chem.* 387 (2007) 861–8.
- [37] B. Ravel, M. Newville, ATHENA, ARTEMIS, HEPHAESTUS: data analysis for X-ray absorption spectroscopy using IFEFFIT., *J. Synchrotron Radiat.* 12 (2005) 537–41.
- [38] M.G. Dowsett, A. Adriaens, in: XTOP, Coventry, 2010.
- [39] European Synchrotron Radiation Facility (ESRF).
- [40] ESRF, ESRF-EBS.
- [41] S.D. Brown, L. Bouchenoire, D. Bowyer, J. Kervin, D. Laundry, M.J. Longfield, D. Mannix, D.F. Paul, a. Stunault, P. Thompson, M.J. Cooper, C. a. Lucas, W.G. Stirling, The XMaS beamline at ESRF: instrumental developments and high-resolution diffraction studies, *J. Synchrotron Radiat.* 8 (2001) 1172–1181.
- [42] K. Lampard, BM28 - XMaS - The UK CRG.
- [43] K. Lampard, XMaS Beamline Details.
- [44] M. Dowsett, A. Adriaens, C. Martin, L. Bouchenoire, The use of synchrotron X-rays to observe copper corrosion in real time., *Anal. Chem.* 84 (2012) 4866–72.
- [45] M. Borsboom, W. Bras, I. Cerjak, D. Detollenaere, D. Glastra Van Loon, P. Goedtkindt, M. Konijnenburg, P. Lassing, Y.K. Levine, B. Munneke, M. Oversluizen, R. Van Tol, E. Vlieg, The Dutch-Belgian beamline at the ESRF., *J. Synchrotron Radiat.* 5 (1998) 518–20.
- [46] DuBBLe, DuBBLe - Overall optics - Station S.
- [47] G. Silversmit, B. Vekemans, K. Appel, S. Schmitz, T. Schoonjans, F.E. Brenker, F. Kaminsky, L. Vincze, Three-Dimensional Fe Speciation of an Inclusion Cloud within an Ultradeep Diamond by Confocal mu-X-ray Absorption Near Edge Structure: Evidence for Late Stage Overprint, *Anal. Chem.* 83 (2011) 6294–6299.



**Synthesis and
characterization of
artificially corroded
copper samples**

CHAPTER 4

Development of new scientific instrumentation is an iterative process in which updates to the hardware need to be evaluated before proceeding to a next step. Because XEOM 1 offers micron-scale lateral resolution at low X-ray power densities compared to X-ray microprobe techniques [1], one of our intended applications is the study of corrosion and its inhibition on copper and cupreous alloys both generally and in context of museum objects and their conservation. During the first stages, evaluation of the hardware and imaging performances of XEOM 1 cannot be done using real artefacts. The lack of any a priori knowledge and the unique nature of such artefacts prevent us from doing that. Instead, well-characterized patterned reference materials, for example, artificially corroded analogues of naturally occurring corrosion are needed for the evaluation and calibration of the instrument. Producing these analogues presents a significant challenge in itself, because corrosion layers on metals are often extremely complex, both chemically and spatially, and may even not be stable in the short term [2]. Moreover, since XEOL appears to be very compound specific, the optical response for each analogue upon X-ray absorption needs to be examined and compared with X-ray absorption spectra obtained via other detection modes. In what follows, an overview is given on the amount of work done on producing and characterizing artificially corroded analogues principally of cupreous artefacts, with a major focus on the development of an alternative protocol to produce cuprite. Furthermore, a sample exhibiting a well-defined geometrical pattern to evaluate the performance of an optical microscope is proposed.

The majority of the findings discussed in this chapter, especially for cuprite, have been published in Applied Surface Science under the title: 'Synthesis and surface characterization of a patterned cuprite sample: preparatory step in the evaluation scheme of an X-ray-excited optical microscopy system' [3].

4.1 COPPER

Copper is a salmon pink metal that has been used by humans since antiquity. The importance of copper to human society dates back more than 10 000 years [4]. The earliest craftsmen in copper soon found that it was malleable and could be easily shaped into tools and other artefacts. Later on, the discovery of a copper-tin alloy and its uses led to end of the stone age and the beginning of the Bronze age, which began in the 4th millennium B.C. in the Middle east [5].

Apart from its utilitarian practice, copper and bronze have been used in the field of art throughout history and left us with a richness of heritage objects. As with many other metals, these copper artefacts might be under the attack of corrosion. Under

certain conditions this will lead to complete destruction of the object whereas in other cases the patina (the surface layer of corrosion) might be protective and desired due to its artistic effect [2, 6]. One of the major challenges in the conservation of corroded artefacts is to distinguish between these different types of corrosion. The success of that effort requires sophisticated tools such as XEOM 1 to gain insight into the nature of the patina.

Due to its importance and omnipresence, copper and its set of corrosion products was considered as an ideal (heritage) metal to explore the capabilities of XEOM 1 as a diagnostic tool in the field of conservation science.

4.1.1 COPPER COUPONS

Artificial patinas were produced on patterned or plain samples. The latter were in the form of 2 mm thick, 12.5 mm diameter circular metallic coupons of 99.9 % pure copper (Goodfellow, Huntingdon, U.K.). The coupons were originally designed to fit the working electrode of the eCell. In order to use the coupons both in the eCell and in XEOM 1, a specific sample holder for the coupons was devised (see 3.1.1.1).

A fresh copper surface was prepared to serve either as a substrate for one of the corrosion patinas (e.g. cuprite, tenorite, etc.) described below or as a copper reference itself. In order to do this, the coupons were mechanically cleaned with P400 grit silicon carbide (SiC) abrasive paper (Buehler, Lake Bluff, Illinois, USA) and subsequently polished with wet P1200 grit. In a final stage, the coupons were manually polished using a microcloth (12", Buehler, Lake Bluff, Illinois, USA) with 1 µm deagglomerated alpha alumina particles (Buehler, Lake Bluff, Illinois, USA) suspended in water. Finally, the remaining adhering alumina particles were removed by rinsing and ultrasonic cleaning in 2-propanol for 15 minutes.

Copper samples and artificially corroded copper samples (see below) were either freshly polished or corroded in the beamline's laboratory just before analysis. Hence could the alteration of the copper coupon or patina by the atmosphere be reduced to a minimum. In case the coupons had to be made in Ghent, an air tight polystyrene box with polyetherane membranes (AGG3319, Agar Scientific, Essex, UK) was used to transport the samples.

4.1.2 COPPER GRIDS: A MESH FOR TRANSMISSION ELECTRON MICROSCOPY EXPERIMENTS

A well-defined geometrical pattern is best for evaluating the performance of an optical imaging system. Therefore, a copper transmission electron microscopy (TEM) sample grid was chosen as a basic, simply available substrate to which cuprite and

other coatings could be applied (Figure 4.1). The grids chosen are $20 \pm 3 \mu\text{m}$ thick, 3.05 mm diameter and have a $127 \mu\text{m}$ pitch (Athene Old 200, Agar Scientific, Stansted, U.K.). The grids themselves can be treated according to the protocols described below to grow a corrosion layer or they were used as supplied. The fragility of the TEM grids prevented them from being subjected to the polishing procedure applied to the coupons. When grids were used in combination with coupons, double sided tape was used as an adhesive between the edge of the grid and the underlying coupon. This resulted in the creation of well-defined regions of $90 \times 90 \mu\text{m}$ (holes in the mesh) and $90 \times 35 \mu\text{m}$ (bars of the mesh) of different states of copper or corrosion product.

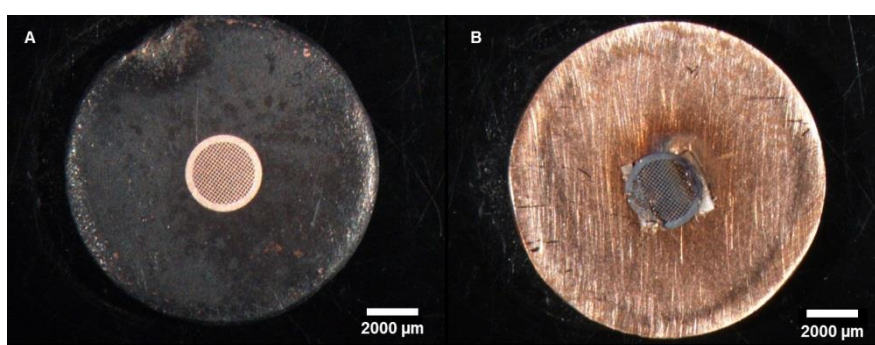


Figure 4.1

[A] Light optical image of a copper coupon with a grey cuprite patina. The geometrical pattern provided by the copper TEM sample holder grid on top of the coupon creates micrometer regions of different, well-defined oxidation states of copper.

[B] Light optical image of a TEM sample holder grid with a grey cuprite patina. The grid was mounted with double-sided tape on a polished copper coupon.

4.1.3 XEOL-XAS OF COPPER

Figure 4.2 displays the XAS and unfiltered XEOL-XAS spectra collected in parallel from a polished copper surface cleaned with 2-propanol across the Cu *K*-edge at 8979 eV. Data points were collected for 5 seconds per point with an energy resolution of 0.5 eV. The data were collected at XMaS during beamtime III (Table 3.6). For both XAS and XEOL-XAS spectra, the raw unsmoothed data were initially normalized to the beam monitor to account for variation in the incoming beam flux. Subsequently, the spectra were normalized to the mean intensity value calculated for the post-edge between 8990 eV – 9100 eV. This procedure allows one to observe the relative changes between the two spectra, without their shape being distorted with respect to the raw data [1].

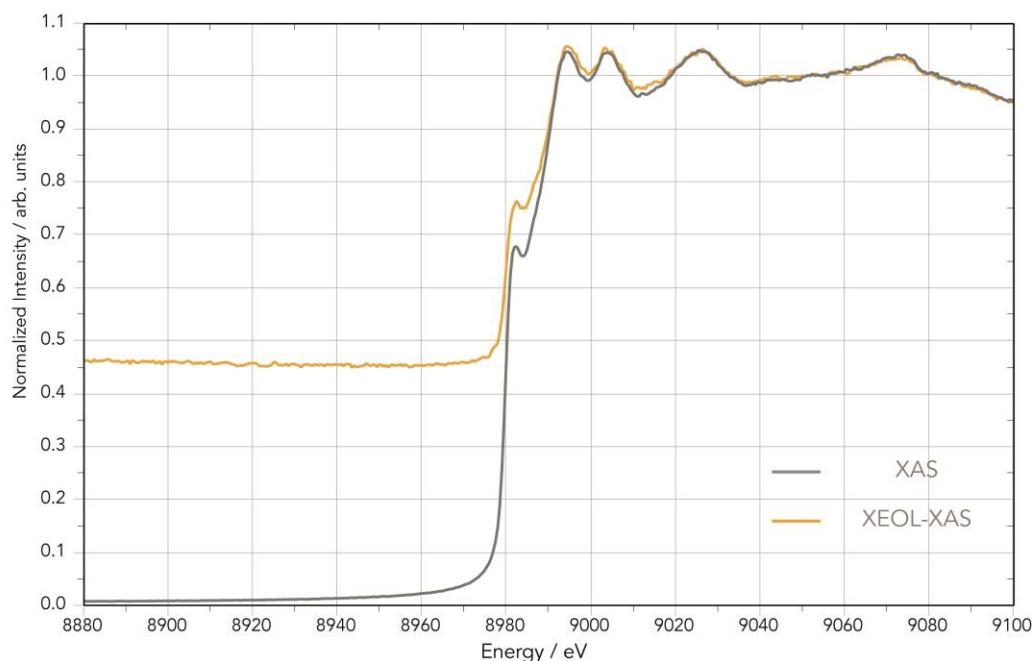


Figure 4.2

Parallel XAS and XEOL-XAS collected from a polished copper coupon.

Among other features, the distinctive mid-edge peak due to the $1s-3d$ resonance followed by the double post-edge features are the modulations characterizing a typical fingerprint of a Cu K -edge spectrum of metallic copper [7]. As can be seen in Figure 4.2, these features can be seen both on the XAS and XEOL-XAS data sets without any remarkable energy shift. The unsmoothed data show the better signal-to-noise ratio obtained for the XAS data with respect to the XEOL-XAS, even though the signal-to-noise ratio for the latter is more than acceptable. A common difference observed between spectra recorded in fluorescence mode and optical yield mode is the difference between pre-edge background emission [1, 8]. This phenomenon is likewise observed for metallic copper. Although a small fraction of pre-edge signal can be attributed to optical fluorescence from organic surface contamination, the majority of the pre-edge XEOL signal is due to surface specific radiative processes related to copper [1]. This can be concluded after carefully studying the relative heights of the spectral features for both spectra, as was done in the study published by the promoters of this work in Analytical Chemistry [1]. Similarly for this data, it can be seen that the mid-edge $1s-3d$ resonance feature occurs at a relative height of approximately 0.68 (XAS) and 0.75 (XEOL-XAS) – a difference of 0.07, whereas a difference of 0.45 a.u. can be observed for the pre-edge emission. From this, one can deduce that that the background signal in the Cu XEOL-XAS is not additive across the Cu K -edge and that optical channels giving rise the pre-edge emission switch off in the vicinity of the absorption edge and hence provide less background luminescence in this region. Consequently, background subtraction operations

during data reduction cannot be performed in a traditional way (see 2.2.4) since this may distort the spectra. An alternative approach is discussed in more detail in [1].

4.2 CUPRITE

Cuprite, Cu_2O or cuprous oxide, is a common corrosion product of copper and its alloys. When fresh copper is exposed to clean damp air, a light brown surface layer of cuprite develops [9]. The growth rate of a cuprite patina is both dependent on the temperature and relative humidity of the ambient environment and the presence of any particulate contamination [10]. Yet, the initial growth rate of the cuprite patina is still unclear. However, as confirmed in paragraph 4.1.3, it is clear that mechanically cleaned copper coupons (according to the cleaning procedure detailed in paragraph 4.1.1) do not show any signs of XEOL visible oxides in the first few hours after the polishing. Depending on the ambient conditions, the stable cuprite can either serve as a passivation layer for the underlying copper or act as a substrate for the further development of the corrosion layer. Therefore, cuprite can be found on many artefacts coming from all kinds of environment, such as rural, urban, marine and industrial [11].

Well-controlled artificial cuprite patinas have been produced in many ways, both for corrosion studies, and because cuprite is a broadly explored semiconductor, e.g. in solar cells. Protocols producing well defined layers of cuprite include electrochemical deposition [12, 13], ultrasonic spray pyrolysis [14], sputter deposition [15], pulsed laser deposition [16], thermal oxidation [17] and many others. Initially, for this research, an electrochemical approach was adopted from [18] to produce cuprite layers by anodic polarization to 320 mV (vs. a normal hydrogen electrode) for 16 hours in a 0.1 M Na_2SO_4 solution (> 99%, Fluka, St. Louis, Missouri). A coupon subjected to this treatment obtained a dull reddish brown cuprite topcoat. Unfortunately, this approach was not feasible when attempting to apply it to a small grid. The major struggle was to make an electrical connection, necessary for polarization, to the tiny grid. Attempting to attach the grid to a thin wire resulted in a poor connection and no significant corrosion layers. More successful was adhering the grid on an electrode made from carbon paste, commonly used to perform Voltammetry of MicroParticles (VMP) experiments. Despite visual inspection confirmed the formation of corrosion product, the chemical reaction made the 20 μm thick grid so brittle) that it was no longer useful. Consequently, a different procedure had to be found. It is generally known that copper has been patinated using flames since antiquity [19]. Within this respect, a simple and quick approach involving heating the grid in a reducing flame followed immediately by air exposure was investigated.

4.2.1 GREY CUPRITE PROTOCOL

Corrosion layers were produced on the copper coupon by heating to bright cherry red (800 – 900 °C) in a reducing Bunsen burner natural gas flame. In order to ensure the copper is heated in a reducing atmosphere, the collar of the Bunsen burner was set to close the air hole. Soot deposition was avoided by heating the coupon well below the tip of the flame. Starving the flame from oxygen avoids the metal of oxidizing in the flame at the point of aspiration where the gas is entirely burnt and oxygen radicals become available. This process produces a scale on the metal surface, which cracks and detaches when the metal cools down. Instead - for a reducing flame - the patina is formed immediately upon removal from the flame, when the hot copper is oxidized in the surrounding air. A patina was induced on the grid by placing it on a coupon without any adhesive and following a similar procedure. Without the coupon, grids melted immediately upon direct contact with the flame. At the ESRF a similar protocol was followed using a micro-horizontal burner with a propane/butane mix (Kager GB2001, Carl Roth GmbH, Karlsruhe, Germany).

The resulting coated coupon and a coated grid can be seen in Figure 4.1. In contrast with the electrochemically deposited layers, which are reddish brown, the flame protocol produces a dark grey surface colour. Literature confirms that cuprite can adopt a variety of colours (including grey) depending on the chemical composition of impurities present [19–21].

4.2.2 XRD ANALYSIS OF GREY CUPRITE

4.2.2.1 Experimental details

X-ray diffraction data were obtained using a Siemens D5000 diffractometer (Bruker, AXS S.A.S., France) with Mo- K_{α} radiation (see 2.4.1.3.1). The sample was mounted in reflection geometry, with the sample rotating at 15 rpm. Data were collected by means of a conventional θ - 2θ scan in the 2θ range 10° - 40° with a 2θ step size of 0.01° and 3001 points at 0.2 s per point. Diffraction patterns are plotted as a function of wave number Q and converted from 2θ according to equation {2.16}. The background was subtracted from the diffraction patterns and they were lightly smoothed using Gaussian convolution. Peak intensities were normalized to the Cu_2O 111 reflection at 2.5 \AA^{-1} . All reflections were eventually identified using reference diffraction patterns from the MinCryst database [22, 23]. All XRD data handling was done with esaProject (see 3.2.2).

4.2.2.2 Results and discussion

Figure 4.3 shows the X-ray diffraction pattern of a copper coupon treated with a reducing flame according to the protocol described above. The square root plot is

used to emphasize minor reflections. The data are plotted versus wave number Q to make them independent of the X-ray wavelength and plot the reflections evenly spaced across the range of data. All reflections observed in the diffraction pattern can be assigned to Cu, Cu₂O and CuO (tenorite, see 4.3). Cuprite is clearly the dominant corrosion product formed, showing major reflections at 2.5 and 4.15 Å⁻¹, although other products are present. Among the other reflections, those at 2.6 and 2.9 Å⁻¹ indicate the presence of crystalline tenorite in the patina. Under reducing flame circumstances, no oxidation reaction will occur at the copper surface when the flame is heating the coupon. Instead, upon removal from the reducing flame, the hot copper (800 – 900 °C) can react with O₂ and H₂O from the environment according to one of the following reactions:



Indeed, Cu₂O and CuO have been described as the sole stable oxides of Cu at high temperatures [24, 25]. Zhu et al.[25], amongst others [17, 24, 26, 27], describe the presence of a two phase scale with an inner Cu₂O layer and an outer CuO layer where Cu₂O is predominantly formed in the temperature range of 350 – 1050 °C. As the oxidation of Cu₂O to CuO (according to Equation {4.4}) is slow compared to the oxidation of Cu to Cu₂O, outward diffusion of copper across the Cu₂O scale determines the overall oxidation rate of Cu, even in the temperature range where CuO is stable [24], hence the predominance of cuprite in the layer. Reactions involving the formation of Cu(OH)₂, a possible contaminant in a moist environment [28], are not included as this compound is not observed in the analytical data.

The presence of copper reflections in the XRD could either be ascribed to the presence of Cu pinholes in the oxide scale or to the short path length of the oxide compared to the escape depth of the reflected Mo- K_α radiation. As no copper contributions are observed in the X-ray absorption spectra (taken at the Cu- K edge with shorter path length compared to the Mo- K_α radiation – see below) the latter hypothesis is likely to be correct.

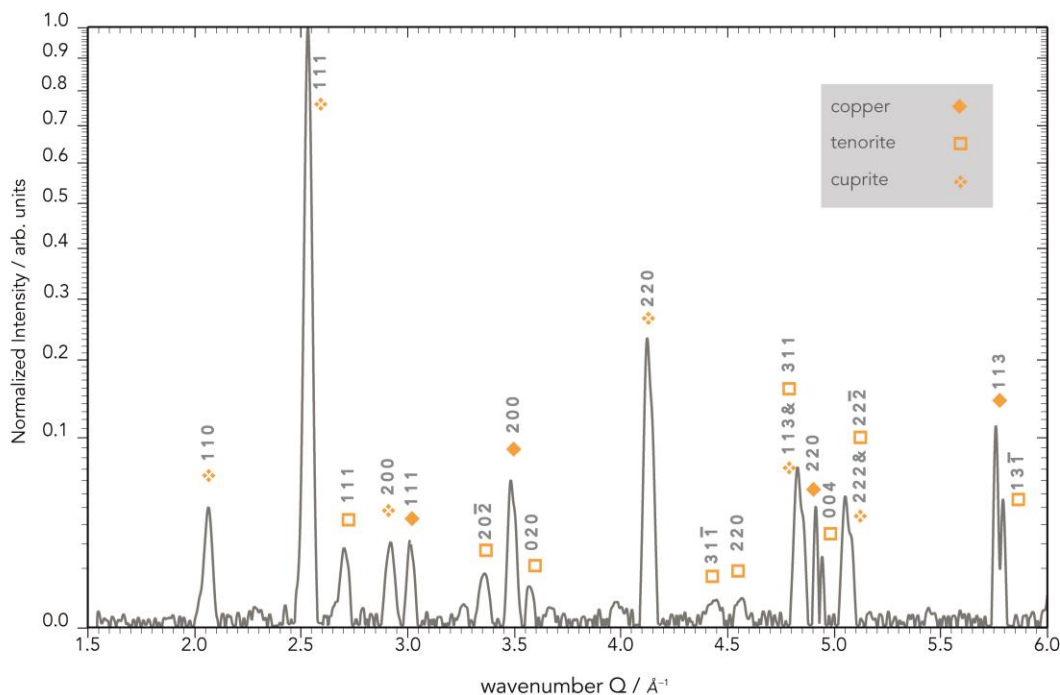


Figure 4.3

X-ray diffraction pattern recorded from a copper coupon treated with a reducing flame. The square root scale of the ordinate axis emphasizes minor reflections. Reference patterns used for peak assignment can be found in A.2.

4.2.3 XPS ANALYSIS OF GREY CUPRITE

4.2.3.1 Experimental details

XPS analysis was performed using an S-probe spectrometer (Surface Science Instruments, VG Scienta, Pleasanton, California, USA) with an Al- K_{α} monochromatic X-ray source ($h\nu=1486.6$ eV). The take-off angle was set at 45° and the primary beam energy at 10 kV with a power of 200 W. The pressure in the analysis chamber was maintained at 2×10^{-9} mbar throughout the measurement. The pass energy spectrum was 107.5 eV with an energy resolution of 0.108 eV per point. The analysed surface was $250 \times 1000 \mu\text{m}^2$. The $1s$ line of aliphatic carbon was set at 285.0 eV. Chemical compositions were analysed using the CasaXPS software package (version 2.3.16, Casa Software Ltd.). XPS curve fitting was performed according to the method described in paragraph 2.4.2.3.

4.2.3.2 Results and discussion

Figure 4.4 displays the results of a survey scan and two high-resolution scans for the O $1s$ and the Cu $2p$ peaks obtained by XPS of a sample coated according to the reducing flame protocol. For the data shown, the information depth is under 3 nm [29]. Similar to XEOL-XANES, XPS is helpful in identifying the oxidation states,

because the binding energy measured for core electrons undergoes a chemical shift because of changes in the chemical environment of atoms. Figure 4.4 A displays the result of the survey (wide scan) measurement in the 0 – 1 keV binding energy (BE) range. Intense spectral lines are observed for Cu $2p$ and O $1s$; the remaining spectral features could be ascribed to the other Cu photoelectrons (Cu $3s$ and Cu $3p$) and Cu Auger electrons (Cu L3V). Finally, an intense spectral line for aliphatic C $1s$ appears at 285.0 eV, which is due to contamination of the sample. XPS peaks for Cu (+II) compounds are typically broader and present prominent shake-up peaks on the higher BE of the Cu $2p$ doublet, whereas the bands are absent from the spectra of Cu(+I) and Cu(0) compounds. Hence, the presence of tenorite (CuO) is readily identifiable in the Cu $2p$ high-resolution spectrum in Figure 4.4, B. The fitting of both Cu $2p_{3/2}$ and Cu $2p_{1/2}$ suggests the presence of cuprite and tenorite, which is in line with the expectations using previous analyses. The BE obtained for the contributors were within the range of values reported in the literature, with 932.6 and 952.7 eV (for Cu $2p_{3/2}$ and Cu $2p_{1/2}$, respectively) as typical chemical shifts for cuprite and 933.9 and 954.1 eV for the corresponding tenorite [30, 31]. Moreover, the presence of cuprite in the top surface layers is confirmed by a characteristic Cu L3V Auger line at 569 eV, with a chemical shift and line shape typical of cuprite as reported by Chawla et al. [31]. The result of the O $1s$ deconvolution analysis is shown in Figure 4.4 C. A double shoulder is observed at high binding energies of the O $1s$ peak. The analysis confirms the presence of Cu₂O (531.2 eV) in addition to CuO (529.5 eV) and suggests the presence of an extra contributor at 532.4 eV. This could be attributed to chemisorbed water originating from ambient water vapour after the production of the patina [28, 32].

Calculations based on the area and the relative sensitivity factor of the cuprite and tenorite contributions in the Cu $2p$ and the O $1s$ peaks suggest relative contributions of 69.4 % CuO and 30.6 % Cu₂O. However, these calculations are based on the assumption that all measured O-atoms are bonded with a Cu-atom as in CuO and Cu₂O. The shoulder at 532.4 eV in the O $1s$ peak and the shoulder at 288 eV in the C $1s$ peak (Figure 4.4 D), suggesting, respectively, the chemisorption of water and the presence of CO-components [33], prove this estimation is not entirely correct and results from fitting procedure are misleading due to the contamination present on the sample.

Solely based on the shape of the overall Cu $2p$ spectrum and the peak height ratio of Cu $2p$ peaks to its corresponding shake up satellites [34], it is more likely to assume the contribution of Cu₂O is in fact much lower. In fact, rather than a surface with a mixture of Cu₂O and CuO present, a stratified structure with nearly pure CuO right at the surface (top 1.5 nm) merging into the underlying Cu₂O is a more plausible explanation. A high tenorite fraction at the surface is consistent with oxidation of the cuprite to tenorite as the sample cooled as described in Equation {4.4}. Moreover,

the presence of the Cu L3W Auger line at BE = 569 eV argues in favour of a stratified structure as the Auger electron (essentially corresponding to a 918 eV electron) has a higher escape depth than the Cu 2*p* photoelectrons.

During this experiment, no attempt was made for XPS depth profiling. Obtaining a depth profile with XPS can be done by either changing the take-off angle (angle-resolved XPS, ARXPS) or sputter profiling whilst recording XPS spectra. ARXPS has a limited depth range and would not have provided much additional information with respect to the presented XPS data. The alternative of retrieving depth information through sputtering would be relevant if the surface layers would be uniform and smooth. Since the layers grown by the grey cuprite protocol are rough surface powders, a poor depth resolution would be observed due to the original and beam induced surface roughness. Hence it seemed irrelevant to obtain a depth profile through XPS. Further experimentation with SEM on an edge or cross-section of the coupon might provide additional information regarding the surface stratigraphy.

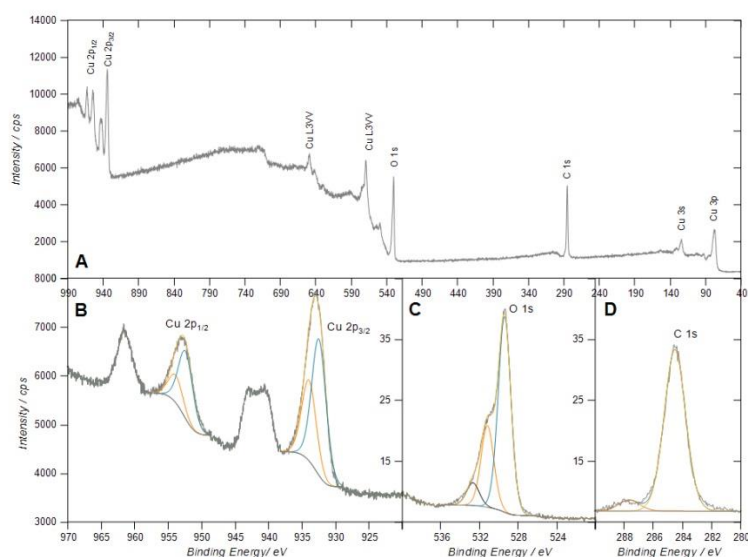


Figure 4.4

[A] XPS survey scan from 0 – 1000 eV (Binding Energy). Strong – line photoelectrons are observed for Cu 2*p*, O 1*s*, and C 1*s*.

[B] High-resolution XPS scan of Cu 2*p* doublet together with the deconvolution of the Cu 2*p*_{3/2} and Cu 2*p*_{1/2} bands with the contribution of Cu (+I) (blue) and Cu (+II) (orange) and the resulting fit (yellow). The shake-up satellites at high BE of the Cu 2*p* are typically observed in Cu (+II) products.

[C] High-resolution XPS scan of O 1*s* spectral line. The contributions of tenorite and cuprite suggested by multiplex analysis are respectively displayed in blue and orange. To get a matching overall fit (yellow), the contribution of the chemisorbed water was also taken into account (black).

[D] High-resolution XPS scan of the C 1*s* spectral line. The shoulder at high binding energy suggests the presence of chemisorbed CO type components.

4.2.4 XAS ANALYSIS OF GREY CUPRITE

4.2.4.1 Experimental details

X-ray absorption spectroscopy experiments in fluorescence mode were performed at beamline BM28, XMAS of the ESRF (see 3.3.2) using modules from the XEOM 1. Data were recorded across the Cu *K*-edge (8.979 keV) in the range of 8960 – 9300 eV with 0.5 eV per step: 680 points measured for 5 s each. The avalanche photodiode detector, described in more detail in section 3.1.4.2.1, mounted at 10° to the sample surface in a geometry to minimize self-absorption effects.

Powder samples of Cu₂O (> 99% purity, Fluka, St. Louis, Missouri, USA) and CuO (99.9999 % purity, Alfa Aesar, Ward Hill, Massachusetts, USA) were used as reference materials. A Cu reference spectrum was recorded from a copper coupon polished as described above. Reference powders were mounted in a purpose made sample holder covered with a layer of Ultralene® (4 μm thick, SPEX SamplePrep, Metuchen, New Jersey) to keep them in place during X-ray bombardment.

Data reduction for normalization and background subtraction of XAS data were carried out in ATHENA (Demeter software package version 0.9.18) [35]. Linear combination fitting of XAS data was performed using the same software package. The reference spectra used to build the fit were those obtained by XAS of the pure materials (copper coupon and cuprite tenorite powder). The analysis was performed on the normalized $\mu(E)$ fitting space in the range of 8960 - 9060 eV.

4.2.4.2 Results and discussion

Figure 4.5 A shows the X-ray absorption near edge spectra (XANES) in fluorescence mode recorded across the Cu *K*-edge (8979 eV) for the flame/air oxidized sample together with the absorption spectra of pure copper, cuprite and tenorite reference samples. The spectra are plotted conventionally as normalized $\mu(E)$ values versus the beam energy. As the absorption length of 9 keV X-rays in copper is about 4 μm, the XAS spectra provide information from < 10 μm depth in the investigated sample. X-ray XANES measured at the Cu *K*-edge are related to the movement of *1s* electrons for electronic states above the Fermi level [36]. The post-edge regions of metallic copper, cuprite and tenorite references exhibit very different resonance characteristics that can be used qualitatively as ‘fingerprints’ to identify the local bonding environment. The main features observed from the coated sample are typical of cuprite: a distinct inter-band transition at the mid-edge around 8980 eV (due to the *1s* → *3d* resonance) and a broad single post-edge feature at 8990 eV (corresponding to the *1s* → *4p* transition). Past the edge, some characteristic peaks are observed at 9010 and 9040 eV. Importantly, the edge position of each X-ray absorption spectrum depends on the oxidation state of the atom. Figure 4.5 A clearly shows the positive shift in edge position with increasing oxidation state (*l* for

copper, *+I* for cuprite and *+II* for tenorite). Although the shape of the coated sample closely follows the oscillations observed in the cuprite reference, some mismatches are observed around the *1s 3d* resonance at 8980 eV and just the past edge around 8990 eV. These are likely due to tenorite and/or copper components in the spectrum already seen in XRD so a linear combination analysis was performed using ATHENA. Figure 4.5 B displays the observed spectrum together with the best fit achieved by a linear combination of the reference spectra. The fit, including the edge shift (*E0*), resulted in a misfit of $\chi^2_v = 0.0000273$. Fitting shows the relative contributions to be $(91.4 \pm 0.1) \%$ Cu_2O and $(8.6 \pm 0.1)\%$ CuO . Although copper reflections were observed in the XRD pattern, copper was omitted from the fit by the software. Combination of this information excludes the possibility of copper being present due to pinholes in the patina. Instead, a continuous cuprite/tenorite layer is present on top of the copper substrate.

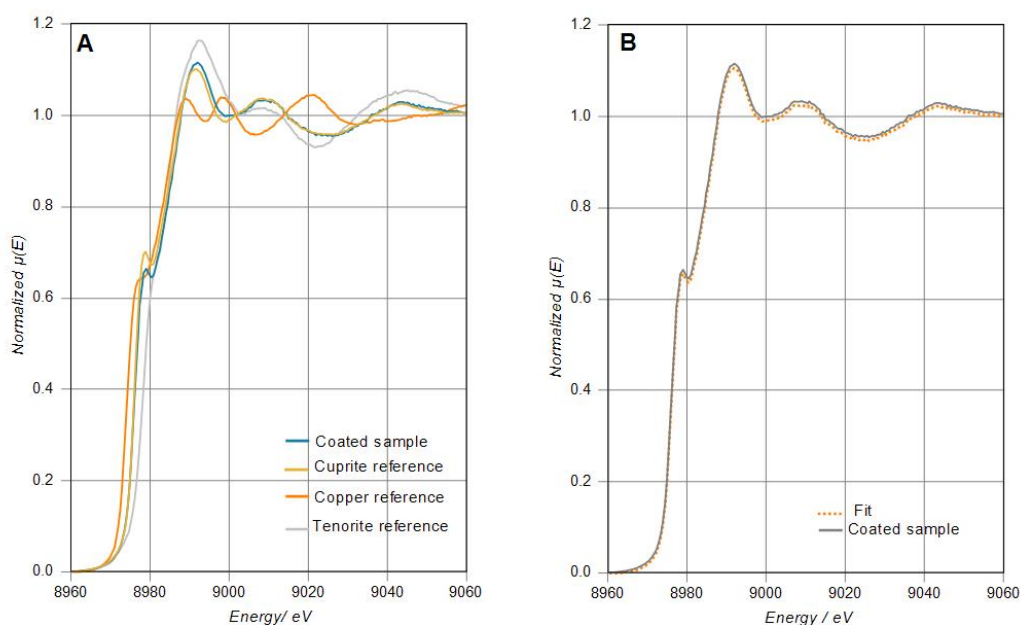


Figure 4.5

[A] X-ray absorption spectra recorded in fluorescence mode of the artificially weathered coupon (blue) together with reference spectra of pure samples of copper, cuprite and tenorite.

[B] X-ray absorption spectra of the grey cuprite coupon and the best fit constructed by linear combination of the cuprite and tenorite reference spectra.

4.2.5 XEOL-XAS ANALYSIS OF GREY CUPRITE

4.2.5.1 Experimental details

XEOL-XAS measurements were simultaneously recorded with the XAS measurements mentioned above. All acquisition parameters are identical. XEOL-XAS spectra were recorded with the Hamamatsu H8259-01 photomultiplier tube (see 3.1.4.1.3). Background (approximately 70 counts/s) was reduced to dark count of the photomultiplier by eliminating all sources of stray light.

The raw XEOL data were processed in esaProject (see 3.2.2). Raw spectra were first normalized to beam monitor to account for variations in primary X-ray beam intensity. Standard normalization techniques were not applied to these spectra, because they distort the XEOL data unacceptably for reasons described in more detail elsewhere [1]. Instead, the complete set of absorption spectra were normalized against the mean value of the post-edge intensity between 8990 and 9060 eV for the most intense spectrum. This left the shape of the spectra unchanged compared with the raw data, and preserved relative changes between the spectra.

4.2.5.2 Results and discussion

Figure 4.6 A shows the XEOL-XANES data from three different cuprite samples: a reference powder, a coupon coated via an electrochemical procedure (see 4.2) and a coupon coated using the protocol described in section 4.2.1. The XEOL emission is likely to be in the range of 350 – 850 nm for Cu_2O as observed in [37]. The photoluminescence spectra recorded by Park et al. of bulk cuprite with a 3.81 eV He-Cd laser at different temperatures between 10 and 300 K are depicted in Figure 4.6 C. At room temperature, bulk cuprite emits in a broad band ranging from 1.5 to 3.5 eV (350 – 850 nm) with dominant oxygen defect peaks at 1.52 and 1.72 eV, accompanied by several weak exciton peaks in the yellow (2.14 eV), green (2.27 eV), blue (2.52 eV) and violet (2.63 eV) portion of the spectrum [38]. The broad range lies wholly inside the spectral response of the detector and the flat transmission band of the window. The optically detected spectra show a clear cuprite fingerprint, consistent with the conventionally detected XAS observations in Figure 4.5 A. Since the spectra arise from the unfiltered broadband optical emission, they are a synthesis of the fluorescence (and phosphorescence) from many excited end-states. The pre-edge signal will arise from indirect optical excitation by Auger electrons released by inefficient L-level ionization and other processes. The relative pre to post edge level will depend on emission from the material itself, as well as any optically emitting contaminants. The electrochemically formed patina has a slightly higher background level (relative to the post-edge signal) compared to the flame produced material, but the reference powder background is still higher. The latter data were measured through an Ultralene® film and optical fluorescence from this has also made a contribution here. Overall, it appears that much of the pre-edge signal is native to

cuprite, with a small amount of that from the electrochemically produced sample being due to residual sodium compounds [1]. Comparing the X-ray fluorescence data with the XEOL-XANES, it is evident that the inter-band $1s\ 3d$ transition occurs at a similar relative height in both spectra with or without a large background contribution. It has already been argued [1] that this demonstrates that the pre-edge background signal arises from emission channels that turn off at the edge. Consequently, other emission channels turn on when the K-level of the Cu-atom is being ionized. Because conventional data processing involves the overall subtraction of the pre-edge level from the data, the near-edge would be irrevocably distorted and the edge step increased [1]. Until suitable data reduction methods have been developed for XEOL-XAS data, no linear combination analysis can be performed on this set of data. Nevertheless, post edge agreement between the X-fluorescence XANES and the XEOL-XANES suggests similar contributions of cuprite and tenorite in the region just below the surface of the sample. A variety of factors can influence the XEOL-XAS intensity and its sampling depth in different samples. Optical transparency of materials is, apart from its morphology, influenced by the prevailing free electron density. Since the free electron density can be drastically increased during X-ray irradiation, the optical transparency of the material might change with respect to its non-irradiated state. X-ray induced conductivity can alter the optical properties of both insulating and conducting materials. Therefore might, even for normally transparent media, the top 200 nm (skin depth at observed optical frequency for conductors) be a good average estimate for the surface specificity of XEOL-XAS during the X-ray analysis [39].

The difference in total optical response originating from the different cuprite samples can be seen in Figure 4.6 B. The difference in intensity between the XEOL-XAS from the different samples (taken under the same conditions) cannot be ascribed to sample thickness because all the samples were thicker than the escape depth of visible photons. The low intensity from the powder, combined with high background may well arise from the presence of the polymer window. We have observed such an effect from a wide variety of optically transparent polymers. It may be that absorption of X-rays excites absorbing states in the windows during the measurements, and the effect is under investigation (see above). The relatively high emission from the flame produced sample compared to the electrochemical one is hard to explain unless the former contains a higher density of excitable optical states (perhaps due to the tenorite component) or the latter contains extra absorbers. Spectral analysis of the XEOL emission itself is an essential accompaniment to the X-ray spectroscopy, but was not available in these experiments due to beam time constraints. Nevertheless, the enhanced optical emission combined with the high cuprite content makes the flame protocol advantageous for the production of reference structures.

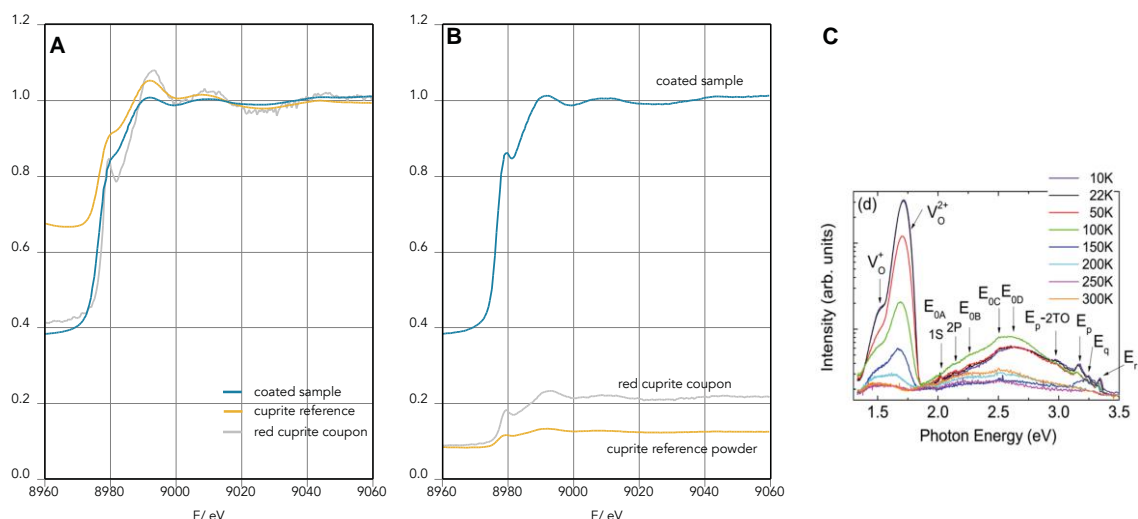


Figure 4.6

[A] XEOL-XANES spectrum of copper treated by: a reducing flame protocol (blue) and an electrochemical method (grey). The XEOL-XANES spectrum of the cuprite reference powder is displayed in orange. All spectra were normalized by the mean post edge value.

[B] XEOL-XANES spectrum of copper coupon treated by: a reducing flame protocol (blue) and an electrochemical method (grey). The XEOL-XAS spectrum of the cuprite reference powder is displayed in orange.

[C] Reproduction of Figure 4 d of [36]. The graph displays the photoluminescence of bulk cuprite upon illumination with a He-Cd laser with excitation energy of 3.81 eV (325 nm) between 10 K and 300 K.

Figure reproduced with permission of copyright clearance center of Journal of Applied Physics (Dec 17, 2017, order number: 4251490507894).

4.2.6 CONCLUSION

A predominantly cuprite patina can be produced on copper by heating in a reducing flame followed by air exposure. The method works for low thermal capacity samples such as TEM grids. Qualitative and quantitative information from the outermost surface to 30 microns below the surface was obtained through XPS, XEOL-XANES, XAS and XRD. XRD analysis identified the presence of cuprite and tenorite with copper also visible, while XAS measurements confirmed the presence of cuprite and tenorite in the top <10 μm of the sample with relative contributions of 91.4 % cuprite and 8.6 % tenorite, and showed that the layer was copper free, confirming that the copper seen in XRD came from the substrate. XPS data showed that the top 3 nm of the patina has a much higher tenorite concentration rising to 100 % in the top 1.5 nm or so. These findings were supported by the XEOL spectra originating in the top < 200 nm of the sample. The intense optical luminescence from this cuprite layer upon X-ray bombardment compared with that from other protocols will be useful for the assessment of XEOM 1 (see Chapter 5) but still requires an explanation.

4.3 TENORITE

Tenorite or cupric oxide, CuO, commonly has a dull black appearance. Tenorite is not often found in natural patinas, since its development in natural corrosion is less favourable than the formation of cuprite. However in the rare case where tenorite is found in non-intentional corrosion crusts, its presence is indicative of heating or firing treatments to the mother-object prior to (or during) burial [2].

4.3.1 PROTOCOL

Because of the black/greyish appearance of the patina grown by the reducing flame protocol, it was initially regarded as tenorite. Since we now know this corroded coating consists for 91.4 % of cuprite, a novel method to create tenorite had to be explored. CuO has been described in the past as a promising semiconductor for solar cell fabrication [40]. Consequently various approaches to produce pure, thin CuO layers on different substrates have been published in a variety of material science oriented journals. The general method to produce tenorite coatings involves the deposition of copper or copper analogues on substrates with subsequent heat treatment to convert into cupric oxide. Literature mentions, among others, mostly the use of: sol-gel methods [40], thermal evaporation [17, 41], chemical deposition [42–45], electrodeposition [46] or reactive sputtering [47] on glass or silica substrates. Subsequent heat treatment vary from applied atmosphere: 100% O₂ [17], 10 %- 90% mixture of O₂ and N₂ [41] or air [17, 40, 42, 44, 45] and applied temperature programs. Literature generally agrees that Cu oxidizes to principally CuO when the temperature exceeds 350 °C [20, 41, 42, 44].

Since the coupon substrate consists of 99.99 % pure Cu, the initial copper depositions steps described above are superfluous and only the thermal oxidation step is of importance. As a result of the literature survey and experimentation with different temperatures, the best results were obtained when a clean, degreased copper coupon was subjected to 450°C for 5 hours and a subsequent linear cooling program for 2 hours to prevent stress cracking of the superficial layer. Oxidation occurred in an air filled tube furnace (Heraeus, Hanau, Germany).

4.3.2 XEOL-XAS OF TENORITE

Figure 4.7 displays the XAS and unfiltered XEOL-XAS spectra acquired simultaneously from a tenorite layer grown as described above. Data were collected during beamtime II (Table 3.6) across the Cu *K*-edge in the range of 8960 – 9040 eV with an energy resolution of 1 eV and an acquisition time of 1 s per data point. Data were gently smoothed using Gaussian convolution and put on a comparable scale using the normalization procedure described above.

One can clearly recognize the surface specificity of XEOL-XAS with respect to its fluorescent complement in Figure 4.7. The contrasting spectral features of the XAS and XEOL-XAS data suggest the presence of a near-surface stratigraphy containing different compounds. The principal features observed in the XAS data are distinctive cuprite features: an inter-band transition on the edge around 8980 eV from a $1s \rightarrow 3d$ resonance [48, 49]; a single post-edge feature around 8990 eV as a result of the enhanced absorption due to promotion of $1s$ core electrons to vacant $4p$ sites [48, 49]. Further downstream of the edge broad peaks can be observed around 9010 eV and 9040 eV. On the contrary, no distinct mid-edge feature at 8980 eV is seen in the XEOL-XAS data. As this feature is typical of Cu(I)-compounds and, additionally, a positive energy shift of approximately 5 eV is observed; the evidence for conversion to tenorite is provided. Moreover, Kau et al. [48] claims Cu(II)-compounds possess weak features at 8979 eV, as a result of a $1s \rightarrow 3d$ transition, and a more intense transition around 8986 eV, possibly due to $1s \rightarrow 4s$ or the $1s \rightarrow 4p$ transition. Although the 8979 eV feature might be evidence for the remains of traces of cuprite, both features are observed in the XEOL-XAS spectrum on Figure 4.7. Therefore, concluding that bulk cuprite is covered with a surface layer of mainly tenorite is justified.

Considering the absorption length of 9 keV X-rays in copper, the XAS spectra provide information from $< 10 \mu\text{m}$ depth in the investigated sample. Conversely, XEOL-XAS typically provides information of the top 200 nm. As described in literature [41, 42] oxidation of copper is a two stage process in which Cu_2O is principally formed at temperatures $< 350^\circ\text{C}$. At more elevated temperatures ($>375^\circ\text{C}$) annealing of the present Cu_2O takes place and recrystallizes into CuO . The stratigraphy observed by both XAS and XEOL-XAS spectra, demonstrates this phenomenon where the outer regions of the coupon possessed sufficient thermal energy to be converted into CuO . However the underlying copper could not be heated substantially to be converted into CuO , plentiful thermal energy was present to oxidize the copper into Cu_2O .

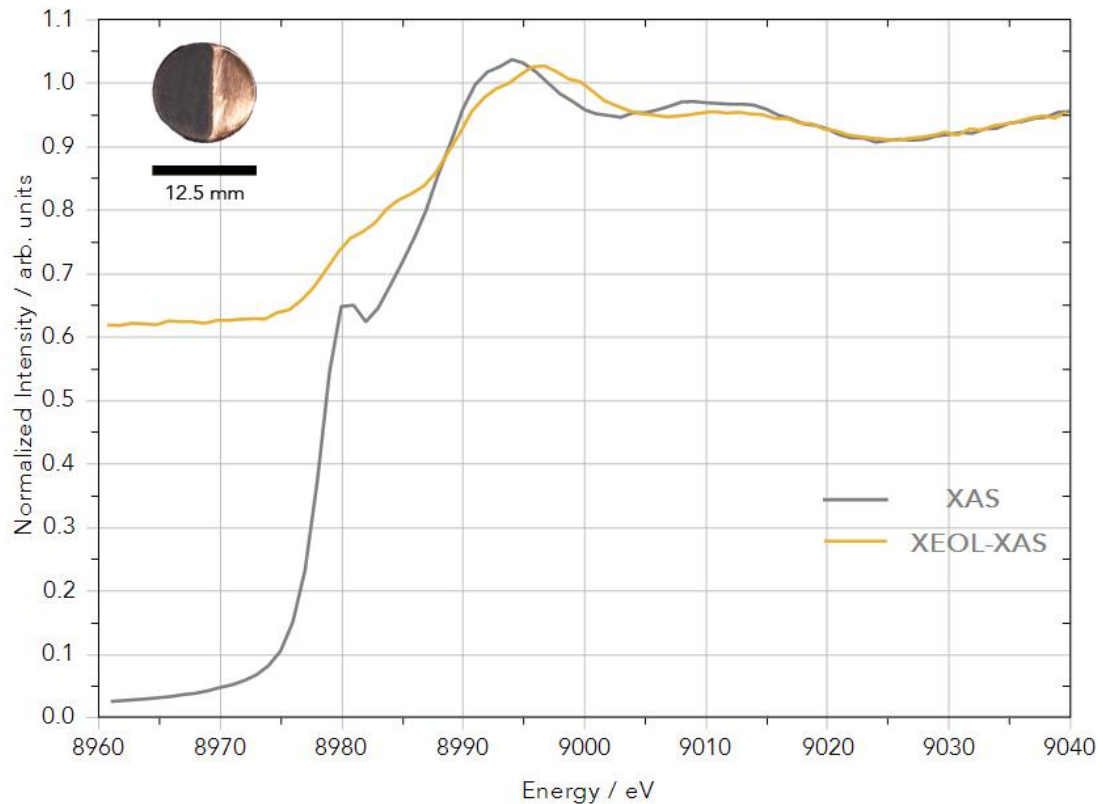


Figure 4.7

Parallel XAS and XEOL-XAS collected spectra from a copper coupon coated with a tenorite layer. In the upper left corner an image is given of a coupon coated with CuO. Part of the coating was removed to display the contrast with the bare Cu substrate.

4.4 NANTOKITE

Nantokite or cuprous chloride, CuCl , is one of the primary active corrosion agents that forms on copper and its alloys. Nantokite is a naturally occurring, pale grey to light green mineral with low solubility in water [50]. Nantokite is typically associated with objects recovered from marine environments but can also be identified on copper/bronze artefacts buried in soil [2, 51]. Although the nantokite layer can be stable for years when buried or immersed, once anaerobic conditions are lost due to excavation, the nantokite layer starts to deteriorate progressively [52]. Nantokite is unstable in air and reacts with oxygen and water vapor to form copper trihydroxychlorides (e.g. atacamite and paratacamite, see below) and hydrochloric acid [51, 53]. Visually this results in the formation of bright green, powdery spots (copper trihydroxychlorides) accompanied by stress cracking of the surface due to volume change and subsequent deeper penetration of chlorides into the metal [54, 55]. This condition is better known as ‘bronze disease’ and can be most troublesome

for the long-term stability of the copper/bronze object. In [55], we have shown that the progression of bronze disease is dependent on the environmental condition upon excavation. In oxygen rich environments, nantokite preferably converts into paratacamite as described above whereas moist environments (excess of water) nantokite hydrolyses into cuprite. Soaking in water (or better a sodium sesquicarbonate solution) is accordingly one of the possible mitigation strategies to tackle bronze disease and convert the cuprous chloride into the more passivating cuprite.

4.4.1 PROTOCOL

Initially the protocol of Lamy [18] was adopted to produce artificial nantokite layers on copper coupons and meshes. According to this protocol, samples were covered with nantokite by immersing the coupon for 60 minutes in a saturated $\text{CuCl}_2 \cdot 2\text{H}_2\text{O}$ solution (VWR International, USA). After removal of the solution, the samples were rinsed with deionised water and exposed to the atmosphere overnight. Although simplicity argues in favour of this protocol, problems were encountered with the purity of the produced patina. The protocol was replaced with the procedure suggested by R.B. Faltermeier [56].

In line with the protocol of Faltermeier, polished copper coupons are degreased in an ultrasonic bath using acetone for 10 minutes, followed by 5 minutes of drying under an infrared lamp (approx. 50 °C) and 10 minutes of drying in a silica buffered desiccator. Subsequently, the coupons are immersed in 25 mL of a 1 M CuCl_2 solution (copper (II) chloride, 97 %, Sigma-Aldrich, Saint Louis, Missouri, USA) for 24 hours. Afterwards, all samples are rinsed three times and once with ethanol. The rinsed samples are then dried for 5 minutes under the infrared lamp and stored in an oven for 30 minutes at 105 °C to ultimately cool down for 10 minutes in a desiccator. When the coating was applied on a microgrid substrate, the immersion time of the grid into the CuCl_2 solution was reduced to 1 hour.

Figure 4.8 displays the X-ray diffraction pattern of a copper coupon treated as reported by Faltermeier. All reflections were scaled relative to the most intense reflection (Cu 200 at 3.4 \AA^{-1}) and the square root plot is used to emphasize minor reflections. All reflections observed belong to copper and to nantokite. The sample was not immediately prepared before analysing hence the oxygen and water vapour of the atmosphere already converted small portions of the nantokite into cuprite or paratacamite.

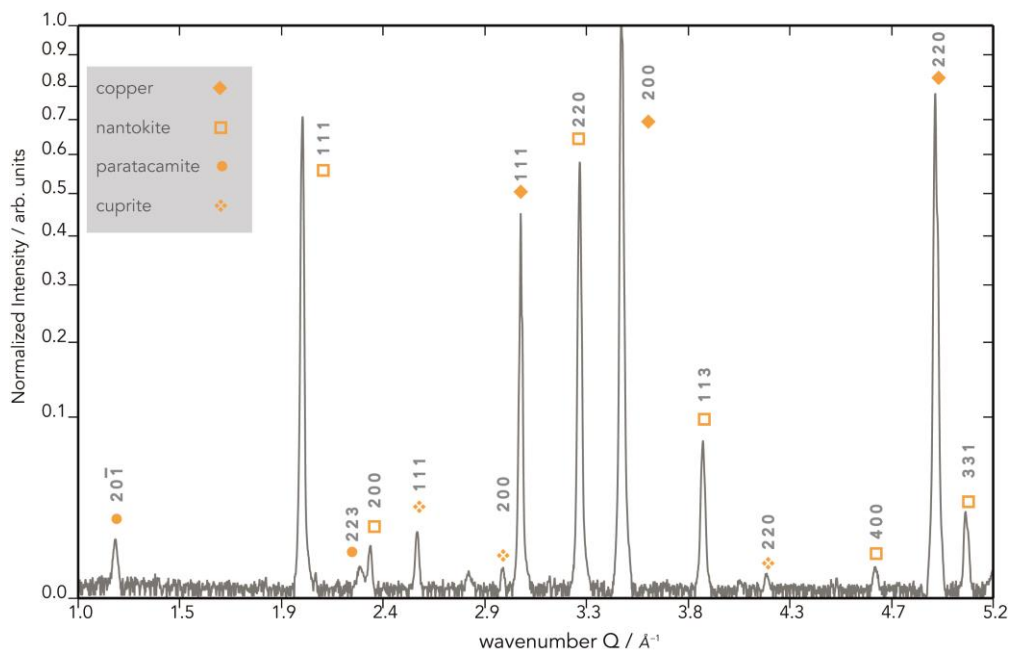


Figure 4.8

X-ray diffraction pattern recorded from a copper coupon treated with the nantokite producing protocol of Faltermeier et al. [53]. The square root scale of the ordinate axis emphasises minor reflections. Reference patterns used for peak assignment can be found in A.2 and A.3.

4.4.2 XEOL-XAS OF NANTOKITE

Figure 4.9 displays the XAS and unfiltered XEOL-XAS spectra collected in parallel from a sufficiently thick nantokite layer on a copper coupon produced according to the Faltermeier protocol [56]. The measurement was carried within an hour following the production of the patina, to minimize formation of cuprite and/or paratacamite. Data points were collected during beamtime X (Table 3.6) across the Cu *K*-edge in the range of 8883 – 9053 eV with an energy resolution of 1 eV and a dwell time of 1 s per data point. As a result of a two stage normalization procedure described above for copper (see 4.1.3), both data sets were put on a comparable scale.

The XAS fingerprint of the coupon is entirely characteristic of nantokite when compared with the XAS data of reference powders on Figure 4.10. In particular, a characteristic ‘white line’ at 8986 eV as a result of the $1s \rightarrow 4p$ intra-atomic transition in Cu(I) compounds is evidential for nantokite [48, 49, 57]. An edge-shift of nantokite, a Cu(I) compound, towards higher energy with respect to Cu (approximately 2 eV) agrees with the expected behavior of increasing edge energy for a higher oxidation state of the metal ion. The XEOL-XAS spectrum of the nantokite layer displays a higher pre-edge background compared to the XAS spectrum, an observance in unison with previously discussed XEOL-XAS spectra. Although the white line is preserved on the edge, the post-edge oscillations are less pronounced with

reference to the spectra recorded in fluorescence mode. Flattened oscillations or distorted amplitudes in X-ray absorption spectroscopy are often attributed to self-absorption effects [58]. However in this particular case, one might attribute the increased absorption in the 8990 – 9000 eV region to the emerging presence of either cuprite and paratacamite in the superficial layer. The features in the reference spectra of cuprite and paratacamite (Figure 4.10) around 8995 and 9050 eV indeed agree with the aberrant behavior of the XEOL-XANES fingerprint of nantokite with respect to its fluorescence counterpart.

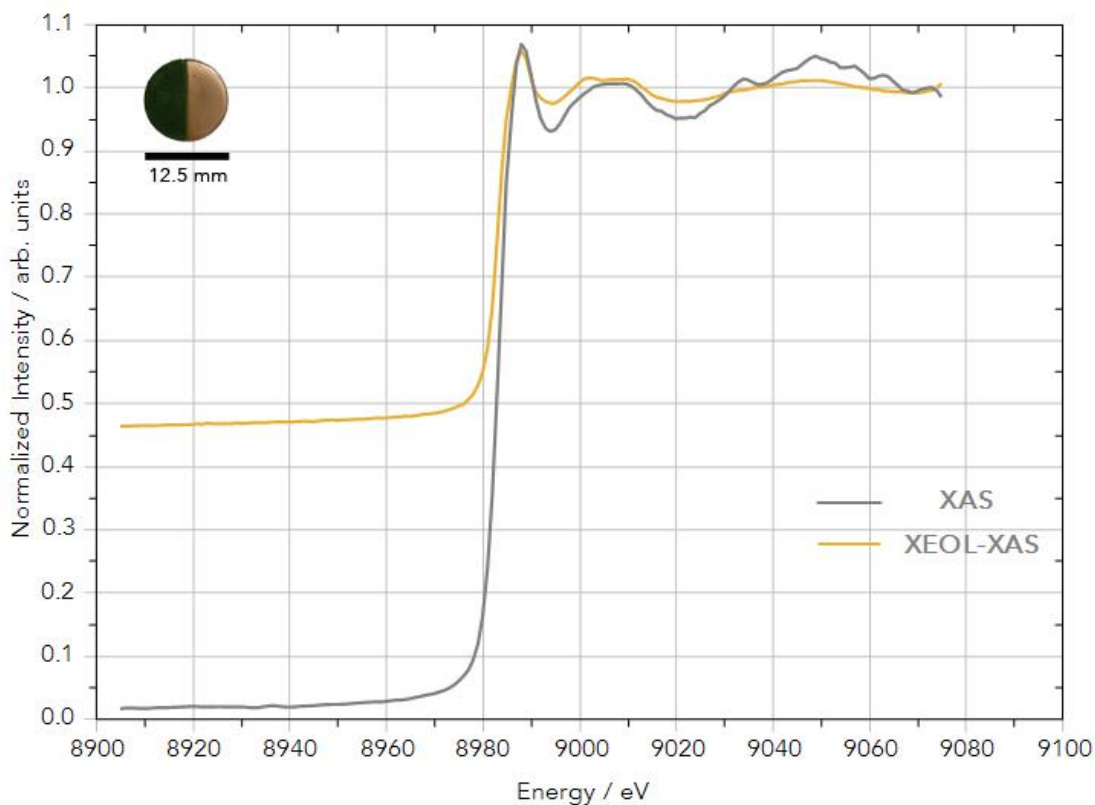


Figure 4.9

Parallel XAS and XEOL-XAS collected spectra from a copper coupon coated with a nantokite layer according to the procedure suggested by Faltermeier et al. [53]. In the upper left corner an image is given of a coupon coated with CuCl. Part of the coating was removed to display the contrast with the bare Cu substrate.

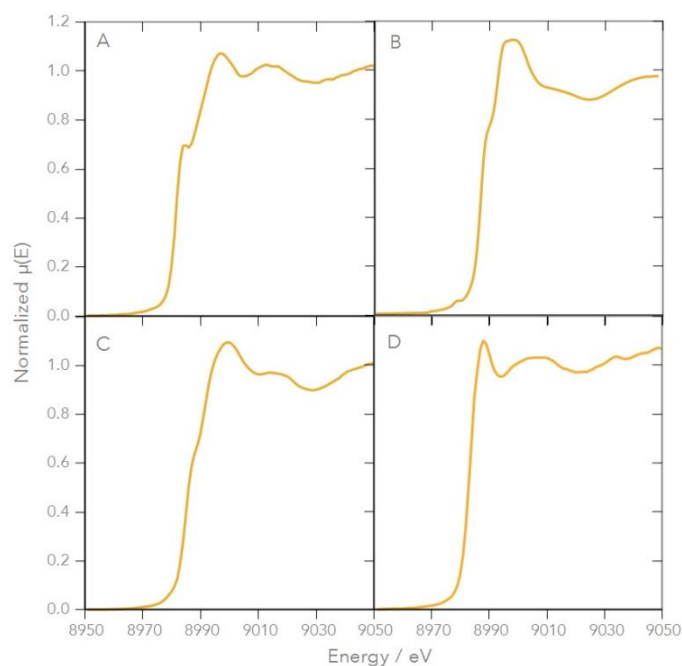


Figure 4.10

Reference spectra from four reference powders in X-ray fluorescence mode: [A] cuprite , [B] paratacamite , [C] tenorite , and [D] nantokite. All spectra were normalized with ATHENA [34] by standard XAS normalization procedures and plotted as normalized $\mu(E)$.

4.5 PARATACAMITE AND ATACAMITE

Atacamite and paratacamite are the most common isomers of copper trihydroxychlorides (sometimes referred to as basic copper chlorides) with molecular formula $\text{Cu}_2\text{Cl}(\text{OH})_3$. Paratacamite occurs as a light green compound on the surface patina of a corroded artefacts and is generally secondary to other substances in the patina, e.g. cuprite. Atacamite is, instead of a continuous coating, mostly observed as a set of dark green patches of glistening crystals [2]. Both isomers are generally found on outdoor bronzes which were moderately affected by rain, i.e. chloride content could accumulate sufficiently without being washed away [51]. Alternatively, as described above, paratacamite might be the result of the oxidation and hydrolysis of nantokite [53]. Their presence is indicative of active corrosion taking place and a signal that conservation treatments, e.g. storage of the object in tap water or dilute sodium sesquicarbonate, are needed [6].

4.5.1 PROTOCOL

The protocol initially used was described by Lamy [18] in 1997. The procedure uses a method in which a solution 10.02 g of $\text{Cu}_2(\text{NO}_3)_2 \cdot 3\text{H}_2\text{O}$ and 10.02 g of NaCl in 100

mL deionized water is prepared and copper coupon are wetted twice a day, for five days, with this solution. Leysens et al. [59] concluded that the patina produced by this protocol is a mixture of both atacamite and paratacamite and NaNO_3 impurities .

In an attempt to produce a patina containing majorly paratacamite, the approach of Faltermeier [56] was pursued. The method builds further on his nantokite recipe, but with an additional step in which the nantokite-coated coupon is held in an environment of high relative humidity (approx. 100 %) for 24 hours. This environment was created in a desiccator buffered with wet K_2SO_4 . Figure 4.11 displays the X-ray diffraction pattern of a copper coupon which has undergone this treatment. All reflections were scaled relative to the most intense reflection (paratacamite 021 and atacamite 011) which has been normalized to 1. All reflections could be assigned to either paratacamite, atacamite, nantokite and copper.

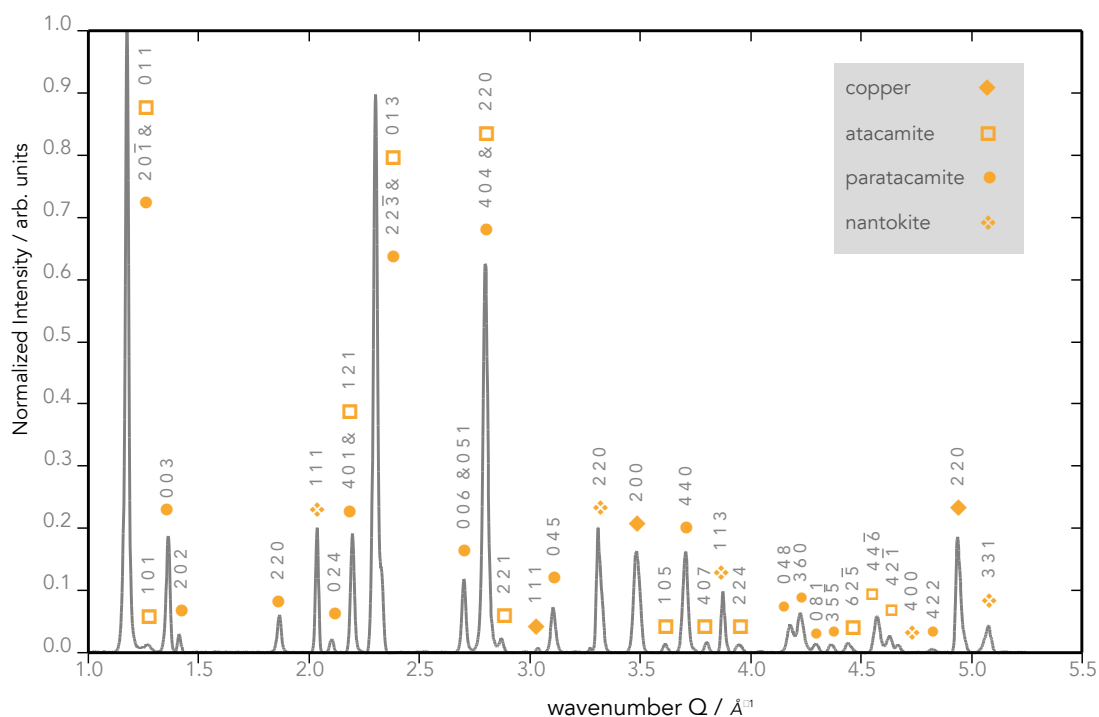


Figure 4.11

X-ray diffraction pattern recorded from a copper coupon treated with the paratacamite producing protocol of Faltermeier et al. [53]. Reference patterns used for peak assignment can be found in A.2 and A.3.

Although the crystal structure of paratacamite (rhombohedral) is different to atacamite (orthorhombic), many reference reflections of both isomers coincide which makes qualitative analysis difficult. Unique reference features for paratacamite can be encountered at 1.36 \AA^{-1} for the 003 reflection and the 006 and 051 reflections around 2.71 \AA^{-1} . Figure 4.11 confirms the presence of these reflections. Furthermore, atacamite can be uniquely defined at 1.26 \AA^{-1} for the 101 reflection and at 1.54 \AA^{-1} ,

1.96 Å⁻¹ and 2.51 Å⁻¹ for respectively the 111, 112 and 202 reflections. Only for the 101 plane of atacamite, a weak reflection can be observed whereas for the other planes no reflections are visible in the diffraction pattern. It is only fair to conclude from this that the coating consists mainly of paratacamite.

4.5.2 XEOL-XAS OF COPPER HYDROXYCHLORIDES

Figure 4.12 displays the XAS and unfiltered XEOL-XAS spectra collected in parallel from a paratacamite (atacamite) layer on a copper coupon produced according to the Faltermeier protocol [56]. Data points were collected during beamtime III (Table 3.6) across the Cu *K*-edge in the range of 8910 – 9070 eV with an energy resolution of 1 eV and a dwell time of 3 s per data point. Although the XEOL-XAS spectrum is not completely free of noise, no smoothing procedures were applied on the data to conserve the spectral features. Both post-edge regions were normalized to one to place spectra on a comparable scale.

The XAS spectrum for the paratacamite layer on a copper coupon is entirely characteristic of paratacamite, when compared with the spectra for the reference powder on Figure 4.10. Due to the thickness of the layer, estimated around a few hundreds of micrometers, no measureable contributions of the underlying copper are observed in the XAS spectrum. The literature available on the analysis of copper hydroxychlorides by X-ray absorption spectroscopy over the Cu *K*-edge is restricted to the data published by our groups [1, 6, 8]. These report the high similarity between the absorption spectra (both optical and fluorescence) of paratacamite and atacamite, which is not completely unexpected due to traces of atacamite in the patina as a result of the protocol (confirmed by the XRD) and the similar coordination of the Cu in both isomers [8]. Hence it is a very difficult task to decide whether atacamite or paratacamite is being looked at solely by investigating the XANES fingerprint and EXAFS analysis might be required. Nevertheless a mixture of copper hydroxychlorides may be uniquely identified from other copper corrosion products. The XANES fingerprint is defined by a weak pre-edge and mid-edge features at 8979 and 8989 eV and a broad indicative white line on the edge around 8992 – 8995 eV. These features can be observed in both the XAS and XEOL-XAS data on Figure 4.12, even though the post-edge features of the XEOL-XAS data are slightly suppressed. The trend in which higher pre-edge signal is observed for optically detected spectra with reference to the fluorescence equivalent is confirmed. However, upon comparing the relative proportions of features native to the XEOL-XAS and XAS spectra of paratacamite, it can be concluded that the background luminescence is partly additive in the XEOL-XAS data. This becomes clear as certain features on the edge, e.g. the faint mid-edge feature at 8980 eV, shift upwards in intensity in the XEOL-XAS data with respect to the XAS data. A phenomenon which

was observed differently in (e.g.) copper where the background in the pre-edge was completely the result of copper-related radiative processes. Moreover, elsewhere [1], the supervisors of this work have shown that a wavelength shift of optical luminescence occurs when the Cu *K*-edge is crossed. The inset in Figure 4.12 displays a reproduction of Figure 5 of the paper published by the supervisors of this work in Analytical Chemistry [1]. The inset displays the result of successive scans recorded from a copper coupon coated with a mixture of paratacamite/atacamite through a red, green and blue optical filter. By optical filtering of the XEOL, it can be concluded that the pre-edge region and white line are predominantly green but when the Cu *K*-edge is exceeded, a wavelength shift from green to blue takes place.

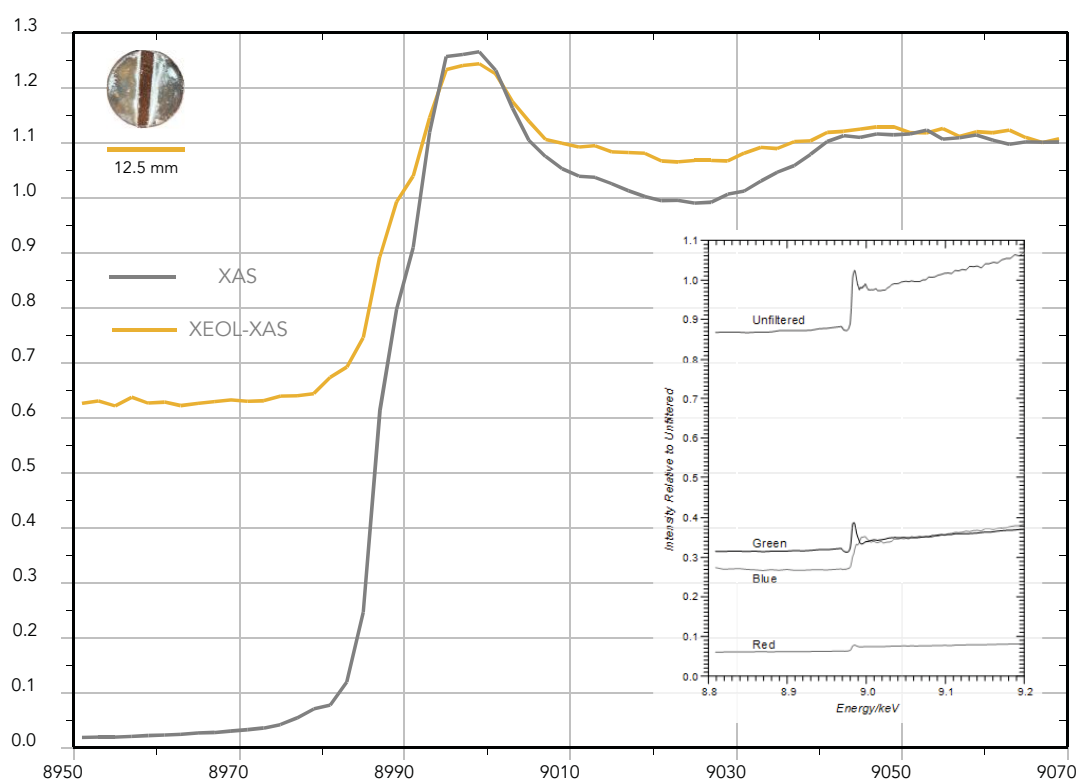


Figure 4.12

Parallel XAS and XEOL-XAS collected spectra from a copper coupon coated with a paratacamite according to the procedure suggested by Faltermeier et al. [53]. In the upper left corner an image is given of a coupon coated with nantokite which was subsequently immersed in a high humidity atmosphere. The brighter green areas of the coupon are paratacamite while the darker green areas display the remains of nantokite. Part of the coating was removed to display the contrast with the bare Cu substrate.

The inset is a reproduction of Figure 5 published in Analytical Chemistry [1] with permission of Dr. Darla Henderson (Assistant Director of Open Access Program of the American Chemical Society). The inset displays the XEOL-XANES data recorded from a copper coupon coated with a mixture of atacamite and paratacamite through a red, green and blue bandpass filters using an X-ray beam with a large footprint. A significant increase in blue emission postedge is observed.

4.6 CONCLUSIONS

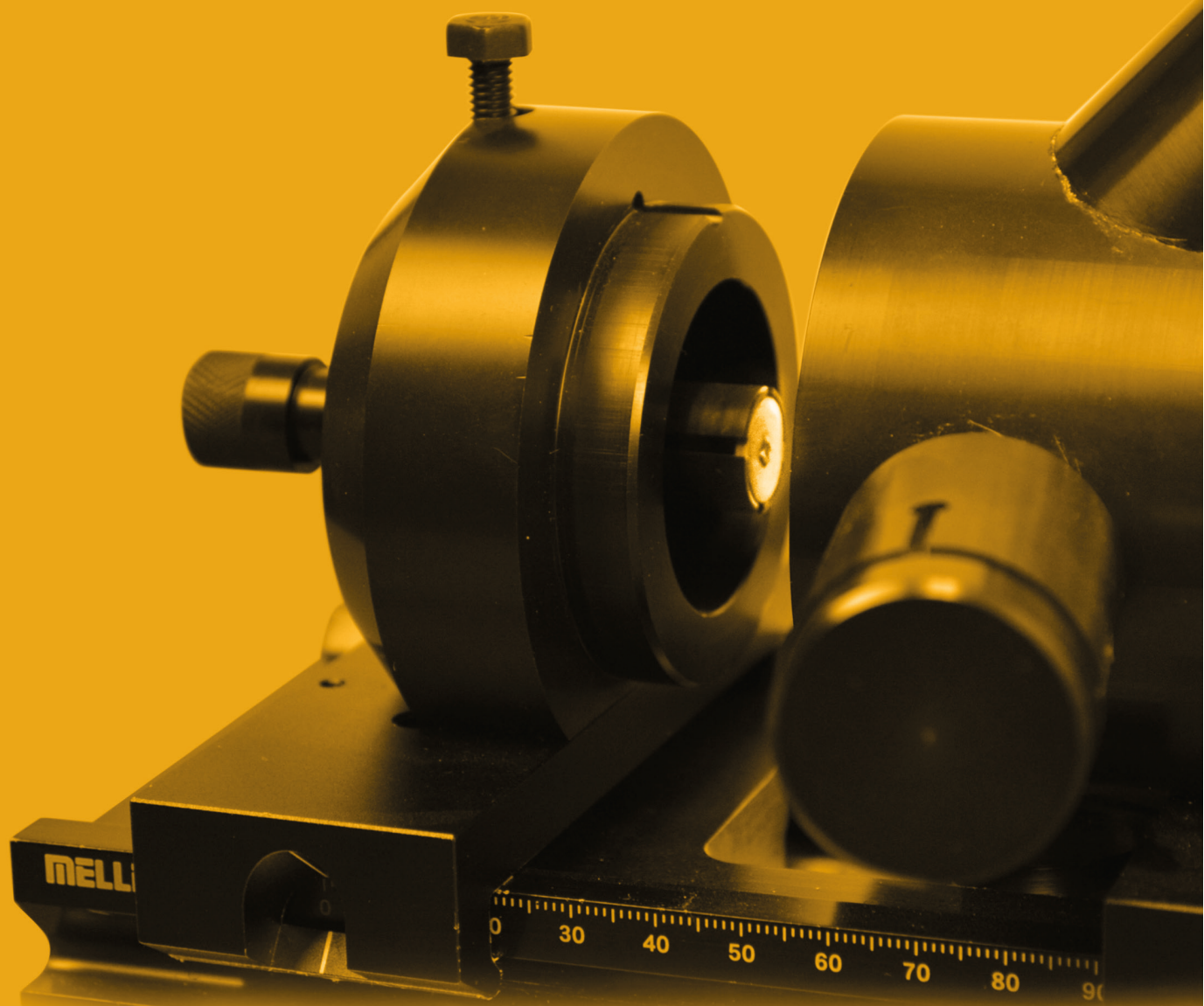
This chapter describes the production and characterization of artificially corroded copper samples necessary for evaluating the imaging and spectroscopic features of XEOM 1. An overview is given of different protocols necessary for producing artificial corrosion coatings on different copper substrates. The use of a patinated copper grid providing a mesh on the micrometre scale (used as a sample holder in transmission electron microscopy) in combination with a flat copper coupons was suggested to assess the lateral and chemical resolution of XEOM 1. In order to gain as much *a priori* knowledge as possible, the product of each protocol was evaluated with either XRD, XAS, XEOL-XAS and XPS or a combination hereof. Where necessary, e.g. due to incompatibility of the protocol with a fragile copper substrate like a microgrid or issues with regard to coating purity, alternative approaches were sought and evaluated. Additionally, the XEOL-XAS spectra of these compounds were discussed in more detail as this is the final product of a XEOM experiment. Cuprite, tenorite, nantokite, paratacamite/atacamite are commonly found on recovered copper, bronze and/or brass artefacts of significant cultural heritage relevance. Apart from this introductory field of application, the relevance of this study and the scope of XEOM 1 can be expanded towards semi-conductor research as pure cuprite and tenorite are of growing importance in solar cell industry [15, 60].

4.7 BIBLIOGRAPHY

- [1] A. Adriaens, P. Quinn, S. Nikitenko, M.G. Dowsett, Real Time Observation of X-ray-Induced Surface Modification Using Simultaneous XANES and XEOL-XANES., *Anal. Chem.* 85 (2013) 9556–9563.
- [2] D.A. Scott, *Copper and Bronze in Art: corrosion, colorants, conservation*, The Getty conservation institute : Los Angeles, 2002.
- [3] P.-J. Sabbe, M.G. Dowsett, M. De Keersmaecker, M. Hand, P. Thompson, A. Adriaens, Synthesis and surface characterization of a patterned cuprite sample: Preparatory step in the evaluation scheme of an X-ray-excited optical microscopy system, *Appl. Surf. Sci.* 332 (2015) 657–664.
- [4] R. Beatty, *Copper*, Benchmark Books, 2001.
- [5] J.R. Davis, A.S.M.I.H. Committee, *Copper and Copper Alloys*, ASM International, 2001.
- [6] A. Adriaens, M. Dowsett, G. Jones, K. Leyssens, S. Nikitenko, An in-situ X-ray absorption spectroelectrochemistry study of the response of artificial chloride corrosion layers on copper to remedial treatment, *J. Anal. At. Spectrom.* 24 (2009) 62–68.
- [7] G.N. Greaves, P. Durham, G. Diakun, P. Quinn, Near-edge X-ray absorption spectra for metallic Cu and Mn, *Lett. To Nat.* 294 (1981) 139–142.
- [8] M.G. Dowsett, A. Adriaens, G.K.C. Jones, N. Poolton, S. Fiddy, Optically Detected X-ray Absorption Spectroscopy Measurements as a Means of Monitoring Corrosion Layers on Copper, *Anal. Chem.* 80 (2008) 8717–8724.
- [9] T. Stambolov, *The Corrosion and Conservation of Metallic Antiquities and Works of Art*, , Central Laboratory for Objects of Art and Science, Amsterdam, 1985.
- [10] R. Lobnig, J.D. Sinclair, M. Unger, M. Stratmann, Mechanism of Atmospheric Corrosion of Copper in the Presence of Ammonium Sulfate Particles, *J. Electrochem. Soc.* 150 (2003) A835.
- [11] C. Leygraf, in: *Corrosion mechanisms in Theory and Practice*, New York, 1955, pp. 421–455.

- [12] K. Leysens, A. Adriaens, C. Degriigny, E. Pantos, Evaluation of corrosion potential measurements as a means to monitor the storage and stabilization processes of archaeological copper-based artifacts., *Anal. Chem.* 78 (2006) 2794–801.
- [13] K. Marušić, H. Otmačić-Ćurković, Š. Horvat-Kurbegović, H. Takenouti, E. Stupnišek-Lisac, Comparative studies of chemical and electrochemical preparation of artificial bronze patinas and their protection by corrosion inhibitor, *Electrochim. Acta* 54 (2009) 7106–7113.
- [14] M. Than Htay, M. Okamura, R. Yoshizawa, Y. Hashimoto, K. Ito, Synthesis of a cuprite thin film by oxidation of a Cu metal precursor utilizing ultrasonically generated water vapor, *Thin Solid Films* 556 (2014) 211–215.
- [15] K. Akimoto, S. Ishizuka, M. Yanagita, Y. Nawa, G.K. Paul, T. Sakurai, Thin film deposition of Cu₂O and application for solar cells, *Sol. Energy* 80 (2006) 715–722.
- [16] W. Seiler, E. Millon, J. Perrière, R. Benzerga, C. Boulmer-Leborgne, Epitaxial growth of copper oxide films by reactive cross-beam pulsed-laser deposition, *J. Cryst. Growth* 311 (2009) 3352–3358.
- [17] A.H. Jayatissa, K. Guo, A.C. Jayasuriya, Fabrication of cuprous and cupric oxide thin films by heat treatment, *Appl. Surf. Sci.* 255 (2009) 9474–9479.
- [18] C. Lamy, *Stabilisation d'Objets Archeologiques Chlorure's en Alliage Cuivreux*, Nantes, 1997.
- [19] F. Mathis, J. Salomon, S. Pagès - Camagna, M. Dubus, D. Robcis, M. Aucouturier, S. Descamps, E. Delange, in: *European Federation of Corrosion (EFC) Series*, Woodhead Publishing, 2007, pp. 219–238.
- [20] K.P. FitzGerald, J. Nairn, G. Skennerton, a. Atrens, Atmospheric corrosion of copper and the colour, structure and composition of natural patinas on copper, *Corros. Sci.* 48 (2006) 2480–2509.
- [21] F. Mathis, E. Delange, D. Robcis, M. Aucouturier, HMTY-KM (black copper) and the Egyptian bronzes' collection of the Musée du Louvre, *J. Cult. Herit.* 10 (2009) 63–72.
- [22] A. V Chichagov, D.A. Varlamov, R.A. Dilanyan, T.N. Dokina, N.A. Drozhzhina, O.L. Samokhvalova, T. V Ushakovskaya, MINCRYST: a crystallographic database for minerals, local and network (WWW) versions, *Crystallogr. Reports* 46 (2001) 876–879.
- [23] MinCryst [online] Available: <http://database.iem.ac.ru/mincryst/index.php>, [accessed june 2014].
- [24] R. Haugsrud, The Influence of Water Vapor on the Oxidation of Copper at Intermediate Temperatures, *J. Electrochem. Soc.* 149 (2002) B14.
- [25] Y. Zhu, K. Mimura, J. Lim, M. Isshiki, Q. Jiang, Brief Review of Oxidation Kinetics of Copper at 350 ° C to 1050 ° C, *Metall. Mater. Trans. A* 37 (2006) 1231–1237.
- [26] J.-P. Wang, W.D. Cho, Oxidation Behavior of Pure Copper in Oxygen and/or Water Vapor at Intermediate Temperature, *ISIJ Int.* 49 (2009) 1926–1931.
- [27] Y. Wan, X. Wang, H. Sun, Y. Li, K. Zhang, Y. Wu, Corrosion Behavior of Copper at Elevated Temperature, *Int. J. Electrochem. Sci.* 7 (2012) 7902–7914.
- [28] T. Robert, M. Bartel, G. Offergeld, Characterization of oxygen species adsorbed on copper and nickel oxides by X-ray photoelectron spectroscopy, *Surf. Sci.* 33 (1972) 123–130.
- [29] C.J. Powell, a. Jablonski, Electron effective attenuation lengths for applications in Auger electron spectroscopy and x-ray photoelectron spectroscopy, *Surf. Interface Anal.* 33 (2002) 211–229.
- [30] V. Hayez, a. Franquet, a. Hubin, H. Terryn, XPS study of the atmospheric corrosion of copper alloys of archaeological interest, *Surf. Interface Anal.* 36 (2004) 876–879.
- [31] S.K. Chawla, N. Sankarraman, J.H. Payer, Diagnostic spectra for XPS analysis of Cu-O-S-H compounds, *J. Electron Spectros. Relat. Phenomena* 61 (1992) 1–18.
- [32] N.S. McIntyre, S. Sunder, D.W. Shoesmith, F.W. Stanchell, Chemical information from XPS-application to the analysis of electrode surfaces, *J. Vac. Sci. Technol.* 18 (1981) 714–721.
- [33] A.V. Naumkin, A. Kraut-Vass, S.W. Gaarenstroom, C.J. Powell, NIST X-ray Photoelectron Spectroscopy Database, [accessed online june 2014].
- [34] M.C. Biesinger, L.W.M. Lau, A.R. Gerson, R.S.C. Smart, Resolving surface chemical states in XPS analysis of first row transition metals, oxides and hydroxides: Sc, Ti, V, Cu and Zn, *Appl. Surf. Sci.* 257 (2010) 887–898.
- [35] B. Ravel, M. Newville, ATHENA, ARTEMIS, HEPHAESTUS: data analysis for X-ray absorption spectroscopy using IFEFFIT., *J. Synchrotron Radiat.* 12 (2005) 537–41.
- [36] B. Ravel, A practical introduction to multiple scattering theory, *J. Alloys Compd.* 20 (2005) 118–126.

- [37] J.-W. Park, H. Jang, S. Kim, S.-H. Choi, H. Lee, J. Kang, S.-H. Wei, Microstructure, optical property, and electronic band structure of cuprous oxide thin films, *J. Appl. Phys.* 110 (2011).
- [38] J.-W. Park, H. Jang, S. Kim, S.-H. Choi, H. Lee, J. Kang, S.-H. Wei, Microstructure, optical property, and electronic band structure of cuprous oxide thin films, *J. Appl. Phys.* 110 (2011) 103503–1 – 103503–7.
- [39] M. Dowsett, M. Hand, P.-J. Sabbe, P. Thompson, A. Adriaens, XEOM 1 - A novel microscopy system for the chemical imaging of heritage metal surfaces, *Herit. Sci.* 3 (2015) 14.
- [40] A.Y. Oral, E. Menşur, M.H. Aslan, E. Başaran, The preparation of copper(II) oxide thin films and the study of their microstructures and optical properties, *Mater. Chem. Phys.* 83 (2004) 140–144.
- [41] G. Papadimitropoulos, N. Vourdas, V.E. Vamvakas, D. Davazoglou, Optical and structural properties of copper oxide thin films grown by oxidation of metal layers, *Thin Solid Films* 515 (2006) 2428–2432.
- [42] J. Medina-Valtierra, S. Calixto, F. Ruiz, Formation of copper oxide films on fiberglass by adsorption and reaction of cuprous ions, *Thin Solid Films* 460 (2004) 58–61.
- [43] T. Maruyama, Copper Oxide Thin Films Prepared from Copper Dipivaloylmethanate and Oxygen by Chemical Vapor Deposition, *Jpn. J. Appl. Phys.* 37 (1998) 4099.
- [44] N. Serin, T. Serin, S. Horzum, Y. Çelik, Annealing effects on the properties of copper oxide thin films prepared by chemical deposition, *Semicond. Sci. Technol.* 20 (2005) 398–401.
- [45] M.T.S. Nair, L. Guerrero, O.L. Arenas, P.K. Nair, Chemically deposited copper oxide thin films: structural, optical and electrical characteristics, *Appl. Surf. Sci.* 150 (1999) 143–151.
- [46] Y.C. Zhou, J.A. Switzer, Galvanostatic electrodeposition and microstructure of copper (I) oxide film, *Mater. Res. Innov.* 2 (1998) 22–27.
- [47] V.F. Drobny, L. Pulfrey, Properties of reactively-sputtered copper oxide thin films, *Thin Solid Films* 61 (1979) 89–98.
- [48] L. Kau, D.J. Spira-Solomon, J.E. Penner-Hahn, K.O. Hodgson, E.I. Solomon, X-ray absorption edge determination of the oxidation state and coordination number of copper. Application to the type 3 site in *Rhus vernicifera* laccase and its reaction, *J. Am. Chem. Soc.* 109 (1987) 6433–6442.
- [49] J. Brugger, B. Etschmann, W. Liu, D. Testemale, J.L. Hazemann, H. Emerich, W. van Beek, O. Proux, An XAS study of the structure and thermodynamics of Cu(I) chloride complexes in brines up to high temperature (400 °C, 600 bar), *Geochim. Cosmochim. Acta* 71 (2007) 4920–4941.
- [50] H.W. Richardson, Copper Compounds, *Encycl. Ind. Chem.* 10 (2012) 273 – 301.
- [51] L. Selwyn, C.C. Institute, *Metals and Corrosion: A Handbook for the Conservation Professional*, Canadian Conservation Institute, 2004.
- [52] R. Grayburn, Spectroelectrochemical techniques for the conservation of metallic artefacts, Ph. D. Dissertation, Ghent Univ.
- [53] D. Scott, Bronze disease: a review of some chemical problems and the role of relative humidity, *J. Am. Inst. Conserv.* 29 (1990) 193–206.
- [54] A. Doménech-Carbó, Electrochemistry for conservation science, *J. Solid State Electrochem.* 14 (2009) 349–351.
- [55] R. Grayburn, M.G. Dowsett, M. Hand, P.-J. Sabbe, P. Thompson, A. Adriaens, Bronze Disease Revealed? A synchrotron X-ray diffraction study of nantokite hydrolysis, *Corros. Sci.* 91 (2014) 220–223.
- [56] R.B. Faltermeier, A corrosion inhibitor test for copper-based artifacts, *Stud. Conserv.* 44 (1998) 121–128.
- [57] S. Hamza, M.A. Khan, S. Lewonczuk, J. Ringeissen, Conduction bands in CuCl and CuI by X-ray absorption at K and L edges, *Solid State Commun.* 75 (1990) 29–33.
- [58] C.S. Schnohr, M.C. Ridgway, *X-Ray Absorption Spectroscopy of Semiconductors*, Springer Berlin Heidelberg, 2014.
- [59] K. Leysens, Monitoring the conservation treatment of corroded cuprous artefacts: The use of electrochemistry and synchrotron radiation based spectroelectrochemistry. Ph.D. Dissertation.
- [60] a. . Musa, T. Akomolafe, M.. Carter, Production of cuprous oxide, a solar cell material, by thermal oxidation and a study of its physical and electrical properties, *Sol. Energy Mater. Sol. Cells* 51 (1998) 305–316.



Evaluation of XEOM 1 for chemical imaging of metal surfaces

CHAPTER 5

XEOL microscopy has the potential to provide laterally resolved surface specific chemical information. The quality of the chemical maps and the degree of lateral resolution is dependent on the condition of the hardware. A vast amount of work has been put into the design of the microscope [1, 2] and the development of suitable specimens [3] for evaluating the prototype. Both preparative steps meet during the experimental testing of the microscope with the samples in the synchrotron. This step is indispensable in the process of developing an innovative technique and building an accompanying instrument which meets the requirements in order to generate reliable data. This chapter begins with an overview of the general details of a typical SR-XEOM experiment and the process of acquiring chemical data with XEOM 1. The subsequent paragraphs detail the results obtained from XEOM image stacks acquired from copper and bronze samples corroded according to the protocols described in chapter 4.

The majority of the findings discussed in this chapter have been published in Analytical Chemistry in 2014 under the title : 'Evaluation of an X-ray-Excited Optical Microscope for Chemical Imaging of metal and Other Surfaces' [4] .

5.1 OPERATION OF A XEOM 1 EXPERIMENT

The establishment of a new analytical tool and its associated applications is anything but a routine task. Nevertheless, the experience of a few beam time allocations demonstrate a certain recurring pattern in the process of generating and analyzing data. The remainder of this section describes which actions are included in a 'standard' experiment and elaborates on the individual steps.

Alignment

Figure 5.1 depicts the process of acquiring chemical data with XEOM 1. The X-ray beam is first aligned precisely with the area of the sample within the field of view. This done by imaging a bare copper TEM grid fixed to a piece of fluorescent paper (Figure 5.2 C) and moving the stages (DUBBLE) or goniometer (XMaS) on which XEOM 1 is mounted until the illuminated region is completely within the field of view of the camera. The clear pattern on the sample is generated by the shadow of the grid on the green fluorescent emission from the paper (Figure 5.2 D).

Focusing and filtered imaging

Often at this stage, the image found is out of focus. Obtaining the optimal position of the focusing lens is done by automatically moving the focusing lens across its range while using the continuous capture functionality of the acquisition software. Binning of the images, i.e. grouping of pixels into a larger pixel whose total intensity

is the integrated value of the intensity of the contributing individual pixels [5], combined with short exposure times allow the frame rate to be high enough to monitor the effects of a different focal position in real time. When longer acquisition times are necessary, e.g. upon imaging low XEOL emitting samples, focusing is done manually by separately moving the focusing lens and subsequently acquiring an image. This prevents the passing of the optimal focal position during the acquisition of the previous image.

Currently, optimal focus is chosen by the user since no algorithm to automatically find the best focus is yet incorporated into the software. Leaving the assessment of image focus to the user's perception is unarguably subjective and challenging, especially in the case of images with naturally low contrast. A robust solution for this problem can be done through finding, a priori, the optimal focal position for the different filters present with a strong emitting sample (see chapter 7). When low emitters are mounted, provided they are in the focal plane and do not have a rough surface, recalling the focal position associated with the applied filter will roughly give a good focus.

When a sample of unknown nature is being imaged for the first time (e.g. chainmail link, Chapter 6), a spectral survey is appropriate to detect in which wavebands the sample is emitting. The new filter wheel allows us to perform this task straightforwardly, even though the focus needs to be readapted for a different filter/waveband. When the necessary alignment and focusing procedures are completed and the desired waveband is chosen by applying the associated filter, a XEOM image stack can be acquired during a trigger capture experiment (see paragraph 3.2.1).

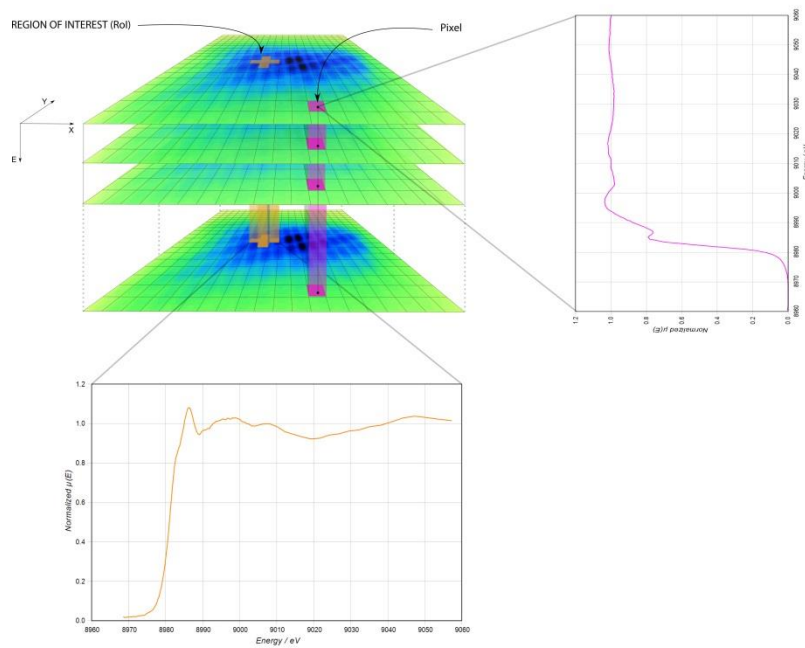


Figure 5.1

Graphical representation of the acquisition of a XEOM image stack with subsequent ROI analysis.

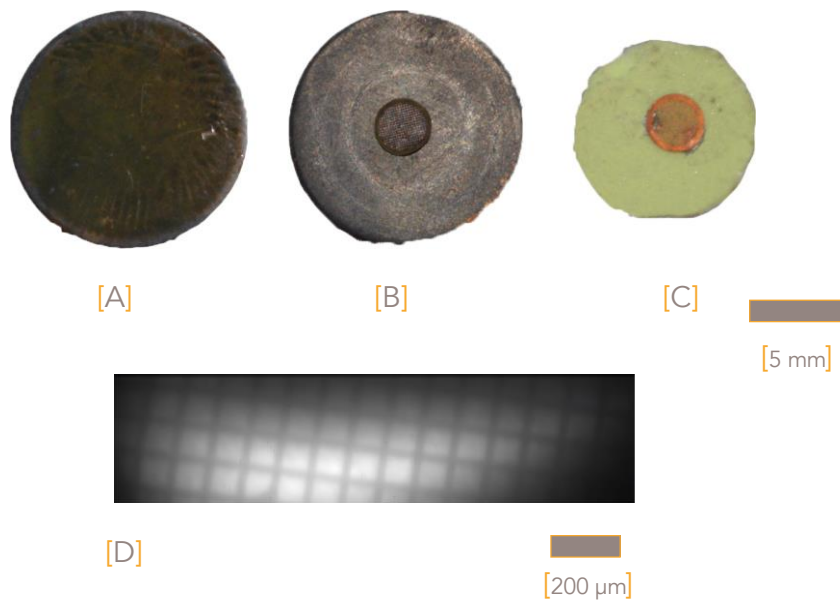


Figure 5.2

[A] Lead bronze coupon coated with an artificial nantokite layer.

[B] Copper coupon coated with an artificial cuprite layer supporting a copper TEM sample holder grid coated with an artificial nantokite layer.

[C] Sample composed of fluorescent paper and a copper TEM grid used for alignment and calibration of XEOM 1.

[D] XEOM image recorded from the sample [C].

XEOM image stack acquisition

Data collection generally proceeds as follows: the photon energy is stepped in 0.5 – 1 eV increments across the energy range of interest, dwelling on each step for a period slightly longer than the acquisition time (typically ≥ 10 s) of the camera. In contrast to the usual practice in XAS acquisition, where the photon energy step size and dwell time are varied in the pre-edge, edge, and postedge regions; the steps and data acquisition times are kept constant so that the background due to slowly decaying phosphorescent modes is smooth (the effect of varying the data acquisition times conventionally can be seen in [6]). Although XEOM and beamline software run independently, the stepping of the monochromator is synchronized with the image capturing during a trigger capture experiment. A more detailed description of the handshaking between both systems is given in section 3.3.

The XEOM images may be delivered raw or pre-processed to correct for instrumental signature and background introduced by the CCD. esaXSec and esaProject can correct for :

- **Bias correction**

Bias noise is present in every – dark or light – image captured from any opto-electronic sensor such as a CCD. Bias noise is the intrinsic noise of the bias level, an electronic offset added to the signal of the CCD to ensure that the analogue-to-digital converter (ADC) always receives a positive value. Bias level correction is done by subtraction of a specifically taken bias-frame, a zero second exposure readout, or by an estimate value generated in the bias regions of the chip (overscanning). For both the Andor and the FLI camera, bias frame subtraction is used as bias correction approach [5, 7]. After bias subtraction, data are directly related to the number of photons detected in each pixel.

- **Flat-field correction**

In general, for any type of CCD, the recorded signal per unit of incident flux is not constant over the complete two-dimensional array of pixels. This variation in relative sensitivity across the chip must be removed. To achieve this correction, a flat-field frame must be recorded in which the CCD sensor is exposed to a uniform light bundle, a flat field source. Flat-field correction is then done by dividing each image frame by this ‘sensitivity map’, thus correcting for pixel response. Various attempts have been done to record flat-field frame, however no satisfactory results were established yet. Obtaining a completely uniform flat-field source has been problematic [5, 7, 8].

- **Dark count correction:**

Dark count correction is the subtraction of electron counts accumulated in each pixel as a result of thermal excitation, rather than optical photon absorption. This effect builds up with longer exposure times and at higher operating temperatures. Modern instrumentation allows deep cooling, either thermoelectrically (Peltier components) or via water/air cooling or both, which mitigates this effect considerably. At low temperatures and short exposure times, this noise source is minimal compared to other noise components contributing to the background level. At longer exposure times, subtraction of a dark frame of equal exposure time is needed to correct for this thermal noise [7].

Data handling and analysis in esaProject

After the entire image stack has been recorded, single images or complete image stacks are imported as `.eccd` files into esaProject. Initially, data are typically normalized to the beam monitor values to correct for changes in the X-ray intensity and for monochromator glitches. From this point on, pixels are stored as binary 64 (8-byte double precision floating point numbers) for speed and accuracy in onward computation. EsaProject allows XEOL-XAS spectra to be extracted through pixel-by-pixel integration of the intensity over an entire image. In this case, a one-dimensional spectrum is obtained without any spatial resolution which is similar to data obtained by a photomultiplier tube in ODXAS experiments [9]. Alternatively, and more powerful, is its feature to extract XEOL-XAS spectra from user-defined regions of interest (ROI) or from individual columns of pixels orthogonal to the image. In these cases a degree of spatial resolution is obtained, its magnitude depending on the size of the ROI or the binning of the images in the stack.

Creation of chemical maps in esaProject

Further processing is possible within the spectrum processing segment of esaProject or other third-party software. However, the XEOM image stack processor portion of esaProject itself allows the user to extract chemical information from the XEOL-XAS spectra, as in the usual way for XAS, with the proviso that the pre-edge background cannot always be subtracted meaningfully from the data [6]. Currently, oxidation state maps of the image stack can be reconstructed by associating the position of an absorption edge in each column of pixels with a value of a false colour scale. Chemical speciation becomes quickly visibly when inspecting such a chemical map.

5.2 IMAGING A HOMOGENEOUS CUPROUS CHLORIDE LAYER ON BRONZE SAMPLE

A preliminary test to deduce some general features of the equipment was done on a leaded bronze coupon coated with a homogenous layer of nantokite free from any obvious lateral inhomogeneity (Figure 5.2 A) at BM26A during beamtime IV (Table 3.6).

Figure 5.3 A displays the image stack recorded from this sample. A series of 102 images were acquired at X-ray beam energies from 8960 to 9010 eV using an exposure time of 25 s per point and no optical filter. The beam footprint is approximately 1 x 2 mm² and images were recorded with the FLI camera. The image stack displayed in Figure 5.3 is represented as a cuboid with the first image of the stack (at 8960 eV) as the top surface and the energy cross sections parallel to the x- and y-axes as the side faces. Illumination of the homogeneous nantokite layer results in the visualization of the beam intensity profile on the top- surface image. The beam follows a Gaussian profile with the highest intensity in the middle around ROI 1 (colored yellow) and fades out towards the edges of the image (purple/blue). This pattern is also observed on the cross section parallel to the x-axis through ROI 1 seen on the front face of the cuboid. Additionally, the absorption edge is clearly visible in this energy cross section with a sharp rise in intensity around 8979 eV. A similar trend is observed on the cross section parallel to the y- axis through ROI 1 at the right face of the cuboid.

Figure 5.3 B shows the normalized integrated XEOL intensity in the range of 8970–9000 eV for the total image and three selected ROIs. The data are a XANES fingerprint of a mixture of nantokite with a minor fraction of paratacamite ($\text{Cu}_2\text{Cl}(\text{OH})_3$) and cuprite (Cu_2O). Nantokite can be discerned by the presence of a characteristic “white line” (nomenclature historically used for a sharp peak occurring on the top of the edge [10]) at 8986 eV (B), resulting from the intra-atomic $1s \rightarrow 4p$ Cu transition [11]. The characteristic shoulder at 8984 eV (A) and the feature at 8991 eV (C) are also observed in the reference spectrum of pure nantokite.

A part of the nantokite produced hydrolyzes rapidly with water from the rinsing procedure to form cuprite [12, 13]. Hence, some features characteristic of cuprite (e.g., shoulder A at 8984 eV and increased intensity around 8995 eV) are observed in the total spectrum. The inset gives the XEOL spectra of the reference powders for comparison. The areas selected for the ROI analysis are on the top-face image of the cuboid. The spectra extracted from the different ROIs can be superimposed to within the noise level, indicating there are no measurable changes among the different areas.

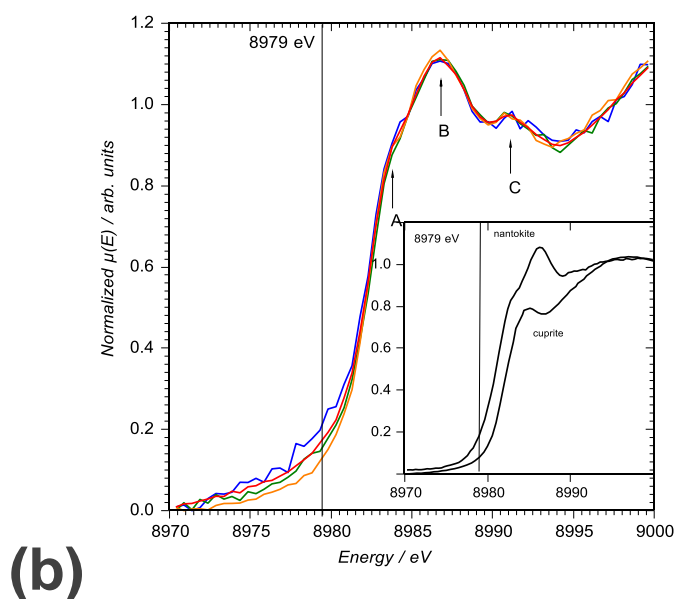
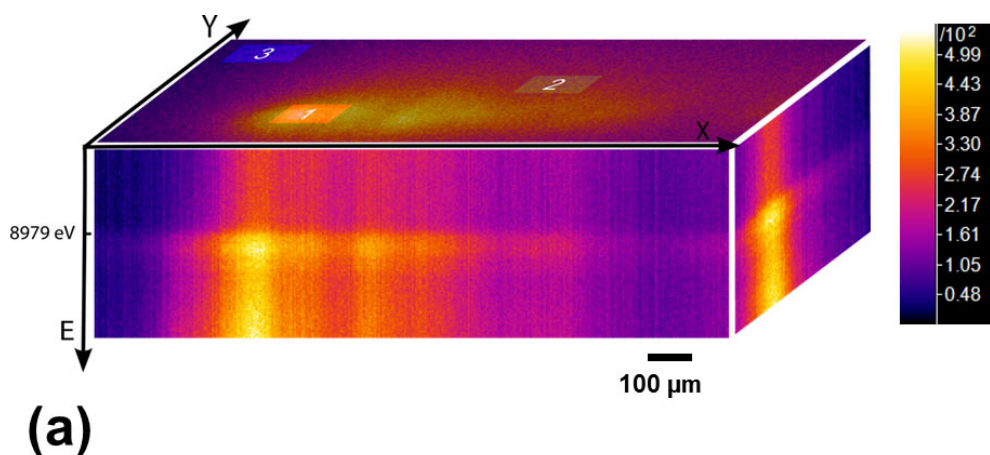


Figure 5.3

[A] XEOM image stack acquired from a lead bronze coupon coated with nantokite.

[B] Normalized, pre-edge subtracted, XEOL-XANES spectra extracted from ROI 1, ROI 2, and ROI 3 and the total image. Inset: XEOL-XANES reference spectra of nantokite and cuprite.

5.3 CHEMICAL MAPPING

Whereas conventional light microscopy yields morphological data, the imaging of the XEOL-XAS provides chemical and physical information. The esaProject software suite provides the necessary tools to extract this information from the raw data and transfer it into a chemical map in which lateral resolution of the data across the surface is retained. At present, more than one approach is available to produce a chemically specific surface mapping.

As detailed in section 2.3, XEOL emission is characteristic of the compounds present in combination with their impurities. Therefore components of different origin or identical components with varying impurities will luminesce in different colours. Imaging these different wavebands by applying different filters is a first and straightforward approach to acquire chemically resolved data. In this respect, a post-edge image can be perceived as a chemical intensity map in which bright areas (high intensity) indicate the presence of a component luminescing in that particular waveband. A clear example of visualizing chemically varying areas by applying different filters can be seen in section 5.3.3. Solid materials typically have spectral bands instead of spectral lines. For example, pure Cu_2O can have emission ranging from 350 nm to 850 nm, as discussed earlier in section 4.2.5.2 and Figure 4.6 C following the finding of Park et al. [14]. As the bands from different compounds and impurities can overlap, application of filters can only enhance the contrast of the chemical image. Unfortunately, it is unlikely to obtain complete chemical speciation by imaging through filters. Nevertheless, the acquisition of a XEOM image stack provides a more powerful pathway to deduce chemical speciation. More details on this approach are given in section 5.3.2 and 5.3.3. In the following section, edge height mapping, a third approach to expose chemical information is presented. Edge height mapping can serve, yet not with similar efficiency but with additional surface specificity, as an alternative method to XRF for elemental mapping.

5.3.1 EDGE HEIGHT MAPPING OF A TOPOLOGICAL INSULATOR

Upon crossing the absorption edge of an element of interest, the efficiency by which incoming X-rays are absorbed increases abruptly. A sudden, steep rise in the absorption spectrum occurs. The absence of such an edge shows that the target element is below the detection limit set in XEOL-XAS by the background fluorescence and phosphorescence. Since X-ray absorption is the primary event leading to XEOL, increased X-ray absorption leads, under the right circumstances, to an augmented XEOL emission as described by Bianconi et al. in 1978 [15]. The edge itself may be negative depending on the availability of post-edge de-excitation channels or reduced efficiency in energy transfer to optical channels as a result of truncated thermalization paths at lower sampling depths [16, 17]. In either case, subtraction of an image recorded below the edge from one recorded above the edge, or vice versa, results in an edge-height contrast chemical map. Contrast indicates where an edge step was recorded within the field of view, which can be understood as the location where the elements of the crossed edge are present in the surface layer.

An example to indicate edge height contrast mapping with XEOM 1 and to demonstrate that the field of application of the microscope is broader than cultural heritage analysis was found within the development of innovative materials. Topological insulators are materials that are insulating in the bulk of the material but support the flow of electrons on their surface [18–20]. Topologically insulating behavior was initially discovered in two-dimensional systems and the extension towards three-dimensional topological insulating materials is already a fact. Although the exact nature of these materials is very complex and beyond the scope of this thesis, it is understood that bulk metallicity underneath topologically ordered surface states is an outstanding problem in this field [18]. Overcoming these issues and further refinement of 3-D topological insulators is subject of investigation, as these materials are thought to hold immense potential for thermoelectric and electronic applications. Copper-doped bismuth selenide, $\text{Cu}_{0.12}\text{Bi}_2\text{Se}_3$, is such a material and currently being investigated for its topologically insulating capability [18].

A sample of $\text{Cu}_{0.12}\text{Bi}_2\text{Se}_3$ (sample name 260410 II) was synthesized in the group of Prof. Geetha Balakrishnan (Department of Physics, University of Warwick, UK) and kindly lent to our group for investigating the distribution of doped-copper within the surface area. Measurements were carried out in BM28 during beam time allocation II (Table 3.6). Images were acquired at both sides of the Cu K-edge, more specifically at 8950 eV and 9000 eV each for 2000 s. Images were recorded with the FLI camera and the beam dimensions were approximately $1 \times 2 \text{ mm}^2$. To improve the S/N ratio, images were binned 4×4 .

Figure 5.4 A & B show respectively the result of the pre- and post-edge acquisition of sample 260410 II. Both frames are normalized for variation in primary X-ray intensity and bias corrected. In order to complete this task, a bias correction frame was constructed by averaging 10 bias frames in which each frame was for 0.1 s with shutter closed. The image acquired in the pre-edge at 8950 eV show no distinct features which are specific to the sample. Clearly visible are the artifactual luminous arc features which were ascribed in section 3.1.4.1.1 to the Hamamatsu chip not being perfectly flat. These artifacts are also present in the post-edge recorded image (Figure 5.4 B) but are accompanied by vague circular marks. Figure 5.4 C is the result of subtracting the pre-edge image from the post-edge image. Apart from reducing the effects of the camera artefacts, this process reveals the position of copper rich areas. The difference image presents three clear bright circular regions suggesting that copper has built-up in certain areas of the surface during the growth process rather than being distributed homogeneously.

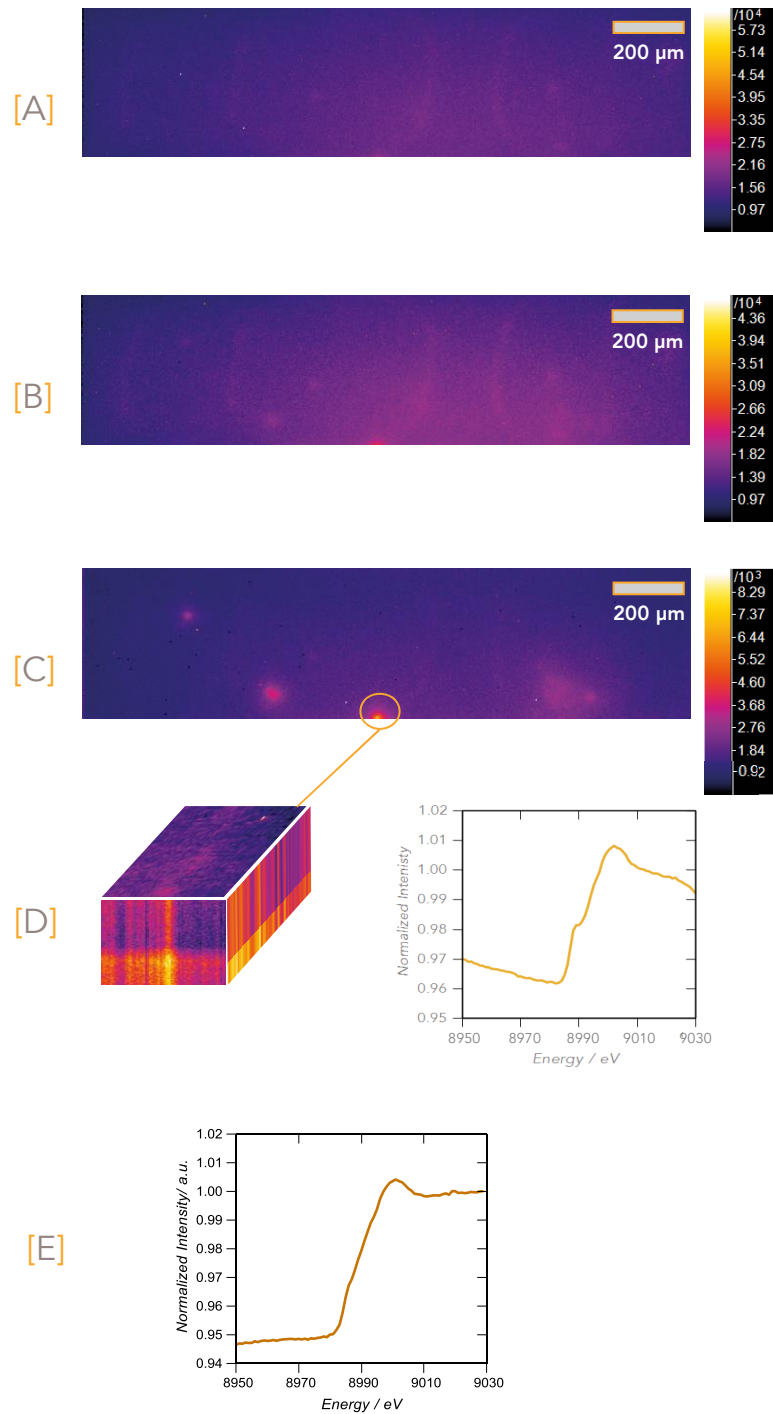


Figure 5.4

[A] Pre-edge image recorded at 8950 eV from topological insulator $\text{Cu}_{0.12}\text{Bi}_2\text{Se}_3$ (sample 260410 II)

[B] Post-edge image recorded at 9000 eV from topological insulator $\text{Cu}_{0.12}\text{Bi}_2\text{Se}_3$ (sample 260410 II)

[C] Edge height map resultant of subtraction of post- and pre-edge image indicating Cu-rich islands in the topological insulator.

[D] Image cube and spectra extracted out of the ROI selected around a bright region in the edge height map.

[E] Average spectrum extracted out of the entire sampled area.

In order to verify which compound is embedded within this bright regions, a region of interest was created around the brightest feature in the bottom of the image and an image stack (100 images) was recorded in the energy range of 8929 eV – 9029 eV with an energy resolution of 1 eV per point and an acquisition time of 140 s per image. The image cube and the spectrum extracted from the total ROI is displayed in Figure 5.4 D and the spectrum extracted from the entire sampled area is displayed in Figure 5.4 E. The XEOL-XANES spectrum shows a positive edge with a mid-edge feature around 8988 eV and broad edge peak around 9000 eV. Determining the origin of these features is a study in itself. This might be a very difficult task due to the complex electronic structure of these materials and is therefore outside the scope of this work.

5.3.2 IMAGE STACK OF A CUPRITE GRID ON A COPPER SURFACE

Assessing the chemical imaging features of XEOM 1 is done by using samples of well-defined areas of different copper chemistry as explained in section 4.1.2. Figure 4.1 B displays a cuprite coated TEM mesh (made with a reducing flame, see 4.2.1) affixed with two fine strips of double-sided tape over a pristine metallic copper coupon.

Firstly a spectral survey was carried out in order to find in which wavebands the sample was emitting. During this survey, the sample was imaged for 15 seconds with 9 keV X-rays with different filters ranging from the deep UV to the far IR. The result of this analysis can be found in Figure 5.5. The experiment suggests that XEOL radiation from either the copper or the cuprite has few or no components in the UV (280 -370 nm), violet (385 – 425 nm) and deep blue (430 – 470 nm). A first component of significant intensity is found in the green / yellow band (515 – 585 nm). The image displays the footprint of the X-ray beam containing poorly visible features of the mesh accompanied with a bright pinpoint mark which was already visible in the deep green. When longer wavelengths are investigated, increasing signal intensity is established from no signal in the yellow/orange band (570 – 630 nm) over emerging signal in the red (615 – 690 nm) and far red (665 – 735 nm) to particularly strong signal in the near IR, both in the range of 770 – 835 nm and 780 – 1050 nm. The stronger signal in the last range must be associated with the presence of larger bandwidth (factor 4), higher transmission of the filter (approx. 10%) and presence of more signal in the 835 – 1050 nm range. This is confirmed when the total count, i.e. integrated intensity of all the pixels in the frame, of the images is examined. These conclusions are consistent with the results of the waveband survey of the flame produced cuprite, which is explained in more detail in section 4.2.5. It could be concluded from this experiment that cuprite, produced with a reducing

flame, provides optical luminescence mainly in the infrared band. However, the featured area observed in the green-yellow band of the sample does not agree with this survey. Apart from the deep green band, the green-yellow band was least intense component contributing to the XEOL of flame produced cuprite. Observation of luminescence and lateral resolution in this band from a cuprite-copper sample might suggest that the majority of the XEOL observed in this band is being emitted from the cupreous areas in the samples.

Unfortunately, due to time constraints during the beamtime allocation, only one image stack could be recorded of two out of the three brighter zones. Since features are only visible in the green/yellow and in the IR and the observed radiation might have different origins on the sample, priority was given to record an image stack with these filters in place. The results of the spectral extraction and generation of oxidation state map are depicted in Figure 5.6 to Figure 5.8.

Green / yellow filtered image stack (515 – 585 nm)

Figure 5.6 displays the result of the ROI analysis performed on three distinct locations in the field of view of an image stack recorded from the sample in the energy range of 8904 eV to 9074 eV, with 1 eV resolution and a dwell time of 100 s per point and the green/yellow filter in place. The first region of interest is created around the bright pinpoint mark feature, the second ROI is selected on the intersection of two bars from the mesh and a third ROI represents the area inside the hole of the mesh, i.e. the copper coupon. The extracted spectra are displayed adjacent to the image.

The spectra yielded from the three ROIs are very similar in shape and exhibit the features of a typical Cu_2O XANES fingerprint with the distinct mid-edge feature around 8980 eV ($1s \rightarrow 3d$ resonance) and the edge peak at 8990 eV ($1s \rightarrow 4p$ transition). The expression of a cuprite fingerprint in ROI 3 is unanticipated since this region contains pure copper. Figure 5.8 A displays the edge map created from the image stack recorded with the green/yellow filter in place. Clearly very poor to no lateral resolution is observed.

On a different note is the existence of the pinpoint mark. The intensity signature of the beam profile is certainly visible in the XEOM image: maximal intensity in the center and slowly decaying X-ray intensity towards the edges. Exactly as one would expect from a Gaussian profile on a homogeneously coated sample. The bright spot is anomalous to this profile and could either be the result of inhomogeneity in the sample or a defect in the imaging system. Visual inspection of the sample prior to XEOM analysis confirmed the presence of a homogenous cuprite layer on the grid and a pristine copper surface. Additionally, the feature is absent in other images which excludes the possibility of an artifact/defect in the optical column or the CCD

system. Moreover, the presence of the feature in the same location with a deep green filter (465 – 535 nm) in place eliminates that the green/yellow filter had been compromised.

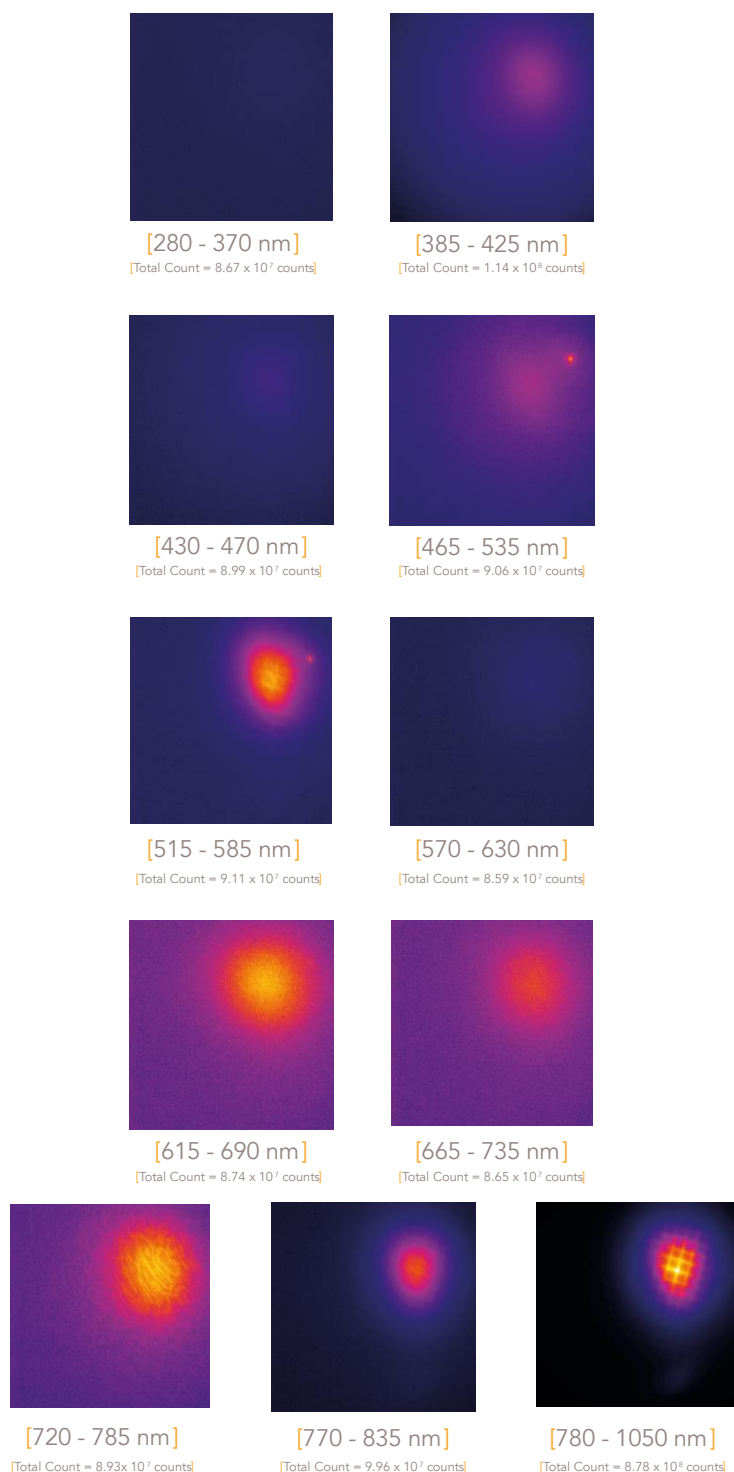


Figure 5.5

Spectral survey of an evaluation sample made from a cuprite grid supported on a copper coupon using a set bandpass filters covering the UV-VIS-IR region of the EM spectrum. Fringes are visible in the image recorded in the 720 – 785 nm. These fringes are due to the etalon effect in the CCD chip. More details on this effect is given in section 6.3.4.1.

Since the spectrum extracted out of ROI 1 exhibits a cuprite fingerprint, yet with lower intensity than the center of the image but with higher intensity than the surroundings, the following hypothesis might provide an explanation for this event. Possibly, this location of the sample was contaminated with a low atomic number product. Possibly the contaminating particle is originating from a green phosphorescent screen used for alignment of the field of view of the microscope with the X-ray beam (see Figure 5.2 C) as these particles strongly emit in this particular region. Fluorescence of this contaminant would occur when secondary fluorescent X-rays, originating in the metallic substrate, would excite valence electrons. Consequently, varying the primary X-ray energy would result in the contaminant luminescing in sympathy with the underlying cuprite. This means that upon crossing the Cu *K*-edge, more secondary X-rays will be produced and luminescence yield of the contaminant will rise accordingly. Eventually the contaminant luminescence yield will be modulated by the absorption probability of copper, therefore showing a cuprite fingerprint in the XAS spectrum.

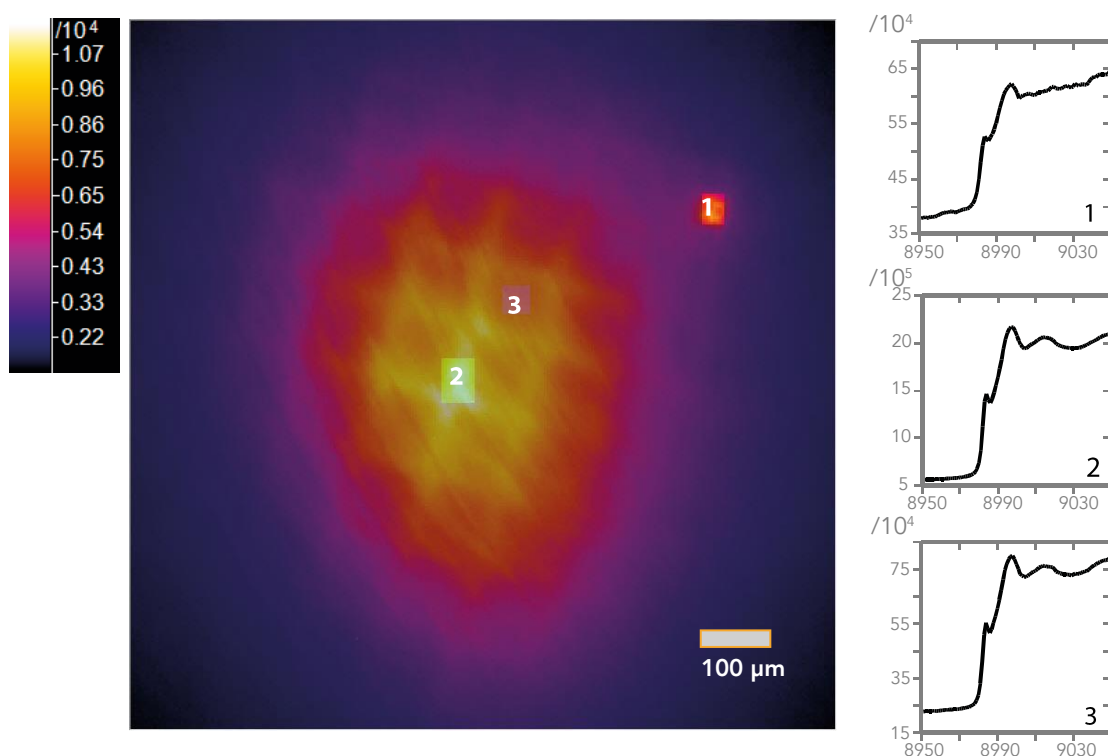


Figure 5.6

ROI analysis of 3 distinct ROIs from the green-yellow filtered image stack of the cuprite/copper sample.

Infrared filtered image stack (780 – 2800 nm)

Figure 5.7 displays a post-edge image of an image stack in the energy range of 8904 – 9074 eV recorded from the evaluation sample with an infrared cutoff filter in place, 1 eV resolution and 15 seconds dwell time per energy point. Consistent with the findings of the spectral survey discussed in section 4.2.5, the major component of cuprite XEOL is found in the IR-region. Consequently acquisition time can be lowered while contrast and good statistics are conserved. Microscopy of the sample with an IR filter in place results in an image of high contrast in which the TEM mesh is clearly discernible. Although lateral resolution is established from a morphological point of view, this is not necessarily the case from a spectroscopic perspective. To confirm this, two distinct ROIs were chosen in the infrared filtered image stack. As illustrated in Figure 5.7, a ROI was drawn in a cuprite rich region (mesh) and a copper rich region (coupon). Both ROIs present spectra which are typical of cuprite, confirming also the absence of any chemical lateral resolution in the image stack recorded of only IR radiation. Figure 5.8 B confirms little lateral resolution visible in the oxidation state map. Nevertheless, a minor improvement is observed with respect to the yellow-orange recorded image stack. Indeed in the center of the beam profile a faintly noticeable grid with similar orientation as the grid in Figure 5.7 is visible.

Since the grid is faintly visible in the area where the beam is expected to possess maximum intensity, absence of chemical lateral resolution might be related to of insufficient counting statistics. Still, spectra extracted out of the ROIs in Figure 5.6 and 5.7 are not obviously noisy, with the exception of the special pinpoint mark case. However, a strong difference in XEOL yield is observed between pure copper and flame produced cuprite. The graph in Figure 5.8 displays XEOL-XANES spectra recorded from a pure copper coupon (grey spectrum) and a coupon treated with a reducing flame (orange spectrum). Both spectra are normalized to a beam monitor to account for differences in acquisition and primary beam intensity. It is obvious that treatment of a copper coupon with a reducing flame creates a layer with a considerable amount of new luminescent chromophores, mainly in the IR waveband. The contrast between XEOL production of copper and cuprite is possibly so large that copper XEOL becomes invisible in the presence of the vast intensity of the cuprite XEOL. In order to provide a solution to this issue, an assessment sample was made which exhibits two copper corrosion products both exhibiting stronger XEOL production efficiency: Cu_2O and CuCl (nantokite).

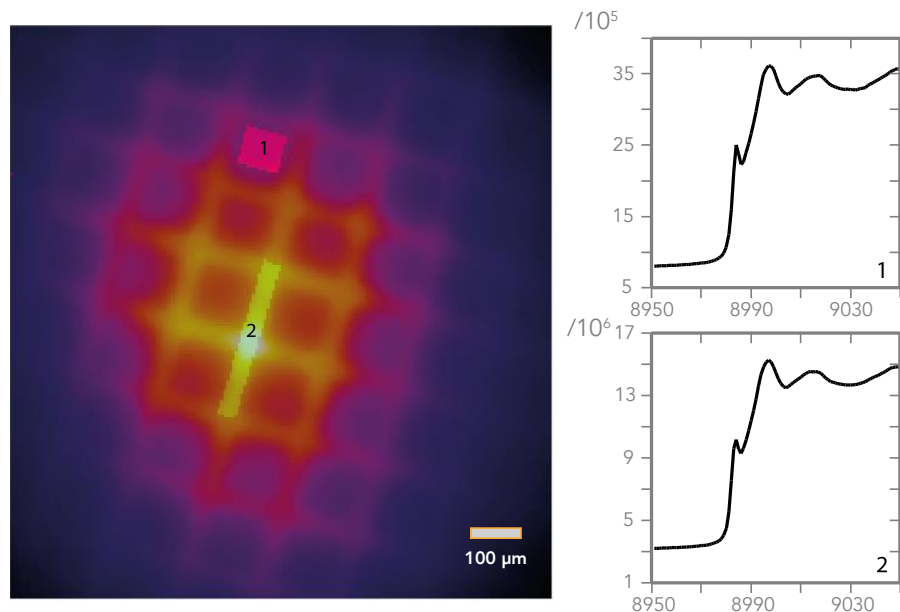


Figure 5.7

ROI analysis of 2 distinct ROIs from the IR filtered image stack of the cuprite/copper sample.

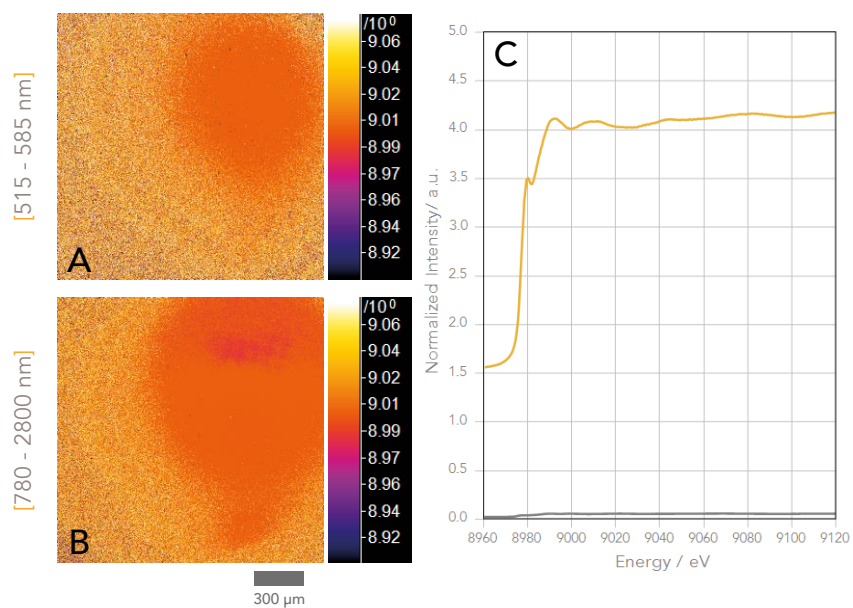


Figure 5.8

[A] Edge position map of the cuprite/copper sample yielded from the image stack recorded with the green-yellow filter in place.

[B] Edge position map of the cuprite /copper sample yielded from the image stack recorded with the green-yellow filter in place.

[C] XEOL-XANES spectra recorded with a photomultiplier tube detector from a clean copper surface (grey) and a copper surface treated with a reducing flame and air exposed whilst hot (orange). Spectra were normalized to a beam monitor to account for variation in the incident beam.

5.3.3 IMAGE STACK OF A NANTOKITE GRID ON A CUPRITE SURFACE

Experiments prior to the development of XEOM 1 revealed that optical filtering is advisable during the recording of XEOL data to alleviate statistical effects of background removal algorithms and to reduce pre-edge background levels [9], apart from the obtaining of a sharp focus with uncorrected optics. Significant chemical differentiation by imaging with XEOM 1 through different optical filters is demonstrated in Figure 5.9 and is one of the chemical imaging approaches that XEOM 1 features. Figure 5.9 displays two images of a nantokite-coated mesh on a cuprite coupon (Figure 5.2 B). The image in Figure 5.9 A was acquired at 9000 eV (out of a series of 112 images collected at 8960–9016 eV) through a red fluorescence line filter (pass band 612–644 nm, see Figure 3.9 and Table 3.3) with an acquisition time of 270 s per image. That in Figure 5.9 B was acquired in a similar way, but with a green fluorescence line filter (pass band 513–556 nm, see Figure 3.8 and Table 3.3) and with an acquisition time of 35 s.

The green emission in Figure 5.9 B is dominated by the coupon, with the mesh only shadowing the underlying surface. The emission is probably close to the 2.27 eV exciton green line (E0B line in Figure 4.6 C) observed in room temperature photoluminescence from bulk cuprite by Park et al. [14] and the rather similar image seen through adjacent filters is consistent with the width of the emission they observed. Red emission from cuprite is suppressed at room temperature. However, the use of a red filter resulted in a significantly different image (Figure 5.9 A) favoring regions of the grid rather than the coupon. The red emission clearly carries the nantokite XANES information (Figure 5.9 C) and is presumably due to a midband gap impurity since the normally observed room temperature photoemission from CuCl is in the far violet (383 nm), as confirmed by the inset of Figure 5.9 D [21–23]. Figure 5.9 D is a reproduction of Figure 6 of [21] which displays the temperature dependence on the photoluminescence of doped and undoped CuCl films deposited by pulsed DC magnetron sputtering. The inset shows that, at room temperature, the main excitonic emission is located just above 380 nm.

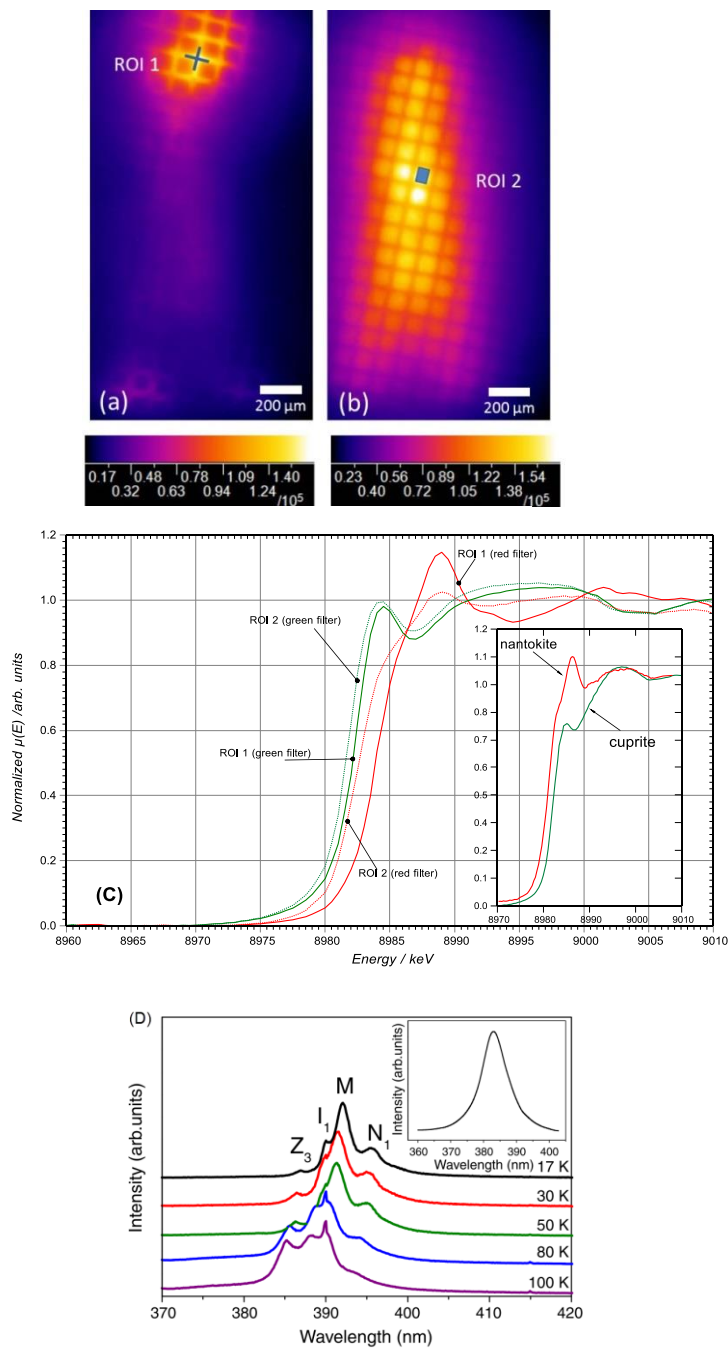


Figure 5.9

[A] Image at 9 keV from a cuprite-coated coupon supporting a nantokite-coated grid acquired through a red fluorescence line filter (Table 3.3).

[B] Image at 9 keV from a cuprite-coated coupon supporting a nantokite-coated grid acquired through a green fluorescence line filter.

[C] Normalized XEOL-XANES spectra extracted from ROI 1 and ROI 2 in the red and green filtered image stacks. Inset XEOL-XANES reference spectra of cuprite and nantokite.

[D] Reproduction of Figure 6 of [21] Temperature dependence and room temperature (inset) PL spectra of CuCl film (3% Zn doped). Photoluminescence spectra were recorded after excitation with 355 nm laser.

Figure reproduced with permission of copyright clearance center of Thin Solid Films (Dec 27, 2017, license number: 4257200552285).

Figure 5.9 C shows the XEOL spectra extracted from ROI 1 and ROI 2 indicated in Figure 5.9 A & B. Using the green filter, both ROIs show the presence of cuprite; i.e., they indicate that cuprite is present on both mesh bars and on the coupon. This is expected due to the rapid hydrolysis of nantokite to cuprite during the rinsing stage. When red filtered, the ROIs give different XEOL–XANES spectra: From ROI 1 (mesh bar) we see nantokite (note the edge shift compared to the spectrum acquired through the green filter from the same region). From ROI 2 the spectrum is (unexpectedly) a mixture of those for nantokite and cuprite. This is possibly due to strong red emission from the nantokite being distributed across the detector from regions outside the intended field of view (possibly due to not having a perfect focus) and swamping the weak red emission from the cuprite. The pre-edge emission mainly results from inefficient excitation of *L*-level Auger transitions in copper, whereas at the edge itself the principal non-radiative electron mechanism switches to *KLL* Auger transition [24]. We have shown elsewhere that the pre-edge and post-edge de-excitation channels can be different and excite different end states as distinguished by the colour of the optical emission [6]. The map in Figure 5.10 was compiled using the image stack acquired through the red fluorescence filter. The position of the edge was determined for each spectrum (column of pixels along the energy axis) using a modified Savitsky–Golay differentiation [25, 26] in *esaProject*, converted to grey scale, and plotted in a 2D map. The difference in binding energy of the two products is observable in the shift of the absorption edge position, as demonstrated in Figure 5.9 C (inset). This corresponds with the observations in Figure 5.10. The darker grey areas clearly correspond to regions on the grid (i.e., a lower edge shift for nantokite), and lighter areas correspond to edge positions extracted from areas where cuprite is present.

The chemical map yielded from the cuprite/nantokite sample is evidently of a higher quality than the chemical map constructed from the copper/cuprite system.

In chapter 7 of this work, it is shown that the ultimate theoretical lateral resolution of XEOM 1 is 1.125 μm for images recorded with a wavelength shorter than this value. Although it is shown in chapter 7 that this resolution can be approached with a UV-C excitation source and a fluorescing glass sample, this level of lateral resolution has certainly not yet been obtained within XEOM imaging experiments. Although the grid could be focused fairly well in the IR band, the level of sharpness of the features is not as good as what would be obtained with other light microscopes. It must be concluded that not all the aberrations, experienced by the optical column of XEOM 1, were addressed or corrected for at the initial design stage of the optical system. Apart from further improving the lens design, a first approach might be the incorporation of additional apertures in order to eliminate out-of-field rays.

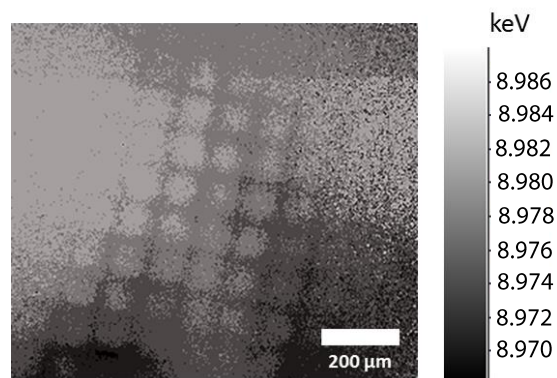


Figure 5.10

Edge position map (oxidation state map) of a nantokite-coated grid on a cuprite coated substrate acquired through a red fluorescence line filter.

5.4 CONCLUSIONS

Data sets collected with XEOM 1 from different samples have been described in this chapter. XEOM 1 adds lateral resolution to the information previously obtained by ODXAS for crystalline and amorphous materials. XEOM 1 acquires images from low-flux-density X-ray beams of millimeter dimensions. The minimum image exposure time for a 2048×2048 image is around 10 s, giving an acquisition time for a stack of images across the absorption edge of 20 minutes to a few hours. This results in statistical precision similar to that obtained with high-flux microbeams, but with a power density of several orders of magnitude lower, which reduces radiation damage to the sample. It is also likely to reduce X-ray-stimulated reactions with the surroundings - an important consideration when attempting to use controlled environments. Image stacks were acquired from samples consisting of copper coupons and grids each provided with different artificial corrosion layers (Cu_2O or CuCl), which facilitated the straightforward evaluation of the imaging characteristics of the microscope. The first XEOM images show chemical contrast from copper corrosion products, and upon optical filtering, the XEOL emission from different corrosion products could be imaged separately. Bespoke image software can process the XEOM image stacks to reduce the data sets, which allows XEOL-XAS spectra to be extracted from the entire image, from a user-defined ROI, or from individual pixel columns; these can subsequently be processed, for example, into 2D edge-shift (oxidation state) images. The results demonstrate that chemical imaging on the micrometer scale is feasible by this relatively nondestructive and potentially

noninvasive technique. Unfortunately, the lateral resolution obtained is currently not near the design limit for XEOM experiments.

5.5 BIBLIOGRAPHY

- [1] M. Hand, Development of an X-ray Excited Optical Luminescence Microscope (XEOM) Ph.D. Dissertation, University of Warwick, June 2014.
- [2] M. Dowsett, M. Hand, P.-J. Sabbe, P. Thompson, A. Adriaens, XEOM 1 - A novel microscopy system for the chemical imaging of heritage metal surfaces, *Herit. Sci.* 3 (2015) 14.
- [3] P.-J. Sabbe, M.G. Dowsett, M. De Keersmaecker, M. Hand, P. Thompson, A. Adriaens, Synthesis and surface characterization of a patterned cuprite sample: Preparatory step in the evaluation scheme of an X-ray-excited optical microscopy system, *Appl. Surf. Sci.* 332 (2015) 657–664.
- [4] P.-J. Sabbe, M. Dowsett, M. Hand, R. Grayburn, P. Thompson, W. Bras, A. Adriaens, Evaluation of an X-ray-Excited Optical Microscope for Chemical Imaging of Metal and Other Surfaces, *Anal. Chem.* 86 (2014) 11789–11796.
- [5] S.B. Howell, *Handbook of Ccd Astronomy*, (2006) 208.
- [6] A. Adriaens, P. Quinn, S. Nikitenko, M.G. Dowsett, Real Time Observation of X-ray-Induced Surface Modification Using Simultaneous XANES and XEOL-XANES., *Anal. Chem.* 85 (2013) 9556–9563.
- [7] S.K. Saha, *High Resolution Imaging: Detectors and Applications*, Pan Stanford Publishing, 2015.
- [8] D. Ratledge, *The Art and Science of CCD Astronomy*, Springer London, 2012.
- [9] M.G. Dowsett, A. Adriaens, G.K.C. Jones, N. Poolton, S. Fiddy, Optically Detected X-ray Absorption Spectroscopy Measurements as a Means of Monitoring Corrosion Layers on Copper, *Anal. Chem.* 80 (2008) 8717–8724.
- [10] T. Sham, R. Gordon, RIXS, XEOL and XEOL Imaging of Rare-earth Phosphors at the L_{3,2}-edges., *AIP Conf. Proc.* 1234 (2010) 133–136.
- [11] S. Hamza, M.A. Khan, S. Lewonczuk, J. Ringeissen, Conduction bands in CuCl and CuI by X-ray absorption at K and L edges, *Solid State Commun.* 75 (1990) 29–33.
- [12] M. Dowsett, A. Adriaens, C. Martin, L. Bouchenoire, The use of synchrotron X-rays to observe copper corrosion in real time., *Anal. Chem.* 84 (2012) 4866–72.
- [13] R. Grayburn, M.G. Dowsett, M. Hand, P.-J. Sabbe, P. Thompson, A. Adriaens, *Bronze Disease Revealed? A synchrotron X-ray diffraction study of nantokite hydrolysis*, 2014.
- [14] J.-W. Park, H. Jang, S. Kim, S.-H. Choi, H. Lee, J. Kang, S.-H. Wei, Microstructure, optical property, and electronic band structure of cuprous oxide thin films, *J. Appl. Phys.* 110 (2011).
- [15] A. Bianconi, D. Jackson, K. Monahan, Intrinsic luminescence excitation spectrum and extended x-ray absorption fine structure above the K-edge in CaF₂, *Phys. Rev. B* 17 (1978) 2022–2024.
- [16] T.-K. Sham, Photon-in/photon-out spectroscopic techniques for materials analysis: some recent developments., *Adv. Mater.* 26 (2014) 7896–901.
- [17] S. Emura, T. Moriga, J. Takizawa, M. Nomura, K.R. Bauchspiess, T. Murata, K. Harada, H. Maeda, Optical-luminescence yield spectra produced by x-ray excitation, *J. Phys. Chem.* 47 (1993) 6918–6930.
- [18] D. Biswas, S. Thakur, G. Balakrishnan, K. Maiti, Exceptional surface and bulk electronic structures in a topological insulator, Bi₂Se₃, *Sci. Rep.* 5 (2015) 17351.
- [19] M.S. Bahramy, P.D.C. King, A. de la Torre, J. Chang, M. Shi, L. Patthey, G. Balakrishnan, P. Hofmann, R. Arita, N. Nagaosa, F. Baumberger, Emergent quantum confinement at topological insulator surfaces., *Nat. Commun.* 3 (2012) 1159.
- [20] C.L. Kane, E.J. Mele, A New Spin on the Insulating State, *Science* (80-.). 314 (2006) 1692–1694.
- [21] K.V. Rajani, F. Olabanji Lucas, S. Daniels, D. Danieluk, a. L. Bradley, a. Cowley, M.M. Alam, P.J. McNally, Growth of n-type γ -CuCl with improved carrier concentration by pulsed DC sputtering: Structural, electronic and UV emission properties, *Thin Solid Films* 519 (2011) 6064–6068.
- [22] L. Kau, D.J. Spira-Solomon, J.E. Penner-Hahn, K.O. Hodgson, E.I. Solomon, X-ray absorption edge determination of the oxidation state and coordination number of copper. Application to the type 3 site in *Rhus vernicifera* laccase and its

reaction, *J. Am. Chem. Soc.* 109 (1987) 6433–6442.

[23] J. Brugger, B. Etschmann, W. Liu, D. Testemale, J.L. Hazemann, H. Emerich, W. van Beek, O. Proux, An XAS study of the structure and thermodynamics of Cu(I) chloride complexes in brines up to high temperature (400 °C, 600 bar), *Geochim. Cosmochim. Acta* 71 (2007) 4920–4941.

[24] A. Rogalev, Goulon, in: T.K. Sham (Ed.), *Chemical Applications of Synchrotron Radiation Part II: X-ray Applications*, World Scientific, Singapore, 2002, pp. 707–760.

[25] W.H. Press, S.A. Teukolsky, W.T. Vetterling, B.P. Flannery, *Numerical recipes in C: the art of scientific computing*, second edi., Cambridge university press, New York, 1992.

[26] D.B. Murphy, M.W. Davidson, *Fundamentals of Light Microscopy and Electronic Imaging: Second Edition*, 2012.

**A multimethod examination
of archaeological samples
retrieved from
King Henry VIII's flagship:
The Mary Rose**

CHAPTER 6



The potential applications of XEOM 1 are broad and might be of value in the area of research to innovative materials: topological insulators (see 5.3.1), nanostructures with particular optical-structural property correlations for optoelectronic devices [1–5], nanosized photocatalysts for water splitting [6], molecular beacons as optical tags for biological studies [7], etc.

Nevertheless, since its design allows one to image sample surfaces with low power density in air or a controlled atmosphere, XEOM 1 is well suited for heritage metal corrosion studies. The information yielded might be an important complement to the information provided by synchrotron X-ray diffraction. In Chapter 5, a first assessment of XEOM 1 is described in which the imaging characteristics were established with well-characterized evaluation samples of distinct chemical speciation. A step further than test structures is the investigation and XEOM analysis of genuine artefacts. This chapter describes the analysis of a pair of chainmail links, one corroded and one conserved, recovered from the wreck of King Henry VIII's flagship the *Mary Rose*. By presenting XAS, XEOL-XAS and XEOM data from one single data acquisition in tandem with the results obtained from subsequent XRF analysis; XEOM 1's capacity to perform simultaneous multimethod analysis is stressed.

Finally, this chapter discusses the results obtained from a SR-XRD study performed on both chain mail links. Data obtained during earlier laboratory XRD measurements appeared to be uninterpretable since the large X-ray footprint of the laboratory source combined with the natural shape of the artefact resulted in a continuum of peak broadening and splitting and superimposed patterns with angular displacement. A relatively novel approach using a 0.25 mm² beam footprint, the extreme intensity of synchrotron radiation and the scanning of a Pilatus 300 K detector provided a solution to this problem.

6.1 THE MARY ROSE : 'THE NOBLEST SHIP OF SAIL'

In an attempt to expand Tudor navy forces in order to face Scottish and French threats, newly crowned King Henry VIII ordered in 1509 two new carracks: the *Peter Pomegranate* and a larger sister ship the *Mary Rose* [8]. The *Mary Rose* (Figure 6.1), presumably named after the Virgin Mary - also known at the time as 'The Mystic Rose'- was built in Portsmouth in 1509-1510 [9]. For over 34 years the *Mary Rose* served the English navy until she sank during the *Battle of the Solent* facing the French fleet on 19th of July 1545. French historians are eager to claim French forces were responsible for sinking the *Mary Rose* while opposite sides declare a strong gust of wind caught sails during a turning maneuver causing the ship to heel over

and water to enter through open gun ports. It's not known whether one of the above reasons, human error or overloading of the ship sank the Mary Rose in the Solent, the strait north of the Isle of Wight [8–10]. What is certain is that the vast majority of the 400 membered crew drowned and only 34 men survived.

After that fatal day, the Mary Rose lay for over 400 years on the seabed until it was salvaged in 1982. During that period, the tidal regime of the Solent, created by its particular geography, gradually buried the wreck and all of its belongings in a layer of sediment. This sheet of silt protected large parts of the ship from abrasion and created an anaerobic environment, impeding oxygen requiring deterioration reactions (e.g. metal corrosion) [11–13]. Moreover, aerobic organisms were inhibited from consuming organic material from the ship and its artefacts. Subsequent formation of a protective crust, composed of compacted clay and crushed shells, concealed the ship and its treasures exceptionally well.

In 1971, the location of the ship wreck was discovered. In the years following, over 19,000 objects were raised from this unique time capsule of life in Tudor England [13]. Depending on the origin of the artefacts, various drying approaches were applied and other treatment steps were taken to stop any further loss [11]. Afterwards, in 1982, an impressive feat of engineering made the raising of the hull relics possible. Excavation of the hull started a period of three decades of preservative actions necessary to dry and restore the timber structure. Since drying of wooden objects which had been waterlogged for centuries would shrink the objects up to 50%, with complementary warping and cracking as result, the wreck was kept wet by spraying it with fresh water [8, 11]. From 1994 until 2013 polyethylene glycol (PEG) was sprayed onto the ship, analogous to the treatment given to the 17th century warship 'Vasa' [11, 14, 15]. Gradually increasing the molecular weight of the PEG over time allowed the PEG to both provide support in the cellular structure of the wood and to strengthen the mechanical properties of the outer surface layers [13]. Finally, a controlled air drying program of 3 years was established to draw out all remaining moisture.



Figure 6.1

The Mary Rose served Tudor naval forces until it sank during the 'Battle of the Solent' on 19 July 1545. Painting by marine artist Geoff Hunt PPRSMA. Reproduced with permission from [16]



Figure 6.2

The Mary Rose museum (left) is located at the Historical Dockyards in Portsmouth [17]. The museum was constructed around the hull (right) while it was still being conserved in a sealed 'hotbox'. In July 2016 the conservation was completed and now the Mary Rose is fully integrated in the museum environment. Images are reproduced with permission from [16].

Nevertheless, preservation work is an ongoing task as the conservators are continuously being challenged with novel threats. For instance, the anaerobic bacteria in the sediment cover produced large amounts of hydrogen sulfide which diffused throughout the hull during its immersion in the sea [12]. Oxidization of the hydrogen sulfide to sulfuric acid as a result of air exposure, imposed a considerable risk as the acid could gradually break down the wooden timbers. In order to resist this, the acid was neutralized during PEG treatment and further mitigation might be done by treating the wood with SrCO₃ nanoparticles [18].

Today the Mary Rose rests in the Mary Rose museum (Figure 6.2) in Portsmouth's Historic Dockyard, just a stone's throw away from where it was first constructed. The 20th of July 2016, after 34 years of 'hospitalization', visitors were able to see the Mary Rose in all her glory, a next stage in her long and remarkable history [16].

6.2 TREASURES HARBOURED BY THE SHIP : TWO CHAIN MAIL LINKS

The anoxic conditions created by the silt were both a blessing and a curse for the Mary Rose. Either anaerobic microorganism on the seabed could metabolize sulfur compounds into hydrogen sulfide or, mediated by iron containing artefacts, into iron sulfides causing a serious 'sulfur problem' once the wreck was raised [12, 19]. On the other hand, the anoxic environment allowed remarkable conservation of the ship and its treasures by impeding wood-boring sea-life to operate, prevent oxidation of the wood and slow down deterioration of other artefacts [13]. Because of the silt, over 19,000 artefacts of different origin could be raised in a well preserved state. Together with the wooden hull, they provide a unique insight into life (at sea) in Tudor England and are therefore of extreme historic value.

Two of those 19,000 artefacts, an as-found and conserved twisted link recovered from the Mary Rose were kindly lent by the Mary Rose Trust and form the subject of this chapter. The twisted links were supposedly identified as chain mail links by the archeology team. Once sewn together chain mail links form a chain mail, also known as a *mail* or a *hauberk*, a protective coat worn by soldiers at the time. Figure 6.3 A displays sample with institution identity number MR81A2249. The sample is as-found and since no conservation treatment was administered, the sample clearly exhibits visible corrosion. Figure 6.3 B displays sample MR81A1436. Contrary to sample MR81A2249, a cleaning and conservation treatment was applied to the chain mail link which is readily visible. According to the conservation card the procedure consisted of :

1. Chemical cleaning via agitation of the link in Modalene, a rust remover containing ammonium citrate, citric acid, oxalic acid and phosphoric acid. Subsequent gentle scrubbing is done to remove concretion. Concretion is a surrounding matrix of shells, sand, mineral cement, dirt, etc. surrounding the artefact.
2. Mechanical cleaning with scalpel to remove larger concretion areas.
3. Agitation in Modalene.
4. Air-abrasion to remove concretion of the area around the twist in the link.
5. Establishment of corrosion inhibitor coating by immersion in a benzotriazole solution [20, 21] and subsequent application of a silicon based oil for protection of the anti-corrosion undercoating.

Both samples are approximately 14 mm by 11 mm and are about 1.5 mm thick. Archeologists investigating the chain mail links established the links are brass, XRF analysis will have to confirm this.



Figure 6.3

[A] Chain mail link MR81A2249 was investigated in the state as it was found when the sample was raised.

[B] Chain mail link MR81A1436 was subjected to a conservation treatment to remove concretion and rust. A benzotriazole layer was applied as anti-corrosion coating and a silicon based oil was applied in order to protect the coating.

[C] The conserved chain mail link fit into the sample stage stub of XEOM 1

6.3 SIMULTANEOUS MULTIMETHOD ANALYSIS OF TWO CHAIN MAIL LINKS

6.3.1 EXPERIMENTAL SETUP

Chain mail link MR81A2249 and MR81A1436 were both analyzed with XEOM 1 at BM28 (XMaS) during beamtime X (Table 3.6) in July 2015. XEOM 1 instrument was installed on the beamline according to the method described in section 3.3.2.1. The X-ray beam was slightly focused into a footprint of approximately 1.25 mm x 0.8 mm. The photomultiplier tube (PMT, see 3.1.4.1.3) was mounted to observe the sample from the large 45° angle port and served both for alignment of the sample and to record XEOL-XAS spectra, averaged over the beam footprint. A Vortex® Si drift detector (SDD, see 3.1.4.2.2) was mounted on a vacant 10° angle port. The SDD was used to acquire both XRF and XAS in fluorescence mode. Since the SDD could not be mounted sufficiently far from the sample, air could not attenuate sufficiently the fluorescent X-rays resulting in saturation effects in the Vortex® detector. In order to prevent saturation of the SDD, a 400 µm thick Al-foil was mounted on the face of the detector. During the measurements, the optical column was filled with He coming from a gas tube fed through a tailored connector (Figure 3.3, IV) in the remaining 10° angle port. In contrast to the case for an O₂ rich environment, synchrotron radiation cannot generate reactive O₃ –radicals (ozone) in a He atmosphere. Hence, ozone cannot react with the sample and induce damage or alter the native chemistry of the surface.

Figure 6.3 C shows the sample mounted in the sample holder end cap of XEOM 1. The object position which is being focused onto the CCD is exactly 25 mm away from the bottom of the end cap. The tailored sample holders for grids, powders, pellets and coupons (Figure 3.3) are machined so that the surface of these samples coincides with this plane. Random samples like a chain mail link require a different approach. During this measurement, the samples were mounted on a threaded rod via a plastic connector. Knowing the sample is 14 mm long, the thread was screwed into the end cap until 11 mm was left of the rod. This way, for both samples, the top of the circular loop of the link intersects with the object plane. Alignment of the X-ray beam with the sample was subsequently done by varying the positions of the different motors of the Huber goniometer and simultaneously monitoring the XEOL response in the PMT (*linescan* or *dscan* SPEC commands). Consequently, the coordinates that correspond with maximum XEOL-intensity give a good estimate for optimal alignment. Ideally, this would be done with the CCD camera. Unfortunately, the camera is not driven by spec. Attempts to synchronize the camera software and the SPEC driven stepper motors would make this much more time consuming.

Finally, a burn paper was spanned over the chain mail link (without physical contact) to indicate the exact imaging location.

6.3.2 X-RAY FLUORESCENCE SPECTROSCOPY

Prior to each synchronized XEOM/XEOL-XAS/XAS experiment, primary X-ray energy was fixed at 14 keV for determining the elemental composition of the links with X-ray Fluorescence spectroscopy. Figure 6.4 displays the result of the XRF elemental analysis of the cleaned (black spectrum) and corroded chain mail link (orange spectrum). Data sets were recorded with an acquisition time of 300 s (corroded link) and 100 s (conserved link). Spectra were normalized to beam monitor values and Cu emission lines were used as internal standards for spectrum calibration. Apart from these operations, evaluation of the XRF spectra was performed by the non-linear least-squares fitting software AXIL (Analysis of X-ray Spectra by Iterative Least Squares) in which the experimental data is fitted with a mathematical function describing assigned fluorescence peaks and spectral background [22].

All photopeaks in both spectra could be assigned to either the K_α and K_β emission lines of: Cu, Zn, Ni, As and to the L_α or L_β emission lines of Pb. The similarity in elemental composition between both chain mail links suggests both links are part of the same batch. The influence of the cleaning and conservation treatment is not visible in the XRF-spectra. This is not surprising since XRF-data are not surface specific due to the large escape depth of the fluorescent X-rays. All the elements observed in the spectra are typical ingredients of archeological copper alloys [23]. Remarkable is the absence of a feature indicating the presence of Sn, which would be expected in a Cu alloy. Sn K_α lines (around 25 keV) are invisible when the incident X-ray energy is 14 keV, however Sn L_α should be visible around 3.44 keV. The exact determination of the alloy would require a quantitative analysis with certified reference materials, which was not done during this study. However one would be tempted to identify the alloy as 'brass' as a result of the larger peaks of n present with respect to the lower amounts of As, Pb and Sn [23].

Apart from the photopeaks, certain artifactual peaks and instrumental signature peaks are visible. Between 6 and 7 keV, two escape peaks related to Cu and Zn were fitted. Detector material atoms, e.g. Si, are inherently sensitive to photoelectric absorption of the detected fluorescent X-rays, hence producing a Si characteristic X-ray of 1739 eV [24]. If this Si fluorescence escapes from the counter, then only the incident energy minus 1739 eV remains for the measured signal. Accordingly every feature in the spectrum will have an associated escape feature at 1739 eV lower energy [25]. At energies higher than the Rayleigh scatter peak, *sum peaks* or *pile up peaks* are visible in which the detector could not discern two individual photons, e.g.

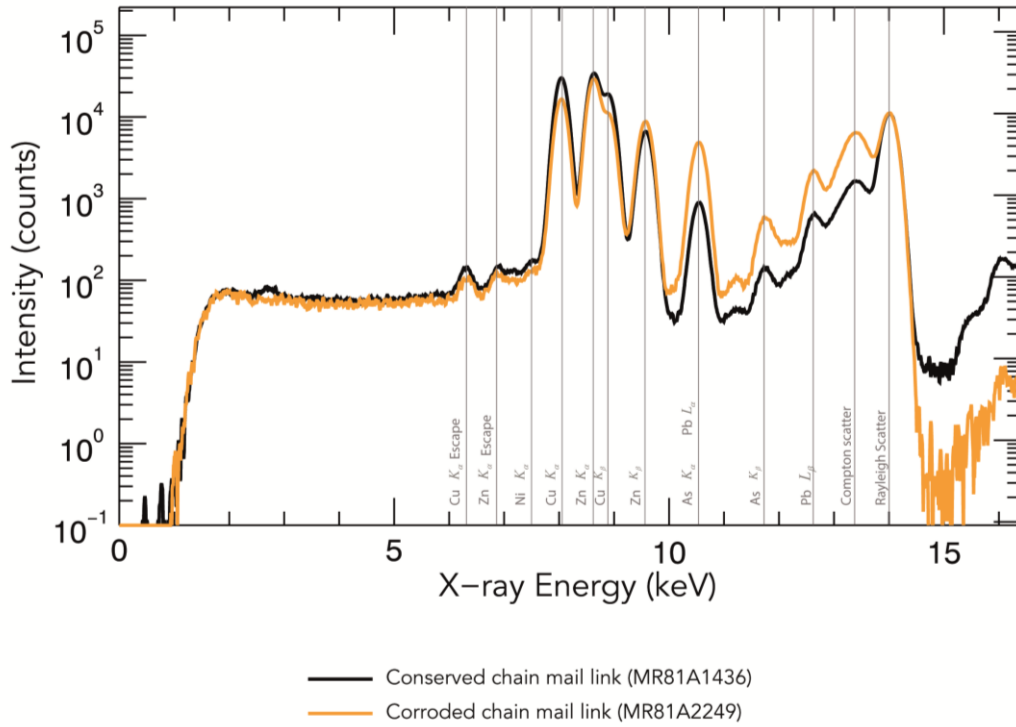


Figure 6.4

XRF spectra collected from the conserved and corroded chain mail link. Both spectra were normalized to the Rayleigh scatter peak at 14 keV.

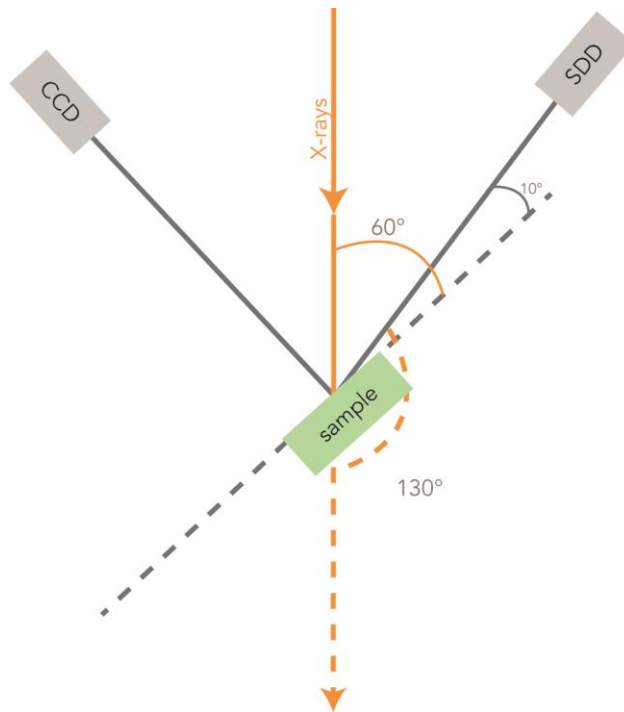


Figure 6.5

Top view of the geometry in which the samples were analysed during beamtime X (Table 3.6) at XMaS.

Cu K_{α} and Zn K_{α} , arriving at exactly the same time in the detector. Next to photoelectric absorption, incident X-rays might be scattered off the sample, as explained into more detail in section 2.2.1. When an X-ray reflects off the sample without losing energy it is referred to as Rayleigh scattering (elastic scattering) [26]. The Rayleigh scatter peak, in Figure 6.4 at 14 keV, is always a good witness for the incident X-ray energy used. When a fraction of the incident X-ray energy is lost, the inelastic scatter event is observed in the Compton scatter peak. The energy of the Compton scatter peak is determined by the Compton Formula (equation {2.9}) and is inherently dependent on the incident X-ray energy and the angle between incident beam and the detector. When installed on XMaS, primary X-rays enter the microscope through the 60° angle port while secondary X-rays are detected with the Vortex® detector mounted on the 10° angle port. Consequently, the detector is oriented at a scattering angle of 130° with respect to the incident X-ray beam (Figure 6.5). Consequently with $E_0 = 14$ keV and $\theta = 130^\circ$, the Compton formula yields 13.45 keV which is in line with the experimentally obtained data.

6.3.3 X-RAY ABSORPTION SPECTROSCOPY : XAS & XEOL-XAS

Figure 6.6 A displays the result of the XANES spectra acquired from the conserved (blue) and corroded (orange) chain mail link. Data was collected across the Cu K-edge in the range of 8960 – 9060 eV with an energy resolution of 1 eV and an acquisition time of 300 second per data point for the corroded link and 200 seconds per data point for the conserved link. The difference in acquisition time is mainly dependent on the (filtered) luminescent intensity observed in the CCD camera. Dependent on that, minimal acquisition time to obtain reasonable statistics is determined. Since all measurements are acquired simultaneously, measurements with the PMT and the SDD follow these time settings. Fluorescent X-rays were detected with a Vortex® energy dispersive detector in which a region of interest was selected around the Cu K_{α} emission line in order to construct the X-ray absorption spectra. At XMaS, three beam monitors are provided for normalization purposes: an ion chamber, a kapton scatter foil and an aluminium foil. X-ray monitoring with the foils appears to be quite noisy, which results in the injection of noise into the spectra during the normalization procedure. Therefore the ion chamber was used to normalize the XAS spectra.

The XANES spectra for both links show a fingerprint typical of Cu obtained across the Cu K-edge. As can be seen in the copper reference in Figure 4.2, typical copper features are the mid-edge feature just past 8980 eV as a result of the $1s-3d$ transition and the double features immediately on the edge. The mid-edge feature is less pronounced in both spectra with respect to the reference in Figure 4.2. This flattened effect may be attributed to self-absorption [27]. Both spectra are

representative of the bulk of the sample and show therefore Cu for both the conserved and the as-found link.

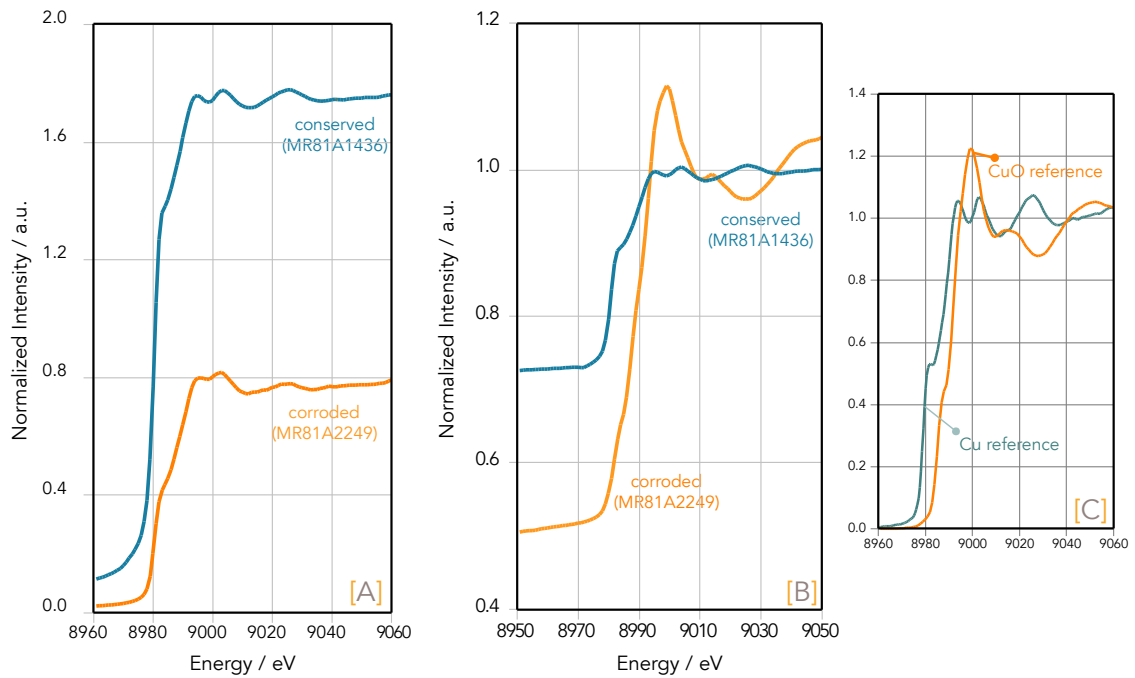


Figure 6.6

[A] X-ray absorption spectra of the conserved link MR81A1436 (blue) and corroded link MR81A2249 (orange) collected in fluorescence mode. Spectra were normalized to beam monitor values.

[B] XEOL-XANES spectra collected of the conserved link MR81A1436 (blue) and corroded link MR81A2249 (orange). Spectra were normalized to average post-edge value.

[C] XEOL-XANES spectra collected of copper (Cu) and tenorite

Figure 6.6 B displays the result of the XEOL-XANES spectra acquired from the conserved (blue) and corroded chain mail link (orange). XEOL-XANES data is acquired with the PMT mounted in the 45° angle port and accordingly represents the unfiltered broadband XEOL emission of the samples. Both XEOL-XAS spectra were normalized against the mean value of the post-edge between 8990 and 9050 eV. Such an approach towards normalization leaves the shape of the spectra generally unchanged compared with the raw data and preserves relative changes between the spectra.

Figure 6.6 B with respect to Figure 6.6 A confirms the surface specificity of XEOL-XAS analysis with reference to XAS in fluorescence mode. Where the conserved chain mail link retains a Cu finger print, the as-found chain mail link clearly has different surface chemistry. Shift of the edge towards higher energy points out the

higher oxidation state of the sample. Where one would expect a XEOL-XANES fingerprint containing various components, the observed XANES spectrum is almost entirely specific for tenorite with a faint mid-edge feature around 8985 eV, a pronounced edge feature at 9000 and positive oscillation followed immediately by a negative oscillation at 9020 eV (Figure 4.10 C).

6.3.4 CHEMICAL MAPPING OF THE CHAIN MAIL LINKS : XEOM ANALYSIS

6.3.4.1 Waveband survey of the corroded link MR81A2249

Analogous to the approach followed in Chapter 5 to image the grid/coupon evaluation samples, a spectral survey was carried out in order to find out which wavebands the sample was emitting. During this survey, the sample was imaged for 200 s with 9 keV X-rays with different filters ranging from the deep UV to the far IR. Figure 6.7 displays the result of this waveband assessment. The survey identifies, according to the total count value recorded, that XEOL emission coming from the corroded link has few or poorly emitting components in the UV (280 – 370 nm), green/yellow (515 – 585 nm), the yellow/orange (570 – 630 nm), the red (615 – 690 nm) and the far red (665 – 735 nm). Components of significant intensity can be found in the violet (385 – 425 nm), the deep blue (430 – 470 nm), the deep green (465 – 535 nm), the IR (720 - 785 nm) and the far IR (780 – 2800 nm).

Notwithstanding the lower XEOL emission, confirmed by total integrated count, imaging with red emission provides substantially more detail than seen in other images. While images captured with violet or IR filters mainly show a homogeneous footprint of the X-ray beam on the link, the red filtered images show a set of bright features within beam footprint. This higher level of detail is a good argument to collect an image stack in this waveband.

The IR-filtered images also provide a set of features. Unfortunately, these features are fringes due to the etalon effect in the CCD chip. These spectral artifacts can arise in images acquired with infrared photons with a back-illuminated CCD.

Typically, a back-illuminated CCD consists of a photosensitive silicon layer (depletion region) sandwiched between an insulating silicon oxide layer and air or a vacuum [28]. This inverse engineering eliminates losses of incoming radiation incurred at the front surface in the traditional front-illuminated geometry. NIR waves entering the depletion region can typically be reflected back towards the front surface (due to its long coherence length with respect to depletion region thickness).

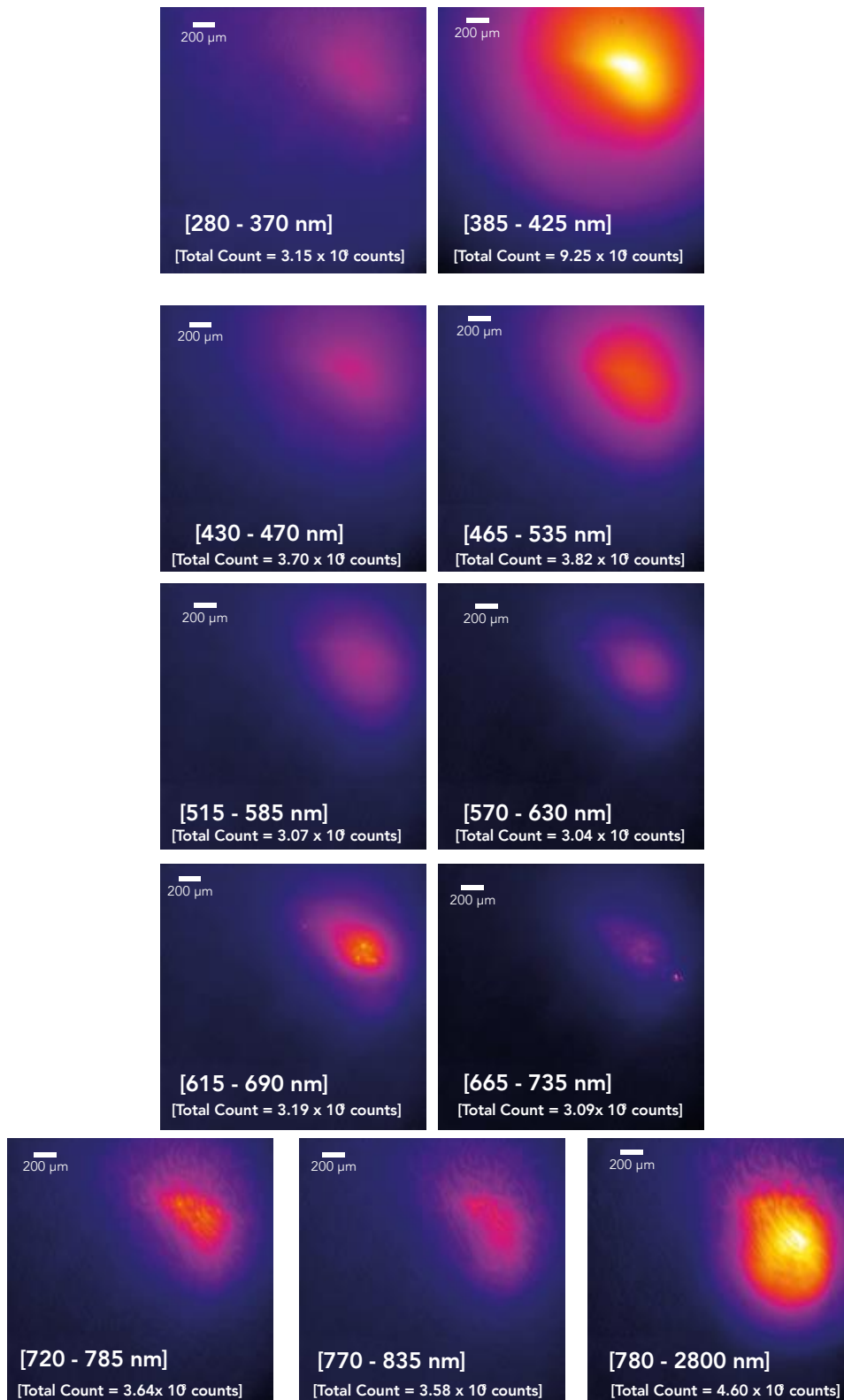


Figure 6.7

Post edge (9 keV) XEOL images (in ironbow colour scale) of the surface of the corroded link MR81A2249 acquired through a series of different optical filters ranging from the UV over the visible to the IR

In areas where the anti-reflectivity coating on the depletion region is not perfect the NIR waves can, in turn, be reflected back. Therefore, a back-and-forth reflection cascade can arise within this ultra-thin cavity, i.e. the etalon. Depending on the conditions dictated by the etalon characteristics this can result in destructive and constructive interference [28, 29]. This interference can either lead to *spectral fringing*, in which the absorption sensitivity (quantum efficiency) of the CCD is increased for NIR photons as a result of the reflection cascade; and *spatial fringing*, which is the aftereffect of varying spectral fringing across the sensor as a result of local variations in depletion region thickness. Accordingly, the IR-filtered images display spatial fringing. Upon purchasing the CCD chip, it was chosen to omit the antifringer coating because it would reduce the chip sensitivity across its bandwidth and it would cost considerably more. The above described experiment was the first time the fringing effect was encountered. Since this was only at the end of this study, a correction scheme for these CCD-artifacts has not yet been provided. Until then, the etalons complicate the data processing of these images to an extent in they are no longer usable. For this reason, acquisition of an image stack in the IR was omitted.

Ultimately, image stacks were acquired from the corroded chain mail link in the red band (615 – 690 nm) and the violet band (385 – 425 nm). After the filter was sent in place a manual focus scan was performed to find optimal focal position for each applied filter.

6.3.4.2 XEOM analysis of the corroded link MR81A2249

Figure 6.8 displays the result of the ROI analysis performed on three distinct locations in the field of view. The upper part of Figure 6.8 displays the analysed area of the link. Unfortunately no image of sufficient quality could be taken of the analysed area with the Andor CCD camera while the link was exposed to broadband white light. Different approaches to illuminate from the side ports have been followed (white LED, tungsten bulb, in presence and absence of diffuser) but were unsuccessful. A novel approach to illuminate the sample through the objective has been designed but is not yet constructed.

When the red filter (615 – 690 nm, Figure 6.8 D) was in place an image stack was recorded in the range of 8905 eV to 9075 eV, with 1 eV resolution and a dwell time of 300 s per point making the acquisition time last over 14 hours. When the violet filter (385 – 425 nm, Figure 6.8 E) was in place, an image stack was recorded as well in the range of 8905 eV to 9075, with a 1 eV resolution, but dwell time could be reduced to 200 s per point due to the higher emission in the violet band. The shorter dwell time decreased the total measurement time to 9.5 hours. Three regions of interest were chosen on different locations in the field of view. The regions of interest were of identical coordinates in both image stacks recorded with different

filters. The first ROI was chosen in the featured area of the red filtered image, ROI 2 was chosen outside this featured area and ROI 3 was chosen outside of the most intense part of the beam footprint for both image stacks.

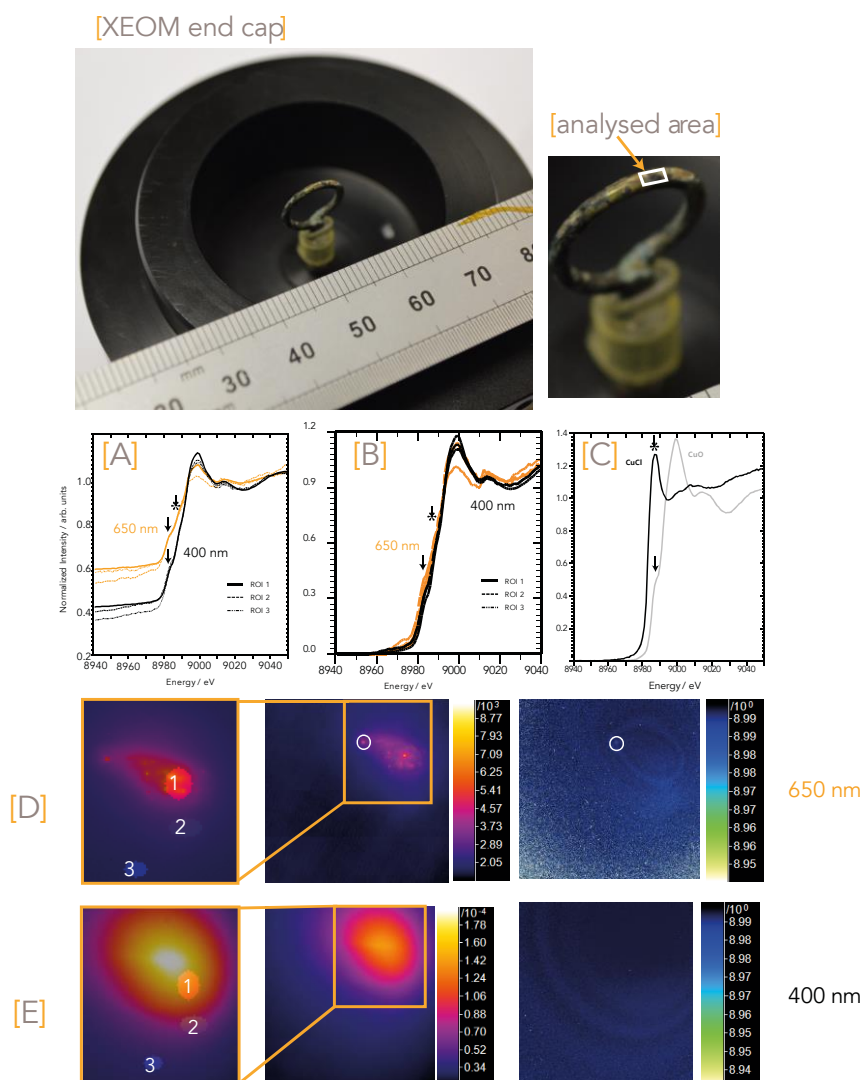


Figure 6.8

Corroded link MR81A2249 mounted in the XEOM 1 end cap and an approximation of the analysed area.

[A] Post-edge normalized spectra extracted out of ROI 1, 2 & 3 indicated in figure D for the red image stack and figure E for the violet image stack.

[B] Background subtracted and post-edge normalized spectra extracted out of ROI 1, 2 & 3 of the red image stack (650 nm, orange spectra) and the violet image stack (400 nm, black spectra).

[C] XEOL-XANES normalized reference spectra of tenorite and nantokite.

[D] Three regions of interest are indicated in enlarged portion of post edge XEOL image acquired through a red filter. The total field of view of the acquired image (in ironbow colour scale) is shown in combination with an edge position map which was created from the red filtered (615 – 690 nm) image stack on the corroded chain mail link MR81A2249.

[E] Three regions of interest indicated in enlarged portion of post edge XEOL image acquired through a violet filter and total field of view of the acquired image (in ironbow colour scale). The edge position map which was created from the violet filtered image stack.

In order to evaluate spectra extracted from the chosen ROI's, the mean post-edge from the spectra in Figure 6.8 A were normalized to 1. The sets of data, both acquired at 400 nm and 650 nm, have significantly different peak to background ratio.

Although the 400 nm signal is overall higher, the 650 nm signal contains a relatively larger pre-edge signal than the 400 nm spectra. Indeed, raw data indicate a significantly reduced edge step for the 650 nm data due to a strongly reduced post-edge signal. In contrast to what has been previously seen for copper chemistry (see chapter 4 and reference [30]) the background observed in both spectra appears to be additive over the whole range of the spectrum; i.e. approximately the same background level is equally present in pre-, mid- and post-edge region. The existence of an additive background is suggested by an upward shift of the 8985 eV edge feature (indicated by an arrow) over a distance which is approximately the same as the difference in pre-edge intensity values of red (650 nm) and violet (400 nm) spectrum. In the alternative case where the background is not additive, i.e. when optical channels giving rise to the pre-edge background switch off upon crossing the absorption edge, edge feature from different spectra would have a similar (normalized) intensity values. Subtraction of the additive backgrounds in all spectra prior to a post-edge normalization results in the spectra plotted in Figure 6.8 B.

As displayed in Figure 6.8 B, both sets of spectra extracted out of the image stacks recorded with red and the violet filter show little chemical differentiation since all spectra can be approximately superimposed. With a faint mid-edge feature around 8985 eV (see arrow), a white line around 9000 eV and a characteristic bump between 9010 and 9020 eV, the spectra extracted from both image stacks are typical of tenorite (see reference in right graph of figure 6.8 C). Although Figure 6.8 A suggested a positive energy shift for the 400 nm spectra, Figure 6.8 B confirms this shift is an artefact due to the difference in peak to background levels. Additional to edge feature at 8985 eV , a hint of another inflection point just before 8990 eV is seen in both spectra. This feature, specified by a star in both Figure 6.8 A & B, corresponds with the white line position of nantokite and therefore suggests its presence in both spectra.

The correspondence between the spectra extracted from the different ROIs within the same image stack is also observed in the edge position maps composed from the image stacks. In both image stacks gentle differentiation is observable. The features in the edge position maps generally correspond with the features seen in the false-colour images, which visualize the profile of the beam convolved with the emission sites on the surface. In the case of red filtered stack (Figure 6.8 D) some extra pinpoint features are visible within the beam profile. The bright pin point features (denoted with white circle) correspond with an edge shift towards lower

energy thus suggesting the presence of nantokite within these spots. Joined with the more homogenous pattern seen in the violet filtered stack, the outcome of these experiments suggest that the surface of the link is covered with a more uniform layer of tenorite combined with a series of nantokite pinholes. Nevertheless, the outcome of the XRF suggests that a substantial amount of Zn, Pb and As is present in the links. Therefore it would be interesting to explore the Zn and As K-edges and/or Pb L-edge. Unfortunately, these measurements could not be performed due to beam time constraints.

6.3.4.3 XEOM analysis of the conserved link MR81A1436

For sake of giving a complete overview of the experiment, Figure 6.9 gives the result of an image stack obtained of the conserved chain mail link MR81A1436. The image shown was recorded for 300 s at 9000 eV X-rays together with the total spectrum extracted out of the image stack. Certainly, this experiment was not as successful as we hoped it would be. The image stack shows clearly an edge around 8979 eV but appears to be tilted with a decaying post edge. With some imagination, the features of a Cu fingerprint can be recognized with a mid-edge feature around 8980 eV and set of double post-edge features. The distorted nature of the spectrum adapts the position of the edge therefore making it impossible to yield a chemical map. As described earlier in section 5.3.2, the XEOL yield of pure copper with respect to its corrosion product is much lower. Either this is the reason of the poor quality of the spectra or the sample was not optimally aligned with the beam. Unfortunately no feature is present yet in the operation software to follow the outcome of the experiment as it is being acquired. Therefore one can only establish if an experiment was suffering from imaging errors after the stack is acquired. In order to confirm this, the experiment should have been repeated. Unfortunately this was impossible due to the limited time available for the experiments.

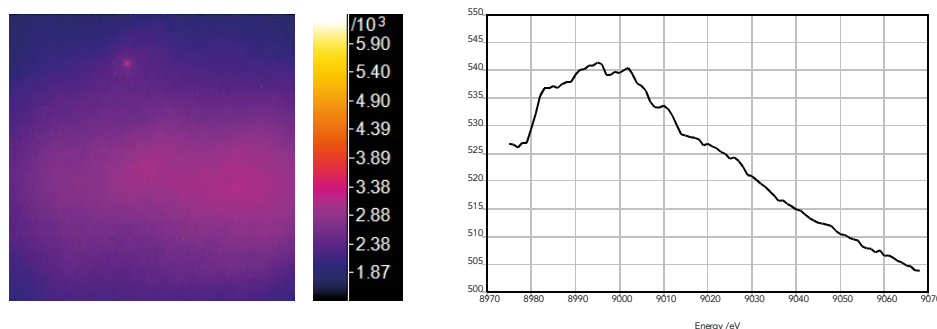


Figure 6.9

Post-edge image recorded at 9 keV from the conserved chain mail link. The spectrum integrated from the total chip area (right) gives hints of copper.

6.4 SR-XRD STUDY OF THE CHAIN MAIL LINKS

In order to better define future conservation routes as well as obtain basic information on Tudor metallurgy, a variety of analytical techniques have been approached to study the corroded and the conserved chain mail link. Information on the elemental composition (XRF) and the short-range atomic order in the bulk (XAS) and on the surface (XEOL, XEOM) have been already been collected and discussed above. Additional information on the long-range atomic order can be obtained with XRD and would provide a more complete set of data on the chain mail link artefacts. Unfortunately, the use of laboratory XRD is problematic for the analysis of (corroded) artefacts with random shapes and geometries. Typically, lab XRD instruments in *Bragg-Brentano* geometry (see 2.4.1.3.1) exhibit a large X-ray footprint on the sample due to the diverging beam. Illuminating samples of complex morphology with such a beam result in a series of height errors causing peak broadening, peak splitting or superposition of patterns with an angular displacement. Therefore, the resultant patterns are often uninterpretable and a different approach is necessary.

During beamtime allocation XI (Table 3.6) a relatively novel method was used in which flat regions of the samples were illuminated with an X-ray beam of relatively small footprint (1.7 mm x 0.5 mm). Data were acquired through an interlaced set of images recorded by scanning a Dectris Pilatus 300K hybrid-pixel detector in 2θ . Subsequent reconstruction of the 1-D XRD pattern in esaProject allows phase analysis via standard methods. Advantageous to this approach is the elimination of height errors with a smaller X-ray beam size; faster acquisition time due to highly intense nature of synchrotron radiation and more precise alignment and selection of the investigated sample area with the eleven-axis Huber diffractometer installed on XMaS.

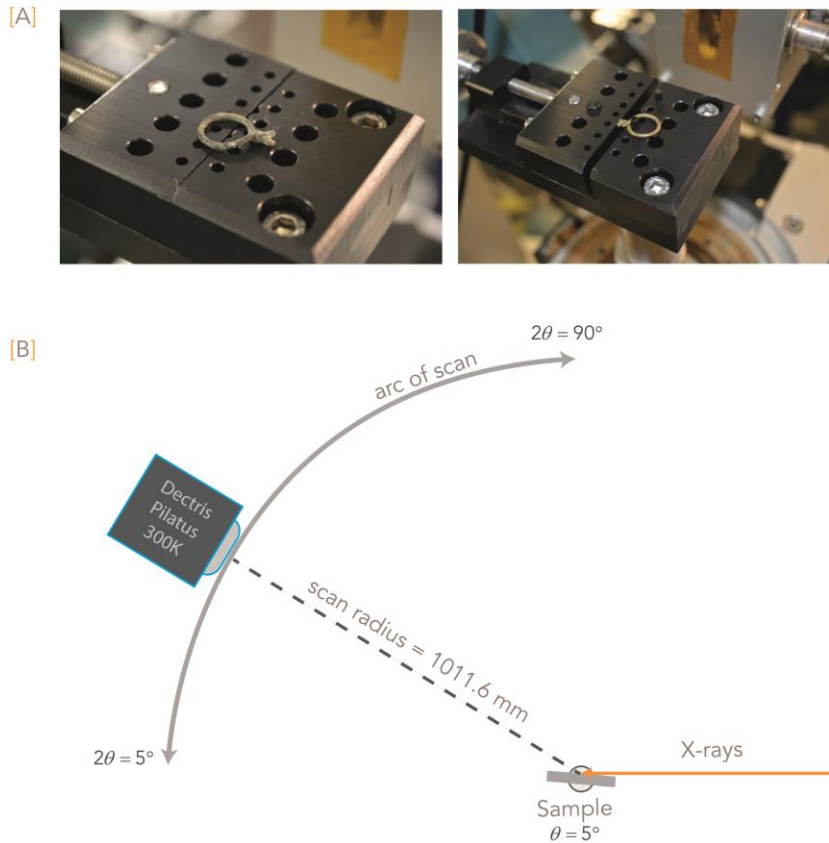


Figure 6.10

[A] All samples were mounted on a soft jawed vice which was fitted onto a motorized xyz-stage.

[B] Schematic overview from the approach followed for acquiring XRD data. The scheme should be perceived as a side view of the experiment.

6.4.1 EXPERIMENTAL APPROACH

Samples were mounted on a tailored soft jawed vise (designed and made by Prof. M.G. Dowsett) which was seated on a motorized xyz stage, in turn, part of the θ -axis of the Huber diffractometer (Figure 6.10 A). A flat region of interest on the chain mail link was aligned with the eucentric position of the goniometer. Subsequently the sample stage was tilted relative to that position so that the incident angle of X-rays was 5° ($\theta = 5^\circ$). Data were collected by scanning a Pilatus 300K hybrid-pixel detector (Dectris, Baden-Daettwil, Switzerland) with its camera face orthogonal to the scan radius (scan radius = 1011.6 mm) from $2\theta = 5^\circ$ to $2\theta = 90^\circ$ in 81 steps (Figure 6.10 B). This implies that the center of the camera face increments each step by $2\theta = 1.042^\circ$. This measure is necessary for subsequent data processing. The Pilatus 300K incorporates three chips, each 487 x 195 pixels, separated by a 17 pixel rows dead space (Figure 6.11 A). In a 1-D pattern these dead spaces would be

visible as large glitches which greatly complicate data processing and phase analysis. Stepping the camera by 1.042° ensures that dead spaces from one image coincide with the chip centres of the next image. Thus, data of the next image can be used to fill the interchip gaps in the current image. A software extension of esaProject (written by Prof. Mark Dowsett) copes with filling the glitches and splices all 81 reprojected images together in one large single merged image, free of dead space. Finally, conversion of the image into a 1-D XRD pattern allows qualitative phase analysis by matching references (Figure 6.11 B).

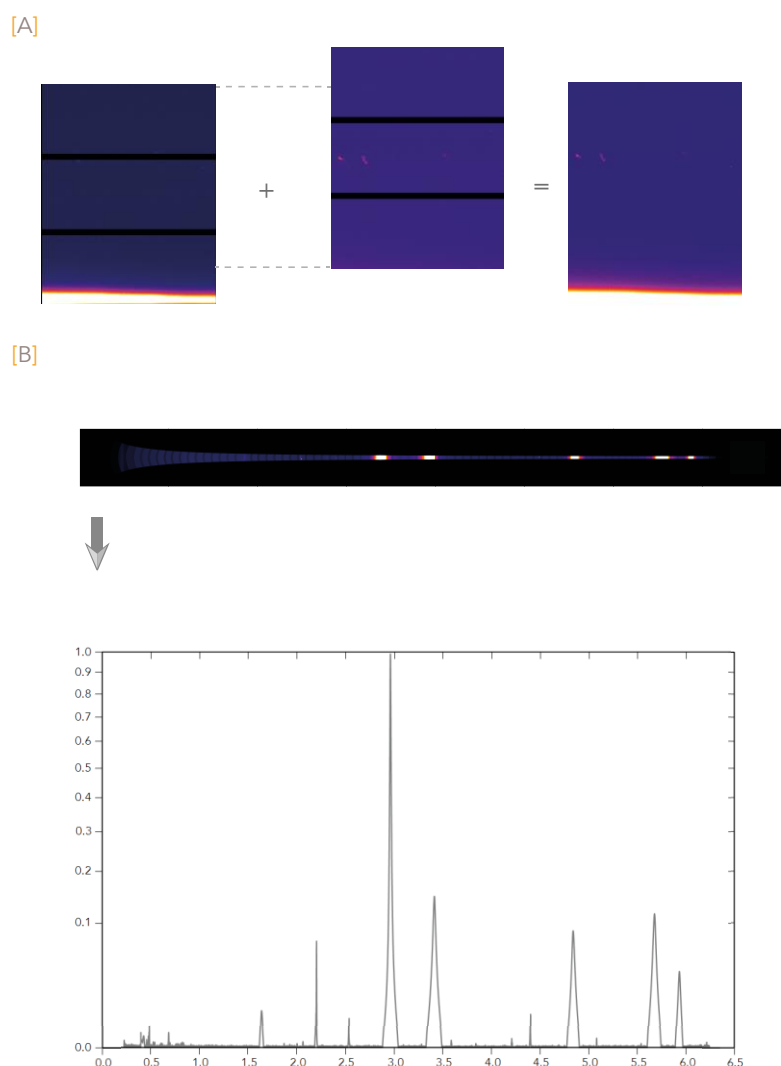


Figure 6.11

[A] First step in combining the separate images together is filling the interchip dead spaces. esaProject uses the next image in the stack to perform this task automatically.

[B] In the following steps, esaProject interlaces all separate image into a single large image containing all information typically seen in 2-D XRD images. Ultimately this can be converted into a 1-D pattern for qualitative and/or quantitative analysis.

6.4.2 XRD ANALYSIS OF THE CORRODED CHAIN MAIL LINK MR81A2249

Figure 6.12 A shows the diffraction patterns of the corroded link MR81A2249 and Figure 6.12 B shows the diffraction pattern of the conserved link MR81A1436. An enlarged version of each separate diffraction pattern can be found in the appendix. Both diffraction patterns are plotted as a function of wave number Q and were converted from 2θ according to equation {2.16}. The background was subtracted and the pattern was normalized to the most intense reflection, the Cu 111 reflection at 3.0 \AA^{-1} . The square root plot is used to emphasize minor reflections. All reflections were subsequently matched to reference diffraction patterns from the MinCryst database [31, 32] in order to identify the unknown phases.

The characteristics of the Pilatus detector allowed us to record data of remarkable quality. Even though a background subtraction procedure was performed, it must be noted that the peak to background ratios of the recorded patterns were very large. Equally notable is the freedom of signal between the assigned reflections in Figure 6.12 and Figure 6.13, which indicates very little inelastic scattering was present during acquisition of the data.

Several corrosion products can be associated with the reflections observed in the diffraction pattern recorded from the as-found chain mail link. This diversity is a logical consequence of the wide variety of dissolved anions (e.g. carbonates, sulfates) present in the sea water or the seabed. Each of which can react either with metallic copper, zinc, lead of the brass structure and precipitate independently as insoluble copper, zinc and lead salts.

Since XRF identified zinc as the main alloying element for copper, it was established that both links are made of brass. Nevertheless, it appears that the corrosion process of the alloy is dominated by the behavior of its major constituent, copper. The substantial presence of metallic copper is also visible in the diffraction patterns with 5 extreme intense reflections. Corrosion of copper under aquatic conditions is a complex interplay between: varying concentration of Cu(I) and Cu(II) species in solution, anions available, oxygen concentration, biological activity on the object and changing chemistry imposed by the local pH. Local fluctuation of these parameters might favor the formation of one corrosion product over another [33]. In this particular case, the majority of copper corrosion products can be associated with compounds found in well-oxygenated marine sites [34–38]. These include copper oxides (cuprite Cu_2O and tenorite, CuO), cuprous chloride (nantokite, CuCl), copper hydroxychlorides (atacamite and paratacamite, both $\text{Cu}_2\text{Cl}(\text{OH})_3$) and copper hydroxycarbonates (malachite, $\text{Cu}_2\text{CO}_3(\text{OH})_2$). However, the Mary Rose was found covered in marine sediments and waste organic materials. In such oxygen depleted

sites, sulfide anions produced by sulfate-reducing bacteria form copper sulphide precipitates with copper ions in solution. Witness of this anaerobic climate is the presence of covellite (CuS) in the diffraction pattern. Nevertheless, the anaerobic patina chemistry is dominated by corrosion formed in an aerobic environment. This might be attributed to the aerobic modifications of the patina following excavation of the chain mail link. Since these artefacts have been recovered from the bottom of *The Solent* over 30 years ago, the latter should not be underestimated. Moreover, formation of chalcocite (Cu₂S) is favored over covellite in pure anoxic conditions [33]. No reflections matching a chalcocite reference are detected in Figure 6.12, an observation which might indicate the subsequent oxidation of chalcocite to covellite [39].

Zinc, the remaining significant alloying element, is only visible in the presence of mostly zincite (ZnO) and to a lesser extent zincosite (ZnSO₄). The presence of zincite might be the result of post-excavation oxidation of zinc phases present in the chain mail link. Other corrosion products of zinc are generally not found on brasses recovered from marine environments, due to the high solubility of zinc compounds. Only traces of calcite (CaCO₃), the major constituent of marine concretion, could be identified on the corroded link. Copper-based artefacts are generally found lightly concreted since most copper compounds are toxic to marine organisms, therefore greatly inhibiting the growth of concretion [33, 40]. Finally, for sake of completion, a set of minor reflections in the corroded link could be addressed to the presence of metallic lead.

6.4.3 XRD ANALYSIS OF THE CONSERVED CHAIN MAIL LINK MR81A1436

Figure 6.12 B shows the 1-D diffraction pattern yielded from the interlaced image stack recorded from the conserved link MR81A1436. The background was subtracted and the pattern was normalized to the most intense reflection, the Cu 111 reflection at 3.0 \AA^{-1} . The square root plot is used to emphasize minor reflections. All reflections were subsequently matched to reference diffraction patterns from the MinCryst database [31, 32] in order to identify the unknown phases.

The data recorded from both chain mail links with XRF suggested an almost identical elemental composition of both chain mail links (Figure 6.4). Analysis of both chain mail links is therefore a good exercise to study the influence of the conservation. Within this context is prevention of *bronze disease* the main aim of marine copper conservation [33]. As confirmed by the previous paragraph, copper-bearing artefacts raised from the sea contain large quantities of chlorides in the form of nantokite, paratacamite and /or atacamite. The chloride-rich corrosion might exist either on the surface of the artefact or in cracks. Nantokite is unstable in air and will react, after excavation, with oxygen and water vapour into copper hydroxychlorides and hydrochloric acid. The released hydrochloric acid may in turn react with free cuprous ions therefore sustaining this cyclic corrosion process better known as '*bronze disease*' [38, 41–43]. The influence of the conservation is visible in the diffraction pattern since no reflections of chloride-based corrosion products are observed. The pattern is dominated by five intense reflections originating from metallic copper. The dominating reflections indicate that surface corrosion is thin with respect to the X-ray escape depth. Non-metallic copper is only present in the form of the passivating cuprite, due to oxidation of metallic copper or conversion of cuprous chlorides, and tenorite. A rather good match of the reflection pair between $1\text{--}1.2 \text{ \AA}^{-1}$ could be found with the reference of copper carbonate ammonia ($\text{CuCO}_3 \cdot 2\text{NH}_3$). Therefore this reflection pair indicate of the conservation treatment with ammonium citrate containing 'Modalene'.

Metallic lead is seen in the diffraction pattern of Figure 6.13. As zinc is added to copper to make brass, a single phase solid solution is created where its diffraction pattern is very similar to pure copper, provided that $\text{Zn} < 35 \text{ \% w/w}$. The strong reflections around 3 \AA^{-1} , 3.5 \AA^{-1} , 4.9 \AA^{-1} and 5.7 \AA^{-1} which are typical for metallic copper and the presence of some Zn (XRF data in paragraph 6.3.2 and unpublished EDX data) justifies the assignment of those reflections to and Hence no separate metallic copper and zinc patterns can be assigned to fcc (face centred cubic) α -brass.

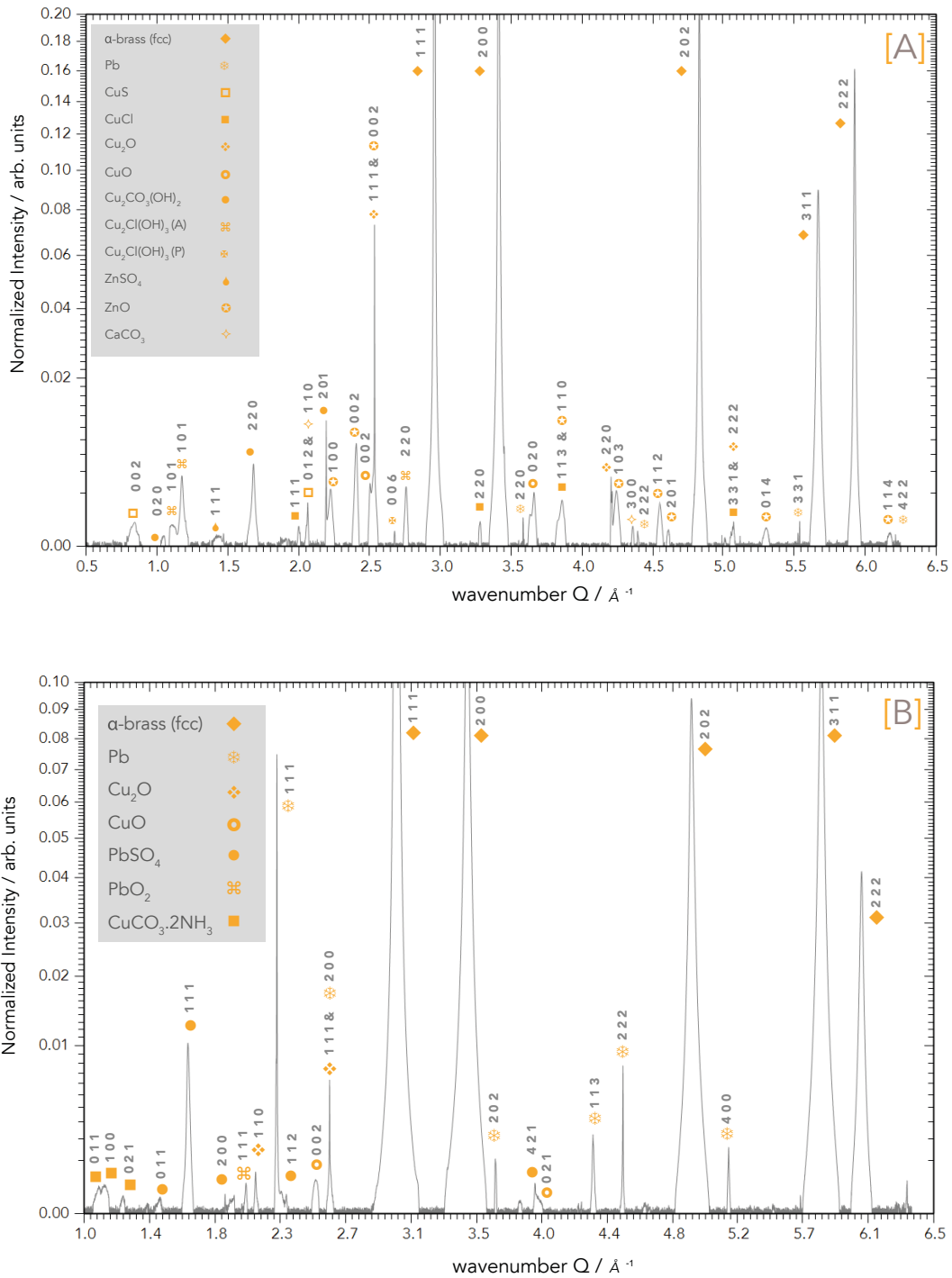


Figure 6.12

[A] 1-D diffraction pattern recorded from the as-found chain mail link MR81A2249.

[B] 1-D diffraction pattern recorded from the conserved chain mail link MR81A1436.

Presumably, the analysed area contained a lead grain since lead has a limited solubility in brass alloys and metallic lead is generally dispersed as discrete droplets [33, 38]. Anaerobic underwater conditions support the growth of anglesite (PbSO_4),

which forms a passivating film protecting the underlying brass from further corrosion [44]. Moreover, N.A. North describes in [45] anglesite not being attacked by citric acid solutions (like Modalene) used during chemical stripping procedures, hence justifying the assignment of PbSO_4 .

Given the high quality of the XRD data, it would be possible to further investigate the brass alpha phase and calculate how much zinc is currently present. Careful analysis of the shift of the α -brass (fcc) diffraction pattern w.r.t. the exact metallic Cu position can reveal how much Zn is present. The original content, intended by the Tudor blacksmith, could however be significantly altered. Selective removal of zinc from the alloy during conservation is likely since zinc corrosion compounds readily dissolve in citric acid [46]. Alternatively, the loss of zinc might be the result of a process known as *dezincification* [47, 48]. Dezincification, a prevalent brass corrosion phenomenon favoured in anaerobic conditions, is the result of the selective dissolution of zinc or the dissolution of both copper and zinc followed by selective deposition of copper. In either case, determination of the alloy composition based on peak shift of α -brass w.r.t. metallic copper is impossible as the sample shape of the chain mail links is not suited for this analysis. The rough and curved shape of the samples results in height errors which would lead to additional peak shifts.

6.5 CONCLUSIONS

Two chain mail links, recovered from the King Henry VIII's flagship the Mary Rose, formed the research topic of this chapter. Both an as-found link MR81A2249 and a conserved link MR81A1436 were subjected to a measuring session in which XAS, XEOL-XAS & XEOM data could be acquired simultaneously. Subsequently shifting the X-ray energy up to 14 keV allowed us to gather elemental information through XRF data. The capability of XEOM 1 to carry out all these different methods without changing the experimental set-up once the sample is installed, is clearly an asset. Moreover, the integrity of the objects is maintained since the larger X-ray beam footprint leads to moderate irradiance of the unique samples. The elemental and short-range atomic order information provided by XRF and XAS/XEOL-XAS/XEOM was supplemented with long-range atomic order of synchrotron X-ray diffraction. In a relatively novel approach, high-resolution crystallographic data was gathered from both chain mail links. This alternative approach simplified substantially data analysis with respect to XRD data collected from a laboratory diffractometer.

Elemental analysis revealed Zn as the major alloying element to copper. Accordingly, the alloy both links were made of is identified as brass. Cu *K*-edge XEOL-XAS and XAS data suggests a metallic copper substrate covered with a tenorite layer in the top 200 nm of the sample. Diffraction data, recorded from a different area on both the corroded and conserved link, suggests that post-excavation corrosion altered the patina of the corroded link, which presumably was formed in anaerobic conditions. The presence of tenorite on the as-found link is confirmed, however it is likely that the beam was focused on a discrete tenorite patch during the XEOM measurement. All approaches applied to the conserved link, endorse the efficiency of the applied conservation method. No signs of destructive chloride-traces, which might cause bronze disease, could be observed. Moderate lateral resolution due to either a lack of contrast or insufficient statistics (or both) is nevertheless confirmed in the XEOM data.

6.6 BIBLIOGRAPHY

- [1] M. Murphy, X. Zhou, F. Heigl, T. Regier, T. Sham, An X-Ray Excited Optical Luminescence (XEOL) Analysis of Mn²⁺ Doped ZnS Nanostructures, *Nanostructures* 882 (2007) 12–14.
- [2] L. Armelao, F. Heigl, A. Ju, R.I.R. Blyth, T. Regier, X. Zhou, X-ray Excited Optical Luminescence Studies of ZnO and Eu-Doped ZnO Nanostructures, (2007) 10194–10200.
- [3] F. Heigl, A. Jürgensen, X.-T. Zhou, S. Lam, M. Murphy, J.Y.P. Ko, T.K. Sham, R.A. Rosenberg, R. Gordon, D. Brewes, T. Regier, L. Armelao, Dynamic View on Nanostructures: A Technique for Time Resolved Optical Luminescence using Synchrotron Light Pulses at SRC, APS, and CLS, *AIP Conf. Proc.* (2007) 1202–1205.
- [4] Z. Wang, X. Guo, T.-K. Sham, 2D XANES-XEOL mapping: observation of enhanced band gap emission from ZnO nanowire arrays, *Nanoscale* 6 (2014) 6531.
- [5] R.A. Rosenberg, G.K. Shenoy, F. Heigl, S.T. Lee, P.S.G. Kim, X.T. Zhou, T.K. Sham, Effects of in situ vacuum annealing on the surface and luminescent properties of ZnS nanowires, *Appl. Phys. Lett.* 86 (2005) 2631151–1 – 263115–3.
- [6] M.J. Ward, W. Han, T. Sham, 2D XAFS - XEOL Mapping of Ga_{1-x}Zn_xN_{1-x}O_x Nanostructured Solid Solutions, *J. Phys. Chem. C* 115 (2011) 20507–20514.
- [7] P.-S.G. Kim, N.O. Petersen, T.K. Sham, Y.F. Hu, Soft X-ray excited optical luminescence (XEOL) studies of fluorescein isothiocyanate (FITC) and FITC-labeled proteins, *Chem. Phys. Lett.* 392 (2004) 44–49.
- [8] D. McElvogue, *Tudor Warship Mary Rose*, Bloomsbury Publishing, 2015.
- [9] D. Childs, *The Warship Mary Rose: The Life and Times of King Henry VIII's Flagship*, Pen & Sword Books Limited, 2014.
- [10] A.J. Stirland, *The Men of the Mary Rose: Raising the Dead*, History Press, 2013.
- [11] J. Evans, *Preserving the Mary Rose*, Mole (2014).
- [12] M. Sandström, F. Jalilehvand, E. Damian, Y. Fors, U. Gelius, M. Jones, M. Salomé, Sulfur accumulation in the timbers of King Henry VIII's warship Mary Rose: a pathway in the sulfur cycle of conservation concern., *Proc. Natl. Acad. Sci. U. S. A.* 102 (2005) 14165–14170.
- [13] A. V. Chadwick, A. Berko, E.J. Schofield, A.D. Smith, J.F.W. Mosselmans, A.M. Jones, G. Cibin, The application of X-ray absorption spectroscopy in archaeological conservation: Example of an artefact from Henry VIII warship, the Mary Rose, *J. Non. Cryst. Solids* (2016) 1–7.
- [14] M. Sandström, F. Jalilehvand, I. Persson, U. Gelius, P. Frank, I. Hall-Roth, Deterioration of the seventeenth-century warship Vasa by internal formation of sulphuric acid., *Nature* 415 (2002) 893–897.
- [15] E. Hocker, G. Almkvist, M. Sahlstedt, The Vasa experience with polyethylene glycol: A conservator's perspective, *J. Cult. Herit.* 13 (2012) S175–S182.
- [16] The Mary Rose, [Http://www.maryrose.org/](http://www.maryrose.org/).
- [17] the mary rose museum, [Http://www.thetimes.co.uk/tto/multimedia/archive/00417/127548747__417959b.jpg](http://www.thetimes.co.uk/tto/multimedia/archive/00417/127548747__417959b.jpg).
- [18] E.J. Schofield, R. Sarangi, A. Mehta, A.M. Jones, F.J.W. Mosselmans, A. V. Chadwick, Nanoparticle de-acidification of the mary rose, *Mater. Today* 14 (2011) 354–358.
- [19] K.M. Wetherall, R.M. Moss, A.M. Jones, A.D. Smith, T. Skinner, D.M. Pickup, S.W. Goatham, A. V. Chadwick, R.J. Newport, Sulfur and iron speciation in recently recovered timbers of the Mary Rose revealed via X-ray absorption spectroscopy, *J. Archaeol. Sci.* 35 (2008) 1317–1328.
- [20] M. Finšgar, I. Milošev, Inhibition of copper corrosion by 1,2,3-benzotriazole: A review, *Corros. Sci.* 52 (2010) 2737–2749.
- [21] H.B. Madsen, A preliminary note on the use of benzotriazole for stabilising bronze objects, *Stud. Conserv.* (1967) 163–166.
- [22] B. Vekemans, K. Janssens, L. Vincze, F. Adams, P. Van Espen, Analysis of X-ray spectra by iterative least squares (AXIL) - New developments, *X-Ray Spectrom.* 23 (1994) 278–285.
- [23] I. Constantinides, A. Adriaens, F. Adams, Surface characterization of artificial corrosion layers on copper alloy reference materials, 189 (2002) 90–101.
- [24] A. Thompson, D. Attwood, E. Gullikson, M. Howells, K.-J. Kim, J. Kirz, J. Kortright, H. Winick, I. Lindau, Y. Liu, P. Pianetta, A. Robinson, J. Scofield, J. Underwood, G. Williams, *X-ray Data Booklet*, 2009.
- [25] R.E. Van Grieken, A.A. Markowicz, *Handbook of X-ray Spectrometry: Methods and Techniques*,

Marcel Dekker Inc., 1993.

[26] B. Beckhoff, B. Kanngiesser, N. Langhoff, R. Wedell, H. Wolff, *Handbook of Practical X-ray Fluorescence Analysis*, Springer - Verlag, Berlin Heidelberg, 2006.

[27] C.S. Schnorr, M.C. Ridgway, *X-Ray Absorption Spectroscopy of Semiconductors*, Springer Berlin Heidelberg, 2014.

[28] Andor Technologies, Optical Etaloning in CCDs and EMCCDs.

[29] R. scientific Germany, Spectroscopic Etaloning in Back Illuminated CCDs.

[30] A. Adriaens, P. Quinn, S. Nikitenko, M.G. Dowsett, Real Time Observation of X-ray-Induced Surface Modification Using Simultaneous XANES and XEOL-XANES., *Anal. Chem.* 85 (2013) 9556–9563.

[31] MinCryst [online] Available: <http://database.iem.ac.ru/mincryst/index.php>, [accessed june 2014].

[32] A. V Chichagov, D.A. Varlamov, R.A. Dilanyan, T.N. Dokina, N.A. Drozhzhina, O.L. Samokhvalova, T. V Ushakovskaya, MINCRYST: a crystallographic database for minerals, local and network (WWW) versions, *Crystallogr. Reports* 46 (2001) 876–879.

[33] C. Pearson, *Conservation of marine archaeological objects*, 1990.

[34] I.D. MacLeod, Formation of marine concretions on copper and its alloys, *Int. J. Naut. Archaeol.* 11 (1982) 267–275.

[35] R.J. Taylor, I.D. Macleod, Corrosion of bronzes on shipwrecks - a comparison of corrosion rates deduced from shipwreck material and from electrochemical methods, *Corrosion* 41 (1985) 100–104.

[36] I.D. Macleod, Conservation of corroded copper alloys: a comparison of new and traditional methods for removing chloride ions, *Stud. Conserv.* 32 (1987) 25–40.

[37] P. Stoffyn-Egli, D.E. Buckley, J.A.C. Clyburne, Corrosion of brass in a marine environment: Mineral products and their relationship to variable oxidation and reduction conditions, *Appl. Geochemistry* 13 (1998) 643–650.

[38] L. Selwyn, C.C. Institute, *Metals and Corrosion: A Handbook for the Conservation Professional*, Canadian Conservation Institute, 2004.

[39] E.D. Mor, A.M. Beccaria, Behavior of copper in artificial sea water containing sulfides., *Br. Corros. J.* 10 (1975) 33–38.

[40] E. Angelini, S. Grassini, S. Tusa, in: European Federation of Corrosion (EFC) Series, Woodhead Publishing, 2013, pp. 236–259.

[41] D. Scott, Bronze disease: a review of some chemical problems and the role of relative humidity, *J. Am. Inst. Conserv.* 29 (1990) 193–206.

[42] D.A. Scott, *Copper and Bronze in Art: corrosion, colorants, conservation*, The Getty conservation institute : Los Angeles, 2002.

[43] R. Grayburn, M.G. Dowsett, M. Hand, P.-J. Sabbe, P. Thompson, A. Adriaens, *Bronze Disease Revealed? A synchrotron X-ray diffraction study of nantokite hydrolysis*, 2014.

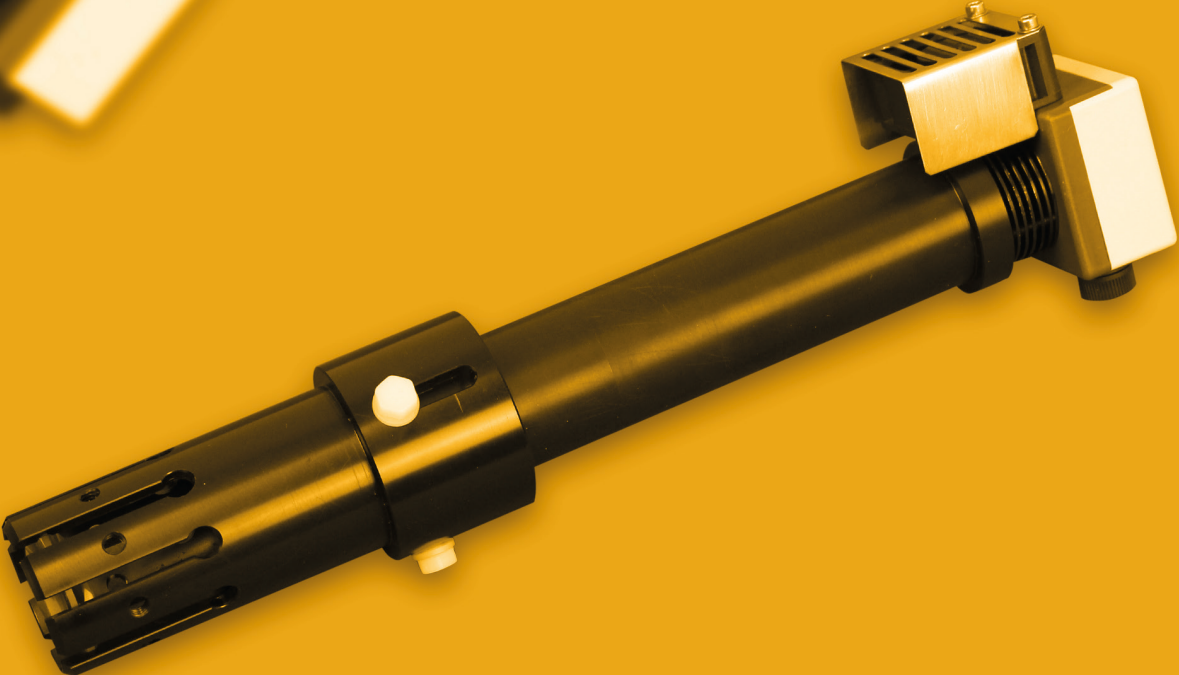
[44] G.L. Gardner, G.H. Nancollas, Complex formation in lead sulfate solutions, *Anal. Chem.* 42 (1970) 794–795.

[45] N.A. North, Butterworth-Heinemann, Oxford, 1987, pp. 207–252.

[46] R. Larba, I. Boukerche, N. Alane, N. Habbache, S. Djerad, L. Tifouti, Citric acid as an alternative lixiviant for zinc oxide dissolution, *Hydrometallurgy* 134–135 (2013) 117–123.

[47] H. Sugawara, H. Ebiko, Dezincification of Brass, *Corros. Sci.* 7 (1967) 513.

[48] G. Joseph, M.T. Arce, Contribution To the Study of Brass Dezincification, *Corros. Sci.* 7 (1967) 597–605.



**Design of an UV-C
illumination module for
laboratory applications and
testing of XEOM 1**

CHAPTER 7

A major difficulty in the development and evaluation of XEOM 1 is the need for beam time when doing experiments which require X-rays. Although we have been fortunate to deploy XEOM 1 during 10 different beamtime allocations on both DUBBLE and XMaS, more beam time is still required for fully understanding, testing and improving all features (hardware, software, sample chemistry, etc.) of this project. Owning a laboratory excitation source would therefore be extremely convenient for long-term assessment of the microscope. Moreover, XEOM 1 could have a broader impact if it could be migrated outside the synchrotron and become available for laboratory or on-site applications. Installing an intense monochromatic laboratory X-ray source would be ideal, but requires substantial funding and would be a Ph.D. study in its own right. Visible light has already been used as a medium to evaluate certain features of XEOM 1's lens system and can be used for traditional microscopy. Unfortunately, visible light only provides morphological information and does not lend itself to do spectroscopy on our samples of interest. Furthermore, with the prospect on a future spectroscopy extension to XEOM 1 (see section 8.2), an illumination source which can cause luminescence or produce photochemical reactions is desirable.

Ultraviolet-induced visible fluorescence has proven useful in art conservation as an examination and photographic technique for over 80 years [1]. With this in mind, the possibility of using UV-C radiation as excitation source for inducing luminescence within heritage and other samples is of great potential. A UV-C-LED emitting 255.6 nm-radiation, already present in our group, provides a base for exploring the feasibility of this approach. However, using the LED in an optimal, convenient and a safe manner requires a separate module. This chapter outlines the designing process of a novel UV-C illumination module serving as an extension to XEOM 1 for laboratory practice. The first experimental results are additionally presented.

7.1 INTRODUCTION

Ultraviolet radiation induces visible fluorescence through excitation of double bonds in conjugated organic systems or band edge excitonic emission in inorganic systems [2, 3]. The latter has been called ultraviolet excited optical emission (UVEOL) [4, 5] and is the same as the end stages of the XEOL mechanism. UVEOL, like XEOL, is influenced by crystal defects such as vacancies and impurities and therefore the luminescence provides information regarding the electronic structure. Especially in the field of art, UV-induced fluorescence is a widely exploited method for studying the surface of artefacts. In the earliest stages, the technique was mainly practiced as a visual tool to detect heterogeneities and diversities in archeological objects. Earlier restorations (retouching, coatings, varnishes) can be discovered or the complex

layering of pigment mixtures in samples can be studied with UV, exploiting the dissimilarity in emission color due to different chemistries [2, 6–8]. Sometime later, UV-induced luminescence spectroscopy was proposed for chemical analysis of cultural heritage [2, 8]. For example paint pigment particles [9], the influence of varnishes on the pigment [7] and the varnishes on Daguerrotypes [3, 10] have been studied. Furthermore, the first UV-induced luminescence spectromicroscopy results have been presented. Thoury et al. [2] developed a synchrotron end-station in which heterogeneities within semiconductor pigments could be mapped at the submicrometer scale. Vacuum ultraviolet (VUV) and UV-visible emission generated by a bending magnet at SOLEIL (Paris, France) was used as an excitation source. The benefits of a synchrotron to carry out such experiments are clear (for more information see paragraph 2.1.3), but would again require beamtime. The objective of this chapter is to design an illumination source to substitute for beam line testing during the development process of XEOM 1.

Fortunately many sources, other than a synchrotron, are able to generate UV light. Generally, radiation within the UV spectrum can be subdivided by wavelength into four distinct regions according to the ISO-21348 standard [11]: UV-A (315– 400 nm), UV-B (280 – 315 nm), UV-C (100 – 280 nm) and Vacuum UV (VUV, 10 – 200 nm). Traditionally, UV light in the range of 200 – 380 nm has been generated using mercury, xenon, deuterium, metal halide and hollow cathode light sources [6, 12]. Recent successes in UV optoelectronics have led to the development of UV light emitting diodes (LEDs) operating below 300 nm [13–15]. Regardless of the fact that a 255 nm UV-C LED could be recycled from an earlier project (i.e. no purchase cost), the use of a LED has a number of benefits in this project [12, 16, 17] :

- The lower voltage required by the LED enables the use of a simple and safe power source. Generally, electronic circuitry can be relatively simple.
- LEDs have lower power consumption, higher power conversion than existing lamp sources and do not require a warm-up phase.
- The lifetime of a LED is up to 10 times higher than e.g. mercury lamps.
- LEDs are much more compact than lamp sources hence allowing flexible design of the new UV-C module.

Because of this advantages, the use of UV-C LEDs are of growing interest in many application fields. Although UV-C LEDs are relatively novel, their use is already incorporated in water treatment applications [17–21]; phototherapy of dermatological disorders [22]; sterilization of medical tools [21]; UV curing of inks, adhesives and coatings [23] and determination of biological macromolecules like proteins, DNA and RNA [12, 24].

When working with UV-C radiation one must not underestimate the damage that UV-C can cause. UV-C radiation is the most hazardous portion of the UV spectrum and can cause severe eye and skin injuries such as erythema, cataracts, photokeratitis or photoconjunctivitis [3]. Moreover, UV-C can create environmental oxygen radicals with the formation of toxic ozone, causing possible respiratory problems. The use of the right protective equipment is essential. Polycarbonate UV-C blocking goggles or face shields and naked skin covering must be worn at all time during experimentation.

7.2 A NOVEL UV-C ILLUMINATION MODULE

7.2.1 DESIGN BRIEF AND CONSIDERATIONS

The design brief was to create an alternative excitation source to X-rays in order to test and evaluate XEOM features and potentially expand the use of XEOM 1 to ultraviolet induced visible luminescence microscopy (UVEOM). A primary design goal for the UV-C illumination module was to keep the module as simple and low-priced as possible. In this regard, recovery of components from previous projects was essential. A High Power UVCLEAN® Lamp (for more details see paragraph 7.2.2.1) was recovered from a Secondary Ion Mass Spectrometry (SIMS) experiment (by Mark Dowsett and Richard Morris) in which a novel approach was tested to perform SIMS analysis on insulating surfaces. The LED was used as an alternative to an electron beam to induce surface conductivity in the studied insulating materials.

However, as detailed further in paragraph 7.2.2.1, the UVCLEAN® lamp actually consists of 9 separate emitters organized in a 3 x 3 pattern (Figure 7.1). Using the LED alone would result in poor irradiance (power per unit area) of the sample when the LED is positioned sufficiently far from the object to avoid imaging of the 3 x 3 pattern on the illuminated sample. Using the lamp in combination with a simple optical column (one fused silica objective lens) placed so as to image the pupil of the LED optical system (formed by the emitter array and the immersion lens of the LED) onto the sample, will eliminate the structure due to the 9 separate emitters. Moreover, an objective lens can confine all emerging UV-C photons into a 1 – 1.5 mm diameter spot increasing the irradiance substantially.

When functioning, a forward current flows through the LED. At short wavelengths, LEDs are still very inefficient and most of the electrical power is dissipated in the form of heat in addition to the UV-C light. Excess heat has a negative impact on the light output and the lifetime of the LED [25]. With a cost of approximately 1000 EUR

per LED, an adequate thermal dissipation system is essential. Therefore, a heatsink and a fan were incorporated in the illumination module for thermal management.

In conclusion, the design features of the illumination module included:

- objective lens for focusing light intensity but located so as not to image the array onto the sample;
- heat dissipation mechanism for efficient cooling of the LED ;
- light-tight housing blocking unwanted stray light and protection the operator from leaking UV-C;
- a solid and compact design for transportability;
- a simple and inexpensive design for proof of concept.

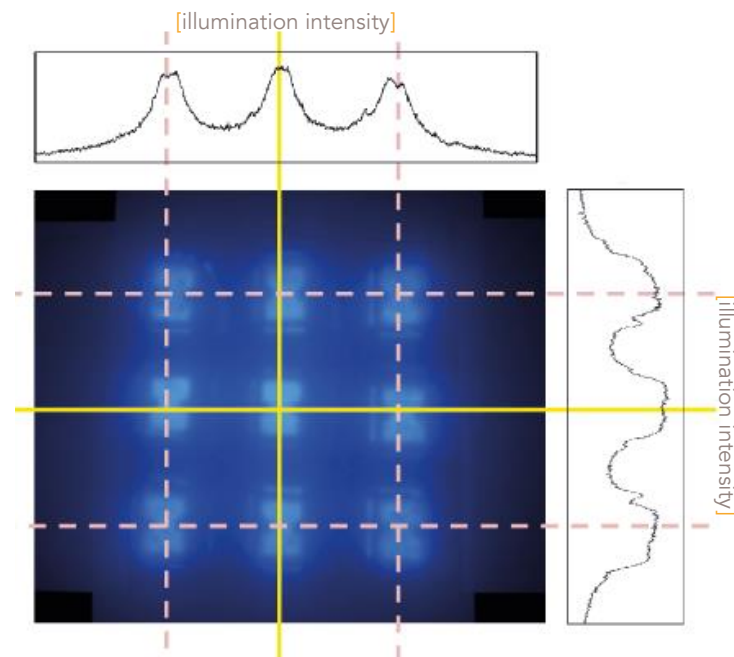


Figure 7.1

The UVCLEAN® exists out of 9 discrete UV-C sources organised in a 3 x3 array. Image and intensity profile were recorded by Michael Abbott (University of Warwick, 2014).

7.2.2 COMPONENTS

7.2.2.1 UV-C LED

A High Power UVCLEAN® Lamp (UVCLEAN255HS-3) manufactured by SETi (Sensor electronic technology, Columbia, South-Carolina, United States) was used in this project. The LED exhibits a peak wavelength of 255.6 nm with a spectral bandwidth of 11.1 nm according to the quality inspection report provided by the supplier, i.e. the source may be considered as quasi-monochromatic. The maximum optical output power of the lamp is 3 mW. Unlike lasers, LEDs possess a wide angle

distribution emitting radiation in all directions [25]. Therefore the UVCLEAN® lamp is fitted with a hemispherical window producing a collimated beam with divergence angles limited to 10°. The UVCLEAN® lamp is a ninefold multi-chip array of UV LEDs enclosed in a metal glass package. Manufacturers produce larger LED sources preferably in arrays rather than as a continuous device due to restrictions in active area size of the LED die (chip) and better handling of waste heat [15, 25]. Figure 7.1 displays the beam profile of the 3 x 3 LED array arrangement of the UVCLEAN® lamp.

7.2.2.2 LENS

As mentioned in paragraph 7.2.1, the beam profile exhibited by the multi-chip array might be more troublesome than one would instantaneously think. Especially during imaging experiments, non-uniform beam profiles might complicate data treatment. Correct application of an objective lens will produce a demagnified image of the virtual pupil of the UV-C LED source onto the sample holder in XEOM. Apart from removing the structure in the beam profile, confining all radiant power into a small beam spot has a beneficial effect on the irradiance of the illumination system. The lens must be sufficiently large in order to maximally collect the light from the diverging beam of the diode, but small enough to fit one of the entrance ports of XEOM 1. Valuing the design condition of keeping the module as cheap as possible, an objective lens was recovered from the ODXAS 1 system (see paragraph 1.3.4 and [26]).

The objective lens is a biconvex LXS4040 lens (Knight Optical, Harrietsham, UK), 40 mm diameter and has a 40 mm focal length. The lens is made from UV-grade fused silica and has no anti-reflection coating. Only the 45° angle port is sufficiently large, diameter between 45.000 mm – 45.039 mm, to fit the lens which means that the wall thickness of any cartridge holding lens will be approximately 2.5 mm which should be sufficient.

7.2.2.3 Current source and Electronics

As mentioned earlier in paragraph 7.1, application of a LED allows one to use relatively simple electronics and cheap and safe power source, i.e. no high voltage is required. The current source necessary to drive the LED was designed and built by Jorge Alves Anjos.

The current source was incorporated as a separate module in the XEOM 1 system. Since the use of the illumination module is associated with the use of the imaging system, it was chosen to use the 24 V DC (direct current) power supply from the electronics interface unit (EIU). Nevertheless the illumination system can be used separately from XEOM 1 with a separate power source or even a battery pack e.g. for field work. Since LEDs are current driven and the EIU provides voltage, a voltage-

to-current converter integrated circuit (XTR110, Texas Instruments, Dallas, Texas, United States) was incorporated into the current source box. The radiant power of the LED varies linearly between 0.2 – 3.16 mW when current is varied between 20 to 270 mA. A potentiometer allows the user to do this and a digital display reads out the current fed to the LED. The LED, fuse and connectors for the current source are enclosed in a small box made from ABS plastic sitting at the end of the illumination module. The box was manufactured by Bopla (Bünde, Germany RS catalog number =161-8179). The fan used for cooling the LED and ABS housing is directly driven by the 24 V. Additionally, a 300 mA fuse was installed to protect the LED against excess current. Figure 7.7.B displays the final result of the current source. Notice its compact design for easy transportability.

7.2.2.4 Heat sink and fan

High temperatures can have a negative effect on the electrical to optical conversion efficiency of the LED and shorten the device lifetime. Proper removal of the waste heat is therefore necessary. A heat sink in combination with a fan is used for transferring the heat away from the diode. The fan will be mounted orthogonal to the heat sink and will blow cool air through its fins to remove thermal energy more efficiently [27].

A radial fin, 38.1 mm diameter x 17.58 mm BGA heat sink (2298 BG) from AAVID Thermalloy (Laconia, New Hampshire, USA, RS components part number 103-960) was used. Holes for fitting the LED and mounting the heatsink onto the illumination module were added in the workshop of the chemistry department by Davy de Pauw. The fan chosen for this project was DC Axial fan (MC25101V1-000U-A99) from the MagLev series by Sunon (Kaohsiung City, Taiwan). The fan has a surface of approximately 25 x 25 mm² and covers the completely the heatsink and additionally cools the ABS box.

7.2.3 DESIGN PROCESS

7.2.3.1 Experiments prior to design

The objective lens in the optical column serves the purpose of making a focused, demagnified image of the UV-C LED virtual source onto the sample holder of XEOM. Since the position of the source is unknown, it has to be determined by experiment so that the optical system can be designed correctly.

Figure 7.2 outlines how the virtual source was located. The virtual source is positioned at a unknown distance L_0 away from the front of the lens of the LED. With

the aid of an optical bench, the L_0 was determined in a two-step experiment. In a first step, a white screen was positioned at a distance L_1 away from the face of the LED. When the LED is powered a projected image of the 3 x 3 array of point sources (similar as in Figure 7.1) is visible on the screen. At this stage d_1 , the height of the projected image, is carefully established with a Vernier caliper. During the second step, this operation is repeated where height of the projected image d_2 is established at a different screen position L_2 . According to the diagram in Figure 7.2 :

$$\begin{aligned} \frac{L_0 + L_1}{d_1} &= \frac{L_0 + L_2}{d_2} \\ \Leftrightarrow L_0 \left(\frac{1}{d_1} - \frac{1}{d_2} \right) &= \frac{L_2}{d_2} - \frac{L_1}{d_1} \quad \{7.1\} \\ \Leftrightarrow L_0 &= \frac{L_2 d_1 - L_1 d_2}{d_2 - d_1} \end{aligned}$$

After repeating the experiment 3 times with values for L_1 varying between 80 and 130 mm and L_2 between 210 and 320 mm, an average value of 5.69 ± 0.61 mm was calculated for L_0 .

Knowing the location of the UV-C source, the position of the objective lens and the LED with respect to XEOM sample holder can be determined. Figure 7.3 displays the effect of the biconvex objective lens on an object. The lens, represented by its two principal planes, has focal lengths of f and f' . Object and image distances are respectively S and S' and heights of object and image are labelled as h and h' . The lateral magnification (m) of the objective lens can be determined by the ratio of image size and object size. According to Figure 7.3 this means that:

$$m = \frac{-x'}{f}. \quad \{7.2\}$$

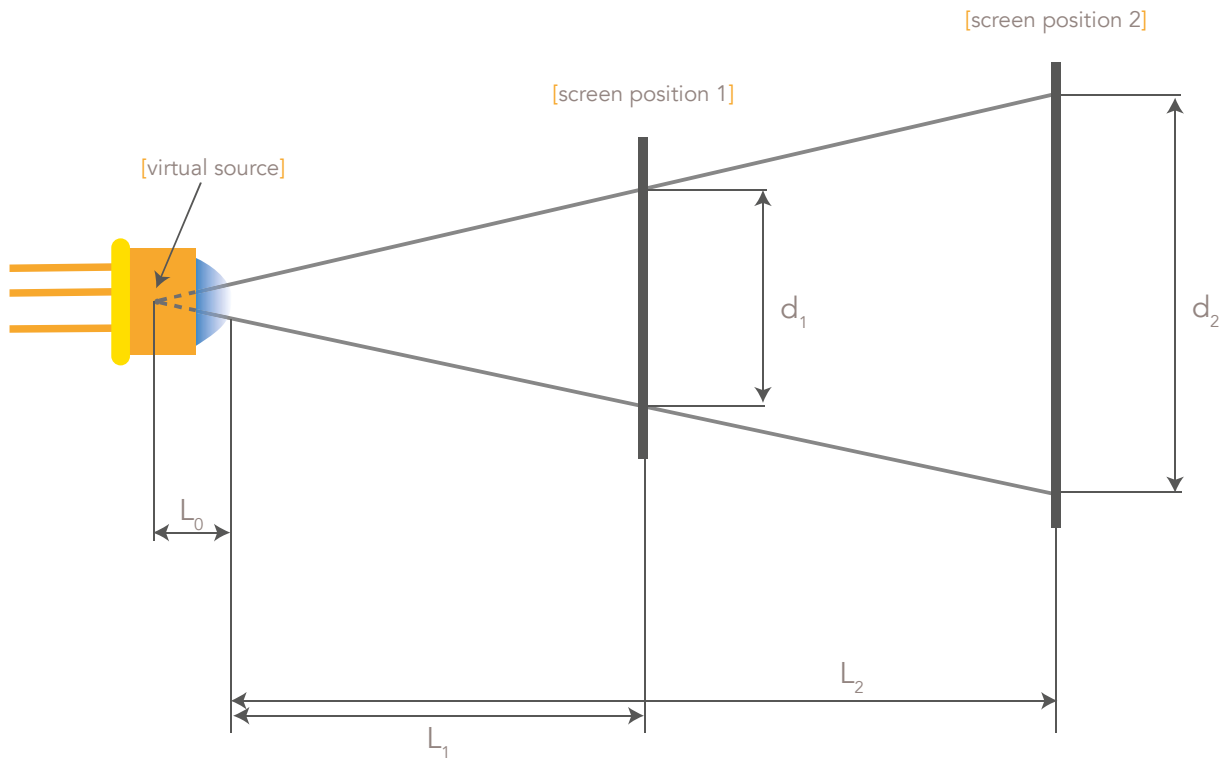


Figure 7.2

Diagram of the approach followed in order to determine the location of the virtual source of the UV-C LED.

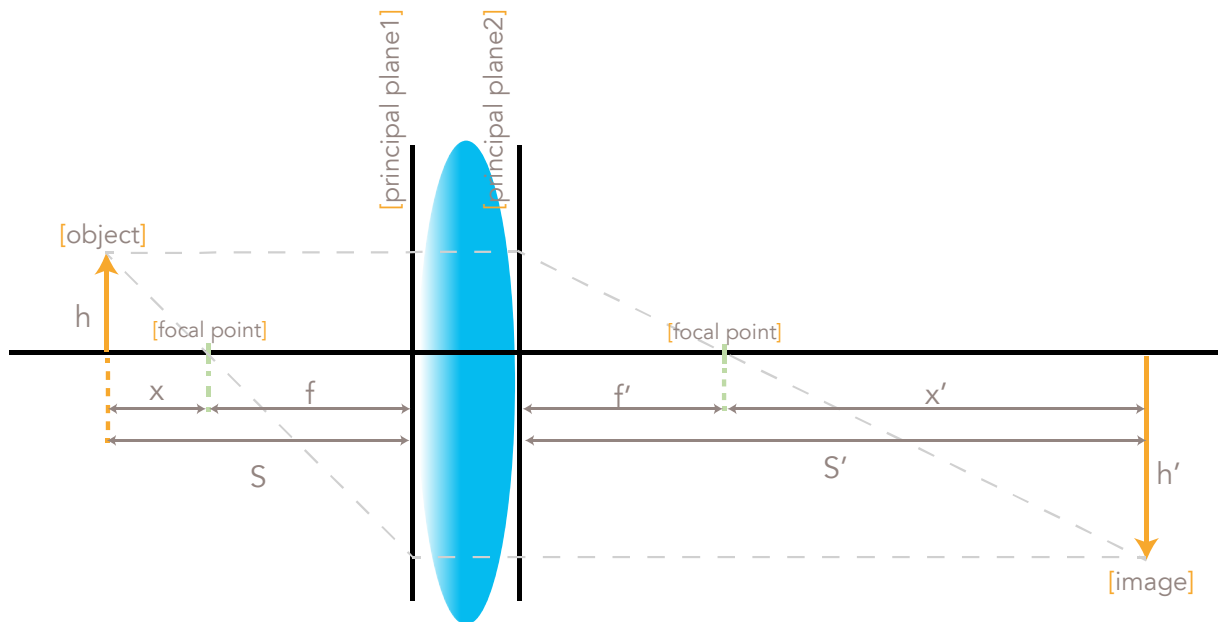


Figure 7.3

Ray tracing diagram displaying the effect of an objective lens. Diagram is reproduced from [28].

As previously discussed in chapter 3 and the accompanying Figure 3.6, the focal distance of a lens is wavelength dependent. The focal distance of objective lens LX4040 is $f = 40$ mm for yellow light of 589 nm. At this wavelength, the refractive index of the lens material (UV-grade fused silica) is 1.458. However, at 255.6 nm the refractive index of fused silica is 1.5045 according to [28]. In order to determine the focal length of a lens in air, the lensmaker's equation {7.3} [29, 30] can be used:

$$\frac{1}{f} = (n-1) \left[\frac{1}{R_1} - \frac{1}{R_2} + \frac{(n-1)d}{nR_1R_2} \right], \quad \{7.3\}$$

where f is the focal length of the lens, R_1 & R_2 are the radii of curvature of the lens surface, d the thickness of the lens and n is the refractive index of the lens material. Using this equation, one can determine that the focal length of lens LX4040 changes to 36.23 mm for 255.6 nm photons in air. We want to demagnify the source footprint to approximately 25 %. According to {7.2} this implies :

$$m = \frac{-x'}{f}$$

$$0.25 = \frac{-x'}{36.23} \Leftrightarrow -x' = 9.06 \text{ mm}$$

$$\{7.4\}$$

$$S' = x' + f'$$

$$S' = 36.23 \text{ mm} + 9.06 \text{ mm}$$

$$S' = 45.28 \text{ mm}$$

Calculation {7.4} indicates that a screen positioned at 45.28 mm from the objective lens will show an image of the object demagnified to 25% of the original size. In the case of the XEOM 1 microscope, 'the screen' is the sample holder of the microscope, i.e. the target of the illumination source. Since the distance between the sample holder and the lens will be fixed, one has to determine the distance S (Figure 7.3) in order to ascertain at which distance from the objective lens the UV-C LED has to be mounted in order to obtain the demagnified image. The 'gaussian' form of the Newtonian lens equation is here appropriate [29] :

$$\frac{1}{s'} = \frac{1}{f} + \frac{1}{s} \Leftrightarrow s = \frac{s'f}{f - s'}$$

$$\{7.5\}$$

$$s = \frac{45.28 \text{ mm} \times 36.23 \text{ mm}}{36.23 \text{ mm} - 45.28 \text{ mm}} = -181.27 \text{ mm}$$

In order to verify this calculations an experiment was set up with an optical bench where the distance between the objective lens and the screen was fixed to 45.28 mm. The screen was covered with white paper with printed squares of 1 x 1 mm².

The experiment consisted of varying the distance between the lens and the LED until the beam profile was well focused into one of the printed squares. An image of the experiment can be seen in Figure 7.4. Experimentally, the best focus, i.e. circle of least confusion [31], was observed when the LED was at a distance of 218 mm from the lens. At distances smaller than 218 mm, the beam spot appeared unfocused and

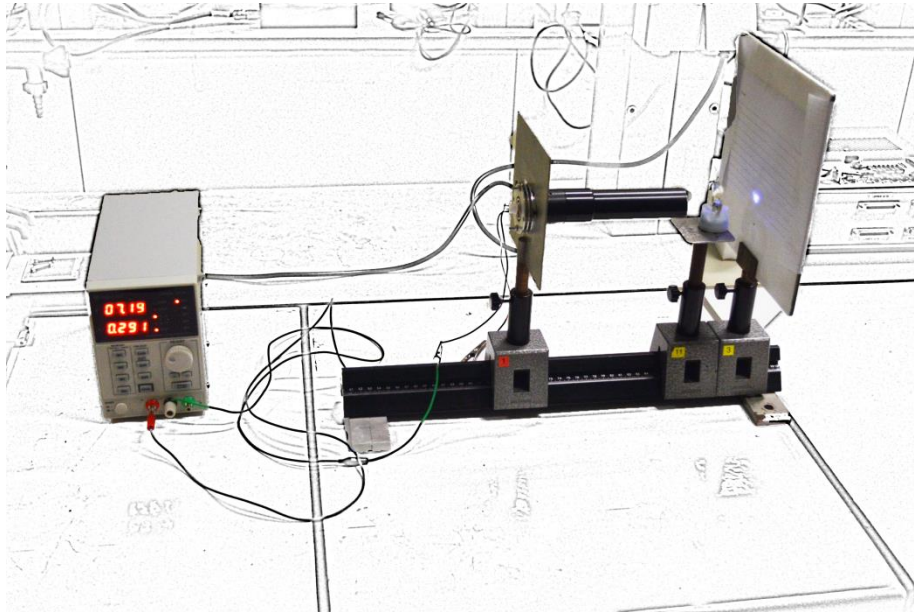


Figure 7.4

Image taken from the experimental setup used to determine certain parameters necessary for the design of the illumination module. An artistic filter was applied to the background of the image in order to draw the attention of the reader to the essential components of the experiment.

surrounded by coma. Since the lens is being used over its whole surface, it is very likely not to get a particularly sharp image. A combination of spherical aberration occurring both on the hemispherical lens of the LED and the objective lens might give rise to this observation. The difference observed between the computed and measured best positions confirms the importance of the experiment.

In conclusion, the illumination module will be designed in such a fashion that the objective lens will be at a fixed distance of 45 mm from the sample position of XEOM 1. The LED will be positioned at 218 mm away from the objective lens. Distances are measured with respect to the face of the hemispherical lens. Accordingly, the (virtual) source is positioned at 223 mm from the objective lens and 269 mm from the sample position of XEOM 1.

7.2.3.2 Design

The prototype of the illumination module holding a simple optical column and a UV-C LED in order to fit the large 45° angle port of XEOM 1 was designed using Inventor®, a computer-aided design (CAD) program by Autodesk (San Rafael, California, U.S.A.) [32].

Figures 7.5 A & B are a three-dimensional exploded-view diagram of the illumination module. The diagram displays all the separate parts necessary to assemble the illumination module. Solid models of purchased parts were made by the author in Inventor® according to specification sheets. Some standard parts (bolts, washers) were imported from a content library incorporated in Inventor®. Solid models from the fuse holder and the LEMO connector were downloaded from the manufacturer's website.

The following parts are visible in the exploded-view of Figure 7.5 B and are hence part of the illumination module :

1. Lens holding cartridge: an 8-teeth collet mechanism, similar to the mechanism used in XEOM 1's optical column, was used to hold the objective lens. Like XEOM 1, the lens holding cartridge is made from black acetal copolymer. Its rigidity, easy machinability, light-tightness and low intrinsic reflectivity make it an appropriate material for this purpose. Each of all 8 teeth is provided with a tapped hole which allow, in combination with the 'lens removal kit' (#16), easy installation and removal of the objective lens. The cartridge, with lens, slides in the large 45° port angle of XEOM 1. When slid in completely, the lens is positioned at 45.3 mm from the sample stub (see previous paragraph). The section of the cartridge with a larger diameter is provided with 3 slots which allow variable positioning of the illumination tube (#3). As an example, a detailed technical drawing for machining the part is given in Figure 7.6. The A4 format of the drawing and the other technical drawing of the other parts can be found in the appendix of this thesis.
2. UV-grade fused silica lens: 40 mm diameter, 40 mm focal length (LXS4040, Knight Optical)
3. Illumination tube: the illumination tube slides in the lens holding cartridge and serves as a mounting point for the LED. The illumination tube positions the LED at a distance of 223 mm from the objective lens when in the middle of the slot. Three nylon bolts (#15) fix the position of the illumination tube in the lens holding cartridge. By sliding the illumination tube in the lens holding cartridge, the distance between the LED and objective lens can be slightly varied, therefore allowing adjustment of the beam footprint of the LED onto the sample holder. The illumination tube is machined from black acetal copolymer.

4. Heat sink: radial fin heatsink (2298 BG, AAVID Thermalloy) surrounding the LED. A counterbored hole and three other holes were machined for respectively fitting the LED and attaching the heat sink on the illumination tube.
5. UV-C LED : 255.6 nm UVCLEAN® lamp (UVCLEAN255HS-3, SETi), see paragraph 7.2.2.1. The UVCLEAN® lamp sits in a three leads LED socket compatible with the UVCLEAN® lamp
6. ABS box: Box made from ABS plastic housing the UV-C LED, the fuse holder with fuse and LEMO connectors. The box serves as a mounting point for the fan.
7. LEMO connector: A Lemo 1B series, 4 pole panel mount connector socket (LEMO, Écublens, Switzerland) was used for connecting the illumination module with the current source necessary for running the LED and the fan.
8. Fuse holder: The fuse holder (Cooper Bussmann, Saint Louis, Missouri, USA) holds the a 300 mA fuse for protecting the LED against excess current.
9. Fan: MagLEV DC Axial fan (MC25101V1-000U-A99, Sunon). The fan is mounted onto the ABS box and is positioned perpendicular to the heat sink. A slot is machined in the ABS box so the fan both blows air through the heat sink fins and in the ABS box for optimal cooling of the LED.
10. Fan protection strip: a folded stainless steel strip is used for attaching the fan onto the ABS box. The metal strip protects the operator from the fan's rotating blades. The metal strip was machined by Davy de Pauw
11. Bolts for attaching the fan and fan protection strip to the ABS box.
12. Bolts and washers for attaching the ABS box and heat sink to the illumination tube.
13. Bolts for locking the position of the LED inside the heat sink
14. ABS box cover
15. Nylon bolts for locking the position of the illumination tube inside the lens holding cartridge
16. Lens removal kit: the lens removal kit is only used for installation and removal of the objective lens inside the lens holding cartridge. Application of eight nylon bolts through each of 8 holes in the 'lens removal ring' into the tapped holes of the cartridge, forces the collet to expand. Once expanded, the lens can be put/removed easily from the machined slot inside the lens holding cartridge. In order to distribute the stress created in the expanded collet, holes were made at the end of all 8 slots in the lens holding cartridge.

7.2.3.3 Final product

Figure 7.7.A displays the final product of the assembled illumination module. Parts not purchased were made by Davy de Pauw in the workshop to the Faculty of Science of Ghent University. Figure 7.7.B and C respectively display the current source of the illumination module and the illuminator inserted inside the 45° angle port of XEOM 1.

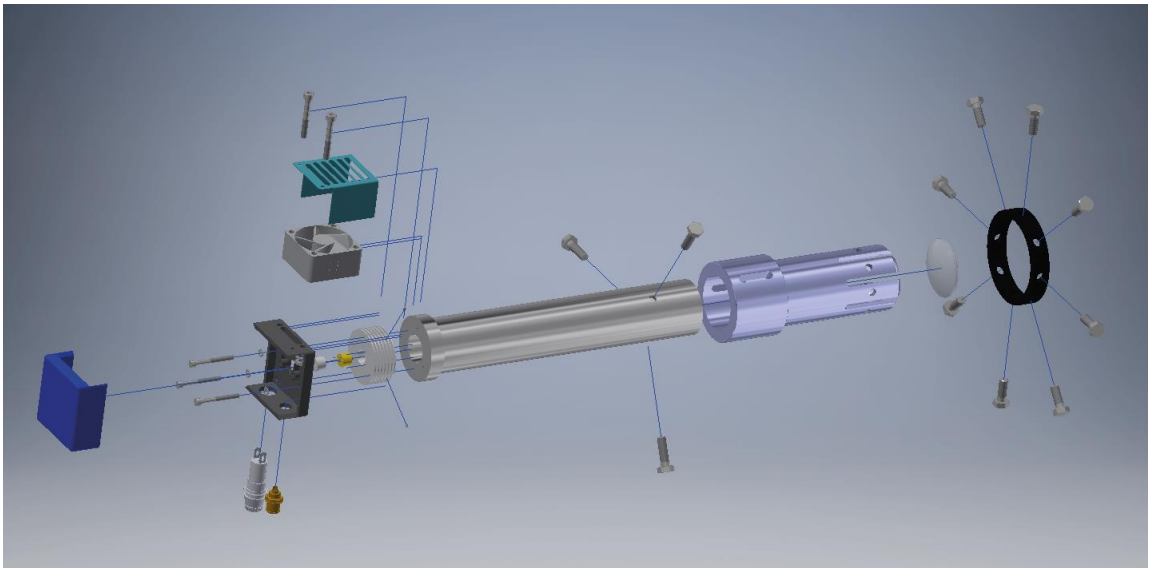


Figure 7.5 A

Three-dimensional exploded view diagram of the illumination module.

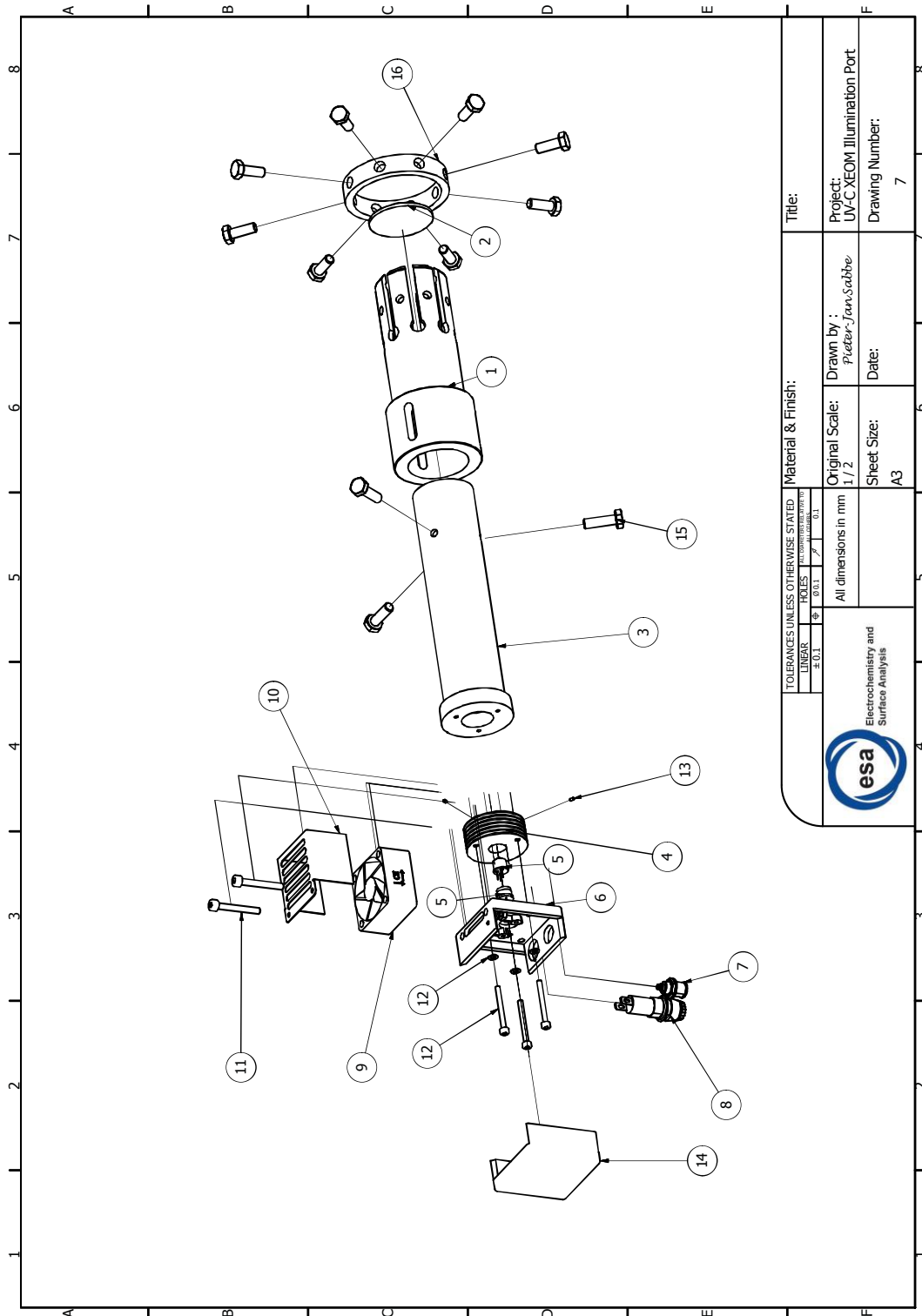


Figure 7.5 B

Three-dimensional exploded view diagram of the illumination module. Each numbered part is further described in 7.2.3.2.

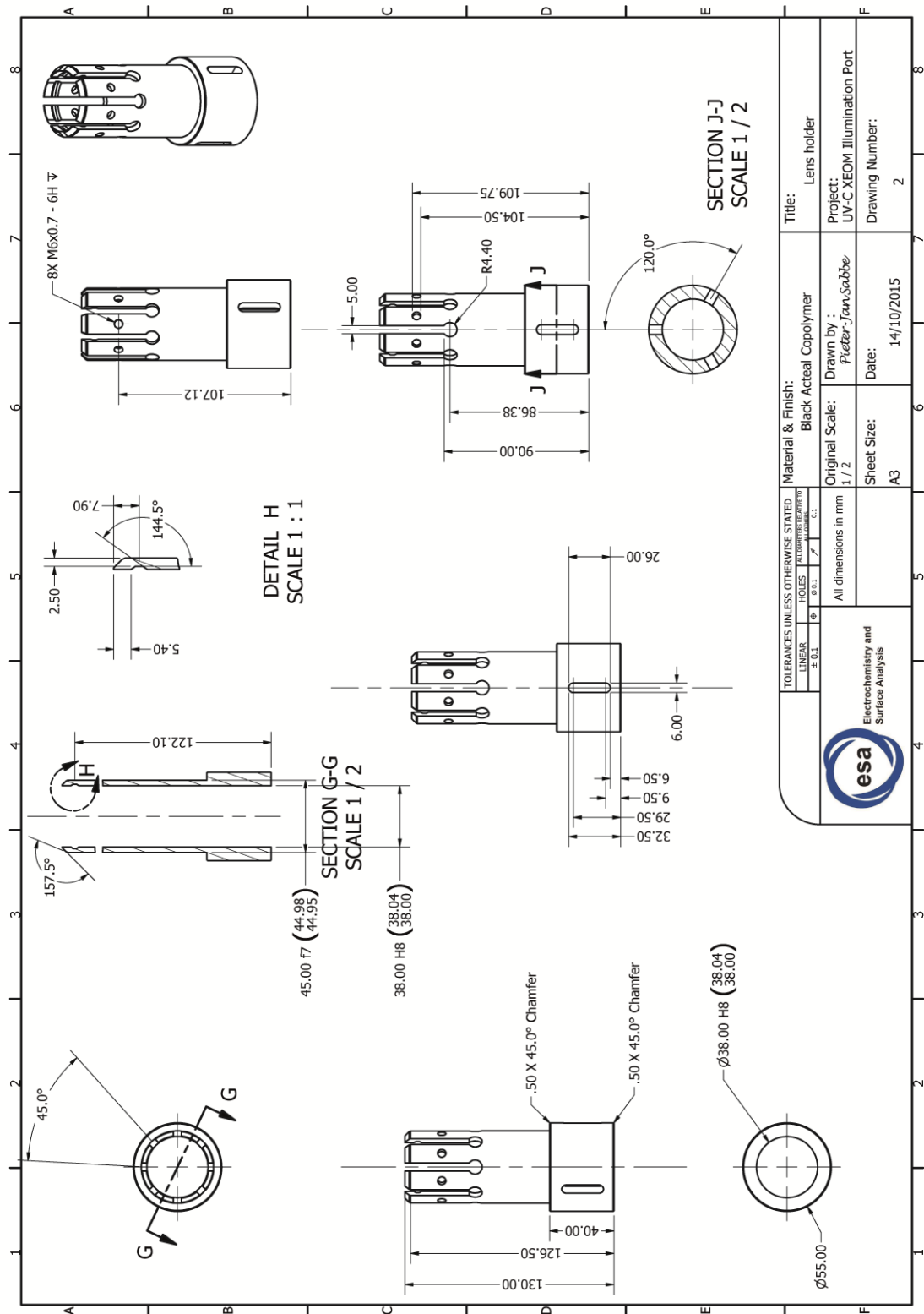


Figure 7.6

Example of technical drawings made by the author necessary for machining the designed parts. The complete set of technical drawings can be found in the appendix of this thesis.

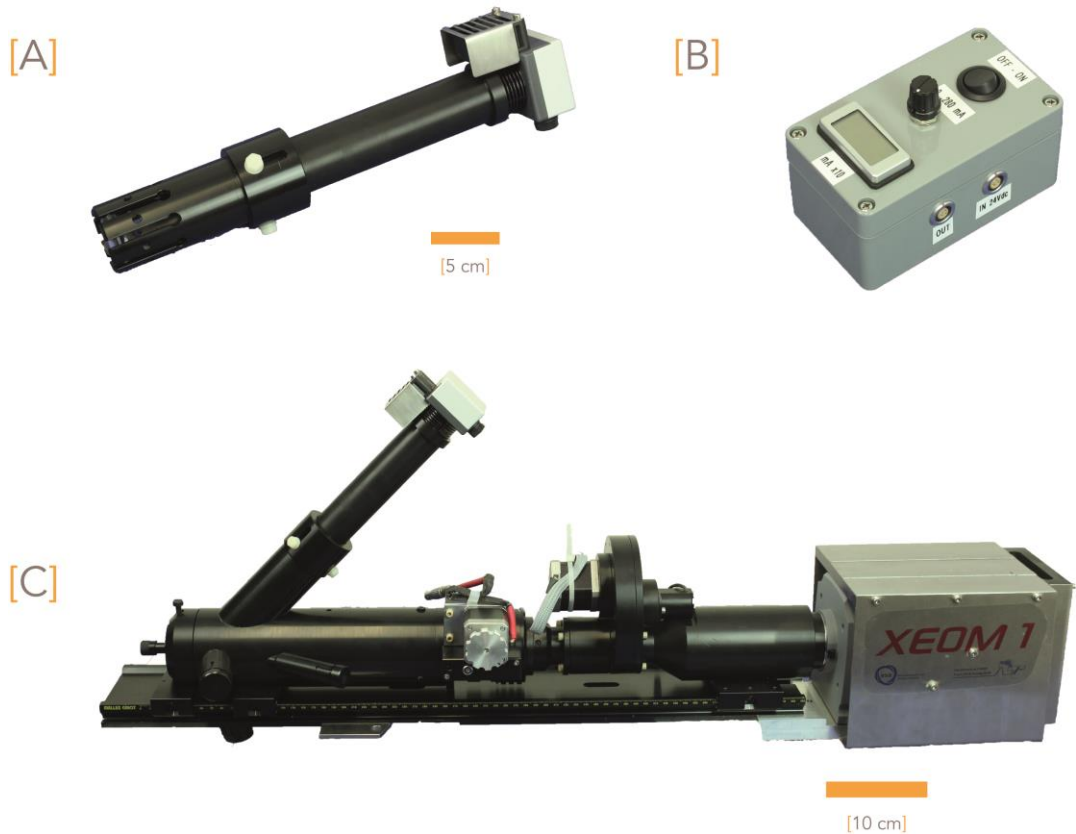


Figure 7.7

- [A] The assembled illumination module.
- [B] Current source for driving the LED (designed and made by J. Anjos)
- [C] Illumination module inserted inside the large 45° angle port of XEOM 1.

7.3 FIRST EXPERIMENTAL RESULTS

The design and the incorporation of the illumination module in XEOM 1 was one of the last exercises done during the course of this study. Extensive testing of the illumination module was therefore not possible. Nevertheless a set of initial tests were performed and already display the added value of the novel illumination source.

7.3.1 MEASUREMENTS TO ESTABLISH THE INFLUENCE OF THE OPTICS' ASPHERICAL CORRECTION ON THE RESOLUTION OF XEOM 1

Simple convex or concave lenses typically have spherical surfaces, i.e. the lens' radius of curvature is constant over the surface. Such lenses are susceptible to spherical aberration [29]. Spherical aberration is the optical effect in which the focal points of rays incident at the margin of the lens is found in different point(s) than the focal point of a ray striking the lens closer to its optical axis [29]. Aspherical corrective lenses exhibit a more complex surface topography which aids in reducing refraction at the edge of the lens, thus reducing spherical aberration [29]. The surface curvature (aspherical correction) of L1 and L2 (see Table 3.1) was computationally optimized in order to reduce overall geometrical aberrations of the complete optical column.

7.3.1.1 Experimental aspects

XEOM 1's first spectroscopy experiment conducted in the Ghent laboratory involved the establishment of the effects of wavelength on the aspherical correction, and therefore also the resolution, of the system. In order to do this experiment, the novel UV-C illumination module was used in combination with an eye piece graticule. An eye piece graticule is a glass disc provided with a fine scale which can be fitted into the eyepiece of an optical microscope. Once calibrated, graticules are typically used to measure specimens in the microscope. The eye piece graticule purchased had a 1 x 1 mm grid of hundred 0.1 x 0.1 mm² squares defined by lines 10 microns wide (part number GEQ1908) by Knight Optical (Harrietsham, United Kingdom). The graticule is fashioned from borosilicate B270 Schott glass (69.13 % SiO₂, 10.75 % B₂O₃, 3.07% BaO, 10.4 % Na₂O, 6.24 % K₂O and 0.36 % As₂O₃) and the pattern (see Figure 7.8 A) is imprinted with black coated chrome [33]. The 255.6 nm radiation of the UV-C LED will induce visible fluorescence in the glass components allowing the user to image the graticule. Images B – J of Figure 7.8 each were recorded by feeding the illuminator with 150 mA while image acquisition was done for 60 s with no binning of pixels in place.

7.3.1.2 Results and discussion

Figures 7.8 B to J display the results of the experiment using the eye piece graticule in combination with different optical waveband filters covering the bandwidth of the Andor camera. As depicted in Figure 7.8 B-J, a sharp image could be yielded for each selected waveband, which implies that the resolution of the optical system is sufficient to distinguish the dark lines at all the wavelengths. Moreover, it can be concluded from these measurements that the general aspherical correction of L1 and L2 is good. The images display that features on the edge and near the centre of the grid are both in focus, confirming that the aspherical correction of L1 and L2 has reduced field curvature to a minimum. Additionally no distortion is observed in the images, since no pincushion or barrel effects are observed as the bars from the graticule grid are perceived as straight and have the same width along their length. Contrary to the results observed for the experiments with Siemens star (see below)

and the chain mail links (see chapter 6), no fringes (due to etalon effect) were observed in images of the graticule recorded in the 700 – 800 nm range. Up till now, no explanation can be provided for this inconsistent observation.

The ability of an imaging system to separate the images of two or more distinct objects is characterized by its resolution. Like other imaging systems, XEOM 1's resolution is limited by a number of factors. Firstly, even in an aberration-free optical system, the resolving power of an imaging system is limited by the diffraction of light by the optical elements within the system. *Lord Rayleigh's criterion* states that the minimum resolvable detail is found when the first imaged diffraction minimum of one point source coincides with the maximum of a second point source; which practically amounts to the wavelength of the light used to create the image [29, 30]. However, this criterion is only valid in perfect systems. In any other case, the resolution of the setup will be limited by optical aberrations within the lens system or the pixelation of the sensor. Time and money investments can always result in approaching the diffraction limit of the system. However, this endeavour might be at the expense of transmitted flux reaching the detector, which negatively influence resolution from a statistical point of view (see below). Furthermore, each of the 4,194,304 pixels of the e2V chip has a physical size of $13.5 \times 13.5 \mu\text{m}^2$ (see paragraph 3.1.4.1.2). Knowing the magnification factor of the optics equals 12, one can conclude that the physical limit of the current system, regardless of the wavelength, is $1.125 \mu\text{m}$. Finally, the influence of statistics on the resolving power of an optical systems may not be underrated, especially in low-light imaging systems like XEOM 1. Poisson noise, introduced by the random nature of XEOL, is signal dependent which implies decreased signal-to-noise ratios upon imaging lower signal. Accordingly, it becomes much more difficult to discern sharp features within such images.

It was theoretically determined by Matt Hand that worst case residual aberration of XEOM 1's optical column corresponds with an image blur of $5.78 \mu\text{m}$, in turn correlating with a value of $0.48 \mu\text{m}$ on the object itself [34]. Since $0.48 \mu\text{m}$ is smaller than the physical limit imposed by the imaging sensor, in theory, the currently present aberrations within the system is not the factor limiting XEOM'1 resolving power. Taking all the above elements into account, it can be concluded that for imaging wavelengths shorter than $1.125 \mu\text{m}$, XEOM 1's theoretical resolution limit is $1.125 \mu\text{m}$. For longer wavelengths, the system is diffraction limited. Determination of the actual resolution of the system at the different wavelengths from the experimental results displayed in Figures 7.8 B to J is difficult. The exact resolving power of XEOM 1 is, per image, a combination of the four limiting factors discussed above. Estimation of the proportion of each factor at each wavelength would be very complex and could only be done by approximation. Nevertheless, the results indicate that geometrical aberration correction is as theoretically intended and sufficient to distinguish the dark lines at all the wavelengths. Since each line is $10 \mu\text{m}$

wide, the resolution must be much better for all the imaged wavebands. After all, discerning dark lines on an emissive background is a very challenging test, hence the value of this result should not be underestimated.

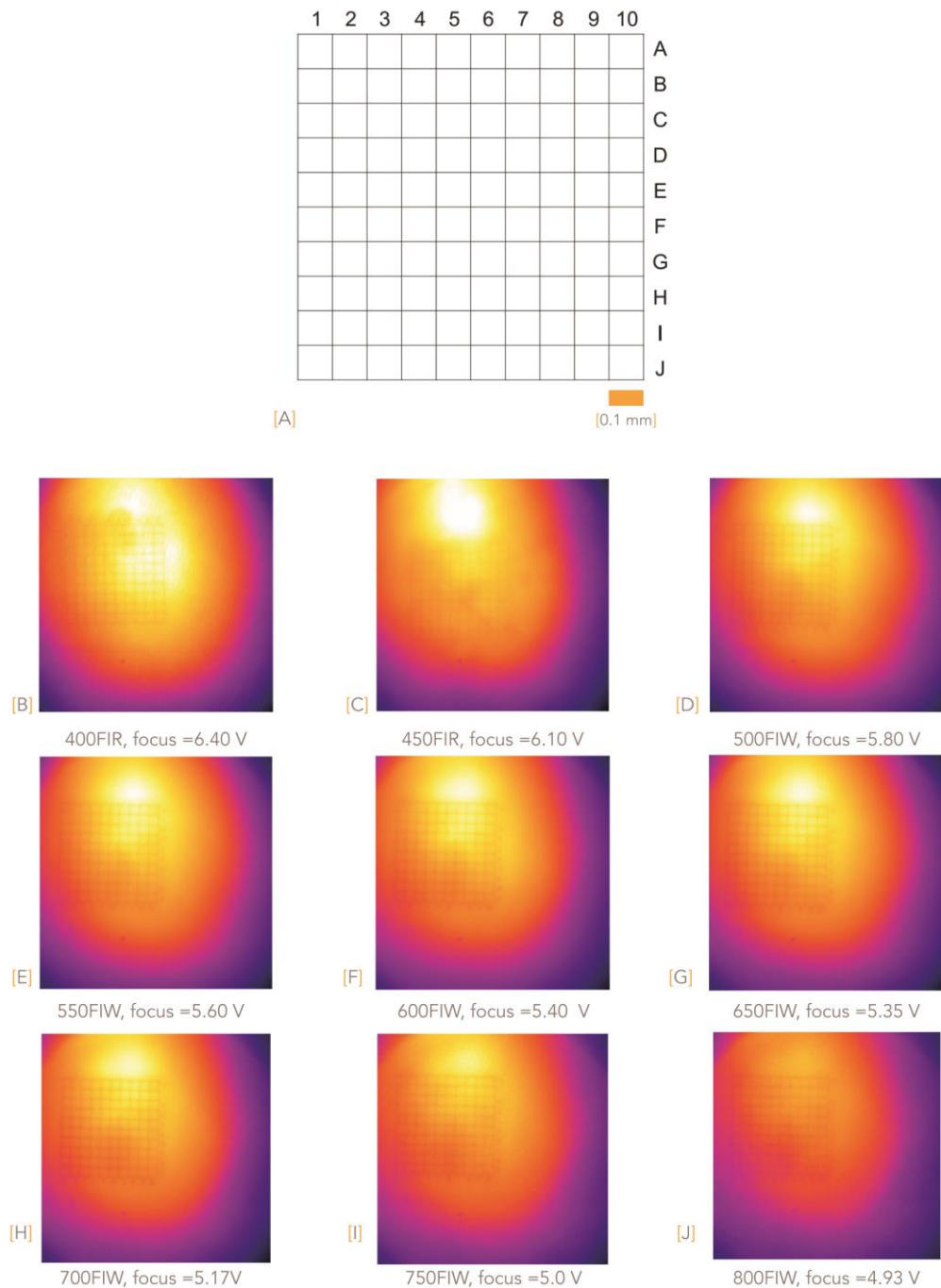


Figure 7.8

[A] Pattern embedded in the eye piece graticule purchased at Knight Optical.

[B] – [J] Results of the experiment carried out to establish the influence of the aspherical correction of the optics on the resolution of XEOM 1. All images are displayed in an ironbow colour scale. [

7.3.2 FINDING OPTIMAL FOCAL POSITION FOR EACH PASS BAND FILTER

One of the demanding and time-consuming tasks during the set-up of a novel XEOM experiment is the spectral survey in order to determine the wavebands in which XEOL is being emitted. The addition of the novel filter wheel carrier (see paragraph 3.1.1.2.2), allowing remote interchangeability of the filters, was already a first step in accelerating this process. Since the optical column is not achromatic, photons of different colour (i.e. wavelength) will be focussed into different spots along the optical axis. Therefore the position of the focussing lens (L3) must be adapted for each different filter in order to obtain a sharp image. The illumination module can aid in finding optimal focus for each optical filter prior to the experiments in the synchrotron. Since the worm drive mechanism of the focal lens L3 is provided with a linear potentiometer for feedback regarding the position of the focussing lens, the position of lens L3 corresponding with the optimal focus for a certain colour can be saved. Later on, during the beamtime allocation, this focal position can be recalled in order to obtain immediate focus.

In order to do this a sample was made consisting of a *Siemens star* printed on white paper. A 'Siemens Star' is a test object used to evaluate the resolution of optical instruments. It consists of a radial pattern of alternating sectors of black and white slots meeting at the true centre of the star [35]. Figure 7.9 A displays an example of a Siemens star [36]. The white paper fluoresces strongly when irradiated with 255.6 nm photons which makes it moderately easy to image the pattern with a low acquisition time. A linear potentiometer is used for feedback regarding the position of lens L3, thus the location of L3 will be expressed in 'Volts'. Prior to this experiment, the extremes of the focal lens have been established. The lower limit at the CCD camera side is 2 V whereas the upper limit at the sample stage side is 7.5 V. Figure 7.9 B – Figure 7.9 J displays the result of the assessment of 9 filters of the filter wheel carrier covering the wavelength range between 400 – 800 nm. The filter names were adopted from Table 3.5 and the corresponding location of focus lens L3 is given. All images were acquired for 1 s with 4 x 4 binning in place. The illumination module was provided with 100 mA. The results of the experiment suggest that lens L3 needs to be translated towards the camera for longer wavelengths (red end) and towards the sample stage for focussing the shorter wavelengths (blue end). Note that the 700-800 nm waveband images exhibit fringes due to the etalon effect (see paragraph 6.3.4.1) as expected.

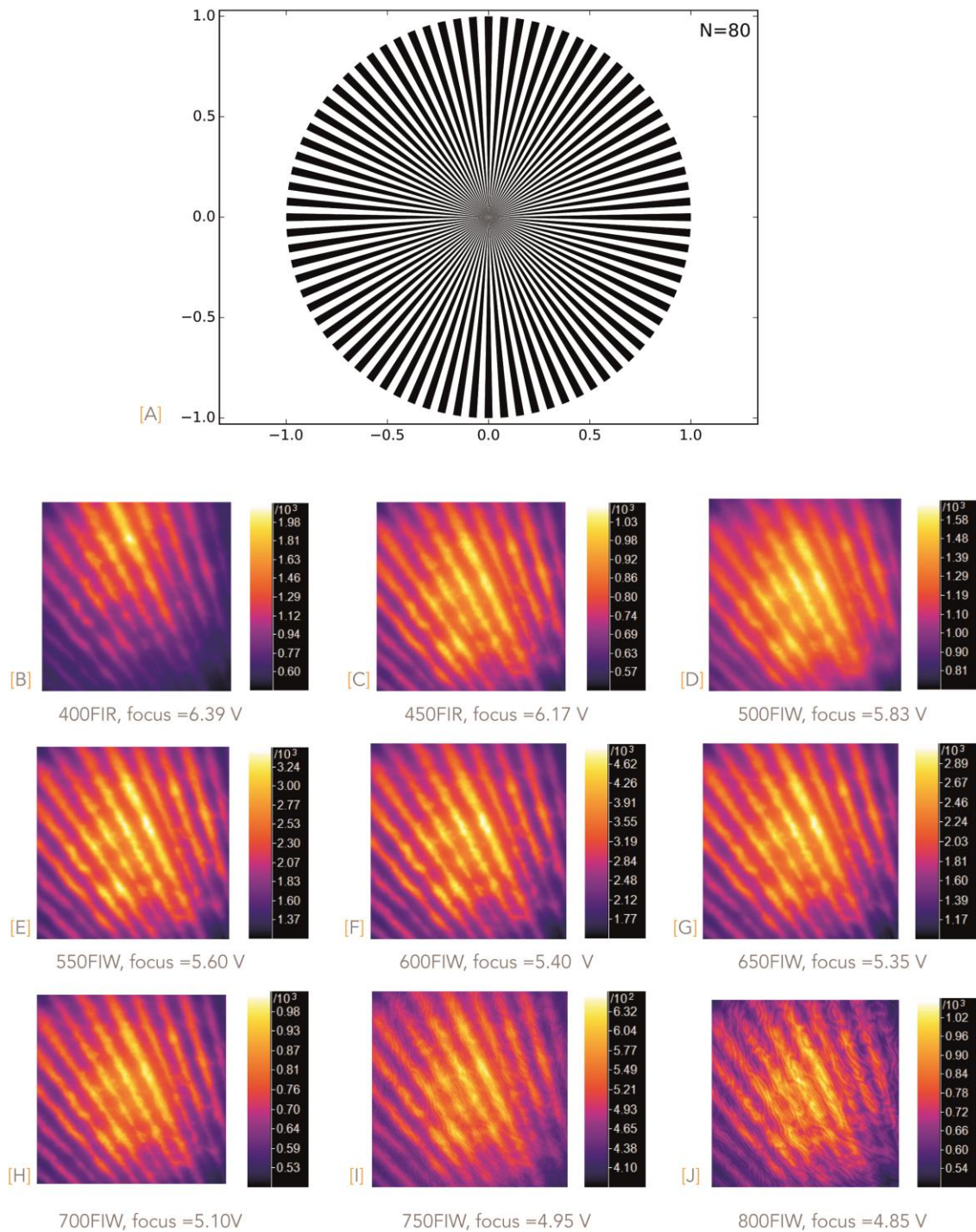


Figure 7.9

[A] Example of a Siemens Star used as evaluation sample. Image is reproduced from [34].

[B] – [J] Results of the experiment carried out to find the optimal position of L3 in combination with different optical filters. All images are displayed in an ironbow colour scale.

7.3.3 ESTABLISHMENT OF 'ASTIGMATISM' IN THE XEOM 1 OPTICAL COLUMN

In paragraph 7.3.1 we conclude that the resolution of the optical system approaches the design limit across the waveband. Nevertheless, in earlier chapters of this work, it was found that obtaining this level of resolution was not achieved for XEOM measurements. This difference implies that the resolution limit for XEOL from grids are due to a combination of poor statistics and poor contrast. Prior to tackling this problem, it needs to be established whether the optical column does not suffer from any additional aberration which prohibits XEOM 1 from making sharp images.

During the experiment discussed in the previous paragraph 7.3.2, the complete focal range of the focusing element L3 (Table 3.1) was scanned until a sharp image was encountered. On certain occasions, sharp images were encountered in two regions of the focal range. These two regions were separated from each other by a region in which a blurred but discernible image was seen. Figure 7.10 A is an image (10 seconds acquisition time, no binning) of an area of the 'Siemens Star' used in paragraph 7.3.2. The image was acquired with the violet filter in place (central wavelength = 400 nm) and focussing lens L3 was positioned at 6.40 V. The printed features of the Siemens Star are visible and the focus is relatively good. Figure 7.9.B is an image acquired under the same circumstances, except that the focus lens L3 was positioned at 5.40 V, i.e. closer to Andor CCD camera. The sharper focus as observed in Figure 7.10 A has degraded. The focus reappears when focus lens L3 is translated even closer towards the red end. Figure 7.10 C displays the image recorded with the focus lens L3 at 4.60 V. The existence of double foci cannot be ascribed to the pass band filters being transparent in multiple regions as described earlier for the corrupted dichroic filters in paragraph 3.1.3.1. The existence of a single pass band was ascertained by acquisition of transmission profiles of each filter in the 200 – 1100 nm range. Details of the experiment are described and depicted in respectively paragraph 3.1.3.1 and Figure 3.11 A & B.

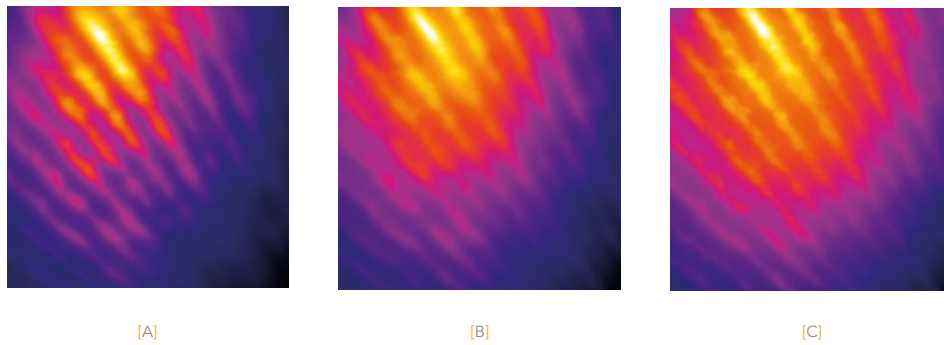


Figure 7.10

[A] Image recorded of the Siemens Star sample with a violet filter. Position of L3 = 6.4 V.

[B] Image recorded of the Siemens Star sample with a violet filter. Position of L3 = 5.4 V.

[C] Image recorded of the Siemens Star sample with a violet filter. Position of L3 = 4.6 V.

The presence of multiple foci might indicate that XEOM 1's optical column additionally suffers from *astigmatism*. Astigmatism is an aberration found in optical system where rays propagating in perpendicular planes, i.e. sagittal and tangential (meridional) plane, are focused in different points along the optical axis [29, 30]. For instance, when an astigmatic lens is used to image a cross, the lens may be focused to yield a sharp image of either the horizontal or vertical details (i.e. either sagittal or tangential details), but not simultaneously. As a consequence, the CCD chip samples a part of space in front of and/or behind the sharp image therefore generally generating blurred images.

In order to confirm whether the optical column suffers from astigmatism and to explain the double foci observed in Figure 7.10, the 'Siemens star' experiment was repeated with the eye piece graticule (see 7.3.1) in the sample position. This is necessary since sharp horizontal and vertical features at sub-millimeter scale are required in order to establish astigmatism.

During the experiment, the two focal positions encountered with the Siemens star experiment are used to image the eye piece graticule within the violet waveband. Figure 7.11 displays the results of the experiment conducted. Initially, with L3 positioned at 6.40 V, the eye piece graticule was rotated until the vertical set of lines were in focus (Figure 7.11 A). At this stage it could already be observed that the vertical lines are noticeably sharper than the set of horizontal lines. In the absence of astigmatism, both set of lines should be equally sharp. Subsequently, the position of L3 was changed to 4.60 V (Figure 7.11 B). With L3 in its new position, it is obvious that the sharp focus seen for vertical set of lines at L3 = 6.40 V has disappeared. Instead, even though the horizontal lines cannot be considered sharp, one might argue that the set of horizontal lines is more in focus at this position of L3. Hence, this experiment suggests that the optical column might suffer from astigmatism. In

the initial position the vertical lines were parallel to the tangential (or sagittal) plane while in the second position the horizontal lines were found (more) in the sagittal (or tangential) focus.

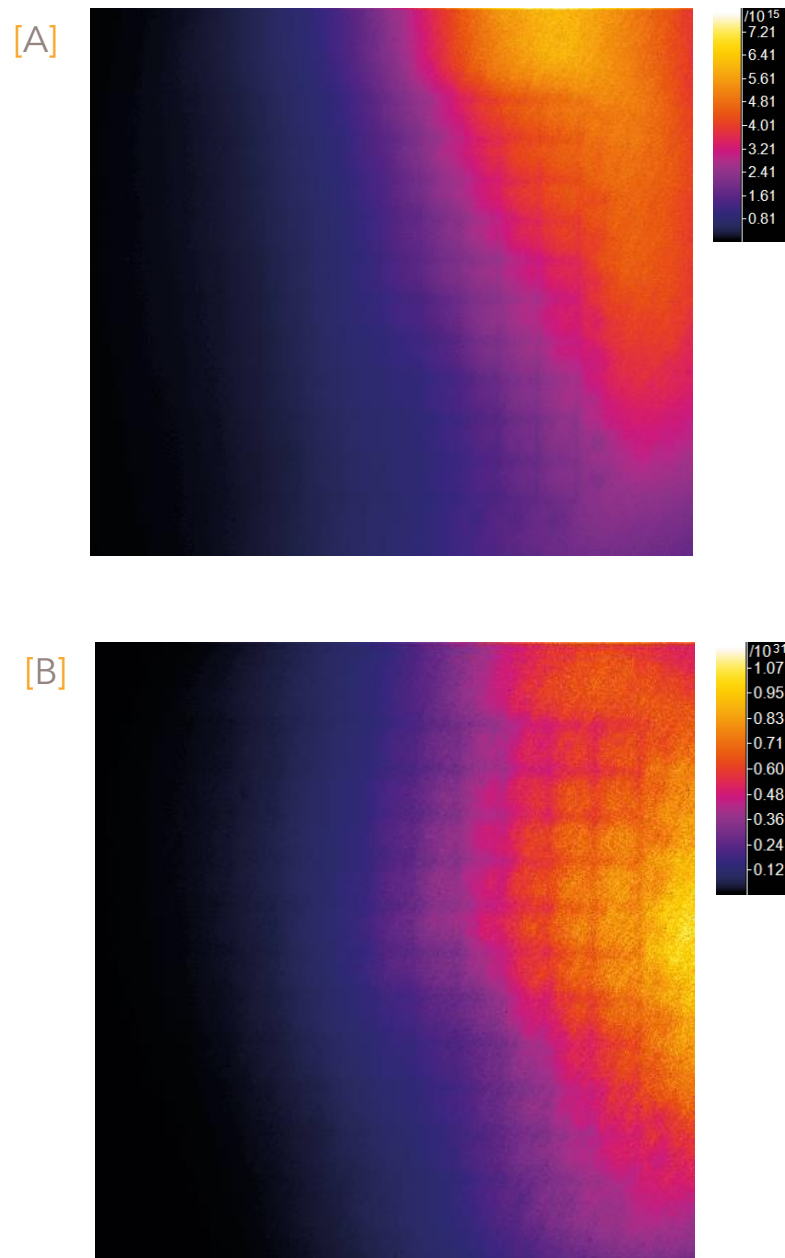


Figure 7.10

[A] Image recorded of the eye pie graticule sample with a violet filter. Position of L3 = 6.4 V.

[B] Image recorded of the eye pie graticule sample with a violet filter. Position of L3 = 4.6 V.

Both images were recorded during 100 s with 1 x 1 binning and 150 mA running through the illuminator.

7.4 CONCLUSION

A novel illumination module was designed as an alternative excitation source for XEOM 1. The target of adding an illumination module is to expand the use of XEOM 1 outside the synchrotron, therefore allowing the microscope to be evaluated away from the synchrotron. The illumination module uses a 255.6 nm UV-C LED as excitation source and a simple optical column for focusing the UV-C radiation into an (approximate) 1 x 1 mm² beam footprint. The design brief of the module was to create a safe, cheap and robust module. Since the most expensive components (UV-C LED and lens) could be recovered from previous projects, the cost of the module could be kept relatively low. The novel illumination module has already proven to be valuable during the evaluation of certain features of the microscope. In this regard, laboratory experiments with a fluorescing glass eye piece graticule confirmed that the aspherical correction of the optical column is as good as what was initially intended during the design process. Moreover, it was shown that the design limit of XEOM 1's lateral resolution (1.125 μm) is approached across the sensor's waveband for experiments with a glass eye piece graticule. The results indicates that resolution limits earlier found for XEOM experiments with the corroded grids are due to a combination of poor statistics and poor contrast. This is subject for further investigation. The possible presence of astigmatism, equally discovered during an experiment with the UV-C illumination module, might be one of the factors contributing to this poor contrast.

Further work will be required to investigate whether UV-C radiation is suitable for metal corrosion research and whether the irradiance of the UVCLEAN® lamp is sufficient to perform spectroscopy on a conceivable timescale. Nevertheless, the equipment necessary for doing this is now in place.

7.5 BIBLIOGRAPHY

- [1] F. Mairinger, in: *Radiation in Art and Archeometry*, 2000, pp. 56–75.
- [2] M. Thoury, J.-P. Echard, M. Réfrégiers, B. Berrie, A. Nevin, F. Jamme, L. Bertrand, *Synchrotron UV - Visible Multispectral Luminescence Microimaging of Historical Samples*, *Anal. Biochem.* 83 (2011) 1737–1745.
- [3] C.B. Tragni, J. Chen, D. Kushel, the Use of Ultraviolet-Induced Visible Fluorescence for Examination of Photographs, *Progr. Adv. Resid. Progr. Photogr. Conserv.* (2005) 64.
- [4] V.A. Fassel, J. Division, M. Laboratories, Determination of Uranium in Ores by an X-ray Excited Optical Luminescence Technique, *Anal. Chem.* 49 (1977) 1–4.
- [5] A. Rogalev, Goulon, in: T.K. Sham (Ed.), *Chemical Applications of Synchrotron Radiation Part II: X-ray Applications*, World Scientific, Singapore, 2002, pp. 707–760.
- [6] D. Creagh, in: A. and C.H. Dudley Creagh and David Bradley BT - *Physical Techniques in the Study of Art* (Ed.), *Physical Techniques in the study of Art, Archaeology and Cultural Heritage*, Elsevier, 2007, pp. 1–95.
- [7] G. Verri, C. Clementi, D. Comelli, S. Cather, F. Piqu??, Correction of ultraviolet-induced fluorescence spectra for the examination of polychromy, *Appl. Spectrosc.* 62 (2008) 1295–1302.
- [8] L. Bertrand, L. Robinet, M. Thoury, K. Janssens, S.X. Cohen, S. Schöder, Cultural heritage and archaeology materials studied by synchrotron spectroscopy and imaging, *Appl. Phys. A* 106 (2012) 377–396.
- [9] A. Pelagotti, L. Pezzati, N. Bevilacqua, V. Vascotto, V. Reillon, C. Daffara, A study of UV fluorescence emission of painting materials, 8th Int. Conf. "Non-destructive Investig. Microanal. diagnostics Conserv. Cult. Environ. heritage" Lecce (Italy), 15-19 May 2005 (2005).
- [10] A. Shugar, K. Lough, J.J. Chen, Characterization of a Surface Tarnish Found on Daguerreotypes Revealed under Shortwave Ultraviolet Radiation, *MRS Proc.* 1656 (2014).
- [11] the International Organization for Standardization, ISO 21348 Definitions of Solar Irradiance Spectral Categories, *Environment* (2007) 6–7.
- [12] M. Belz, F. a Klein, H.S. Eckhardt, K.-F. Klein, D. Dinges, K.T. V Grattan, Optical detection techniques and light delivery with UV LEDs and optical fibres, *J. Phys. Conf. Ser.* 85 (2007) 012034.
- [13] H. Hirayama, S. Fujikawa, N. Kamata, Recent progress in AlGaIn-based deep-UV LEDs, *Electron. Commun. Japan* 98 (2015) 1–8.
- [14] H. Hirayama, T. Yatabe, N. Noguchi, T. Ohashi, N. Kamata, 231-261 nm AlGaIn deep-ultraviolet light-emitting diodes fabricated on AlN multilayer buffers grown by ammonia pulse-flow method on sapphire, *Appl. Phys. Lett.* 91 (2007) 2007–2009.
- [15] M. Kneissl, T. Kolbe, C. Chua, V. Kueller, N. Lobo, J. Stellmach, A. Knauer, H. Rodriguez, S. Einfeldt, Z. Yang, N.M. Johnson, M. Weyers, Advances in group III-nitride-based deep UV light-emitting diode technology, *Semicond. Sci. Technol.* 26 (2011) 014036.
- [16] H. Venugopalan, Ultraviolet LEDs enable cost-effective spectroscopic instruments, (2015) 0–3.
- [17] M.A. Würtele, T. Kolbe, M. Lipsz, A. Külberg, M. Weyers, M. Kneissl, M. Jekel, Application of GaN-based ultraviolet-C light emitting diodes - UV LEDs - for water disinfection, *Water Res.* 45 (2011) 1481–1489.
- [18] A.C. Chevremont, A.M. Farnet, B. Coulomb, J.L. Boudenne, Effect of coupled UV-A and UV-C LEDs on both microbiological and chemical pollution of urban wastewaters, *Sci. Total Environ.* 426 (2012) 304–310.
- [19] C. Bowker, A. Sain, M. Shatalov, J. Ducoste, Microbial UV fluence-response assessment using a novel UV-LED collimated beam system, *Water Res.* 45 (2011) 2011–2019.
- [20] I. Carra, J.A. Sánchez Pérez, S. Malato, O. Autin, B. Jefferson, P. Jarvis, Application of high intensity UVC-LED for the removal of acetamiprid with the photo-Fenton process, *Chem. Eng. J.* 264 (2015) 690–696.
- [21] N. Yagi, M. Mori, A. Hamamoto, M. Nakano, M. Akutagawa, S. Tachibana, A. Takahashi, T. Ikehara, Y. Kinouchi, Sterilization using 365 nm UV-LED, *Annu. Int. Conf. IEEE Eng. Med. Biol. - Proc.* (2007) 5841–5844.
- [22] M.D. Zanolli, S.R. Feldman, *Phototherapy Treatment Protocols for Psoriasis and Other Phototherapy-Responsive Dermatoses, Second Edition*, Taylor & Francis, 2004.
- [23] C. Sampson, Ultraviolet curing, (2006).
- [24] M. Belz, F.A. Klein, H. Habliegger, UV LED fiber optic detection system for DNA and protein - art. no. 64330H, *Opt. Fibers Sensors Med. Diagnostics Treat. Appl.* VII 6433 (2007) H4330–H4330.

- [25] R. Sahara, UV LED Lens Technology, Radtech e5 (2008).
- [26] A. Adriaens, P. Quinn, S. Nikitenko, M.G. Dowsett, Real Time Observation of X-ray-Induced Surface Modification Using Simultaneous XANES and XEOL-XANES., *Anal. Chem.* 85 (2013) 9556–9563.
- [27] H.S. Lee, *Thermal Design: Heat Sinks, Thermoelectrics, Heat Pipes, Compact Heat Exchangers, and Solar Cells*, Wiley, 2010.
- [28] I.H. Malitson, Interspecimen Comparison of the Refractive Index of Fused Silica, *J. Opt. Soc. Am.* 55 (1965) 1205.
- [29] W.J. Smith, *Modern Optical Engineering*, 2000.
- [30] E. Hecht, *Optics*, Addison-Wesley, 2002.
- [31] M.E. Wilkinson, A.P. Doan, *Essential Optics Review for the Boards*, F.E.P. International, Incorporated, 2006.
- [32] Autodesk, Inventor, (2016).
- [33] GVB, Schott B270 properties.
- [34] M. Hand, Development of an X-ray Excited Optical Luminescence Microscope (XEOM) Ph.D. Dissertation, University of Warwick, June 2014.
- [35] S.S. Ahmed, *Electronic Microwave Imaging with Planar Multistatic Arrays*, Logos Verlag Berlin, 2014.
- [36] L. Wagner, Siemens Star, (2015).

Conclusions

CHAPTER 8



8.1 PROJECT SUMMARY

A full understanding of the details of corrosion encountered on metallic objects requires studies ranging from the macroscopic to the microscopic level. When corrosion is approached at the molecular level, more sophisticated tools are required. Many such tools benefit from the unique properties of synchrotron radiation. Current techniques (e.g. XRD, XAS, XPS) already provide a great deal of insight in the composition and properties of corrosion layers. However, especially in the field of heritage science, the use of these techniques is sometimes limited by: the lack of lateral resolution and surface specificity, the requirement of a high vacuum, the potentially damaging character of the beam required to execute the measurements and/or time necessary to produce chemical maps of large surfaces. Development of novel tools overcoming these limitations is therefore of extreme importance. In this thesis, the objectives encompassed the application, evaluation and further development of a novel modular system for the non-destructive chemical imaging of corroded heritage and other metal surfaces. The X-ray-excited optical luminescence microscope 1 (XEOM 1) is a microscope designed to be deployed independently in a synchrotron beam line and is a system which collects light produced by X-ray-excited optical luminescence (XEOL). XEOL refers to the trans-visible emission generated as a consequence of X-ray bombardment and provides an alternative detection mode for X-ray absorption spectroscopy (XAS). A major reason to adopt XEOL spectroscopy for studying corrosion phenomena lies within the additional surface specificity it provides in addition to the information yielded with conventional XAS. Proving the concept of using XEOL to study chemical systems relevant to the corrosion of heritage artefacts was done prior to this doctoral study (by Prof. Adriaens and Prof. Dowsett) with XEOM 1's precursor: ODXAS 1[1].

XEOM 1 builds further on ODXAS 1 by replacing the photomultiplier tube with a CCD-camera. Using a CCD-camera, which provides instant lateral resolution through its two-dimensional array of photosensitive pixels, allows one to acquire full field images. In contrast to scanning probe microscopy, full-field microscopy creates images by illuminating a relatively large area of the sample using large footprint X-ray beams (few mm²). This approach is particularly useful in the field of heritage science since earlier work indicated that the X-ray power density of micro-size beams (necessary for scanning probe microscopy) can alter corrosion products through a variety of processes [2]. Apart from damaging the sample under investigation, analytical information extracted from such surface specific maps may be biased.

The outcome of this dissertation is the result of a close collaboration between two research groups led by the supervisors of this thesis: Analytical Science Projects (ASP, University of Warwick, led by Prof. Dowsett) and Electrochemistry and Surface analysis (ESA, led by Prof. Adriaens). At commencement of this doctoral study, a

substantial amount of design and construction work had already been done by Prof. Dowsett and M. Hand [3, 4]. A part of the hardware of XEOM 1, including: a set of custom optics, an optical column for housing the optics and supporting multiple detectors and other hardware and a basic control system (both software and hardware) was already in place. During the course of this doctoral study the hardware and software of the XEOM 1 system underwent many upgrades for a variety of reasons including :

- Increase automation and functionality : A crucial achievement to improve automation was the synchronization of XEOM 1 with the beamline systems (first BM28 then BM26A) for automated acquisition of image stacks. Further automation was obtained by the incorporation of a remotely controllable filter wheel for automated replacement of light optical filters.
- Defects in earlier components: A serious obstacle encountered during the research was the deficiency of the Hamamatsu sensor installed in the FLI CCD camera. The defects in the chip introduced severe imaging and data artefacts. The camera was eventually replaced by an Andor ikon-L with an e2v chip. In a similar way were additional pass bands outside the 400 – 700 nm region discovered in the set of dichroic filters which were initially used for optical filtering of the XEOL emission. As this can lead to multiple foci and blurred images, the set was replaced by novel standard bandpass, extra broadband bandpass and fluorescence line filters.
- Increase versatility : A novel UV-C illumination source was designed, built and added in order to allow operation of the system outside the synchrotron. Within this regard, a new electronics interface unit and accompanying software were made. The new interface is more robust than the initial system and accommodates independent modules for XEOM and eCell experiments. Incorporation of counting channels was one of the most recent additions to the electronics interface unit. Apart from making the system completely independent from the beamline system, the counters will be useful for future experiments with the UV-C illumination source. Addition of the counters may also be perceived as one of the first preparatory steps necessary for incorporation of a spectroscopic module into XEOM 1.
- Certain features were added as the result of continuous development. For example, a lead housing for the camera was constructed to prevent X-rays from erasing the camera memory. The initial lens carrier for the biconcave focusing lens was replaced by an updated model so optical light at the blue and UV end could be better focused. Apart from this hardware updates,

software necessary for data acquisition (esaXAS & esaXSec) and data processing (esaProject) .

The initial field of XEOM 1 consists of studying corrosion processes on metals, mainly corroded copper being a part of our cultural heritage. Instead of genuine corroded heritage artifacts, evaluation of the imaging and spectroscopic features of XEOM 1 demands well characterized assessment samples. Chapter 4 describes the production and characterization of artificially corroded analogues of naturally occurring copper corrosion. The chapter describes in the detail the principal sample used for evaluation of the microscope and the data it produces. The sample comprises two components: a micrometer scale copper grid in combination with a flat copper coupon. Providing one of these components with a corrosion layer and combining them appeared to be an effective way to create micron scale regions of different corrosion products in order to assess the lateral and chemical resolution of XEOM 1. The reaction products for protocols for nantokite, paratacamite/atacamite, tenorite, and especially cuprite were carefully analyzed with either XRD, XAS, XEOL, XAS and XPS or a combination hereof. Where necessary the protocol was adapted to produce pure layers of these corrosion products on fragile substrates like the microgrid.

The results from the first image stacks acquired from the evaluation sample are described in Chapter 5. Images could be acquired with a minimum exposure time of 10 s for a 2048 x 2048 image, resulting in a stack acquisition time ranging from 20 minutes to a few hours. The first XEOM images present chemical contrast from the different copper corrosion products, and consequent to optical filtering, XEOL emission originating from different corrosion products could be imaged separately. Subsequent data processing with esaProject allowed extraction of XEOL-XAS spectra from either the entire image, a user-defined region of interest, or an individual pixel. The software supports subsequent processing of extracted spectra into two-dimensional edge-shift images displaying variations in oxidation state of the imaged surface. Although the feasibility of imaging surfaces on a micrometer scale in a nondestructive way is demonstrated, high spatial resolution measurements showing good signal-to-noise ratio have not been achieved yet. Attainment of limited lateral resolution was ascribed to both the nature of the studied materials and certain specifications of the optical column. It was indeed observed that in certain cases the signal of low efficient XEOL emitters (e.g. copper) was swamped by the emission of an intense XEOL emitter (e.g. cuprite). In addition it was established that general poor contrast in the measurements prohibits us from achieving high lateral resolution. A new optical column which includes set of achromatic lenses, improved correction for astigmatism (see below) and additional field stops and apertures can be a next step.

After the initial evaluation phase, imaging artificially corroded reference samples, artefacts of significant heritage relevance were also subjected to XEOM analysis. Chapter 6 describes the results from a simultaneous XEOM, XAS, XEOL-XAS measuring session in tandem with XRF acquisition on two chain mail links recovered from King Henry VIII's flagship the Mary Rose. The information provided by these parallel measurements on both an as-found chain mail link and conserved link was supplemented by high-resolution SR-XRD data collected in a relatively novel approach. The results suggested both links were constructed from brass and both corroded under anaerobic conditions, although post-excavation corrosion altered the patina composition of the as-found link. The effect of conservation was clearly visible in the recovered data and the non-destructive character of the method is confirmed. Unfortunately, similar lateral resolution problems as observed in the initial evaluation phase were seen in the composed chemical maps of the chain mail links.

Since access to a synchrotron is intrinsically quite limited, efforts were made to migrate evaluation of the equipment to our home laboratory by the addition of a shortwave UV sample illumination module. Chapter 7 presents the illumination module which houses a LED source, producing 255.6 nm UV-C radiation, and a simple optical column for focusing the UV-C radiation in a confined 1 x 1 mm² beam footprint. Since most expensive components (UV-C LED and lens) could be recycled from earlier projects, the condition of keeping the module as cheap as possible could be met. The added value of the novel illumination module turned out during laboratory experiments for assessing the aspherical correction of the lens system, establishment of astigmatism within the column and finding the optimal focal position of focus lens L3 in combination with different optical bandpass filters. Moreover, addition of the system allowed us to prove that the resolution design limit can be approached for measurements with a fluorescing glass sample. Further experiments will be required to assess whether the illumination module is appropriate for metal corrosion research.

8.2 FUTURE WORK

Ever since the first version of XEOM 1 was constructed, continuous testing of the system resulted in a series of important updates and improvements. Partly because of these improvements it has become clear that XEOM 1 has the potential to become a powerful, nondestructive technique for chemical analysis of corroded heritage and other metal surfaces. Nevertheless, the system could be further improved. One of the major limitations encountered during the project is the restricted chemical differentiation currently achieved. To obtain an acceptable level of chemical resolution and further improvement of general system features, several paths can be followed in the future. These paths involve :

Addition of XEOL spectroscopy section

Over the course of the project, a general approach was developed in order to perform a XEOM experiment. One of the key steps during this approach, as explained in more detail in paragraph 5.1, is performing a spectral survey in order to gain information on the luminescent features of the sample. Knowledge of the composition of different wavelengths from which the XEOL signal is built up provides useful information for appropriate optical filtering during image stack acquisition. Moreover, as explained more in depth in the introductory section 1.3.1, XEOL is a spectroscopic tool in its own right and has been used on different occasions in the past to study e.g. rare-earth elements [5–7] and a variety of nano-sized materials [8–12]. Incorporation of a XEOL spectroscopy section into XEOM 1 could -additional to information required for sharp imaging- provide insight into the composition, optical properties and electronic structure of the investigated material. The passbands of the current optical filters are too wide (> 30 nm FWHM) to perform XEOL spectroscopy with a high energy resolution. The current system can nevertheless serve as a medium to collect waveband resolved XEOL-XANES intensity maps which can aid in better understanding of fundamental properties of materials. Addition of a spectroscopic arm would essentially require a device for wavelength dispersion of the polychromatic XEOL and a sensor for its detection. Similar to the approach seen in integral field spectroscopy (IFS) [13], it is possible to obtain full two-dimensional spectroscopic images, i.e. wavelength resolved XEOL spectrum for each pixel obtained in parallel. As such a solution is far too expensive, wavelength resolved XEOL averaged over the imaged area in XEOM is a cheaper alternative. A diffraction grating in combination with a CCD sensor can be used in order to create an energy dispersive system in which a XEOL spectrum can be acquired per energy point across the absorption edge of the investigated element. Unfortunately, the dynamic range of CCD detectors is currently not sufficient and background noise is generally

too high to observe monochromatic XEOL emission coming from the metals we have studied. Once single photon counting pixelated detectors are available (and affordable), a spectroscopy arm could become part of the current system in which energy dispersed XEOL and XEOM stacks can be acquired in parallel. In this case a beam splitter (e.g. half-silvered mirror) and some additional optics would guide one part of the XEOL emission towards the spectroscopy module and the other part to the imaging module. It is not surprising that first attempts with a portable spectroscope and an optical fiber, as proposed by other groups [5], were not successful since not enough XEOL emission could be captured. Application of a lens focusing the emission on the optical fiber could potentially provide a solution, but this will need to be further investigated.

Improving resolution of XEOM 1

It has been stated earlier in this work that the current optical column of XEOM 1 is not aberration free. Part of this project was to recognize which aberrations are present in the optical column and which influence they have on data quality. In this respect, results presented in chapter 7 prove that the aspheric correction of the optical column is sufficiently good to discern 10 micron thick black lines on an emissive background. Unfortunately such results were not obtained for XEOL imaging of corroded metallic samples. Combination of poor contrast and poor statistics result in poor focus which has direct effect on the quality and resolution of the obtained data. The presence of astigmatism might be amplifying this observed effect.

Improving the resolution and quality of images, which are limited by statistics, can only be done by detecting more signal. Detecting more signal can be done by either increasing transmission of the optical column or having a more sensitive detector. Replacing the current optical column with an achromatic system would allow us to acquire total yield images. However it is questionable whether the increase in signal for unfiltered total yield images is substantial to overcome the signal loss introduced by additional surfaces in an achromatic column. Whether total yield imaging and imaging at identical magnification for different colours justifies the cost of an achromatic column is doubtful. Especially, when we have shown that focusing with the current column works sufficiently well when using a filter. Even when total yield imaging would be possible, addressing certain wavebands through filtering the XEOL-emission might always be interesting and/or necessary for certain experiments.

Apart from acquiring a different detector, an initial and cheaper approach might be improving the poor contrast due to scatter inside the optical column. The addition and careful placement of apertures and field stops can significantly improve contrast.

Moreover, addition of apertures will have a beneficial effect on the observed astigmatism.

Ultraviolet excited optical emission spectroscopy for heritage corrosion

Another area of work which can be continued from this research is the exploration of using the novel shortwave UV-C illumination system for (heritage) metal corrosion research. Luminescence imaging spectroscopy and chemical identification of the materials by studying their UV-induced spectral features have been carried out for organic and inorganic heritage materials like pigments, dyes and varnishes [14–18]. To our knowledge no data has been published regarding the use of shortwave ultraviolet excited optical luminescence on heritage corrosion products. The chemical similarity between certain paint pigments like e.g. zinc white (ZnO), which have been investigated with shortwave UV radiation, and certain corrosion products do suggest it is a pathway worthwhile exploring. This consideration is supported with the information depicted in Figure 8.1, which shows a preliminary result of the assessment sample (cuprite grid on copper coupon) imaged for 300 seconds with the UV-C illuminator (with forward current of approximately 200 mA) in a dark environment with no filter in place. Although the grid pattern is not as sharp as during imaging with X-rays, the pattern is discernible and opens perspectives for further investigation.

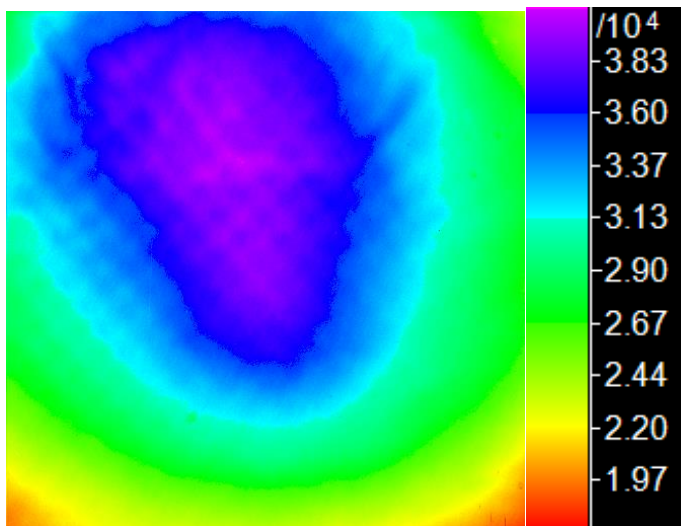


Figure 8.1

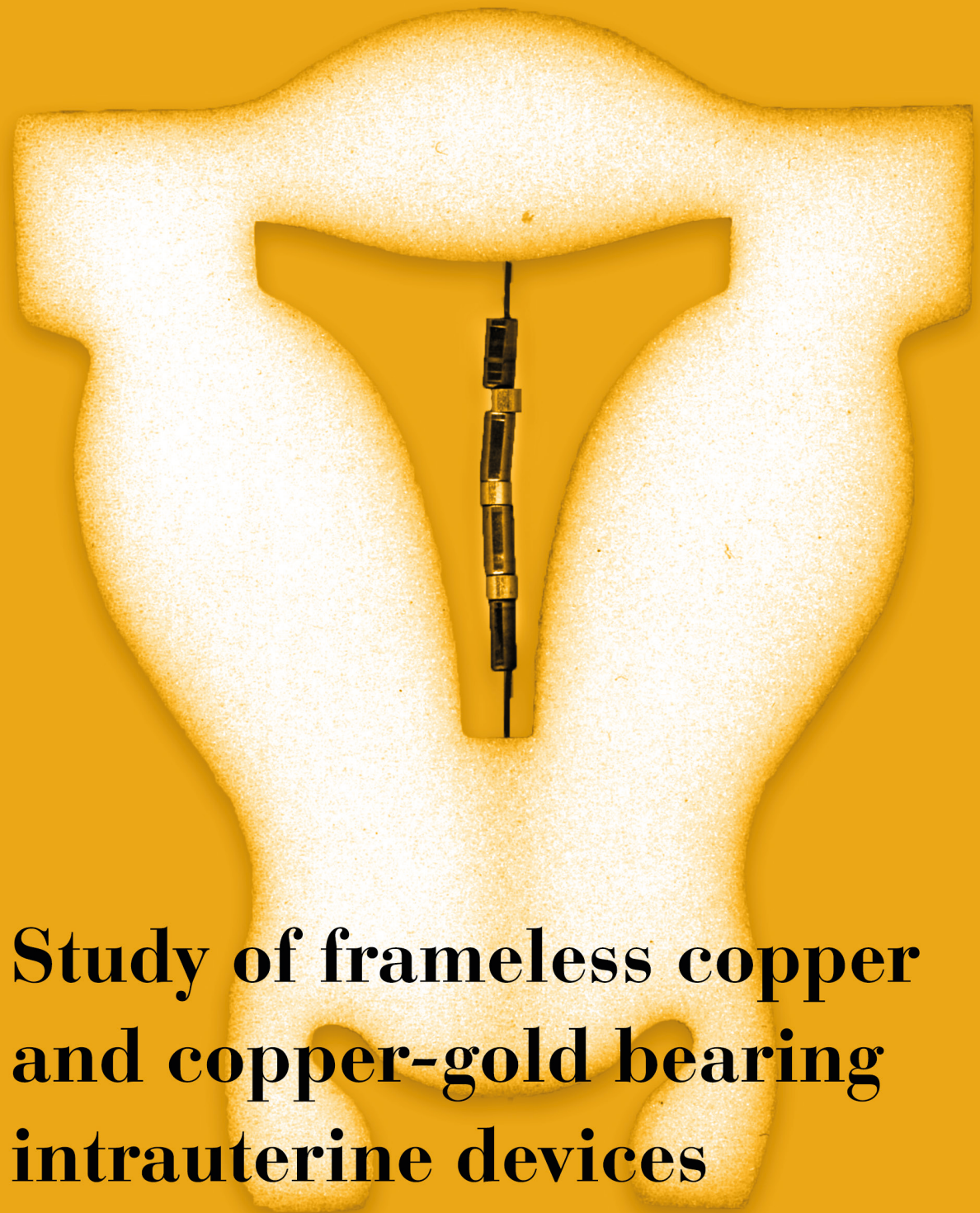
Preliminary result of imaging a cuprite-copper assessment sample with the UV-C illumination source.

8.3 FINAL THOUGHTS

Acquiring a complete understanding of corrosion layers formed on cultural heritage artefacts is, partly because of their heterogeneity, a very difficult assignment. Approaching this complexity through investigation of the sample with a set of different analysis techniques helps to break down this complexity. In this regard, the continued development of novel analytical techniques for investigating corrosion layers from a different point of view is necessary. Soderholm, Liu and Antonio predicted a difficult future for XEOL as a detection scheme for XAS spectroscopy in the late 1990s [19]. Nevertheless, we have managed to create a solid base for using XEOL as information carrier in order to produce laterally resolved surface specific maps visualizing the chemical variation in corrosion crusts of heritage and other metal surfaces. We agree further work will be required for increasing the quality of such surface chemical maps. Yet, once this is completed, this novel method can find its place in the analytical sequence of studying heritage materials. Apart from imaging a topological insulator in chapter 5, this thesis focussed on the application of XEOM in the area of heritage corrosion science. It is evident that XEOM 1's application field can be expanded to other scientific areas which desire knowledge on the surface chemistry or luminescent features of specific samples.

8.4 BIBLIOGRAPHY

- [1] M.G. Dowsett, A. Adriaens, G.K.C. Jones, N. Poolton, S. Fiddy, Optically Detected X-ray Absorption Spectroscopy Measurements as a Means of Monitoring Corrosion Layers on Copper, *Anal. Chem.* 80 (2008) 8717–8724.
- [2] A. Adriaens, P. Quinn, S. Nikitenko, M.G. Dowsett, Real Time Observation of X-ray-Induced Surface Modification Using Simultaneous XANES and XEOL-XANES., *Anal. Chem.* 85 (2013) 9556–9563.
- [3] M. Hand, Development of an X-ray Excited Optical Luminescence Microscope (XEOM) Ph.D. Dissertation, University of Warwick, June 2014.
- [4] M. Dowsett, M. Hand, P.-J. Sabbe, P. Thompson, A. Adriaens, XEOM 1 - A novel microscopy system for the chemical imaging of heritage metal surfaces, *Herit. Sci.* 3 (2015) 14.
- [5] R.P. Taylor, A.A. Finch, J.F.W. Mosselmans, P.D. Quinn, The development of a XEOL and TR XEOL detection system for the I18 microfocus beamline Diamond light source, *J. Lumin.* 134 (2013) 49–58.
- [6] F. Ions, V.A. Fassel, Analytical Applications of X-Ray Excited Optical Luminescence Direct Determination of Rare Earth Nuclear Poisons in Zirconia, *Anal. Biochem.* 46 (1974) 997 – 999.
- [7] A.P. D’Silva, V.A. Fassel, X-ray excited optical fluorescence of trace rare earths in yttrium phosphate and yttrium vanadate hosts. Part per giga level determination of rare earth impurities in yttrium oxide, *Anal. Chem.* 45 (1973) 542–547.
- [8] T.K. Sham, Nanoparticles and nanowires: synchrotron spectroscopy studies, *Int. J. Nanotechnol.* 5 (2008) 1194.
- [9] M. Murphy, X. Zhou, F. Heigl, T. Regier, T. Sham, An X-Ray Excited Optical Luminescence (XEOL) Analysis of Mn²⁺ Doped ZnS Nanostructures, *Nanostructures* 882 (2007) 12–14.
- [10] Z. Wang, X. Guo, T.-K. Sham, 2D XANES-XEOL mapping: observation of enhanced band gap emission from ZnO nanowire arrays, *Nanoscale* 6 (2014) 6531.
- [11] F. Heigl, A. Jürgensen, X.-T. Zhou, S. Lam, M. Murphy, J.Y.P. Ko, T.K. Sham, R.A. Rosenberg, R. Gordon, D. Brewe, T. Regier, L. Armelao, Dynamic View on Nanostructures: A Technique for Time Resolved Optical Luminescence using Synchrotron Light Pulses at SRC, APS, and CLS, *AIP Conf. Proc.* (2007) 1202–1205.
- [12] L. Armelao, F. Heigl, A. Ju, R.I.R. Blyth, T. Regier, X. Zhou, X-ray Excited Optical Luminescence Studies of ZnO and Eu-Doped ZnO Nanostructures, (2007) 10194–10200.
- [13] R. Bacon, G. Monnet, *Optical 3D-Spectroscopy for Astronomy*, Wiley, 2017.
- [14] M. Thoury, J.-P. Echard, M. Réfrégiers, B. Berrie, A. Nevin, F. Jamme, L. Bertrand, Synchrotron UV - Visible Multispectral Luminescence Microimaging of Historical Samples, *Anal. Biochem.* 83 (2011) 1737–1745.
- [15] L. Bertrand, L. Robinet, M. Thoury, K. Janssens, S.X. Cohen, S. Schöder, Cultural heritage and archaeology materials studied by synchrotron spectroscopy and imaging, *Appl. Phys. A* 106 (2012) 377–396.
- [16] A. Pelagotti, L. Pezzati, N. Bevilacqua, V. Vascotto, V. Reillon, C. Daffara, A study of UV fluorescence emission of painting materials, 8th Int. Conf. “Non-destructive Investig. Microanal. diagnostics Conserv. Cult. Environ. heritage” Lecce (Italy), 15-19 May 2005 (2005).
- [17] G. Verri, C. Clementi, D. Comelli, S. Cather, F. Piqué, Correction of ultraviolet-induced fluorescence spectra for the examination of polychromy, *Appl. Spectrosc.* 62 (2008) 1295–1302.
- [18] A. Shugar, K. Lough, J.J. Chen, Characterization of a Surface Tarnish Found on Daguerreotypes Revealed under Shortwave Ultraviolet Radiation, *MRS Proc.* 1656 (2014).
- [19] L. Soderholm, G.K. Liu, M.R. Antonio, X-ray excited optical luminescence (XEOL) detection of x-ray absorption fine structure (XAFS), *J. Chem. Phys.* 109 (1998) 6745 – 6752.



Study of frameless copper and copper-gold bearing intrauterine devices

CHAPTER 5

A part from the research done concerning imaging of corroded metal surfaces with XEOM 1, a significant amount of work has been done studying corrosion phenomena associated with copper-based intrauterine devices (IUDs), a popular method for birth-control. Since this body of work is difficult to unify with the rest of this thesis, it was chosen to add this material as a supplementary chapter. This additional chapter is the result of a successful collaboration over the past years with, among others, Dr. Dirk Wildemeersch (MD-PhD, gynaecologist and medical advisor at Control Research). The collaboration has so far resulted in the publication of two research papers:

- Assessment of copper corrosion from frameless copper IUDs after long-term in utero residence by D. Wildemeersch, P.J. Sabbe, M.G. Dowsett, V. Flexer, P. Thompson, D. Walker, P. A. Thomas and A. Adriaens. The paper was peer-reviewed and published in *Contraception* (90, 454 – 459) in 2014 [1].
- XRD in situ monitoring of copper-IUD corrosion in simulated uterine fluid using a portable spectroelectrochemical cell by A. Grayburn, M.G. Dowsett, P.-J. Sabbe, D. Wermeille, J.A. Anjos, V. Flexer, M. De Keersmaecker, D. Wildemeersch and A. Adriaens. The paper was peer-reviewed and published in *Bioelectrochemistry* (110, 41-45) in 2016 [2].

This chapter consists of a part of these published results supplemented by the findings of new experiments

S.1 GENERAL INTRODUCTION

Intrauterine devices (IUD) are the most popular method for long acting reversible contraception (LARC) and are, after sterilization, the most widely used form of birth control. The contraceptive effect of the IUDs is established either by the presence of hormones (levonorgestrel releasing intrauterine system, LNG-IUS) or copper (Cu-IUD) [3–11]. The primary contraceptive effect of Cu-IUDs is prevention of fertilization and implantation through the release of copper ions into the fluid medium of the uterus. Cupric ions primarily perturb sperm motility, hence compromising the survival of the spermatozoa and preventing fertilization and implantation. Moreover, the presence of an intrauterine foreign body triggers the endometrium to release leukocytes and prostaglandins in the uterus, oviduct and cervix accordingly impeding sperm and egg development [12]. Earlier generations of Cu-IUD models consisted of a plastic frame, either 'double S'-shape (Lippes loop [13]) or T-shaped (TCu200 [14] & TCu380A[15], Figure S.1 C), serving as a support for anchoring a solid copper source inside the uterus. Even though it is known that uterine cavities can differ considerably

in size and shape between women and the uterus' size and volume is influenced by the menstrual cycle, framed-IUDs are only available in one standard size [7]. Disproportionality between the IUD and the uterine cavity has proven to be the cause of expulsion of the IUD, unusual pain, unintended pregnancy consequently to partial expulsion and abnormal uterine bleeding [5, 7, 16]. Next generation frameless Cu-IUDs strive to counter these problematic effects observed in framed Cu-IUDs. Frameless Cu-IUDs typically consist of a polypropylene suture threaded with a number of hollow copper cylinders. Its flexible and smaller design with respect to framed IUDs allows the use of the IUD in uterine cavities varying size and shape.

GyneFix® (by Dirk Wildemeersch, Contrel Research, Ghent, Belgium) belongs to this next generation of frameless Cu-IUDs and was used throughout this research project (Figure S.1 A) The standard version contains six hollow copper sleeves (GyneFix® 330) and the small version contains four copper sleeves (GyneFix® 200). Anchoring of the device is done by inserting a knot, made at the proximal end of the IUD's thread, in the fundal myometrium [7]. Below the anchor is a small stainless steel tube threaded on the suture that serves as a marker for radiographic visualization of the anchor at insertion and follow up (Figure S.1 B). Top and bottom sleeves are crimped onto the suture to prevent the other sleeves from sliding off (Figure S.1 D).

S.2 EVALUATION OF SITE-SPECIFIC IN UTERO CORROSION BEHAVIOUR OF COPPER SLEEVES FROM FRAMELESS INTRAUTERINE DEVICES .

S.2.1 INTRODUCTION

In Cu-IUDs, the copper dissolution rate is directly proportional to the exposed surface area. Accordingly will the risk of unwanted pregnancies decrease with increasing copper area in a device [17]. Although the minimal copper load for an IUD to prevent pregnancy is still unknown, literature suggests that good contraceptive efficacy is obtained when IUDs have a minimal exposed surface area of 200 mm². However, when the surface area exceeds 380 mm², no additional reduction in failure rate (unwanted pregnancies) is perceived. This observation can be ascribed to the limited amount of dissolving agent present necessary for in utero corrosion [18–20].

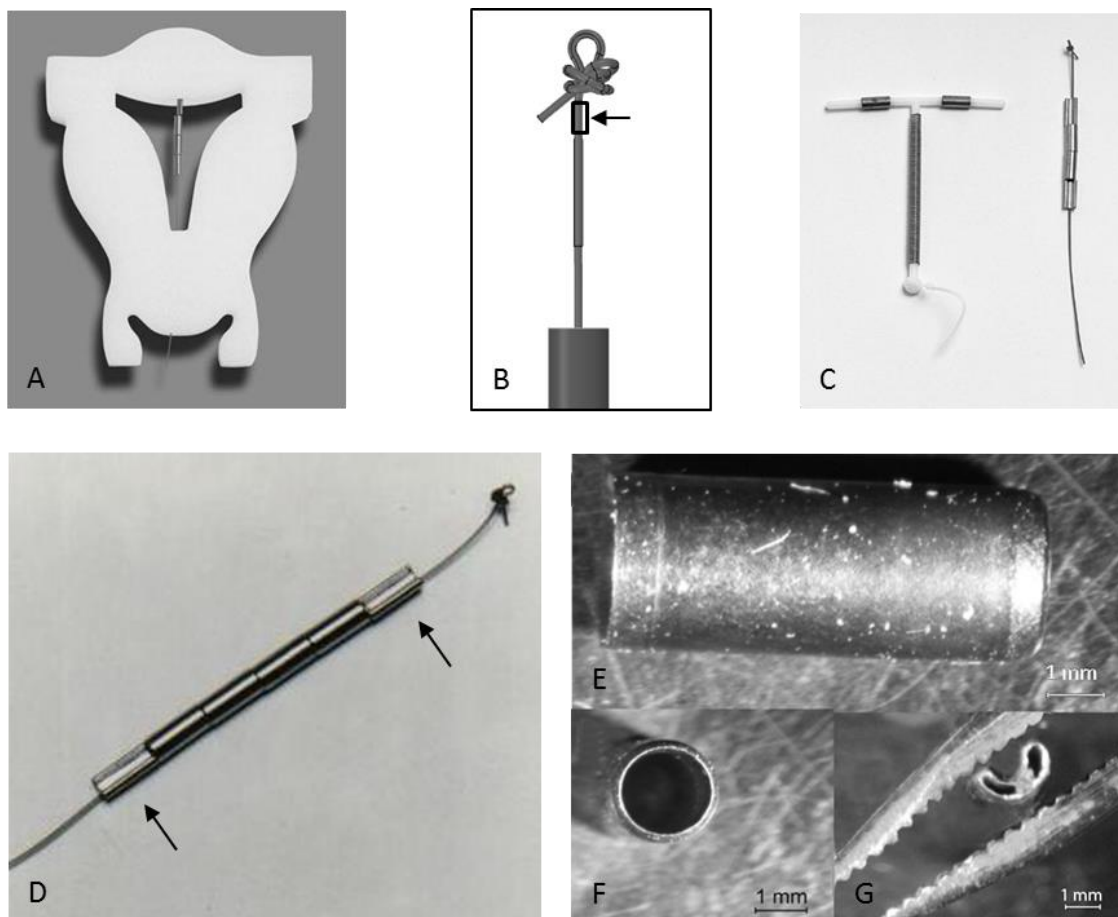


Figure S.1

[A] Frameless Cu IUD of the GyneFix® 200 type inserted in a foam uterus.

[B] The IUD has a knot on the top that serves to anchor the IUD in the fundus. Below the anchor is a small metal tube (arrow) threaded on the suture that serves as a marker to visualize the anchor at insertion and follow-up.

[C] The total foreign body surface area (copper and plastic frame) of the TCu380A IUD is approximately 3 times greater than that of a small GyneFix® IUD.

[D] GyneFix® 330 IUD that has two copper tubes more than the smaller version. The top and bottom tubes are crimped onto the suture thread (arrow) to avoid sliding off of the tubes from the suture.

[E] Depending on their position on the suture, the tubes are present in two different shapes. The middle tubes are cylindrical, while the end tubes are pinched cylinders. The former are named O-shaped tubes (F) while the latter are referred to as U-shaped tubes (G).

Reprinted from *Contraception*, 90, Wildemeersch D., Sabbe P.-J., Dowsett M.G., Flexer V., Thompson P. Walker D., Thomas P. and Adriaens A., *Assessment of copper corrosion from frameless copper IUDs after long-term in utero residence*, 454 – 459, Copyright (2014), with permission from Elsevier.

When using copper sleeves strung onto a suture, the effective copper surface area should be identical to the nominal copper surface area. This design feature makes frameless IUDs essentially different from conventional framed IUDs. By definition all available surface area, 330 mm² for the 6-sleeved IUD and 200 mm² for the 4-sleeved version, is exposed to the uterine environment. However it is unknown whether the

restricted access for uterine fluid on the inside of the copper cylinders used in frameless IUDs affects the local dissolution rate, especially in the sleeves pinched onto the suture at top and bottom of the device. If in utero corrosion of frameless Cu-IUDs is not site-dependent, i.e. the inside of the copper cylinder contribute significantly in the released copper, the high efficacy of these small IUDs can be explained. Improvements in design for novel IUDs require knowledge regarding the site-specificity of in-utero corrosion in such devices.

Maximizing surface area to volume ratio is the prime design brief of novel universal IUDs fitting a large variety of uterine cavities. Larger foreign uterine bodies generally cause more menstrual blood loss. Erratic and increased menstrual blood loss is the main reason why women request removal of a copper IUD. Maximizing copper release while minimizing the size of the intrauterine foreign body is therefore an important objective to enhance acceptability of the IUD. Earlier clinical studies already confirmed higher acceptance of frameless IUD with respect to framed IUDs, [5]. Difference in size between framed and frameless-IUD can be seen in Figure S.1 C.

Frameless IUDs, like GyneFix®, were first developed in 1985 [21, 22] and have been in use in Europe and China since 1995 [7]. Until recently, first research has been done on long term in utero corroded copper sleeves from frameless Cu-IUDs. Although results coming from in vitro studies in simulated uterine solutions (see paragraphs below) prove to be valuable, it remains a difficult exercise to mimic a complex biological environment like a uterus. Even though the number of in utero corroded samples received to analyse is limited, their relevance cannot be underestimated. In this section, a qualitative evaluation of corrosion profiles found on the inner and outer surface of 4 different frameless IUD samples is presented and discussed. The analyzed IUDs corroded in utero up to 150 months.

S.2.2 MATERIAL AND METHODS

S.2.2.1 Analysed samples

Frameless Cu-IUDs of the GyneFix® type consist of 99.99% pure copper sleeves, each 5.00 ± 0.01 mm long, outer diameter of 2.188 ± 0.008 mm and inner diameter of 1.655 ± 0.007 mm as stated by the technical data sheet provided by the copper supplier. Additionally, the sheet mentions that 0.01 % of impurities present consist mainly of Ag (50 ppm); Fe (10 ppm) and Ni, Zn, Se, P (≤ 5 ppm). Depending on the position on the suture, the tubes are present in 2 different shapes; The middle tubes are cylindrical while the end tubes are swaged to a U-shape to grip the suture. In what follows, the former are named O-shaped tubes (Figure S.1 F) while the latter are referred to as U-shaped (Figure S.1 G). The samples were removed from 4

different users after an in utero residence time ranging from 98 to 149 months. After removal, samples were patted dry with soft cotton pads and rinsed with distilled water. Samples were stored in a dry, sterile environment until the measurements were performed. Overall, the samples could be divided into ten different groups depending on a combination of the following parameters: origin of the sample (patient); its shape and inside/outside orientation. An overview of the samples analysed is listed in Table S.1.

Nr.	Sample	Residence time in utero (months)	Shape	Orientation	Intensity of Cu (111) reflection (counts)
1	DCM W27	144	U	IN	19875.3
2	DCM W27	144	U	OUT	2329.2
3	DCM W27	144	O	IN	8458.5
4	DCM W27	144	O	OUT	5576.4
5	DR W24	150	U	IN	2655.4
6	DR W24	150	U	OUT	387.4
7	BF W134	98	U	IN	29115.3
8	BF W134	98	U	OUT	32997.3
9	BF W134	98	O	IN	35855.2
10	BF W134	98	O	OUT	13718.5
11	Cu - ref	0	O	IN/OUT	92.3
12	NW W202	149	O	N.A.	N.A.
13	NW W202	149	U	N.A.	N.A.

Table S.1

Overview of the samples corroded in utero (1 – 10) and reference sample (11). U-shaped samples are at the ends of the polypropylene suture, O-shaped ones are in the middle. Sample n°12 and n°13 were used for determination of differential copper loss analysis. Sample names are based on the initials of the user and an index number. The last column lists the intensity values of the Cu 111 reflection at 3Å, necessary for normalization.

S.2.2.2 X-ray diffraction experiments

X-ray diffraction patterns were measured at BM28 (XMaS) end-station at the European Synchrotron Radiation Facility (Grenoble, France) [23]. Diffraction rings were recorded with a Mar CCD 165 camera (Mar USA Inc., Evanston, Illinois, USA), oriented at an angle of 45° to the input beam with its surface at 130 ± 0.5 mm from the sample surface. The X-ray beam was incident at 10° to the sample surface resulting in an elliptical beam footprint (Figure S.2 A). Dimensions of the beam were set to 1 mm wide and 1.15 mm long by adjusting the vertical slit height. The monochromator was set to 8 keV ($\lambda = 1.5498 \text{ \AA}$)

In order to examine the inner surface of a copper sleeve, the sleeves were opened longitudinally with a utility knife degreased with 2-propanol. The resulting half-cylinders were mounted on a sample carousel (Figure S.2 B) for remote sample changing. The inside or the outside surface was pointed towards the incoming X-ray beam.

The Mar CCD camera produces two-dimensional diffractograms (example in Figure S.2 C). Data acquired with the MAR CCD were processed with esaProject²⁰¹³ (by M. Dowsett) [24]. EsaProject²⁰¹³ reprojects the images produced by the MAR CCD to 2θ or d -spaced images, which are integrated in a subsequent step to one-dimensional diffraction patterns vs. 2θ , d or wave number (Q). The later were compared to reference patterns downloaded from the MinCryst database [25, 26].

Diffraction patterns from uncorroded Cu-IUD sleeves were recorded with a Panalytical X'Pert PRO MPD (PANalytical, Almelo, The Netherlands) laboratory instrument (University of Warwick). The instrument uses monochromated Cu- $K_{\alpha 1}$ radiation ($\lambda = 1.540598 \text{ \AA}$) selected by a curved Ge-monochromator. Reflections were recorded with a PIXcel® solid state detector (PANalytical, Almelo, The Netherlands).

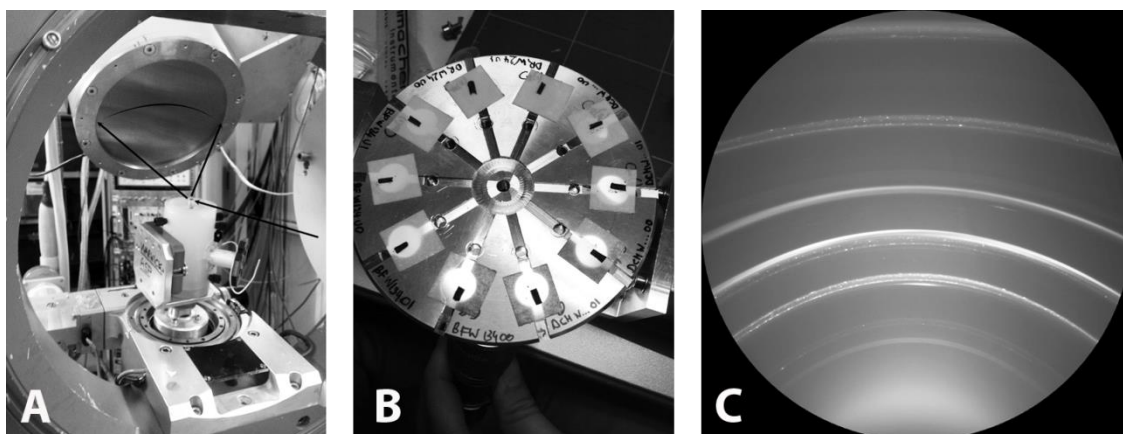


Figure S.2

[A] 2D-XRD setup at BM28 (XMaS) in ESRF with Huber Goniometer tilted so that the incoming X-ray beam strikes the sample at 10°. The Mar-camera detects the diffracted X-rays under an angle of 45°.

[B] Remotely controlled sample carousel with 10 GyneFix® samples from Table S.1

[C] A two dimensional diffractograms recorded from sample n°1

In order to facilitate comparison of diffraction patterns recorded with the Mar CCD and those collected with the PANalytical X'Pert PRO, patterns are plotted as a function of wavenumber Q where:

$$Q = \frac{2\pi}{d}, \quad \{2.16\}$$

and d is the plane spacing. Prior to the normalization process, all diffraction patterns were subjected to a background removal operation. Diffraction patterns recorded with the X'Pert PRO were smoothed using a Gaussian convolution algorithm. Normalization was done by determining the value of the height of the Cu 111 reflection at 3\AA^{-1} (Table S.1, final column) and subsequently all reflections in the diffraction pattern were divided by this value. All these tasks were carried out in esaProject²⁰¹³.

S.2.2.3 Scanning electron microscopy

Scanning electron micrographs were recorded with a Phenom FEI bench top scanning electron microscope (SEM) (Phenom World BV, the Netherlands). Backscattered electrons (BSE) images were collected using 5 kV electrons and a solid state detector. The magnification of the microscope was calibrated with a reference

tube measured with a high precision micrometer (Mitutoyo Quantum, Mitutoyo Corp., resolution $\pm 1 \mu\text{m}$).

S.2.2.4 Differential copper loss measurements

The differential copper loss from the inside and outside of an IUD tube was estimated by measuring separately the inner diameter (ID) and outer diameter (OD) of a reference tube and an uncut in utero corroded tube (149 months). The ID and OD of the reference tube was accurately measured with both a set of high precision pin gauges and a high precision micrometer. The ID and OD of the corroded tube were estimated from end-on micrographs.

S.2.3 RESULTS AND DISCUSSION

S.2.3.1 X-ray diffraction patterns

The diffraction pattern of a pristine frameless Cu-IUD sleeve accompanied by the pattern recorded from the inside of U-shaped in utero corroded (for 150 months, Sample n°5 in Table S.1) sleeve is displayed in Figure S.3. Apart from two minor reflections at low wave number originating from the sample mounting grease, the pattern of the uncorroded sleeve solely displays metallic copper reflections. The pattern confirms the composition of the raw material from which the IUD was manufactured. The diffraction pattern of sample n°5 equally shows these metallic copper reflection in addition to a set of reflections which can be assigned to cuprite (Cu_2O). Cuprite, a crystalline Cu^{I} oxide, has been suggested as an intermediate in the dissolution process of copper in an uterine environment [27–29]. Even though it has been suggested elsewhere [30, 31], it is very unlikely that cuprite is the firsthand source of dissolved copper ions in the uterus necessary for contraception [2]. Cuprite generally exhibits poor solubility at pH and temperature values observed in uterine environments [32]. It is more likely that the simultaneously formed and far more soluble copper sulfates and chlorides serve as immediate copper ion sources [2]. Oxidation of copper is often suggested as an initial step in the release of metallic copper atoms from its neighboring atoms. Subsequently cuprite may evolve to the unstable and soluble paratacamite ($\text{Cu}_2(\text{OH})_3\text{Cl}$) in more saline environments [33–35]. Nevertheless, cuprite has been observed in many Cu-IUD corrosion studies and therefore it can be regarded as an important component in the corrosion process of Cu-IUDs [9, 16, 27, 28, 33, 36, 37]. The presence of cuprite on in utero resided IUDs hence hint dissolution had taken place and suggest a proper functioning of the device on that site.

Figure S.4 displays the X-ray diffraction pattern of the inside and outside of an O-shaped GyneFix sleeve with an in utero residence time of 98 months (sample n°9 and sample n°10 in Table S.1). On both sides of the corroded cylinder, copper and

cuprite reflections are detected. Similar observations are made on both inside and outside of an U-shaped tube originating from the same IUD (Figure S.5, sample n°7 and sample n°8). As discussed above, the presence of cuprite on both sides of the IUD sleeve suggests that the reduced space on the inside of a copper cylinder is not restricting the entry of the dissolving agent and copper dissolution is not inhibited. In the extreme case where the copper tubes are compressed (U-shaped cylinders), initial corrosion results in the formation of a thicker oxide layer. The thicker layer fills the internal space of the swaged tube entirely and essentially prevents any further reaction by blocking the gaps. This observation is not necessarily negative since significant internal dissolution of U-shaped end-cylinders could result in its fragmentation. Disintegration of an end-tube could make the other sleeves fall off the device, making it unsafe and unreliable. The presence of cuprite and copper is observed on all other analysed samples of Table S.1. The results can be found in the appendix of this thesis.

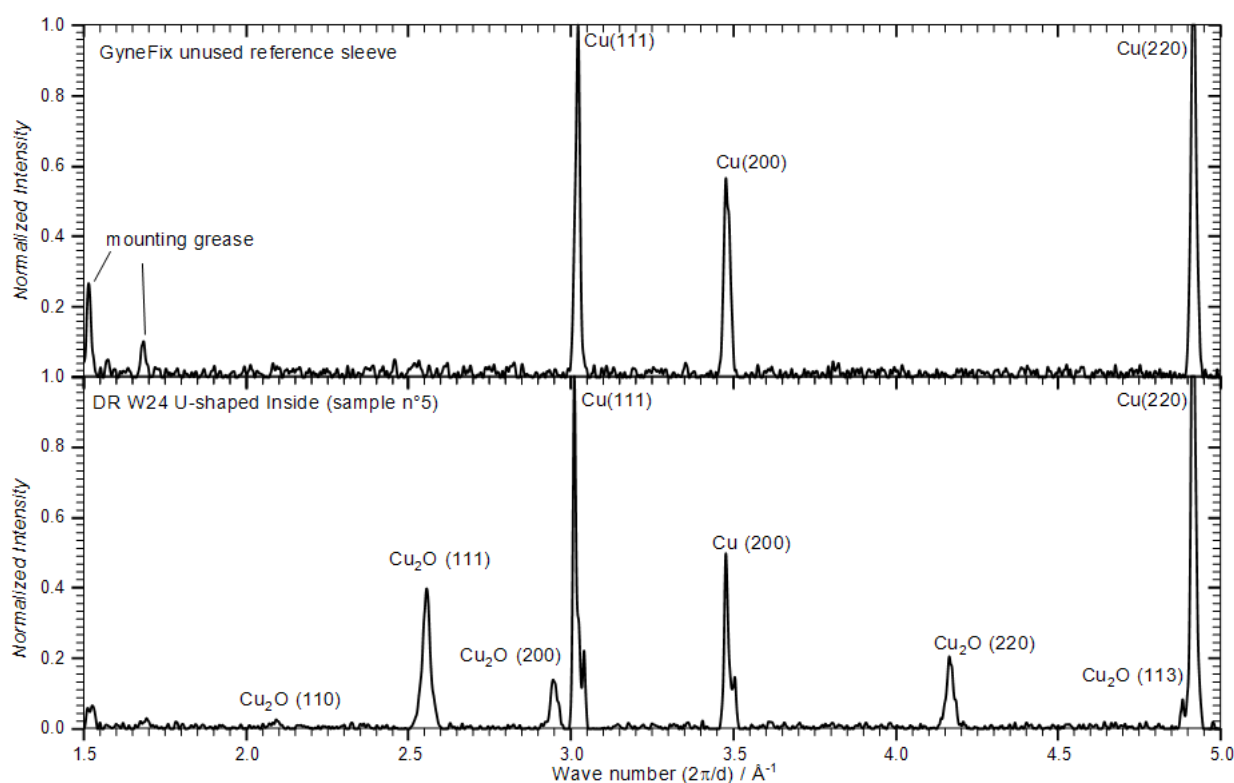


Figure S.3

X-ray diffraction pattern from a fresh reference sleeve of a GyneFix® IUD (top) and the inside of a sleeve corroded for 150 months in utero (sample n°5).

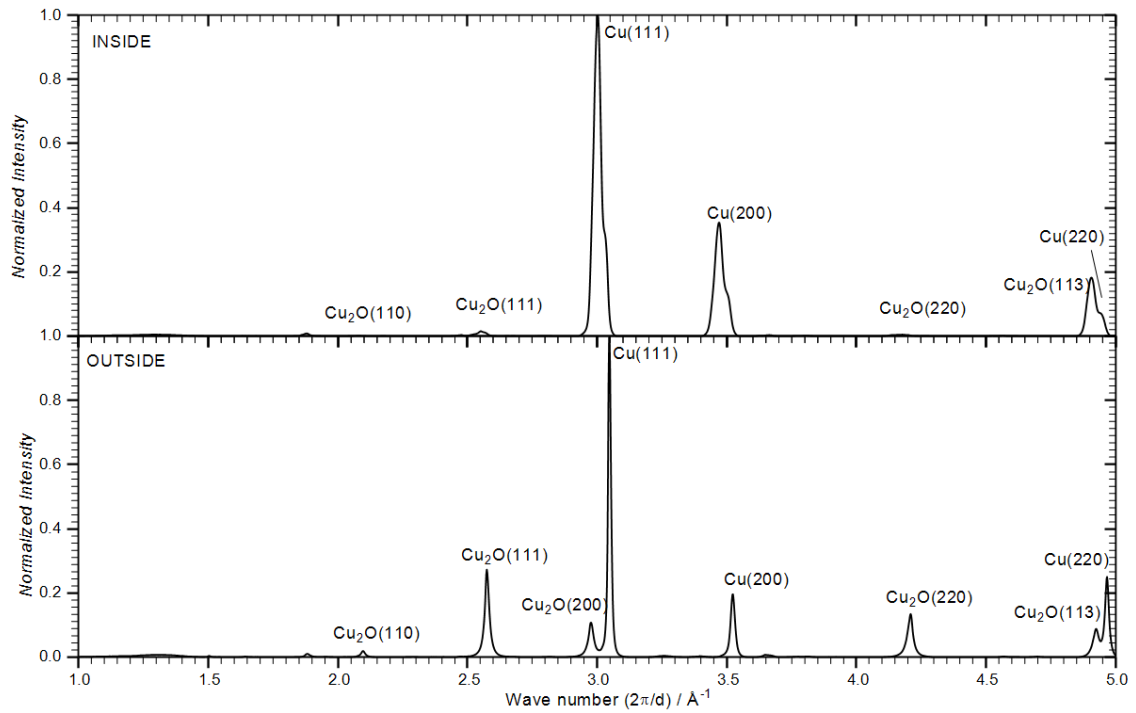


Figure S.4

X-ray diffraction pattern recorded from the inner (top) and outer (bottom) surface of an O-shaped GyneFix® sleeve corroded for 98 months in utero (sample n°9 and n°10).

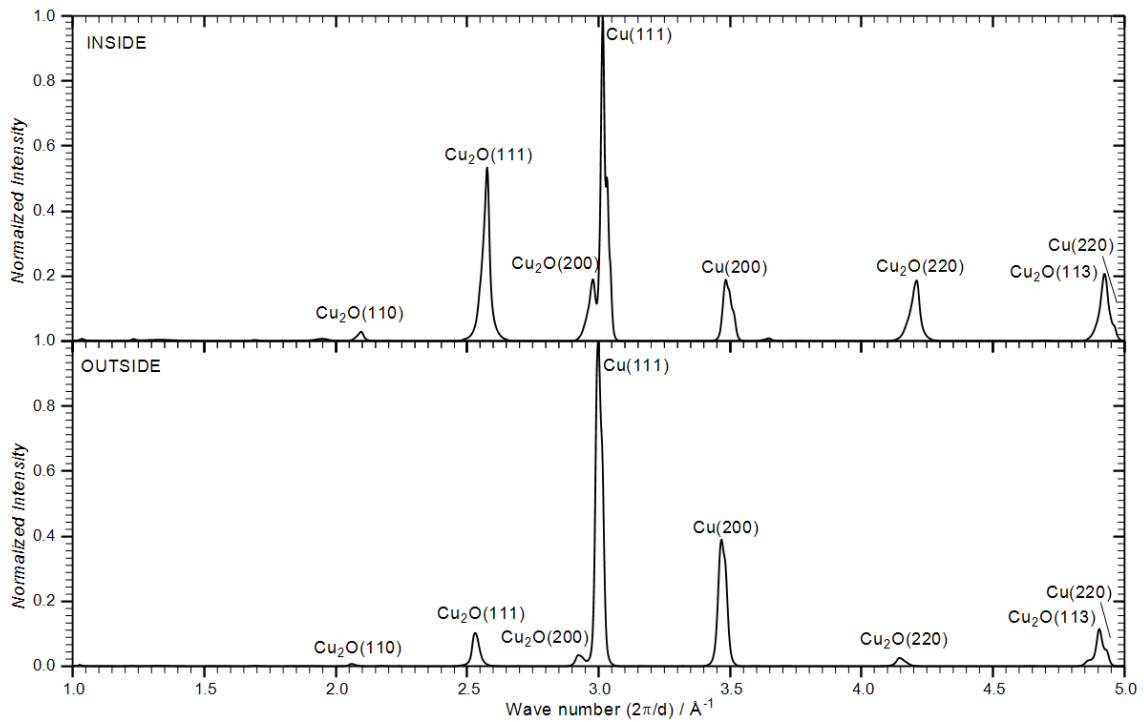


Figure S.5

X-ray diffraction pattern recorded from the inner (top) and outer (bottom) surface of a U-shaped GyneFix® sleeve corroded for 98 months in utero (sample n°7 and n°8).

Essentially, the intensity of XRD-reflections holds information concerning the amount of corrosion product within the investigated area of the IUD's surface [38]. Hence, quantitative differences in corrosion products will reflect site-specific variations in corrosion, i.e. contraceptive, efficiency. Unfortunately, quantitative XRD analysis of curved samples is not straightforward as sample curvatures (due to corrosion, sample opening and original geometry) will cause the X-ray beam to impact at a range of heights resulting in peak broadening or peak splitting when larger polycrystals with preferred orientation are irradiated [39]. Moreover, since uterine environments vary over time and between individuals, in utero studies usually show some scatter in the data. Corrosion reaction rates are oxygen concentration dependent and differences in oxygen partial pressure and pH affect the kinetics of the corrosion process of the Cu-IUD [40]. Drawing conclusions based upon quantitative results would require us to account for differences in oxygen partial pressure and pH. In-utero differences could arise because of: the position of the examined tube with relation to the cervix (oxygen partial pressure is higher near the cervix), differences in menstrual cycles (supply of oxygen-rich hemoglobin in red blood-cells), diet (pH variation of uterine fluid, blood), etc. For all these reasons it was chosen to omit a quantitative XRD analysis. Instead, site-specific quantitative data was obtained from an in vitro corrosion experiment of frameless Cu-IUDs in simulated uterine solutions. The results of this experiment are explained in paragraph S.3.

S.2.3.2 SEM-analysis

Additional information on the corrosion products formed, and possible differences on in utero corrosion due to site-specific effects was gained by a morphological study with SEM in BSE mode. Figure S.6 gives an overview of electron micrographs taken on the inside and outside of the in utero corroded IUDs. A micrograph number corresponds with the sample number as listed in Table S.1. The micrographs show that all samples have been affected by the uterine fluid and therefore participated in the contraceptive effect of the IUD. However, it seems that not all samples have been corroded to the same extent and, at time of removal, these could be classified within different stages of the corrosion process.

It can be generally concluded that corrosion is in an advanced stage on both sides of the analysed Cu IUD sleeves. In most cases, the damage is no longer restricted to discrete points but has taken place over large areas. However, no rupture of any of the sleeves was found, even when some devices had been inserted for more than 10 years. A remarkable feature can be noted on micrographs recorded on the inside of the cylinders (samples n° 1, 5, 7 and 9). The micrographs display the development of a fairly thick cuprite layer which cracks and peels off partially exposing the underlying copper to further corrosion. Conversely, the cuprite scale seems to already have detached on large areas of the outside (samples n°2, 4, 8, and 10). It should be

noted that the bulk copper exposed shows a different morphology to that of the reference Cu (sample n°11). The porosity of the cuprite scale allows further corrosion of bulk copper. This is confirmed by the crumbly state of copper found underneath a cuprite 'dome' (see detail Figure S.7 A). Differences in the general corrosion tendency observed in the micrographs, as seen in sample n°3 and sample n°6, can be attributed to changes in uterine environments between patients.

Cuprite is more likely to detach from the inside of O-shaped samples than from the inside of U-shaped samples. The corrosive environment of samples n°1/n°3 and n°7/n°9 was identical (same individual), which means both pairs of samples can be directly compared. The cuprite layer had detached completely from the inside of O-shaped sample n°3 while detachment on the inside of U-shaped sample n°1 is only partial. A similar tendency was noted on the inside of U-shaped sample n°7 and inside O-shaped sample n°9, where the cuprite scale was still intact in the U-shape and disintegration had already commenced in the O-shape. These observations are supported by the results of the XRD analysis. The cuprite reflections recorded from the U-shaped samples n°1 (Figure Appendix.9, top) and n°7 (Figure S.5) top show distinctly higher intensities than from the O-shaped samples n°3 (Figure Appendix.10, top) and n°9 (Figure S.4, top). Even though the issues regarding comparison of XRD reflections for extracting semi-quantitative information were discussed earlier, the additional information provided by the electron micrographs justifies the comparison made. Knowing that both copper tubes were adjacent in the identical corrosive environment, it is reasonable to conclude that more intense cuprite reflections represent a thicker cuprite scale on the IUD wall.

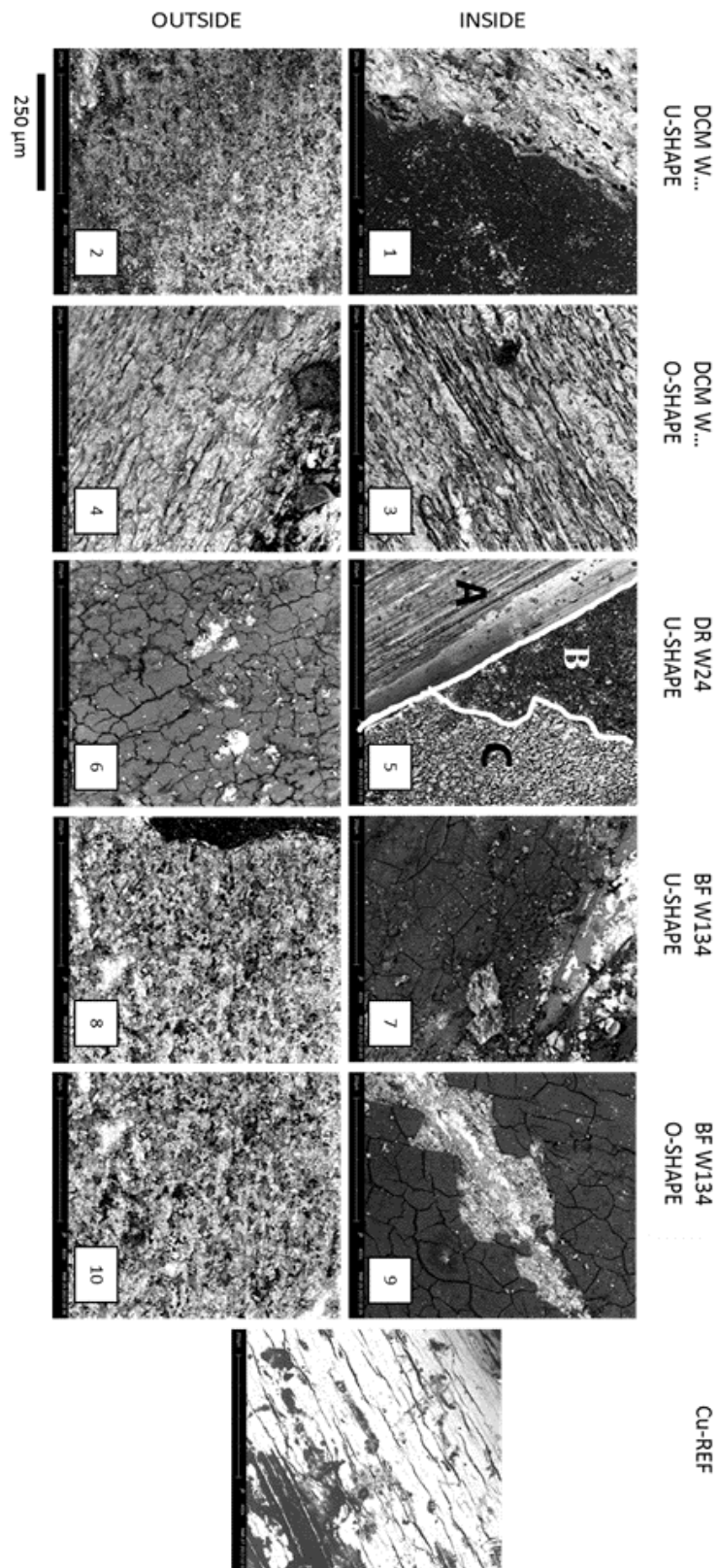


Figure S.6

Overview of electron micrographs recorded from all corroded samples and a reference sample. The numeration corresponds with Table 1. Micrograph n°5 displays the various stages of the in utero corrosion process. Micrographs are recorded with a 400x magnification. Part of this results were reprinted from [1] with permission from Elsevier.

The end views of an uncorroded reference sleeve and a GyneFix® sleeve (sample n°9) are depicted respectively in Figure S.7 B and Figure S.7 C. An attempt was made to determine differential copper loss of the IUD tube by measuring the inner and outer diameter of an uncut in utero corroded tube (sample n°12, 149 months corroded in utero) from the end-on micrograph with respect to the ID and OD of a reference sleeve. The ID of the reference sleeve was found to be 1.642 ± 0.002 mm, while the OD was found to be slightly tapered and on average 2.188 ± 0.008 mm with a wall thickness of 0.273 ± 0.008 mm. The ID and OD of a corroded tube was respectively estimated to be 1.674 ± 0.024 mm and 2.146 ± 0.046 mm. The error on the measurements of the corroded tubes are compounded of the standard errors on the mean of the independent measurements which largely arise from roughness and lack of circularity and concentricity in the corroded tube and the error on the scale factor. The expansion factor of 1.64, resulting from the conversion of copper (8.49×10^{22} Cu atoms per cm^3) to cuprite (5.16×10^{22} Cu atoms per cm^3) was taken into account in this calculation to determine the original copper thickness. Hence, the differential copper loss from the inner wall was found to be 0.016 ± 0.012 mm and 0.021 ± 0.027 mm from the outer wall. These values support the assumption that Cu is being dissolved in utero from both the inside and outside of the tube. While the relative errors of the ID and OD are small (1.4 and 2.1 % respectively), they translate into much larger relative errors for the dissolved copper. Considering these large errors, statistics should be obtained from a large number of samples for an accurate quantitative analysis of the differential copper loss. Unfortunately not enough samples are available for this.

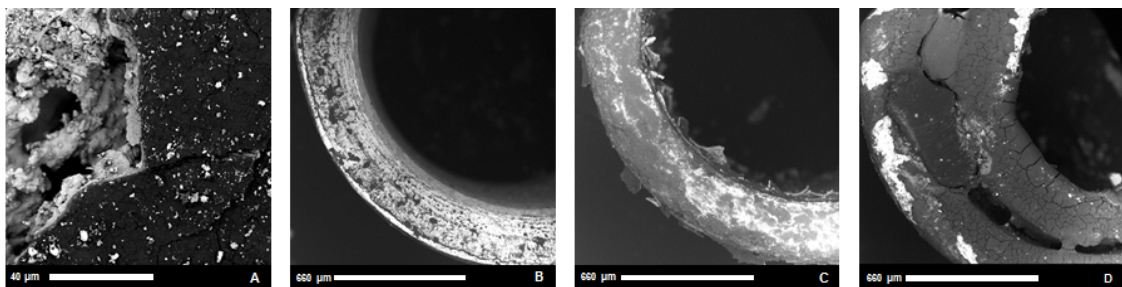


Figure S.7

[A] Detail of cuprite layer formed after 144 months in utero (sample n°1). Magnification is 2000x.

[B] Micrograph of end plane of copper reference sleeve. Magnification is 150x.

[C] Micrograph of end plane of O shaped sample corroded for 149 months in utero (sample n° 12). Magnification is 150x.

[D] Micrograph of end plane of U-shaped tube , corroded for 149 months in utero (sample n°13). Magnification is 150x.

S.2.3.3 Discussion

S.2.3.3.1 Monitoring the rinsing-effect on in vitro corroded copper with time-lapse SR-XRD

The results from the XRD experiments were perfectly conclusive: apart from metallic copper, solely Cu_2O was observed in the corrosion crust. Cuprite itself is not prone to dissolve cupreous ions since it is almost insoluble at the pH and temperature inside the uterus [32]. It is more likely that copper reacts alternatively to easily solvated solid corrosion products. Strikingly none of these products were observed in any of the recorded XRD patterns. It is even more surprising since the presence of organic compounds, copper phosphates, copper chlorides, copper sulfides and calcareous deposits (CaCO_3 a.k.a. vaterite) on in utero and in vitro corroded Cu-IUDs was reported elsewhere [33, 37, 41].

Experience in the field of heritage corrosion science taught us that cuprite can be formed during the hydrolysis of nantokite (CuCl), an important step in the progression of bronze disease [42, 43]. Therefore one must be aware that rinsing a fresh copper corrosion layer with water can drastically alter its composition. Unfortunately such a rinsing treatment was carried out (not by the author of this work) on the removed in utero samples before storage and XRD analysis. It is very likely that much of the soluble copper corrosion components were rinsed away during this procedure. Moreover, similar to the case for bronze disease, it is possible that other of the copper corrosion salts were converted into cuprite. If this presumption could be validated, this would immediately explain the sole observation of cuprite in the diffraction patterns.

In order to confirm this presumption, a time-lapse SR-XRD experiment was carried out to monitor the evolution of rinsing an in vitro corroded copper sample. In vitro corrosion of the copper coupon (12.5 mm diameter, 99.99% pure by Goodfellow, Cambridge) was done in a portable cell filled with a simulated uterine solution at pH = 6.2 and heated to 37°C in order to mimic uterine conditions [2]. The composition of the SUS is prepared according to the recipe by Mora et al. and contains: 0.167 g/L CaCl_2 (Merck, Darmstadt, Germany), 0.224 g/L KCl (Merck, Darmstadt, Germany) , 4.97 g/L NaCl (VWR, Radnor, USA), 0.48 g/L Urea (Merck, Darmstadt, Germany) , 0.5 g/L glucose (Sigma Aldrich, St-Louis, USA), 0.072 g/L $\text{NaH}_2\text{PO}_4 \cdot 2\text{H}_2\text{O}$ (Merck, Darmstadt, USA), 0.25 g/L NaHCO_3 (Merck, Darmstadt, Germany) and 35 g/L albumin (Sigma Aldrich, St- Louis, USA) [31]. The experiment was carried out at the XMaS beamline (station BM28, ESRF) using a Mar CCD 165 (Mar USA Inc.) 2D detector. The camera was mounted at 44.5° to the incident X-ray beam with a detector-sample distance of 132 mm. The primary X-ray energy was set to 8 keV and were directed onto the sample at an angle 10° with respect to the sample surface

into a 3 x 0.5 mm² footprint. A total of 85 diffraction patterns were recorded using an exposure time of 10 seconds per diffractogram. The time in between each measurement was 30 s and the beam was shuttered during this period to minimize sample damage and radiolysis. The first 10 diffraction patterns were recorded from a coupon pre-corroded in SUS for 28 hours drying to air. Between pattern 10 and 11 the sample was thoroughly rinsed with deionized ultrapure water. Accordingly the hydrolysis reaction of the corrosion product can be followed downstream from scan 11.

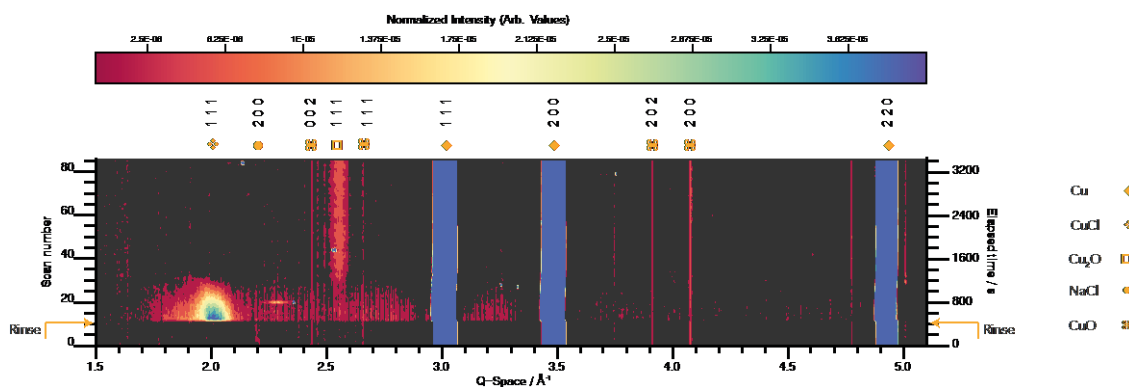


Figure S.8

Pattern set image of all diffraction patterns recorded during the progressive conversion of the IUD corrosion layer consequently to rinsing with deionized water. Each diffraction pattern has been used to modulate colour scale to form one row of the image. Rinsing took place after 10 scans.

Figure S.8 shows a pattern set image of all diffraction patterns recorded during the progressive conversion of the IUD corrosion layer as a consequence of rinsing. Each diffraction pattern has been used to modulate a colour scale to form one row of the pattern set image. Accordingly the figure displays the intensity per wavenumber in function of elapsed time (scan number). The square root intensity scale has been chosen in order to make minor reflections visible. A black coloured frame was added as a background in order to increase contrast. Apart from three extremely intense metallic Cu reflections, mainly tenorite (CuO) and some crystallized NaCl (halite) is visible in the dry pattern. It must be noted that the corrosion crust is the result of 28 h corroding in SUS. In other similar experiments, as described in more detail in paragraph S.4 and in [2], a more diverse spectrum in corrosion products was only observed after 72 h corrosion in SUS. The action of rinsing the in vitro corroded copper after 400 s (from scan 10 on) has a thorough influence on the diffraction patterns recorded. Almost immediately an intense reflection appears around 2.0 Å⁻¹ . Apart from this reflection a range of minor reflections appear simultaneously in the range 1.7 – 3.3 Å⁻¹ . Some of these reflections might presumably be ascribed to

diffuse scattering, a sequence of scattered X-rays falling between the Bragg peaks and raising the background, as a result of the wetted surface [44]. While another fraction might be assigned to certain crystalline products, it is not possible to do this with the raised background. Nevertheless, the strong reflection at 2.0 \AA^{-1} can be assigned to nantokite 111. After 1000 seconds, the diffuse background in combination with the nantokite 111 reflection disappears abruptly. This phenomenon is accompanied by the appearance of a strong reflection around 2.55 \AA^{-1} . The reflection can be ascribed to the cuprite 111 crystallographic plane. The nantokite produced upon rinsing the pre-corroded coupon progressively hydrolyzed into cuprite following a reaction described in more detail in [43, 45]. The reflection around 2.2 \AA^{-1} disappeared after rinsing. This confirms the solubility of this product and the ascribing the reflection to NaCl 200. Other reflections observed prior to the rinsing procedure were ascribed to CuO. The reflections of this insoluble product remained visible after rinsing.

The results of the experiment confirm that immediate rinsing of in utero removed Cu-IUDs can drastically alter its corrosion profile. Even though cuprite is typically observed as a corrosion product on the scale of in utero corroded Cu-IUDS, it must be acknowledged that a fraction of the cuprite here might be present as a result of the ex utero corrosion consequently to rinsing the devices upon removal.

S.2.3.3.2 Discussion of SEM results

Berthou et al. screened 461 T-shaped IUDs with SEM and described the results in [46]. They claim in utero corrosion of Cu-IUDs is a multi-step process. The authors propose that initiation of the corrosive attack by the uterine fluid is marked by a frosted, generally blackish surface with zones of slight wear (Stage I). Subsequently, pitting corrosion is initiated at several discrete points of attack, possibly due to differential aeration of the Cu-IUD [29] (stage II). Damaged areas develop into partly visible halo-shaped craters where, at the bottom, the metal appears crumbly. During the next stage, corrosion will penetrate deeper, creating voids in the metal covered by thin domes of cuprite (stage III). These then burst and entire pieces detach and disappear into the uterine fluid (stage IV). Deep circular and elliptical craters become apparent. Their subsequent coalescence eventually exposes the core of the copper over large areas. Eventually, the oxidation of solid copper will continue until the substrate is so thin that it breaks (stage V). An illustration of the process can be found in the supplementary information in the appendix of the thesis (Figure Appendix.12).

The three major stages of the corrosion process described by Berthou et al. are visible in three different contiguous regions of a BSE micrograph taken on the inside of the U-shaped sample n°5 (Figure S.6 5) Region A is the area where the polypropylene suture was squeezed on the copper wall and hence remained

uncorroded since no electrolyte could initiate corrosion. The longitudinal strips visible are the 'scarfs' from the drawing process of the copper, a feature also visible in the copper reference micrograph (Figure S.6 11). Region B is between stages II and III, where a thin layer of cuprite covers an underlying void and crumbly copper. This stage was imaged more clearly in sample 1 (Figure S.7 A). Region C becomes visible when the cuprite vault collapses and portions of blackish crust detach from the surface of the IUD. Still in the frame of this model, the SEM images suggest that the insides of the IUD sleeves are likely to be in stage III of the in utero corrosion process, with the exception of sample n°3. Accordingly all samples with an outside orientation are allocated to stage IV, with the exception of sample n°6.

S.2.4 CONCLUSION

The site-specific corrosive behaviour of 4 different in utero corroded IUD was analysed in order to verify whether an unconventional IUD design is efficient in contraceptive terms. In utero corroded copper sleeves were divided into ten different groups based on their shape (U or O), orientation (inside and outside) and in utero residence time (patient). X-ray diffraction only showed cuprite (Cu_2O) as corrosion product on both the inside and the outside of the copper sleeves, regardless of their shape. The exclusive presence of cuprite can be misleading and must be perceived with the knowledge that the in utero corroded IUDs were rinsed (for cleaning) after removal. A time-lapse SR-XRD experiment recorded on a copper samples corroded in a simulated uterine solution confirmed that rinsing of corrosion layer can intensely alter its composition. The hydrolysis of nantokite into cuprite was observed as one of the results and might be an additional source of the observed cuprite. Nevertheless, the site indifference of in utero corrosion in frameless Cu-IUDs was confirmed by backscattered electron micrographs recorded on the outside, inside and end plane of the IUD sleeve. Synchrotron X-ray diffraction (SR-XRD) and scanning electron microscopy (SEM) were considered as useful tools to evaluate the site specific corrosion behaviour of in-situ corroded medical devices after extraction. The apparent copper loss from both sides of the IUD sleeves suggest that the nominal copper surface area of the frameless IUD may be considered approximately equal to the efficient copper surface area.

S.3 SITE-SPECIFIC IN VITRO COPPER RELEASE STUDY OF FRAMELESS INTRAUTERINE DEVICES IN A SIMULATED UTERINE SOLUTION.

S.3.1 INTRODUCTION

The value of in vivo studies lies within the fact that certain body specific experimental conditions may be difficult to mimic in a laboratory set-up. In the particular case of simulating uterine environments, a substantial amount of work has been published [30, 31, 40, 47, 48]. It remains nevertheless quite difficult to mimic certain physical (viscosity, surface tension, etc.) and physiological (composition) parameters of the uterine environment. The importance and significance of analysing in utero (in vivo) corroded devices, as in paragraph S.2, is hence yielding results where these particular parameters are being accounted for. Unfortunately, in vivo studies show limitations when the corrosion behaviour of IUDs needs to be studied systematically. The obstruction of collecting data over longer periods and the individual variability have been mentioned as notable restrictions [36, 49]. Moreover, in the previous paragraph we concluded that XRD is not a suitable tool, in this particular case, to collect quantitative data mirroring the site-specific release behaviour of copper.

When intending to improve existing designs of Cu-IUDs, significant quantitative data for regarding site-specific release behaviour of cupric ions in frameless IUDs is required. This section describes the experiment in which the site-specific cupric ion release behaviour of frameless Cu-IUDs in simulated uterine solutions (SUS) was determined using flame atomic absorption spectroscopy (FAAS). Site-specific quantitative results were obtained by partially embedding the inside or the outside of a frameless Cu-IUD cylinder with a chemically resistant epoxy resin.

S.3.2 MATERIAL AND METHODS

S.3.2.1 Materials

All the devices could be subdivided into three groups depending on the site exposed to the simulated uterine medium.

Three IUDs of the GyneFix® 200 type with 2 O-shaped and 2 U-shaped tubes were used in subgroup 'ALL'. The samples in this subgroup were not embedded into epoxy resin and thus were fully immersed, i.e. both inside and outside oriented copper surface were in contact with the SUS. Three IUDs were assembled from 4 O-shaped copper cylinders and a suture thread to create subgroup 'OUTSIDE'. For each IUD, the inside of every copper cylinder was filled with epoxy. Consequently only the outside copper surface is accessible for the corrosive solution. Finally, the

outside of 4 O-shaped copper sleeves for each of three IUDs was selectively coated with epoxy resin. Therefore, the results from the subgroup 'INSIDE' represent the cupric ion concentration released from the inner surface.

Based on the measurements of the internal and external diameter of a copper cylinder in paragraph S.2.3.2, the exposed copper surface from the different subgroups was calculated. Each copper cylinder in the subgroup 'OUTSIDE' has an exposed outer surface of $34.37 \pm 0.14 \text{ mm}^2$. Both ends of the cylinder account for $3.28 \pm 0.02 \text{ mm}^2$ of exposed copper. Consequently the exposed copper area of the subgroup 'OUTSIDE' is $150.62 \pm 0.14 \text{ mm}^2$ copper per IUD .

Each cylinder within the subgroup 'INSIDE' has an exposed surface of $25.79 \pm 0.06 \text{ mm}^2$. In this subgroup, the ends of each cylinder were covered in epoxy, hence total exposed copper surface in this subgroup is $103.17 \pm 0.06 \text{ mm}^2$.

Since it was chosen to use the GyneFix® 200 with 2 O-shaped and 2 U-shaped tubes it is more difficult to calculate exactly the exposed area. As shown in Figure S.1 G, a U-shaped tube is crimped onto the suture, hence a part of the inner copper surface is shielded by the suture. Assuming that the change in exposed surface area as a result of shape transition (O-shape to U-shape) is negligible with respect to the loss of copper area due to suture shielding, an approximation of the exposed copper surface area of subgroup 'ALL' can be made. The suture diameter was established at $0.38 \pm 0.01 \text{ mm}$, hence the inner copper surface shielded by the suture in a U-shaped tube is $3.80 \pm 0.05 \text{ mm}^2$. Consequently, the total (approximated) exposed surface area of each IUD within the subgroup 'ALL' is $246.19 \pm 0.16 \text{ mm}^2$.

Slow-curing transparent epoxy of the type EpoFix (Struers Inc., Ballerup, Denmark) was used for selective screening of the copper cylinders. Figure S.9 A and Figure S.9 B respectively display a copper sleeve from the 'INSIDE' and 'OUTSIDE' subgroups.

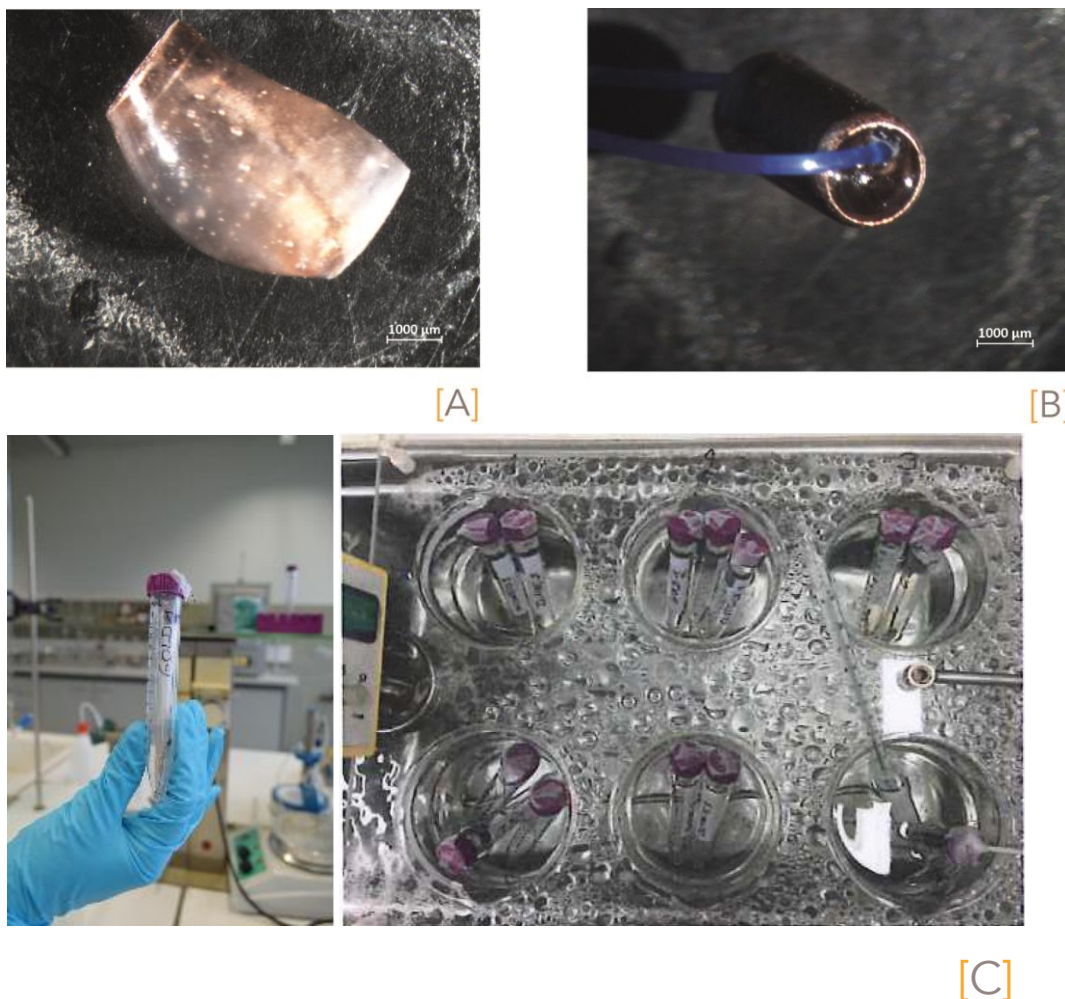


Figure S.9

[A] Image of a copper IUD sleeve from the INSIDE category. The sleeve is coated on the outside. The sleeve is accordingly only able to release cupric ions from the inside surface.

[B] Image of a copper IUD sleeve from the OUTSIDE category. The sleeve is coated on the inside. The sleeve is accordingly only able to release cupric ions from the outside surface.

[C] Experimental setup of the in vitro experiment. IUDs were immersed in 15 mL SUS in a container which was, in turn, immersed in a water bath thermostatically regulated at 37°C.

S.3.2.2 Preparation of simulated uterine solution and stock solution.

The in vitro corrosion experiments were carried out in simulated uterine solution (SUS). SUS was prepared by mixing: 0.167 g/L CaCl₂ (Merck, Darmstadt, Germany) 0.224 g/L KCl (Merck, Darmstadt, Germany), 4.97 g/L NaCl (VWR, Radnor, USA), 0.5 g/L glucose (Sigma Aldrich, St.-Louis, USA), 0.072 g/L NaH₂PO₄·2H₂O (Merck, Darmstadt, Germany), 0.25 g/L NaHCO₃ (Merck, Darmstadt, Germany) and 0.5 g/L albumin from bovine serum (BSA) (Sigma Aldrich, St.-Louis, USA). The solution was prepared with deionized water and reagent grade chemicals. This solution (without BSA) has been proposed by Zhang et al. [47] and used frequently in the past as a medium to simulate uterine conditions [8, 50, 51]. Bastidas and co-workers

demonstrated the importance of albumin in simulated uterine solutions [40]. Due to demanding sample pretreatment for FAAS and the poor reproducibility and data scatter observed in the results for reference samples, it was chosen not to use the solution in which 35 g/L albumin from egg was dissolved [40] (i.e. the solution used in the in-situ experiment explained in paragraph S.4). Instead, it was chosen to add 0.5 g/L of BSA to the solution in agreement with the experiment described by Xu et al [33]. The pH was adjusted in the range of 6.0 – 6.2 by adding dilute HCl (0.5 M) or NaOH (0.5 M) [31].

S.3.2.3 Instrumentation

The cupric ion concentration of the SUS was determined by flame atomic absorption spectroscopy (FAAS). The used instrument was an AAnalyst 200 by Perkin Elmer (Waltham, Massachusetts, U.S.A.). A copper hollow-cathode lamp operating at a wavelength of 324.75 nm was installed. Samples were introduced into an air-acetylene flame (air : 10 L/min , acetylene: 2.5 L/min).

S.3.2.4 Standard curve for cupric ions

Standard solutions of cupric ions with concentrations of 0.1, 0.5, 1, 5, 10, 15, 20 and 50 ppm were made by dilution of a 1000 ppm certified reference cupric ion solution (Certipur® reference materials, Merck, Darmstadt , Germany). The dilutions were prepared with the simulated uterine solution as described in paragraph S.3.2.2. A standard curve was obtained by individually spraying the standard solutions into the FAAS in order to determine their ion absorbance. Figure S.10 displays the calibration plot showing the FAAS absorbance vs. cupric ion concentration. The method produced satisfactory linearity in the interval of 0.1 – 50 ppm with linearity $R^2 = 0.9904$.

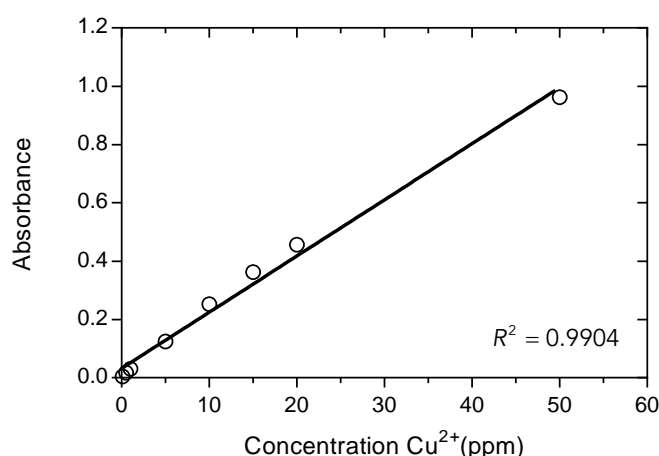


Figure S.10

Calibration curve showing absorbance as function of concentration of cupric ions. A satisfying linearity was obtained in the 0 – 50 ppm Cu²⁺ range.

S.3.2.5 Sample analysis and sampling

Figure S. 9 C shows the setup of the in vitro experiment. Each IUD of the three subgroups was immersed in 15 mL simulated uterine solution in separate containers and incubated at 37 ± 0.2 °C in a thermostatic water bath (Unitronic 320, Selecta, Barcelona, Spain) for 50 days. In order to determine its cupric ion concentration, samples of the simulated uterine solution were taken at: 1, 2, 3, 4, 5, 6, 7, 15, 22, 29, 36, 43 & 50 days after initial immersion of the IUDs. During sampling, aliquots of 2 mL of homogenized SUS were taken from each of the IUD container. Once the aliquot was diluted fivefold with nitric acid (0.5 M), sample was ready for FAAS analysis. After sampling, pH (6 - 6.2) and the original volume (15 mL) of the SUS was reinstalled in each container. All IUDs were immersed in fresh SUS after 7 days.

S.3.3 RESULTS AND DISCUSSION

The release profiles of cupric ions as a function of elapsed time for three subgroups of Cu-IUDs (ALL: nothing embedded, OUTSIDE exposed, INSIDE exposed) are shown in Figure S.11. The data demonstrate that all samples of the various subgroups follow a similar trend in cupric ion release behaviour. During the first week, the cupric ion is unstable. It typically grows to a maximum during the first three days followed by a steep decrease in copper dissolution. After the first week, it gradually evolved to an average value which remained relatively stable for the remaining time of the experiment. The intense release observed initially is typical of the behaviour of Cu-IUDs and is referred to as 'burst release' [16, 33, 51–53]. It is believed that the 'burst release' phenomenon is correlated with some discomforting side-effects of Cu-IUDs, such as excessive bleeding, intermenstrual spotting and pelvic pain [33, 49, 51]. The subsequent decrease is interpreted as an inhibiting effect of the corrosion products being deposited on the copper surface [31]. Since this behaviour is being reproduced in the different subgroups, one could conclude that the orientation of the copper surface does not influence its corrosion behaviour. In the period where Cu²⁺-ion release appears to be stable, from 20 days past initial immersion onwards, the average cupric ion release values were determined. The average level of subgroup 'ALL' was 141 ± 17 µg/day, where the average levels of 'OUTSIDE' and 'INSIDE' were respectively: 121 ± 14 µg/day and 50 ± 19 µg/day.

As calculated in section S.3.2.1, the exposed outer area is a factor 1.45 larger than the inner exposed area. Consequently, if orientation of the exposed surface would not influence the cupric ion release behaviour, a release of 83 µg/day would be expected for subgroup INSIDE. The experimental obtained value of 50 ± 19 µg/day hence indicates that orientation of the copper surface has a significant effect on the cupric ion release.

Based on these values one can quantify the relative release behaviour of the IUDs by dividing the experimentally obtained values for cupric ion release and exposed surface. Accordingly the samples of the subgroups 'INSIDE', 'OUTSIDE' and 'ALL' respectively have a cupric ion release of $0.48 \pm 0.18 \mu\text{g}\cdot\text{Day}^{-1}\cdot\text{mm}^{-2}$, $0.80 \pm 0.09 \mu\text{g}\cdot\text{Day}^{-1}\cdot\text{mm}^{-2}$, $0.57 \pm 0.07 \mu\text{g}\cdot\text{Day}^{-1}\cdot\text{mm}^{-2}$ in the stable phase after insertion (> 20 days). A lower relative release is observed for 'INSIDE' with respect to 'OUTSIDE'. This confirms the earlier conclusion that copper release is less efficient on the inside of the copper cylinder and that the relative release of differently oriented surfaces is not additive. Indeed, a higher relative release for 'OUTSIDE' is found with respect to subgroup 'ALL'. Whether the U-shaped end tubes have a bigger impact on the release than we think or whether the release rate being intensely modified by the speed by which the solute can diffuse out of the ends of the IUD cannot be concluded from this experiment. An in-vitro release study where the different release behaviour of U-shaped tubes with respect to O-shaped tubes is monitored will therefore be a valuable next step in this research. Outcome of the experiment might indicate if a novel design of IUD would benefit from solely O-shaped tubes and an alternative method for fixing the tubes onto the suture would be required.

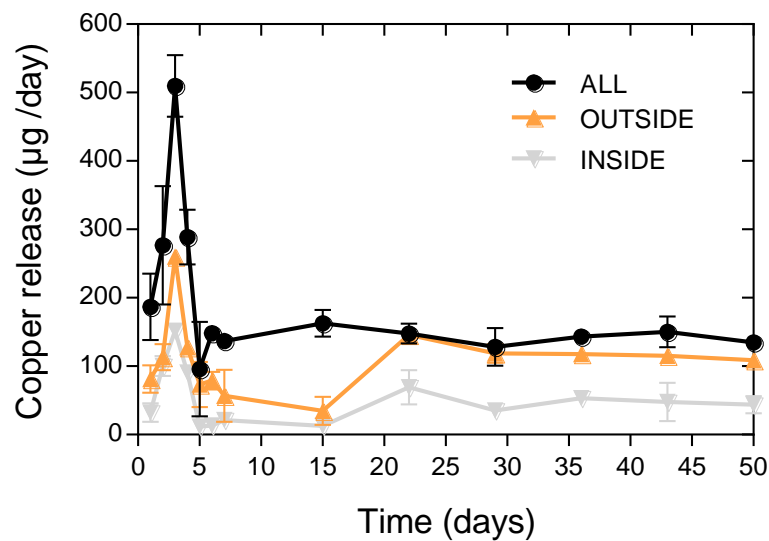


Figure S.11

Cupric ion release curve for the three categories of frameless IUDs: ALL (no coating, black), OUTSIDE (inside coating, orange) and INSIDE (outside coating, grey). Data points on the graph are mean values for all three IUDs per subgroup (per day) and error bars are composed from the standard deviation of the mean value.

S.3.4 CONCLUSION

In this experiment the site-specific cupric ion release rate was quantitatively determined during an in vitro study. Different categories within the samples were created by specifically embedding the outside and inside oriented surfaces of the copper cylinders in an epoxy resin. Subsequently, all samples from each category (outside exposed group, inside exposed group and control group) were immersed for 50 days in a simulated uterine solution and incubated at body temperature and pH values typical for a uterine environment. Cupric ion content of the simulated uterine solution was determined with flame atomic absorption spectroscopy at various time intervals during the experiment. After an initial burst release in the first week, an average cupric ion release rate of $141 \pm 17 \mu\text{g Cu}^{2+}/\text{day}$ was observed for the uncoated control group. Release rates of $121 \pm 14 \mu\text{g Cu}^{2+}/\text{day}$ and $50 \pm 19 \mu\text{g Cu}^{2+}/\text{day}$ were determined respectively for the outside exposed and inside exposed subgroup. The results of the study indicate that the inside of a copper tube contributes to the total cupric ion release. The release from an inner surface is however not as efficient as the outer surface of a copper cylinder and hence it could be concluded that the copper surface orientation has a significant influence on the release behaviour.

S.4 EVALUATION OF CORROSION BEHAVIOR OF COPPER-GOLD BEARING INTRAUTERINE DEVICES

S.4.1 INTRODUCTION

Metallic copper has been used as contraceptive agent in commercially available non-medicated IUDs since 1969 [36]. The popularity of copper-bearing intrauterine devices has increased intensely since 1969 and is now with nearly 160 million users the most widely used form of long acting reversible birth control [4–6]. Efforts have been made to adapt the design of the devices in order to improve the comfort of the users, especially in the creation of smaller devices. However, the exposed copper surface must be sufficiently large to release enough cupric ions to be anticonceptively efficient over several years. Increasing surface area to volume ratio by application of hollow copper cylinders strung on a flexible suture (i.e. frameless Cu-IUD) has been shown to be a valid improvement and was discussed in the previous paragraphs (S.2 & S.3). Increasing transfer efficiency of cupric ions would allow one to further minimize the size of the IUD. Moreover, increased uterine cupric ion concentrations potentially provide protection against sexually transmitted diseases [7, 54–58]. This section discusses the potential of bimetallic copper-gold bearing IUDs. Bringing copper into contact with the gold should substantially increase copper dissolution. In such a Cu-Au system, a galvanic corrosion reaction

will be induced in which Cu acts as a sacrificial anode (lower electrode potential) to the more noble gold [59–63].

In order to explore the possibility of using differential corrosion as the driving force to increase copper dissolution in bimetallic Cu-Au IUDs, a better understanding of the interaction of such a device with uterine fluid is required. Paragraph S.4.2 describes the results of an SR-XRD experiment in which initial corrosion of Cu-Au IUDs was monitored in situ of a simulated uterine solution. The measurements were carried out in a portable electrochemical and environmental cell (peCell) designed by Rosie Grayburn and Mark Dowsett and the results were published in *Bioelectrochemistry* [2]. Since it is complex to accommodate and record XRD patterns from actual frameless Cu-Au IUDs in the peCell, gold-coated copper coupons were used as samples as a model for the IUDs. Subsequently, frameless Cu-Au IUDs designed by Dr. Dirk Wildemeersch were used to determine the copper release rate of the devices in simulated uterine solution by flame atomic absorption spectroscopy.

S.4.2 SR-XRD STUDY OF CU-AU CORROSION IN SIMULATED UTERINE SOLUTIONS USING A PORTABLE SPECTROELECTROCHEMICAL CELL

S.4.2.1 Material and methods

peCell

In situ SR-XRD experiments were carried out in a heated portable electrochemical/environmental cell (peCell) filled with simulated uterine solution to simulate the uterine environment. Figure S.12 shows the portable cell, which is a multiple Bragg-type cell and was designed by Rosie Grayburn and Mark Dowsett [64]. The peCell serves as a 'sister' instrument to the earlier developed electrochemical/environmental cell for spectroelectrochemistry experiments, i.e. the eCell (Mk IV) by Dowsett and Adriaens [24, 42, 43, 65–68]. The emphasis of the peCell, different than the eCell, lies on long-term corrosion studies in a controlled atmosphere through spectroelectrochemistry. Since the long-term aspect includes moving the cell between the synchrotron and the home institution, portability was set as a priority in the design brief. The cell accommodates three pistons, each holding a working electrode with a sample, which can be remotely driven to either a surface analysis position (approximately 100 μm thick electrolyte layer) or an electrochemical/environmental exposure position (10 mm thick layer). By this means the dynamics of the corrosion can be monitored either through SR-XRD (upper surface analysis position) or by observing variations in corrosion potential (E_{corr} , lower

electrochemical/environmental position). A detailed description of the design specifications of the peCell can be found elsewhere [2, 64].

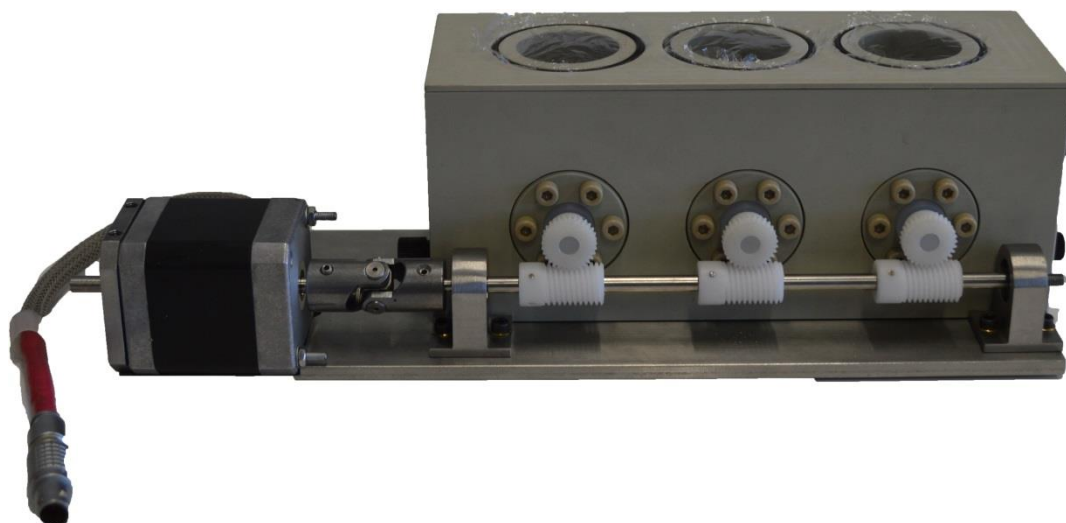


Figure S.12

The portable environmental/electrochemical cell (peCell) was designed by Rosie Grayburn and Mark Dowsett for long term corrosion studies. A detailed description of the peCell can be found in [2] and [64].

Cu/Au samples

Actual Cu-Au IUDs (Figure S.13) do not lend themselves to situ SR-XRD experimentation. Three gold-coated copper coupons of differing Cu/Au surface area ratio, each fitting in one of the three working electrodes of the peCell, were used to substitute the IUDs. Standard copper coupons (12.5 mm diameter, 99.99 % pure Cu, Goodfellow, Cambridge, United Kingdom) were polished following the procedure described in paragraph 4.1.1. Subsequently, each coupon was masked with a copper tape provided with an opening necessary to recreate a certain Cu/Au surface area ratio. Each taped sample was then sputter-coated with gold using a JFC – 1300 Auto Fine Coater (JEOL, Akishima, Tokyo, Japan) typically used for increasing conductivity in samples to be imaged with SEM. The masked coupons were sputtered at 30 mA for 600 s to deposit a layer of 100 ± 50 nm gold. Figure S.13 displays all samples after removal of the copper tape. The author greatly acknowledges Prof. Rino Morent and Prof. Nathalie de Geyter (Plasmapor research group, Department of Applied Physics, Ghent University) for lending the JEOL instrument and Gaelle Aziz and Pieter Cools for their assistance during operation of the sputter coater. Sample A was coated with a gold surface area in order serve as an analogue for a typical frameless IUD of the GyneFix® type, i.e. 2.83 mm diameter circular gold spot. Sample B and Sample C were respectively designed to exhibit a lower (1.5 mm

diameter circular gold spot) and higher (6.25 mm diameter circular gold spot) Cu/Au surface area ratios (Figure S.14).

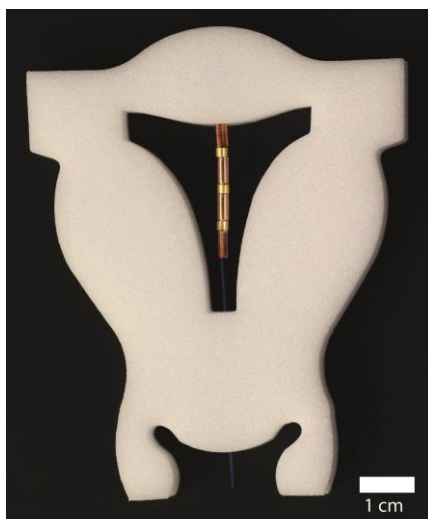


Figure S.13
Example of a frameless Cu-Au IUD.

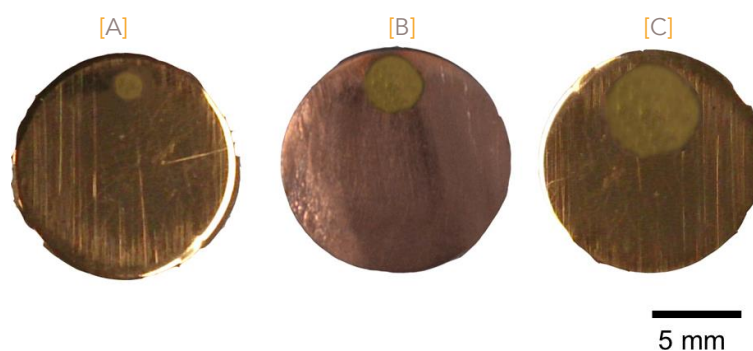


Figure S.14
Cu coupons provided with different areas of sputter-coated with gold were installed in the working electrodes of the peCell in order to study the influence of galvanic corrosion on the corrosion profile.

SR-XRD experiment

SR-XRD measurement were carried out at XMaS (BM 28, ESRF, see paragraph 3.3.2). The complete setup (see Figure S.15) included the peCell and a pump installation for providing the sealed peCell of fresh simulated uterine solution. The Cu/Au samples were mounted in the peCell in the Ghent laboratory two days prior to the beamtime and transported by car to the ESRF. The peCell was filled with simulated uterine solution (SUS) as described by Bastidas and co-workers [30]. SUS was prepared by

mixing: 0.167 g/L CaCl_2 , 0.224 g/L KCl, 4.97 g/L NaCl, 0.5 g/L glucose, 0.072 g/L $\text{NaH}_2\text{PO}_4 \cdot 2\text{H}_2\text{O}$, 0.25 g/L NaHCO_3 and 35 g/L crystallized egg albumin. The solution was prepared with deionized water and reagent grade chemicals and pH was set at pH = 6.2. During SR-XRD measurements, SUS was preheated to 37°C on a controlled hotplate (ESK Heicon, Heidolph Instruments, Schwabach, Germany) and circulated through the peCell using a peristaltic pump (502S by Watson Marlow, Wilmington Massachusetts, USA) with 5.5 mL/min flow rate for consistent supply of fresh SUS. The peCell was accommodated with a custom cartridge heater (made by Jorge Alves Anjos) for maintaining the temperature of SUS at 37°C both during transportation and experimentation. More details on the transportation unit for the heated peCell and the pump - peCell setup can be found in [64].

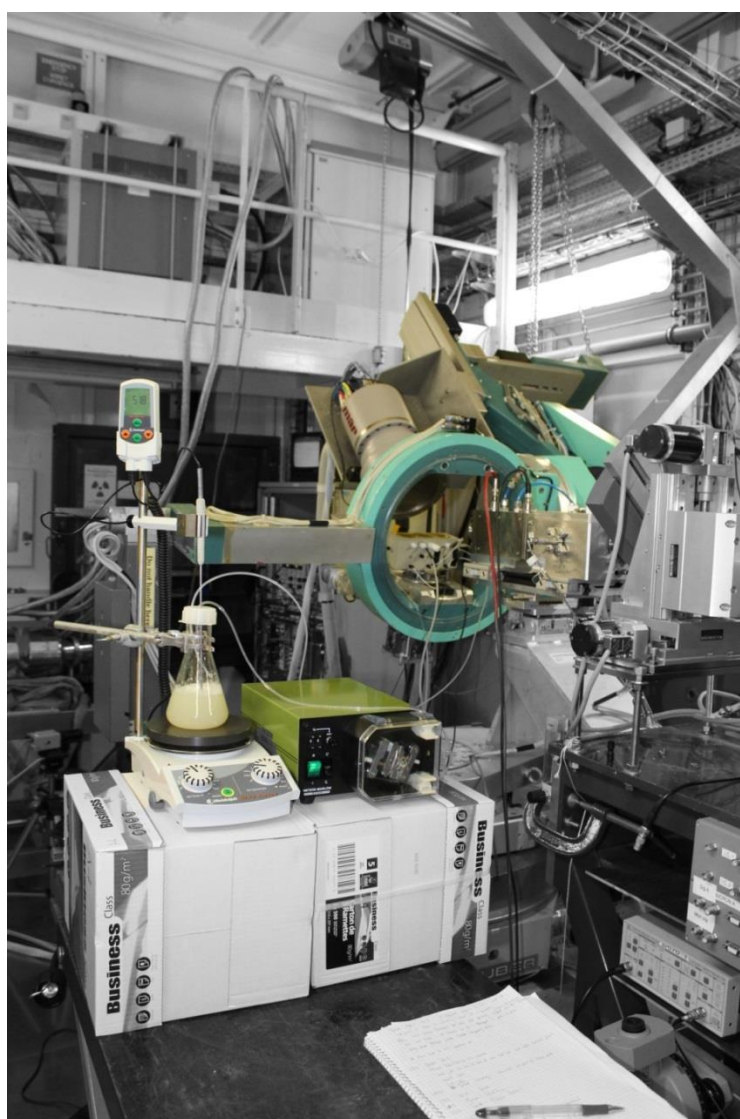


Figure S.15

The peristaltic pump and peCell on the XMaS beamline. The background was artificially set to black/white colours in order draw the attention to key parts of the setup.

In situ SR-XRD patterns were recorded from all samples at time intervals of approximately 24 h during the entire 5-day course of beam time allocation IX (Table 3.6). Diffraction patterns were collected using a Mar CCD 165 (Mar USA Inc.) 2D detector. The Mar was mounted at exactly 132 mm from the sample and at an angle of 44.5° with respect to the incident X-ray beam. An 8 keV X-ray beam was directed at the sample at 10° to the sample surface. This resulted in a X-ray beam footprint of approximately $3 \times 0.5 \text{ mm}^2$. All patterns were collected using an exposure time of 10 s. For each sample, a set of 9 diffraction patterns were collected at different positions across the Cu-Au boundary within a range of approximately 2 mm from the sample centre. Where necessary, a set of ten images per position were recorded to improve sensitivity. Ultimately, all patterns recorded during the line scan were summed to produce a single diffraction pattern representing the average corrosion on the Cu/Au sample. This procedure was done by Rosie Grayburn using esaProject software (see paragraph 3.2.2 and [24]) and was repeated for each sample and each day.

S.4.2.2 Results and discussion

Figure S.16 displays the summed diffraction patterns from the line scan across the Cu-Au boundary in samples A, B & C for each elapsed day with respect to the initial immersion time. Sample A was created to serve as an analogue for the frameless Cu-Au IUD model used during the in vitro experiments in paragraph S.4.3 (designed by Dirk Wildemeersch who based its design on the GyneFix® 200 type). The gold surface area accounted for 5% of the total coupon area. Significant reflections in the diffraction pattern indicating the initiation of corrosion appeared after 3 days in situ residence. This 3-day period coincides with the cupric ion 'burst release' peak observed in the release curve for Cu-Au IUDs in Figure S.17. Starting from day 4 in the release curve a steep drop in cupric ion release is observed. This event occurs simultaneously with the first signs of cuprite (Cu_2O) reflections therefore confirming the inhibiting effect of the cuprite scale on copper release. Apart from cuprite, main corrosion products could be assigned to CuS and Cu_2S . The development of a sulphur containing layer in utero was observed earlier by Chantler and co-workers [69] but it remained unclear whether it was a copper sulphide or deposited barium sulfate. The origin of sulfide ions can most likely be found within the disulfide bonds, known to be abundantly present in albumin [70]. The sputter-coated gold spot in sample B accounted for 1.4 % of the total coupon surface. Compared to sample A, a similar corrosion growth, including copper (I) & copper (II) sulphides, was observed in the first four days. Additional to crystallized NaCl , reflections indicating the growth of nantokite (CuCl) were observed. Development of nantokite at this stage might indicate delayed corrosion since nantokite is typically precursor to cuprite at $\text{pH} = 6.5$ and no cuprite was observed by day 7. Indeed, earlier research described the hydrolysis of nantokite to cuprite in circumstances comparable to intrauterine solutions [42, 71]. The most interesting results were observed on sample C which'

surface was covered with 25% of gold, the largest Cu/Au surface ratio of all samples. Although the surface was clearly covered with amorphous material (see below), no indications of crystalline products were seen before day 7 of the experiment. After 7 days, reflections in the diffraction patterns could be assigned to either calcareous deposits (CaCO_3) and a set of Cu^{2+} -compounds : CuCl_2 , CuO and CuS . The observation of CuCl_2 is especially interesting considering its high solubility in water, i.e. 76 g / 100 mL at 25°C [72]. Such a values suggest that CuCl_2 could equally be formed prior to day 7 but immediately dissolved before it could have been observed with XRD. In contrast, after 7 days, CuCl_2 was formed faster than it could dissolve and therefore appeared on the diffraction pattern. Moreover, absence of Cu_2O in the first seven days suggest no factors could impede copper dissolution. It can be concluded that the increase Cu/Au surface ratio established a notable shift in corrosion profile with respect to lower Cu/Au surface area ratio values. The observed set of corrosion products indicate copper dissolution rate had increased with reference to samples A & B. For a more detailed description of the evolution of E_{corr} , the reader is redirected to [2].

S.4.2.3 Conclusions

A portable multicell was used to monitor the evolution of corrosion occurring on three samples with each a different Cu/Au surface area ratio. After 2 days precorroding in the heated peCell and transportation to the ESRF, SR-XRD patterns were recorded from the three different samples every 24 hours for 5 consecutive days. Notable differences in composition of the corrosion crust were observed between the different samples. The gold coating strongly modifies the corrosion behavior in simulated uterine solutions. Increased dissimilar corrosion as a result of increasing gold area drives the surface reactions towards the formation of more soluble compounds which directly results in the augmented release of dissolved cupric ions.

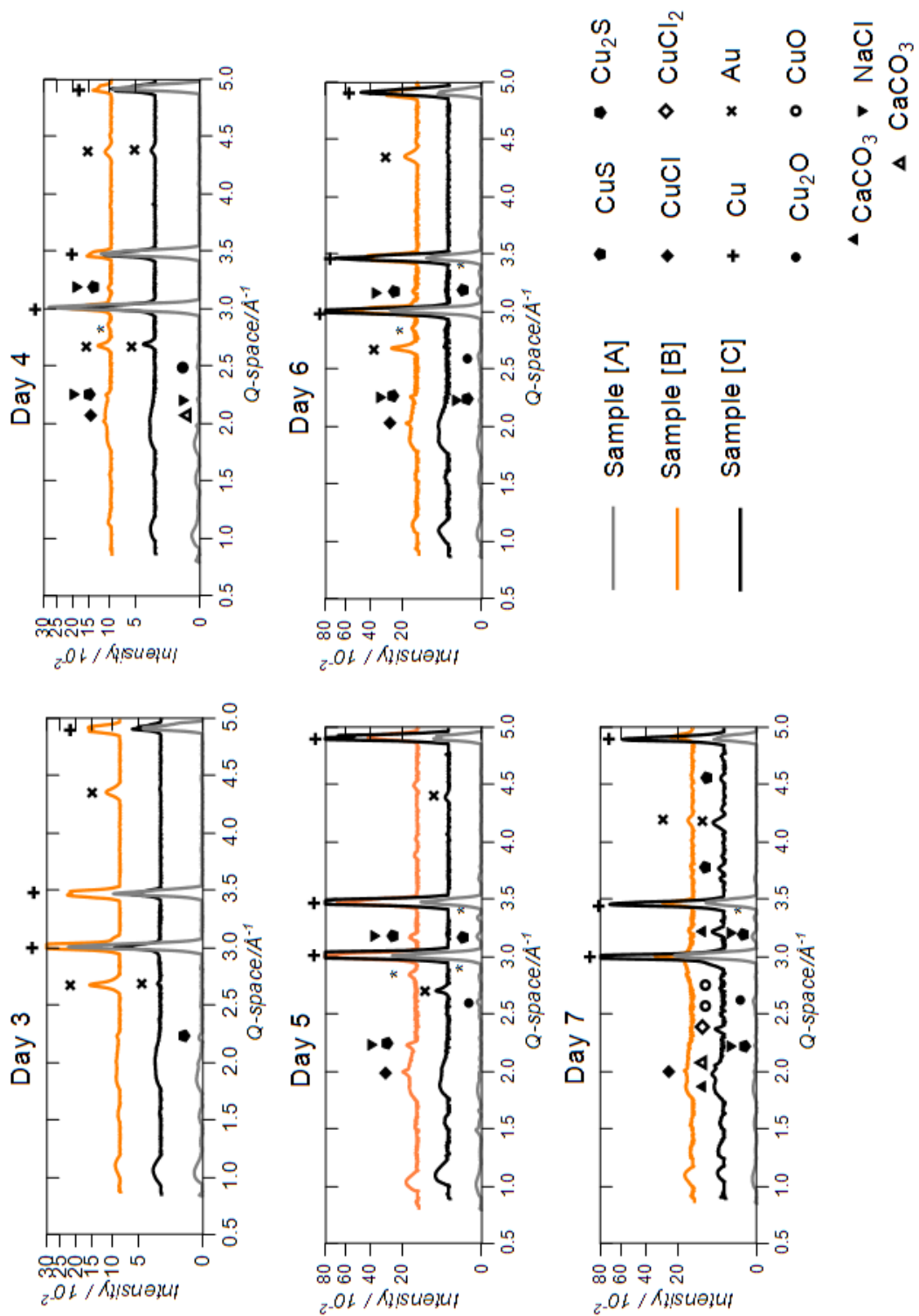


Figure S.16

Summed diffraction patterns across a 4 mm range on the surface of the samples A-C for five consecutive days. Corrosion products are labelled as shown. Unidentified peaks are marked with a *. Reprinted from [2] Copyright (2016) with permission from Elsevier.

S.4.3 IN VITRO COPPER RELEASE STUDY OF Cu-AU FRAMELESS INTRAUTERINE DEVICES IN SIMULATED UTERINE SOLUTIONS

This section describes the results obtained from the comparing release study of Cu and Cu-Au IUDs in simulated uterine solutions.

S.4.3.1 Material and methods

S.4.3.1.1 Frameless IUD samples

The design of the Cu-Au IUDs is very closely related to the design of the GyneFix®200. In essence, the Cu-Au IUD is a GyneFix®200 where each copper sleeve is in contact with one of in total 3 gold segments. Each gold ring is 99.99 % pure (Wieland Dental + Technik GmbH & Co, Pforzheim, Germany) and each ring is 2.20 mm high with an internal diameter of 1.66 mm and outer diameter of 1.90 mm. Figure S.13 displays an example of the used Cu-Au IUDs.

S.4.3.1.2 Methodology

The release study of the Cu-Au IUDs was performed in the same solution and under the same instrumental conditions as earlier described in S.3.2.2.

S.4.3.1.3 Sample analysis and sampling

Each IUD of the three subgroups was immersed in 15 mL simulated uterine solution in separate containers and incubated at 37 ± 0.2 °C in a thermostatic water bath (Unitronic 320, Selecta, Barcelona, Spain) for 50 days. Samples of the simulated uterine solution in order to determine its cupric ion concentration were taken at: 1, 2, 3, 4, 5, 6, 7, 15, 22, 29, 36, 43 & 50 days after initial immersion of the IUDs. During sampling, aliquots of 2 mL of homogenized SUS were taken from each of the IUD container. Once the aliquot was diluted fivefold with nitric acid (0.5 M), sample was ready for FAAS analysis. After sampling, pH (6 - 6.2) and the original volume (15 mL) of the SUS was reinstalled in each container. All IUDs were immersed in fresh SUS after 7 days.

S.4.3.1.4 Data evaluation

The average levels of cupric ion release rate of both Cu and Cu-Au IUDs was evaluated by a nonparametric test (Mann-Whitney U test) using the statistical part of the GraphPad Prism software (La Jolla, California, United States).

S.4.3.2 Results and discussion

The cupric ion release profiles of both the Cu and Cu-Au IUDs are shown in Figure S.17. The experiments were carried out simultaneously with the site-specific cupric ion release rate study, which was discussed in paragraph S.3. The release rate curve plotted for the Cu IUD is identical to the release rate curve for the 'ALL' of the experiment in paragraph S.3. The cupric ion release rate trend including an initial 'burst release' followed by a long period of stable cupric ion release is equally observed for the Cu-Au IUDs. Interestingly, the addition of Au had no influence on the time profile of this release behaviour. Burst release and cupric ion release rate stabilisation of the Cu-Au IUD was observed almost simultaneously to the Cu IUD. During the first two measurements, a notably higher cupric ion release rate was observed for the Cu-Au IUD w.r.t. the Cu IUD. At later points during the experiment, both Cu and Cu-Au IUDs were fluctuating around a similar average value. The average cupric ion release rate for the Cu-IUDs in the stable phase (> 7 days) was $143 \pm 18 \mu\text{g/day}$ while the average rate for the Cu-Au IUDs were $158 \pm 35 \mu\text{g/day}$. Although this value is slightly higher, there was no statistically significant difference between the release rate of both groups ($P = 0.3846$, $P > 0.05$). Even for the first data points at day 1 and day 2 no significant difference could be observed ($P = 0.1$ and $P = 0.2$ respectively). This observation is in contrast with the results from the SR-XRD study of the corrosion profiles discussed in the previous paragraph. The simple initial design of the Cu-Au IUD is most likely the reason why no difference in release rates were observed. Geometrical factors like anode/cathode surface area ratio, anode/cathode distance, geometrical forms of the dissimilar metals and the anode/cathode joint type (weld, fastener, etc.) strongly influence galvanic corrosion [63]. The smaller the ratio of the anode to cathode area, the faster galvanic corrosion will occur at the anode [63]. This statement was confirmed by our SR-XRD experiments where the sample with the lowest Cu-Au area ratio (largest Au area) showed the presence of the extremely soluble CuCl_2 [2]. Poor contact and low contact surface between the Cu and Au cylinders in the Cu-Au are probably the main reasons why galvanic corrosion between this dissimilar metals is not occurring and the current Cu-Au IUDs behave in an identical fashion as the Cu-IUDs. Moreover, as corrosion advances, contact between the Cu and Au cylinders can be hindered by the formation of a poorly conducting corrosion crust (e.g. Cu_2O) on the edge of the Cu cylinders. Improving design of the Cu-Au IUDs will require a fixed and larger Cu-Au contact surface than the current design.

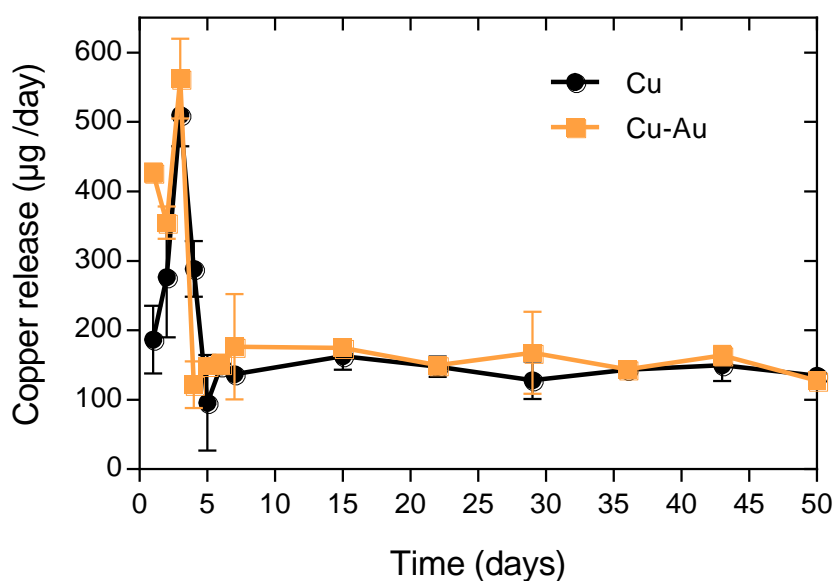


Figure S.17

Cupric ion release curve for frameless Cu (black) and Cu-Au (orange) IUDs. Data points on the graph are mean values for all three IUDs per subgroup (per day) and error bars are composed from the standard deviation of the mean value.

S.4.3.3 Conclusions

This experiment describes the results obtained during a quantitative comparative study of the cupric ion release rate between frameless Cu and Cu-Au IUDs. Both sets of IUDs were immersed for a period of 50 days in simulated uterine solution (SUS). The cupric ion content of the SUS solution was determined at various time points with flame atomic absorption spectroscopy. The Cu-Au IUD followed a similar cupric ion release rate trend as Cu IUDs with an initial burst release followed by a period of constant, lower release values. Even though increased Cu^{2+} release was suggested by the in situ SR-XRD experiments, no significant difference in release rate was observed between both groups of IUDs. Most likely the limited Cu-Au contact surface and absence of a fixed joint between both dissimilar metals prohibit galvanic corrosion to take place. A novel design of the Cu-Au in which the Cu-Au contact surface area is fixed and increased is designated. Sputtering or otherwise coating Cu IUD sleeves with gold may be an interesting approach in creating a more efficient Cu-Au IUD.

S.5 BIBLIOGRAPHY

- [1] D. Wildemeersch, P.J. Sabbe, M.G. Dowsett, V. Flexer, P. Thompson, D. Walker, P. a. Thomas, A. Adriaens, Assessment of copper corrosion from frameless copper IUDs after long-term in utero residence, *Contraception* 90 (2014) 454–459.
- [2] R.A. Grayburn, M.G. Dowsett, P.-J. Sabbe, D. Wermeille, J.A. Anjos, V. Flexer, M. De Keersmaecker, D. Wildemeersch, A. Adriaens, SR-XRD in situ monitoring of copper-IUD corrosion in simulated uterine fluid using a portable spectroelectrochemical cell, *Bioelectrochemistry* 110 (2016) 41–45.
- [3] K. Andersson, V. Odling, G. Rybo, Levonorgestrel-releasing and copper-releasing (Nova T) IUDs during five years of use: A randomized comparative trial, *Contraception* 49 (1994) 56–72.
- [4] G. Dean, E.B. Schwarz, in: R. Hatcher, J. Trussel, A. Nelson (Eds.), *Contraceptive Technology*, Ardent Media, New York, 2011, pp. 147 – 191.
- [5] D. Wildemeersch, A. Pett, T. Hasskamp, P. Rowe, M. Vrijens, Precision intrauterine contraception may significantly increase continuation of use: a review of long-term clinical experience with frameless copper-releasing intrauterine contraception devices, *Int. J. Womens. Health* 5 (2013) 215–225.
- [6] C. d’Arcangues, Worldwide use of intrauterine devices for contraception., *Contraception* 75 (2007) S2–7.
- [7] D. Wildemeersch, New frameless and framed intrauterine devices and systems - an overview., *Contraception* 75 (2007) S82–92.
- [8] S. Cai, X. Xia, C. Xie, Corrosion behavior of copper/LDPE nanocomposites in simulated uterine solution., *Biomaterials* 26 (2005) 2671–6.
- [9] J.M. Bastidas, J. Simancas, Characterization of corrosion products on a copper-containing intrauterine device during storage at room temperature., *Biomaterials* 18 (1997) 247–50.
- [10] B.L. Sheppard, The intrauterine contraceptive device, *Clin. Mater.* 3 (1988) 1–13.
- [11] D. Campoccia, L. Montanaro, C.R. Arciola, A review of the clinical implications of anti-infective biomaterials and infection-resistant surfaces., *Biomaterials* 34 (2013) 8018–29.
- [12] M.E. Ortiz, H.B. Croxatto, Copper-T intrauterine device and levonorgestrel intrauterine system: biological bases of their mechanism of action., *Contraception* 75 (2007) S16–30.
- [13] J. Lippes, Contraception with Intrauterine Plastic Loops, *Am. J. Obstet. Gynecol.* 93 (1965) 1024–1030.
- [14] J.A. Zipper, H.J. Tatum, L. Pastene, M. Medel, M. Rivera, Metallic copper as an intrauterine contraceptive adjunct to the “T” device., *Am. J. Obstet. Gynecol.* 105 (1969) 1274–1278.
- [15] W.H.O.S. Programme, D. Training, H. Reproduction, W. Bank, The TCu 380A IUD and the frameless IUD “the FlexiGard”: interim three-year data from an international multicenter trial. UNDP, UNFPA, and WHO Special Programme of Research, Development and Research Training in Human Reproduction, World Bank: IUD Research , *Contraception* 52 (1995) 77–83.
- [16] J. Li, J. Suo, X. Huang, C. Ye, X. Wu, Comparison of the release behaviors of cupric ions from metallic copper and a novel composite in simulated body fluid., *J. Biomed. Mater. Res. B. Appl. Biomater.* 85 (2008) 172–9.
- [17] H. Tatum, Metallic copper as an intrauterine contraceptive agent, *Am. J. Obstet. Gynecol.* 117 (1973) 602–618.
- [18] D. Wildemeersch, Effective copper surface area of IUDs., *J. Fam. Plann. Reprod. Health Care* 32 (2006) 54.
- [19] H. Timonen, Copper release from Copper-T intrauterine devices, *Contraception* 14 (1976) 25–38.
- [20] X. Cao, W. Zhang, X. Zhao, N. Lin, L. Wang, C. Li, L. Song, W. Zhang, Z. Zhang, D. Wildemeersch, Three-year efficacy and acceptability of the GyneFix 200 intrauterine system., *Contraception* 69 (2004) 207–11.
- [21] D. Wildemeersch, H.V.A.N.D.E.R. Pas, M. Thiery, H.V.A.N. Kets, W. Parewijck, W. Delborge, The Copper-Fix (Cu-Fix): a new concept in IUD technology, 4 (1988) 197–205.
- [22] D. Wildemeersch, I. Batar, B. Affandi, A. Andrade, W. Shangchun, H. Jing, C. Xiaoming, The “frameless” intrauterine system for long-term, reversible contraception: a review of 15 years of clinical experience., *J. Obstet. Gynaecol. Res.* 29 (2003) 164–173.
- [23] S.D. Brown, L. Bouchenoire, D. Bowyer, J. Kervin, D. Laundry, M.J. Longfield, D. Mannix, D.F.

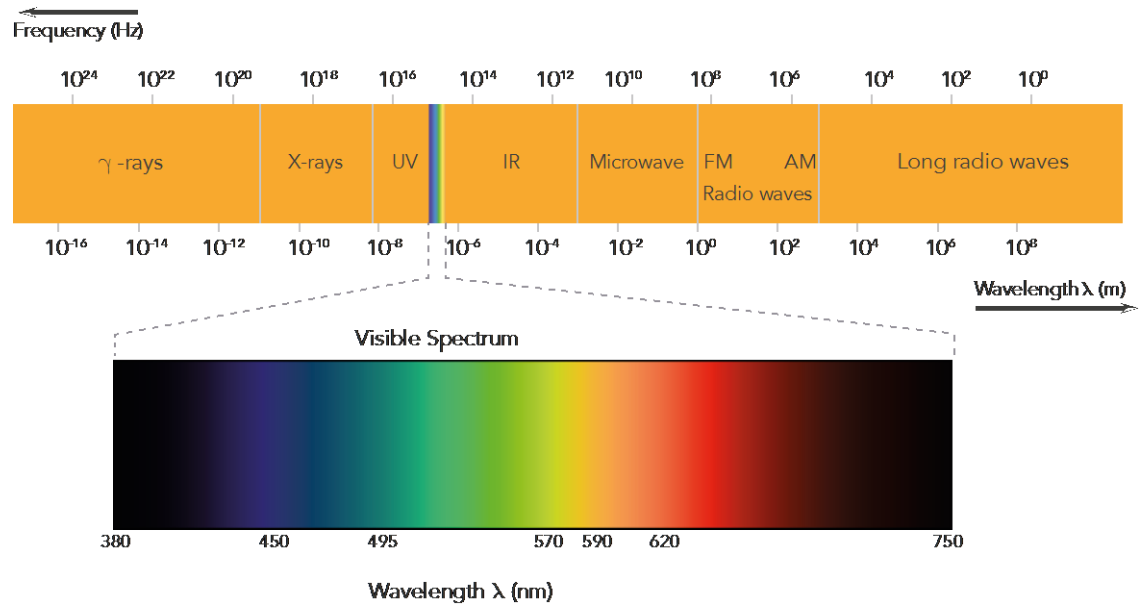
- Paul, a. Stunault, P. Thompson, M.J. Cooper, C. a. Lucas, W.G. Stirling, The XMaS beamline at ESRF: instrumental developments and high-resolution diffraction studies, *J. Synchrotron Radiat.* 8 (2001) 1172–1181.
- [24] A. Adriaens, M.G. Dowsett, K. Leyssens, B. Van Gasse, Insights into electrolytic stabilization with weak polarization as treatment for archaeological copper objects., *Anal. Bioanal. Chem.* 387 (2007) 861–8.
- [25] MinCryst [online] Available: <http://database.iem.ac.ru/mincryst/index.php>, [accessed june 2014].
- [26] A. V Chichagov, D.A. Varlamov, R.A. Dilanyan, T.N. Dokina, N.A. Drozhzhina, O.L. Samokhvalova, T. V Ushakovskaya, MINCRYST: a crystallographic database for minerals, local and network (WWW) versions, *Crystallogr. Reports* 46 (2001) 876–879.
- [27] G. Oster, M.P. Salgo, The copper intrauterine device and its mode of action., *N. Engl. J. Med.* 293 (1975) 432–8.
- [28] Oster, GK, Chemical reactions of copper intrauterine device, *Fertil. Steril.* 23 (1972) 18–23.
- [29] A. Kosonen, in: E. Hafez, W. van Os (Eds.), *Medicated Intrauterine devices*, Martinus Nijhoff, The Hague, The Netherlands, 1980, pp. 22–29.
- [30] J.M. Bastidas, E. Cano, N. Mora, Copper corrosion-simulated uterine solutions., *Contraception* 61 (2000) 395–9.
- [31] N. Mora, E. Cano, E.M. Mora, J.M. Bastidas, Influence of pH and oxygen on copper corrosion in simulated uterine fluid, *Biomaterials* 23 (2002) 667–671.
- [32] D.A. Palmer, Solubility Measurements of Crystalline Cu₂O in Aqueous Solution as a Function of Temperature and pH, *J. Solution Chem.* 40 (2011) 1067–1093.
- [33] X.X. Xu, F.L. Nie, Y.B. Wang, J.X. Zhang, W. Zheng, L. Li, Y.F. Zheng, Effective inhibition of the early copper ion burst release with ultra-fine grained copper and single crystal copper for intrauterine device application., *Acta Biomater.* 8 (2012) 886–96.
- [34] E.M. Sherif, S.-M. Park, 2-Amino-5-ethyl-1,3,4-thiadiazole as a corrosion inhibitor for copper in 3.0% NaCl solutions, *Corros. Sci.* 48 (2006) 4065–4079.
- [35] E.-S.M. Sherif, Effects of 2-amino-5-(ethylthio)-1,3,4-thiadiazole on copper corrosion as a corrosion inhibitor in 3% NaCl solutions, *Appl. Surf. Sci.* 252 (2006) 8615–8623.
- [36] B. Cao, T. Xi, Y. Zheng, Release behavior of cupric ions for TCu380A and TCu220C IUDs., *Biomed. Mater.* 3 (2008) 044114.
- [37] J.M. Bastidas, N. Mora, E. Cano, J.L. Polo, Characterization of copper corrosion products originated in simulated uterine fluids and on packaged intrauterine devices., *J. Mater. Sci. Mater. Med.* 12 (2001) 391–7.
- [38] W.H. Zachariasen, *Theory of X-Ray Diffraction in Crystals*, Dover Publications, 2004.
- [39] A. Duran, J. Castaing, P. Walter, X-ray diffraction studies of Pompeian wall paintings using synchrotron radiation and dedicated laboratory made systems, *Appl. Phys. A* 99 (2010) 333–340.
- [40] D.M. Bastidas, E. Cano, E.M. Mora, Influence of oxygen, albumin and pH on copper dissolution in a simulated uterine fluid., *Eur. J. Contracept. Reprod. Health Care* 10 (2005) 123–30.
- [41] K. Patai, M. Berényi, M. Sipos, B. Noszál, Characterization of calcified deposits on contraceptive intrauterine devices, *Contraception* 58 (1998) 305–308.
- [42] R. Grayburn, M.G. Dowsett, M. Hand, P.-J. Sabbe, P. Thompson, A. Adriaens, *Bronze Disease Revealed? A synchrotron X-ray diffraction study of nantokite hydrolysis*, 2014.
- [43] M. Dowsett, A. Adriaens, C. Martin, L. Bouchenoire, The use of synchrotron X-rays to observe copper corrosion in real time., *Anal. Chem.* 84 (2012) 4866–72.
- [44] D. Vaknin, *X-Ray Diffraction and Spectroscopic Techniques for Liquid Surfaces and Interfaces*, *Charact. Mater.* (2012).
- [45] R. Grayburn, M.G. Dowsett, M. Hand, P.-J. Sabbe, P. Thompson, A. Adriaens, *Bronze Disease Revealed? A synchrotron X-ray diffraction study of nantokite hydrolysis*, *Corros. Sci.* 91 (2014) 220–223.
- [46] J. Berthou, F.C. Chrétien, P.A. Driguez, Dégradation in utero des DIU au cuivre en fonction du temps . Le phénomène de corrosion métallique . Étude au microscope électronique à balayage Degradation of copper IUDs in utero . The process of metallic corrosion . A scanning electron microscope study, *Gynécologie, Obs. Fertil.* 31 (2003) 29–42.
- [47] C. Zhang, N. Xu, B. Yang, The corrosion behaviour of copper in simulated uterine fluid, *Corros. Sci.* 38 (1996) 635–641.
- [48] H. Xue, N. Xu, C. Zhang, Corrosion Behavior of Copper in a Copper Bearing Intrauterine Device in the presence of indomethacin, *Contraception* (1998).

- [49] L. Jinying, L. Ying, G. Xuan, G. Yanli, L. Jianping, Investigation of the release behavior of cupric ion for three types of Cu-IUDs and indomethacin for medicated Cu-IUD in simulated uterine fluid., *Contraception* 77 (2008) 299–302.
- [50] Z. Yang, C. Xie, Zn²⁺ release from zinc and zinc oxide particles in simulated uterine solution, *Colloids Surfaces B Biointerfaces* 47 (2006) 140–145.
- [51] F. Alvarez, P.L. Schilardi, M.F.L. de Mele, Reduction of the “burst release” of copper ions from copper-based intrauterine devices by organic inhibitors., *Contraception* 85 (2012) 91–8.
- [52] F. Alvarez, C. Grillo, P. Schilardi, A. Rubert, G. Benítez, C. Lorente, M.F.L. de Mele, Decrease in cytotoxicity of copper-based intrauterine devices (IUD) pretreated with 6-mercaptopurine and pterin as biocompatible corrosion inhibitors., *ACS Appl. Mater. Interfaces* 5 (2013) 249–55.
- [53] T. Xu, H. Lei, S.Z. Cai, X.P. Xia, C.S. Xie, The release of cupric ion in simulated uterine: New material nano-Cu/low-density polyethylene used for intrauterine devices., *Contraception* 70 (2004) 153–7.
- [54] J.-L. Sagripanti, M.M. Lightfoote, Cupric and Ferric Ions Inactivate HIV, *AIDS Res. Hum. Retroviruses* 12 (1996) 333–337.
- [55] J. Sagripanti, Mechanism of copper-mediated inactivation of herpes simplex virus, *Antimicrob. Agents Chemother.* 41 (1997) 812–817.
- [56] G. Borkow, H.H. Lara, C.Y. Covington, A. Nyamathi, J. Gabbay, Deactivation of human immunodeficiency virus type 1 in medium by copper oxide-containing filters., *Antimicrob. Agents Chemother.* 52 (2008) 518–25.
- [57] C.D. Lytle, Mechanism of copper-mediated inactivation of herpes simplex virus . Mechanism of Copper-Mediated Inactivation of Herpes Simplex Virus, 41 (1997).
- [58] a R. Karlström, R.L. Levine, Copper inhibits the protease from human immunodeficiency virus 1 by both cysteine-dependent and cysteine-independent mechanisms., *Proc. Natl. Acad. Sci. U. S. A.* 88 (1991) 5552–6.
- [59] R. Gonen, L. Gal-or, A. Zilberman, S. Mordechai, A copper-based intrauterine device with gold or platinum core: in vitro and in vivo studies, *Contraception* 24 (1981) 657–671.
- [60] C. Goh, W. Chong, T. Lee, C. Breach, Corrosion Study and Intermetallics Formation in Gold and Copper Wire Bonding in Microelectronics Packaging, *Crystals* 3 (2013) 391–404.
- [61] R. Bakish, W.D. Robertson, Galvanic Potentials of Grains and Grain Boundaries in Copper Alloys, *J. Electrochem. Soc.* 103 (1956) 320.
- [62] K. Oldham, J. Myland, M. Bond, *Electrochemical Science and Technology*, John Wiley & Sons, West-Sussex, 2012.
- [63] A. Groysman, *Corrosion for Everybody*, Springer Netherlands, 2009.
- [64] R. Grayburn, Spectroelectrochemical Techniques for the conservation of metallic artefacts (PhD Thesis), (2015).
- [65] M.G. Dowsett, A. Adriaens, Cell for simultaneous synchrotron radiation X-ray and electrochemical corrosion measurements on cultural heritage metals and other materials., *Anal. Chem.* 78 (2006) 3360–5.
- [66] A. Adriaens, M. Dowsett, The coordinated use of synchrotron spectroelectrochemistry for corrosion studies on heritage metals., *Acc. Chem. Res.* 43 (2010) 927–35.
- [67] R. Wiesinger, R. Grayburn, M. Dowsett, P.-J. Sabbe, P. Thompson, A. Adriaens, M. Schreiner, In situ time-lapse synchrotron radiation X-ray diffraction of silver corrosion, *J. Anal. At. Spectrom.* 30 (2015) 694–701.
- [68] A. Adriaens, M. Dowsett, G. Jones, K. Leyssens, S. Nikitenko, An in-situ X-ray absorption spectroelectrochemistry study of the response of artificial chloride corrosion layers on copper to remedial treatment, *J. Anal. At. Spectrom.* 24 (2009) 62–68.
- [69] E. Chantler, P. Kenway, Z. Larouk, E.B. Faragher, J. Morris, A. Kosonen, H. Allonen, M. Elstein, An analysis of the corrosion process of the nova-T IUD, *Adv. Contracept.* 10 (1994) 287–301.
- [70] X.M. He, D.C. Carter, Atomic structure and chemistry of human serum albumin., *Nature* 358 (1992) 209–215.
- [71] G. Bianchi, P. Longhi, Copper in sea-water, potential-pH diagrams, *Corros. Sci.* 13 (1973) 853–864.
- [72] J.A. Dean, *Handbook of Organic Chemistry*, McGraw-Hill Book Co., New York, 1987.

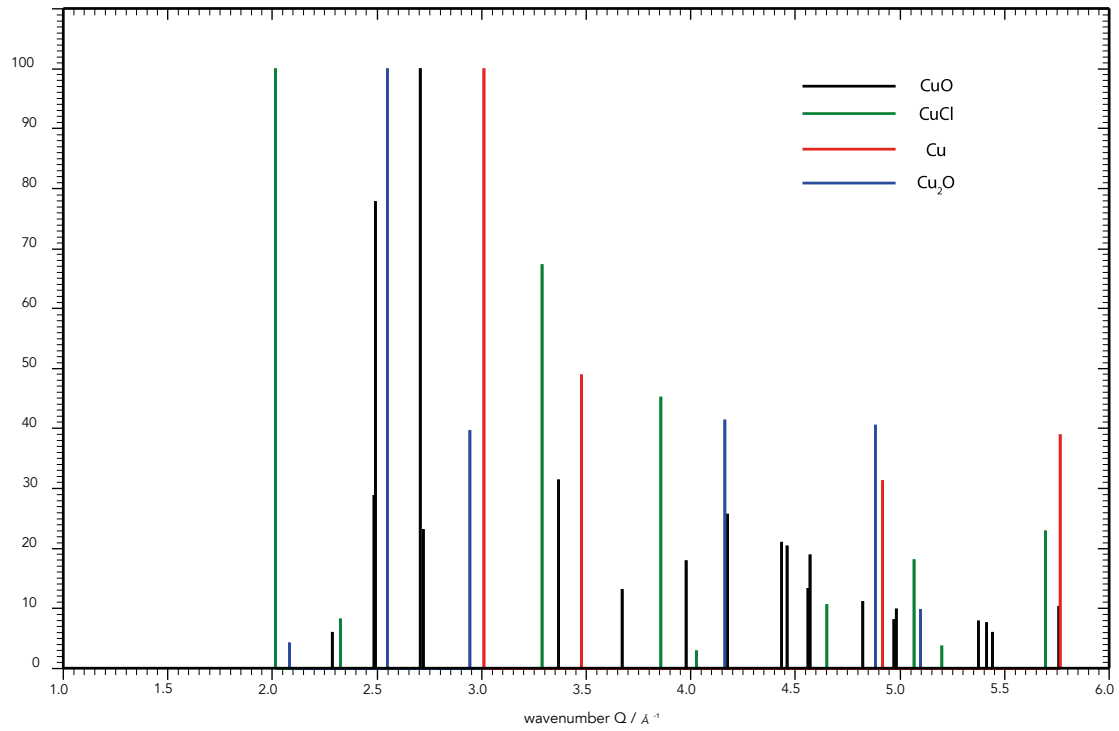
Appendix

—

Appendix



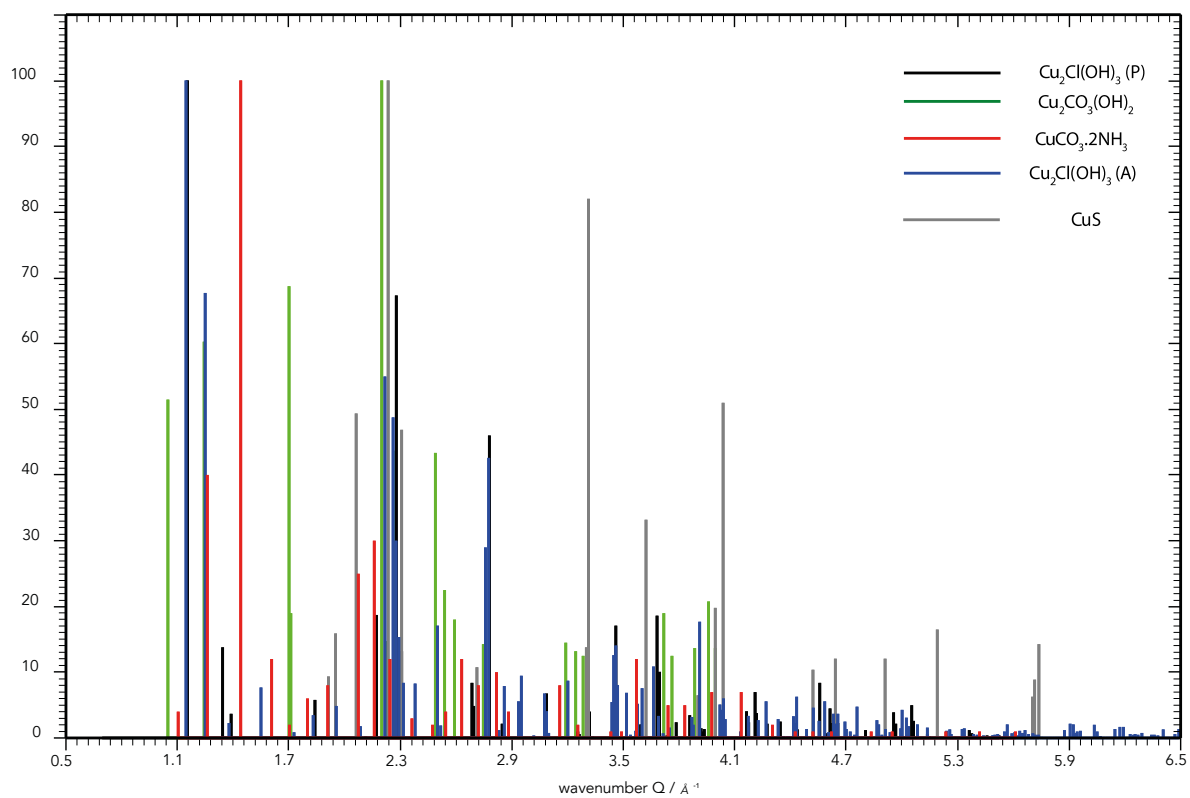
A.1 Electromagnetic spectrum



	HKL	Q(Å ⁻¹)
Cu		
	1 1 1	3.01
	2 0 0	3.48
	1 1 3	5.76
	2 2 0	4.92
Cu ₂ O		
	1 1 1	2.55
	2 2 0	4.16
	1 1 3	4.88
	2 0 0	2.94
	2 2 2	5.1
CuCl	1 1 0	2.08
CuCl		
	1 1 1	2.01
	2 2 0	3.29
	1 1 3	3.85
	2 2 4	5.69
	3 3 1	5.07
	4 0 0	4.65
	2 0 0	2.32
	4 2 0	5.2

CuO		
	1 1 1	2.71
	1 1 -1	2.49
	2 0 -2	3.37
	0 0 2	2.48
	1 1 -3	4.17
	2 0 0	2.72
	0 2 2	4.43
	3 1 -1	4.46
	2 2 0	4.57
	2 0 2	3.98
	1 1 3	4.56
	0 2 0	3.67
	3 1 1	4.82
	1 3 -1	5.76
	2 2 -2	4.98
	0 0 4	4.97
	3 1 -3	5.37
	2 2 2	5.41
	4 0 0	5.44
	1 1 0	2.28

A.2 XRD reference patterns of tenorite (CuO), nantokite (CuCl), copper (Cu) and cuprite (Cu₂O).

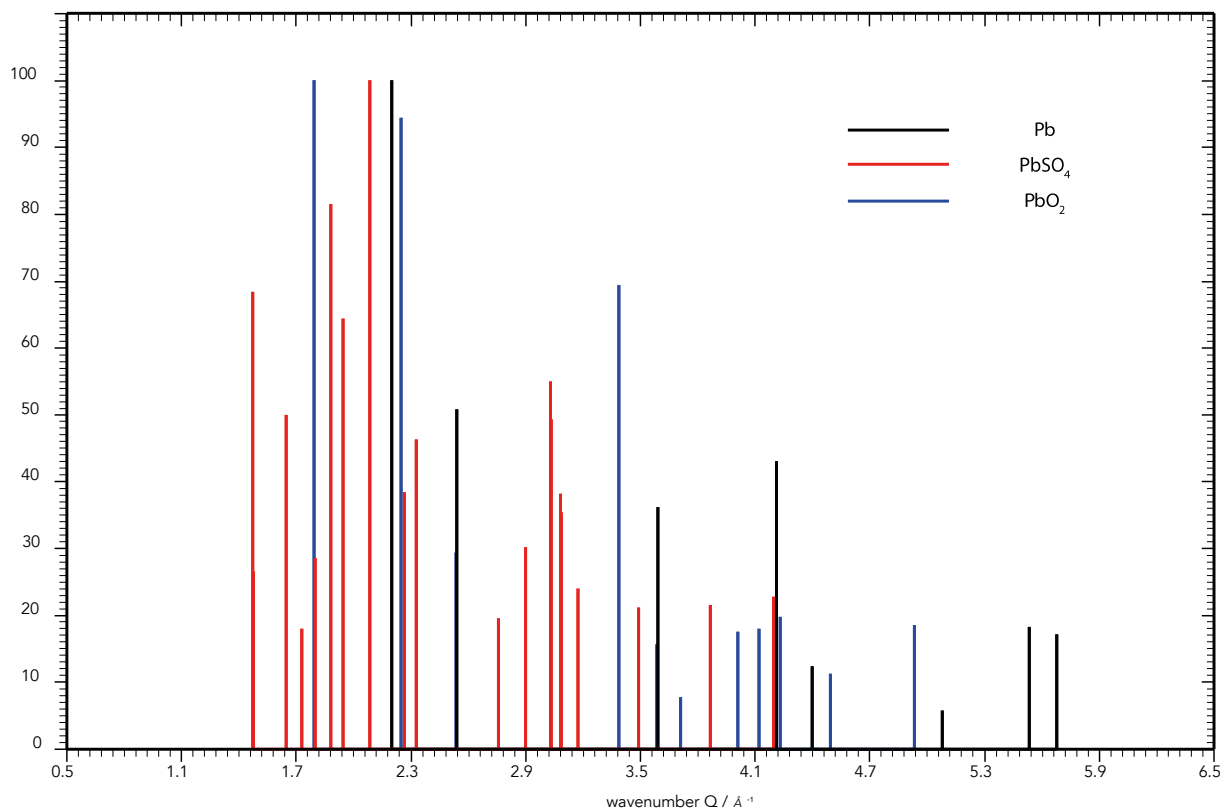


	HKL	Q(Å ⁻¹)
Cu₂Cl(OH)₃ (P)		
Paratacamite	2 0 -1	1.15
	4 0 4	2.78
	2 2 3	2.28
	2 2 -3	2.28
	4 4 0	3.68
	4 0 1	2.17
	6 0 3	3.46
	4 0 -2	2.31
	0 0 3	1.34
	0 0 6	2.68
	2 0 -7	3.31
	4 0 -5	3.09
	8 0 -4	4.61
	4 4 -6	4.56
	4 4 6	4.56
	4 0 -8	4.16
	4 2 -7	0.35
	2 4 7	4.21
	6 0 -3	3.46

$\text{Cu}_2\text{Cl}(\text{OH})_3$ (A)	0 1 1	1.15
Atacamite	1 0 1	1.25
	1 2 1	2.22
	2 2 0	2.77
	0 1 3	2.26
	0 0 4	2.76
	2 1 0	2.28
	2 2 4	3.91
	2 0 2	2.50
	2 2 3	3.46
	0 4 0	3.66
	0 2 2	2.29
	2 3 0	3.45
	2 4 2	4.43
	3 0 1	3.20
	1 2 3	2.95
	0 4 4	4.58
	2 2 1	2.86
	1 0 5	3.60
	2 3 1	3.52
$\text{Cu}_2\text{CO}_3(\text{OH})_2$		
	2 0 -1	2.20
	2 2 0	1.70
	1 2 0	1.24
	0 2 0	1.05
	2 1 -1	2.26
	2 4 0	2.49
	2 0 1	2.54
	0 1 2	3.96
	1 3 0	1.71
	4 4 -1	3.72
	2 1 1	2.59
	0 2 1	2.23
	3 2 1	3.19
	2 2 1	2.75
	4 3 1	3.88
	3 5 1	4.00
	4 2 -1	3.24

	1 1 1	2.23
	5 2 -1	3.76
	1 5 -1	3.28
CuS		
	1 0 3	2.23
	1 1 0	3.31
	1 1 6	4.04
	1 0 2	2.06
	0 0 6	2.31
	1 0 8	3.62
	2 0 3	3.99
	2 1 3	5.19
	1 0 1	1.95
	3 0 0	5.74
	1 0 7	3.30
	1 0 11	4.64
	2 0 8	4.91
	1 0 5	2.71
	1 1 8	4.52
	1 0 0	1.91
	1 0 14	5.71
	2 0 2	3.90
	2 0 11	5.70
	0 0 8	3.08

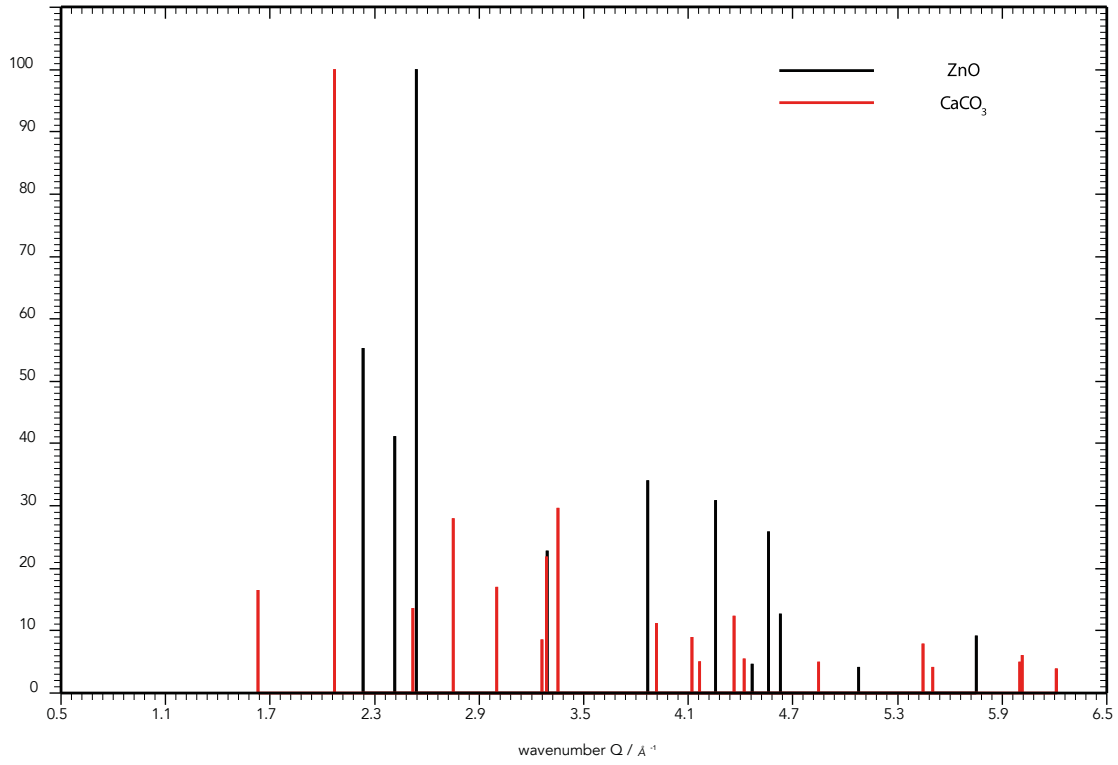
A.3 XRD reference patterns of paratacamite ($\text{Cu}_2\text{Cl}(\text{OH})_3$ (P)) , malachite ($\text{Cu}_2\text{CO}_3(\text{OH})_2$), ammonium copper carbonate ($\text{CuCO}_3 \cdot 2\text{NH}_3$) , atacamite ($\text{Cu}_2\text{Cl}(\text{OH})_3$ (A)) and covellite (CuS).



	HKL	$Q(\text{\AA}^{-1})$
Pb	1 1 1	2.20
	2 0 0	2.54
	1 1 3	4.21
	2 2 0	3.59
	3 3 1	5.53
	4 2 0	5.68
	2 2 2	4.40
	4 0 0	5.08
	PbO₂	1 1 0
1 0 1		2.25
2 1 1		3.39
2 0 0		2.53
3 0 1		4.23
3 2 1		4.93
1 1 2		4.12
3 1 0		4.01
2 2 0		3.58
2 0 2		4.49
0 0 2		3.71

PbSO ₄		
	2 1 1	2.08
	2 1 0	1.88
	0 1 1	1.47
	1 0 2	1.94
	1 1 3	3.03
	1 1 1	1.65
	1 2 2	3.03
	0 2 0	2.33
	1 1 2	2.27
	3 1 2	3.08
	4 0 1	3.09
	2 2 1	2.90
	0 0 2	1.80
	2 0 0	1.48
	4 1 0	3.17
	3 2 3	4.19
	4 2 1	3.86
	3 0 3	3.49
	2 2 0	2.76
	2 0 1	1.73

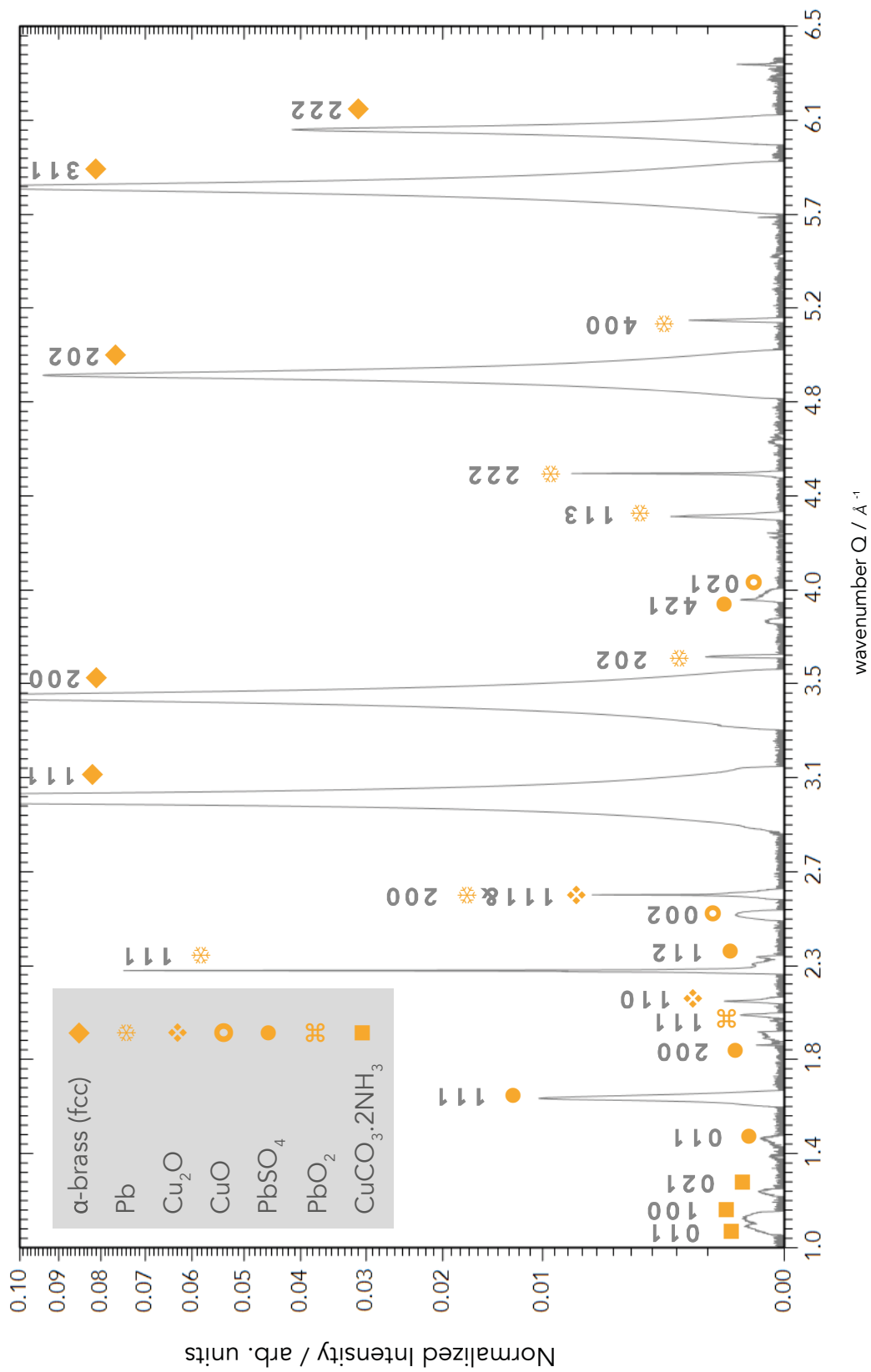
A.4 XRD reference pattern of lead (Pb), anglesite (PbSO₄) and plattnerite (PbO₂)



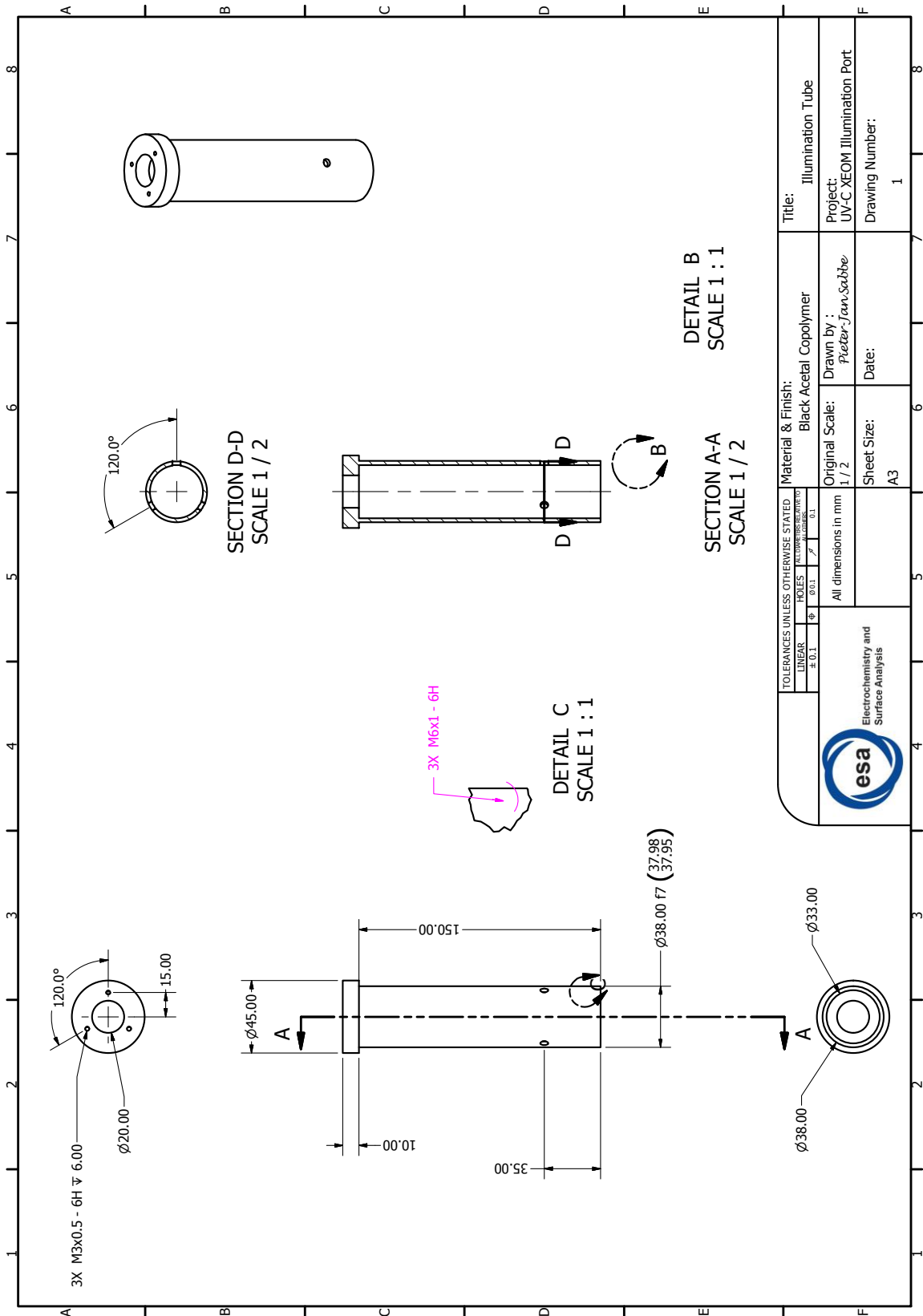
	HKL	$Q(\text{\AA}^{-1})$
ZnO		
	1 0 1	2.54
	1 0 0	2.23
	0 0 2	2.41
	1 1 0	3.87
	1 0 3	4.26
	1 1 2	4.56
	1 0 2	3.29
	2 0 1	4.63
	2 0 3	5.75
	2 0 0	4.47
	2 0 2	5.08
CaCO ₃		
	1 0 4	2.07
	1 1 6	3.35
	1 1 3	2.75
	1 0 -8	3.29
	2 0 -2	3.00
	1 0 -2	1.63
	1 1 0	2.52
	3 0 0	4.36
	2 1 -2	3.92

	2 1 4	4.12
	2 0 -4	3.26
	3 1 -4	5.45
	3 1 8	6.01
	0 0 12	4.42
	1 1 9	4.16
	2 1 -8	4.85
	4 0 4	6.00
	2 2 6	5.50
	3 0 -12	6.21
	3 0 12	6.21

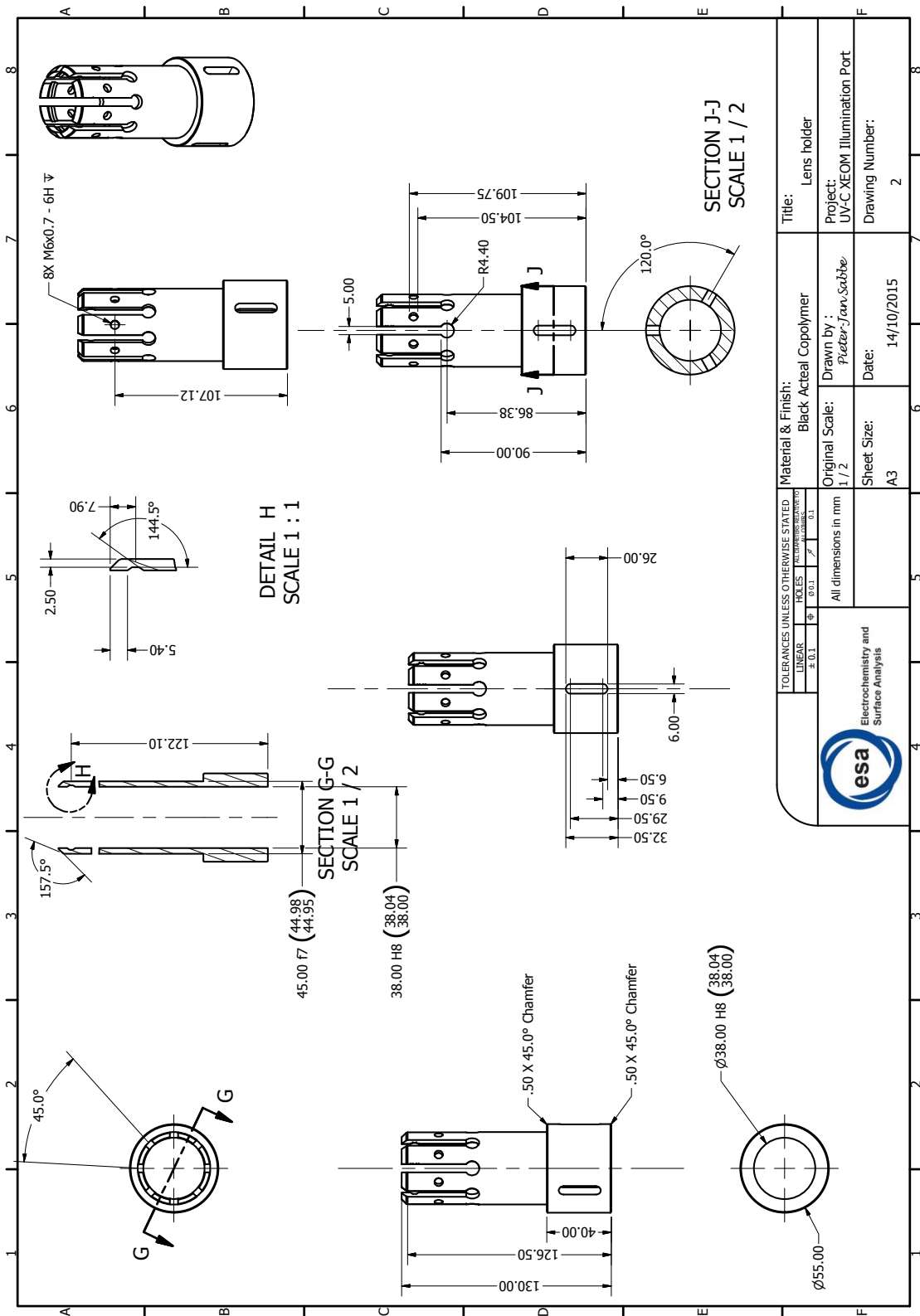
A.5 XRD reference pattern of zincite (Zn) and calcite (CaCO_3) .



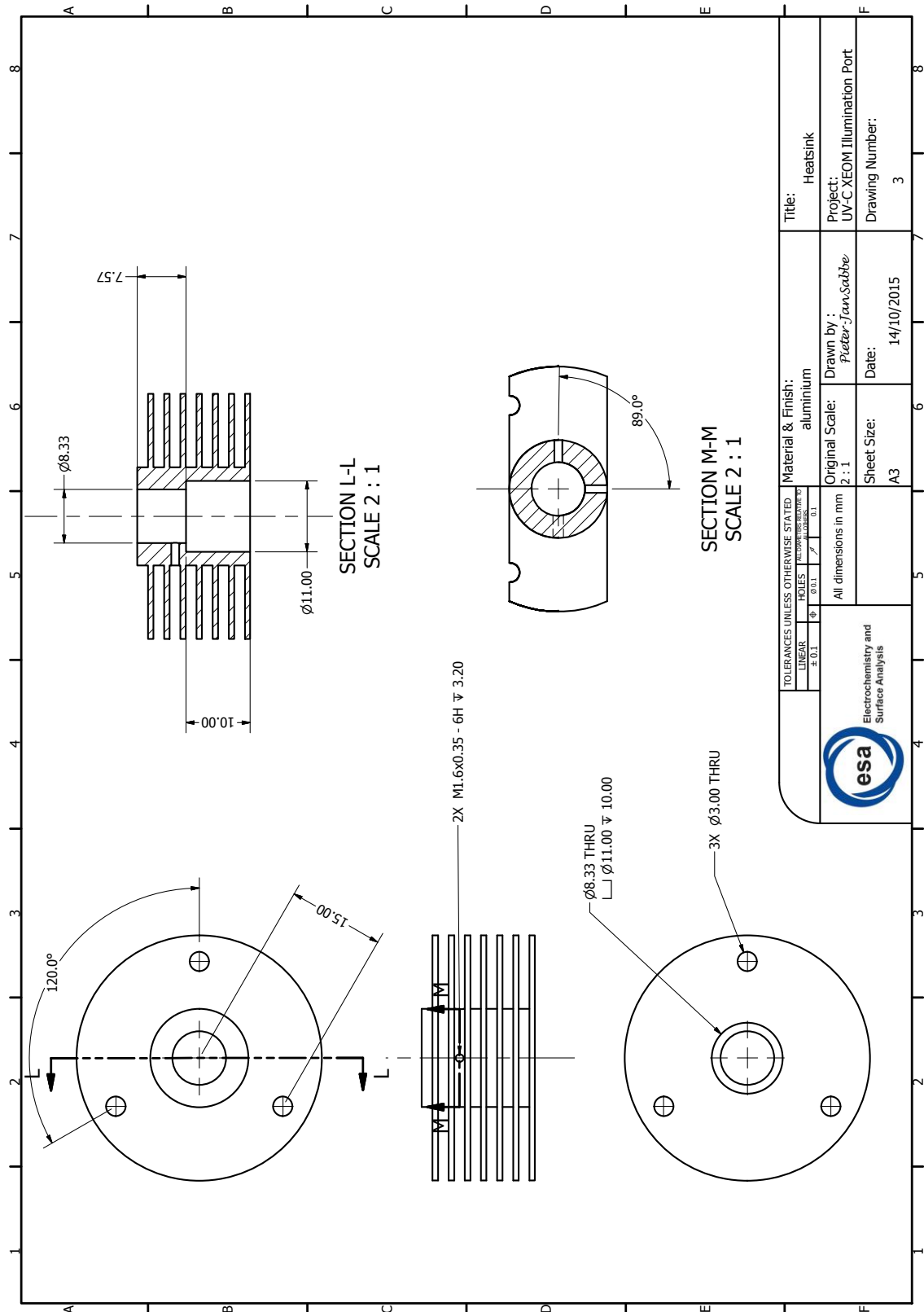
A.7 1-D diffraction pattern recorded from the conserved chain mail link MR81A1436.



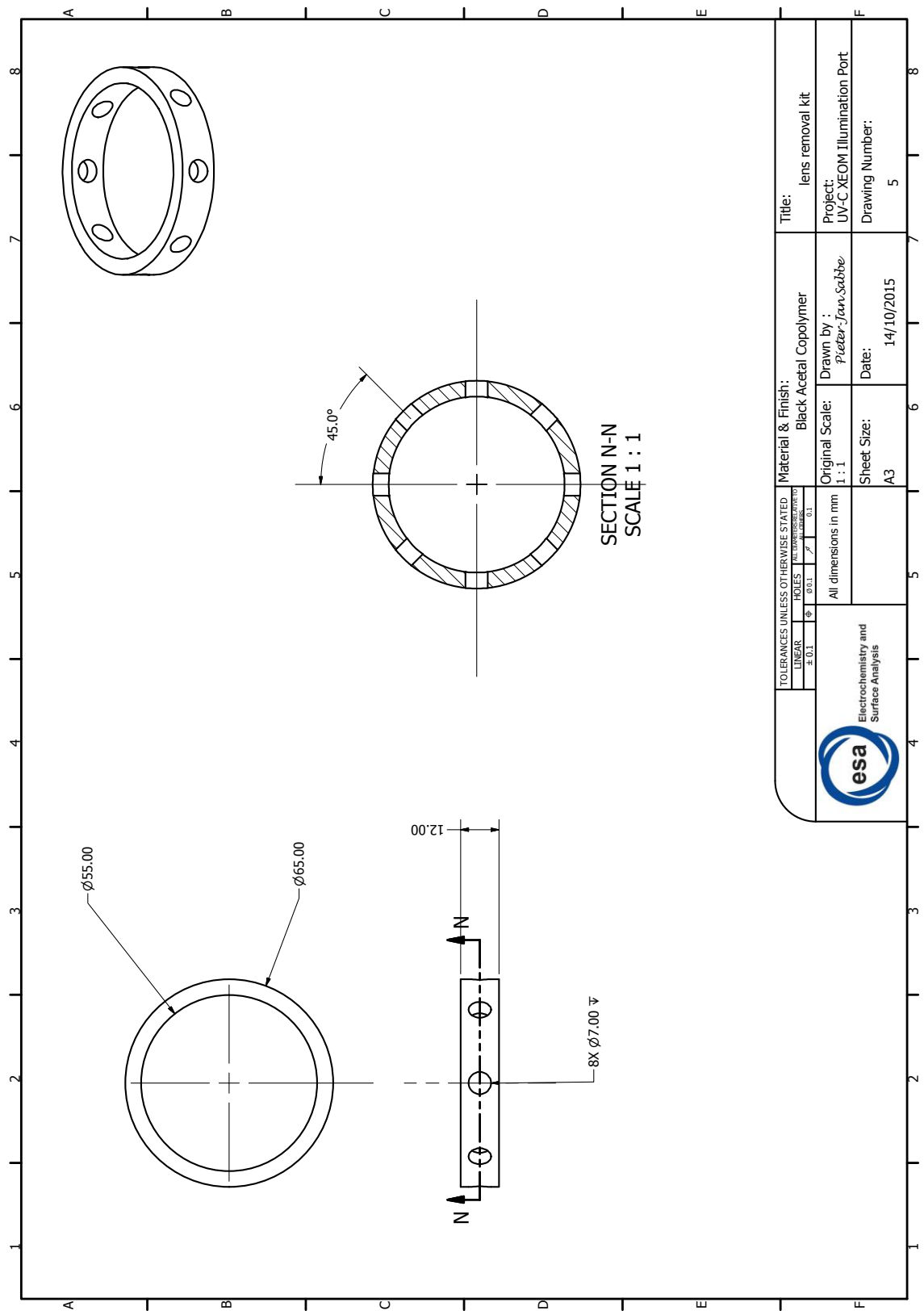
A.8 Technical drawing: illumination tube




A.9 Technical drawing: lens holder

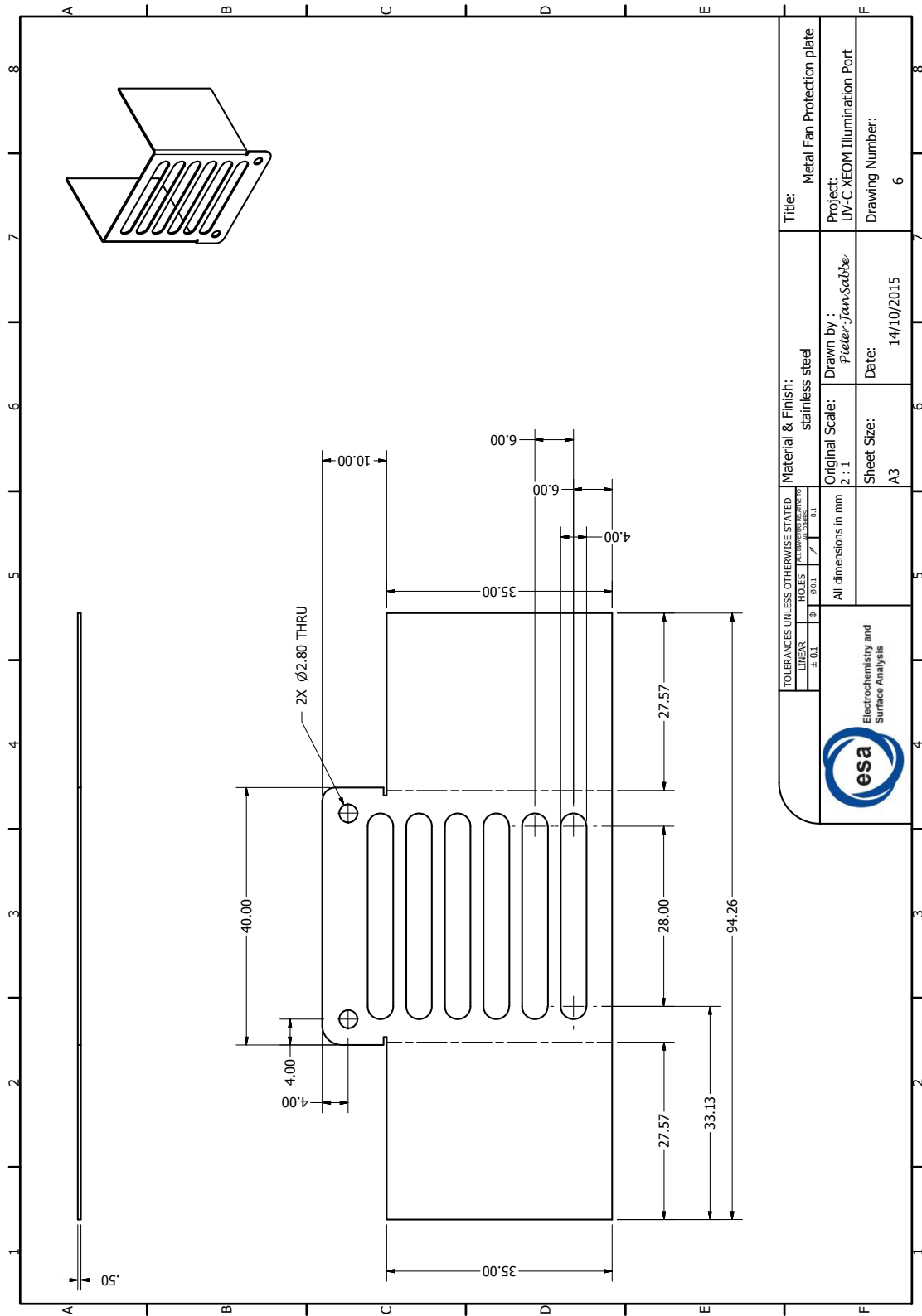


A.10 Technical drawing: heatsink



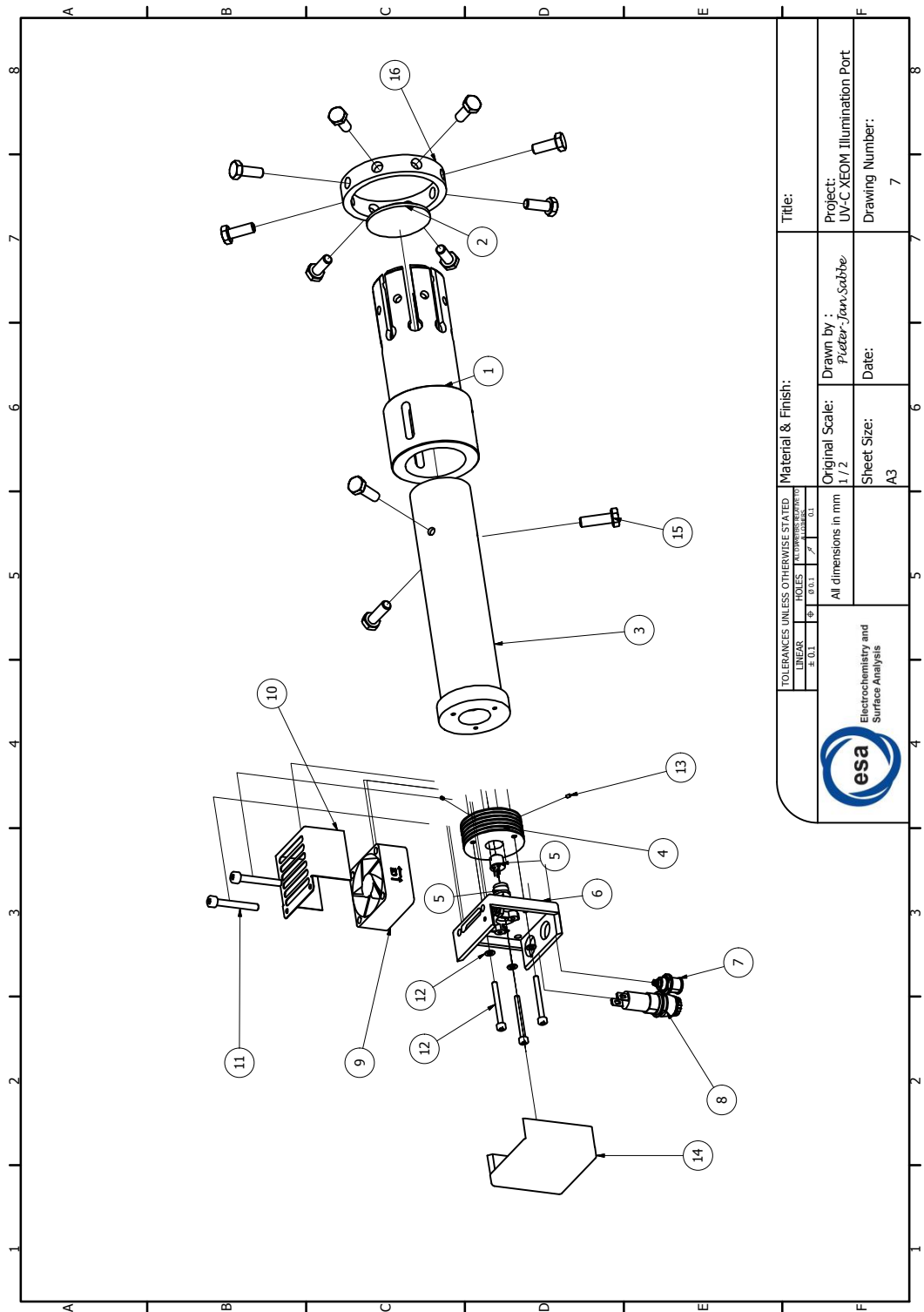
A.11 Technical drawing: lens removal kit

 Electrochemistry and Surface Analysis	TOLERANCES UNLESS OTHERWISE STATED LINEAR ± 0.1 HOLES ALL DIMENSIONS UNLESS OTHERWISE STATED Ø 0.1 / / 0.1		Material & Finish: Black Acetal Copolymer	Title: lens removal kit
	All dimensions in mm		Original Scale: 1 : 1	Project: UV-C XEOM Illumination Port
		Sheet Size: A3	Drawn by: Peter-John Scabbie	Drawing Number: 5
			Date: 14/10/2015	



A.12 Technical drawing: metal fan protection plate

TOLERANCES UNLESS OTHERWISE STATED		Material & Finish: stainless steel	Title: Metal Fan Protection plate
LINEAR ± 0.1	HOLES ± 0.1		
All dimensions in mm		Original Scale: 2 : 1	Project: UV-C XEOM Illumination Port
esa Electrochemistry and Surface Analysis		Drawn by : Pieter-Jan Sabbe	Drawing Number: 6
		Date: 14/10/2015	
		Sheet Size: A3	




A.13 Exploded view : UV-C XEOM illumination port

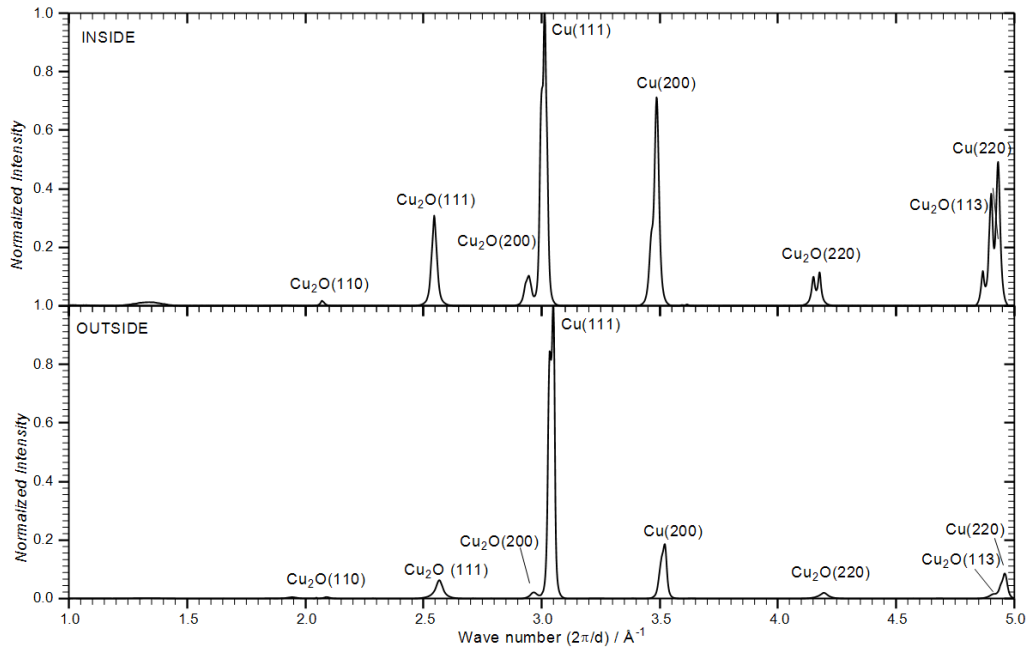
TOLERANCES UNLESS OTHERWISE STATED		Material & Finish:		Title:	
LINEAR	± 0.1	HOLES	± 0.1	Drawn by :	Project:
				Preter-Jan-Sabbe	UV-C XEOM Illumination Port
				Original Scale:	Drawing Number:
				1 / 2	7
				All dimensions in mm	
				Sheet Size:	
				A3	



PARTS LIST			
ITEM	QTY	PART NUMBER	DESCRIPTION
1	1	Lens Holder	Drawing : 2
2	1	Lens	
3	1	Illumination Tube	Drawing: 1
4	1	Heatsink	Drawing: 3
5	1	UV-C LED+ socket	
6	1	ABS box bottom	Drawing: 4
7	1	LEMO connector	
8	1	Fuse Holder	
9	1	Fan	
10	1	Metal fan protection plate	Drawing: 6
11	2	bolted_fan_connection	AS1420 Metric M4 x 30 : 1 AS1237 (2:1) 4:1 AS 1112 Metric M4 : 1
12	3	bolted_absbox_connection	AS1237 (2:1) 3:1
13	2	ANST B18.3.6M - M1,6x0,35 x 3	Forged Hexagon Socket Set Screw - Cone Point - Metric
14	1	ABS box Top	
15	3	AS 1110 - M6 x 20	ISO metric hexagon precision bolts and screws
16	1	Lens Removal Kit	Drawing: 5
17	8	AS 1110 - M6 x 16	ISO metric hexagon precision bolts and screws

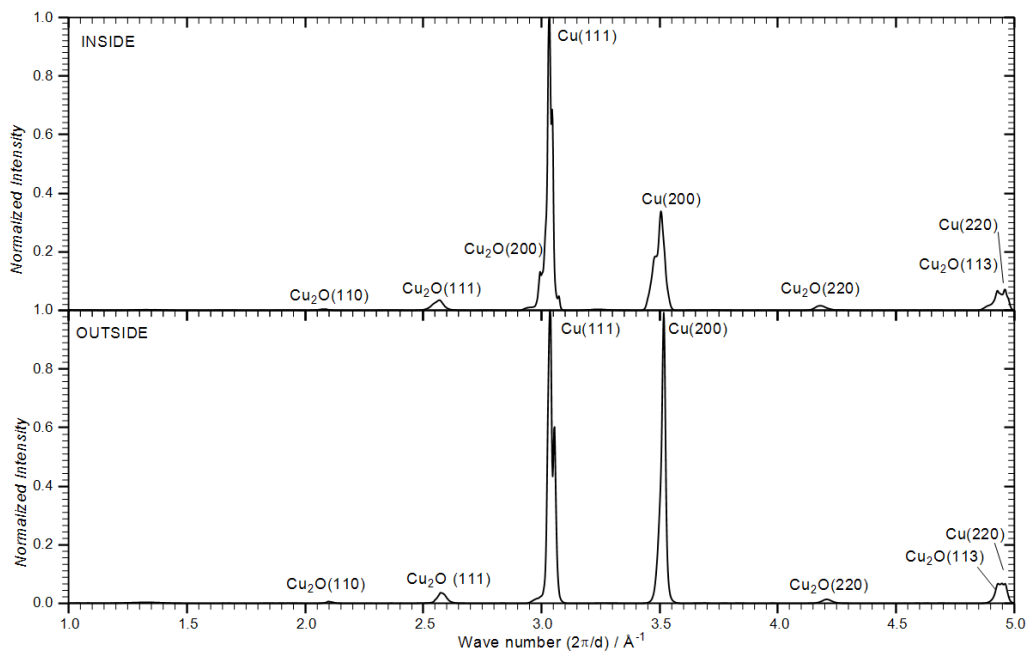
	TOLERANCES UNLESS OTHERWISE STATED LINEAR ± 0.1 HOLES ± 0.1 ANGLES ± 0.1	
	Material & Finish:	
Title:		Drawn by : <i>Pietzer-Jean,Sabbe</i>
Original Scale:		Date: 14/10/2015
Sheet Size: A3		Project: UV-C XEOM Illumination Port Drawing Number: 8

A.14 Bill of materials: UV-C XEOM illumination port



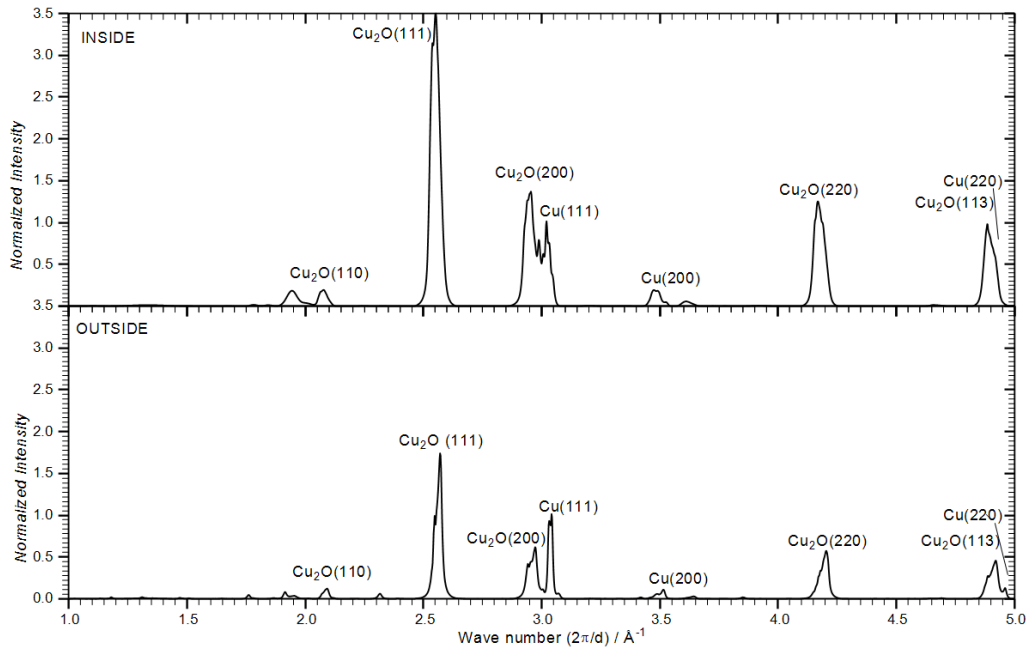
A.15

X-ray diffraction pattern recorded from the inner (top) and outer (bottom) surface of an U-shaped sleeve corroded for 144 months in utero (sample n°1 and n°2 in Table S.1)



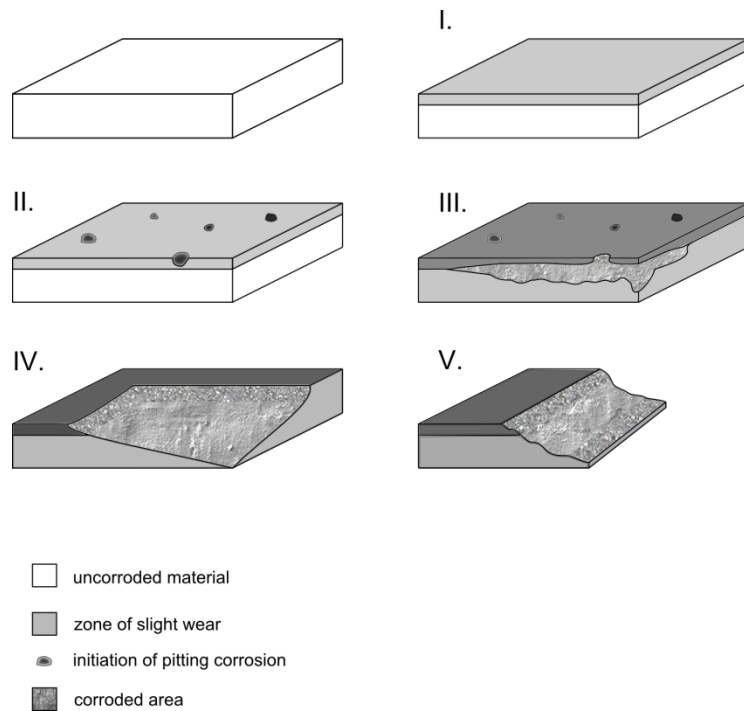
A.16

X-ray diffraction pattern recorded from the inner (top) and outer (bottom) surface of an O-shaped sleeve corroded for 144 months in utero (sample n°3 and n°4 in Table S.1).



A.17

X-ray diffraction pattern recorded from the inner (top) and outer (bottom) surface of an U-shaped GyneFix® sleeve corroded for 150 months in utero (sample n°5 and n°6 in Table S.1).



A.18

Schematic of in utero corrosion process described by Berthou et al. [46]. In utero corrosion of IUDs can be divided into 5 different stages, initiated by a tarnished surface (I) and terminated by rupture of the copper piece (V).

Personal Info

LIST OF PUBLICATIONS

- **P.-J. Sabbe**, M. Dowsett, M. Hand, R. Grayburn, P. Thompson, W. Bras, A. Adriaens, Evaluation of an X - ray-Excited Optical Microscope for Chemical Imaging of Metal and Other Surfaces, *Anal. Chem.* 86 (2014) 11789–11796
- **P.-J. Sabbe**, M.G. Dowsett, M. De Keersmaecker, M. Hand, P. Thompson, A. Adriaens, Synthesis and surface characterization of a patterned cuprite sample: Preparatory step in the evaluation scheme of an X-ray-excited optical microscopy system, *Appl. Surf. Sci.* 332 (2015) 657–664.
- M. Dowsett, M. Hand, **P.-J. Sabbe**, P. Thompson, A. Adriaens, XEOM 1 - A novel microscopy system for the chemical imaging of heritage metal surfaces, *Herit. Sci.* 3 (2015) 14.
- D. Wildemeersch, **P.J. Sabbe**, M.G. Dowsett, V. Flexer, P. Thompson, D. Walker, P. a. Thomas, A. Adriaens, Assessment of copper corrosion from frameless copper IUDs after long-term in utero residence, *Contraception* 90 (2014) 454–459.
- R.A. Grayburn, M.G. Dowsett, **P.-J. Sabbe**, D. Wermeille, J.A. Anjos, V. Flexer, M. De Keersmaecker, D. Wildermeersch, A. Adriaens, SR-XRD in situ monitoring of copper-IUD corrosion in simulated uterine fluid using a portable spectroelectrochemical cell, *Bioelectrochemistry* 110 (2016) 41–45.
- R. Grayburn, M.G. Dowsett, M. Hand, **P.-J. Sabbe**, P. Thompson, A. Adriaens, Tracking the progression of bronze disease - A synchrotron X-ray diffraction study of nantokite hydrolysis, *Corros. Sci.* 91 (2014) 220–223
- R. Wiesinger, R. Grayburn, M. Dowsett, **P.-J. Sabbe**, P. Thompson, A. Adriaens, M. Schreiner, In situ time-lapse synchrotron radiation X-ray diffraction of silver corrosion, *J. Anal. At. Spectrom.* 30 (2015) 694–701.
- R. Wiesinger, R. Grayburn, M. Dowsett, **P.-J. Sabbe**, P. Thompson, A. Adriaens, M. Schreiner, Silver corrosion in real time, *XMaS Newsletter* (2014)

CONFERENCE ATTENDANCE

- **P.-J. Sabbe**, M. Dowsett, M. Hand, R. Grayburn and A. Adriaens, X-ray-excited Optical Microscopy (XEOM), poster at Chemcys, Blankenberge, Belgium, 1–2 march 2012
- **P.-J. Sabbe**, M. Dowsett, M. Hand, R. Grayburn and A. Adriaens, X-ray-excited Optical Microscopy (XEOM): corrosion mapping, oral presentation at 53rd Corrosion Science Symposium, National Physics Laboratory, Teddington, United Kingdom, 6-7 September 2012
- **P.-J. Sabbe**, M. Dowsett, M. Hand and A. Adriaens, Identifying surface corrosion in cultural heritage by X-ray-excited optical microscopy (XEOM), oral presentation at ECASIA 13, Pula (Cagliari), Italy, 13- 18 October 2013
- **P.-J. Sabbe**, M. Dowsett, M. Hand and A. Adriaens, Towards non-destructive analysis of cultural heritage metals by X-ray excited optical microscopy (XEOM), oral presentation at Chemcys 2014, Blankenberge, Belgium, 27 - 28 February 2014
- **P.-J. Sabbe**, M. Dowsett, M. Hand, D. Wermeille, M. Jones and A. Adriaens, Chemical imaging of heritage metal surfaces with X-ray-excited optical microscopy, oral presentation at XAFS 16, Karlsruhe, Germany, 23 - 28 August 2015
- **P.-J. Sabbe**, M. Dowsett, M. Hand, D. Wermeille, M. Jones and A. Adriaens, Chemical imaging of heritage metal surfaces with X-ray-excited optical microscopy, oral presentation at InArt 2, Ghent, Belgium, 21 - 25 March 2016

